Metabolic profiling of cancer cells and its implications for targeted metabolic therapies

Yitao Xu

A thesis submitted for the degree of

Doctor of Philosophy

October 2024

Imperial College London

Department of Surgery and Cancer

Declaration of Originality

I, Yitao Xu, declare this thesis and body of work are my own. Any work that was provided through collaboration is appropriately referenced and acknowledged.

Declaration of Copyright

The copyright of this thesis rests with the author. Unless otherwise indicated, its contents are licensed under a Creative Commons Attribution-Non Commercial 4.0 International Licence (CC BY-NC).

Under this licence, you may copy and redistribute the material in any medium or format. You may also create and distribute modified versions of the work. This is on the condition that: you credit the author and do not use it, or any derivative works, for a commercial purpose.

When reusing or sharing this work, ensure you make the licence terms clear to others by naming the licence and linking to the licence text. Where a work has been adapted, you should indicate that the work has been changed and describe those changes.

Please seek permission from the copyright holder for uses of this work that are not included in this licence or permitted under UK Copyright Law.

Abstract

Metabolic reprogramming is a hallmark of cancer and is partially regulated by the PI3K/Akt pathway. Epithelial ovarian cancer (EOC) is one of the most common gynaecological cancers and dysregulated PI3K/Akt signalling is frequently detected. However, the metabolic impact remains unclear. Here, using the ID8 *in vitro* and *in vivo* model of EOC, I found that the deletion of Pten (i.e., the negative regulator of Akt) enhanced glycolysis, and modulated NAD^+ metabolism and arginine synthesis.

The enhanced glycolysis induced by the hyperactive PI3K/Akt and Ras signalling may create a metabolic bottleneck by increasing the demand for NAD^+ (a key glycolytic co-factor). Indeed, we previously showed NAD^+ depletion by FK866, which inhibits NAD^+ salvage synthesis, sensitized EOC cells to the PARP inhibitor Olaparib. Using a panel of EOC cells, I confirmed the higher sensitivity of the combination treatment in Ras/PI3K mutant cells. Mechanistically, higher DNA damage and oxidative stress were observed. The combination treatment improved median survival in the ID8 mouse model.

Lactate has been reported to fuel the TCA cycle in cancer cells. More recently, lactate acidosis uncouples glycolysis from the TCA cycle, which the lactate metabolon model can rationalize. Exogenous lactate forms a kinetically resolved pool from that derived from glycolysis and its derived pyruvate enters mitochondria before mixing with the glycolysis-derived pool. To test this hypothesis, I traced the relative contribution of glucose and exogenous lactate to citrate. A higher correlation was observed between labelling in citrate and pyruvate compared to exogenous lactate, which is inconsistent with the lactate metabolon model. Examining the roles of MCT1 and MCT4 (main lactate transporters) in this phenomenon I found that MCT1 was the major lactate transporter, and they were functionally redundant, which implies dual targeting may be necessary for therapeutic benefits.

Acknowledgements

I would like to express my gratitude to Professor Hector Keun and Professor Iain McNeish for offering me the opportunity to work on this exciting PhD project. I also want thank Professor Hector Keun and Professor Iain McNeish for the support and guidance during my study at Imperial College London. It is a great pleasure to work with Dr Cristina Nadal, Dr Michael Gruet and Yurui Ma. Cris you are an amazing scientist who knows all everything about MS and I would like to thank you for your help and support for all the metabolomics work. Mike you are so knowledgeable and professional, and it is always full of laughter when working with you. Yurui you are the most hard-working, helpful and supportive person and it is my honor to work with you. I would also like to thank MRes students Antong (Chris) Lyu and Elina Hazeri for your contributions. Chris you are an amazing and intelligent MRes student, and you will surely excel in your PhD.

I also want to thank Imperial College London for providing the funding (i.e., the President PhD Scholarship) for my PhD project and offering me place to study for PhD.

I would also like to thank the rest of members of the Keun group who make the Keun group an enjoyable place to be. Thanks to Dr Yuweui Xu and Flora McKinney for kindly providing mice tissue samples. I want to thank Dr Anke Nijhuis, Chiharu Wickremesighe, Dr Yuweui Xu, Flora McKinney, Dr Panagiotis Vorkas, Dr Alexis Siskos, Chandler Bray, Julia Babuta for your help and technical support. I also want to thank Aitana Cheesman, Laila Evangelista and Nikos Zourdoumis for fun chats during lunch. Thanks to Katherine Tyson, Roxanne Wood, David Macdonald for supporting the mice studies.

I also want to thank my parents for their continued support and guidance since the day I was born. I would never be where I am without their love and help. Thanks to all my friends (especially Lingyu Tan) for all the fun travelling around Europe. I would be insane without you.

Publications

Published:

1. **Xu Y**, Balcells C, Barnes EME, Selivanov V, Benito A, Cascante M, Keun HC. Exploring the kinetics of lactate metabolism in cancer cells. [Conference abstract]. 5th Metabolism and cancer conference, Nice, France. Nov 2023.
2. Balcells C, **Xu Y**, Gil-Solsona R, Maitre L, Gago-Ferrero P, Keun HC. Blurred lines: Crossing the boundaries between the chemical exposome and the metabolome. Curr Opin Chem Biol. 2024 Feb;78:102407. doi: 10.1016/j.cbpa.2023.102407. Epub 2023 Dec 11. PMID: 38086287.
3. Xu Y, Spear S, Ma Y, Lorentzen MP, Gruet M, McKinney F, **Xu Y**, Wickremesinghe C, Shepherd MR, McNeish I, Keun HC, Nijhuis A. Pharmacological depletion of RNA splicing factor RBM39 by indisulam synergizes with PARP inhibitors in high-grade serous ovarian carcinoma. Cell Rep. 2023 Oct 31;42(10):113307. doi: 10.1016/j.celrep.2023.113307. Epub 2023 Oct 19. PMID: 37858464.

Manuscripts in preparation:

1. Gruet MJ, **Xu Y**, An L, Ma Y, Balcells C, Spear S, Tyson K, Xu Y, McKinney F, Bray C, Wickremesinghe C, Siskos AP, Nijhuis A, McNeish I, Tate EW, Benito A, Keun HC. RAS/PI3K mutations sensitise epithelial ovarian cancer cells to NAMPT inhibition and a PARP/NAMPT inhibitor combination. Paper in preparation. Co-first author.

Table of Contents

Declaration of Originality 2
Declaration of Copyright 2
Abstract 3
Acknowledgements 4
Publications 5
Table of Figures 10
List of tables 13
List of Appendix Figures 14
List of Appendix Tables 15
List of Appendix Reports 15
List of Abbreviations 16
Chapter 1 Introduction 27
1.1 Metabolic reprogramming is a hallmark of cancer 27
1.1.1 Increased uptake of glucose and amino acids 27
1.1.2 Upregulated biosynthesis of macromolecules 28
1.1.3 Increased reliance on the maintenance of redox balance 34
1.2 Cancer metabolism is regulated by PI3K/Akt signalling pathway 37
1.2.1 The PI3K/Akt signalling pathway 37
1.2.2 The PI3K/Akt pathway enhances glucose uptake and glycolysis 40
1.2.3 The PI3K/Akt pathway promotes anabolic metabolism 43
1.2.4 The PI3K/Akt signalling regulates redox homeostasis 45
1.3 Dysregulation of the Ras and PI3K pathways are common in epithelial ovarian cancer (EOC) 48
1.3.1 Introduction to ovarian cancer 48
1.3.2 Genetic events leading to dysregulated Ras and PI3K pathways in EOC 48
1.4 PARP inhibitors: targeted therapy against ovarian cancer 51
1.4.1 PARP1 is key to DNA damage repair 51
1.4.2 NAD^+ is a substrate of PARP1 and synthesized through multiple pathways 54
1.4.3 PARP inhibitors: mechanisms of action 56
1.4.4 Clinical development of PARP inhibitors 59

1.4.5 The impact of the Ras and PI3K pathways on PARP inhibitor responses 63
1.5 Lactate is more than a metabolic waste in cancer 64
1.5.1 Lactate fuels the TCA cycle in cancer cells 64
1.5.2 LDH: key enzymes in lactate metabolism 66
1.5.3 Monocarboxylate transporters (MCTs): key lactate transporters 69
1.5.4 Uncoupling of glycolysis and TCA cycle: potential subcellular compartmentation of lactate metabolism 71
1.6 Metabolomics: a system biology tool for cancer research 75
1.6.1 Metabolic profiling 75
1.6.2 Metabolic flux analysis 76
1.6.3 Analytical platforms used in this study 77
1.7 Hypotheses and aims 83
1.7.1 Chapter 3 83
1.7.2 Chapter 4 83
1.7.3 Chapter 5 86
1.7.4 Chapter 6 87
Chapter 2 Methods 92
2.1 Cell culture 92
2.2 Animal studies 93
2.3 Sulforhodamine B (SRB) assay 95
2.4 Caspase glo-3/7 assay 96
2.5 Mitochondrial membrane potential (ΔΨm) assay 97
2.6 Oxidative stress assay 97
2.7 Immunofluorescence (IF) 98
2.8 Annexin V-Propidium Iodide staining assay 99
2.9 Cell cycle assay 99
2.10 Protein extraction and Western Blot (WB) 100
2.11 ^{1}H NMR: sample preparation and NMR analysis 103
2.12 ^{13}C labelling studies: ^{13}C tracer incubation, sample preparation and analysis 105
2.13 Untargeted metabolic profiling using LC-MS/MS 108
2.14 Statistics 113

Chapter 3 Akt pathway activation results in metabolic reprogramming of ovarian HGSC cells....116
3.1 Introduction....116
3.2 Results....117
3.2.1 A distinct metabolic landscape was detected in ID8 *Trp53*$^{-/-}$; *Pten*$^{-/-}$ tumours....117
3.2.2 Enrichment analysis revealed that several metabolic pathways are altered due to Pten loss....122
3.2.3 Pten loss increased glycolytic flux and glucose contribution to FA synthesis132
3.2.4 Glutamine metabolism is not significantly altered in ID8 *Trp53*$^{-/-}$; *Pten*$^{-/-}$ cells....140
3.2.5 Investigating the alternative carbon source of citrate synthesis in ID8 cells..145
3.3 Discussion....147
Chapter 4 Mutations in the Ras/PI3K pathway sensitized the combination of FK866 and Olaparib in ovarian cancer cells....159
4.1 Introduction....159
4.2 Results....160
4.2.1 Mutations in the Ras/PI3K pathway sensitised human EOC cells to dual PARP and NAMPT inhibition....160
4.2.2 Olaparib and FK866 combination induced higher DNA damage in EOC cells with mutations in the Ras/PI3K signalling....165
4.2.3 FK866 and Olaparib combination caused cell cycle arrest at the G2/M phase in ovarian cancer cells with Ras/PI3K mutations....171
4.2.4 No enhancement in PARP trapping could be detected with combined PARP inhibitor/FK866 treatment....173
4.2.5 The combination of Olaparib and FK866 resulted in more ROS accumulation in Ras/PI3K mutant ovarian cancer cells....175
4.3 Discussion....181
Chapter 5 Investigating NAD^+ depletion as a strategy to improve Olaparib sensitivity in isogenic models of ovarian HGSC....188
5.1 Introduction....188
5.2 Results....188
5.2.1 Mutations in Ras/PI3K pathway enhanced apoptosis induction capacity of FK866 and Olaparib combination in ID8 ovarian HGSC cells *in vitro*....188

5.2.2 FK866 induced similar levels of NAD^+ decrease in ID8 ovarian HGSC cells *in vitro* 192
5.2.3 FK866 and Olaparib combination caused ROS accumulation in ID8 cells *in vitro* 194
5.2.4 The combination of FK866 and Olaparib inhibited growth of ID8 *Trp53*$^{-/-}$; *Pten*$^{-/-}$ tumours and increased overall survival *in vivo* 196
5.2.5 FK866 and Olaparib combination resulted in higher DNA damage *in vivo* 201
5.2.6 The combination of FK866 and Olaparib resulted in NAD^+ depletion in ID8 *Trp53*$^{-/-}$; *Pten*$^{-/-}$ tumours 204
5.3 Discussion 218
Chapter 6 Investigating the kinetics of lactate metabolism in cancer cells 227
6.1 Introduction 227
6.2 Results 228
6.2.1 Dual labelling experiments supported the canonical model of lactate metabolism 228
6.2.2 Dual inhibition of MCT1 and MCT4 increased glucose contribution to the TCA cycle 234
6.3 Discussion 241
Chapter 7 Final discussion and future directions 249
7.1 Characterisation of metabolic reprogramming in ovarian HGSC cells with Pten loss 249
7.2 Mutations in the Ras/PI3K signalling sensitized ovarian cancer cells to the combination of FK866 and Olaparib 250
7.3 Investigating the kinetics of lactate metabolism in cancer cells 252
7.4 Future work 253
7.5 Conclusions 256
Appendix Figurers and Tables 293
Appendix Reports 335
Reference 258

Table of Figures

Figure 1.1 FA *de novo* synthesis pathways in cancer cells. 30
Figure 1.2 Metabolic pathways contributing to NADPH production in cancer cells. 33
Figure 1.3 Oxidative stress protection mechanisms in cancer cells. 36
Figure 1.4 The PI3K/Akt pathway and the major downstream effectors in regulating cancer metabolism. 40
Figure 1.5 The PI3K/Akt pathway stimulates glucose metabolism via glycolysis in cancer cells. 42
Figure 1.6 The PI3K/Akt signalling promotes de novo FA synthesis. 44
Figure 1.7 The PI3K/Akt pathway regulates the redox balance in cancer cells. 47
Figure 1.8 The Ras signalling pathway in cancer cells. 50
Figure 1.9 The roles of PARP1 in DNA damage repair in cancer cells. 53
Figure 1.10 The metabolic pathways of NAD^+ synthesis. 56
Figure 1.11 Mechanisms of PARP inhibitors. 58
Figure 1.12 Exogenous lactate is a carbon source of the TCA cycle in cancer cells. 66
Figure 1.13 Structure and functions of LDH isoforms. 68
Figure 1.14 Two models of lactate metabolism in cancer cells. 74
Figure 1.15 Isotopomer spectral analysis of FA de novo synthesis. 77
Figure 1.16 The principle of SWATH MS. 81
Figure 1.17 FK866 increased the sensitivity of Olaparib in a panel of EOC cells, especially those with mutations in genes involved in the Ras/PI3K pathway. 85
Figure 1.18 Glycolysis was uncoupled from the TCA cycle in HCT116 cancer cells. 88
Figure 1.19 MCT1, but not MCT4, is the key determinant of glucose entry into the TCA cycle. 89
Figure 3.1 PLSDA modelling reveals differences in the metabolic profiles in ID8 *Trp53*$^{-/-}$ tumour samples based on the genetic status of *Pten*. 120
Figure 3.2 Key metabolites with significantly changed abundance in in ID8 *Trp53*$^{-/-}$*; Pten*$^{-/-}$ tumours in comparison to ID8 *Trp53*$^{-/-}$ tumours. 121
Figure 3.3 Metabolic pathways enriched in ID8 *Trp53*$^{-/-}$*; Pten*$^{-/-}$ tumours. 125
Figure 3.4 Metabolites in the glycerophospholipid pathway were enriched in ID8 *Trp53*$^{-/-}$*; Pten*$^{-/-}$ tumours. 126
Figure 3.5 Metabolites in the salvage pathway of NAD synthesis were enriched in ID8 *Trp53*$^{-/-}$*; Pten*$^{-/-}$ tumours. 127
Figure 3.6 Metabolites in the arginine metabolism pathway were enriched in ID8 *Trp53*$^{-/-}$*; Pten*$^{-/-}$ tumours. 128
Figure 3.7 Metabolites in histidine metabolism pathway were enriched in ID8 *Trp53*$^{-/-}$*; Pten*$^{-/-}$ tumours. 129
Figure 3. 8 Metabolites in pantothenate metabolism pathway were enriched in ID8 *Trp53*$^{-/-}$*; Pten*$^{-/-}$ tumours. 130
Figure 3.9 Metabolites in β-alanine metabolism pathway were enriched in ID8 *Trp53*$^{-/-}$*; Pten*$^{-/-}$ tumours. 131
Figure 3.10 Pten loss upregulated the rates of glucose uptake and lactate release in ID8

cells. 135
Figure 3.11 Schematics of the ^{13}C labelling patterns of central carbon metabolism using $^{13}C_6$-glucose as a tracer. 136
Figure 3.12 Pten loss did not impact glucose contribution to the TCA cycle as a carbon source. 137
Figure 3.13 Schematics of the ^{13}C enrichment patterns of the TCA cycle and FA synthesis using $^{13}C_6$-glucose as a tracer. 138
Figure 3.14 Pten loss upregulated glucose contribution to FA de novo synthesis in ID8 cells. 139
Figure 3.15 Pten loss did not impact glutamine consumption and metabolism through the TCA cycle in ID8 cells. 142
Figure 3.16 Schematics of the ^{13}C enrichment patterns of the TCA cycle and FA *de novo* synthesis using $^{13}C_5$-glutamine as a tracer. 143
Figure 3.17 There was a downward trend, albeit not significant, of glutamine contribution to FA de novo synthesis in ID8 *Trp53*$^{-/-}$*; Pten*$^{-/-}$ cells. 144
Figure 3.18 Exogenous lactate was a carbon source for the TCA cycle in ID8 *Trp53*$^{-/-}$ cells. 147
Figure 4.1 The combination of FK866 and Olaparib induced caspase-3/7 activation in ovarian cancer cells with mutations in the Ras/PI3K pathway (except OVCAR8 cells). 162
Figure 4.2 FK866 and Olaparib combination upregulated the proportion of apoptotic cells in Ras/PI3K mutant ovarian cancer cells. 163
Figure 4.3 Supplementation of NMN rescues apoptosis induced by FK866 and Olaparib combination in A2780 cells. 164
Figure 4.4 The combination of FK866 and Olaparib upregulated γH2AX intensity in Ras/PI3K mutant ovarian cancer cells. 168
Figure 4.5 The combination of FK866 and Olaparib did not induce further activation of DDR signalling in ovarian cancer cells. 170
Figure 4.6 The combination of FK866 and Olaparib caused cell cycle arrest at G2/M phase in ovarian cancer cells with mutant Ras/PI3K. 172
Figure 4.7 No increase in PARP trapping could be detected with FK866 and Olaparib combination treatment. 174
Figure 4.8 The combination of FK866 and Olaparib induced ROS accumulation in ovarian cancer cells with mutations in the Ras/PI3K pathway. 177
Figure 4.9 The combination of FK866 and Olaparib caused mitochondrial dysfunction in Ras/PI3K mutant ovarian cancer cells. 178
Figure 4.10 Supplementation of NAC rescued apoptosis in A2780 cells treated with the combination of FK866 and Olaparib. 179
Figure 4.11 NAC supplementation rescued caspase-3/7 induction by the combination of FK866 and Olaparib in A2780 cells. 180
Figure 5.1 The combination of FK866 and Olaparib might induce higher levels of apoptosis in ID8 *Trp53*$^{-/-}$*; Pten*$^{-/-}$ cells compared to ID8 *Trp53*$^{-/-}$ cells. 190
Figure 5.2 FK866 enhanced the growth inhibitory effects of Olaparib in a panel of ID8 cells. 191

Figure 5.3 FK866 reduces NAD pool size and interferes with NAD^+/NADH ratio in ID8 cells. 193
Figure 5.4 The combination of FK866 and Olaparib induced ROS accumulation in ID8 cells. 195
Figure 5.5 The combination of FK866 and Olaparib reduced tumour weight in the ID8 *Trp53*$^{-/-}$*; Pten*$^{-/-}$ model..... 199
Figure 5.6 FK866 improved Olaparib sensitivity in mice with ID8 *Trp53*$^{-/-}$*; Pten*$^{-/-}$ tumours. 200
Figure 5.7 The impact of FK866 and Olaparib combination on DDR, Akt and Erk signalling pathway in ID8 *Trp53*$^{-/-}$*; Pten*$^{-/-}$ tumours. 203
Figure 5.8 The combination of FK866 and Olaparib depleted NAD^+ in omental tumours. . 208
Figure 5.9 The combination of FK866 and Olaparib may induce oxidative stress in omental tumours. 209
Figure 5.10 The combination of FK866 and Olaparib may cause oxidative damage to lipids in omental tumours. 211
Figure 5.11 FK866 doses were correlated to a subset of metabolites in omental tumour tissue. 213
Figure 5.12 NAD^+ levels were correlated to a subset of metabolites in omental tumour tissue. 216
Figure 5.13 PCA analysis and hierarchical clustering analysis of the untargeted metabolomics dataset..... 217
Figure 6.1 Schematics of ^{13}C enrichment patterns in dual labelling studies using $^{13}C_6$-glucose and 3-^{13}C-lactate as tracers. 230
Figure 6.2 The metabolic fluxes of exogenous lactate fuelling the TCA cycle were high initially and there was a time-dependent increase in glucose contribution. 231
Figure 6.3 There was a time-dependent increase in glucose derived pyruvate and lactate in media..... 232
Figure 6.4 Higher agreement between the ratio of glucose/exogenous lactate derived citrate and that of intracellular pyruvate. 233
Figure 6.5 Dual inhibition of MCT1 and MCT4 may reduce net lactate and pyruvate export and glucose uptake rates. 237
Figure 6.6 Dual MCT1 and MCT4 inhibition reduced lactate uptake. 238
Figure 6.7 Dual MCT1 and MCT4 inhibition decreased lactate and pyruvate export. 239
Figure 6.8 Dual MCT1 and MCT4 inhibition shifted the relative contribution of glucose and exogenous lactate to the TCA cycle. 240

List of tables

Table 1.1 Summary of the clinical trials of PARP inhibitors in ovarian cancer. 62
Table 1.2 Substrate affinity and gene sequence identity to MCT1 of different MCT isoforms. 71
Table 2.1 Composition of ‘routine media' and ‘physiological glucose media’ during adaption. 93
Table 2.2 Dosing regimen of the toxicology study. 94
Table 2.3 Dosing regimen of the survival study. 95
Table 2.4 The seeding density of EOC cells for 96-well plate based assays. 96
Table 2.5 The seeding density of EOC cells for 6-well plate based assays. 99
Table 2.6 Antibodies for WB. 103
Table 2.7 ^{13}C tracer supplementation. U: unlabelled metabolites added, L: ^{13}C labelled metabolites added, N/A: not added. 105
Table 2.8 Components and concentrations of the internal standard mix for LC-MS/MS analysis. 109
Table 2.9 Mobile phase composition. 110
Table 2.10 LC gradient for the positive mode. 110
Table 2.11 LC gradient for the negative mode. 110
Table 2.12 DP and CE for Q1 windows in positive mode. 111
Table 2.13 DP and CE for Q1 windows in negative mode. 112

List of Appendix Figures

Appendix Figure 3. 1 PCA analysis showed that there was no separation between the ID8 *Trp53*$^{-/-}$ and *Trp53*$^{-/-}$*; Pten*$^{-/-}$ tumours. 309
Appendix Figure 3.2 Validation of the panel of ID8 cell lines. 310
Appendix Figure 3.3 Extremely low levels of pyruvate carboxylase activity were observed in ID8 cells. 311
Appendix Figure 3.4 Exogenous acetate might not be a carbon source of the TCA cycle. . 312
Appendix Figure 3.5 Net consumption of BCAA was observed in ID8 Trp*53*$^{-/-}$ cells. 313
Appendix Figure 3.6 Extremely low levels of ^{13}C enrichment of citrate could be detected after short incubation with ^{13}C tracers. 314
Appendix Figure 4.1 EOC cell lines with mutations in Ras/PI3K pathways are more sensitive to FK866. 315
Appendix Figure 4.2 Gating strategy of the flow analysis as described in Figure 4.1. 316
Appendix Figure 4.3 OVCAR8 (Ras mutant) cells had a smaller pool of NAD^+ and were more sensitive to NAD^+ depletion by FK866. 317
Appendix Figure 4.4 No association between Ras/PI3K pathway mutations and NAMPT or NAPRT expression in a panel of ovarian cancer cells. 318
Appendix Figure 4.5 Inconsistent activation of the Ras/PI3K pathway across ovarian cancer cell line with or without Ras/PI3K mutations. 320
Appendix Figure 4.6 The combination of FK866 and Olaparib upregulated γH2AX intensity in Ras/PI3K mutant ovarian cancer cells. 321
Appendix Figure 4.7 The combination of FK866 and Olaparib did not induce further activation of DDR signalling in ovarian cancer cells. 322
Appendix Figure 4.8 The combination of FK866 and Olaparib did not induce further activation of DDR signalling in ovarian cancer cells. 323
Appendix Figure 4.9 Gating strategy of the flow analysis as described in Figure 4.6. 324
Appendix Figure 4.10 Gating strategy of the flow analysis as described in Figure 4.10. 325
Appendix Figure 5.1 Gating strategy of the flow analysis as described in Figure 5.1. 326
Appendix Figure 5.2 FK866 reduces NAD pool size and interferes with NAD^+/NADH ratio in ID8 cells. 327
Appendix Figure 5.3 No correlation between NAMPT/NAPRT expression and Pten mutational status in ID8 cells. 328
Appendix Figure 5.4 Gating strategy of the flow analysis as described in Figure 5.1. 329
Appendix Figure 5.5 Pyruvate withdrawal enhanced sensitivity of FK866 in ID8 *Trp53*$^{-/-}$*; Pten*$^{-/-}$ cells but not ID8 *Trp53*$^{-/-}$ cells. 330
Appendix Figure 5.6 Relative changes of mouse weight during the toxicology study. 331
Appendix Figure 5.7 Adenine Supplementation rescued apoptosis in A2780 cells treated with FK866 and Olaparib combination. 332
Appendix Figure 6.1 Initial high fluxes of exogenous lactate fuelling the TCA cycle were observed and there was a time-dependent increase in glucose contribution. 333
Appendix Figure 6.2 Dual MCT1 and MCT4 inhibition altered the relative contribution of glucose and exogenous lactate to the TCA cycle. 334

List of Appendix Tables

Appendix Table 3.1 Survival days of mice injected with ID8 tumour cells. 293
Appendix Table 3.2 List of metabolites that were annotated by MS Dial with both MS1 and MS2 matching to the public library (version 17). 304
Appendix Table 3.3 List of metabolites that were cross-validated with MS1 and MS2 matching to the in-house built library. 308

List of Appendix Reports

Appendix Report 1. STR profiling of KURAMOCHI, OVSAHO, COV318, COV504 and COV644 cell lines (highlighted by red rectangles). 335
Appendix Report 2. STR profiling of 59M, A2780 and HEY-A8 cell lines (highlighted by red rectangles). 336
Appendix Report 3. STR profiling of TOV21G cell lines (highlighted by red rectangles). 337
Appendix Report 4. STR profiling of the panel of ID8 cell lines. 339

List of Abbreviations

^{13}C-MFA	^{13}C-Metabolic Flux Analysis
4e-BP	4e-Binding Protein
7-KCh	7-Ketocholesterol
7-OHCh	7-Hydroxycholesterol
8-oxo-dG	8-Oxo-2'-Deoxyguanosine
ACC	Acetyl-Coa Carboxylase
ACL	ATP-Citrate Lyase
ACSS1	Acetyl-Coa Synthetase 1
ACSS2	Acetyl-Coa Synthetase 2
AD	Auto-Modification Domain
AMDIS	Automated Mass Spectral Deconvolution And Identification System
ARA	Arachidonic Acid
ARG	Arginase
ASCT2	Alanine Serine-Cysteine Transporter 2
ASL	Argininosuccinate Lyase
ASNS	Asparagine Synthetase
ASS1	Argininosuccinate Synthetase 1
ATF4	Activating Transcription Factor 4
ATM	Ataxia Telangiectasia Mutated
ATR	Ataxia Telangiectasia And Rad3-Related Protein Serine/Threonine Kinase
AUC	Area Under Curve
BCAA	Branched-Chain Amino Acid
BCAT1/2	BCAA transaminases 1 and 2
BCKA	Branched-Chain Keto Acid
Bcl-2	B Cell Lymphoma 2
BER	Base Excision Repair
BRCA1/2	Breast Cancer Gene 1/2

BRCT	BRCA1 Carboxy-Terminal
BSA	Bovine Serum Albumin
c-Abl	Abelson Non-Receptor Tyrosine Kinase
CAD	Carbamoyl-Phosphate Synthetase 2, Aspartate Transcarbamylase And Dihydroorotase
CAT	Cationic Amino Acid Transporter
CCOC	Clear-Cell Ovarian Cancer
CCT	CTP:phosphocholine cytidylyltransferase
CD	Catalytic Domain
CD147	Basigin
CDK	Cyclin-Dependent Kinase
CDP	Cytidine Diphosphate
CE	Collision Energy
CHK	Choline Kinase
Chk1	Checkpoint Kinase 1
Chk2	Checkpoint Kinase 2
CID	Collision Induced Dissociation
CoA	Coenzyme A
CORE	Consumption Or Release
COX	Cyclooxygenase
CPT	Diacylglycerol Cholinephosphotransferase
CPT1	Carnitine Palmitoyltransferase 1
DAG	Diacylglycerol
DAG-CPT	Diacylglycerol Cholinephosphotransferase
DBD	DNA binding domain
DDR	DNA damage repair
DIA	Data Independent Acquisition
DP	Declustering Potential
DSB	Double Strand Breaks
DSS	Deuterated 4,4-Dimethyl-4-Silapentane-1 Sulfonic Acid

EAA	Essential Amino Acids
ECM	Extracellular Matrix
EDI3	Endometrial Differential 3
EI	Electron Impact Ionization
EMA	European Medicine Agency
EMT	Epithelial-Mesenchymal Transition
EnOC	Endometroid Ovarian Cancer
EOC	Epithelial Ovarian Cancer
ER	Endoplasmic Reticulum
ERBB2	Epidermal Growth Factor Receptor 2
ESI	Electrospray Ionization
F2,6BP	Fructose 2,6-Bisphosphate
FA	Fatty Acids
FADS	Fatty Acid Desaturases
FAME	Free Fatty Acid Methyl Esters
FAO	Fatty Acid Oxidation
FASN	Fatty Acid Synthase
FC	Fold Change
FDA	Food And Drug Administration
FDG	Fludeoxyglucose F18
FDR	False Discovery Rate
FID	Free Induction Decay
FMN	Flavin Mononucleotide
FOXO	Forkhead Box O
G6P	Glucose 6-Phosphate
G6PD	Glucose 6-Phosphate Dehydrogenase
GAVIN	GC-MS Assignment Validator and Integrator
GC	Gas-Chromatography
GDP	Guanosine Diphosphate

GDPD	Glycerophosphodiester Phosphodiesterase
GEM	Genetic Engineered Mouse
GLS	Glutaminase
GLUT	Glucose Transporters
GMP	Guanosine Monophosphate
GP70	Embigin
GPC	Glycerophosphocholine
GPC-PDE	Glycerophosphocholine Phosphodiesterase
GSH	Glutathione
GSK3	Glycogen Synthase Kinase 3
GSSG	Oxidised Glutathione
GTP	Guanosine Triphosphate
H_2O_2	Hydrogen Peroxide
HD	Helical Domain
HETE	Hydroxyeicosatetraenoic Acid
HGSC	Ovarian High-Grade Serous Carcinoma
HIF1α	Hypoxia-Inducible Factor 1A
HILIC	Hydrophilic Interaction Liquid Chromatography
HK2	Hexokinase 2
HMDB	Human Metabolome Database
HMGB2	High-Mobility Group Box 2
HODE	Hydroxyoctadecadienoic Acid
HPETE	Hydroperoxyeicosatetraenoic Acid
HPLC	High Performance Liquid Chromatography
HPODE	Hydroperoxyoctadecadienoic Acid
HR	Homologous Recombination
HRD	Hr Deficient
HRE	Hypoxia Response Element
HRP	Horseradish Peroxidase

I.P.	Intraperitoneal
IDH	Isocitrate Dehydrogenase
IDO	Indoleamine-2,3-Dioxygenase
IF	Immunofluorescence
IMP	Inosine Monophosphate
IMPDH	IMP dehydrogenase
IS	Internal Standards
ISA	Isotopomer Spectral Analysis
isoP	Isoprostanes
LAT	L-Type Amino Acid Transporter
LC	Liquid-Chromatography
LCFA	Long Chain Fatty Acid
LDH1	Lactate Dehydrogenase 1
LDLR	Low-Density Lipoprotein Receptor
LGSC	Ovarian Low-Grade Serous Carcinoma
LIG3	DNA ligase 3
LOD	Long Chain Fatty Acid
LOH	Loss Of Heterozygosity
lysoPC	Lysophosphatidylcholine
LysoPL	Lysophospholipase
m/z	Mass-To-Charge
MALDI	Matrix-Assisted Laser Desorption/Ionization
MCT	Monocarboxylate Transporters
ME	Malic Enzyme
MFA	Metabolic Flux Analysis
MID	Mass Isotopomer Distribution
MIEF2	Mitochondrial Elongation Factor 2
MOC	Mucinous Ovarian Cancer
MOX	Methoxamine Reagent

MPC	Mitochondrial Pyruvate Carrier
MRE11	Meiotic Recombination 11
MS	Mass-Spectroscopy
MSEA	Metabolite Set Enrichment Analysis
MSI	Mass Spectrometry Imaging
MSTFA	N-Methyl-N-(Trimethylsilyl)Trifluoroacetamide
MTBSTFA	N-Tert-Butyldimethylsilyl-N-Methyltrifluoroacetamide
MTHFD2	Methylenetetrahydrofolate Dehydrogenase 2
mTORC1	Mammalian Target Of Rapamycin Complex 1
mTORC2	Mechanistic Target Of Rapamycin Complex 2
NA	Nicotinic Acid
NAAD	Nicotinic Acid Adenine Dinucleotide
NAC	N-Acetylcysteine
NAD^+	Nicotinamide Adenine Dinucleotide
NADH	Reduced Nicotinamide Adenine Dinucleotide
NADK	NAD kinase
$NADP^+$	Nicotinamide Adenine Dinucleotide Phosphate
NADPH	Reduced Nicotinamide Adenine Dinucleotide Phosphate
NADS	NAD synthetase
Nam	Nicotinamide
NAMN	Nicotinic Acid Mononucleotide
NAMPT	Nicotinamide Phosphoribosyl Transferase
NAPRT	Nicotinic Acid Phosphoribosyltransferase
NEAA	Non-Essential Amino Acids
NEF	Nucleotide Exchange Factor
NER	Nucleotide Excision Repair
NF1	Neurofibromin 1
NHEJ	Non-Homologous End Joining
NIST	National Institute Of Standards And Technology

NMN	Nicotinamide Mononucleotide
NMNAT	NMN adenylyltransferases
NMR	Nuclear Magnetic Resonance
NOS	Nitric Oxide Synthases
NRF2	Nuclear-Factor Erythroid 2-Related Factor 2
NRF2	Nicotinamide Riboside
NRK	Nicotinamide Riboside Kinase
NSCLC	Non-Small-Cell Lung Cancer
$O_2^{\bullet-}$	Superoxide Anion
OAA	Oxaloacetate
ODC	Ornithine Decarboxylase
$OH^{\bullet}$	Hydroxyl Radical
ORA	Overrepresentation Analysis
ORR	Objective Response Rate
OS	Overall Survival
OTC	Ornithine Carbamoyltransferase
oxoHODE	Oxo-Octadecadienoic Acid
PA	Phosphatidic Acid
PANK	Pantothenate Kinase
PAR	Poly(Adp-Ribose)
PARG	Poly(Adp-Ribose) Glycohydrolase
PARP	Poly(Adp-Ribose) Polymerase
PBEF	Pre-B Cell Colony-Enhancing Factor
PC	Pyruvate Carboxylase
PCA	Principal Component Analysis
PDH	Pyruvate Dehydrogenase
PDK1	Pyruvate Dehydrogenase Kinase 1
PDPK1	Phosphoinositide-Dependent Protein Kinase 1
PFK1	Phosphofructokinase 1

PFKFB2	6-Phosphofructo-2-Kinase/Fructose-2,6-Biphosphatase
PFS	Progression Free Survival
PGD_2	Prostaglandin D2
PH domain	Pleckstrin Homology Domain
PH pathway	Preiss-Handler (Ph) Pathway
PhoC	Phosphocholine
PI	Propidium Iodide
PI3K	Phosphatidylinositol 3-Kinases
PIP_2	Phosphatidylinositol 4,5-Bisphosphate
PIP_3	Phosphatidylinositol 3,4,5-Trisphosphate
PLA_2	Phospholipase A2
PLA2	Phospholipase A2
PLSDA	Partial Least Squares Discriminant Analysis
PO_2	Partial Pressure Of Oxygen
POLβ	Gap-Filling Dna Polymerase B
PPP	Pentose Phosphate Pathway
PRA	Phosphoribosylamine
PRAS40	Proline-Rich Akt Substrate Of 40 Kda
PRPP	Phosphoribosyl Pyrophosphate
PSAT	Phosphoserine Aminotransferase
PtdCho	Phosphatidylcholine
PTEN	Phosphatase And Tensin Homologue
PTM	Post-Translational Modification
PUFA	Polyunsaturated Fatty Acids
Q	Quadruple
QA	Quinolinic Acid
QC	Quality Control
QEA	Quantitative Enrichment Analysis
RALGDS	RAL GTPase guanine nucleotide dissociation stimulator

RET	Reverse Electron Transport
RF	Radio Frequency
ROS	Reactive Oxygen Species
RP	Reversed-Phase Chromatography
RPE	Ribulose-Phosphate 3-Epimerase
RPI	Ribose-5-Phosphate Isomerase
RT	Retention Time
RTK	Receptor Tyrosine Kinases
S6K	Ribosomal Protein S6 Kinase
SCD	Stearoyl-Coa Desaturases
SCFA	Short Chain Fatty Acids
SCS	Selective Cell Sampling
SDS	Sodium Dodecyl Sulfate
SGLT	Sodium–Glucose Linked Transporter
SIRM	Stable Isotope Resolved Metabolomics
SIRT	Sirtuin
SLC	Solute Carrier
SMS	Spermine Synthase
SOS	Son Of Sevenless
SRB	Sulforhodamine B
SREBP	Sterol Regulatory Element-Binding Protein
SRM	Spermidine Synthase
SSB	Single Strand Breaks
SSR	Sum Of Squared Residuals
STAT3	Signal Transducer And Activator Of Transcription 3
STR	Short Tandem Repeat
SWATH	Sequential Window Acquisition Of All Theoretical Mass Spectra
TAG	Triglyceride
TALDO	Transaldolase

TBDMS	N-Methyl-N-(Tert-Butyldimethylsilyl)Trifluoroacetamide
TCA	Trichloroacetic Acid
TCA cycle	Tricarboxylic Acid Cycle
TDO	Tryptophan Dioxygenase
TKT	Transketolase
TMCS	Trimethylchlorosilane
TME	Tumour Microenvironment
TNBC	Triple-Negative Breast Cancer
TOF	Time Of Flight
TSC2	Tuberous Sclerosis Complex 2
TSP	3-(Trimethylsilyl)-2,2′,3,3′-Tetradeuteropropionic Acid
TXNIP	Thioredoxin-Interacting Protein
WB	Western Blot
WGR	Tryptophan-Glycine–Arginine-Rich
WT	Wild-Type
xCT	Cystine/Glutamate Antiporter
XRCC1	X-Ray Repair Cross Complementing Protein 1
α-KG	α-ketoglutarate
ΔΨm	Mitochondrial Membrane Potential

CHAPTER 1

Introduction

Chapter 1 Introduction

1.1 Metabolic reprogramming is a hallmark of cancer

Research into cancer metabolism can be traced back to more than a century ago. In 1923, Otto Warburg made a landmark discovery that cancer cells increase glucose uptake and metabolise it to lactate in the presence of oxygen (aerobic glycolysis or the Warburg effect) (*1*). However, it was not until the early 2000s that this field gained substantial attention (*2*). Later on, alterations in metabolism are observed across different cancer types, which leads to the idea that metabolic reprogramming is a hallmark of cancer (*3*).

The overarching theme is that the rewired metabolism provides cancer cells with a selective advantage during tumorigenesis (*4*). In this regard, cancer cells increase nutrient uptake, upregulate the biosynthesis of macromolecules and actively maintain redox balance (*5*), which in turn supports their rapid proliferation and survival.

1.1.1 Increased uptake of glucose and amino acids

Glucose and glutamine are the major carbon and nitrogen source consumed by cancer cells, respectively. In addition to generate ATP, they provide intermediates for anabolic metabolism. Therefore, cancer cells increase the uptake of glucose and glutamine by upregulating transporter expression and translocation to plasma membranes.

There are two classes of glucose transporters and both have been reported to be overexpressed in tumour cells: 1) facilitated diffusion glucose transporters (GLUT), 2) sodium–glucose linked transporter (SGLT) (*6*). GLUT1 is ubiquitously expressed and has a high affinity for glucose (*7*). The overexpression of GLUT1 has been shown in a variety of cancer types, including breast, lung, pancreatic cancer (*8*). Cancer cells also overexpress other GLUT proteins. The expression of GLUT3, for instance, is increased in many cancer types (e.g. ovarian, breast and lung cancer) (*9*). SGLT1 is powered by the sodium gradient across the cell membrane to mediate active transport of glucose. Its overexpression is reported in various

tumour types, including colorectal, lung and prostate cancer (*10*).

The entry of glutamine can be mediated by multiple transporters which are upregulated in cancer cells. Solute carrier 1A5 (SLC1A5, also known as alanine serine-cysteine transporter 2 (ASCT2)), for instance, is a sodium-dependent neutral amino acid transporter and has a high affinity for glutamine (*11*). Its expression has been reported to be increased in solid tumours (*12-14*). Other glutamine transporters including SLC38A1 (SNAT1), SLC38A2 (SNAT2) and SLC38A5 are overexpressed in a variety of tumours (*15-20*).

Additionally, cancer cells have a high demand for essential amino acids (EAA) for anabolism and enhance the expression of EAA transporters, including SLC6A14 (*21-23*) and SLC7A5 (also known as L-type amino acid transporter (LAT))/SLC3A2 heterodimeric transporter (*24*). Noticeably, SLC7A5/SLC3A2 transporter is an amino acid exchanger and imports a range of EAA (e.g. leucine, valine, methionine) while exporting intracellular glutamine (*25*). Therefore, increased glutamine uptake also supports EAA import.

1.1.2 Upregulated biosynthesis of macromolecules

The majority of nutrients are used for energy generation in resting cells. However, cancer cells divert nutrients for anabolic metabolism to provide macromolecules (e.g. fatty acids (FAs), proteins and nucleotides) necessary for rapid proliferation and tumour growth (*5*).

Fatty acids are a key component of membrane lipids and therefore, are essential for the synthesis of plasma membrane (*26*). Unlike resting cells which obtain FAs from dietary intake or FAs synthesised from the liver, cancer cells enhance FA *de novo* synthesis to support bulk membrane production and tumorigenesis (*26, 27*). Indeed, cancer cells upregulate key lipogenic enzymes, including acetyl-CoA carboxylase (ACC), ATP-citrate lyase (ACL) and fatty acid synthase (FASN) (*28*). Various studies have shown that the inhibition of lipogenic enzymes leads to decreased cancer cell proliferation and tumour size (*29-33*).

The carbon source of FAs synthesis is cytoplasmic acetyl-CoA which is formed by the ACL-catalysed cleavage reaction of cytoplasmic citrate (Figure 1.1) (*26*). Of note, citrate is produced in mitochondria as a TCA cycle intermediate and therefore, it is exported into cytosol to fuel

FA synthesis. Next, acetyl-CoA is activated by ACC to generate malonyl-CoA which then undergoes a series of condensation reactions catalysed by FASN to produce the 16-carbon saturated FA palmitate (C16:0). Palmitate can be subsequently elongated by fatty acid elongases (ELOVL1–7) to form the 18-carbon FA stearate (C18:0) (Figure 1.1). Saturated FAs can undergo desaturation catalysed by stearoyl-CoA desaturases (SCD) or fatty acid desaturases (FADS1–3) to produce unsaturated FAs, including palmitoleate (C16:1) and oleate (C18:1) (Figure 1.1) (*26*). Collectively, they form the cellular pool of non-essential FA.

Citrate can be derived from a variety of nutrients, including glucose, glutamine, and acetate (*34-36*). Glucose contributes to citrate production by oxidation of the glycolysis end-product pyruvate through the tricarboxylic acid (TCA) cycle in mitochondria (Figure 1.1). It has been reported as the major lipogenic acetyl-CoA source in cultured cancer cells (*36, 37*). However, under conditions of mitochondrial defects (e.g. mutations in enzymes of the TCA cycle), glutamine is the major contributor to citrate synthesis (*35*). In this regard, α-ketoglutarate (α-KG) derived from glutamine undergoes isocitrate dehydrogenase (IDH)-catalysed reductive carboxylation to generate citrate (Figure 1.1). Moreover, during hypoxia, cancer cells enhance the expression of acetyl-CoA synthetase 2 (ACSS2) to directly generate cytoplasmic acetyl-CoA from acetate (Figure 1.1) (*38*).

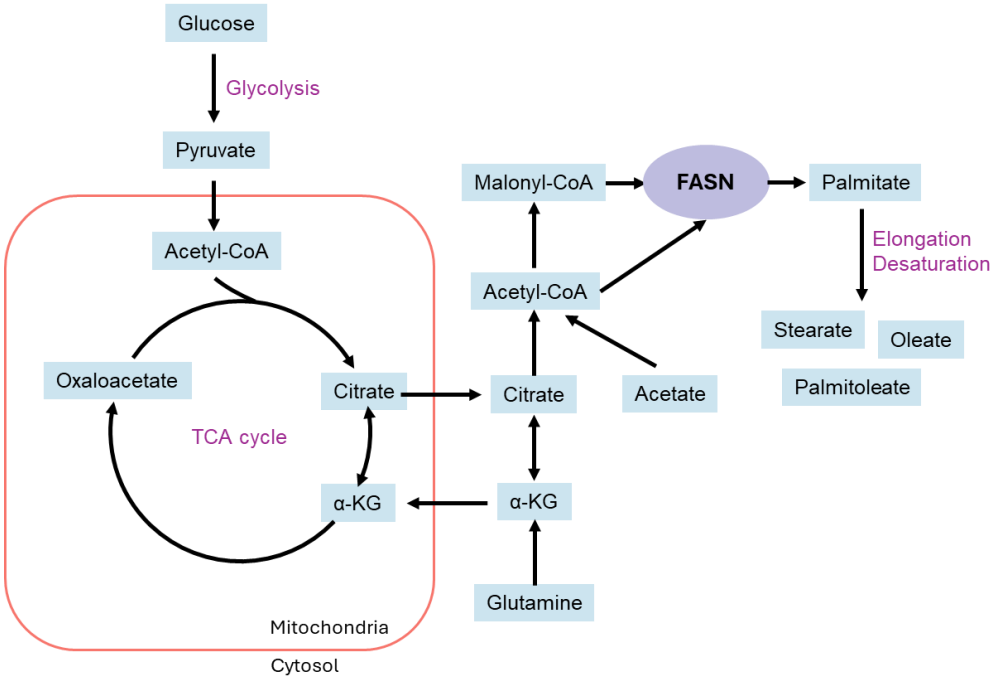


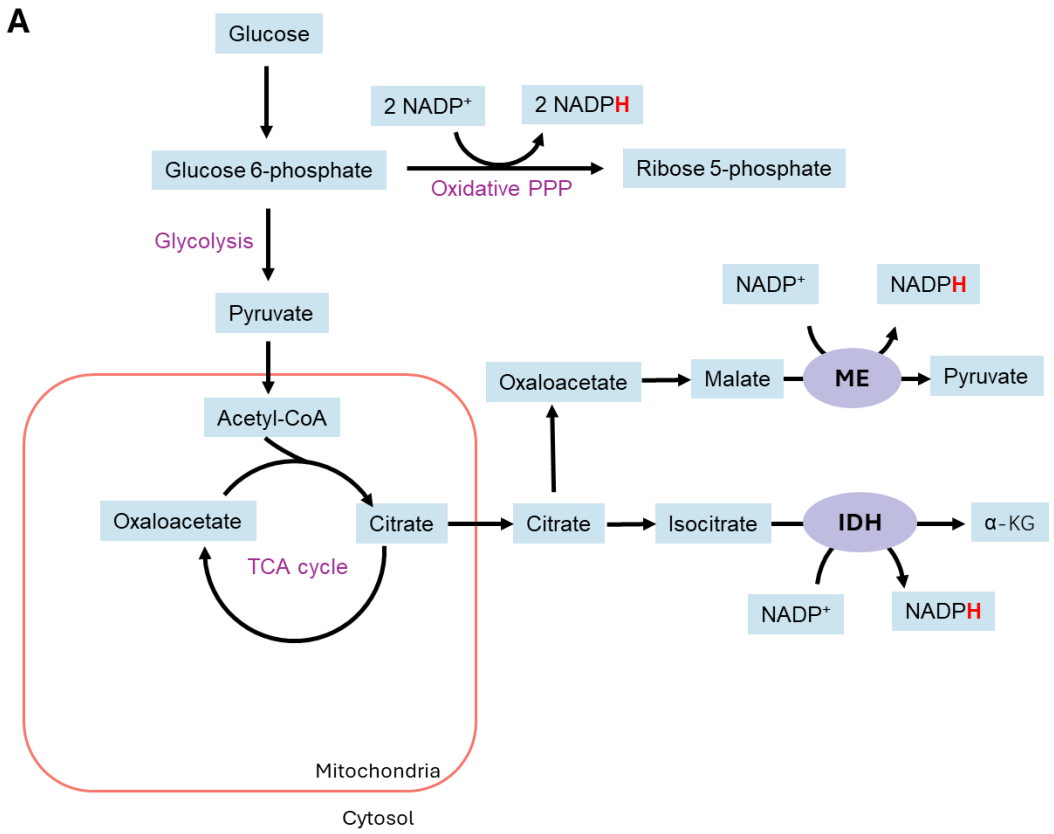
Figure 1.1 FA *de novo* synthesis pathways in cancer cells.

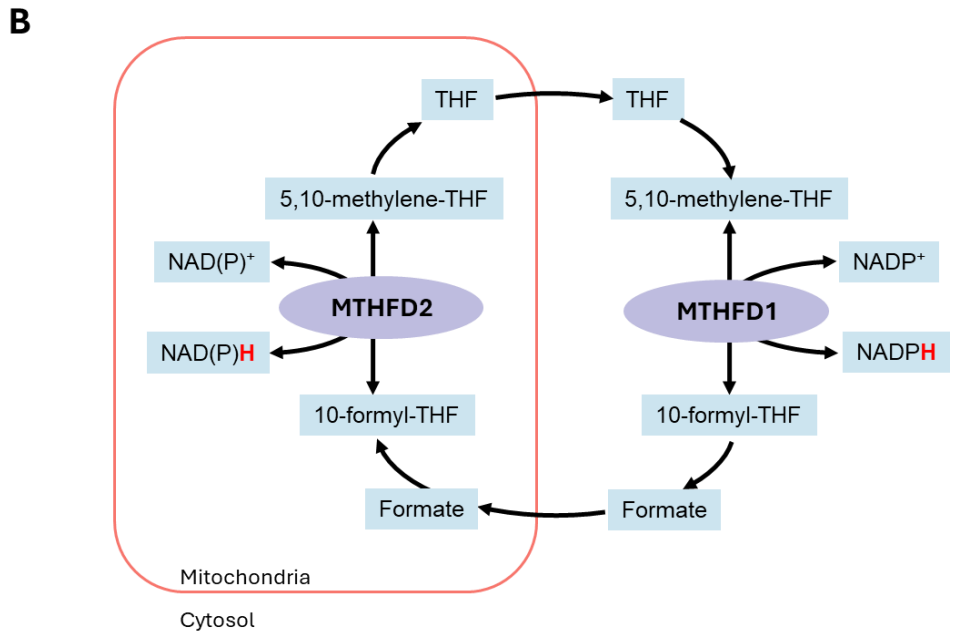
The carbon sources of FA *de novo* synthesis include glucose, glutamine and acetate. The lipogenic substrate is cytosolic acetyl-CoA which can be derived from citrate or acetate. Glucose is converted to pyruvate through glycolysis and on to citrate via the TCA cycle. Glutamine can be converted into α-KG which in turn undergoes reductive carboxylation to produce citrate. Citrate is then exported into cytosol where it is cleaved into acetyl-CoA by ACL. Acetate can be converted to acetyl-CoA directly via ACSS2. Acetyl-CoA is then converted to malonyl-CoA by ACC which in turn undergoes a series of FASN catalysed condensation to produce palmitate. Palmitate can undergo further elongation or desaturation. ACL: ATP-citrate lyase, ACSS2: acetyl-CoA synthetase 2, ACC: acetyl-CoA carboxylase, FASN: fatty acid synthase, FA: fatty acid, α-KG: α-ketoglutarate. Metabolites and enzymes are shown in blue rectangles and purple ovals, respectively.

To sustain lipogenesis, cancer cells rely on two types of supporting metabolic processes: anaplerosis and production of reduced nicotinamide adenine dinucleotide phosphate (NADPH). In the TCA cycle, citrate is formed by the condensation of acetyl-CoA and oxaloacetate (OAA). While acetyl-CoA can be supplied from pyruvate, citrate export from the mitochondria necessitates the replenishment of OAA to ensure the continued reactions of the TCA cycle (i.e. anaplerosis) (*39*). In this regard, previous studies revealed that glutamine is the major source of OAA in cancer cells (*37*). Specifically, glutamine is converted to α-KG which is subsequently processed in the TCA cycle to generate OAA.

FA *de novo* synthesis is highly dependent on the supply of NADPH. Indeed, 14 molecules of

NADPH is consumed to produce one molecule of palmitate. Previous studies demonstrated that the major source of NADPH is the pentose phosphate pathway (PPP) (*40, 41*). PPP branches from the glycolysis intermediate glucose 6-phosphate and produces NADPH via the oxidative part (Figure 1.2). Indeed, cancer cells upregulate the expression of the rate-limiting enzyme glucose 6-phosphate dehydrogenase (G6PD) (*42-44*). Additionally, malic enzyme (ME) in the cytosol produces NADPH (*5*). OAA in the mitochondria can be exported into the cytosol and converted into malate. NADPH is generated by the ME-catalysed oxidation of malate to pyruvate (Figure 1.2). Indeed, depletion or inhibition of ME reduced FA synthesis and tumour growth (*45, 46*). Furthermore, cytosolic citrate can be converted to isocitrate that is in turn converted to α-KG with the production of NADPH by IDH1 (Figure 1.2) (*47*). In addition, the folate cycle is a source of NADPH production and transfers one-carbon unit across tetrahydrofolate (THF) and its derivatives. Methylenetetrahydrofolate dehydrogenase 1 and 2 (MTHFD1/2) are two isoforms of the key enzyme MTHFD and are located in cytosol and mitochondrial, respectively (*48*). Both isoforms are bifunctional and catalyse the reversible conversion between 5,10-methylene-THF and 5,10-methenyl-THF via the dehydrogenase function and subsequently 5,10-methenyl-THF to 10-formyl-THF via the cyclohydrolase function (*48*). MTHFD1 and MTHFD2 are $NADP^+$ and $NADP^+$/NAD^+-dependent enzymes and regulate the ratio of $NADP^+$/NADPH and NAD^+/NADH (*48*). Indeed, shRNA knockdown of either isoform of MTHFD resulted in increased $NADP^+$/NADPH ratio and oxidized/reduced glutathione ratios (GSSG/GSH), which in turn sensitises cancer cells to oxidative stress (*40*). Likewise, depletion of MTHFD2 causes disrupted redox balance in colon cancer cells as evidenced by increased $NADP^+$/NADPH and GSSG/GSH ratio (*49*).





(Figure legends: see the next page)

Figure 1.2 Metabolic pathways contributing to NADPH production in cancer cells.
(A) The PPP pathway and cytosolic citrate are sources of NADPH production. The PPP pathway branches off glycolysis at the point of glucose-6-phosphare and generates NADPH. In addition, cytosolic citrate can be converted to oxaloacetate via the ACL catalysed cleavage reaction. Oxaloacetate undergoes further reaction to produce malate which can be oxidised to produce NADPH and pyruvate. Cytosolic isocitrate is derived from citrate and undergoes cytosolic IDH catalysed reaction to produce NADPH and α-KG. (B) The folate cycle is another source of NADPH production. In the cycle, one-carbon unit is transferred across THF and its derivatives. MTHFD1 and MTHFD2 are $NADP^+$ and $NADP^+/NAD^+$ dependent enzymes, respectively. The two isoforms of MTHFD regulate $NADP^+$/NADPH and NAD^+/NADH ratio. ACL: ATP-citrate lyase, PPP: pentose phosphate pathway, IDH: isocitrate dehydrogenase, ME: malic enzyme, α-KG: α-ketoglutarate. THF: tetrahydrofolate, MTHFD1/2: methylenetetrahydrofolate dehydrogenase 1/2. Metabolites and enzymes are shown in blue rectangles and purple ovals, respectively. NADPH is highlighted in red.

Protein is the most abundant cellular macromolecules and compromises almost 60% of dry mass in a mammalian cell (*4*). Its synthesis is necessary for cell division and requires the supply of essential and non-essential amino acids. While EAAs are imported from extracellular space (as described in section 1.1.1), non-essential amino acids (NEAAs) can be synthesized using glutamine as a source. Glutamine is a 5-carbon molecule with two amino groups (i.e. α-amino group and γ-amide groups). The γ-amide group is used as a nitrogen source for asparagine synthesis (*50*). Additionally, glutamine undergoes deamidation to remove the γ-amide group and form glutamate in cancer cells, which is mainly catalysed by the mitochondrial glutaminase (GLS). Glutamate is further converted to α-KG and NEAAs, including aspartate, alanine, and serine (*50*). Previous studies demonstrated that the expression of aminotransferases and deaminases, including phosphoserine aminotransferase (PSAT) (*51*), GLS (*52, 53*) and asparagine synthetase (ASNS) (*54*), is enhanced in a wide range of cancer types.

Protein synthesis not only requires the supply of amino acids as substrates, but also relies on the activation of signalling pathways, mainly the mammalian target of rapamycin complex 1 (mTORC1). mTORC1 is a key regulator of cellular anabolism, including promoting protein synthesis (*55*). It is activated by the presence of various amino acids, including glutamine, leucine, alanine, arginine, asparagine, histidine, methionine, serine, threonine, and valine (*56*). Therefore, amino acids also regulate protein synthesis in cancer cells by acting as signalling

molecules.

Cell proliferation also requires the supply of DNA which is synthesized using purine and pyrimidine nucleotides as substrates. Nucleotides consist of nitrogen-containing bases and deoxyribose groups covalently linked to phosphate groups (i.e. phosphoribosylamine (PRA)). The *de novo* synthesis of nucleotides requires the input from multiple metabolic pathways. In this regard, the PRA backbone is generated from ribose-5-phosphate that is an intermediate of the non-oxidative branch of PPP (*57*). Previous studies found that various types of cancer cells upregulate the expression of enzymes involved in this pathway, including ribose-5-phosphate isomerase (RPI) (*58*), ribulose-phosphate 3-epimerase (RPE) (*58*), transketolase (TKT) (*42, 59*) and transaldolase (TALDO) (*60*). The synthesis of purine and pyrimidine bases requires amino acids (glutamine, aspartate and glycine) as carbon and nitrogen sources. For purine bases synthesis, methyl group donated from the one-carbon/folate pool is also necessary. Methylenetetrahydrofolate dehydrogenase 2 (MTHFD2), the major mitochondrial enzyme involved in the folate cycle, has been reported to be upregulated in multiple cancer types (*61-63*).

1.1.3 Increased reliance on the maintenance of redox balance

Redox homeostasis refers to the balance of reducing and oxidizing reactions in cells and is key to cellular biological functions (*64*). Therefore, cancer cells actively regulate redox homeostasis to promote survival and tumour development (*65*). Reactive oxygen species (ROS) is a group of highly reactive oxidants and free radicals that oxidize other molecules by accepting electrons during chemical reactions. ROS is generated during oxygen metabolism as by-products and includes superoxide anion ($O_2^{\bullet-}$), hydrogen peroxide (H_2O_2) and hydroxyl radical ($OH^{\bullet}$) (*66*). To counteract ROS and balance the redox status, cells employ various antioxidation systems, including the glutathione system (GSH) (Figure 1.3) (*67*). GSH peroxidase catalyses the conversion of H_2O_2 to water using reduced GSH as a reducing equivalent (Figure 1.3). The oxidised GSH (GSSG) can be reduced to GSH using NADPH by GSH reductase (Figure 1.3).

Cancer cells modulate intracellular ROS levels to maintain cellular homeostasis because ROS at different concentrations leads to different effects. When present at low to moderate levels, ROS upregulate cell division and survival by reversibly oxidizing cysteine residues of kinases and phosphatases (*68-70*). However, excess amount of ROS (i.e. oxidative stress) may damage macromolecules (e.g. proteins, lipids and DNA) and result in the loss of cellular integrity (*71*). Thus, cancer cells employ antioxidation systems to tightly control ROS levels. One mechanism is to activate the transcription factor nuclear-factor erythroid 2-related factor 2 (NRF2) and activating transcription factor 4 (ATF4) which in turn promotes the expression of enzymes and transporters involved in GSH *de novo* synthesis (Figure 1.3) (*72*). Of note, GSH regeneration from the oxidized form GSSG require the supply of NADPH from the PPP pathway (as described in section 1.1.2) (Figure 1.3). Interestingly, cancer cells not only upregulate the capacity of NADPH re-generation from nicotinamide adenine dinucleotide phosphate ($NADP^+$), but also increase the pool size of total NADP (i.e. NADPH and $NADP^+$) (*5*). $NADP^+$ is synthesized using nicotinamide adenine dinucleotide (NAD^+) as a substrate which is catalysed by NAD kinase (NADK1 and NADK2). Previous studies have shown that the activity of NADK1 is stimulated in cancer cells to expand NADP pool size (*73*).

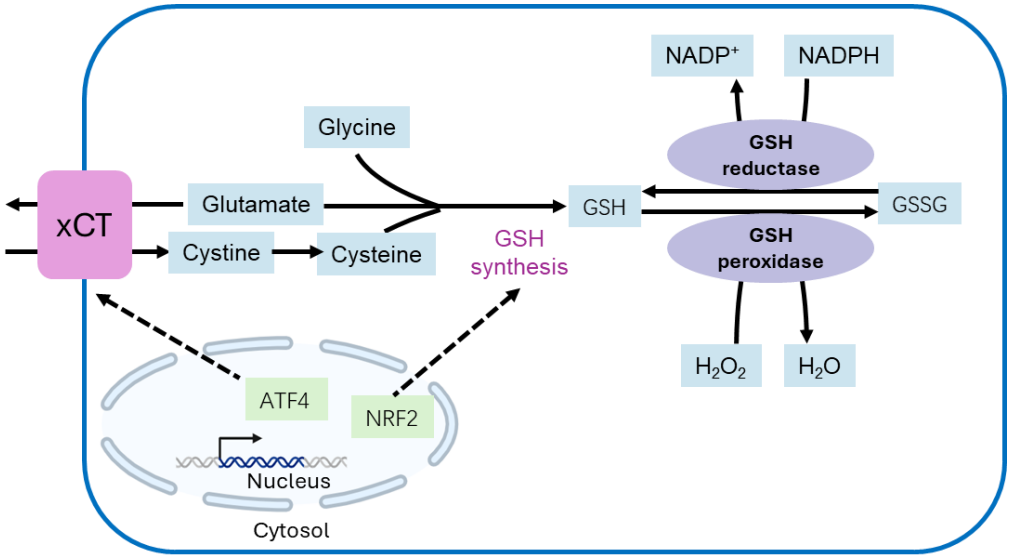


Figure 1.3 Oxidative stress protection mechanisms in cancer cells.
Various mechanisms help cancer cells defend oxidative stress, including enhanced GSH synthesis and NADPH production. The transcription factors NRF2 and ATF4 regulate key enzymes involved in GSH *de novo* synthesis and promote the transporter xCT expression which is a cystine/glutamate antiporter. The imported cystine is then reduced to cysteine which is a substrate of GSH synthesis. H_2O_2 is reduced to water by GSH peroxidase with the production of oxidised GSSG. GSSG can be converted back to GSH catalysed by GSH reducatase with the consumption of NADPH. For simplicity, NADPH production is not shown and can be found in Figure 1.2. xCT: cystine/glutamate antiporter, GSH: glutathione, GSSG: oxidised glutathione, ATF4: activating transcription factor 4, NRF2: nuclear factor erythroid 2-related factor 2. Metabolites and enzymes are shown in blue rectangles and purple ovals, respectively.

Moreover, cancer cells actively regulate reducing equivalents to avoid their accumulation to excessive levels (i.e. reductive stress) which interferes with metabolism, disrupts proliferation, and inhibits cell survival (*74-76*). Reductive stress can result from an imbalance of reduced nicotinamide adenine dinucleotide (NADH)/NAD^+, NADPH/$NADP^+$ or GSH/GSSG (*77-80*). NAD^+ is an essential co-factor for glycolysis and the TCA cycle. It is reduced to NADH as carbon sources (e.g. glucose and glutamine) are oxidized. In cancer cells, the increased uptake and oxidization of carbon sources favours the production of NADH (*81*). Indeed, the oversupply of NADH may exceed the capacity of cancer cells to regenerate NAD^+. Thus, the resulting imbalance of NADH/NAD^+ not only causes reductive stress, but also interferes with metabolic reactions that require NAD^+.

Cancer cells possess multiple mechanisms to regenerate NAD^+ from NADH. The Warburg effect is one prominent example. Pyruvate reduction to lactate is coupled with the oxidation of NADH to NAD^+ (*5*). Therefore, the diversion of pyruvate for lactate production maintains the constant supply of NAD^+ in cancer cells. In addition, the malate-aspartate shuttle facilitates regeneration of NAD^+ through ETC by transporting electrons in the cytosolic NADH into mitochondria (*5*).

1.2 Cancer metabolism is regulated by PI3K/Akt signalling pathway

The PI3K/Akt signalling is one of the most commonly deregulated pathways across various types of cancer (*82*). Once activated, it promotes survival, growth, and proliferation of cancer cells. Of note, the PI3K/Akt pathway also induces metabolic reprogramming to upregulate nutrient uptake and anabolic metabolism, which in turn supports the metabolic demands for rapid proliferation (*83*).

1.2.1 The PI3K/Akt signalling pathway

The activation of the phosphatidylinositol 3-kinases (PI3K)/Akt pathway starts when receptor tyrosine kinases (RTKs) bind to the ligands (e.g. growth factors and insulin) (Figure 1.4) (*84*). Ligand engagement induces dimerization of RTKs and juxtaposes the cytoplasmic tyrosine kinase domains (*84*). As a result, it facilitates the autophosphorylation of the tyrosine residues which function as a binding site for downstream effectors or adaptor proteins.

PI3K is one of the effectors recruited to the activated RTKs (Figure 1.4). Based on their structures and substrate preference, PI3K is grouped into three classes: class I (a and b), II and III (*85, 86*). However, only class Ia PI3K has been demonstrated to have implications for cancer biology (*87*). Class Ia PI3K is a heterodimer and consists of a regulatory subunit (p85α (or its shorter variants p55α, p55γ and p50α) or p85β) and a catalytic subunit (p110α, p110β or p110δ) (*88*). In the absence of stimulants, the regulatory subunit binds to the catalytic subunit

to inhibit its kinase activity. However, the binding of PI3K to activated RTKs relieves such inhibition and allows the phosphorylation of plasma membrane lipid phosphatidylinositol 4,5-bisphosphate (PIP_2) to generate phosphatidylinositol 3,4,5-trisphosphate (PIP_3) (Figure 1.4) (*88*). The activity of the PI3K/Akt pathway can be attenuated by phosphatase and tensin homologue (PTEN). PTEN is a phosphatase that mediates dephosphorylation of PIP_3 to PIP_2 (Figure 1.4) (*89*).

PIP_3 is a second messenger and recruits the downstream effector with pleckstrin homology (PH) domain, such as the serine/threonine kinase Akt (*90*). Once localised to plasma membrane, Akt can be fully activated by phosphoinositide-dependent protein kinase 1 (PDPK1)-mediated threonine 308 phosphorylation (*91, 92*) or mechanistic target of rapamycin complex 2 (mTORC2)-mediated serine 473 phosphorylation (Figure 1.4) (*93*). Subsequently, Akt phosphorylates and modulates the activity of a wide variety of effectors. There are three isoforms of Akt (Akt1, Akt2 and Akt3) (*94*) and their expression in organs differs with Akt1 and Akt2 broadly expressed and Akt3 mainly found in brain (*94, 95*). However, most of the downstream effects are redundantly regulated by three isoforms of Akt (*83*).

Among the effectors regulated by Akt, the key regulators of cellular metabolism include mTORC1, glycogen synthase kinase 3 (GSK3) and forkhead box O (FOXO) family of transcription factors (FOXO1, FOXO3A and FOXO4) (Figure 1.4) (*96*). mTORC1 can be directly activated by Akt-mediated phosphorylation of its component proline-rich Akt substrate of 40 kDa (PRAS40) (*97*). Alternatively, Akt phosphorylates tuberous sclerosis complex 2 (TSC2) which forms a complex with TSC1 and negatively regulates mTORC1 activity in the absence of stimulants (*98, 99*). Therefore, TSC2 phosphorylation disrupts the complex formation and activates mTORC1. Subsequently, mTORC1 phosphorylates downstream effectors including ribosomal protein S6 kinase (S6K) and eukaryotic translation initiation factor 4e-binding protein (4e-BP), which regulates protein and lipid synthesis (*100*). mTORC1 activation also regulates FA synthesis via sterol regulatory element-binding protein (SREBP) family of transcription factors (Figure 1.4) (*100*). MYC expression is also modulated by mTORC1 activation (Figure 1.4) (*100*).

Under basal conditions, GSK3 is active and phosphorylates its targets to direct them for proteasomal degradation (*101, 102*). Upon stimulation, GSK3 is phosphorylated and inhibited by Akt. The targets of GSK3 include transcription factors which regulate cellular metabolism, such as MYC, NRF2 and SREBP (Figure 1.4) (*103*).

Upon Akt phosphorylation, FOXO transcription factors are sequestered from the nucleus which prevents the expression of their target genes (*104*). It has been shown that the target genes are involved in suppressing cellular metabolism, cell growth, survival, and proliferation (*105*).

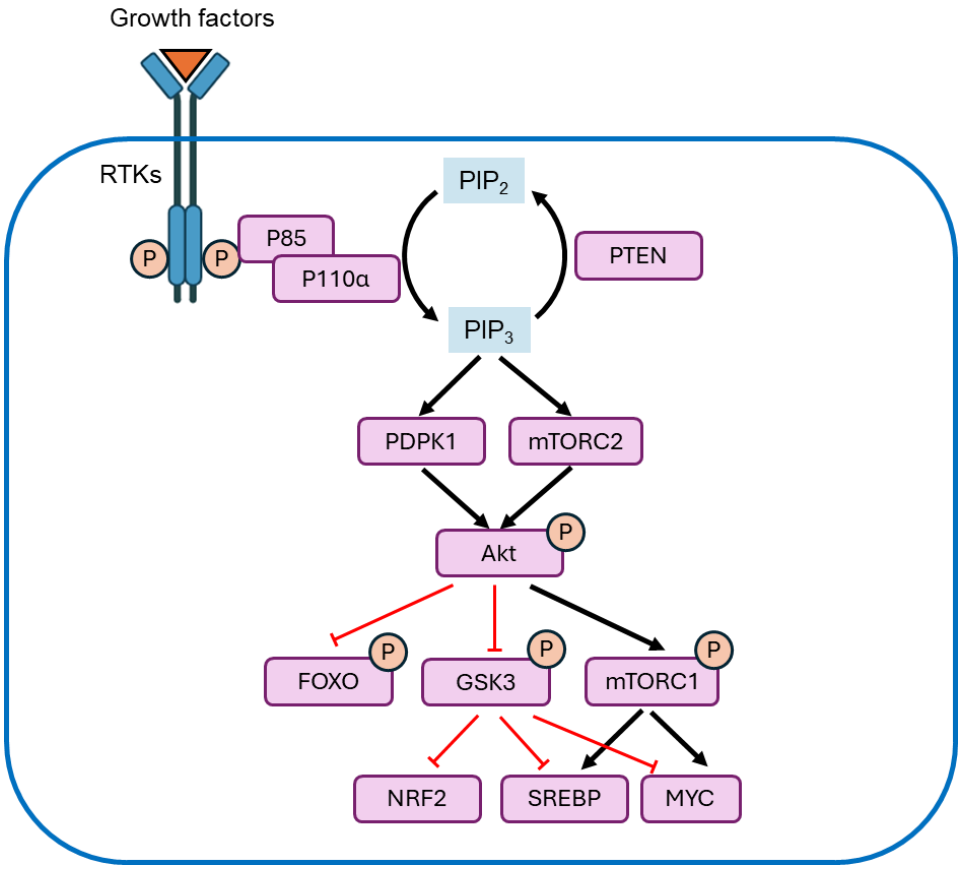


Figure 1.4 The PI3K/Akt pathway and the major downstream effectors in regulating cancer metabolism.

Once activated by ligands (e.g., growth factors), RTKs dimerise and undergo autophosphorylation of the cytoplasmic domain to recruit PI3K. PI3K phosphorylates PIP_2 to PIP_3 which is a second messenger to recruit Akt. PIP_3 can be dephosphorylated to PIP_2 by PTEN. Akt is then fully activated by PDPK1 and mTORC2 mediated phosphorylation at T308 and S473. Akt regulates cancer metabolism through three key effectors: FOXO, GSK3 and mTORC1. mTORC1 promotes the processing and activation of SREBP and the expression of MYC. GSK3 mediated phosphorylation of NRF2, SREBP and MYC directs them for proteasomal degradation under basal conditions. Akt-mediated GSK3 phosphorylation inhibits GSK3 activity. PDPK1: phosphoinositide-dependent protein kinase 1, PIP_2: phosphatidylinositol 4,5-bisphosphate, PIP_3: phosphatidylinositol 3,4,5-trisphosphate, RTK: receptor tyrosine kinase, PTEN: phosphatase and tensin homologue, GSK3: glycogen synthase kinase 3, FOXO: forkhead box O transcription factors, SREBP: sterol regulatory element-binding protein. Phosphorylation is indicated as a P in circle.

1.2.2 The PI3K/Akt pathway enhances glucose uptake and glycolysis

Akt pathway has been shown to activate multiple control points in glucose uptake and glycolysis (Figure 1.5). Glucose entry into cancer cells is mainly mediated by GLUT1 (*106*).

Upon Akt stimulation, GLUT1 localization to plasma membrane is increased, which as a result upregulates glucose uptake (*107, 108*). Such effect is mediated by Akt-induced phosphorylation and inhibition of thioredoxin-interacting protein (TXNIP) which promotes endocytosis of plasma membrane-bound GLUT1 (*107, 108*). Indeed, inhibition of TXNIP has been demonstrated to increase glucose uptake in non-small-cell lung cancer cells (*109*).

Moreover, Akt stimulates glycolysis by phosphorylating and activating key glycolytic enzymes (Figure 1.5). Hexokinase 2 (HK2) is the initial glycolytic enzyme and catalyses the phosphorylation of glucose to glucose 6-phosphate (G6P). Because G6P cannot be exported to extracellular space, HK2 promotes the retention of glucose in cells. HK2 is one of the rate-limiting enzymes in glycolysis and can be activated by Akt-mediated phosphorylation (*110, 111*). In addition, Akt indirectly activates phosphofructokinase 1 (PFK1) which is another important regulatory enzyme of glycolysis (*112, 113*). Akt phosphorylates and stimulates the activity of 6-phosphofructo-2-kinase/fructose-2,6-biphosphatase (PFKFB2) to promote the synthesis of fructose 2,6-bisphosphate (F2,6BP). F2,6BP is an allosteric activator of PFK1 and therefore, PFK1-driven glycolysis is increased (*113*).

Apart from direct activation by phosphorylation, Akt also stimulates glucose uptake and glycolysis by modulating downstream transcription factors to regulate enzyme expression (Figure 1.5). In this regard, mTORC1 has been demonstrated to upregulate the translation of *HIF1A* mRNA which increases the protein levels of hypoxia-inducible factor 1α (HIF1α) even under conditions of normoxia (*114-116*). HIF1α is a transcription factor that is degraded depending on cellular oxygen levels and stabilised in the absence of oxygen (*117*). It upregulates the expression of GLUT1 and almost all the glycolytic enzymes and directs glucose away from the TCA cycle by enhancing the expression of lactate dehydrogenase 1 (LDH1) and pyruvate dehydrogenase kinase 1 (PDK1) (*117*). Another key transcription factor regulated by Akt is MYC which promote the expression of GLUT1 and most glycolytic enzymes (*118*). Akt activation has been shown to increase the protein levels of MYC by multiple mechanisms, including transcription, translation, and post-translational modification (PTM) (*118*). The translation of MYC can be increased by mTORC1 signalling (*119, 120*). Under basal conditions, GSK3 phosphorylates MYC and directs it for proteasomal degradation (*121-123*).

Therefore, Akt-mediated phosphorylation and inhibition of GSK3 stabilises MYC. In addition, FOXO has been shown to reduce the expression of enzymes involved in glycolysis by antagonizing MYC function (*124-126*). Thus, Akt-mediated phosphorylation of FOXO abolishes the inhibitory effects on glycolysis (*126*).

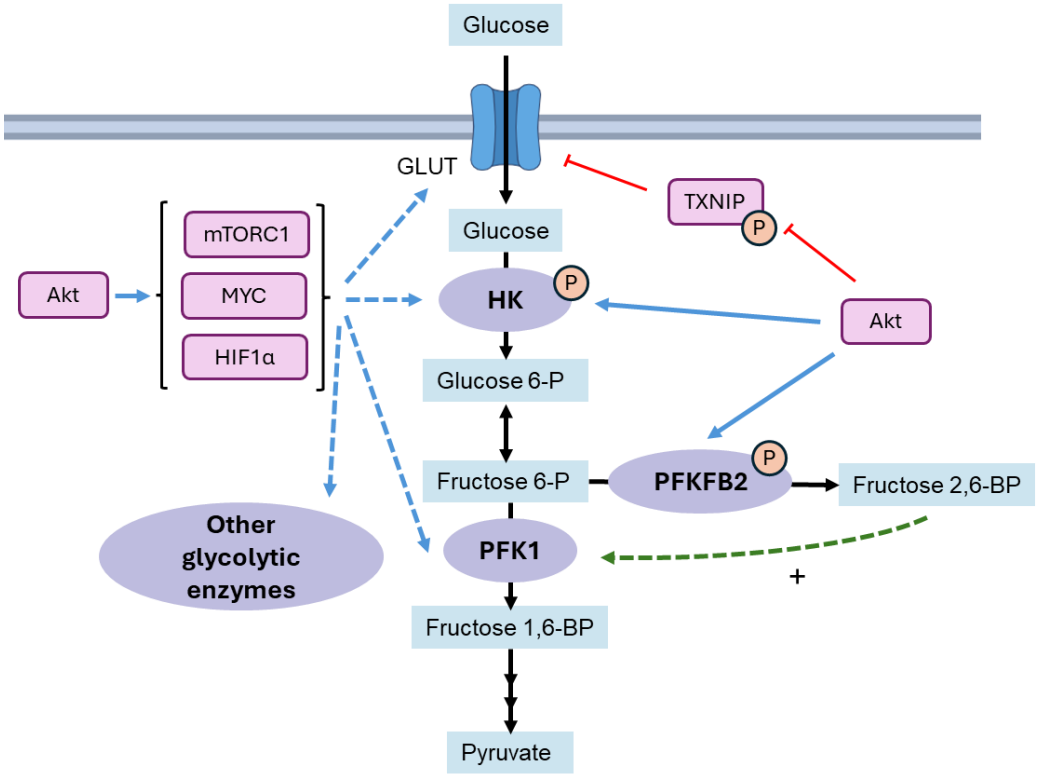


Figure 1.5 The PI3K/Akt pathway stimulates glucose metabolism via glycolysis in cancer cells. The Akt signalling promotes glycolysis via direct phosphorylation and transcriptional mechanisms. Akt enhances GLUT1 localization to plasma membrane and glucose uptake. TXNIP promotes endocytosis of GLUT and its phosphorylation by Akt inhibits its activity. Akt also stimulates HK to increase the retention and activation of imported glucose. HK phosphorylates glucose to glucose 6-phosphate which cannot be exported. PFKFB2 is phosphorylated and activated by Akt to produce fructose 2,6-bisphosphate which is an allosteric activator of PFK1. The downstream effectors of Akt (e.g., mTORC1, MYC, HIF1α) increase the expression GLUT and most glycolytic enzymes. TXNIP: thioredoxin-interacting protein, HK: hexokinase, GLUT: glucose transporter, PFK1: phosphofructokinase 1, PFKFB2: 6-phosphofructo-2-kinase/fructose-2,6-biphosphatase, Glucose 6-P: glucose 6-phosphate, Fructose 6-P: fructose 6-phosphate, Fructose 2,6-P: fructose 2,6-bisphosphate, Fructose 1,6-P: fructose 1,6-bisphosphate. Metabolites and enzymes are shown in blue rectangles and purple ovals, respectively. Blue solid and dashed arrows indicate Akt mediated regulation by direct phosphorylation and transcription, respectively. Green dashed arrow indicates allosteric activation of PFK1 by fructose 2,6-bisphosphate.

1.2.3 The PI3K/Akt pathway promotes anabolic metabolism

The PI3K/Akt signalling has been shown to upregulate the synthesis of macromolecules, including FAs, nucleotides, and proteins (*83*). Akt activation promotes *de novo* synthesis of FAs to support the production of plasma membranes (Figure 1.6). Cytosolic acetyl-CoA is the substrate for FA synthesis and is generated from ACL-catalysed cleavage of citrate (refer to section 1.1.2 for details). Akt-mediated phosphorylation of ACLY enhances its activity, which in turn increases the supply of acetyl-CoA for FA synthesis (Figure 1.6) (*127, 128*). Additionally, Akt stimulates FA synthesis by activating transcription factor SREBP to promote the expression of almost all the lipogenic enzymes and enzymes involved in NADPH production (Figure 1.6) (*129, 130*). Under basal conditions, SREBP remains as an inactive trans-membrane protein in endoplasmic reticulum (ER). Its activation involves the transport to Golgi apparatus and release of its N-terminal fragment by proteolytic cleavage. The N-terminal fragment is the mature active form of SREBP and can translocate to the nucleus to induce the expression of target gene (*129*). Akt signalling promotes SREBP activation via multiple mechanisms. mTORC1 has been shown to enhance the proteolytic processing and trafficking of the mature form of SREBP (Figure 1.6) (*116, 131, 132*). GSK3 phosphorylates the active form of SREBP and directs it for proteasomal degradation and thus, Akt-mediated inhibition of GSK3 enhances its stability (Figure 1.6) (*133, 134*). MYC has been recently reported to promote the expression of SREBP and the binding of SREBP to promoters of lipogenic genes, thereby upregulating FA synthesis (*135*).

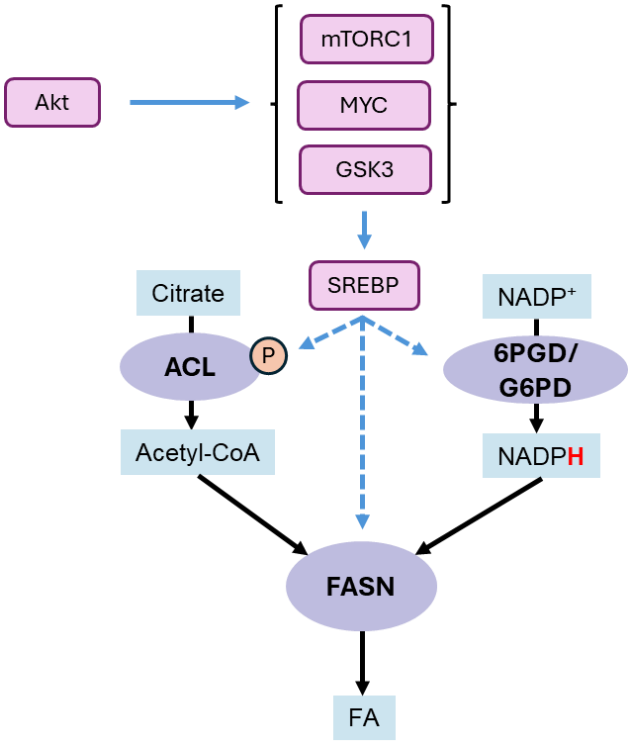


Figure 1.6 The PI3K/Akt signalling promotes de novo FA synthesis.
Akt phosphorylates and activated ACL which catalyses the cleavage of cytosolic citrate to produce acetyl-CoA for FA synthesis. The downstream effectors mTORC1 promotes the processing and nuclear localisation of SREBP to enhance the expression of lipogenic enzymes (e.g., ACL, FASN, 6PGD/G6PD). GSK3-mediated phosphorylation of the mature active form of SREBP directs it for degradation and thus, Akt-mediated phosphorylation and inhibition of GSK3 enhances the retention of the active SREBP. MYC also induces the expression of SREBP. ACL: ATP-citrate lyase, SREBP: sterol regulatory element-binding protein, G6PD: glucose-6-phosphate dehydrogenase, 6PGD: 6-phosphogluconate dehydrogenase. Metabolites and enzymes are shown in blue rectangles and purple ovals, respectively. Blue solid and dashed arrows indicate Akt mediated regulation by direct phosphorylation and transcription, respectively.

Additionally, Akt activation enhances *de novo* synthesis of nucleotides to support DNA production in rapid proliferating cells (*83*). Nucleotide synthesis depends on the coordinated input from multiple metabolic pathways which are stimulated by Akt signalling. The PPP pathway produces ribose-5 phosphate as a substrate for the synthesis of deoxyribose moiety of nucleotides (as described in section 1.1.2). mTORC1 activation has been shown to induce the expression of the rate-limiting enzyme G6PD of PPP pathway (*116*). Akt also promotes PPP flux by directly phosphorylating and activating the key enzyme TKT (*136*). The synthesis of pyrimidine bases is enhanced by mTOCR1 which phosphorylates and activates the rate-

limiting enzyme carbamoyl-phosphate synthetase 2, aspartate transcarbamylase and dihydroorotase (CAD) (*137, 138*). The supply of one carbon units, which are necessary for purine base synthesis, is enhanced by mTORC1-mediated stimulation of activating transcription factor 4 (ATF4) (*139*). ATF4 promotes the expression of MTHFD2 which is a key enzyme involved in the one-carbon/folate cycle (*139*). Akt-mediated activation of MYC also promotes the expression of enzymes involved in purine and pyrimidine synthesis (*140*). The uptake of glutamine, which serves as a nitrogen source, is increased by MYC activation (*140*).

Moreover, Akt signalling promotes the uptake of amino acids for protein synthesis. mTORC1-mediated induction of MYC upregulates the expression of amino acid transporters, including LAT1 and SLC1A5 (*141*). MYC induction also increases the levels of glutamine and glutamine dehydrogenase to enhance the entry of glutamine into the TCA cycle for production of intermediates of NEAA synthesis (*142*). ATF4 induction downstream of mTORC1 activation also promotes the expression of amino acid transporters, such as LAT1, cystine/glutamate antiporter (xCT) and cationic amino acid transporter 1 (CAT1 or SCL7A1; transporters for arginine, lysine, histidine) (*143, 144*).

1.2.4 The PI3K/Akt signalling regulates redox homeostasis

Akt pathway has been shown to promote antioxidant capacity in cancer cells by enhancing the production of reducing equivalents, namely NADPH (*83*).

Akt activation upregulates the synthesis of cytosolic NADPH via multiple mechanisms (Figure 1.7A). The oxidative branch of PPP is the major source of NADPH production from $NADP^+$. mTORC1 stimulates oxidative PPP by inducing the expression of G6PD via SREBP (*116*). In addition, mTORC1-mediated activation of SREBP increases the expression of ME and IDH which contributes to cytosolic NADPH generation (*145, 146*). Of note, Akt signalling also increases the pool size of total $NADP^+$ and NADPH available for redox reactions. NADK catalyses $NADP^+$ production from NAD^+ and can be phosphorylated and activated by Akt (Figure 1.7A) (*73*).

In addition, Akt stabilizes and activates NRF2 which is a key transcription factor and

coordinates cellular antioxidation responses. GSK3 phosphorylates NRF2 and directs it for proteasomal degradation (*147*). Thus, Akt-mediated phosphorylation and inhibition of GSK3 results in NRF2 accumulation (Figure 1.7B). NRF2 induces the expression of multiple genes involved in ROS detoxification, including NADPH regeneration and GSH *de novo* synthesis and regeneration from the oxidised GSSG (*148*). In this regard, NRF2 induces the expression of G6PD, ME and IDH to support NADPH production (Figure 1.7B) (*149*). NRF2 also increases uptake of cystine, a key substrate for GSH production, by transcriptional regulation of its transporter xCT (Figure 1.7B) (*150*). Moreover, NRF2 positively regulates the levels of glutamate-cysteine ligase which is the rate-limiting enzyme in GSH synthesis (Figure 1.7B) (*151, 152*).

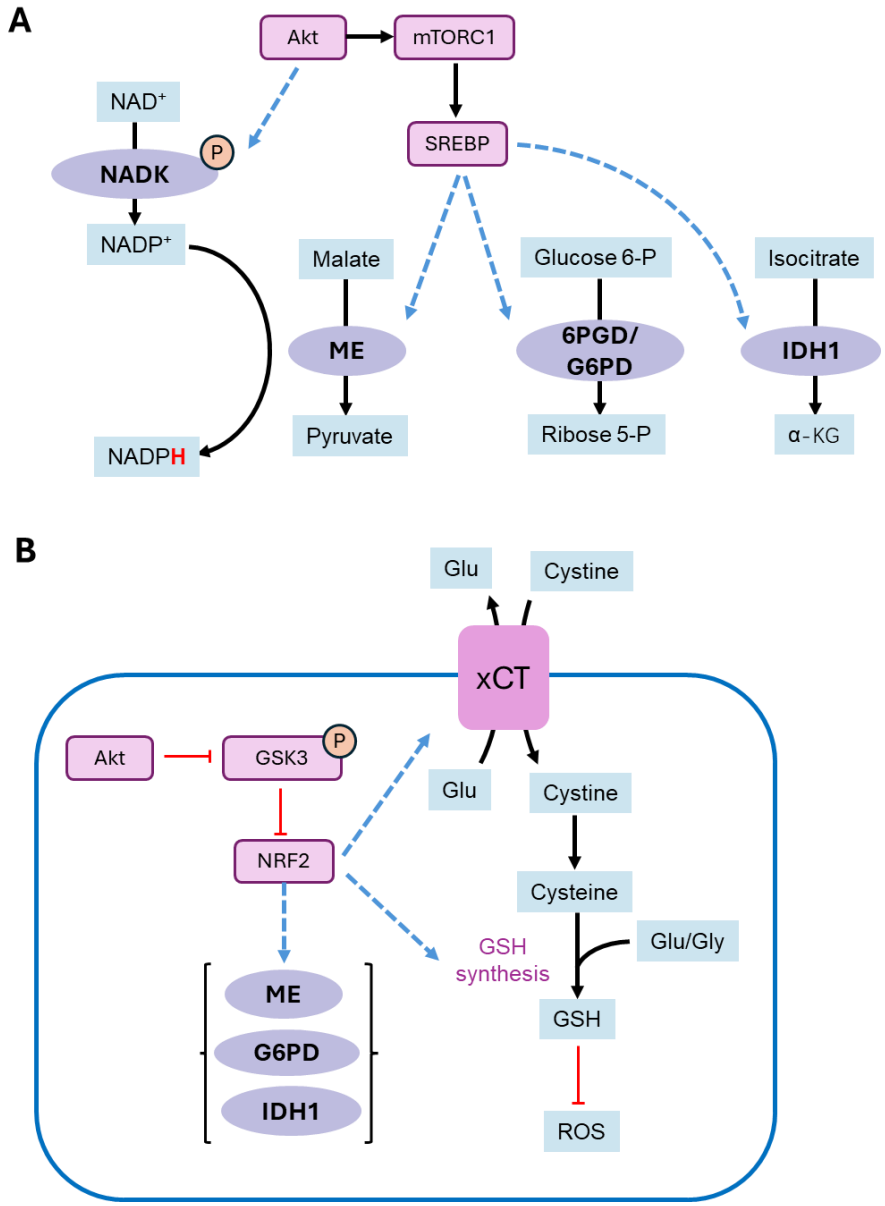


Figure 1.7 The PI3K/Akt pathway regulates the redox balance in cancer cells.

(A) The Akt signalling promotes the production of reducing power NADPH via SREBP. The Akt downstream effector mTORC1 stimulates the activity of SREBP which in turn induces the expression of ME, IDH1, G6PD and 6PGD for NADPH production. Akt also increases the pool size of total NADP by phosphorylating and activating NADK which phosphorylates NAD^+ to $NADP^+$. (B) The Akt signalling enhances *de novo* synthesis of GSH via NRF2. Under basal conditions, GSK3 phosphorylates and directs NRF2 for proteasomal degradation. Once phosphorylated by Akt, GSK3 is inhibited and thus NRF2 is stabilised. NRF2 enhances the expression of ME, G6PD and IDH to promote NADPH production. NRF2 also increases the expression of enzymes involved in GSH *de novo* synthesis (e.g., glutathione synthetase) and xCT transporters to upregulate the uptake of cystine. xCT: cystine/glutamate antiporter, GSH: glutathione, Glu: glutamate, Gly: glycine. Metabolites and enzymes are shown in blue rectangles and purple ovals, respectively. Blue solid and dashed arrows indicate Akt mediated regulation by direct phosphorylation and transcription, respectively.

1.3 Dysregulation of the Ras and PI3K pathways are common in epithelial ovarian cancer (EOC)

1.3.1 Introduction to ovarian cancer

Ovarian cancer is the fourth leading cause of death associated to cancer and the seventh most common diagnosed malignancy in female in developed countries (*153*). In the UK, it has been estimated that 1 in 60 women will develop ovarian cancer during their lifetime (*153*). This equates to approximately 7,000 newly diagnosed cases each year in the UK (*154*). Of these patients, around 4,200 patients die (*154*), and the high death rate is partially caused by the late diagnosis when the disease is highly metastatic and hard to manage. Indeed, the 5-year survival rate for patients diagnosed at early stage is 92% in comparison to 29% in those presenting at advanced stage (*155*). However, ovarian cancer diagnosis is challenged by the lack of effective screening methods and the asymptomatic nature at early stage (*155*).

Ovarian cancer is a group of diseases with heterogeneous molecular landscape, clinicopathological features and developmental origins. The most common type is epithelial ovarian cancer (EOC) which account for roughly 90% of ovarian cancer cases and can be further divided into several subtypes (*156*). Approximately 70% of EOC cases are ovarian high-grade serous carcinoma (HGSC) (*157*). Ovarian HGSC is characterized by genomic instability which in turn leads to copy number alterations (*158*). Apart from the nearly universal loss-of-function mutations in *TP53*, oncogenic mutations in HGSC patients are relatively rare (*157*). Ovarian low-grade serous carcinoma (LGSC), clear-cell ovarian cancer (CCOC), endometroid ovarian cancer (EnOC) and mucinous ovarian cancer (MOC) are less frequent and account for approximately 5%, 10%, 10% and 5% of all EOC cases (*159*). The rest 10% of ovarian cancer cases are non-epithelial and include sex cord-stromal ovarian cancer and germ cell ovarian cancer (*159*).

1.3.2 Genetic events leading to dysregulated Ras and PI3K pathways in EOC

Integrated genomics analysis has identified genetic signatures associated with each subtype of EOC. However, genetic alterations in the Ras and PI3K signalling pathways are frequently detected across EOC subtypes (*160*). The Ras pathway is a signalling cascade and regulates biological processes in cancer cells, including proliferation and survival. It is activated at upstream RTKs by growth factors, cytokines and hormones (Figure 1.8) (*161*). As described in Section 1.2.1, activated RTKs dimerise and auto-phosphorylate the cytoplasmic domains which function as docking sites for adaptor proteins. SOS (son of sevenless) is one of the recruited proteins and functions as a nucleotide exchange factor (NEF) (Figure 1.8) (*161, 162*). Ras is a GTPase and exists in its inactive guanosine diphosphate (GDP)-bound form under basal conditions. Upon stimulation, SOS facilitates the exchange of Ras-bound GDP with guanosine triphosphate (GTP) which in turn activates Ras (i.e., GTP bound active form) (*162*). Neurofibromin 1 (NF1) is a GTPase activating protein and enhances the hydrolysis of Ras bound GTP to GDP, which inactivates Ras (Figure 1.8) (*163*). GTP-bound Ras binds and activates multiple downstream effectors, including PI3K (see section 1.2.1 for the signalling pathway) and RAF protein family (BRAF, ARAF and c-RAF1) (*161, 164*). Subsequently, RAF functions as a protein serine/threonine kinase and phosphorylates and activates MEK1/2 (Figure 1.8) (*161, 164*). Finally, MEK1/2 phosphorylates and activates Erk1/2, which regulates multiple transcription factors (e.g., MYC, c-Jun and ELK1) (Figure 1.8) (*161, 164*).

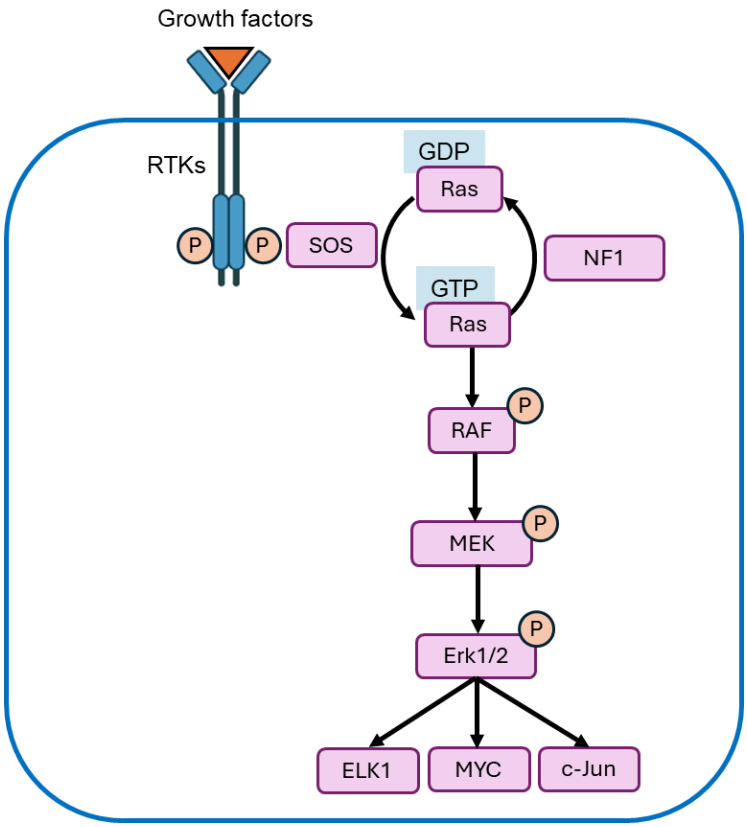


Figure 1.8 The Ras signalling pathway in cancer cells.
RTKs can be activated by ligands (e.g., growth factors) and undergo dimerization and autophosphorylation. SOS is recruited to the phosphorylated cytoplasmic domains and exchanges Ras bound GDP with Ras bound GTP to activate Ras. NF1 is a GTPase activating protein and stimulates the hydrolysis of Ras bound GTP to Ras bound GDP. The activated GTP-bound Ras phosphorylates and stimulates RAF, MEK and Erk1/2 in the manner of signalling cascade. Finally, multiple transcription factors (e.g., ELK1, MYC and c-Jun) are activated. RTK: receptor tyrosine kinase, SOS: son of sevenless, NF1: neurofibromin 1. Phosphorylation is indicated as a P in circle.

Multiple genetic alterations can lead to the hyperactive Ras signalling in EOC. For instance, amplification and activating mutations in epidermal growth factor receptor 2 (ERBB2), which functions as an RTK, are common in LGSC, CCOC and MOC. Mutations in the Ras isoform KRas and NRas have also been reported in LGSC, EnOC, CCOC and MOC (*153, 156, 159, 165, 166*). Mechanistically, the Ras mutations impair the GTPase activity of Ras and cause its constitutive activation (*167, 168*). In addition, amplification of KRas has been detected in HGSC and MOC (*169-171*). Deletion of NF1, the negative regulator of Ras, has also been detected in 8% of HGSC patients (*172*). BRAF mutations have been observed in LGSC and MOC (*173-*

175). The majority mutation (about 90%) is the substitution of valine with glutamate ($BRAF^{V600E}$) (*173, 174*). c-MYC amplification is also a common genetic alteration event in EOC (*169, 176*).

Genetic alterations at multiple components of the PI3K pathway have been reported in EOC. In this regard, approximately 40-50% of HGSC patients have constitutive activation of the PI3K/Akt pathway. Amplifications in p110 subunit of PI3K (*PIK3CA*) and one of the AKT isoforms (*AKT1-3*) are detected in 20% and 15-20% of cases, respectively (*177, 178*). Activating mutations in the *PIK3CA* and *RAPTOR* (encoding one component of mTORC1) are less common but present in 4% and 4% patients, respectively (*172, 179*). Loss of negative regulators in the PI3K/Akt pathway is also detected. In this regard, 8% patients harbour deleterious or loss-of-function mutations in *PTEN (179).* Mutations in the regulatory subunit p85 (encoded by *PIK3R1*), which binds and inhibits the catalytic subunit p110 in resting state, are present in roughly 4% cases (*172*). Moreover, dysregulation of the PI3K/Akt pathway may result from amplification or activating mutations in the upstream RTKs (e.g. EGFR, ERBB3, ERBB2 and IGF1) which are present in about 16-21% cases (*172*). Hyperactivity in the PI3K pathway is also prevalent in less frequent subtypes of EOC. PIK3CA mutations are detected in approximately 35% and 20% of clear-cell and endometroid ovarian cancer cases, respectively (*180, 181*). Deletions or loss-of-function mutations in PTEN are also common and observed in roughly 40% and 20% patients with endometroid and clear-cell ovarian cancer, respectively (*182*). Mutations in RTKs (i.e. ERBB2) and the Ras/Raf/Mek/Erk pathway (i.e. Ras) are frequent in ovarian LGSC and mucinous ovarian cancer patients (*183, 184*).

In addition, cross-talk and feedback mechanisms exist between the PI3K/Akt pathway and the Ras/Raf/Mek/Erk pathway. Thus, they may contribute to the hyperactivity in the Ras and PI3K signalling.

1.4 PARP inhibitors: targeted therapy against ovarian cancer

1.4.1 PARP1 is key to DNA damage repair

Poly(ADP-ribose) polymerase (PARP) is a large protein family consisting of 17 members based on similarity in sequence (*185*). Among these, PARP1 is essential to DNA damage repair (DDR) in mammalian cells (*186*). PARP1 is localized in the nucleus and contains three domains with different functions (Figure 1.9A) (*187*). In the N-terminus DNA binding domain (DBD), there are three zinc fingers that are capable of binding to DNA strands. The first two zinc fingers are required for binding to DNA breaks while the third one couples DNA binding to alterations in PARP1 function (*188-191*). In the middle auto-modification domain (AD), there are glutamate and lysine residues which accept ADP-ribose moieties (*192, 193*). There is also a BRCA1 carboxy-terminal (BRCT) repeat motif for protein-protein interaction. The catalytic domain (CD) is located in the C-terminus (*194*). Using NAD^+ as a substrate, CD transfers multiple ADP-ribose moieties to substrate proteins, thereby forming poly(ADP-ribose) (PAR) chains (*194*). The CD also contains a tryptophan-glycine–arginine-rich (WGR) domain for DNA binding and a helical domain (HD) which inhibits PARP1 activity in the absence of DNA damage by blocking the access of NAD^+ to PARP1 (*195*).

In response to DNA damage (e.g., single strand breaks (SSBs) and double strand breaks (DSBs)), PARP1 is recruited to the damage sites and undergoes allosteric changes in its structure, which abolishes the inhibitory effect of HD and upregulates its catalytic activity (Figure 1.9B) (*196*). As a result, poly(ADP-ribose) (PAR) chains are synthesized and attached covalently to PARP1 itself (i.e., autoPARylation) and histones (*197, 198*). The PAR chains serve as a scaffold for recruiting DDR proteins to DNA breaks through non-covalent interaction (Figure 1.9B) (*195*). For example, X-ray repair cross complementing protein 1 (XRCC1) binds to PAR chains and activates base excision repair (BER) by recruiting more BER proteins, including gap-filling DNA polymerase β (POLβ) and DNA ligase 3 (LIG3) (*199, 200*). Because SSBs are generated as an intermediate of BER, PARP1-mediated recruitment of XRCC1 is also essential for repair of SSBs (*201*). PAR chains also interact with meiotic recombination 11 (MRE11) and ataxia telangiectasia mutated (ATM) to initiate DSB repair by homologous recombination (HR) and restart of stalled replication forks (*202-204*). Eventually, PARP1 is released from the repaired DNA strands due to the negative charge of PAR chains (Figure 1.9B) (*187*). The PAR chains on PARP1 are hydrolysed by poly(ADP-ribose) glycohydrolase

(PARG) and free ADP-ribose monomers are released (Figure 1.9B) (*205*).

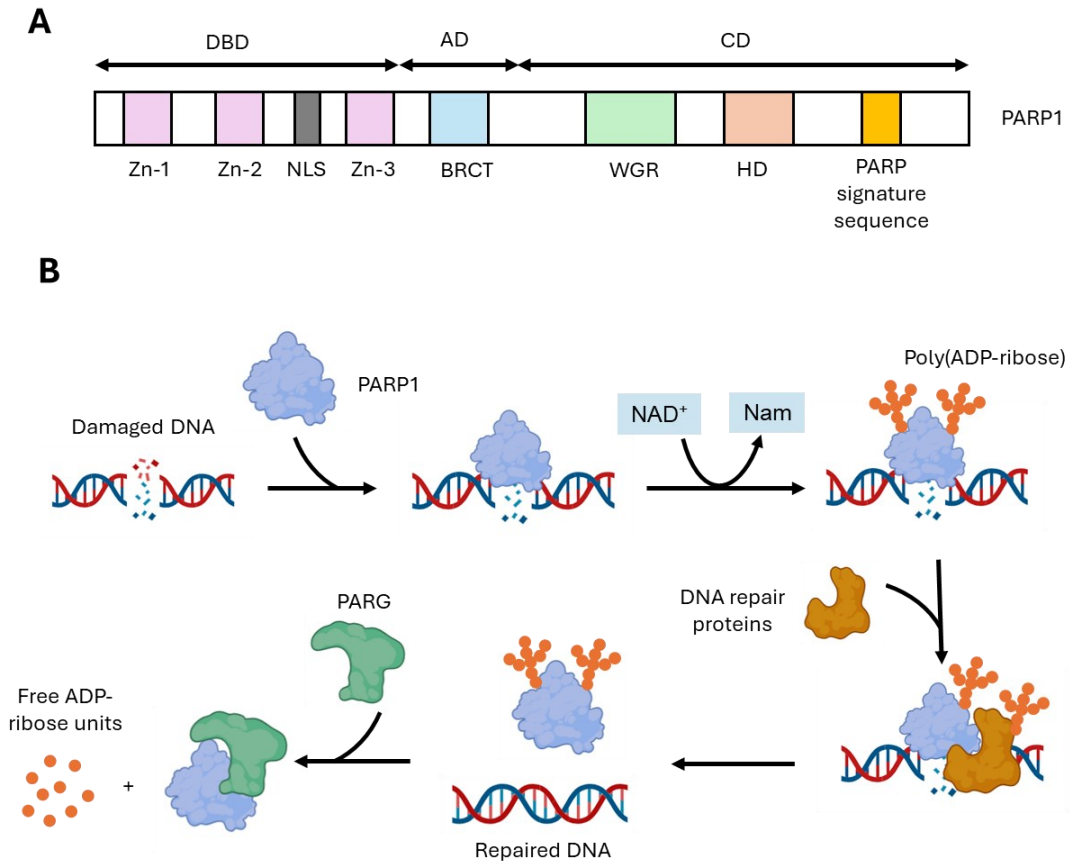


Figure 1.9 The roles of PARP1 in DNA damage repair in cancer cells.

(A) The domain structure of PARP1. PARP1 consists of three domains: DBD, AD and CD. There are three zinc fingers in the DBD domain for DNA binding. The nuclear localization signal is also in the DBD domain. A BRCT repeat motif is in the AD domain for protein-protein interaction. The WGR and HR domains inside the CD are for DNA binding and the inhibition of PARP1 activity in the absence of DNA damage. The PARP signature sequence is the most conserved sequence among PARP isoforms and locates in the CD. (B) PARP1 plays a key role in DNA damage repair. PARP1 detects and binds to damaged DNA strands and utilise NAD^+ as a substrate to synthesize PAR chains on itself and histone (not shown for simplicity). The PAR chains recruits DNA damage repair proteins which also undergo PARylation by PARP1. After the resolution of DNA damage, autoPARylated PARP1 is released, and the PAR chains are hydrolysed by PARG. DBD: DNA binding domain, AD: auto-modification domain, CD: catalytic domain, Zn: zinc finger, NLS: nuclear localization signal, BRCT: BRCA1 carboxy-terminal repeat motif, WGR: tryptophan-glycine–arginine-rich domain, HD: helical domain, PAR: poly(ADP-ribose), PARG: poly(ADP-ribose) glycohydrolase, Nam: nicotinamide.

PARP2 has also been shown to have implications in DDR, including BER (*206, 207*). In this regard, knock out of Parp2 in mice results in phenotypes similar to *Parp1*$^{-/-}$ mice, such as enhanced sensitivity to alkylating agents and ionizing radiation and increased genomic instability (*207, 208*). Functional redundancy between PARP1 and PARP2 has also been suggested. Knock out of both *Parp1* and *Parp2* genes in mice results in embryonic lethality related to genomic instability while the depletion of either Parp1 or Parp2 is not sufficient to impair DDR (*208*). However, PARP2-catalysed PARylation accounts for at most 15% of total PARylation, which suggests that PARP1 is the major PARP protein activated due to DDR (*209, 210*).

1.4.2 NAD^+ is a substrate of PARP1 and synthesized through multiple pathways

The activity of PARP1 is dependent on the supply of its substrate NAD^+ and PAR chain synthesis consumes a substantial amount of NAD^+. Indeed, PARP1 hyperactivation in response to excessive DNA damage depletes cellular NAD^+ pool and its replenishment requires the input of ATP (*211, 212*). As a result, NAD^+ synthesis exhausts cellular ATP content, which in turn can lead to oncosis (*212-215*). Oncosis is a programmed cell death mechanism under conditions of rapid ATP depletion (*216*). Consequently, ion balance across the plasma membrane is disrupted, and membrane integrity is lost, which collectively causes cell death accompanied by membrane blebbing (*216*).

In mammalian cells, there are three pathways to generate NAD^+: 1) the salvage pathway; 2) the Preiss-Handler (PH) pathway; and 3) the *de novo* synthesis pathway (Figure 1.10) (*217*). Most of cellular NAD^+ is synthesized through the salvage pathway which recycles the by-product nicotinamide (Nam; also known as niacinamide) released from PARylation and other NAD^+ consuming enzymes (e.g., CD38 and sirtuin (SIRT)) (*217*). Indeed, the NAD^+ turnover in human liver is estimated to be approximately 8g per day (*217*). The synthesis of the same amount of NAD^+ without recycling requires 1.5g Nam which is almost 100 times of the recommended daily uptake (i.e., 15mg) (*218*). The rate-limiting enzyme is nicotinamide

phosphoribosyl transferase (NAMPT; also called visfatin or Pre-B cell colony-enhancing factor (PBEF)) which catalyses the condensation of Nam with phosphoribosyl Pyrophosphate (PRPP) to produce nicotinamide mononucleotide (NMN) (*219-221*). Additionally, Nam and nicotinamide riboside (NR) from dietary uptake are also converted to NMN which is catalysed by nicotinamide riboside kinase (NRK) (*222*). Subsequently, NMN adenylyltransferases (NMNAT) catalyses the transfer of ADP moiety from ATP to NMN and produces NAD^+ (*217*).

The PH pathway uses nicotinic acid (NA) as a source of NAD^+ synthesis and the rate-limiting step is catalyzed by nicotinic acid phosphoribosyltransferase (NAPRT) (Figure 1.10) (*223, 224*). The product is nicotinic acid mononucleotide (NAMN) and is generated by condensation with PRPP. The *de novo* synthesis pathway starts with tryptophan (Figure 1.10) (*225*). The first reaction is catalysed by rate-limiting enzymes tryptophan dioxygenase (TDO) or indoleamine-2,3-dioxygenase (IDO) and produces N-formylkynurenine which undergoes multiple enzymatic reactions to generate NAMN via quinolinic acid (QA). NAMN is also a substrate of NMNAT and its adenylation produces nicotinic acid adenine dinucleotide (NAAD) (*217*). The last step to synthesise NAD^+ requires glutamine as the second substrate and is catalysed by NAD synthetase (NADS) (*217*).

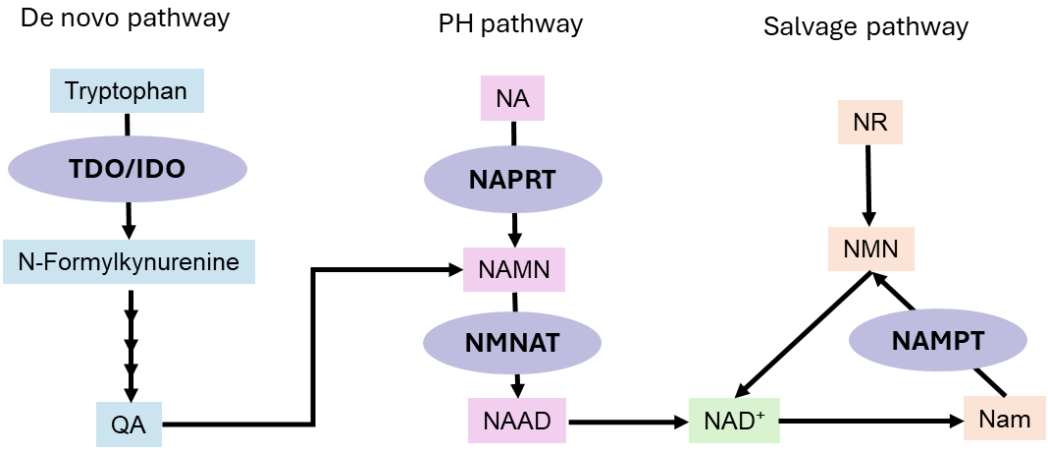


Figure 1.10 The metabolic pathways of NAD^+ synthesis.
The majority of NAD^+ is synthesized via the salvage pathway. The by-product of NAD^+ consuming enzymes (e.g., PARP), nicotinamide, is recycled to produce NAD^+. In addition, NAD^+ can also be synthesized via the *de novo* pathway where tryptophan is a substrate. In the PH pathway, nicotinic acid is the substrate, and this pathway converges with the de novo pathway at NAMN. The rate-limiting enzymes in the salvage, de novo and PH pathway are NAMPT, IDO/TDO and NAPRT, respectively. NA: nicotinic acid, NR: nicotinamide riboside, NAAD: nicotinic acid adenine dinucleotide, Nam: nicotinamide, QA: quinolinic acid, NAMN: nicotinic acid mononucleotide, NMN: nicotinamide mononucleotide, NAPRT: nicotinic acid phosphoribosyltransferase, NAMPT: nicotinamide phosphoribosyl transferase, NMNAT: NMN adenylyltransferases, NRK: nicotinamide riboside kinase, TDO: tryptophan dioxygenase, IDO: indoleamine-2,3-dioxygenase. The salvage, de novo and PH pathway are shown in blue, pink and orange rectangles. Enzymes are indicated in purple ovals.

Interestingly, NAD^+ synthesis is compartmentalized in mammalian cells. In this regard, there are three isoforms of NMNAT (i.e., NMNAT1-3) which are localized in different subcellular structures (*226, 227*). NMNAT1 exist in the nucleus and provides NAD^+ to fuel PARP1 activity. Indeed, PARP1 recruits NMNAT1 to generate NAD^+ locally (*228, 229*). NMNAT3 is expressed in mitochondria to support OXPHOS which requires NAD^+ as a co-factor (*230*). NMNAT2 is localized to cytosol where NAD^+ is required for glycolysis (*230*). NAMPT has been shown to exist in both nucleus and cytosol, which also supports the local demand of NAD^+ (*230*).

1.4.3 PARP inhibitors: mechanisms of action

The mechanism of PARP inhibitors is based on the concept of synthetic lethality (*231*). In this model, the perturbation of target A or B alone is not sufficient to induce cytotoxicity. However,

the perturbation of target A and B in combination leads to the loss of cell viability. In 2005, the synthetic lethality was described between PARP inhibitors and BRCA1/2 deficiency as evidenced by the enhanced sensitivity (i.e., greater reduction of cell survival) to PARP inhibitors (*232, 233*). Indeed, a 1000-fold decrease in SF_{50} values (the dose where 50% cells can survive) of KU0058684, a PARP1 inhibitor, was reported in Chinese hamster ovary cells with breast cancer gene 2 (BRCA2) deficiency (*233*). PARP inhibitors are designed to mimic the structure of its substrate NAD^+ and inhibit the catalytic domain (*234*). Initially, the proposed mechanisms are associated with the blockage of PARP1 enzymatic activity. Because PARP1 is essential for SSB repair, such inhibition leads to the persistence of DNA damage (*232, 233*). When encountered by a replication fork, the SSBs can cause the collapse of the fork, which in turn can create a DSB (*233*). In HR competent cells, the consequent DSBs are repaired by the error-free HR mechanisms which requires a sister chromatid as its template for high fidelity repair (*235*). However, in BRCA1/2 deficient cells, the DSBs can persist and be lethal (*232, 233*). Part of the DSBs remain unrepaired as chromatid breaks while the rest are repaired by non-homologous end joining (NHEJ) pathway (*232, 233*). NHEJ directly re-ligates DSBs without the need for a homologous template (*236*). As a result, NHEJ is error-prone and increases the risks of nucleotide deletions and insertions, which in turn results in genomic instability and cell death (*237*). Thus, the ability to activate HR following treatment of PARP inhibitors is essential for its survival.

However, the above-described mechanism has been challenged by the data showing PARP1 deficient cells are resistant to PARP inhibitors (*238, 239*). In addition, it has been reported that Rucaparib, Niraparib, Talazoparib and Olaparib inhibit PARP1 autoPARylation and prevent its release from the DNA strands (*238, 240-242*). Therefore, a modified model of mechanism was proposed (Figure 1.11). Once trapped on DNA by PARP inhibitors, PARP1 blocks the progression of replication forks, which in turn leads to the formation of DSBs (Figure 1.11) (*233*). The failure of BRCA1/2 deficient cells to engage the error free HR repair pathway leads to cell death. In ovarian HGSC, approximately 50% of patients harbour deficient HR (HRD) mainly due to loss of BRCA1 or BRCA2 (*172*). Therefore, PARP treatment induces genomic instability and cancer cell death in HRD patients. Indeed, several studies established the

correlation between PARP trapping potency of PARP inhibitors and cytotoxicity with Talazoparib being the most effective inducer of PARP trapping and cell death (*243, 244*).

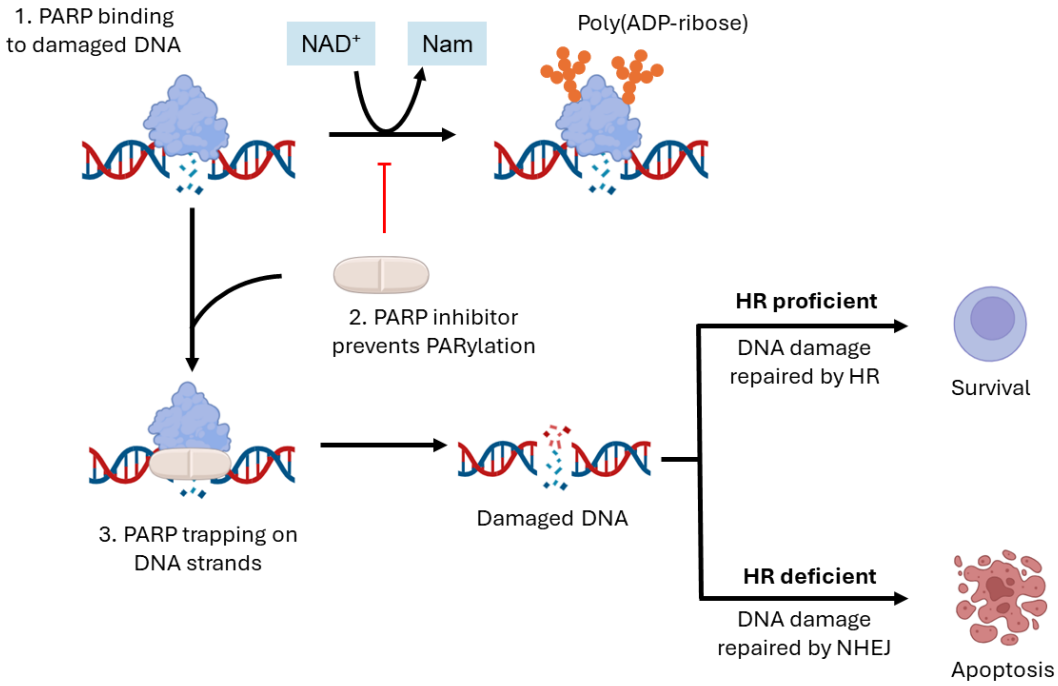


Figure 1.11 Mechanisms of PARP inhibitors.
PARP inhibitors mimic the structure of NAD^+, the substrate of PARP. Therefore, PARP inhibitors block autoPARylation of PARP1 which in turn causes its trapping on the DNA strands. Trapped PARP1 blocks the progression of replication forks and induces DNA damage. In HR proficient cells, the DNA damage can be repaired by the high-fidelity HR pathway. However, in HR deficient cells, such DNA damage is repaired by the error-prone alternative NHEJ pathway, which leads to genomic instability and cell death. HR: homologous recombination pathway, NHEJ: non-homologous end joining pathway.

Other mechanisms of action of PARP inhibitors have also been reported. For example, in HRD cancer cells, PARP inhibition enhances NHEJ by upregulating the phosphorylation and activation of DNA-dependent protein kinase (DNAPK) (*245*). This in turn results in large-scale genomic rearrangement and cell death. Indeed, resistance to PARP inhibition can be observed when NHEJ proteins (e.g., DNAPK and Ku80) are depleted (*246*). Interestingly, contradiction exists in terms of the effects of PARP inhibition on replication fork progression. In this regard, PARP inhibition upregulates the speed of replication fork progression, which increases the chance of DSB, genomic instability and cytotoxicity (*247, 248*).

1.4.4 Clinical development of PARP inhibitors

Multiple PARP inhibitors have been approved to treat ovarian cancer patients by the European Medicine Agency (EMA) and the Food and Drug Administration (FDA) (Table 1.1). Olaparib is the first approved PARP inhibitor in the clinic. In 2014, it was approved by FDA for advanced ovarian cancer patients who harbour germline or somatic mutations in BRCA1/2 and have received previous treatment of three of more lines of chemotherapy (*249, 250*). At the same time, EMA approved Olaparib as maintenance therapy for ovarian HGSC patients who have germline or somatic mutations in BRCA1/2 and show complete or partial responses to platinum-based chemotherapy (*249*). The approval is supported by several clinical trials that showed favourable responses of Olaparib. In the phase I clinical trial carried out by Fong et al, 8 out of 15 ovarian cancer patients with BRCA1/2 mutations showed complete or partial responses (*251*). Later, a phase II clinical trial (study 42) showed an objective response rate (ORR) of 34% (46 of 137) in ovarian cancer patients with germline BRCA1/2 mutations (*252, 253*). In 2018, Olaparib was approved as the first-line maintenance therapy for advanced ovarian cancer patients with mutations in BRCA1/2 (*249*). The decision was based on the SOLO-1 trial which assessed Olaparib as a maintenance therapy for newly diagnosed ovarian cancer patients. A 70% reduction in the risk of disease progression or death was observed in patients treated with Olaparib at three years (Olaparib = 60% vs placebo = 27%) (*254*).

In 2017, Olaparib was approved as a maintenance therapy for recurrent and platinum sensitive ovarian cancer patients (*249*). The approval decision was based on the SOLO-2 trial and study 19. The phase III SOLO-2 trial recruited recurrent and platinum sensitive ovarian cancer patients with BRCA1/2 mutations. Results showed that Olaparib as a maintenance therapy increased progression free survival (PFS) (Olaparib = 19.1 months vs placebo = 5.5 months) (*255*). Study 19 is a phase II clinical trial and recruited recurrent ovarian HGSC patients who had received two or more lines of chemotherapy. Results showed Olaparib improved PFS (Olaparib = 8.4 months vs placebo = 4.8 months), especially in patients with BRCA1/2 mutations (Olaparib = 11.2 months vs placebo = 4.8 months) (*256*). Moreover, a confirmatory trial SOLO-3 examined Olaparib for relapsed ovarian cancer patients with mutations in

BRCA1/2 and showed improved PFS (Olaparib = 13.4 months vs chemotherapy = 9.2 months) and objective response rate (ORR; Olaparib = 84.6% vs chemotherapy = 61.5%) (*257*).

Rucaparib was approved by FDA as a maintenance therapy for ovarian cancer patients with BRCA1/2 mutations after two or more lines of chemotherapy in 2016 (*249*). The approval was based on study 10 and the ARIEL2 trial. In study 10, BRCA1/2 mutated ovarian HGSC patients who had received more than two lines of chemotherapy were selected and an ORR of 59.5% was observed in patients treated with Rucaparib (*258*). In the ARIEL2 trial, relapsed and platinum sensitive ovarian HGSC patients were recruited and categorized into three groups: 1) mutated BRCA1/2; 2) wild-type BRCA1/2 with high levels of loss of heterozygosity (LOH); 3) wild-type BRCA1/2 with low levels of LOH. Results showed Rucaparib conferred more beneficial responses in BRCA1/2 mutated group (median PFS: BRCA mutant = 12.8 months vs LOH high = 5.7 months vs LOH low = 5.2 months) (*259*). Additionally, in the ATHENA trial, rucaparib was assessed as a first-line maintenance therapy for newly diagnosed ovarian cancer patients. Results showed that rucaparib significantly increased median PFS in HR deficient (HRD) patients (Rucaparib = 28.7 months vs placebo = 11.3 months) (*260*). Of note, patients with wild-type BRCA1/2 and high level of LOH were deficient in HR and showed improved median PFS (Rucaparib = 13.6 months vs placebo = 5.4 months) (*259*).

In 2018, FDA approved Rucaparib as a maintenance therapy for recurrent and platinum sensitive ovarian cancer patients (*249*). This is supported by the ARIEL3 trial which investigated the efficacy of Rucaparib as a maintenance therapy for recurrent and platinum sensitive ovarian HGSC patients. Patients with BRCA1/2 mutations showed a significant increase in median PFS (Rucaparib = 16.6 months vs placebo = 5.4 months) (*261*). In the ARIEL4 trial, the efficacy of rucaparib was compared against standard-of-care chemotherapy in relapsed ovarian cancer patients with BRCA1/2 mutations. Clinical benefits were observed as evidenced by the increase in median PFS (Rucaparib = 7.4 months vs chemotherapy = 5.7 months) (*262*).

Niraparib was approved by FDA as a maintenance therapy for relapsed and platinum-sensitive ovarian cancer patients in 2017 (*249*). The approval was based on the ENGOT-OV16/NOVA trial which recruited relapsed and platinum sensitive patients after two or more

lines of chemotherapy. Results showed a significant increase in median PFS in BRCA1/2 mutant patients (Niraparib = 21.0 months vs placebo = 5.5 months) (*263*). Of note, in patients with wild-type BRCA1/2, Niraparib also increased median PFS (Niraparib = 9.3 months vs placebo = 3.9 months), especially in those with HRD (Niraparib = 12.9 months vs placebo = 3.8 months) (*263*).

In 2020, FDA approved Niraparib as a first-line maintenance therapy for advanced ovarian cancer who show complete or partial response to platinum-based chemotherapy (*249*). The decision was based on the results from the PRIMA trial which recruited newly diagnosed and platinum sensitive advanced ovarian cancer patients. Niraparib improved median PFS regardless of HR status (Niraparib = 13.8 months vs placebo = 8.2 months) although the benefit was more profound in HRD patients (Niraparib = 21.9 months vs placebo = 10.4 months) (*264*). Niraparib was also investigated in the treatment of recurrent ovarian cancer in the QUADRA trial. Patients with response to platinum-based chemotherapy were selected and median overall survival (OS) of 15.5, 19.0 and 26.0 months was observed in patients with negative HRD, positive HRD and BRCA mutations, respectively (*265*).

	Study	Phase	Study arms	Cancer criteria	HR status	Endpoint
Front-line maintenance therapy	SOLO-1	III	Olaparib vs Placebo	HGSC or EnOC	BRCAm	PFS: 49.9 vs 13.8 m
	Study-42	II	Olaparib	HGSC	gBRCAm	ORR: 34%
	PRIMA	III	Niraparib vs Placebo	HGSC or EnOC	All	PFS: 13.8 vs 8.2 m (All); 21.9 vs 8.2 m (HRD)
	ATHENA	III	Rucaparib vs Placebo	HGSC	All	PFS: 28.7 vs 11.3 m (HRD positive); 12.1 vs 9.1 m (HRD negative)
Maintenance therapy for recurrent disease	Study-19	III	Olaparib vs Placebo	HGSC	All	PFS: 8.4 vs 4.8 m
	SOLO-2	III	Olaparib vs Placebo	HGSC or EnOC	BRCAm	PFS: 19.1 vs 5.5 m
	NOVA	III	Niraparib vs Placebo	HGSC	All	PFS: 21.0 vs 5.5 m (gBRCAm); 12.9 vs 3.8 m (HRD positive, non-gBRCAm); 9.3 vs 3.9 m (non-gBRCAm)
	ARIEL3	III	Rucaparib vs Placebo	HGSC or EnOC	All	PFS: 10.8 vs 5.4 m (All); 16.6 vs 5.4 m (BRCAm)
	ARIEL4	III	Rucaparib vs Placebo	HGSC or EnOC	BRCAm	PFS: 7.4 vs 5.7 m
Treatment of recurrent disease	SOLO-3	III	Olaparib vs Placebo	HGSC or EnOC	BRCAm	PFS: 13.4 vs 9.2 m; ORR: 84.6% vs 61.5%
	QUADRA	III	Niraparib	HGSC	HRD	ORR: 24%
	Study-10	I/II	Rucaparib	HGSC	gBRCAm	ORR: 59%
	ARIEL2	III	Rucaparib	HGSC	All	PFS: 12.8 m (BRCAm); 5.7 m (BRCAwt, LOH high); 5.2 m (BRCAwt, LOH low)

Table 1.1 Summary of the clinical trials of PARP inhibitors in ovarian cancer.

Table adapted from Smith and Pothuri (248) with additions from other trials (255, 257, 258, 260, 261). HGSC: ovarian high grade serous cancer, EnOC: endometrioid ovarian cancer, PFS: progression free survival, ORR: objective response rate, m: months, LOH: loss of heterozygosity, HRD: homologous recombination deficiency, gBRCAm: germline BRCA mutation, BRCAm: BRCA mutations, BRCAwt: BRCA wild type.

1.4.5 The impact of the Ras and PI3K pathways on PARP inhibitor responses

Aberrant activation of the Ras and PI3K pathways is associated with impaired responses to PARP inhibitors and therefore, novel combination therapies are required. In this regard, the ARIEL2 trial showed that the hyperactive Ras signalling and amplification of *AKT1/2/3* genes impaired responses to Rucaparib in patients with wild-type BRCA (*266*). In pre-clinical studies, the dysregulation of the Ras and PI3K signalling has been reported to induce resistance to PARP inhibitors and the downregulation of the signalling is associated with enhanced sensitivity (*267*). In this regard, Sun et al demonstrated that KRas mutations are correlated with acquired resistance to the PARP inhibitor Talazoparib in EOC cells and the treatment of MEK inhibitors re-sensitized PARP inhibitors (*268*). Mechanistically, MEK inhibition impaired HR capacity by downregulating the expression of HR components (*268*). Moreover, Olaparib synergises with the PI3K inhibitor BKM120 to induce DNA damage and inhibit proliferation and survival of ovarian cancer cells with PIK3CA mutations (*269*). The proposed mechanism is downregulation of BRCA1/2 levels and HR capacity due to PI3K inhibition. Moreover, in BRCA1-deleted breast cancer cells, BKM120 enhanced Olaparib induced DNA damage and attenuation of tumour growth (*270*). Indeed, several clinical trials showed promising results. For instance, a phase I trial assessed the combination of Olaparib with an Akt inhibitor Capivasertib. Safety and tolerability were confirmed and 50% (11 of 22) of ovarian cancer patients showed complete/partial response or stable disease (*271*). Two ongoing clinical trials assessing the combination of Olaparib with MEK inhibitor selumetinib in Ras mutant patients (Phase I trial SOLAR, NCT03162627; Phase II trial ComboMATCH, NCT05554328) showed safety and anti-tumour activity (*272, 273*).

In addition to directly targeting the signalling pathways, dysregulated Ras and PI3K pathways reprogramme tumour metabolism, which may be exploited to sensitize PARP inhibitor in this subgroup of EOC patients. As described in sections 1.2.2 to 1.2.4, the PI3K signalling regulates cancer metabolism, including enhanced glycolysis (*96*). Likewise, hyperactive Ras signalling promotes glucose metabolism by upregulating the expression of GLUT1 and key glycolytic

enzymes (e.g., HK and PFK1, section 1.2.2) (*58, 274, 275*). Given that NAD^+ is a key cofactor of glycolysis (*217*), the dysregulated Ras and PI3K signalling may increase the demand for NAD^+ and thus, create a metabolic bottleneck. Moreover, both Ras and PI3K pathways have been reported to modulate cellular NAD^+ levels. As described in section 1.2.4, the PI3K signalling activates NADK to enhance the production of $NADP^+$ from NAD^+ (*73*). Ras signalling also promotes $NADP^+$ synthesis by phosphorylating and activating NADK (*276*). Of note, $NADP^+$ has been reported as an endogenous inhibitor of PARP1 (*277*). Decreased levels of NAD^+ have been reported in KRas-mutant colorectal and non-small cell lung cancer cells (*278, 279*). The expression of NAMPT, the rate-limiting enzyme of the NAD^+ synthesis, has been reported to be regulated by multiple transcription factors downstream of the Ras and PI3K pathways. For instance, MYC overexpression promotes NAMPT expression at the transcription level and increases cellular NAD^+ levels in colorectal cancer cells (*280*). STAT3-5, NF-κB and HIF-1α also upregulate NAMPT protein levels (*281-284*). BRAF mutant tumours overexpress NAMPT and display higher sensitivity to NAMPT inhibitors (*282*).

Given the above, one hypothesis tested in this thesis is that metabolic reprogramming by hyperactive Ras and PI3K signalling may confer higher vulnerability to NAD^+ depleting agents. Since NAD^+ is a substrate of PARP1, its depletion may block autoPARylation and induce PARP trapping (*234*). This in turn synergies with PARP trapping induced by PARP inhibitors, which causes enhanced DNA damage and cytotoxicity. Thus, NAD^+ depletion may increase the sensitivity to Olaparib, especially in EOC cells with hyperactive Ras and PI3K signalling. Previously, the combination of FK866, a NAMPT inhibitor, has been shown to sensitize Olaparib in models of TNBC, Ewing sarcoma and ovarian HGSC (*285-287*). However, the combination of FK866 and Olaparib has not yet been tested in EOC cells with mutations in the PI3K/Akt pathway.

1.5 Lactate is more than a metabolic waste in cancer

1.5.1 Lactate fuels the TCA cycle in cancer cells

Historically, lactate was considered as a 'waste' product of aerobic glycolysis (i.e., the Warburg effect) in cancer cells. However, this notion is being challenged by the recent data that show it is a metabolic fuel for cancer cells (Figure 1.12). In this regard, Chen et al reported that in H460 human lung cancer cells, extracellular lactate is imported and oxidized to pyruvate which in turn fuels the TCA cycle (*288*). Indeed, a substantial amount of lipids are synthesized using lactate-derived citrate as a substrate. Additionally, Sonveaux et al and Pavlides et al reported the utilization of lactate via the TCA cycle in mice tumour tissue (*289, 290*). Moreover, using $^{13}C_3$-lactate as a tracer, Faubert et al demonstrated that ^{13}C enrichment into pyruvate and TCA cycle intermediates in patients with non-small-cell lung cancer (NSCLC) (*291*), which provides the direct evidence of lactate contribution to central carbon metabolism in human tumours *in vivo*. Furthermore, the comparison of TCA cycle intermediates labelling from $^{13}C_3$-lactate and $^{13}C_6$-glucose indicated that lactate is a preferential substrate (*291*). Using metabolic flux analysis techniques, Hui et al quantitated the relevant contribution of lactate and glucose and found that lactate contribution to central carbon metabolism exceeded that of glucose in mice with lung tumours (*292*). However, there is scepticism about lactate as a preferential fuel of the TCA cycle. In this regard, Liu et al performed metabolic flux analysis (MFA) and demonstrated that TCA fluxes from glucose are higher than those from lactate in various strains of mice, which suggests that glucose contributes more than lactate as the TCA cycle substrate (*293*). Additionally, Ying et al argued that isotope labelling experiments overestimated net contribution of lactate and underestimated that of glucose due to isotope exchange between pyruvate and lactate (*294*). Nevertheless, these studies provided several lines of evidence supporting lactate as a metabolic fuel in cancer cells.

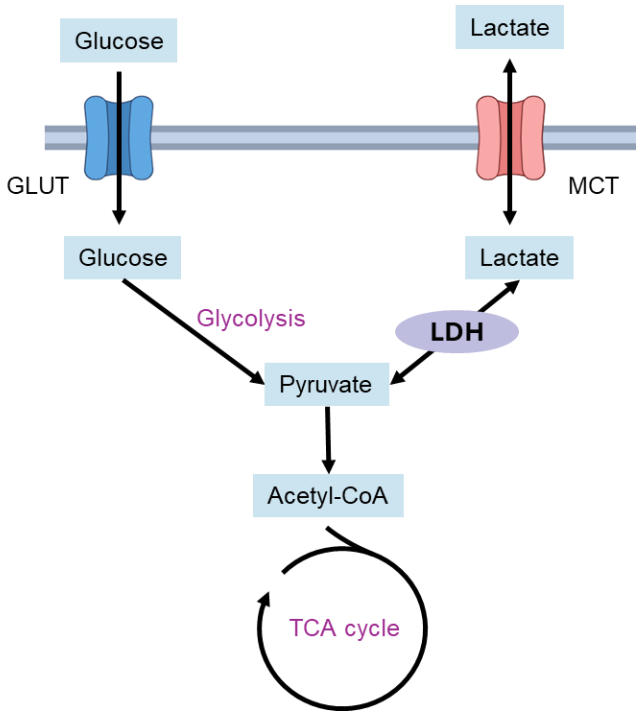


Figure 1.12 Exogenous lactate is a carbon source of the TCA cycle in cancer cells.
In addition to utilizing glucose derived carbons for the TCA cycle, cancer cells uptake extracellular lactate via MCT and oxidize it to pyruvate via LDH which subsequently enters the TCA cycle. GLUT: glucose transporter, MCT: monocarboxylate transporter, LDH: lactate dehydrogenase. Metabolites and enzymes are shown in blue rectangles and purple ovals, respectively.

1.5.2 LDH: key enzymes in lactate metabolism

The interconversion of pyruvate and lactate is catalysed by LDH with the concomitant interconversion of NADH and NAD^+ (Figure 1.13) (*295*). LDH is a tetramer and consists of M and/or H subunits that are encoded by LDHA and LDHB genes, respectively (*295*). Thus, there are five isoforms of LDH based on the combinations of M and H subunits: two homo-tetramers composed of four M or H subunits (LDHA/LDH5 and LDHB/LDH1, respectively) and three hetero-tetramers, LDH2 (1 M subunit and 3 H subunits), LDH3 (2 M subunit and 2 H subunits) and LDH4 (3 M subunit and 1 H subunit) (Figure 1.13) (*296*). LDH isoforms display various levels of expression in different types of organs. In this regard, LDH1 and LDH2 are highly expressed in heart and LDH3 is predominantly expressed in brain and kidneys (*297*). LDH4 and LDH5 are preferentially expressed in liver and skeletal muscle (*297*). The organ-

specific expression pattern is linked to the metabolic needs. Although all five LDH isoforms can catalyse the reversible conversion between pyruvate and lactate, they differ in the relative affinity to pyruvate and lactate due to the differences in the number of charged amino acid residues in the catalytic domain (*298*). LDH1 preferentially catalyses the oxidation of lactate to pyruvate for OXPHOS and thus, is highly expressed in, the largest lactate consuming organ, heart (*299*). In contrast, LDH4 and LDH5 have a greater affinity for pyruvate and preferentially catalyse the reduction of pyruvate to lactate coupled to NAD^+ regeneration from NADH (*295*). The high levels of LDH4 and LDH5 is essential for energy production in skeletal muscle under anaerobic conditions. Due to insufficient oxygen supply, glycolysis instead of OXPHOS is the main energy source. Given NAD^+ is a key cofactor for glycolysis, its regeneration from NADH maintains the high glycolytic flux (*298*). In malignant cells, the expression of LDH with high content of M subunit (e.g., LDH5 and LDH4) is favoured in general (*295*). Likewise, the rapid regeneration of NAD^+ from NADH through pyruvate reduction maintains the enhanced glycolysis activity (i.e., the Warburg effect).

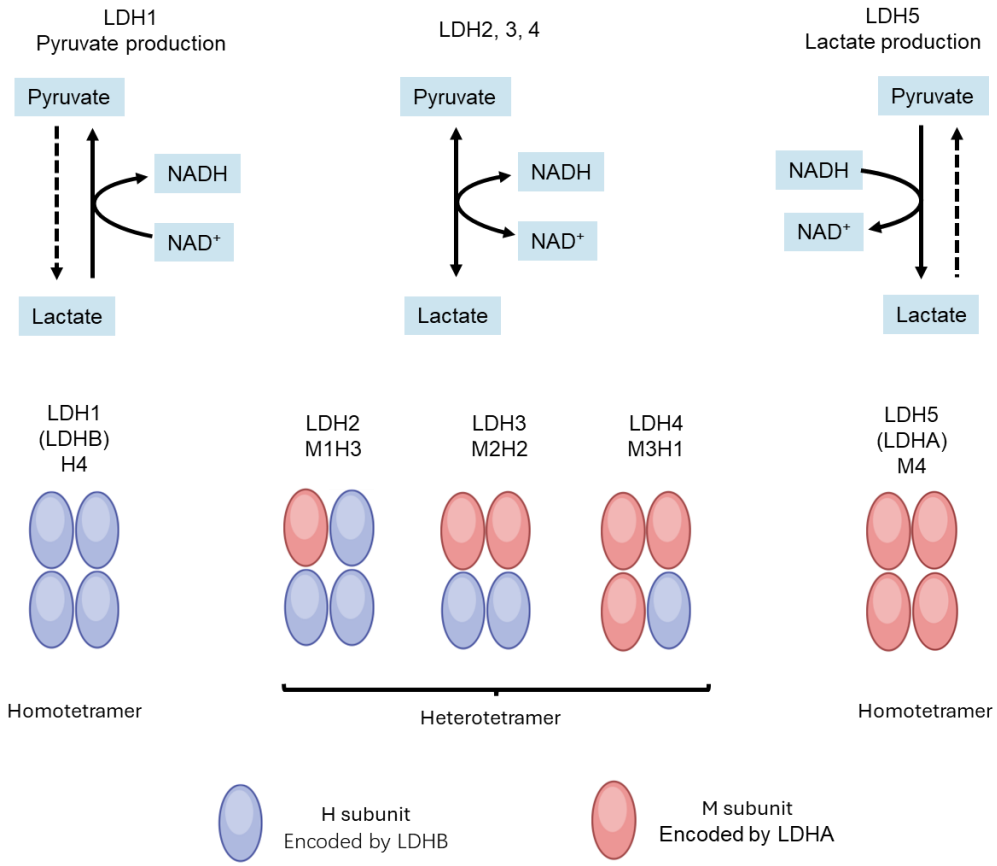


Figure 1.13 Structure and functions of LDH isoforms.
LDH consists of four subunits and catalyses the conversion of pyruvate and NADH to lactate and NAD^+. LDHA and LDHB genes encode M and H subunit, respectively. The two types of subunits differ in the amino acid residues surrounding the active sites, which impacts the substrate affinity. LDH1 and LDH5 are homotetramers consisting of four H and M subunits, respectively. Thus, LDH1 and LDH5 preferentially catalyse lactate oxidation and pyruvate reduction, respectively. The three heterotetramers (i.e., LDH2-4) catalyse the reversible conversion between pyruvate and lactate. LDH: lactate dehydrogenase.

In cancer cells, the expression of LDH isoforms is altered and regulated by a combination of transcriptional, post-transcriptional and translational mechanisms. In this regard, several transcription factors have been reported to modulate LDHA/LDH5 expression (*298*). For instance, HIF1 binds to the hypoxia response element (HRE) in the promoter region of LDHA gene and promotes its expression, which in turn adapts cancer cells to the hypoxic tumour microenvironment (TME) (*300*). c-MYC and FOXM1 are also positive regulators of LDHA expression (*301-304*). The promoter region of LDHB has been shown to undergo hypermethylation in prostate and pancreatic cancer cells, thereby inhibiting its expression

(*305, 306*). However, signal transducer and activator of transcription 3 (STAT3) and high-mobility group box 2 (HMGB2) promote LDHB expression in some types of cancer cells (*307, 308*). Moreover, microRNA (miRNA) has been demonstrated to regulate mRNA levels of LDHA and LDHB. For example, miR-200b reduces LDHA mRNA levels in glioma models, which in turn inhibits glycolysis and promotes invasiveness (*309*). PTM is an additional mechanism of LDHA and LDHB regulation. Acetylation and phosphorylation of LDHA have been shown to inhibit and enhance its activity, respectively (*310, 311*). LDHB deacetylation by SIRT5 promotes its activity and stimulates autophagy and proliferation of colorectal cancer cells (*312*).

Dysregulated expression of LDHA and LDHB is associated with enhanced cancer cell survival and tumour progression. In this regard, pharmacological inhibition or genetic ablation of LDHA has been shown to induce oxidative stress and inhibit cancer cell survival (*313, 314*). High levels of LDHA also stimulates epithelial-mesenchymal transition (EMT), a key process in cancer cell migration and invasion, in various types of cancer cells (*315, 316*). Angiogenesis is also enhanced by elevated expression of LDHA in endometrial cancer cells (*317*).

1.5.3 Monocarboxylate transporters (MCTs): key lactate transporters

MCTs are a family of 14 transporters with sequence homology and are encoded by the SLC16A gene (*318*). However, only four of the MCTs (i.e., MCT1-4) have been shown to mediate cross-membrane transport of monocarboxylate, including lactate, pyruvate and ketone bodies (*318, 319*). The transmembrane trafficking mediated by MCT1-4 is coupled to proton movement in the same direction (i.e., monocarboxylate and proton symport) and involves an ordered mechanism (*295, 320*). Sequential binding of protons and monocarboxylate anions causes conformation change of MCT1-4, which in turn exposes them to the opposite side of the plasma membrane (*321-323*). This is followed by sequential release of monocarboxylate anions and protons (*321-323*). Of note, MCT1-4 mediated transport can be bi-directional and the direction (i.e., influx or efflux) is dependent on the relative levels of monocarboxylate and proton gradient across the plasma membrane (*318*).

Additional ancillary proteins are necessary for the correct localization of MCT1-4 to the plasma membrane. In this regard, basigin (CD147) binds to MCT1, MCT3 and MCT4 while embigin (GP70), the homolog of basigin, binds preferentially to MCT2 (*324*).

MCT1-4 display distinct expression profile across tissue and organs. In this regard, MCT1 is the most widely expressed MCT isoform and the expression of MCT4 is upregulated in highly glycolytic and anaerobic tissue (e.g., white skeletal muscle) (*325, 326*). MCT2 expression is mainly in neurons at postsynaptic density, red skeletal muscle and heart, and MCT3 is expressed exclusively in retinal pigment epithelium and choroid plexus epithelia (*325*). The affinity to substrates also varies across MCT1-4. MCT1 has a higher affinity for both lactate and pyruvate than MCT4 as evidenced by a lower K_m value (i.e., the substrate concentration where transport reaches 50% of maximum) (Table 1.2) (*318, 327-330*). Interestingly, MCT1 shows higher affinity to pyruvate than lactate while MCT4 exhibits the opposite trend with a much lower affinity to pyruvate (*329*). MCT2 shows an even higher affinity for both lactate and pyruvate in comparison to MCT1 (*318, 330*). The heterogenous affinity profile correlates with the tissue and organ expression patterns, which reflect the metabolic activities. For example, high levels of MCT1 and/or MCT2 in heart facilitates the uptake of exogenous lactate to fuel the TCA cycle (*320*). The low affinity MCT4 enriched in white skeletal muscle mediates the secretion of high concentrations of lactate under conditions of strenuous activities while preserving pyruvate (*318, 328*).

The expression of both MCT1 and MCT4 has been shown to be modulated by transcriptional mechanisms in cancer cells. In this regard, the promoter regions of MCT1 can be bound by several transcription factors, including MYC, PGC-1α, CREB and NRF2 (*320, 326, 331, 332*). For instance, c-MYC augments MCT1 expression and lactate export by regulating the promoter of MCT1. p53 directly interacts with MCT1 promoter and modulates the stability of MCT1 mRNA (*331*). Under conditions of hypoxia, p53 loss enhances MCT1 expression and facilitates lactate secretion in highly glycolytic cancer cells (*333*). Moreover, HIF-1α binds to the promoter regions of MCT4 and enhance its expression under conditions of hypoxia (*326*).

In cancer cells, MCT1 and MCT4 are the major isoforms of MCT and display functional

redundancy and heterogeneity. In this regard, Sheng et al showed that in osteosarcoma cells, MCT1 inhibition by AZD3965 reduced the consumption rates of exogenous lactate and blocking MCT4 by VB124 decreased lactate concentrations in media, which indicates that MCT1 and MCT4 mainly mediate lactate uptake and release, respectively (*334*). However, dual inhibition of MCT1 and MCT4 caused a further reduction in extracellular uptake and a greater accumulation of intracellular lactate, thereby indicating the functional redundancy (*334*). However, selectivity of the inhibitors of MCT1 and MCT4 is a major limitation of these studies. In this regard, VB124 inhibits MCT4 with greater potency than MCT1 (EC_{50}: MCT1 = 24μM vs MCT4 = 19nM (lactate efflux)) (*335*). Given the high dose applied by Sheng et al (10μM), potential off-target inhibition on MCT1 was possible (*334*). Another gap is the lack of data about the functional differences between MCT1 and MCT4 in other types of cancer cells.

MCT isoforms	**K_m lactate (mM)**	**K_m pyruvate (mM)**
MCT1	3-6	1-2.5
MCT2	0.5-1	0.02-0.1
MCT3	2-10	NA
MCT4	25-30	150

Table 1.2 Substrate affinity and gene sequence identity to MCT1 of different MCT isoforms. MCT: monocarboxylate transporter, NA: not available. Table adapted from Draoui and Feron (*295*).

1.5.4 Uncoupling of glycolysis and TCA cycle: potential subcellular compartmentation of lactate metabolism

Multiple lines of evidence suggests that glycolysis and the TCA cycle are uncoupled at the point of lactate. Initial observations showed that glucose catabolism via glycolysis proceed to lactate production even under conditions of ample oxygen supply (*336*). In both resting and exercising muscle, the partial pressure of oxygen (PO_2) is approximately 40 Torr and 3-4 Torr respectively which is well above the critical PO_2 for maximal mitochondrial respiration (1-2 Torr) (*337-339*). However, net lactate production and secretion were observed and most lactate is re-imported by muscle and heart for oxidation in the TCA cycle (*337-339*). More

recently, using $^{13}C_6$-glucose and $^{13}C_3$-lactate as tracers, Hui et al found that a substantial amount of serum lactate is derived from glucose via glycolysis and circulating lactate is the major fuel of the TCA cycle in all mice tissues except brain (*292*). Furthermore, the quantitative analysis of metabolic fluxes indicates that TCA cycle labelling from $^{13}C_6$-glucose is primarily indirect via circulating lactate in both fed and fasting mice (*292*).

The above-described uncoupling occurs between different tissues and/or organs. Additionally, there is evidence of such uncoupling phenomenon in the same cell. For instance, Bouzier et al reported lower ^{13}C enrichment in glutamate from 1-^{13}C-glucose than that of alanine (i.e., 36.7% and 22.5%, respectively) in glioma cells (*340, 341*). Given glutamate and alanine equilibrates with α-KG and pyruvate, these data suggest the isotopic dilution effect in central carbon metabolism due to carbon entry from unlabelled source. As lactate is the precursor of pyruvate and if exogenous lactate mixes with glycolysis derived lactate, isotopic dilution would be expected, and acetyl-CoA labelling would correlate with that of intracellular lactate. However, when 3-^{13}C-lactate was used as a tracer, higher ^{13}C enrichment in glutamate was observed than that of alanine (i.e., 69% and 32%, respectively) (*340*). Furthermore, poor association between intracellular lactate labelling and acetyl-CoA was detected (i.e., 59% and 77.5% respectively) (*340*). Collectively, these data could not fit with the canonical model of lactate metabolism and indicates the existence of two separate pools of lactate and pyruvate (i.e., the lactate metabolome model). In addition, Bünger reported low rates of 3-^{14}C-lacate production when cardiomyocytes were incubated with 3-^{14}C-pyruvate at the concentration with no evident inhibition of LDH (*342*). This result suggests the existence of a non-labelled or low labelled pool of pyruvate which is separate from the imported pyruvate pool (*342*).

Such uncoupling phenomenon in the same cell can be rationalized by subcellular compartmentation of lactate metabolism (i.e., the lactate metabolon model; metabolon: the assembly of sequential metabolic enzymes and cellular structural elements (e.g., actin) into a supramolecule complex (*343*)). The canonical model of central carbon metabolism states that pyruvate derived from glucose enters mitochondria via mitochondrial pyruvate carrier (MPC) where it condenses with oxaloacetate to fuel the TCA cycle (Figure 1.14A). Excessive pyruvate can be reduced to lactate which is then exported to extracellular space (Figure 1.14A).

Exogenous lactate can be imported and oxidised to pyruvate which presumably mixes with the pool of glycolysis derived pyruvate before entering the TCA cycle (Figure 1.14A). In contrast, the lactate metabolon model suggests that imported lactate forms a separate pool without mixing with glycolysis-derived lactate and is readily oxidized to pyruvate which is subsequently rapidly oxidized via the TCA cycle in mitochondria (Figure 1.14B). Thus, the export of glucose-derived lactate and re-import of exogenous lactate uncouple glycolysis and TCA cycle.

However, these above two studies in glioma and cardiomyocytes rely solely on isotopic labelling patterns which could not directly imply metabolic flux, especially in non-steady state. Additionally, they lack the support from genetic and cell imaging studies to understand the mechanisms.

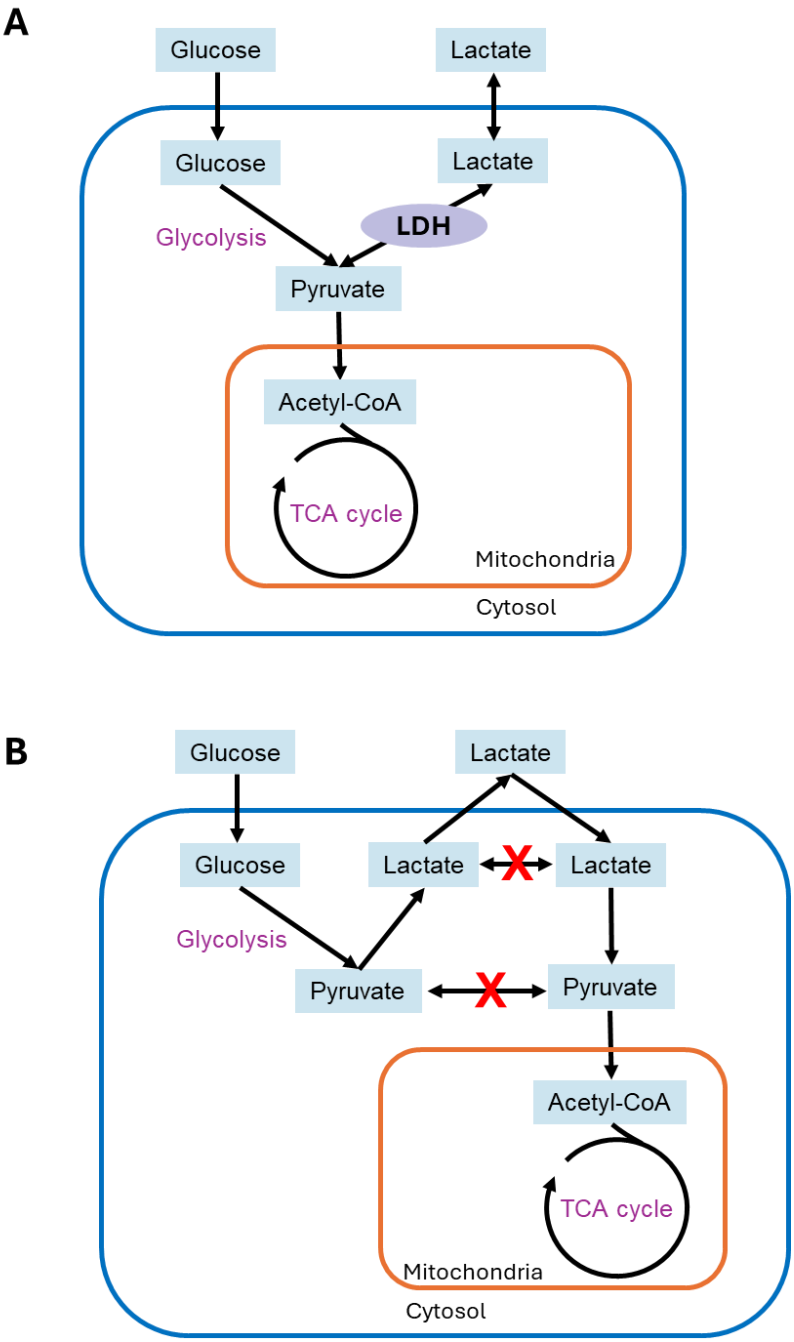


Figure 1.14 Two models of lactate metabolism in cancer cells.

(A) The canonical model. Glucose is converted to pyruvate through glycolysis which then enters the TCA cycle. Excessive pyruvate can be reduced to lactate which is then released into the extracellular space. The exogenous lactate can also be imported and oxidized to pyruvate which mixes with the glycolysis derived pool before entry into the TCA cycle. (B) The lactate metabolon model. Glycolysis is uncoupled with the TCA cycle. Glycolysis derived pyruvate is preferentially converted to lactate which is then exported to the extracellular space. The exogenous lactate can be oxidized to pyruvate to fuel the TCA cycle. Of note, the exogenous derived lactate and pyruvate form a separate pool without mixing with the glycolysis-derived pool. Red crosses indicate no exchange between the two pools.

1.6 Metabolomics: a system biology tool for cancer research

1.6.1 Metabolic profiling

Metabolomics is a high-throughput technique used to study metabolome in biological samples, including cells, organs, tissues and biofluids. Metabolome refers to small molecule metabolites with molecular weight between 50 and 1500Da (*344*). As metabolic activities are downstream of genomic, transcriptomic and proteomic regulators, the identification and quantitation of the metabolome offers a direct measurement of the molecular phenotypes, which is an advantage over other omics studies (*345*). Therefore, metabolomics is a powerful technique in cancer research and has been applied for quantitative phenotyping, biomarker discovery and revealing mechanisms underlying oncogenesis (*346, 347*).

A typical metabolomics workflow includes experimental design, sample collection and quenching, metabolite extraction, data acquisition, and data analysis (*348, 349*). During the experiment design stage, it should be decided whether to perform targeted or untargeted metabolomics. Targeted metabolomics identifies and quantifies a limited number of metabolites (usually less than 100) (*345*). Its advantage is the use of internal standards (IS) for validation to reduce false positives and therefore, the results are more accurate (*345, 350*). However, prior knowledge and hypothesis are required to select the set of metabolites for analysis and its partial metabolome coverage may increase the risk of misinterpretation of metabolic activities (*345*). In contrast, untargeted metabolomics offers a wider coverage of metabolome, and no prior knowledge or hypothesis are necessary (*351*). However, no single method can provide whole metabolome coverage. Given that sample preparation and analytical techniques may affect the subset of metabolites identified, the proper methods should be chosen carefully. The choice of sample preparation method should also be based on the nature of the biological samples (i.e., cells, organs and biofluids) (*345*).

The most critical steps in the metabolomics workflow are sample quenching and metabolite extraction. Rapid quenching is necessary to terminate all metabolic activities and prevent

perturbations of metabolite abundance (*349, 352*). Data acquisition can be performed on mass-spectroscopy (MS) based techniques or nuclear magnetic resonance (NMR) techniques (see section 1.6.3) (*345*). Data analysis is performed with bioinformatics tools and starts with metabolite identification which is dependent on metabolite libraries (e.g., public library: the Human metabolome database) (*353, 354*). Statistical analysis is subsequently performed to identify significantly changed metabolites which are then linked to biological context by enrichment and pathway analysis (*354, 355*). Metabolomics can also be integrated with other omics studies (e.g., proteomics) for a deeper understanding of molecular mechanisms (*354, 356*).

1.6.2 Metabolic flux analysis

Although measuring metabolite concentrations is informative, these concentrations do not necessarily align with metabolic pathway activity (i.e., metabolic flux). For example, the accumulation of a metabolite can result from upregulated production or inhibited consumption (*357*). Therefore, metabolite concentration data should be integrated with flux data to achieve a deeper understanding of the metabolic phenotype (*357*). Metabolic fluxes are inferred by isotope tracers. For instance, $^{13}C_6$-glucose and $^{13}C_5$-glutamine tracers are commonly used for investigating fluxes of upper metabolism (i.e., glycolysis and PPP) and lower metabolism (i.e., TCA cycle), respectively (*358, 359*). The ^{13}C atoms in ^{13}C labelled substrates are transferred to downstream metabolites and therefore, the levels of ^{13}C enrichment provides an intuitive interpretation of the metabolic activity (*357, 360*).

Additionally, metabolic fluxes can be quantitatively determined by computational models. In this regard, isotopomer spectral analysis (ISA) is a commonly used computational tool for analysis of *de novo* FA synthesis (Figure 1.15) (*361*). Based on the mass isotopomer distribution (MID) data of FA from labelling studies, two parameters can be determined by ISA. As cytosolic acetyl-CoA is a substrate for FA synthesis, the D value in ISA estimates the fractional contribution of the isotope tracer to the pool of lipogenic acetyl-CoA (*361, 362*). The g(t) value quantifies the relative proportion of FA that is newly synthesised during the labelling time t (*361, 362*). Typically, ISA is performed with multiple parallel labelling

experiments using different tracers (*363*). These studies reveal the relative contribution of different nutrients for FA *de novo* synthesis (*363*).

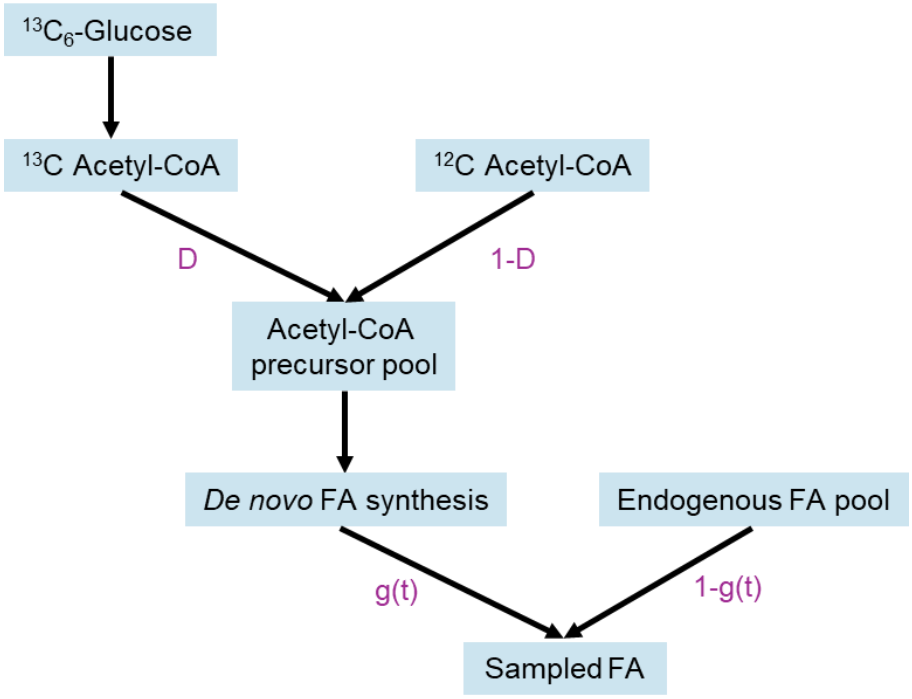


Figure 1.15 Isotopomer spectral analysis of FA de novo synthesis.
The ISA model is a computational model to estimate two parameters based on the MIDs of FA. Acetyl-CoA is a substrate for FA *de novo* synthesis and partially labelled from the ^{13}C tracer (e.g., $^{13}C_6$-glucose in this case). The fractional contribution of the ^{13}C tracer to lipogenic acetyl-CoA is estimated by the parameter D. The FA pool sampled from cancer cells consists of newly synthesized FA during the labelling study and endogenous FA. The parameter g(t) provides an estimate of proportion of *de novo* synthesized FA during the exposure to the ^{13}C tracer. ISA: isotopomer spectral analysis, FA: fatty acid.

1.6.3 Analytical platforms used in this study

Multiple types of MS techniques are available for metabolomics (*349*). For simplicity, only the analytical platforms relevant to this study are described here (i.e., gas-chromatography (GC)-MS (single quadruple (Q)) and liquid-chromatography (LC)-MS/MS (Q-time of flight (TOF))). Separation-based MS is a key analytical platform to study metabolomics. MS achieves metabolite identification based on the mass-to-charge (*m/z*) ratio of analytes (*345*). Due to the complexity of biological samples, multiple analytes may exhibit the same *m/z* ratio which limits the accuracy of identification (*364*). One strategy is to add another parameter: retention

time (RT). In this regard, metabolites are first separated by chromatographic system and elute at different timepoints for MS analysis (*345*). Such separation also avoids overloading MS or ion suppression, which reduces sensitivity (*365*).

The chromatographic system consists of stationary phase housed in a column and mobile phase. Due to the unique physicochemical properties of metabolites, they interact differently with the stationary phase and therefore, separation is achieved (*345*). Based on the mobile phase, the chromatographic system is divided into two categories: GC and LC. In GC, the mobile phase is inert gas (e.g., helium and hydrogen) and the stationary phase can be a liquid that coats the capillary column or a solid (*366*). Separation is achieved by gradually increasing column temperature to facilitate the dissociation of metabolites (*366*). The analytes are first vaporised and therefore, GC can be used for separation of volatile analytes (*366*). Given the high boiling points of many metabolites (e.g., amino acids and TCA cycle intermediates), chemical derivatization is required to increase the volatility and thermal stability (*367*). Tert-butyldimethylsilylation and trimethylsilylation are common derivatization methods (*367, 368*). LC enables the analysis of non-volatile or thermally unstable compounds which cannot be performed by GC. Reversed-phase chromatography (RP) is a common technique which uses non-polar stationary phase and polar mobile phase (e.g., water) (*369*). C18 is a widely used RP column for metabolomics that separates various analytes, include semipolar metabolites (e.g., phenolic acids) (*370*). Polar metabolites (e.g., amino acids) can be separated by the hydrophilic interaction liquid chromatography (HILIC) technique that uses polar stationary phase (*370*). By applying a high pressure and reducing the size of the particles (i.e., the stationary phase), the resolution of LC and column capacity can be improved, and it is called high performance liquid chromatography (HPLC) (*371*).

The MS system consists of an ion source, a mass analyser and a detector. After eluting out of GC or LC, the compounds first gain positive or negative charge (i.e., ionization) in the ion source. Electron impact ionization (EI) is commonly used in GC-MS and is a type of hard ionization method (*372*). In EI, molecules in gaseous phase collide with high energy electrons and are excited which subsequently dissociate to generate charged fragments. The fragmentation pattern is highly specific (i.e., molecular fingerprint) and therefore, enables the

identification of metabolites (*372, 373*). MS with an electrospray ionization (ESI) source is commonly coupled with LC. The liquid eluting out of LC is introduced to a strong electric field in a fine spray, which generates droplets with electric charge. By applying drying gas (i.e., nitrogen), the solvent in the droplets is evaporated and thus, the droplet size decreases and the electric density increases (*370, 374*). Finally, columbic explosion of the droplet occurs, and solvent-free analytes are produced (*370, 374*).

The charged analytes or fragments are next introduced to the mass analyser. A quadrupole is a type of commonly used mass analyser and consists of four parallel cylindrical rods (*375*). Oscillating electric field is created by applying a voltage of opposite polarity to adjacent rods (*375*). Analyte ions are selected based on their trajectory stability in the oscillating filed and the modulation of voltages allows the selection of a specific *m/z* or a range of *m/z* (*375*). TOF is another common type of mass analyser and consists of a field-free flight tube. The charged analytes are introduced to the flight tube by applying an electric field (*376, 377*). All like-charged ions reach the flight tube with the same kinetic energy but various velocity due to different mass (*376, 377*). Therefore, the ions reach the detector at different timepoints and are separated. Q mass analyser offers high sensitivity and TOF mass analyser achieves high resolution and fast scan rates (*345*).

Configuration of single (MS or MS1) and tandem (MS/MS or MS2) mass analysers can be used for metabolomics. GC is commonly coupled with a single Q while LC can be linked to tandem configure rations (e.g., QTOF) (*370*). QTOF is ideal for global profiling of metabolomics (i.e., untargeted method) and consists of two Q coupled to a TOF (*378*). The first Q (Q1) operates as a mass filter to select ions with a particular *m/z* or a range of *m/z* (*379*). The second Q (Q2) is a collision cell where the precursor ions from Q1 are fragmented by bombarding with neutral gas molecules (e.g., nitrogen) (*379*). This type of fragmentation is called collision induced dissociation (CID). The ion fragments (i.e., product ions) are then analysed by TOF. The Q2 can also operate in radio frequency (RF) only mode without fragmenting ions from Q1. Therefore, QTOF can operate in two modes to analyse the unfragmented ions or fragments for untargeted profiling. One data acquisition strategy is the sequential window acquisition of all theoretical mass spectra (SWATH) (Figure 1.16) (*380*). SWATH is a type of

data independent acquisition (DIA) mode where no pre-determined criteria is required (*381*). SWATH starts with an initial ion scan without ion fragmentation in Q2 to collect information about precursor ions (*380*). Next, the precursors ions selected in small consecutive windows (approximately 20Da but can be adjusted) in Q1 are introduced to and fragmented in Q2 (*382, 383*). The precursor and product ions are then simultaneously monitored in the TOF. The advantage is the full coverage of precursor ion mass range. However, decoding the fragmentation patterns can be challenging and searching multiple libraries of MS1 and MS2 data may be necessary (*351*).

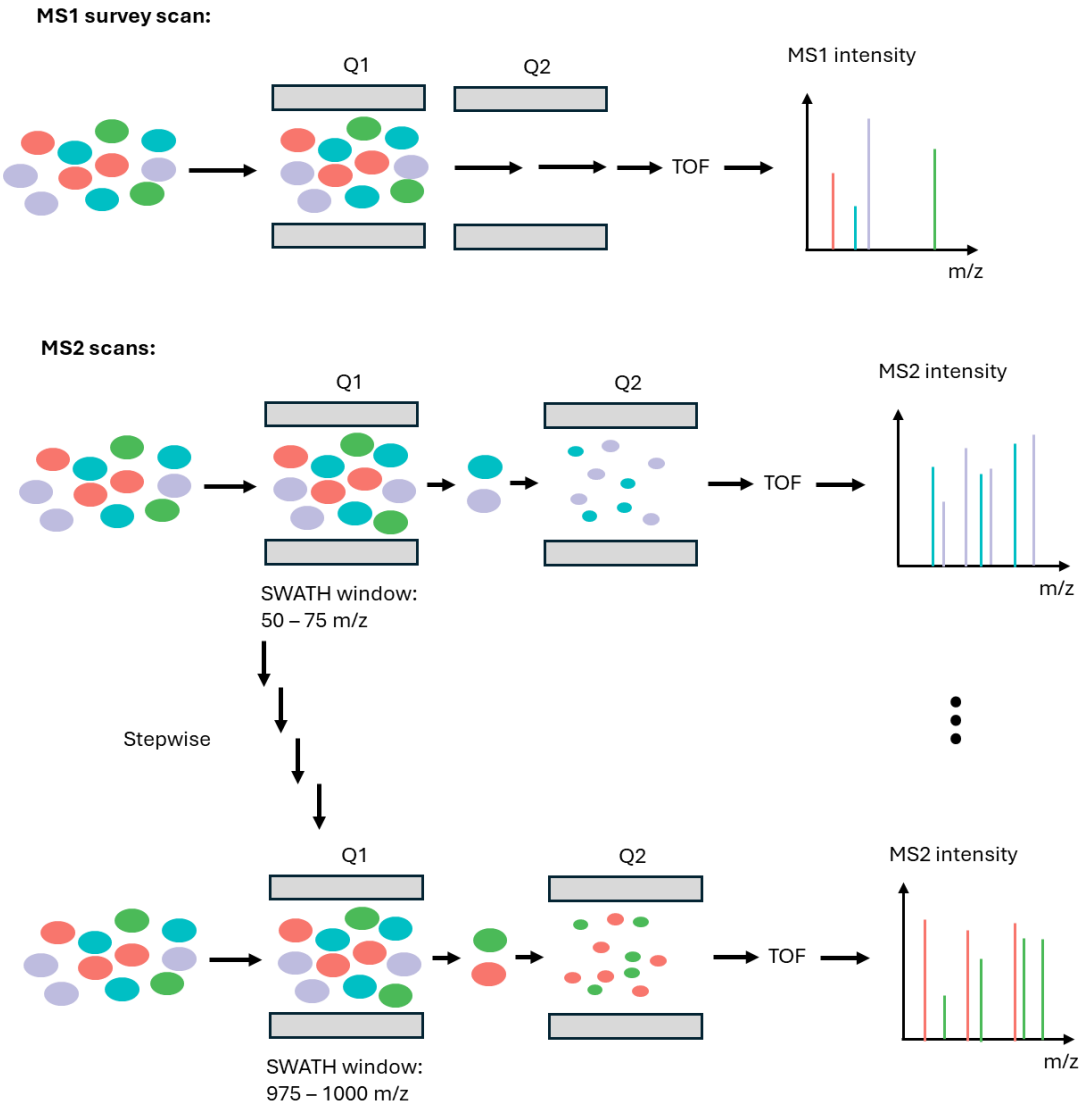


Figure 1.16 The principle of SWATH MS.

The SWATH method is a data-independent acquisition method and is typically performed on a hybrid MS (e.g., Q-TOF in this study). It starts with an initial survey scan where no fragmentation in Q2 occurs. Thus, a spectrum of all the precursor ions (MS1) is recorded. This survey scan is followed by a series of scans of the fragmented ions (MS2). In detail, the precursor ions are selected in small consecutive windows (e.g., 25 *m/z*) and then introduced to Q2 for fragmentation. The fragmented and precursor ions are then monitored and spectra of MS2 ions are recorded. SWATH: sequential window acquisition of all theoretical mass spectra, TOF: time-of-flight MS. Different coloured ovals indicate different precursor ions.

NMR is an analytical tool based on the transition in energetic status of nuclear spins in a strong external magnetic field. For nuclei with non-zero spin (e.g., ^{1}H: spin = 1/2), two spin states exist: +1/2 with low energy and -1/2 with high energy (*384*). The difference in energy is usually given as a frequency and correlates with the strength of the external magnetic field (*384, 385*). Given the small energy difference, strong external magnetic field is necessary for NMR. Under conditions of thermal equilibrium, there is no coherence in the nuclear spins, i.e. no bulk signal (*384, 385*). However, in an NMR spectrometer, nuclear spin excitation (i.e., transitions from low to high energy state) can be achieved by applying a RF radiation corresponding to the energy difference, creating a coherence in nuclear spins (*384, 385*). The termination of the RF radiation allows nuclear spin relaxation to equilibrium, which generates an oscillating and decaying signal (i.e., a free induction decay (FID)) (*384, 385*). The FID is a time-domain signal and transformation into a frequency-domain signal via Fourier Transformation is required to interpret the data (*384, 385*).

The protons (^{1}H) in metabolites are surrounded by electrons and a secondary magnetic field is generated due to the movement of electrons in the external field. The secondary field reduces the effective strength of the nucleus from the external applied field (i.e., shielding) and the frequency of the oscillating signals within the FID is changed (*384, 385*). Therefore, protons in different chemical environment induce distinct signals (resonances). NMR spectra are plotted as chemical shift (δ) which is based on the difference in the resonance signal frequency relative to the reference standard (e.g., 3-(trimethylsilyl)-2,2′,3,3′-tetradeuteropropionic acid (TSP) or deuterated 4,4-dimethyl-4-silapentane-1 sulfonic acid (DSS)) (*384-386*). Spin (J) coupling occurs due to the magnetic interaction between neighbouring nuclei in different magnetic or chemical environments, which causes the splitting of NMR signals (*384, 385*). Thus, a metabolite can be identified by the combination of chemical shift and signal splitting patterns.

1.7 Hypotheses and aims

1.7.1 Chapter 3

As described in sections 1.2.2 to 1.2.4, dysregulated PI3K/Akt signalling causes metabolic reprogramming in cancer cells. In this regard, the PI3K/Akt pathway promotes glucose metabolism and anabolic metabolism (e.g., *de novo* FA synthesis), and regulates redox balance. In EOC patients, Gungar et al reported that the Akt inhibitor GSK795 reduces the uptake of fludeoxyglucose F^{18} (FDG), which is a radiotracer for monitoring glucose uptake (*387*). However, little is known about glucose metabolic fate and the wider impact on cellular metabolism in EOC cells with mutations in the PI3K/Akt pathway.

Hypothesis:

Enhanced activation of the PI3K/Akt signalling promotes glucose and glutamine uptake, and anabolic metabolism in EOC cells.

Objectives:

- Examine the global impact of genomic activation PI3K/Akt signalling on cell metabolism in a model of EOC.
- Probe central carbon metabolism in this model with hyperactive PI3K/Akt signalling.

1.7.2 Chapter 4

As described in section 1.4.5, NAD^+ depletion by FK866, the NAMPT inhibitor, enhances sensitivity to Olaparib in multiple types of tumour cells (*285, 286, 388*). Also, dysregulated Ras and PI3K pathways increases the demands for NAD^+ by modulating tumour metabolism, which may create metabolic vulnerabilities and imply an improved response to the

combination. However, the combination has not been tested in cancer cells with mutations in the Ras and PI3K signalling pathways and thus, it remains unclear whether these cancer cells are more vulnerable. Preliminary data from our laboratory confirmed the efficacy of the combination in a panel of 10 EOC cell lines as evidenced by FK866 induced decreases in Olaparib IC_{50} values (Figure 1.17A). Of note, OVCAR-8 cells (KRas mutant) showed higher sensitivity to the combination treatment as evidenced by enhanced caspase activation in comparison to COV318 cells (wild-type (WT) in genes involved in the Ras and PI3K signalling; referred to as 'Ras/PI3K WT' in this thesis) (Figure 1.17B). Thus, these data warrant further investigation.

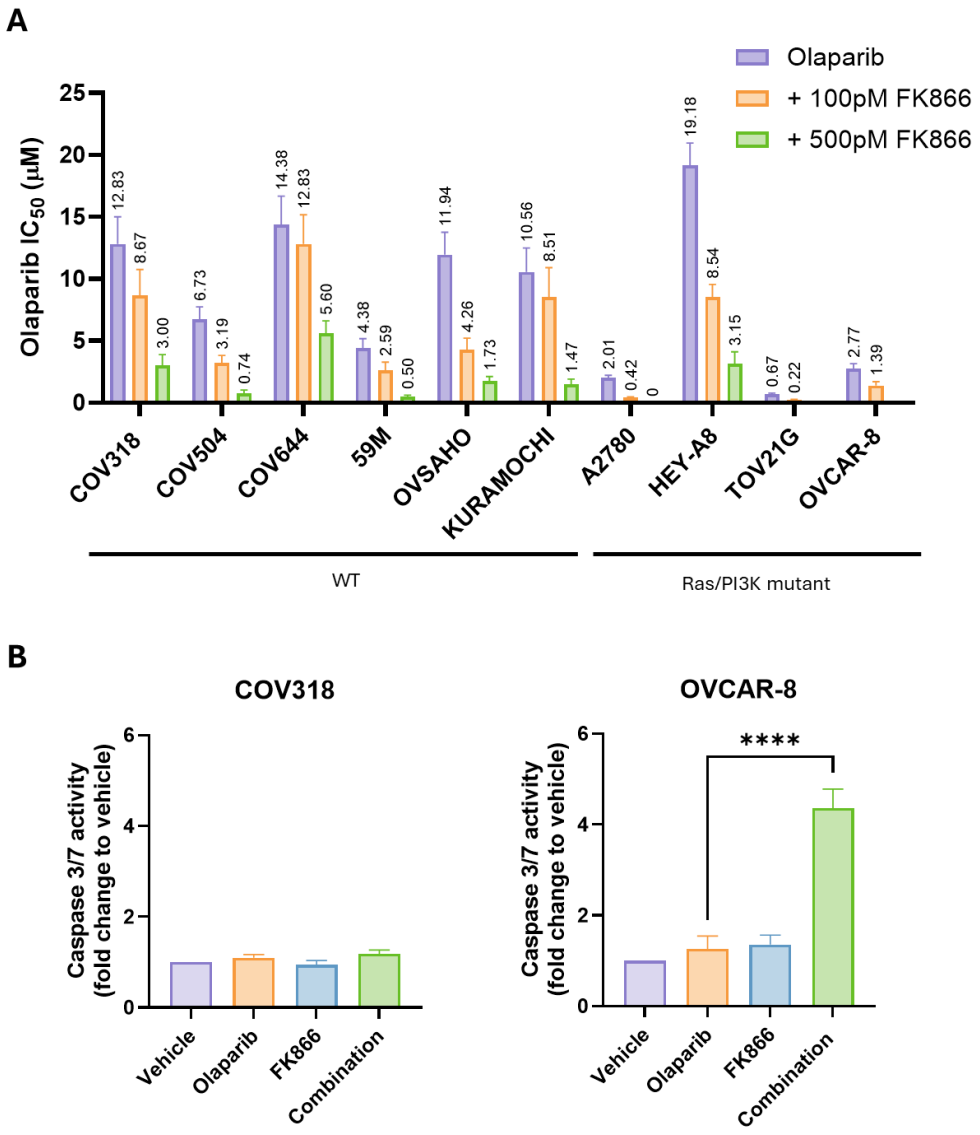


Figure 1.17 FK866 increased the sensitivity of Olaparib in a panel of EOC cells, especially those with mutations in genes involved in the Ras/PI3K pathway.

(A) IC_{50} values of Olaparib in the absence or presence of FK866. A panel of EOC cells were treated with 1μM Olaparib and/or 100pM/500pM FK866 for 6 days. Cell density was measured by SRB assay and IC_{50} values were calculated by least squares fit using GraphPad Prism (version 10.0.0). Data represent mean ± 95% confidence interval from three biological repeats. (B) Caspase-3/7 activity of COV318 (Ras/PI3K WT) and OVCAR-8 (KRas mutant) cells. The cells were treated with 1μM Olaparib and/or 1nM FK866 for 6 days. Caspase-3/7 activity and cell density were measured by the Caspase-Glo® 3/7 assay and SRB assay, respectively. The caspase-3/7 readout was normalised against cell density and the data were expressed as fold changes. Data represent the mean ± SD of three independent replicates. Statistical significance was calculated by one-way ANOVA followed by post-hoc Tukey test. **** $p < 0.0001$. The data were preliminary data obtained by Dr Michael Gruet in the Keun laboratory and the figures were re-plotted.

Hypothesis:

Mutations in the Ras and PI3K pathways enhance the sensitivity to combined FK866 and Olaparib treatment in EOC cells.

Objectives:

- Investigate whether the combination of FK866 and Olaparib is more effective in EOC cells with mutations in the Ras and PI3K signalling.
- Examine the mechanisms of the combination effect and any sensitization effects of mutations in the Ras and PI3K signalling.

1.7.3 Chapter 5

The panel of EOC cell lines tested in chapter 4 and previously in our lab are not isogenic. Thus, the interpretation of the data is confounded by the complex genetic landscape. Also, these data were obtained from *in vitro* studies and the efficacy of the combination should be tested by *in vivo* models. To this end, a panel of ID8 cells, which is a murine model of ovarian HGSC, was chosen. Given the near universal loss of p53 in ovarian HGSC, *Trp53* has been deleted in ID8 cells. CRISPR knockout technology has been applied to generate isogenic pairs with deletion of *Nf1* and *Pten* (negative regulator of the Ras and PI3K pathway, respectively). Additionally, the ID8 cells can be injected into immunocompetent mice (i.e., syngeneic) and develop ascites and omental metastasis which recapitulates human ovarian HGSC patients.

Hypothesis:

Loss of Nf1 or Pten in ID8 cells enhances sensitivity to the combination of FK866 and Olaparib.

Objectives:

- Investigate the responses to the combination of FK866 and Olaparib in the panel of ID8 cells.
- Examine the mechanisms of the combination in ID8 cells.
- Investigate whether the combination inhibits tumour growth and improves overall survival in mice with ID8 *Trp53*$^{-/-}$*; Pten*$^{-/-}$ tumours.
- Probe the metabolic impact of the combination.

1.7.4 Chapter 6

As described in section 1.6.4, cytosolic compartmentation of lactate metabolism has been proposed over two decades ago. However, they lack the support from genetic and cell imaging studies and thus are largely ignored. Preliminary data from our laboratory and other groups showed the uncoupling of glycolysis and the TCA cycle which was associated with a discrepancy in pyruvate and citrate labelling (*292, 340, 342*). This phenomenon could be rationalized by compartmentation of lactate metabolism (Figure 1.18A-B). In this regard, using $^{13}C_6$-glucose and $^{13}C_3$-lactate as single tracers, the TCA cycle intermediates citrate and α-KG were largely derived from exogenous lactate than glucose although both glucose and lactate made similar contribution to pyruvate (Figure 1.18A-B). Therefore, these data indicate the urgent need to further investigate the kinetics of lactate metabolism.

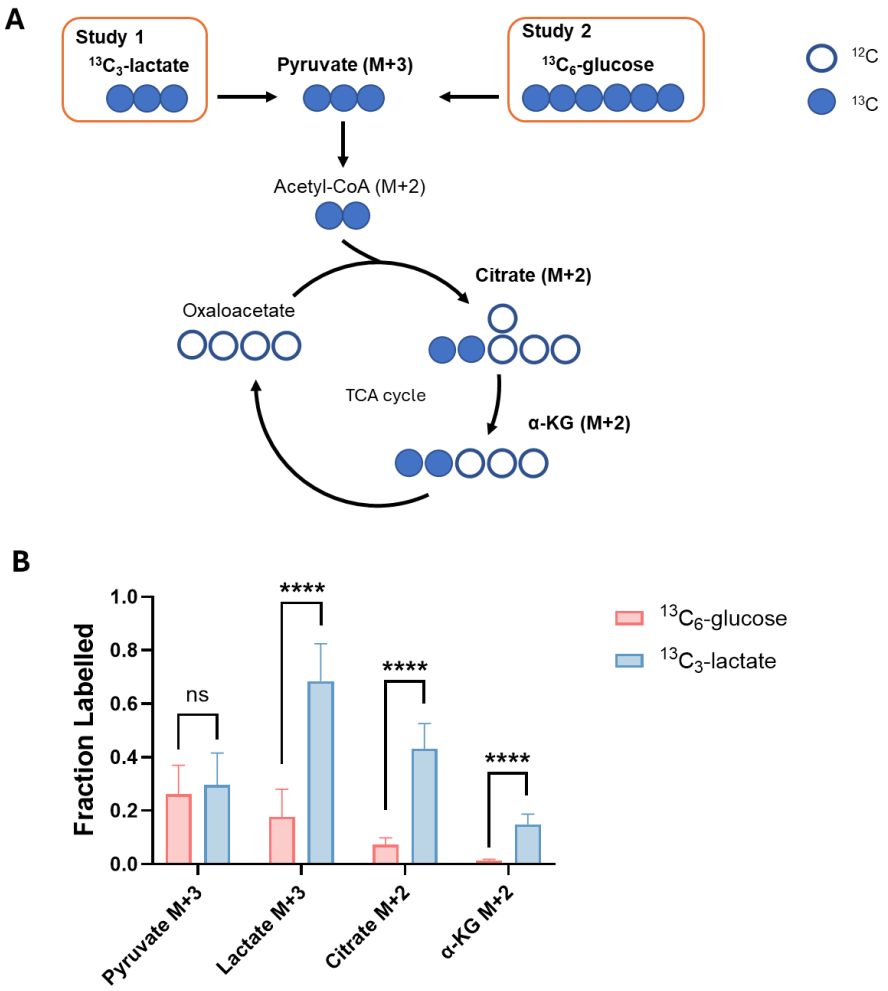


Figure 1.18 Glycolysis was uncoupled from the TCA cycle in HCT116 cancer cells.
(A) Schematic showing ^{13}C labelling patterns using $^{13}C_6$-glucose or $^{13}C_3$-latcate as a single tracer in parallel studies. Both $^{13}C_6$-glucose or $^{13}C_3$-latcate produce M+3 labelled pyruvate which enters the TCA cycle. Thus, the TCA cycle intermediates (e.g., citrate) are labelled M+2. Blue and empty circles indicate ^{13}C and ^{12}C atoms, respectively. (B) Fraction of M+3 pyruvate and lactate, and M+2 citrate and α-KG. The HCT116 colon cancer cells were incubated with $^{13}C_6$-glucose and unlabelled lactate or $^{13}C_3$-lactate and unlabelled glucose for 2h. The concentrations of glucose and lactate were kept the same in the two labelling studies (i.e., 5.6mM glucose and 10mM lactate). The intracellular metabolites were extracted and analysed by GC-MS. Data represent the mean ± SD of three independent replicates. Statistical significance was calculated by t tests. **** $p < 0.0001$, ns: not significant. (Data from Yitao Xu, MRes thesis 2019 (*389*)).

MCT1 and MCT4 are the main lactate transporters in cancer cells. Our preliminary data showed that pharmacological inhibition or genetic deletion of MCT1, but not MCT4, increased glucose contribution to pyruvate and the TCA cycle intermediate citrate (Figure 1.19). Also, deletion of both MCT1 and MCT4 led to a further increase (Figure 1.19). These data suggest that the compartmentation of lactate metabolism may be dependent on MCT and MCT4, especially MCT1. Thus, it would be interesting to understand their roles in regulating compartmentation of lactate metabolism.

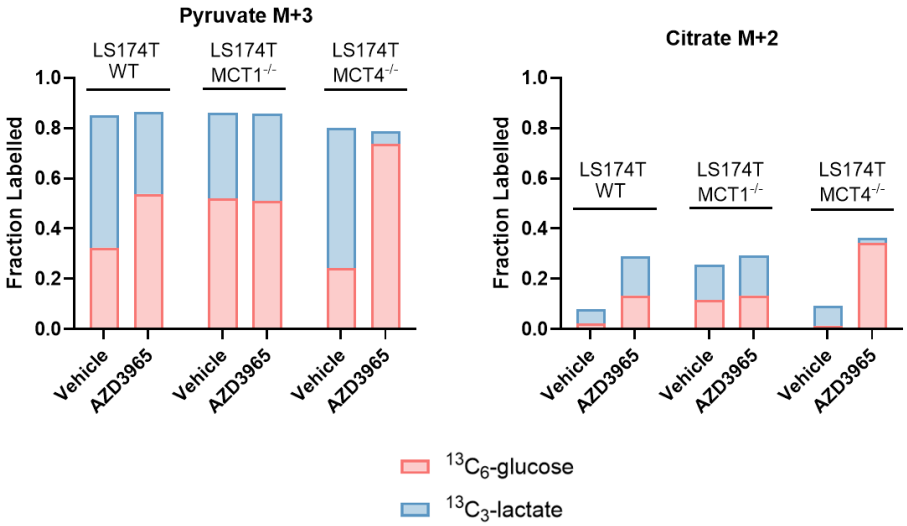


Figure 1.19 MCT1, but not MCT4, is the key determinant of glucose entry into the TCA cycle. Fraction of M+3 pyruvate and M+2 citrate is shown. A panel of LS174T colon cancer cells (i.e., LS174T WT, LS174T MCT1$^{-/-}$, LS174T MCT4$^{-/-}$) were incubated with $^{13}C_6$-glucose and unlabelled lactate or $^{13}C_3$-lactate and unlabelled glucose for 2h. The concentrations of glucose and lactate were kept the same in the two labelling studies (i.e., 5.6mM glucose and 10mM lactate). The intracellular metabolites were extracted and analysed by GC-MS. The schematics of labelling patterns are shown in Figure 1.18A. Data represent mean from one biological repeat. (Data from Yitao Xu, MRes thesis 2019 (*389*)).

Hypothesis:

There are two kinetically resolved cytosolic pools of lactate and thus, the exogenous lactate is preferentially channelled into mitochondria for the TCA cycle without mixing with glycolysis derived lactate.

Objectives:

- Investigate whether extracellular lactate is preferentially transported into mitochondria without mixing with glycolysis derived lactate.
- Examine the roles of MCT1 and MCT4 in regulating cytosolic compartmentation of lactate metabolism.

CHAPTER 2

Methods

Chapter 2 Methods

2.1 Cell culture

A panel of EOC cells (A2780, TOV21G, OVCAR8, COV504, COV644, 59M, OVSAHO, KURAMOCHI, HEY-A8, and COV318 cells) and HCT116 colon cancer cells were used in this study. HCT116 and OVCAR8 cell lines were part of the NCI-60 human tumour cell lines screen panel obtained from NCI DTP Tumour Repository. OVSAHO cells were obtained from Japanese Collection of Research Bioresources. KURAMOCHI cells were a generous gift from Dr Haonan Lu at Imperial College London. COV318, COV504, COV644 and 59M cell lines were purchased from the European Collection of Authenticated Cell Culture. A2780, TOV21G and HEY-A8 cell lines were obtained from ATCC. All the cell lines were maintained in DMEM media (Thermo Fisher, A1443001) supplemented with 5.6mM glucose (Thermo Fisher, A2494001), 2mM glutamine (Thermo Fisher, 25030-081), 10% foetal bovine serum (FBS; Thermo Fisher, 10270106), 100µg/mL streptomycin and 100 units/ mL penicillin (Thermo Fisher, 15070-063).

An isogenic panel of ovarian HGSC cells (ID8 *Trp53*$^{-/-}$, ID8 *Trp53*$^{-/-}$*;Nf1*$^{-/-}$, ID8 *Trp53*$^{-/-}$*;Pten*$^{-/-}$, *Trp53*$^{-/-}$*;Brca1*$^{-/-}$ and ID8 *Trp53*$^{-/-}$*;Brca2*$^{-/-}$cells) was developed in Prof Iain McNeish group at Imperial College London (*390, 391*). For *in vivo* study, the isogenic cell lines were cultured in their routine condition to enable comparison with historical data in our and Prof Iain McNeish groups. Specifically, the ID8 cells were cultured in the 'routine media': DMEM media (Thermo Fisher, A1443001) supplemented with 25mM glucose (Thermo Fisher, A2494001), 1mM pyruvate (Thermo Fisher, 11360070), 2mM glutamine (Thermo Fisher, 25030-081), 4% FBS (Thermo Fisher, 10270106), 100µg/mL streptomycin, 100 units/ mL penicillin (Thermo Fisher, 15070-063) and 1x Insulin-Transferrin-Selenium (Thermo Fisher, 41400045).

To better mirror physiological glucose concentrations in healthy human plasma (i.e. 4.4-6.6mM) (*392*) for *in vitro* studies, the ID8 cell lines were adapted to physiological glucose condition (i.e. 5.6mM glucose). The 'physiological glucose media' is prepared by supplementing DMEM media (Thermo Fisher, A1443001) with 5.6mM glucose (Thermo Fisher, A2494001), 1mM pyruvate (Thermo Fisher, 11360070), 2mM glutamine (Thermo Fisher,

25030-081), 10% FBS (Thermo Fisher, 10270106), 100µg/mL streptomycin and 100 units/ mL penicillin (Thermo Fisher, 15070-063). Briefly, the adaption was performed by gradually decreasing the fraction of 'routine media' in the mixture of 'routine media' and 'physiological glucose media' over four passages (Table 2.1).

Passage number since adaption started	Percentage of 'routine media'	Percentage of 'physiological glucose media'
1	75	25
2	50	50
3	25	75
4	0	100

Table 2.1 Composition of 'routine media' and 'physiological glucose media' during adaption.

The authenticity of the cells (except OVCAR-8 and HCT116 cells) was verified by short tandem repeat (STR) profiling by Eurofins Genomics (Appendix Report 1-4). All the cell lines were cultured at 37°C in a humidified cell incubator with 5% CO_2. The passage number of all the cells was kept below ten after thawing to limit genetic drift and mycoplasma screen was performed routinely.

2.2 Animal studies

In collaboration with Dr Michael Gruet in our group, the *in vivo* studies were performed in compliance with UK animal welfare guidelines and under project licence (PA780D61A) and personal licences in dedicated facility at Imperial College London. Female 6–8-week-old C57BL/6 mice were used, and a 7-day acclimatization period was allowed before ear notching for identification purposes. At passage number 3 since thawing, 5 million ID8 *Trp53*$^{-/-}$;*Pten*$^{-/-}$ cells were injected intraperitoneally (I.P.) into each mouse. The mice were weighed and monitored 2-3 times every week for two weeks before drug injection.

The vehicle solution, FK866 and Olaparib suspension were prepared by Dr Michael Gruet (*393*). Briefly, the vehicle solution was prepared by combining 6.5% Tween 80 (Sigma-Aldrich, P4780) and 3.5% DMSO in 0.9% saline (NaCl in H_2O; Sigma-Aldrich, S9888) in a biosafety cabinet to

ensure sterility. FK866 and Olaparib suspension were prepared using the vehicle solution. Due to limited solubility of FK866 and Olaparib in the vehicle solution, the drug suspension was vigorously vortexed and sonicated for 4h in cold water bath (i.e. ice-water mix) to absorb heat generated by continuous sonication and prevent drug degradation at high temperature. To ensure no large particle existed, the drug suspension was checked in a haemocytometer under light microscopy. The vehicle solution and drug suspension were then aliquoted and stored at -20°C.

Different dosing regimens were used for the toxicology and survival study. For the toxicology study, the mice were randomised and allocated to 7 treatment groups (i.e., 3 mice in each treatment group) (Table 2.2). For reasons of animal ethical guidelines (i.e., the 3Rs) and having enough biological replicates for statistical power to examine pharmacodynamic properties of drugs (i.e., at least three), 3 mice were included in each treatment group. Each mouse received daily drug I.P. injection from day 14-18 and 21-25. There was a two-day drug holiday from day 19-20 to limit drug related toxicity. One day after the last drug injection (i.e. day 26), the mice were culled, and ascites was drained and collected from mice with apparent ascites in abdominal cavity (i.e. the presence of bloody liquid). Peritoneal lavage was performed in mice without ascites using 5mL sterile FACS buffer (50mL of 0.1M EDTA in PBS) and the buffer was collected. The ascites and peritoneal lavage buffer were centrifuged at 1,500rpm for 5min at 4°C to separate the cells. The supernatant after centrifugation was snap frozen in dry ice and kept at -80°C. The cells were then resuspended in freezing media (10% DMSO in FBS) and slowly frozen to -80°C. Omentum tumour and liver samples were collected and snap frozen in dry ice and kept at -80°C.

Drug dose (mg/kg)	**Vehicle**	**Olaparib**	**FK866**	**Combination A**	**Combination B**	**Combination C**	**Combination D**
Olaparib	0	50	0	50	50	50	50
FK866	0	0	30	30	20	10	5

Table 2.2 Dosing regimen of the toxicology study.

For the survival study, the mice were randomly allocated into 6 treatment groups (in groups

of 6) (Table 2.3). To determine the group size, the power calculation was performed and based on mean and standard deviation (SD) of survival days. Based on our historical data, the SD of survival of untreated mice with ID8 tumours is 4. Thus, the difference in mean survival of 8 days (i.e., twice the SD) is required to reach significance. The calculation of group size was performed using the online calculator (https://sample-size.net/sample-size-means/). The input parameters are: E (i.e., effect size; the difference in mean survival) = 8, q_1 (the proportion of subjects in treated group) = 0.5, q_0 (the proportion of subjects in untreated group) = 0.5, α (type I error rate) = 0.05, β (type II error rate) = 0.2 and SD = 4. The output of group size in both untreated and treated group is 6. From day 14-17 and day 21-24, the mice were administered daily I.P. injections and had a three-day drug holiday from day 18-20. The decrease in total injection number is due to the unexpected drug toxicity of FK866 observed in the toxicology study (refer to Section 5.2.4 for data about FK866 toxicity). To limit drug toxicity and keep the mice hydrated, the mice received wetted food and HydroGel® (Clear H_2O, 70-01-1062) during drug injection period. After drug treatment, group blinding was performed by the technicians in the animal facility to prevent bias. The mice were then monitored every day to inspect health and weight. When the mice reached humane endpoint as defined in the project licence (i.e. abdomen reached the same size as that of a mouse in late pregnancy, narrowed eyes, nose bulging, hunching, inactive), they were culled by cervical dislocation. All decisions about the mice culling were made by me and Dr Michael Gruet independently and confirmed by the animal facility technicians to avoid bias.

Drug dose (mg/kg)	**Vehicle**	**Olaparib**	**FK866 (low)**	**FK866 (high)**	**Combination (low)**	**Combination (high)**
Olaparib	0	50	0	0	50	50
FK866	0	0	10	20	10	20

Table 2.3 Dosing regimen of the survival study.

2.3 Sulforhodamine B (SRB) assay

The EOC cell lines were seeded into 96-well plates in quadruplicate at the density shown in Table 2.4 and incubated overnight to allow attachment. On the following day, the media was

removed and fresh media with 0.2% DMSO, FK866 (0.5-15nM) and/or Olaparib (0.1-50μM). After treatment for 3 days, the cells were fixed with 50% (w/v) trichloroacetic acid (TCA) solution (Sigma-Aldrich, T6399) at 4°C for 1h. Next the plates were washed with tap water and left to air dry at room temperature overnight. To stain the cells, 100ul of 0.4% SRB (Sigma-Aldrich, 230162) solution (w/v) in 1% (v/v) acetic acid (ThermoFisher, 10005920) was added to each well. After staining at room temperature for 30min, the SRB solution was removed, and the plates were washed with 1% (v/v) acetic acid (ThermoFisher, 10005920) for 4 times. The plates were then kept at room temperature to allow air dry overnight. Next 200ul of 10mM Tris Base solution (Sigma-Aldrich, T1699) was added to each well and the plates were kept on a shaker to dissolve the SRB dye. A SpectraMax Gemini XPS Microplate Reader (Molecular Devices) was used to read the absorbance at 565nm. The data were normalised to vehicle treated groups after background correction using readings from cell- and treatment-free wells. To calculate IC_{50} values, the data were then fitted to nonlinear regression model (i.e. log[inhibitor] vs. normalised response (three parameters)) using GraphPad Prism 10.0.0 software.

Cell line	Seeding density (cells/well)
A2780	5,000
TOV21G	2,000
OVCAR8	2,000
COV318	3,500
ID8 cell panel	500

Table 2.4 The seeding density of EOC cells for 96-well plate based assays.

2.4 Caspase glo-3/7 assay

The panel of EOC cell lines (A2780, TOV21G, OVCAR8 and COV318 cells) and ID8 cells were seeded in triplicate into white 96-well plates at the density shown in Table 2.4. To allow normalization by cell density, the cells were seeded in quadruplicate at the same density in a parallel clear 96-well plate. The cells were allowed to attach to the plates overnight. Next the media was removed and replaced with fresh media supplied with 0.2% DMSO, FK866 (1 or 5nM) and/or Olaparib (10μM). After drug treatment for 24-48h, caspase glo-3/7 assay (Promega, G8092) was performed on the white plate following manufacturer's protocols.

Briefly, an equal volume of caspase-glo® assay reagent (i.e. 100ul) was added to each well and the plates were incubated at room temperature for 30min. The luminescence was measured by FLUOstar CLARIOstar Plus Microplate Reader (BMG LABTECH). Cell-free wells were subject to the same processing for background correction. The parallel clear 96-well plates were processed using the SRB assay protocol as described previously. The caspase data were normalised to SRB readings to correct the effects of cell number on caspase activity.

2.5 Mitochondrial membrane potential (ΔΨm) assay

The panel of EOC cells (A2780 and COV318 cells) and ID8 cells were seeded in triplicates into black 96-well plates at the density shown in Table 2.4. The cells were also seeded into parallel clear 96-well plates at the same density for normalization against cellularity. After overnight incubation to allow attachment to the plates, the media were replaced with fresh DMEM media with 0.2% DMSO, FK866 (5nM) and/or Olaparib (10μM). At the end of 48h drug treatment, ΔΨm was measured using JC-10 assay kit (Abcam, ab112134) according to the manufacturer's manual. In brief, 50ul of assay buffer A with JC-10 dye was added to each well and incubated at room temperature for 1h. Next, 50ul of assay buffer B was added to each well to lyse the cells and fluorescence at excitation/emission=490/525nm (cut off at 515nm) was measured by FLUOstar CLARIOstar Plus Microplate Reader (BMG LABTECH). The parallel clear plates were processed according to the SRB assay in section 2.4. Cell-free wells were used for background subtraction. The fluorescent intensities were normalised against SRB data for correction of cell biomass.

2.6 Oxidative stress assay

The EOC cell lines (A2780 and COV318 cells) were seeded into white 96-well plates in triplicates at the density shown in Table 2.4. A parallel clear 96-well plate was also seeded for normalisation against cell density. After overnight incubation and cell attachment to the plates, media were removed and 80ul of fresh DMEM media with 0.2% DMSO, FK866 (5nM) and/or Olaparib (10μM) was added to each well. H_2O_2 was measured using ROS-Glo H_2O_2 assay (Promega, G8820) according to manufacturer's manual. Briefly, after 18h, 20ul of combined

H_2O_2 substrate (provided in the kit) and test compound were added to reach the final concentration of H_2O_2 substrate at 25uM and keep drug concentrations unchanged. After a further 6h incubation, 100ul of ROS-Glo™ detection solution (provided in the kit) was added, and the plates were incubated at room temperature for 20min. Next, luminescence was measured using FLUOstar CLARIOstar Plus Microplate Reader (BMG LABTECH). To subtract background signals, cell-free wells were processed using the same protocol. To correct cell biomass, the luminescence signals were normalised to SRB readings from the parallel plates processed using SRB assay.

2.7 Immunofluorescence (IF)

The EOC cell lines (A2780, TOV21G and COV318 cells) were seeded into clear 96-well plates in quadruplicate at the density shown in Table 2.4. The cells were allowed to attach to the plates by incubation overnight. The media were then replaced with DMEM media supplemented with 0.2% DMSO, FK866 (5nM) and/or Olaparib (10μM). After 24h drug treatment, immunofluorescence analysis of γH2AX was performed by PhD student Yurui Ma as described previously (*394*). In brief, the cells were fixed with 4% formaldehyde (Fisher Scientific, 11586711) for 15min after one PBS wash. The formaldehyde was then removed, and the cells were washed with PBS twice. Next the cells were permeabilized by incubating with 0.1% Triton X-100 (Sigma-Aldrich, T8787) in PBS for 20min. After blocking with 1% BSA (Sigma, A2153) and 2% FBS (Thermo Fisher, 10270106) in PBS for 1h, the samples were incubated with mouse anti-gH2AX antibody (1:500; Sigma-Aldrich, 05–636) at 4°C overnight (around 16h). The samples were then incubated with AF488-conjugated goat anti-mouse secondary antibody (1:500; Invitrogen, A11001) and DAPI (Sigma-Aldrich, D9542; 1:1000 in blocking buffer (BD Bioscience, 347580)) for 2h at room temperature. Next the samples were washed with PBS for three times and imaged in 200ul PBS by IN Cell Analyzer 1000 (GE Healthcare) using a 20X objective. At least 16 images were acquired for each well and the data were analysed by CellProfiler (V3.1.8.).

2.8 Annexin V-Propidium Iodide staining assay

The panel of EOC cells (A2780, TOV21G and COV318 cells) were seeded into 6-well plates at the density shown in Table 2.5. The cells were allowed to attach after overnight incubation and the media were replaced with DMEM media supplemented with 0.2% DMSO, FK866 (5nM) and/or Olaparib (10uM). After 24h drug treatment, annexin v apoptosis assay was performed by the PhD student Yurui Ma as described previously (*394*). In brief, media were collected to harvest non-adherent cells, and adhering cells were then collected by trypsinization using TrypLE Express (Gibco, 12604013). Both non-adherent and adhering cells were combined and washed with cold PBS twice. The cells were then resuspended in annexin v binding buffer (BD Biosciences, 556454) and single-cell suspension was made by passing the cell solution through a 30um cell strainer. To stain the cells, 2.5ul of Cy5™ Annexin V (BD Biosciences, 559933) and propidium iodide (PI) staining solution (Invitrogen, 00-6990-50) was added to each sample. After 15min incubation in the dark, analysis was performed by BD FACS Canto analyser and positive control was processed for colour compensation. Gating and data analysis were performed using FlowJo V10.6.2.

Cell line	**Seeding density (cells/well)**
A2780	350,000
TOV21G	250,000
COV318	250,000

Table 2.5 The seeding density of EOC cells for 6-well plate based assays.

2.9 Cell cycle assay

EOC cell lines (A2780, TOV21G and COV318 cells) were seeded into 6-well plates at the density shown in Table 2.5. After cell attachment by overnight incubation, media was replaced with DMEM media added with 0.2% DMSO, FK866 (5nM) and/or Olaparib (10uM). Cell cycle assay was performed by the PhD student Yurui Ma as described previously (*394*). Briefly, after 23h of drug treatment, the cells were incubated with 200 mM IdU (Sigma, I7125) and washed with PBS twice before collection by trypsinization (Gibco, 12604013). After fixing overnight at

4°C by incubating with 70% ethanol, chromosomes were denatured by adding 2M HCl with 0.5% Triton X-100 (Sigma-Aldrich, T8787) with agitation and incubating for 30min. Next, the samples were added with 0.1M NaB4O7 (pH 8.5; Sigma, B9876) and incubated for 5min to neutralise the HCl. The samples were then incubated with 1% BSA (Sigma, A2153) and 0.2% Tween 20 (Sigma, P1379) in PBS for 30min to block. To probe IdU, the samples were incubated with mouse anti-IdU antibody (Abcam, ab6326; 1:25 in blocking buffer (BD Bioscience, 347580)) for 60min each at room temperature. The samples were then washed with blocking buffer (BD Bioscience, 347580) twice and incubated with AF488-conjugated goat anti-mouse antibody (Invitrogen, A11001; 1:100 in blocking buffer (BD Bioscience, 347580)) before the 15min incubation with FxCycle PI/RNase staining solution (Invitrogen, F10797) in the dark. The samples were then analysed using BD FACS Canto analyser and data were analysed by FlowJo V10.6.2.

2.10 Protein extraction and Western Blot (WB)

To extract protein from cells in 2D-culture (i.e. *in vitro* studies), A2780 and COV318 were seeded into 6-well plates at the density shown in Table 2.5 and treated with 0.2% DMSO, FK866 (5nM) and/or Olaparib (10uM) for 24h. At the end of drug treatment, the media were removed, and the cells were transferred to a ThermalTray™ pre-cooled on ice to prevent protein degradation. The cells were then washed with ice-cold PBS once to remove residual media. For protein extraction from cells under basal conditions, the panel of EOC cells and ID8 cells were pelleted during routine cell passaging by centrifuging at 800rpm for 5min. The media were removed, and the cell pellets were than washed with PBS once. To extract proteins, the cells in 6-well plates and cell pellets were lysed by adding ice-cold radioimmunoprecipitation assay (RIPA) buffer supplemented (Sigma-Aldrich, R0278) with Halt™ Protease and Phosphatase Inhibitor Cocktail (ThermoFisher, 78440). The cell lysates were scrapped with cell lifter (Corning, CLS3008) and transferred to 1.5ml EP tubes. After vertexing for 30sec, the lysates were kept on ice for 10min and centrifuged at 16,000xg for 10min at 4°C. Next the supernatant was collected and the pellet (i.e. cell debris) was discarded. The protein extract was kept at -80°C until further analysis by WB.

For protein extraction from the omentum tumour tissue, 15-25mg of the tissue was weighed and transferred to the 2ml homogenising tubes (Bertin Technologies, P000945-LYSK0-A). To homogenise the tissue, 0.1mm Precellys® Glass Beads (Bertin Technologies, VK01) were added to the homogenising tubes containing ice-cold RIPA buffer (Sigma-Aldrich, R0278) with Halt™ Protease and Phosphatase Inhibitor Cocktail (ThermoFisher, 78440). For every 10mg tissue, 100ul of RIPA buffer was added. The tubes were placed in the Precellys Evolution tissue homogeniser (Bertin) coupled to the Cryolys Evolution cooling system (Bertin) and the homogenising was performed using a programme (4 X 20sec at 8,000rpm with 30sec pause, 4°C, two cycles). Next, the tumour lysates were centrifuged at 16,000xg for 10min at 4°C and supernatant was collected. The protein extract was stored at -80°C.

To quantify the concentrations of proteins, a Pierce™ BCA Protein Assay Kit (ThermoFisher, 23225) was used according to the manufacturer's manual. Briefly, cell and tissue protein extracts were diluted at 1:2 and 1:5 by RIPA buffer, respectively, and added in duplicates to 96-well plates. Bovine serum albumin (BSA) standards (125, 250, 500, 750, 1000, 1500, 2000μg/ml) were added in duplicates to generate the standard curves. Next, 200ul of BCA reagent (made by combining reagent A with reagent B at 50:1) was added to each well. After incubation at 37°C for 30min, the absorbance at 562nm was measured using a SpectraMax Gemini XPS Microplate Reader (Molecular Devices). After background correction using readings of cell-free wells, protein concentrations were calculated in Microsoft Excel 365 (Microsoft, version 2310) using the standard curves.

For WB analysis, 30ug of proteins were taken and mixed with Laemmli buffer (BIO-RAD, 1610747) supplemented with 10% (v/v) β-mercaptoethanol (BIO-RAD, 1610710). The samples were then diluted by ddH2O to achieve an equal volume and heated at 95°C for 10min to denature the proteins. Subsequently, the protein samples and Amersham™ ECL™ Rainbow™ Marker (Merck, GERPN800E) were loaded onto 4–20% Mini-PROTEAN® TGX™ Precast Protein Gels (BIO-RAD, 4561094 or 4561096). The proteins were then resolved by electrophoresis at 200V for 40-60 minutes using a PowerPac HC Power Supply (BIO-RAD). The running buffer was prepared in house by dissolving tris base (Sigma, 93362), glycine (Sigma, 50046) and sodium dodecyl sulphate (SDS; Sigma, L3771) in ddH_2O to the final concentrations at 25mM,

192mM and 0.1 % (v/v), respectively.

Wet transfer (100V for 60min) was performed to transfer resolved proteins onto nitrocellulose membranes (BIO-RAD, 1620115). The transfer buffer was prepared in house by dissolving glycine, tris base and methanol (Sigma, 179337) in ddH2O to the concentrations at 190mM, 25mM tris base and 20% (v/v) and adjusting pH levels to 8.3. The protein transfer efficiency was confirmed by briefly staining the membranes with Ponceau S solution (Sigma-Aldrich, P7170). The membranes were then blocked in 5% milk (Mercy, 70166) or 5% BSA (Sigma-Aldrich, SRE0096) in tris-buffered saline with 0.1% tween-20 (TBST; prepared in-house) at room temperature for 1h. Next the membranes were cut into sections according to the molecular weight of the proteins of interest.

The membranes for phosphor-proteins and total proteins were incubated with primary antibodies (Table 2.6) in 5% BSA or 5% milk in TBST at 4°C overnight (around 16h), respectively. Next the membranes were washed with TBST for 10min for three times at room temperature to eliminate non-specific binding of antibodies. The membranes were then incubated with anti-mouse or anti-rabbit horseradish peroxidase (HRP) conjugated secondary antibodies for 1h at room temperature according to the species in which the primary antibodies were obtained (Table 2.6). Next the membranes were washed for 10min for three times with TBST. To visualise, the membranes were incubated in Supersignal^{TM} West Pico plus chemiluminescent substrates (ThermoFisher, 34580) for 2min at room temperature. The blots were then developed using Amersham Hyperfilm ECL film (GE Healthcare, 28-9068) and Optimax X-ray film processor (Protec).

Antibody	Supplier	Catalogue No.	Species	Dilution
PARP1	Cell Signalling	9542S	Rabbit	1:1,000
Phospho-Chk1 (Ser345)	Cell Signalling	133D3	Rabbit	1:2,500
Chk1	Cell Signalling	2360	Mouse	1:2,500
Phospho-Chk2 (Thr68)	R&D Systems	AF1626	Rabbit	1:2,500
Chk2	R&D Systems	MAB1358	Rabbit	1:2,500
Phospho-ATM (Ser1981)	Invitrogen	MA1-2020	Mouse	1:2,500
ATM	GeneTex	GTX70103	Mouse	1:2,500
Phospho-ATR (Ser482)	Cell Signalling	2853	Rabbit	1:2,500
ATR	Cell Signalling	13934	Rabbit	1:2,500
NAMPT	Invitrogen	MA5-24108	Rat	1:2,500
NAPRT	Invitrogen	PA5-70595	Rabbit	1:2,500
PTEN	Cell Signalling	9552	Rabbit	1:2,500
NF1	Abcam	ab238142	Rabbit	1:1,000
Phospho-γH2AX	Sigma-Aldrich	05-636	Mouse	1:1,000
Histone H3	Merck	07-690	Rabbit	1:5,000
Phospho-Erk1/2 (Thr202/Tyr204)	Cell Signalling	4695S	Rabbit	1:1,000
Erk1/2	Cell Signalling	4370S	Rabbit	1:1,000
Phospho-Akt (Ser473)	Cell Signalling	4060	Rabbit	1:1,000
Akt	Cell Signalling	4691	Rabbit	1:1,000
β-actin	Abcam	ab6276	Mouse	1:10,000
α-tubulin	Santa Cruz Biotechnology	T9026	Mouse	1:1,000
HRP-conjugated anti-rabbit	Invitrogen	31460	Goat	1:2,500
HRP-conjugated anti-mouse	Invitrogen	31340	Goat	1:2,500
HRP-conjugated anti-rat	Proteintech	SA00001-15	Goat	1:2,500

Table 2.6 Antibodies for WB.

2.11 ^{1}H NMR: sample preparation and NMR analysis

The ID8 cells were seeded in duplicates into 6-well plates at the density of 25,000 cells/well. After incubation overnight to allow attachment, fresh media was added, and the cells were incubated for a further 24h. At the end of incubation, the media was collected and centrifuged at 800rpm for 5min to remove floating cells in media. Next the supernatant was collected and kept at -80°C. A parallel plate was used to count the cell numbers at the start (0h) and end of incubation (24 h) using the Vi-cell XR cell viability analyser (Beckman) according to the manufacturer's instrument. Briefly, 400ul of TrypLE™ Select Enzyme (Gibco, 12563011) was added and the plates were incubated for 5min at 37°C to detach the cells. Next, 600ul of PBS

was added to terminate the reaction and the cell suspension was well-mixed and counted.

For referencing and quantitation, the NMR media buffer was prepared in house as described previously (*395*). Briefly, NaH_2PO_4 (Sigma, 52074) and DSS (Sigma, 178837) were dissolved in deuterated water (dH2O; Sigma, 756822) to reach a final concentration of 0.5M and 12mM, respectively. The pH levels were adjusted to 7.0 using NaOH pellets (Sigma, S5881). The purity of the buffer was checked by confirming no contaminant peaks were higher than 0.5% of DSS peak in intensity by ^{1}H NMR spectroscopy (parameters are described in the next paragraph).

On the day of NMR spectroscopy analysis, 550ul of media was transferred to a clean EP tube and 50ul of NMR media buffer was added. The samples were then centrifuged at 16,000xg for 1min to remove insoluble. Next, 550ul of the samples were loaded into NMR tubes (Sigma, Z562262) and analysed by 14.1 T Bruker AVANCE 400 MHz spectrometer (Bruker Biospin). To suppress the intensity of water signal, a ZGPR solvent pre-saturation method was used to acquire NMR spectra at 298K. The ZGPR method involves a single RF pulse with a recycle delay at 4sec and 32 FIDs. A total of 64,000 data points were acquired, and the spectra width was 6402.049 Hz. The spectra were Fourier transformed, and phase correction, baseline correction and DSS normalisation were performed using MATLAB scripts (MathWorks) written by T.M.D. Ebbels, J.T. Pearce, R. Cavill, and H.C. Keun. Peaks were identified by referencing to Human Metabolome Database (HMDB) (*353*) and integrated using MATLAB scripts (MathWorks) written by C. Lau.

The consumption or release (CORE) rates of metabolites were calculated as described previously. In brief, the cell numbers at the start and end of incubation were plotted against the function of time to calculate area under curve (AUC) using equation 1. Next, the difference between the concentrations of metabolites at the start and end of incubation was divided by AUC to calculate the CORE rates using equation 2.

$$Equation\ 1 \qquad AUC = \frac{1}{2} \times 24 \times \left(Cell\ number\ (0h) + Cell\ number\ (24h)\right)$$

$$Equation\ 2 \qquad CORE = \frac{Concentration\ (24h) - Concentration\ (0h)}{AUC}$$

2.12 ^{13}C labelling studies: ^{13}C tracer incubation, sample preparation and analysis

The ID8 cells were seeded in duplicates into 6-well plates at the density of 125,000 cells/well. After incubation overnight, the media was replaced by DMEM supplemented with 10% FBS and ^{13}C tracers as described in Table 2.7.

^{13}C tracer	Supplier and catalogue No.	Condition 1	Condition 2	Condition 3	Condition 4	Condition 5
$^{13}C_6$-glucose (5.6mM)	Sigma, 660663	L	U	N/A	U	U
$^{13}C_5$-glutaime (2mM)	Sigma, 605166	U	L	U	U	U
1,2-$^{13}C_2$-glucose (5.6mM)	Sigma, 453188	N/A	N/A	L	N/A	N/A
3-^{13}C-lactate (10mM)	Sigma, 490040	N/A	N/A	L	L	N/A
$^{13}C_2$-acetate (1mM)	Sigma, 282022	N/A	N/A	N/A	N/A	L

Table 2.7 ^{13}C tracer supplementation. U: unlabelled metabolites added, L: ^{13}C labelled metabolites added, N/A: not added.

After incubation of 4-24h, the plates were placed on ice and media was collected and centrifuged at 800rpm for 5min. The supernatant was then collected and stored at -80°C. To extract the intracellular metabolites, the cells were washed once with ice-cold Ringer's buffer (Sigma, 1.15525) and HPLC-grade methanol (Honeywell, 34898) pre-cooled on dry ice was added to quench the metabolism (1ml/well). The cells were scrapped, and methanol solution was transferred to EP tubes. To improve extraction efficiency, a further 500ul of methanol was added to each well, and scrapping was repeated. The solution was combined and dried using under N_2 flow. Extraction blanks were prepared from cell-free wells using the same protocol. The samples were then stored at -80°C.

To extract metabolites in media, media was defrosted at room temperature and 50ul of media from each sample was transferred to clean EP tubes. Next 50ul of HPLC-grade water

(Honeywell, 34877) and 300ul of dry-ice cooled methanol (Honeywell, 34898) was added to each sample. After mixing by vertexing and incubation at -20°C for 20min, the samples were centrifuged at 16,000xg and 4°C for 10min. Next the supernatant was collected. An extraction blank was generated by extracting 100ul of HPLC-grade water and using the same protocol. The samples were then dried under N_2 flow and stored at -80°C.

To separate the aqueous (polar) and organic (nonpolar) metabolites, dual-phase extraction was performed as described previously (*396*). In brief, the dried methanol extracts were placed on ice. Next 300ul of chloroform (Acros Organic, 10071511) /methanol 2:1 (v/v) mix and 300ul HPLC-grade water (Honeywell, 34877) were added. The samples were vigorously vortexed for 30sec and centrifuged at 16,000xg for 10min at 4°C. The upper aqueous and lower organic phases were separated and transferred to salinized glass vials (Agilent, 5183-2071) using glass pipettes (Fisher, 1156-6963). The extraction was repeated to improve recovery efficiency. Next 10ul of 1.5 mg/mL myristic acid d27 (Sigma, 366889) was added to each sample as an injection and derivatization standard. The samples were then dried under N_2 flow and stored at -80°C.

Different protocols were used to derivatize aqueous and organic metabolites. For aqueous metabolites, 20ul of methoxamine reagent (MOX, 2% methoxyamine·HCl in pyridine; Thermo, TS-45950) was added, and the samples were vortexed and incubated at 30°C for 90min. This is to convert the ketone groups in pyruvic acid to methoxymated ketone groups which prevents the formation of multiple trimethylsilyl groups and distinguishes pyruvic acid derivatives with lactic acid derivatives. After the incubation, the samples were centrifuged briefly and cooled to room temperature. Next 80ul of N-tert-Butyldimethylsilyl-N-methyltrifluoroacetamide (MTBSTFA) with 1% N-Methyl-N-(tert-butyldimethylsilyl)trifluoroacetamide (TBDMS) silylation reagent (Thermo, TS-48920) was added and the samples were included at 70°C for 1h.

For organic metabolites, lipids (e.g. triglyceride (TAG)) are difficult to vaporise and analyse on GC-MS as a result of the high boiling point. Therefore, transesterification was performed to convert TAG into free fatty acid methyl esters (FAME) which are easier to vaporise and analyse by GC-MS. To this end, each sample was added with 300ul anhydrous methanol (Sigma,

322415): toluene (Sigma, 244511) mix (1:1, v/v) and 200 µL of sodium methoxide (Sigma, 164992) solution (0.5M, in anhydrous methanol (Sigma, 322415)). The samples were then vortexed and incubated at room temperature for 1h. Next, transesterification was terminated by adding to each sample 500ul of sodium chloride (Sigma, S9625) solution (1M, in HPLC-grade water (Honeywell, 34877)) and 25ul of 37% hydrochloric acid (Sigma, 258148). Next each sample was added with 500ul of hexane (Honeywell, 34484) and centrifuged briefly to separate the layers. Glass pipettes were used receive the upper organic layer into new vials with anhydrous magnesium sulfate (Sigma, M7506) which absorbs moisture and residual aqueous phase material (*397*). To improve recovery efficiency, the extraction step was repeated, and the organic phase was combined. Next the vials were briefly centrifuged to precipitate magnesium sulfate and the supernatant was collected into new glass vials. The samples were then dried under N_2 flow. To perform derivatization by silylation, each sample was added with 80ul of N-Methyl-N-(trimethylsilyl)trifluoroacetamide (MSTFA) with 1% trimethylchlorosilane (TMCS) (Thermo, TS-48915) and incubated at 37°C for 30min.

After derivatization, a quality control (QC) sample was prepared by pooling an equal volume from each sample. The samples were then transferred to clean vial inserts (Agilent, 5183-2086) using glass pipettes. The samples were randomised and immediately analysed by GC-MS as described previously (*398*). In brief, the Agilent 7890A GC system coupled to the Agilent 5975 MSD triple-axis detector was used and the Agilent 7693 autosampler injector was used to inject the samples in a spitless mode. Metabolite separation was achieved on a 30 m DB-5MS capillary column integrated with a 10 m DuraGuard column (Agilent, 122-5532G) using the Fiehn method (*399*).

Automated Mass Spectral Deconvolution and Identification System (AMDIS) was used for mass spectra deconvolution and metabolite identification based on the in-house built library developed with reference to the National Institute of Standards and Technology (NIST) mass spectral library. Peak integration, correction for natural abundance and calculation of MID were performed by the GC-MS Assignment Validator and Integrator (GAVIN) script in MATLAB (*400*).

To model the synthesis of fatty acids, ISA was performed using ConvISA algorithm on MATLAB (*401*). The fraction of *de novo* synthesised fatty acid and ^{13}C tracer derived lipogenic acetyl-CoA were estimated based on the MIDs of methyl palmitate.

2.13 Untargeted metabolic profiling using LC-MS/MS

Mice omentum tumour tissue from the in vivo survival study described in section 5.2.4 were used for metabolite extraction. In addition, mice omentum tumour tissue kindly provided by PhD student Flora McKinney and Dr Yuwei Xu in our group was used (refer to Appendix Table 3.1 for mice survival period).

To extract metabolites, approximately 10-15mg of tissue was weighed and transferred to 2ml homogenising tubes containing 0.8ml of dry-ice cooled methanol (80% in HPLC-grade water, v/v) and 0.1mm Precellys® Glass Beads. Next 10ul of internal standard mix (Table 2.8) was added to each sample. The samples were then homogenised using Precellys Evolution tissue homogeniser (Bertin) coupled to the Cryolys Evolution cooling system (Bertin). The parameters for the homogenising programme were two cycles of 4 X 20sec on at 8,000rpm with 30sec off intervals at 4°C. Next the samples were centrifuged at 16,000xg for 10min at 4°C and supernatant was collected. The extraction was repeated to improve recovery. An extraction blank was prepared on tissue-free homogenising tubes using the same protocol. The samples were then dried under N_2 flow and kept at -80°C. To separate the aqueous with organic metabolites, the dried samples were subjected to dual-phase extraction using the same method as described in section 2.12.

Labelled Standard	Concentration (µg/mL)	Source	Identifier
L-alanine-2,3,3,3-d_4	30	Sigma	485845
L-isoleucine-$^{13}C_6$,^{15}N	5	Sigma	608092
Citric-2,2,4,4,-d_4 acid	30	Sigma	485438
Glycine-1-^{13}C,2,2-d_2	50	Sigma	608076
L-glutamine $^{13}C_5$	40	Sigma	604690
L-aspartic acid-$^{13}C_4$	5	Sigma	604852
L-glutamic acid-$^{13}C_5$	20	Sigma	604860
L-valine-$^{13}C_5$	20	Sigma	758159
Fumaric acid-$^{13}C_4$	10	Sigma	606014
Succinic acid-$^{13}C_4$	20	Sigma	491983
Sodium pyruvate-3-^{13}C,3,3,3-d_3	30	Sigma	608483
L-serine-$^{13}C_3$, ^{15}N,2,3,3-d_3	10	Sigma	749877
L-malic acid-$^{13}C_4$	5	Sigma	750484
Lactic acid $^{13}C_3$	50	Sigma	746258
Uracil ^{13}C, $^{15}N_2$	10	Sigma	608459
Uridine 5,6-d_2	10	Santa Cruz Biotechnology	sc-213138
TMP $^{13}C_{10}$, $^{15}N_2$	10	Sigma	648590
Carnitine d_3	10	Sigma	617466
SAH d_4	5	Santa Cruz Biotechnology	sc-296290
SAM $^{13}C_5$	5	Sigma	798231
tyrosine d_4	10	Sigma	489808
Lysine HCl d_4	10	Sigma	616192
nicotinamide $^{13}C_6$	5	Supelco	V-034
Creatinine d_3	10	Supelco	C-165
nicotinate d_3	5	Sigma	489077

Table 2.8 Components and concentrations of the internal standard mix for LC-MS/MS analysis.

To analyse the aqueous metabolites by LC-MS, 50ul of HPLC-grade water was added and the samples were vortexed vigorously for 30sec. A QC sample was prepared by taking an equal volume from each sample. The samples were then transferred to glass vial inserts (Agilent, 5190-2242) and randomised before loading into the autosampler (kept at 10°C). The chromatographic separation was performed on an Exion LC system (Sciex) using a Luna™ 150 X 2.1mm polar C18 column (particle size = 1.6um, Phenomenex, 00F-4748-AN) integrated with a SecurityGuard™ Ultra polar C18 pre-column (Phenomenex, AJ0-9505). The flow rate was 0.45ml/min and injection volume was 5ul for each sample for both positive and negative ion mode. The mobile phase composition and LC gradient was shown in Table 2.9-2.11.

	Mobile phase A	Mobile phase B
Positive ion mode	Water (Fisher, 10505904) with 0.2% (v/v) formic acid (FA; Fisher, 15646720)	Acetonitrile (Fisher, 10001334) with 0.2% (v/v) FA
Negative ion mode	Water with 0.2% (v/v) FA and 10mM ammonium formate (Fisher, A11550)	Acetonitrile

Table 2.9 Mobile phase composition.

Time (min)	Flow rate (ml/min)	Mobile phase A (%)	Mobile phase B (%)
0.00	0.45	99.8	0.2
2.00	0.45	99.8	0.2
5.00	0.45	98.0	2.0
11.00	0.45	75.0	25.0
13.00	0.45	2.0	98.0
17.00	0.45	2.0	98.0
18.00	0.45	99.8	0.2
20.00	0.45	99.8	0.2

Table 2.10 LC gradient for the positive mode.

Time (min)	Flow rate (ml/min)	Mobile phase A (%)	Mobile phase B (%)
0.00	0.45	95.0	5.0
8.00	0.45	80.0	20.0
10.00	0.45	0.0	100.0
12.00	0.45	0.0	100.0
12.10	0.45	95.0	5.0
14.00	0.45	95.0	5.0

Table 2.11 LC gradient for the negative mode.

The MS analysis was performed using a ZenoTOF 7600 MS system (Sciex) with a OptiFlow Turbo V source (Sciex). The ion source was operated in positive or negative electrospray mode according to the mobile phase composition. To improve the coverage of metabolites detected, a SWATH method was applied. Spray voltage was 5500V and -4500V for positive and negative mode, respectively. In the initial survey scan, the precursor ions (MS1) were

acquired from *m/z* 50 to 1000 for both positive and negative mode with declustering potential (DP) at 25V (-25V for negative mode) and collision energy (CE) at 10V (-10V for negative mode). The accumulation time was set to 0.1s. In the subsequent MS2 scan, the precursor ions were acquired from *m/z* 20 to 1000 for both positive and negative mode. The Q1 window width was optimized using the SWATH variable window calculator provided by the instrument supplier Sciex. The fragmentation method is CID and the DP and CE for each Q1 window was previously optimized by Dr Cristina B Nadal in our group. In brief, human serum standards SRM 1950 were analysed by various combinations of DP and CE. The DP and CE combinations where the maximal number of features was detected were chosen as the optimal and are shown in Table 2.12-2.13. The accumulation time was 0.02s. The ZenoTrap, which is a novel ion accumulation device developed by Sciex, was turn on to improve sensitivity. For quality control, the peaks of internal standards were manually inspected.

SWATH window	Precursor ion start mass (Da)	Precursor ion stop mass (Da)	Deculstering potential (V)	DP spread (V)	Collision energy (V)	CE spread (V)
1	49.5	56.2	25	0	35	0
2	55.2	70	25	0	15	0
3	69	97	25	0	15	0
4	96	125.1	25	0	35	0
5	124.1	149.8	25	0	35	0
6	148.8	179.2	25	0	35	0
7	178.2	218.6	25	0	35	0
8	217.6	257.1	25	0	75	0
9	256.1	285.6	25	0	15	0
10	284.6	314.1	10	0	35	0
11	313.1	350.2	10	0	75	0
12	349.2	389.7	50	0	75	0
13	388.7	421.5	50	0	75	0
14	420.5	448.6	25	0	15	0
15	447.6	475.2	50	0	75	0
16	474.2	498.4	50	0	15	0
17	497.4	517.4	25	0	15	0
18	516.4	535	50	0	15	0
19	534	555.9	50	0	35	0
20	554.9	583	10	0	75	0
21	582	624.3	10	0	15	0
22	623.3	688.4	50	0	75	0
23	687.4	790.1	50	0	75	0
24	789.1	881.8	25	0	15	0
25	880.8	999.6	50	0	15	0

Table 2.12 DP and CE for Q1 windows in positive mode.

SWATH window	Precursor ion start mass (Da)	Precursor ion stop mass (Da)	Deculstering potential (V)	DP spread (V)	Collision energy (V)	CE spread (V)
1	49.5	119.8	-25	0	-15	0
2	118.8	147.4	-25	0	-35	0
3	146.4	178.7	-25	0	-35	0
4	177.7	195.1	-25	0	-35	0
5	194.1	230	-25	0	-35	0
6	229	276.6	-25	0	-35	0
7	275.6	308.4	-50	0	-15	0
8	307.4	339.3	-50	0	-15	0
9	338.3	348.8	-100	0	-35	0
10	347.8	362.1	-100	0	-35	0
11	361.1	375.9	-100	0	-35	0
12	374.9	389.2	-100	0	-35	0
13	388.2	395.8	-100	0	-35	0
14	394.8	403	-50	0	-35	0
15	402	411.5	-50	0	-35	0
16	410.5	446.2	-100	0	-35	0
17	445.2	490.8	-100	0	-35	0
18	489.8	536.4	-100	0	-35	0
19	535.4	565.9	-100	0	-35	0
20	564.9	595.8	-100	0	-35	0
21	594.8	664.2	-50	0	-35	0
22	663.2	792.9	-50	0	-35	0
23	791.9	999.6	-50	0	-35	0

Table 2.13 DP and CE for Q1 windows in negative mode.

Library matching was performed by MS Dial (version 5.2.240424.3) against MS Dial spectral library (version 17) (*402*). A spectral match score of 20% was used as a threshold with dot product score of 400 and reverse dot product score of 600. The library matching was cross referenced to the MSMLS™ Mass Spectrometry Metabolite Library which covers broad metabolite spectrum and consists of 600 metabolites. The MS spectra of the MSMLS™ Mass Spectrometry Metabolite Library was acquired by Dr Cristina B Nadal in our laboratory. Next, the data were blanked filtered with the threshold of 10 times in the blank samples using an in-house R package developed by Dr Cristina B Nadal and me. To correct the systematic drift of signal intensity during a LC-MS run, data from the QC samples were used to perform drift correction using the notame R package (*403*). Finally, areas of each metabolite peak were normalised to the sum of peak areas and the data were visualised by MetaboAnalyst (version 5.0.) (*356, 404*).

2.14 Statistics

The statistical analysis of metabolomics data (Section 3.2.1-3.2.2 and Section 5.2.6) was performed using MetaboAnalyst (version 5.0.). The data were first normalized to the sum of peaks and then auto-scaled (i.e., for each metabolite, the data were mean-centered and divided by its standard deviation). Single factor statistical analysis was used to perform univariate analysis, including t tests and volcano plots (for metabolomics data in Chapter 3) and one-way ANOVA tests (for metabolomics data in Chapter 5). Correction for multiple tests were conducted using False Discovery Rate (FDR). Multivariate statistics was also performed using the single factor statistical analysis module. Briefly, principal component analysis (PCA), partial least squares-discriminant analysis (PLSDA) and clustering (e.g., dendrogram and heatmap) were performed. Spearman's correlation analysis was performed using the function cor.test() from the package *stats* (version 4.3.2) in R for windows (version 4.3.1). Enrichment analysis was performed using the quantitative enrichment analysis (QEA) method in MetaboAnalyst (version 5.0.) and mapped to the public database of KEGG human metabolic pathways. For the metabolomics data in Chapter 3, 6 and 7 biological repeats with 1 technical replicate were used in control samples and samples with *Pten* deletion. For the metabolomics data in Chapter 5, 3 biological replicates with 1 technical replicate were used except in FK866 monotherapy group where 1 biological replicate was used.

Except for the metabolomics data, the statistical analysis was performed using GraphPad Prism (version 10.3.1). Mean and standard deviation were calculated using this software. To calculate the statistical significance between two groups, t tests were performed. One-way ANOVA and post-hoc Tukey tests were performed to calculate significance across three or more groups when only one parameter was involved (e.g., drug treatment). When there are two parameters (e.g., drug treatment and cell lines), two-way ANOVA and post-hoc Tukey tests were performed. For data that are not normally distributed (i.e., skewed), Kruskal-Wallis test and Dunn's multiple comparisons tests were performed to calculate p values (e.g., γH2AX foci data). For the Kaplan-Meier survival curves in Chapter 5, the Log-rank (Mantel-Cox) test were performed to calculate significance. The statistical significance (i.e., p values) are

presented as * $p<0.05$, ** $p<0.01$, *** $p<0.001$, **** $p<0.0001$ and ns: not significant. Unless stated otherwise, data were represented using scatter plot with bar representing mean (Chapter 4 and 5) or barchart (Chapter 3 and 6). In all the plots, error bars represent standard deviation (SD). Unless stated otherwise in figure legends, 3 independent biological replicates with 3 technical replicates were used.

CHAPTER 3

Akt pathway activation results in metabolic reprogramming of ovarian HGSC cells

---

Chapter 3 Akt pathway activation results in metabolic reprogramming of ovarian HGSC cells

3.1 Introduction

As described in sections 1.2.2 to 1.2.4, activation of the Akt signalling leads to metabolic rewiring in cancer cells (*83*). For instance, glucose uptake and metabolism via glycolysis are promoted due to enhanced expression and activation of GLUT1/4 and glycolytic enzymes (e.g., HK2) (*106*). Additionally, multiple downstream effectors of Akt (e.g., mTORC1, MYC) stimulate anabolic metabolism to increase nucleotide, protein and lipid synthesis (*98, 128, 140*). The Akt pathway also regulates cellular redox balance by modulating the production of the key redox equivalent NADPH (*148, 405*).

Ovarian HGSC is the commonest type of ovarian cancer and is the leading cause of cancer-associated death in women (*153, 157*). The genomic landscape is characterised by frequent DNA copy number changes and nearly universal loss-of-function mutation of *TP53* gene (*153, 406*). Aberrant activation of the Akt pathway is detected in approximately 40-50% of ovarian HGSC patients (*407*). This mainly result from amplification of *PIK3CA* and *AKT* genes and loss-of-function mutations of *PTEN* (encoding the negative regulator) (*177-179*).

Although the impact of Akt pathway activation in metabolic reprogramming has been studied in various cancer types (*96*), such effects are less clear in ovarian HGSC cells. Therefore, the hypothesis of this chapter is that Akt signalling activation leads to metabolic rewiring in ovarian HGSC cells. To this end, untargeted metabolic profiling by LC-MS was performed to improve metabolite coverage and examine the changes in abundance. Stable isotope resolved metabolomics (SIRM) was also employed to study central carbon metabolism. A panel of ID8 cells was used to model ovarian HGSC. The ID8 cell model was originally

generated by multiple passaging ovarian epithelial cells derived from a C57BL/6 mouse (*408*). Later, it was improved by introducing *Trp53* deletion using CRISPR technology to recapitulate the nearly ubiquitous *TP53* loss in human patients (*390*). *Pten* deletion was also introduced to model hyperactive Akt signalling (*391*). In addition to the traditional 2D culture *in vitro* model, tumour tissue from ID8 mouse model was also used. This is because 2D cell culture system deviates from the tumour microenvironment (e.g., high O_2 tension, high glucose and glutamine concentrations, buffered pH, and no cancer-stromal interaction) (*409, 410*). Metabolism is influenced by environmental factors and therefore, artifacts of metabolism may be detected using in vitro system (*4, 411*). ID8 mouse model is generated by injecting ID8 cell into immunocompetent mice, which keeps the immune cell component. Another advantage of ID8 mouse model is that it recapitulates the production of ascites and omental metastasis in human patients (*390, 412*). Therefore, the ID8 cells and tumour tissue were chosen as the ovarian HGSC model to investigate the metabolic reprogramming secondary to Akt pathway activation.

3.2 Results

3.2.1 A distinct metabolic landscape was detected in ID8 *Trp53*$^{-/-}$; *Pten*$^{-/-}$ tumours

To investigate the effects of Akt signalling activation in metabolic reprogramming, untargeted metabolic profiling was performed for the unbiased measurement of metabolites. The biological samples were ID8 *Trp53*$^{-/-}$ and ID8 *Trp53*$^{-/-}$; *Pten*$^{-/-}$ tumour tissue (refer to Appendix Table 3.1 for the list of samples). The tumours were generated using the methods described in Section 2.2 (also refer to Appendix Table 3.1 legend for details). In brief, ID8 *Trp53*$^{-/-}$ or ID8 *Trp53*$^{-/-}$; *Pten*$^{-/-}$ cells were intraperitoneally injected into female 6-8-week-old C57BL/6 mice. Because ID8 *Trp53*$^{-/-}$; *Pten*$^{-/-}$ tumours were established approximately 7 days earlier than ID8 *Trp53*$^{-/-}$ tumours (personal communication with Dr Yuewei Xu in our group), the tumours were collected when the mice reached humane endpoints (refer to Appendix Table 3.1 for mice

survival). Here, 6 samples of ID8 *Trp53*$^{-/-}$ tumours (kindly provided by Dr Yuewei Xu) and 7 samples of ID8 *Trp53*$^{-/-}$*; Pten*$^{-/-}$ tumours (2 samples from the survival study described in Section 5.2.4 and 5 samples kindly provided by Flora McKinney in our group) were analysed.

The extracted metabolites were measured by an in-house built SWATH method that optimises feature coverage and repeatability, and the data were analysed by MS Dial for peak deconvolution and integration. In total, 19955 features were identified. Annotation was then performed by referencing to the MS Dial public metabolite database (version 17) and cross-validated to an in-house built metabolite library (i.e., acquired by analysing the MSMLS™ Mass Spectrometry Metabolite Library which consists of 600 metabolites), respectively. A total of 359 features were annotated by MS Dial with both MS1 and MS2 matching to the library (Appendix Table 3.2). Among these, 165 features were cross-validated with MS1 and MS2 matching to the standards of the in-house built library (Appendix Table 3.3). The metabolomics data were then subject to blank filter and QC drift correction by an in-house written R script based on the 'notame' R package (*403*). Low quality features with CV larger than 0.2 were excluded for further analysis, and all the 165 features passed these tests. The data were subsequently visualised using MetaboAnalyst (*404*).

To examine the variance across the samples, the metabolomics data table was subject to partial least squares discriminant analysis (PLSDA) for dimension reduction. PLSDA was chosen instead of principal component analysis (PCA) because the class label information is kept in PLSDA and it better extracts inter-group variance (*354*). In practice, PLSDA achieves cluster separation even when there are few data points and low levels of separation (*413*). The results showed that the samples within each genotype group were clustered closely (Figure 3.1A), thereby confirming the limited intra-group variance. Interestingly, ID8 *Trp53*$^{-/-}$*; Pten*$^{-/-}$ tumours were clustered separately with ID8 *Trp53*$^{-/-}$ tumours (Figure 3.1A), which suggests the existence of differences in metabolite abundance. Interestingly, principal component analysis (PCA) showed no separation between ID8 *Trp53*$^{-/-}$ and *Trp53*$^{-/-}$*; Pten*$^{-/-}$ tumours (Appendix Figure 3.1), which suggests that there is no large systematic difference between the data.

However, PLSDA is prone to over-fitting (*413*) and therefore, cross-validation is necessary. Here, a 5-fold cross validation was performed on the first 5 components. Accuracy, predictive ability (Q^2) and coefficient of determination (R^2) were calculated and presented as the cumulative effects of including more components. The data showed that the PLSDA model with the first component achieved 73% accuracy and 31% predictive ability and explained 84% of the response variance (R^2) (Figure 3.1B), which suggests that a significant amount of information is captured by the first component. The inclusion of the second components improved Q^2 and R^2 to 45% and 94%, respectively (Figure 3.1B). This suggests that a substantial improvement in predictive ability and explanatory capability. Further addition of components showed only slight improvement. Overall, the cross-validation results confirmed the good fitting (R^2), predictive power (Q^2) and classification (accuracy) of the PLSDA model.

To reveal the metabolites that are significantly altered, non-parametric tests (i.e., Wilcoxon rank-sum test) were performed. The data showed that the abundance of 19 metabolites is significantly changed (p(FDR)<0.05, Figure 3.2A) and they were displayed in the heatmap (Figure 3.2B). Noticeably, acyl-carnitine (especially long chain acyl-carnitines), NAD and phosphatidylinositol are significantly increased in the tumours with Pten loss (Figure 3.2B). In contrast, amino acids (including histidine, aspartate, serine), nucleotides (cytidine and deoxycytidine) and nucleosides (inosine monophosphate (IMP), guanosine monophosphate (GMP)), metabolic cofactors and precursors (flavin mononucleotide (FMN) and pantothenic acid) and lipid mediators (cortisol, Prostaglandin D_2 (PGD_2)) are downregulated (Figure 3.2B). To visualise the metabolites with large fold changes (threshold=2) that are also statistically significant, a volcano plot was displayed (Figure 3.2C). The data showed that NAD and acyl-carnitines are upregulated more than two-fold, and IMP, pantothenic acid, ascorbic acid and PGD_2 are more than two-fold decreased in tumours with Pten loss (Figure 3.2C).

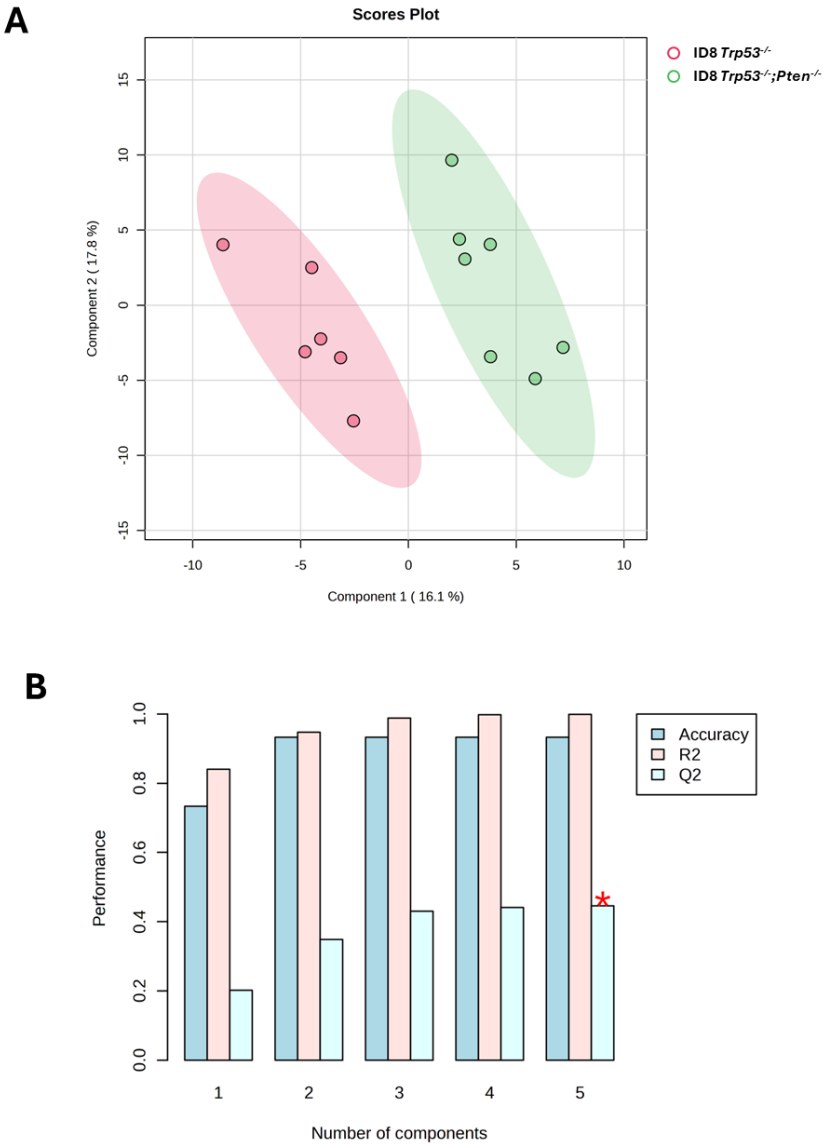


Figure 3.1 PLSDA modelling reveals differences in the metabolic profiles in ID8 *Trp53*$^{-/-}$ tumour samples based on the genetic status of *Pten*.

(A) PLSDA plot. Untargeted metabolic profiling was performed using mouse tumour tissue and PLSDA plot was generated by Metaboanalyst (v.5.0.). Samples within each group cluster closely while ID8 *Trp53*$^{-/-}$ tumours separate with ID8 *Trp53*$^{-/-}$*; Pten*$^{-/-}$ tumours. Coloured circles represent 95% confidence intervals. (B) Cross validation of PLSDA. Cross validation was performed Metaboanalyst (v.5.0.) and showed that the inclusion of the first two components achieved good fitting (R^2), predictive power (Q^2) and classification (accuracy). Further inclusion of more components only marginally improved the PLSDA model. Red asterisk represents the best predictive power.

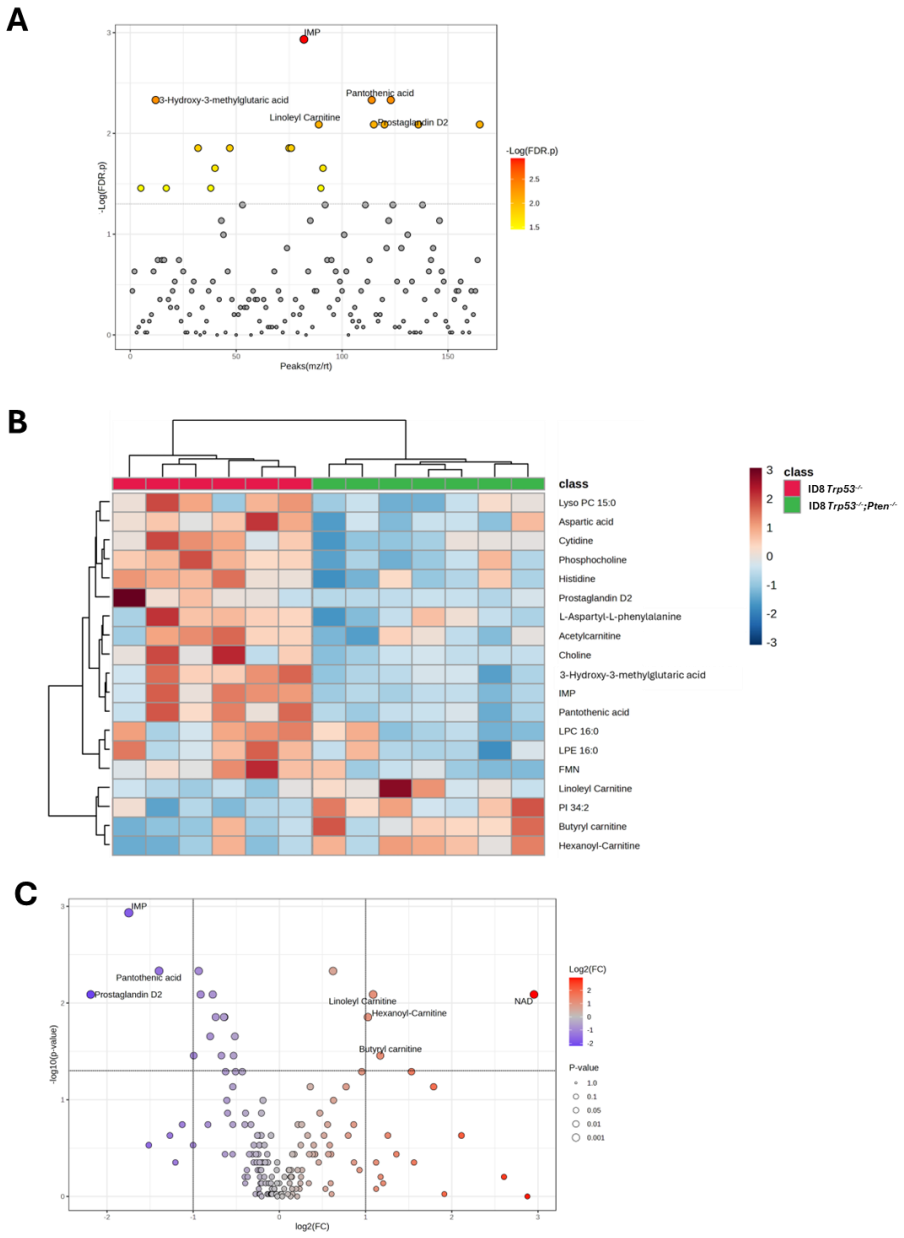


Figure 3.2 Key metabolites with significantly changed abundance in in ID8 *Trp53*$^{-/-}$*; Pten*$^{-/-}$ tumours in comparison to ID8 *Trp53*$^{-/-}$ tumours.

(A) Results of the non-parametric tests (i.e., Wilcoxon rank-sum test) of the untargeted metabolic profiling data was performed by Metaboanalyst (v.5.0.). Significantly changed metabolites are highlighted. (B) Heatmap showing the metabolites with significantly altered abundance. Hierarchical clustering was performed by Pearson distance and Ward clustering. The raw data were normalised against the sum of peaks and then auto-scaled. Thus, 0 in the scale bar indicates mean and the values indicates how many times of SD (e.g., 1 = 1 SD). Positive and negative values suggest higher and lower than mean values, respectively. (C) Volcano plot showing differently expressed metabolites based on fold-change analysis and Wilcoxon rank-sum test. Red and blue dots represent significantly upregulated and downregulated metabolites in ID8 *Trp53*$^{-/-}$*; Pten*$^{-/-}$ tumours, respectively. p-values represent FDR. FC: fold change, FDR: false discovery rate.

3.2.2 Enrichment analysis revealed that several metabolic pathways are altered due to Pten loss

To understand the link between the alteration of metabolite abundance and biological context, the metabolomics data was analysed by metabolite set enrichment analysis (MSEA) using MetaboAnalyst. In brief, metabolites were mapped to the public database of KEGG human metabolic pathways. Quantitative enrichment analysis (QEA) was chosen as the MSEA method because it captures enriched metabolite sets not only when metabolites are significantly changed but also when many metabolites are slightly (i.e., statistically insignificant) but consistently altered (*414*). Thus, QEA provides the unique advantage over the traditional overrepresentation analysis (ORA) which works by comparing the occurrence of metabolites with significance (p-value) above a certain threshold (*414*).

The data showed that significantly enriched metabolite sets include intermediates involved in glycerophospholipids, nicotinic acid and nicotinamide, arginine, histidine, beta-alanine, and pantothenic acid and coenzyme A metabolic pathways (Figure 3.3). Phosphatidylcholine (PtdCho) is a major lipid member of glycerophospholipids and key components of cellular membrane (*415*). Phosphocholine (PhoC) is derived from free choline and is required for *de novo* synthesis of PtdCho (Figure 3.4A) (*416*). In the Kennedy pathway, PtdCho is synthesised using the high-energy intermediate cytidine diphosphate (CDP)-choline (also known as citicholine) (Figure 3.4A) (*416*). Choline can be regenerated via the breakdown of PtdCho and it involves a three-step enzymatic cleavage process with the generation of intermediates lysophosphatidylcholine (lysoPC, also known as 1-acyl-glycerophosphocholine) and glycerophosphocholine (GPC) (Figure 3.4A) (*417*). Here, my data showed that choline and PhoC were significantly downregulated while there is an upward trend in citicholine and GPC in tumours ID8 *Trp53*$^{-/-}$*; Pten*$^{-/-}$ tumours (Figure 3.4B). Pten loss also resulted in an downward trend of lysoPC(18:1) (Figure 3.4B). However, the peak intensity ratio of PhoC to choline was not significantly changed in Pten deficient tumours (Figure 3.4C). These data suggest that the activity of citicholine synthesis and lysoPC breakdown may be altered in Pten deficient tumours.

NAD^+ is an essential metabolic co-factor and can be synthesized via multiple pathways as described in the introduction chapter. In brief, the majority of NAD^+ is synthesised via the salvage pathway by recycling the breakdown product nicotinamide (Figure 3.5A) (*217*). My data showed that there is an upward trend of NAD^+ and a downward trend of nicotinamide in tumours with Pten loss (Figure 3.5B). Interestingly, the ratio of NAD^+ to nicotinamide is significantly higher in tumours with Pten deficiency (Figure 3.5C). Collectively, these data suggest that the flux of the salvage pathway or the activity of NAD^+ catabolism mediated by PARP and/or SIRT may be changed in ID8 *Trp53*$^{-/-}$*; Pten*$^{-/-}$ tumours.

Arginine is a semi-essential amino acid because *de novo* synthesis is not sufficient to compensate for the limited dietary uptake and increased demands under certain conditions (e.g., pregnancy) (*418*). The key substrate of endogenous arginine synthesis is citrulline that is derived from glutamate or proline (Figure 3.6A) (*418*). Aspartate is the nitrogen donor and condenses with citrulline to produce arginosuccinate which is cleaved to generate arginine and fumarate (*419*). Apart from protein synthesis, arginine can be hydrolysed via the arginase pathway for ornithine and urea. Ornithine undergoes further enzymatic reactions for regenerate proline, glutamate and citrulline (*420*). Ornithine can also be diverted to the polyamine pathway and generate spermidine (*418*). Additionally, arginine can be catabolised by nitric oxide synthases (NOS) to nitric oxide and citrulline (*421*). My data showed that aspartate and citrulline abundance is significantly decreased and increased in ID8 *Trp53*$^{-/-}$*; Pten*$^{-/-}$ tumours, respectively (Figure 3.6B). There is an increasing trend in glutamate and spermidine, and a decreasing trend in arginine, fumarate, spermine and urea in Pten deficient tumours (Figure 3.6B). This suggests that the activity of arginine metabolism and polyamine pathway may be altered in tumours with Pten loss.

Histidine is an essential amino acid and undergoes catabolism in addition to protein synthesis. The first step is rate-limiting and catalysed by histidase to produce ammonia and urocanate (Figure 3.7A) (*422*). In the subsequent enzymatic reactions, urocanate is converted to glutamate (Figure 3.7A) (*422*). My data showed that histidine abundance is significantly reduced in Pten deficient tumours. There is also an upward trend of glutamate and urocanate abundance in tumours with Pten loss (Figure 3.7B). However, histidase is mainly expressed in

liver and skin tissue (*422*). Nevertheless, my data showed that Pten loss significantly downregulated histidine concentrations in ID8 tumours.

Pantothenic acid (also known as vitamin B5) is a precursor of coenzyme A synthesis (*423*). The first step is rate-limiting and catalysed by pantothenate kinase to produce 4'-phosphopantothenate which undergoes further reactions to CoA (Figure 3.8A) (*424*). In my data, pantothenate showed significantly reduced abundance (Figure 3.8B), thereby suggesting Pten loss may regulate pantothenic acid metabolism.

β-alanine is a structural intermediate between α-amino acid and γ-amino acid and can be synthesized using multiple substrates (Figure 3.9A) (*425*). Uracil is one of the substrate to produce β-alanine via deamination and carboxylation (*426*). Additionally, the cleavage of the dipeptide carnosine by carnosinase generates histidine and β-alanine (*427*). My data showed that histidine is significantly decreased and there is a downward trend of uracil in tumours with Pten loss (Figure 3.9B). However, carnosinase is mainly expressed in enterocytes and serum (*427*). Given that β-alanine abundance could not be determined in this study, the enrichment of β-alanine pathway may have limited relevance to ovarian tumours.

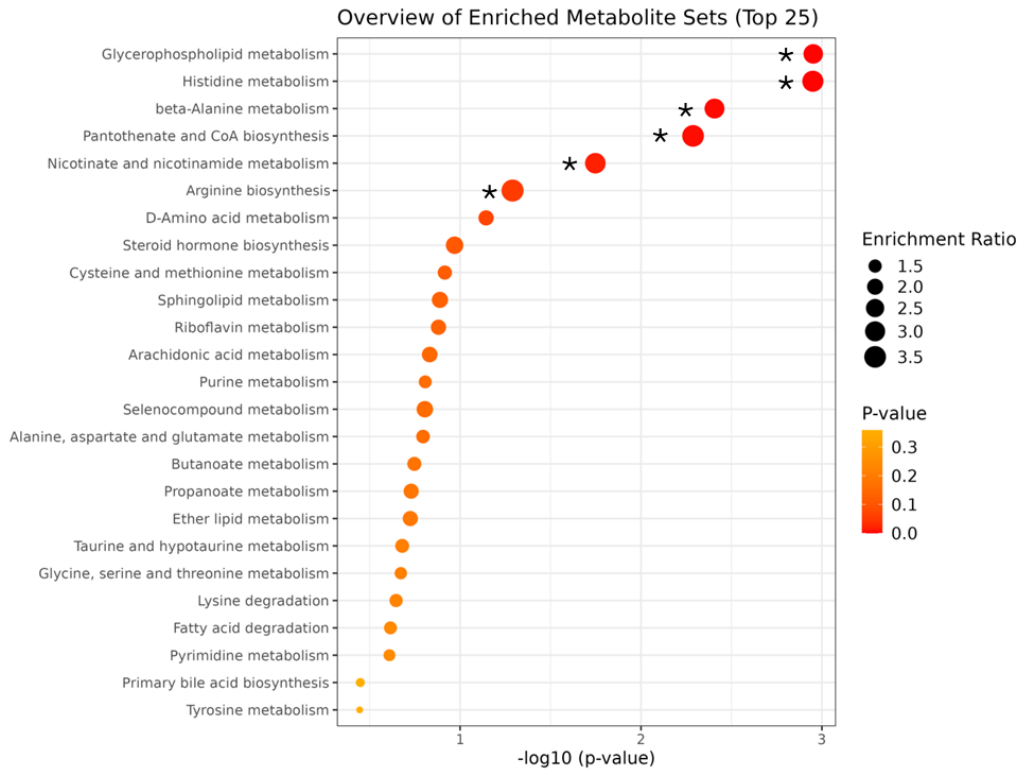


Figure 3.3 Metabolic pathways enriched in ID8 *Trp53*$^{-/-}$*; Pten*$^{-/-}$ tumours.
Metabolite set enrichment analysis was performed using the quantitative enrichment analysis method by Metaboanalyst (v.5.0.). The metabolites were mapped to the KEGG database of human metabolic pathways. The significantly enriched metabolic sets with an FDR<0.05 were highlighted by an asterisk. The number of hits is: 5 in the glycerophospholipid pathway, 2 in NAD synthesis pathway, 8 in arginine metabolism pathway, 3 in histidine pathway, 1 in pantothenate pathway and 2 in β-alanine pathway. All the hits with relative abundance in each pathway are shown in Figures 3.4-3.10.

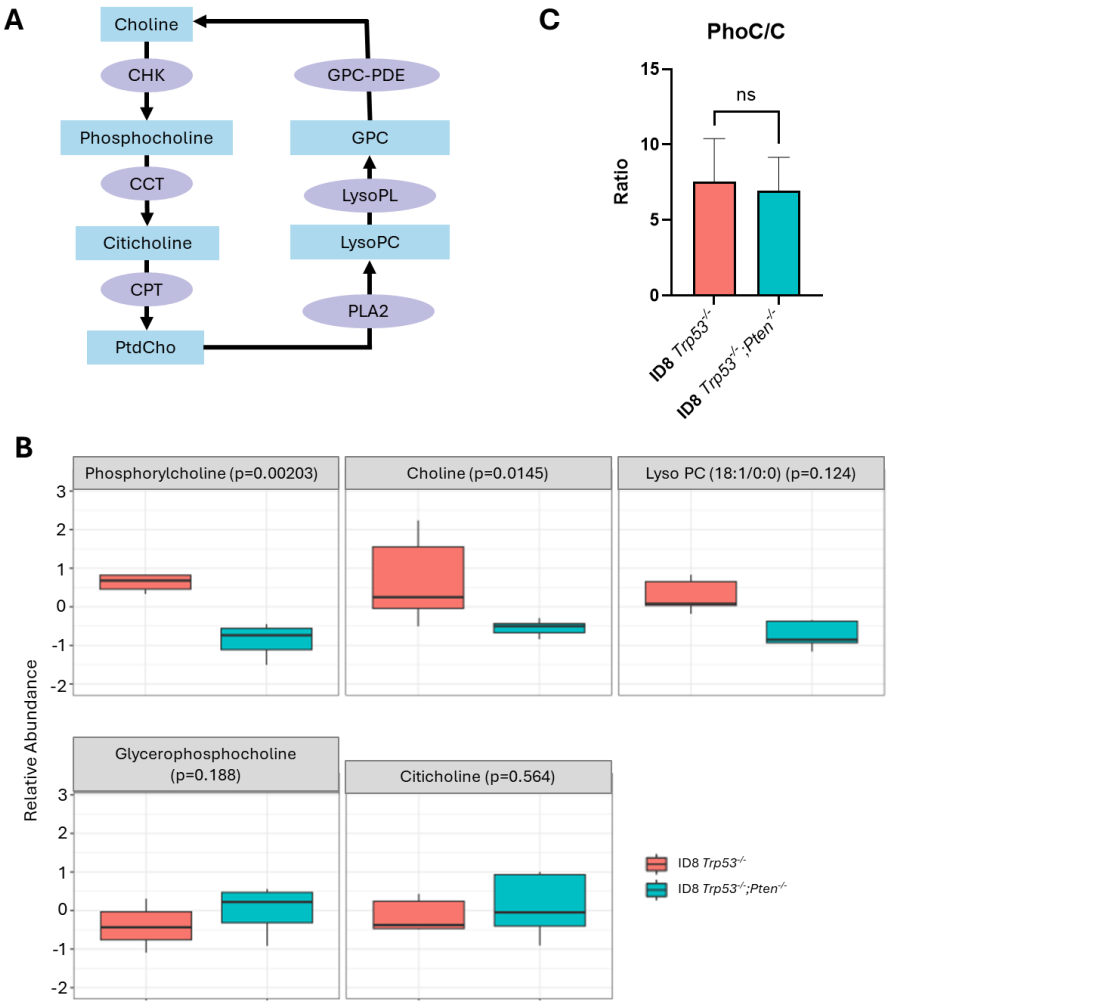


Figure 3.4 Metabolites in the glycerophospholipid pathway were enriched in ID8 *Trp53*$^{-/-}$; *Pten*$^{-/-}$ tumours.

(A) Schematics of the glycerophospholipid pathway. Choline is the substrates for PtdCho synthesis, respectively. Choline kinase catalyses the phosphorylation of choline to produce phosphocholine which enters the Kennedy pathway for PtdCho synthesis via the intermediate CDP-Choline. Catabolic metabolism of PtdCho regenerates choline via the intermediates LysoPC and GPC. Metabolites and enzymes are shown in blue boxes and purple ovals, respectively. (B) Relative abundance of metabolites in the pathway. P values were calculated by Metaboanalyst (v.5.0.) and represent FDR. Data were auto-scaled and represented using box plots with the line inside the box representing media. The box represent the middle 50% of the data with the left and right edge of the box showing the lower (i.e., the 25 percentile) and upper quartile value (i.e., the 75 percentile), respectively. The whiskers extend from the box to the highest and lowest data value.(C) The peak intensity ratio of phosphocholine (PhoC) to free choline (C). Data represent mean ± SD. Statistical significance was calculated by t tests. ns, not significant. (B-C) 6 and 7 biological replicates were used in ID8 *Trp53*$^{-/-}$ tumours and ID8 *Trp53*$^{-/-}$; *Pten*$^{-/-}$ tumours, respectively. CHK: choline kinase, CCT: CTP:phosphocholine cytidylyltransferase, CPT: diacylglycerol cholinephosphotransferase, GPC: glycerophosphocholine, PLA2: phospholipase A2, GCP-PDE: Glycerophosphocholine phosphodiesterase, LysoPL: lysophospholipase.

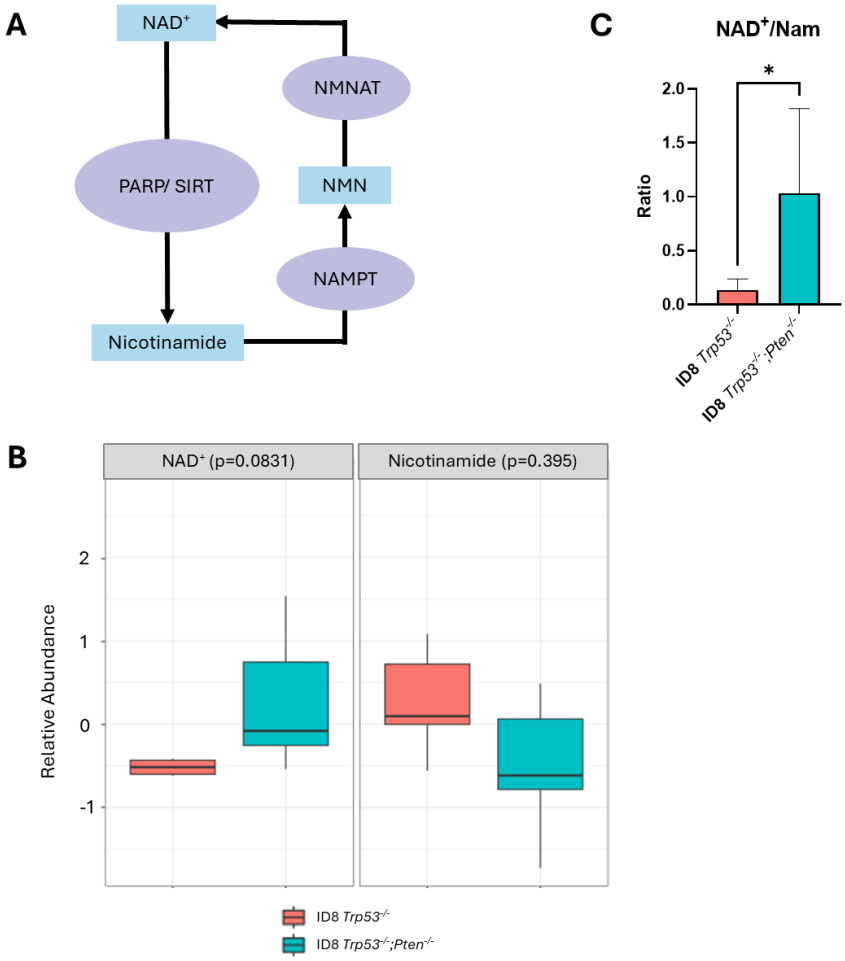


Figure 3.5 Metabolites in the salvage pathway of NAD synthesis were enriched in ID8 *Trp53*$^{-/-}$*; Pten*$^{-/-}$ tumours.

(A) Schematics of the salvage pathway of NAD synthesis. NAD^+ is a substrate of multiple enzymes including PARP and the breakdown product is nicotinamide (Nam). NAMPT catalyses the conversion of NAM to NMN for regeneration of NAD^+. The majority of NAD^+ is synthesised by the salvage pathway. Metabolites and enzymes are shown in blue boxes and purple ovals, respectively. (B) Relative abundance of metabolites in the pathway. P values were calculated by Metaboanalyst (v.5.0.) and represent FDR. Data were auto-scaled and represented using box plots with the line inside the box representing media. The box represent the middle 50% of the data with the left and right edge of the box showing the lower (i.e., the 25 percentile) and upper quartile value (i.e., the 75 percentile), respectively. The whiskers extend from the box to the highest and lowest data value. (C) The ratio of peak intensity of NAD^+ to Nam. Data represent mean ± SD. Statistical significance was calculated by t tests. * $p<0.05$. (B-C) 6 and 7 biological replicates were used in ID8 *Trp53*$^{-/-}$ tumours and ID8 *Trp53*$^{-/-}$*; Pten*$^{-/-}$ tumours, respectively. NAMPT: nicotinamide phosphoribosyl transferase, MNM: nicotinamide mononucleotide, NMNAT: NMN adenylyltransferases, PARP: poly(ADP-ribose) polymerase, SIRT: sirtuin.

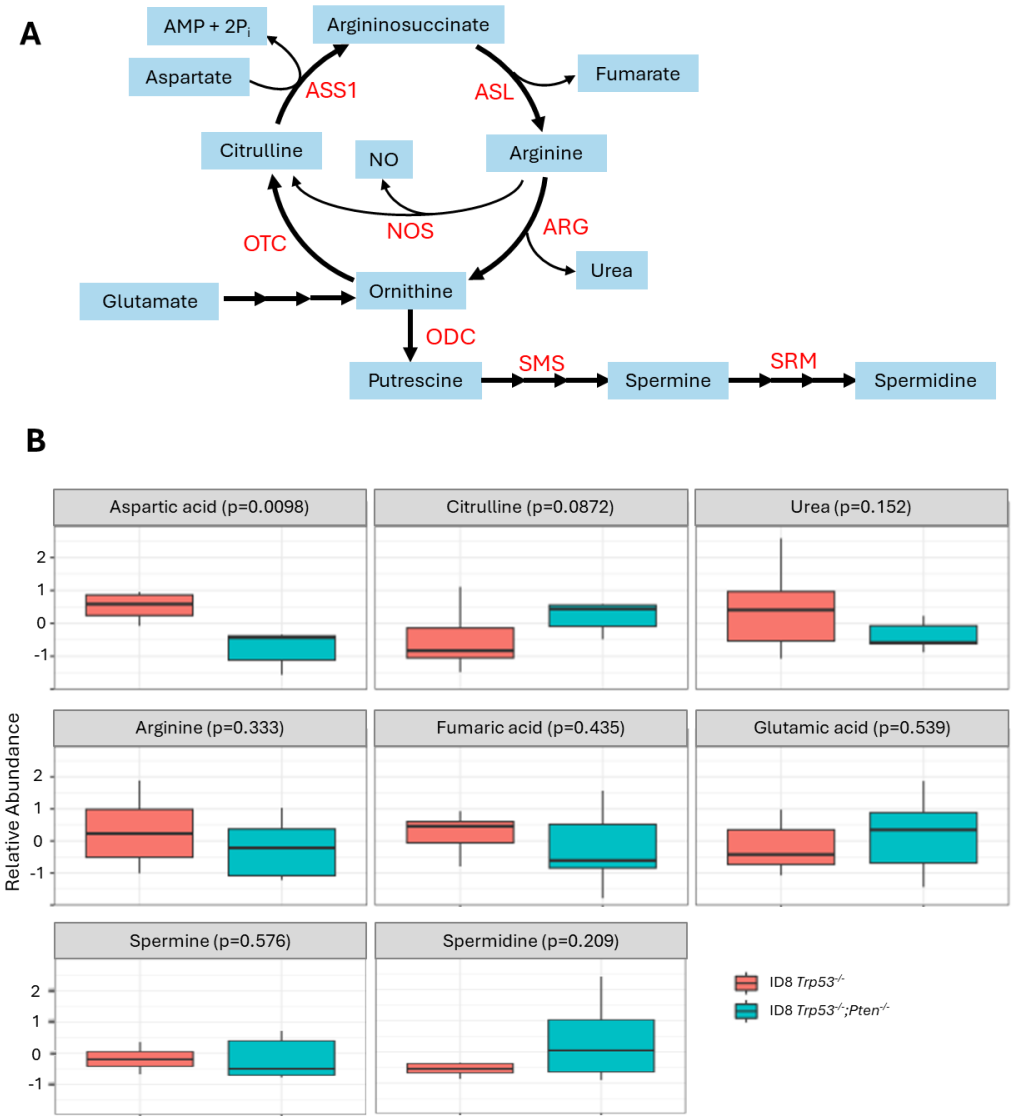


Figure 3.6 Metabolites in the arginine metabolism pathway were enriched in ID8 *Trp53*$^{-/-}$; *Pten*$^{-/-}$ tumours.

(A) Schematics of arginine metabolism pathway. Citrulline, derived from glutamine or proline is the substrate of arginine biosynthesis. Aspartate is the nitrogen source and condenses with citrulline to produce argininosuccinate which is then cleaved to arginine. Arginine is hydrolysed to ornithine and urea and further metabolism of ornithine via the polyamine pathway generates spermidine. Arginine can also be catabolised by NOS to citrulline and NO. Metabolites and enzymes are shown in blue boxes and red text, respectively. (B) Relative abundance of metabolites in the pathway. P values were calculated by Metaboanalyst (v.5.0.) and represent FDR. Data were auto-scaled and represented using box plots with the line inside the box representing media. The box represent the middle 50% of the data with the left and right edge of the box showing the lower (i.e., the 25 percentile) and upper quartile value (i.e., the 75 percentile), respectively. The whiskers extend from the box to the highest and lowest data value. 6 and 7 biological replicates were used in ID8 *Trp53*$^{-/-}$ tumours and ID8 *Trp53*$^{-/-}$; *Pten*$^{-/-}$ tumours, respectively. ASS1: argininosuccinate synthetase 1, ASL: argininosuccinate lyase, OTC: ornithine carbamoyltransferase, NOS: nitric oxide synthase, ARG: arginase, ODC: ornithine decarboxylase, SMS: spermine synthase, SRM: spermidine synthase.

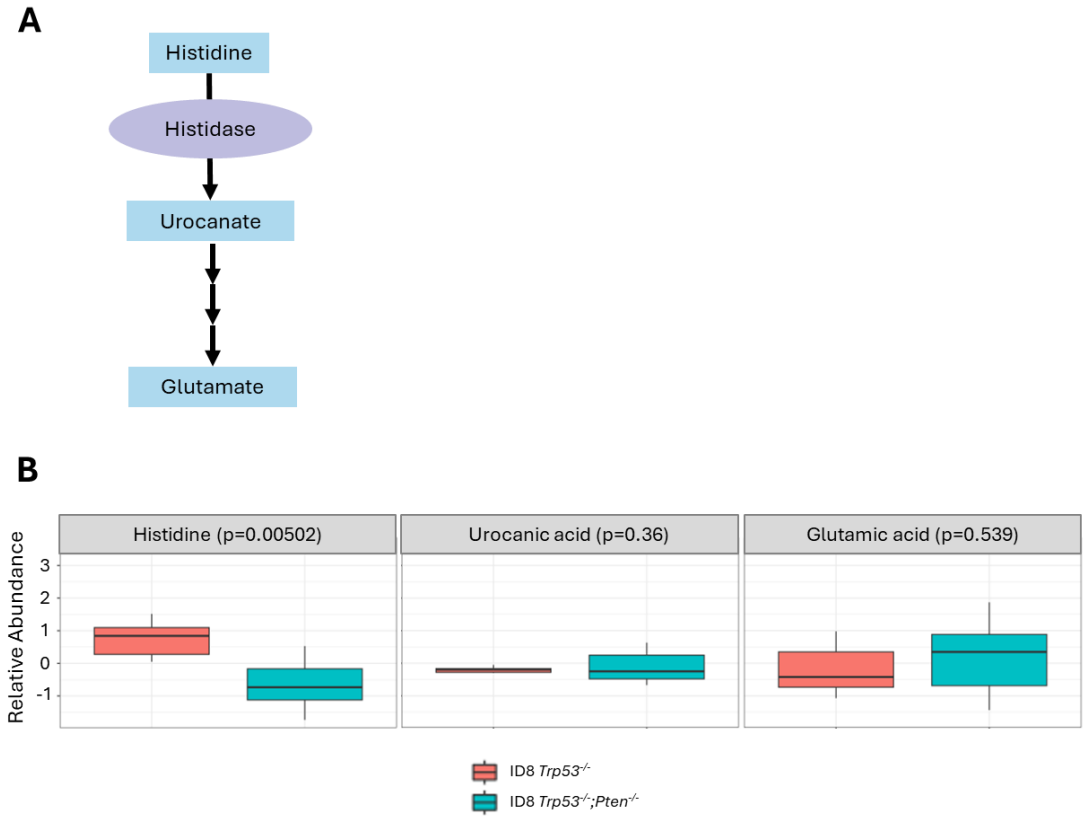


Figure 3.7 Metabolites in histidine metabolism pathway were enriched in ID8 *Trp53*$^{-/-}$*; Pten*$^{-/-}$ tumours.

(A) Schematics of histidine metabolism pathway. Histidine is catabolised by histidase to urocanate which undergoes further enzymatic reactions to produce glutamate. Metabolites and enzymes are shown in blue boxes and purple ovals, respectively. (B) Relative abundance of metabolites in the pathway. P values were calculated by Metaboanalyst (v.5.0.) and represent FDR. Data were auto-scaled and represented using box plots with the line inside the box representing media. The box represent the middle 50% of the data with the left and right edge of the box showing the lower (i.e., the 25 percentile) and upper quartile value (i.e., the 75 percentile), respectively. The whiskers extend from the box to the highest and lowest data value. 6 and 7 biological replicates were used in ID8 *Trp53*$^{-/-}$ tumours and ID8 *Trp53*$^{-/-}$*; Pten*$^{-/-}$ tumours, respectively.

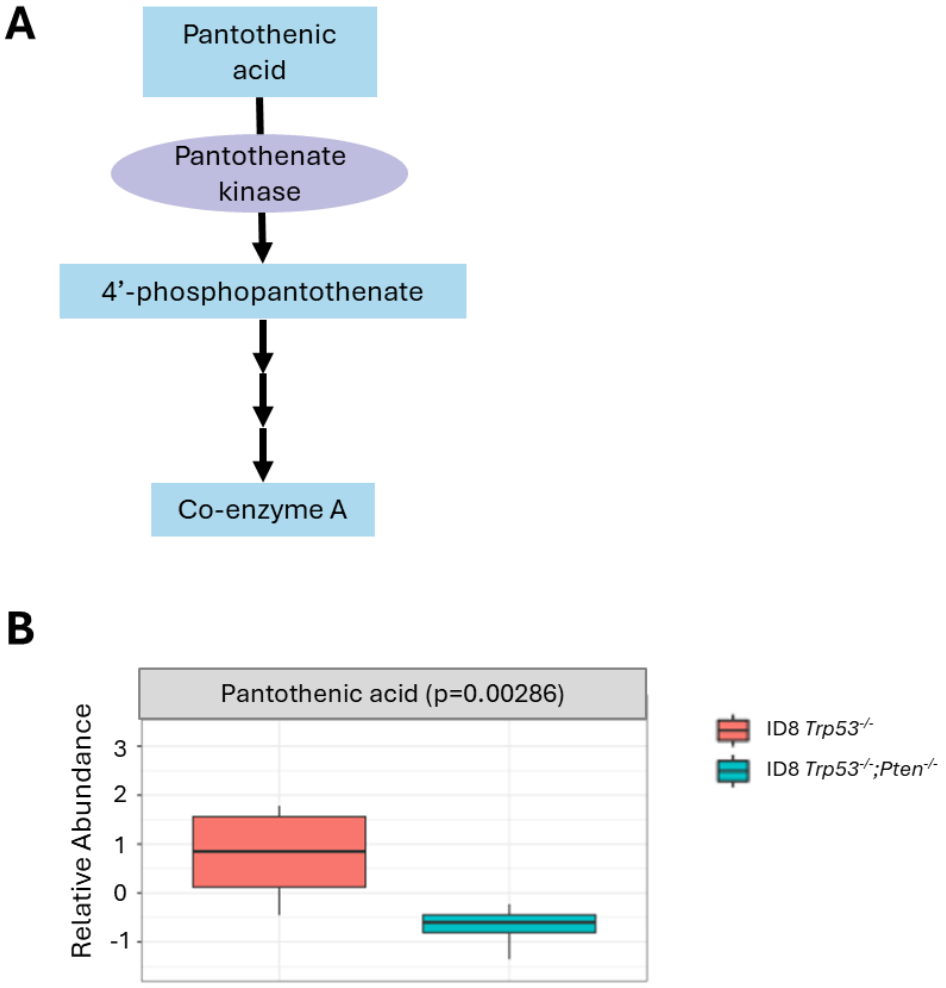


Figure 3. 8 Metabolites in pantothenate metabolism pathway were enriched in ID8 *Trp53*$^{-/-}$; *Pten*$^{-/-}$ tumours.

(A) Schematics of pantothenate metabolism pathway. The first and rate-limiting step is catalysed by pantothenate kinase and produces 4'-phosphopantothenate which undergoes further enzymatic reactions to generate coenzyme A. Metabolites and enzymes are shown in blue boxes and purple ovals, respectively. (B) Relative abundance of metabolites in the pathway. P values were calculated by Metaboanalyst (v.5.0.) and represent FDR. Data were auto-scaled and represented using box plots with the line inside the box representing media. The box represent the middle 50% of the data with the left and right edge of the box showing the lower (i.e., the 25 percentile) and upper quartile value (i.e., the 75 percentile), respectively. The whiskers extend from the box to the highest and lowest data value. 6 and 7 biological replicates were used in ID8 *Trp53*$^{-/-}$ tumours and ID8 *Trp53*$^{-/-}$; *Pten*$^{-/-}$ tumours, respectively.

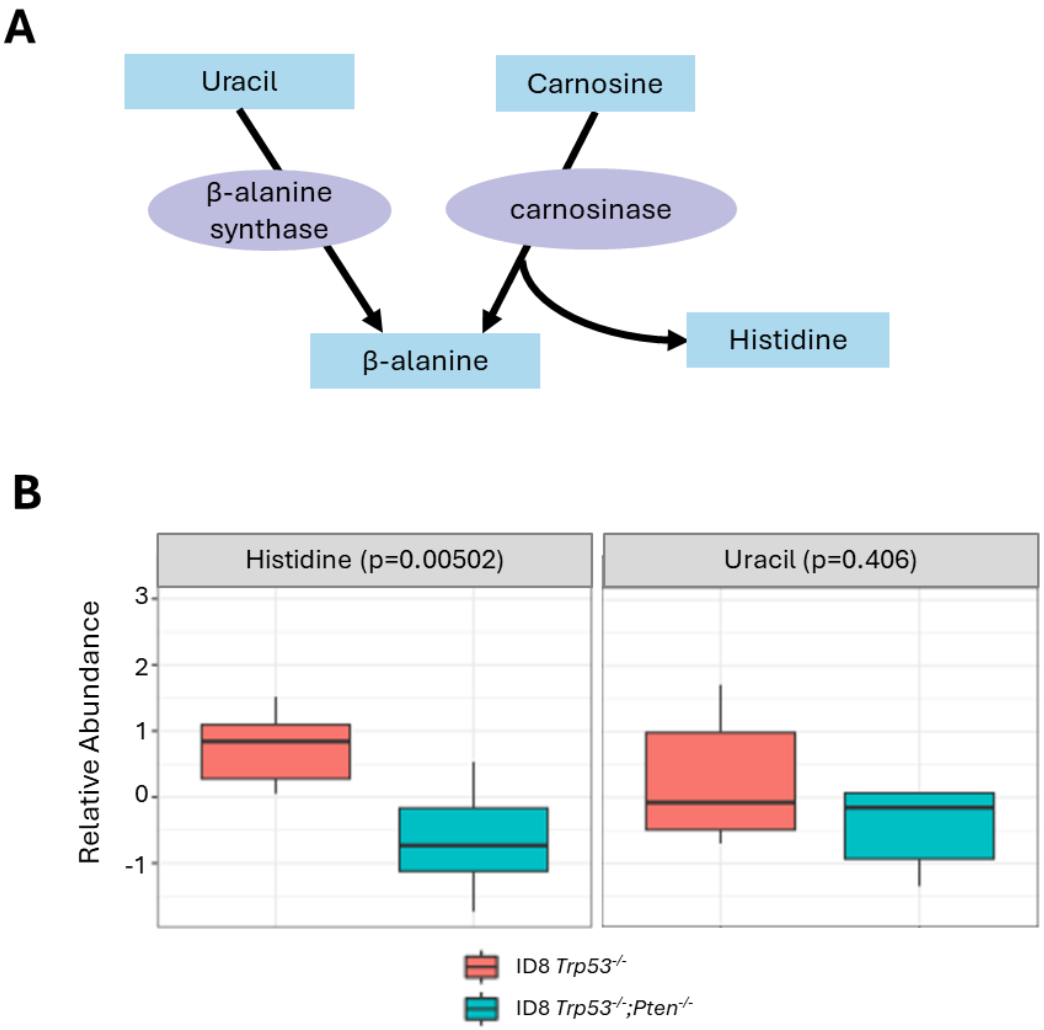


Figure 3.9 Metabolites in β-alanine metabolism pathway were enriched in ID8 *Trp53*$^{-/-}$*; Pten*$^{-/-}$ tumours.

(A) Schematics of β-alanine metabolism pathway. β-alanine can be synthesized from uracil via deamination and carboxylation. Alternatively, the cleavage of the dipeptide carnosine produces β-alanine and histidine. Metabolites and enzymes are shown in blue boxes and purple ovals, respectively. (B) Relative abundance of metabolites in the pathway. P values were calculated by Metaboanalyst (v.5.0.) and represent FDR. Data were auto-scaled and represented using box plots with the line inside the box representing media. The box represent the middle 50% of the data with the left and right edge of the box showing the lower (i.e., the 25 percentile) and upper quartile value (i.e., the 75 percentile), respectively. The whiskers extend from the box to the highest and lowest data value. 6 and 7 biological replicates were used in ID8 *Trp53*$^{-/-}$ tumours and ID8 *Trp53*$^{-/-}$*; Pten*$^{-/-}$ tumours, respectively.

3.2.3 Pten loss increased glycolytic flux and glucose contribution to FA synthesis

As Akt pathway activation has been reported to regulate glucose metabolism in cancer cells (*428*), glycolysis and the TCA cycle metabolism were investigated. Here, ID8 *Trp53*$^{-/-}$ cells and ID8 *Trp53*$^{-/-}$*; Pten*$^{-/-}$ cells were used as a model. The depletion of Pten protein and activation of Akt pathway were verified by WB. The results showed no detectable expression of Pten and increased levels of pAkt in ID8 *Trp53*$^{-/-}$*; Pten*$^{-/-}$ cells (Appendix Figure 3.2), which confirmed the validity of this model.

To examine the glycolytic flux, the uptake rates of glucose and excretion rates of lactate (i.e., the product of glycolysis) were measured. In brief, the cells were incubated for 24h and media were collected at the start and end of incubation to measure glucose and lactate concentrations by NMR. My data showed that glucose uptake and lactate secretion rates were significantly increased in cells with Pten loss (Figure 3.10A-B). This suggests that Pten loss increases glycolytic flux. Because the glycolytic intermediates are substrates of other metabolic pathways (e.g., PPP pathway, serine synthesis and alanine synthesis), the ratio of lactate production to glucose consumption (L/G ratio) indicates the relative activity of glycolysis to the other pathways requiring glycolytic intermediates (*429*). My data showed there is no significant difference in L/G ratio between the two genotypes (Figure 3.10C), thereby suggesting Pten loss did not alter the relative activity of glycolysis. Additionally, it has been reported that the ratio between lactate and pyruvate concentrations in media (L/P ratio) reflects cytosolic NADH/NAD^+ redox status (*430*). This is because the equilibrium of LDH-catalysed interconversion of lactate and pyruvate is dependent on NADH/NAD^+ ratio (*430*). The results showed that Pten loss did not change the L/P ratio (Figure 3.10D), thereby suggesting the intracellular NADH/NAD^+ ratio remains the same in the two cell lines.

To further probe for the intracellular metabolic fate of glucose, stable isotope labelling experiments were performed. In brief, ID8 *Trp53*$^{-/-}$ cells and ID8 *Trp53*$^{-/-}$*; Pten*$^{-/-}$ cells were incubated with $^{13}C_6$-glucose for 24h. Intracellular metabolites were extracted and separated into aqueous and organic fractions. As the glycolysis and TCA cycle intermediates are water

soluble, the aqueous fraction was then measured by GC-MS. The ^{13}C enrichment patterns of glycolysis and TCA cycle intermediates are illustrated in Figure 3.11. Pyruvate, the end-product of glycolysis, is fully labelled with ^{13}C atoms (i.e., M+3) Next, pyruvate feeds the TCA cycle in the form of acetyl-CoA via the pyruvate dehydrogenase (PDH) flux, which labels the TCA cycle intermediates (e.g., citrate) with the pattern of M+2. My data showed that ^{13}C enrichment of pyruvate or lactate is not significantly changed in cells with Pten loss (Figure 3.12). Moreover, there is no significant difference in the fraction of M+2 labelled TCA cycle intermediates, including citrate and α-KG (Figure 3.12). This indicates that Pten loss fails to alter glucose contribution to the TCA cycle.

Additionally, M+3 citrate is derived from pyruvate carboxylase (PC flux) where pyruvate is converted to OAA and enters the TCA cycle (Appendix Figure 3.3A) (*431*). M+5 citrate results from the condensation of M+3 OAA (i.e., the PC flux) with M+2 acetyl-CoA (i.e., the PDH flux) (Appendix Figure 3.3B). My data showed very low levels of M+3 and M+5 citrate and that there was no significant difference in the fraction of M+3 or M+5 citrate between the two cell lines (Appendix Figure 3.3C), which suggests that pyruvate mainly enters the TCA cycle via the PDH flux and Pten loss cannot change the relative activity of the PDH and PC flux.

Citrate can be exported into cytosol and metabolised to acetyl-CoA for FA and cholesterol *de novo* synthesis (*432*). Additionally, Akt signalling activation has been reported to upregulate FA and cholesterol synthesis in multiple cancer types (*83, 433*). Therefore, the activity of FA synthesis and glucose contribution as a carbon source were examined. Briefly, the organic fraction that contains lipids and was obtained as described in the previous paragraph was analysed by GC-MS. Endogenously synthesised FA is a substrate of synthesis of triacylglycerol (TAG) which consists of a glycerol backbone and three fatty acyl chains (*434*). Technically, it is challenging to detect TAG using GC-MS due to its high boiling point and low levels of volatility. Thus, the samples were subject to transmethylation to release the fatty acyl chains in the form of methyl FA to enable GC-MS measurement. The schematics of labelling patterns of newly synthesized FA (e.g., palmitate (16:0) and stearate (18:0)) are depicted in Figure 3.13. Acetyl-CoA derived from labelled citrate is fully labelled (i.e., M+2) and palmitate synthesis involves sequential condensation of multiple acetyl-CoA molecules, thereby

creating the ordered labelling pattern (i.e., M+2, M+4, M+6 etc). Subsequent elongation requires the condensation of palmitate with an additional molecule of acetyl-CoA to produce stearate. My data showed that significant levels of ^{13}C enrichment into methyl FA (i.e., methyl palmitate, and methyl stearate) in both cell lines (Figure 3.14A), thereby confirming the activity of FA synthesis. However, ^{13}C enrichment of cholesterol cannot be detected (data not shown), which suggests that the activity of cholesterol synthesis using glucose as a substrate is low during the 24h incubation.

Because acetyl-CoA is unstable and difficult to measure by GC-MS, its labelling was modelled using ISA based on MIDs of palmitate (*401*). In addition, ISA also calculate the fraction of newly synthesised FA during the incubation period. The results showed that a significantly higher proportion of lipogenic acetyl-CoA is derived from glucose in ID8 *Trp53*$^{-/-}$*; Pten*$^{-/-}$ cells (Figure 3.14B), which indicates that Pten loss increases glucose contribution to FA synthesis. However, the percentage of de novo synthesised FA remained unchanged between the two cells lines (Figure 3.14B), thereby suggesting that Pten loss has no significant impact on the flux of FA synthesis.

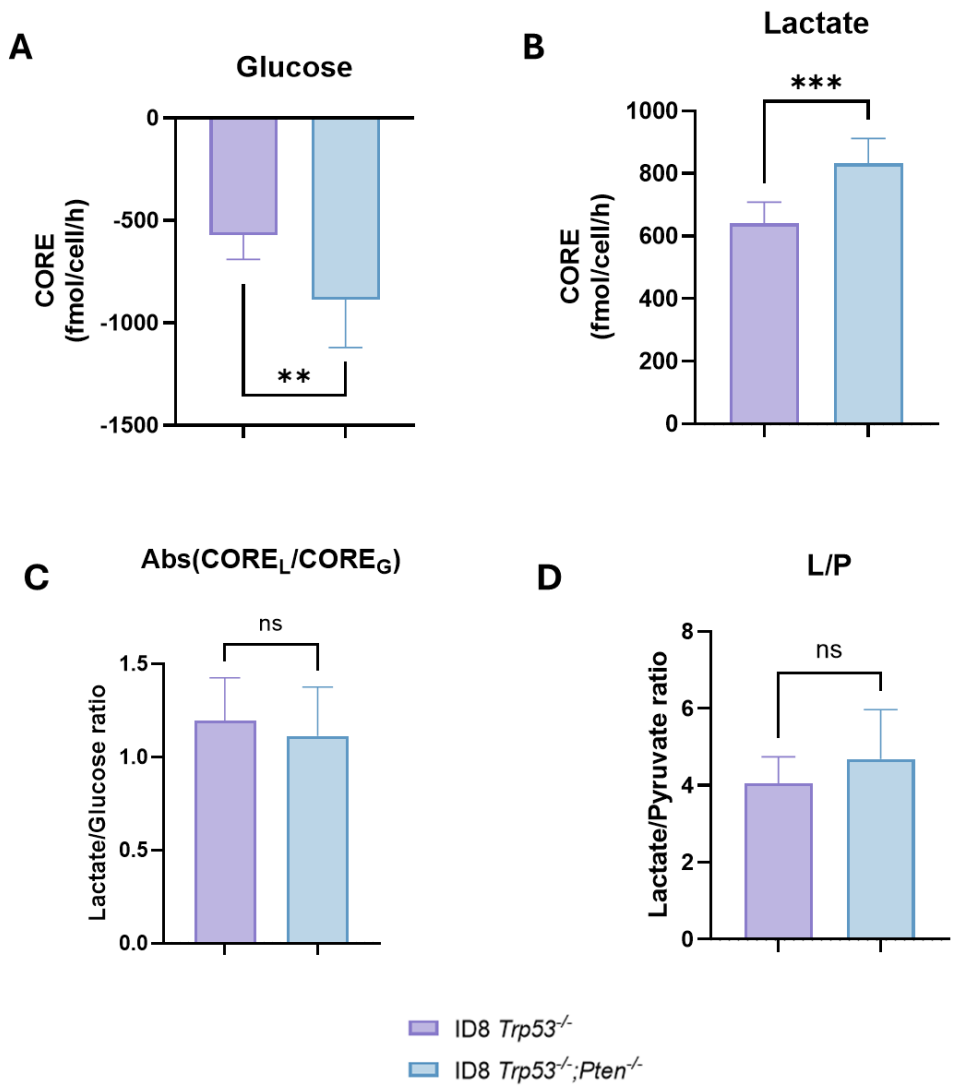


Figure 3.10 Pten loss upregulated the rates of glucose uptake and lactate release in ID8 cells. (A-B) CORE (Consumption or Release) rates of glucose (A) and lactate (B) in ID8 *Trp53*$^{-/-}$ cells and ID8 *Trp53*$^{-/-}$*; Pten*$^{-/-}$ cells without drug treatment. Media were collected at the start and end of the 24h incubation period. NMR spectroscopy was used to measure the concentrations of glucose and lactate. CORE rates were calculated by dividing the changes in metabolite levels with cell density. Positive and negative CORE values indicate net release and consumption, respectively. (C) Ratio of lactate release and glucose consumption rates measured from (A-B). Please note the ratio is calculated using absolute values of CORE rates. Abs: absolute, CORE$_L$/CORE$_G$: CORE rates of lactate/glucose. (D) Ratio of lactate and pyruvate concentrations in media. Levels of lactate and pyruvate in media at the end of the 24h incubation were examined by NMR spectroscopy. Data represent mean ± SD from three biological repeats. Statistical significance was calculated using t tests. ** p<0.01, *** p<0.001, ns: not significant.

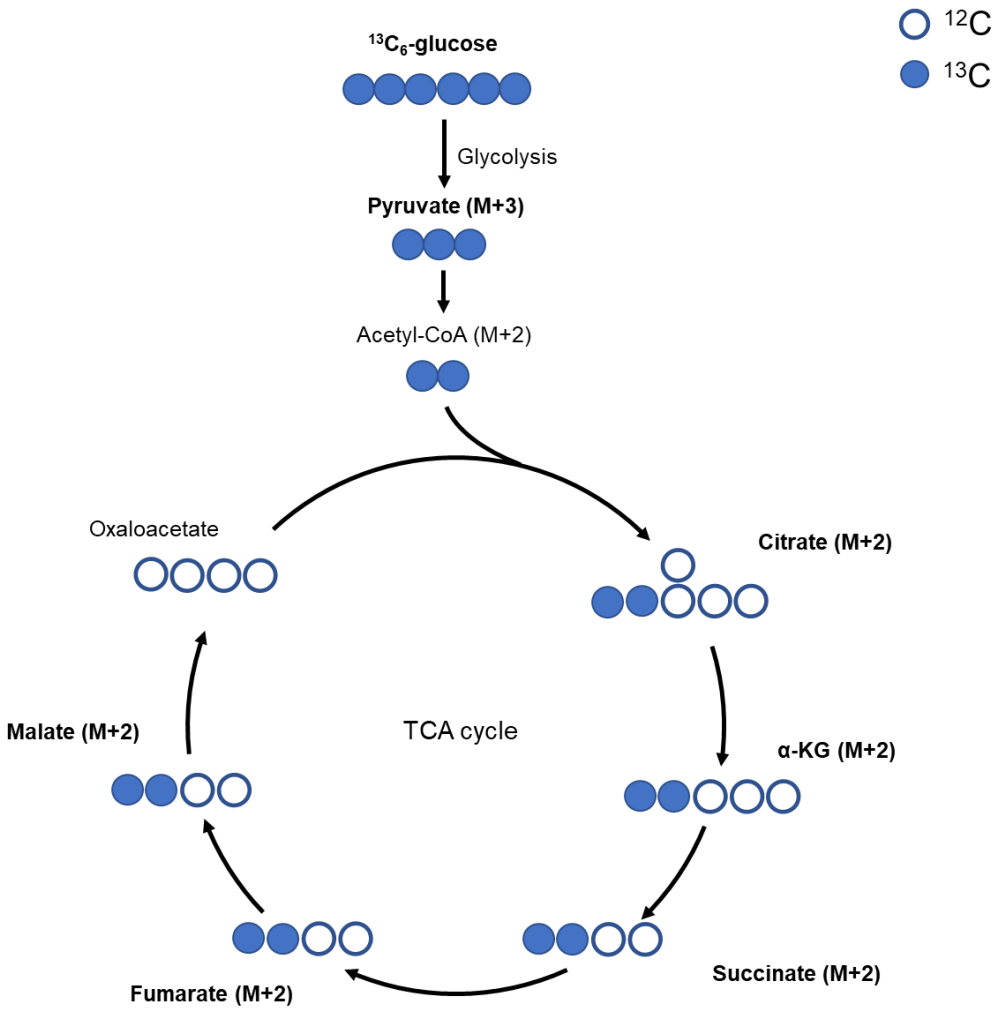


Figure 3.11 Schematics of the ^{13}C labelling patterns of central carbon metabolism using $^{13}C_6$-glucose as a tracer.

^{13}C atoms in $^{13}C_6$-glucose are transferred to downstream metabolites. Pyruvate and the product acetyl-CoA are uniformly labelled (i.e., M+3 and M+2, respectively). Unlabelled oxaloacetate condenses with labelled acetyl-CoA and generated M+2 labelled TCA cycle intermediates. For simplicity, labelling patterns of the first round of the TCA cycle are shown. Metabolites detected in this study are highlighted in bold.

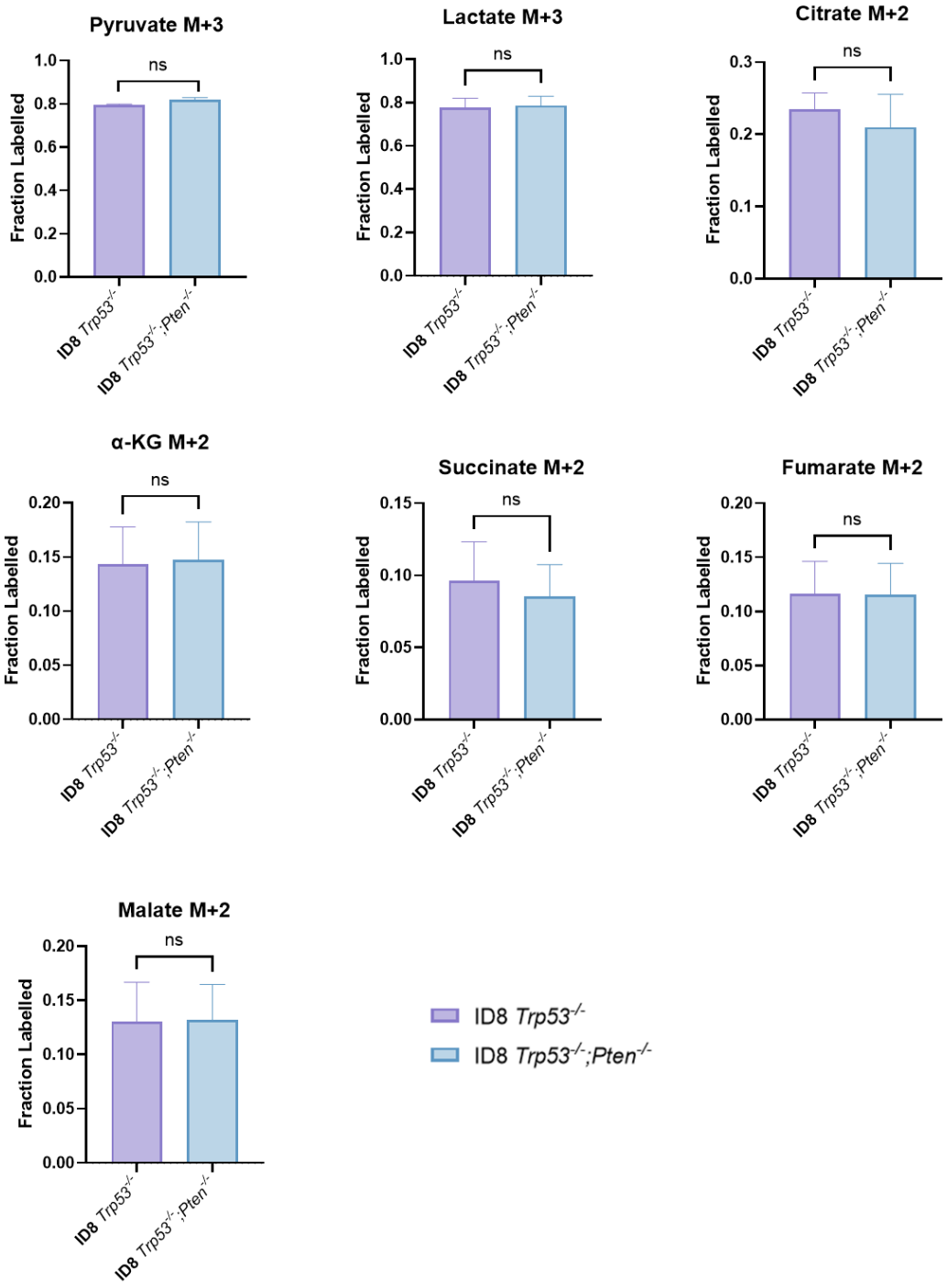


Figure 3.12 Pten loss did not impact glucose contribution to the TCA cycle as a carbon source. Fraction of M+3 labelled pyruvate and lactate, and M+2 labelled TCA cycle intermediates (e.g., citrate) are shown. ID8 *Trp53*$^{-/-}$ cells and ID8 *Trp53*$^{-/-}$*; Pten*$^{-/-}$ cells were cultured in media with 5.6mM $^{13}C_6$-glucose for 24h. Intracellular metabolites were then extracted and analysed by GC-MS. Data represent mean ± SD from three independent biological repeats. Statistical significance was calculated by t tests. ns, not significant.

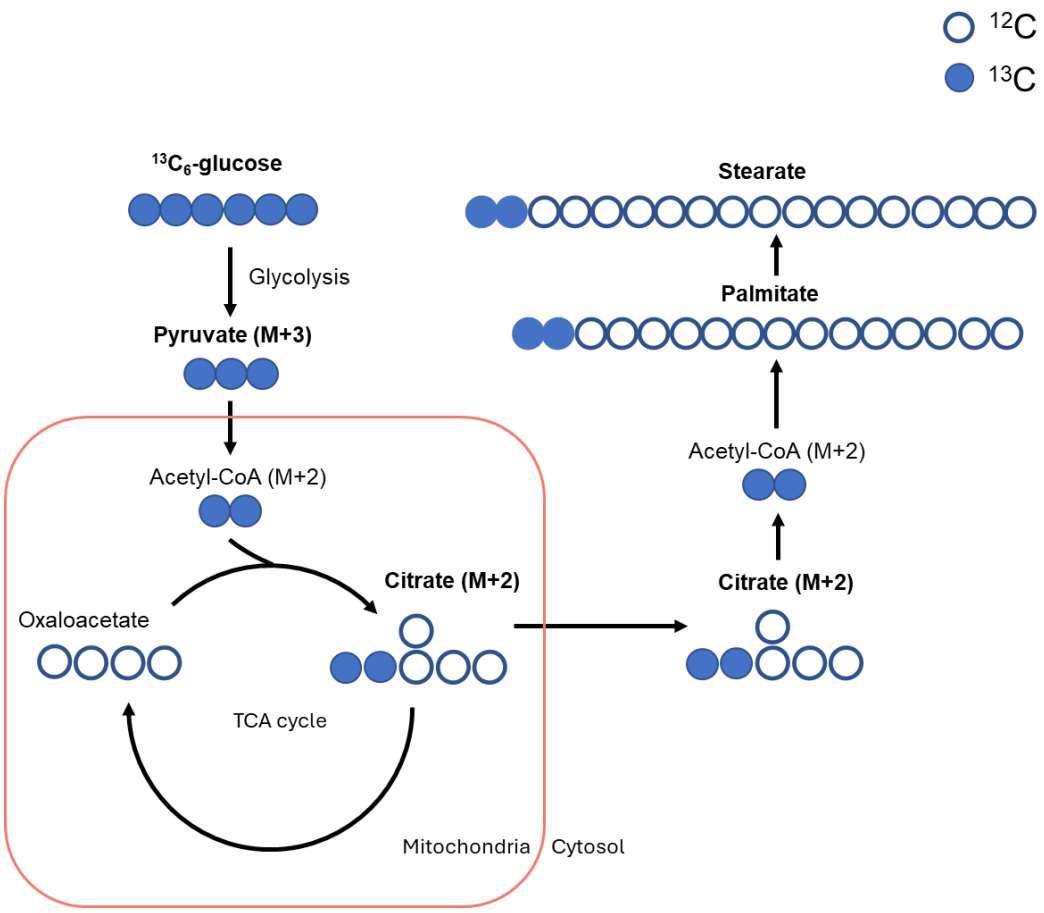


Figure 3.13 Schematics of the ^{13}C enrichment patterns of the TCA cycle and FA synthesis using $^{13}C_6$-glucose as a tracer.

M+2 citrate is generated via glycolysis and pyruvate dehydrogenase flux. Citrate is subsequently transported out of mitochondria and is cleaved into acetyl-CoA in the cytosol. Acetyl-CoA is the substrate of FA *de novo* synthesis. Multiple acetyl-CoA molecules condense via several iterations to produce palmitate (16:0). Palmitate can undergo elongation by incorporating a molecule of acetyl-CoA to generate stearate (18:0).

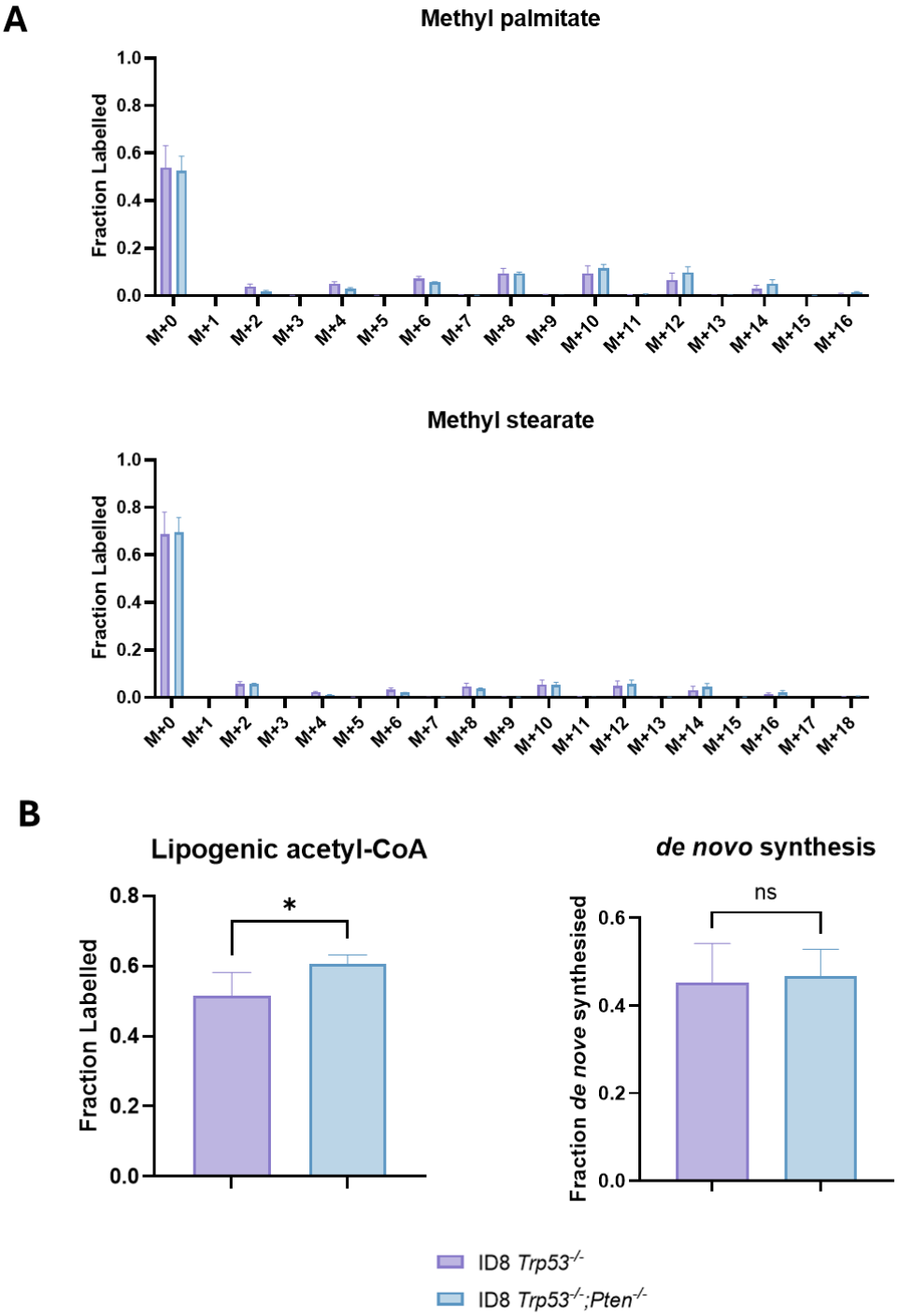


Figure 3.14 Pten loss upregulated glucose contribution to FA de novo synthesis in ID8 cells. (A) MID of methyl palmitate and methyl stearate. ID8 *Trp53*$^{-/-}$ cells and ID8 *Trp53*$^{-/-}$*; Pten*$^{-/-}$ cells were cultured in media with 5.6mM $^{13}C_6$-glucose for 24h. Intracellular metabolites were then extracted and analysed by GC-MS. (B) The fraction of lipogenic acetyl-CoA (left, parameter D) and newly synthesized FA during tracer incubation (right, parameter g(t)). D and g(t) were estimated by ISA modelling using the MID of methyl palmitate. Data represent mean ± SD from three independent biological repeats. Statistical significance was calculated by t tests. *, $p<0.05$, ns, not significant.

3.2.4 Glutamine metabolism is not significantly altered in ID8 *Trp53*$^{-/-}$*; Pten*$^{-/-}$ cells

The activation of Akt pathway has been reported to stimulate glutamine uptake indirectly via MYC and its metabolism through the TCA cycle (*83, 140*). Therefore, glutamine utilization was examined using ID8 *Trp53*$^{-/-}$ cells and ID8 *Trp53*$^{-/-}$*; Pten*$^{-/-}$ cells. To start with, the uptake rates of glutamine was investigated by measuring the change of glutamine concentrations in media during 24h incubation using NMR. The results showed that there is no significant change in the glutamine uptake rate between the two cell lines (Figure 3.15A).

To understand the metabolic fate of glutamine, stable isotope labelling techniques were employed. The ID8 cells were cultured in media with $^{13}C_5$-glutamine for 24h and the aqueous phase metabolites were measured by GC-MS. The ^{13}C enrichment patterns are illustrated in Figure 3.15B. Briefly, $^{13}C_5$-glutamine enters the TCA cycle after conversion to fully labelled α-KG (i.e., M+5). In the canonical TCA cycle, the downstream intermediates (i.e., succinate, fumarate, malate, OAA and citrate) are labelled M+4 as one of the ^{13}C atom of M+5 α-KG exists the cycle in the form of CO_2. In contrast, α-KG undergoes reductive carboxylation and incorporates one ^{12}C atom from CO_2, which generated M+5 citrate (*35*). My data showed that the fraction of M+4 or M+5 citrate or the ratio between M+4 and M+5 citrate remain unchanged in ID8 *Trp53*$^{-/-}$*; Pten*$^{-/-}$ cells (Figure 3.15C), which suggests that Pten loss has no significant impact on glutamine metabolism via the TCA cycle.

To examine glutamine contribution to FA and cholesterol synthesis, the organic phase of metabolites from the labelling experiment described in the above paragraph was analysed by GC-MS. Figure 3.16 illustrates the ^{13}C enrichment pattern of FA using $^{13}C_5$-glutamine as a tracer. M+5 citrate undergoes cleavage by ACL to produce M+2 acetyl-CoA. This generates the ordered labelling pattern of FA as described in section 3.2.3 (i.e., M+2, M+4, M+6 etc). However, unlabelled acetyl-CoA is produced by cleaving M+4 citrate and therefore, no labelling into FA is generated. Here, the ^{13}C enrichment patterns of methyl palmitate in ID8 cells are shown in Figure 3.17A. No significant levels of ^{13}C enrichment of cholesterol were detected (data not shown), thereby suggesting the flux of cholesterol synthesis during the

24h incubation is low. ISA analysis of palmitate MID showed that there was a decreasing trend in the fraction of lipogenic acetyl-CoA from glutamine in ID8 *Trp53*$^{-/-}$*; Pten*$^{-/-}$ cells, although it was not statistically significant (Figure 3.17B). Given that Pten loss significantly enhanced glucose contribution to FA *de novo* synthesis (refer to Section 3.2.3), these results suggest that Pten loss may alter substrate preferences for FA synthesis. My data also showed that the proportion of newly generated FA is not significantly altered in ID8 *Trp53*$^{-/-}$*; Pten*$^{-/-}$ cells (Figure 3.17B). This is in line with the unchanged fraction of *de novo* synthesised FA using $^{13}C_6$-glucose as a tracer (refer to Section 3.2.3) and indicates that Pten loss did not regulate the flux of FA synthesis.

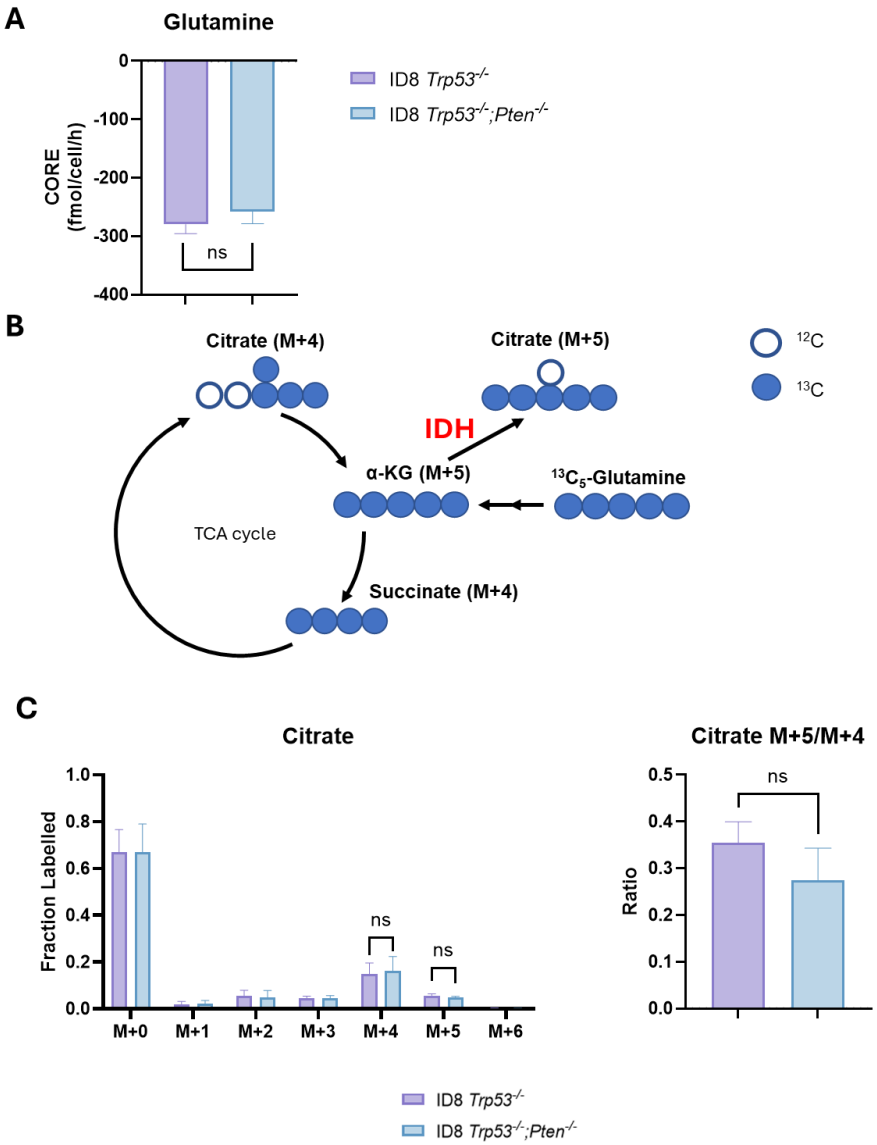


Figure 3.15 Pten loss did not impact glutamine consumption and metabolism through the TCA cycle in ID8 cells.

(A) CORE rates of glutamine. ID8 *Trp53*$^{-/-}$ cells and ID8 *Trp53*$^{-/-}$*; Pten*$^{-/-}$ cells were cultured without drug treatment for 24h. Concentrations of glutamine in media were measured by NMR spectroscopy and cells were counted to calculate CORE rates Negative CORE values indicate net consumption. (B) Schematics of the labelling patterns using $^{13}C_5$-glutamine as a tracer. α-KG is labelled M+5 and the downstream TCA cycle intermediates are labelled M+4. When condensing with unlabelled acetyl-CoA, M+4 citrate is generated. α-KG can undergo reductive carboxylation catalysed by Isocitrate dehydrogenase (IDH) to produce M+5 citrate. (C) MID of citrate and ratio of M+5 and M+4 citrate. ID8 *Trp53*$^{-/-}$ cells and ID8 *Trp53*$^{-/-}$*; Pten*$^{-/-}$ cells were cultured with 2mM $^{13}C_5$-glutamine for 24h. Cellular metabolites were extracted and analysed by GC-MS. Data represent mean ± SD from three independent biological repeats. Statistical significance was calculated by t tests (CORE rates and citrate M+5/M+4 ratio) or one way ANOVA with post-hoc Tukey rests (citrate MID). ns, not significant.

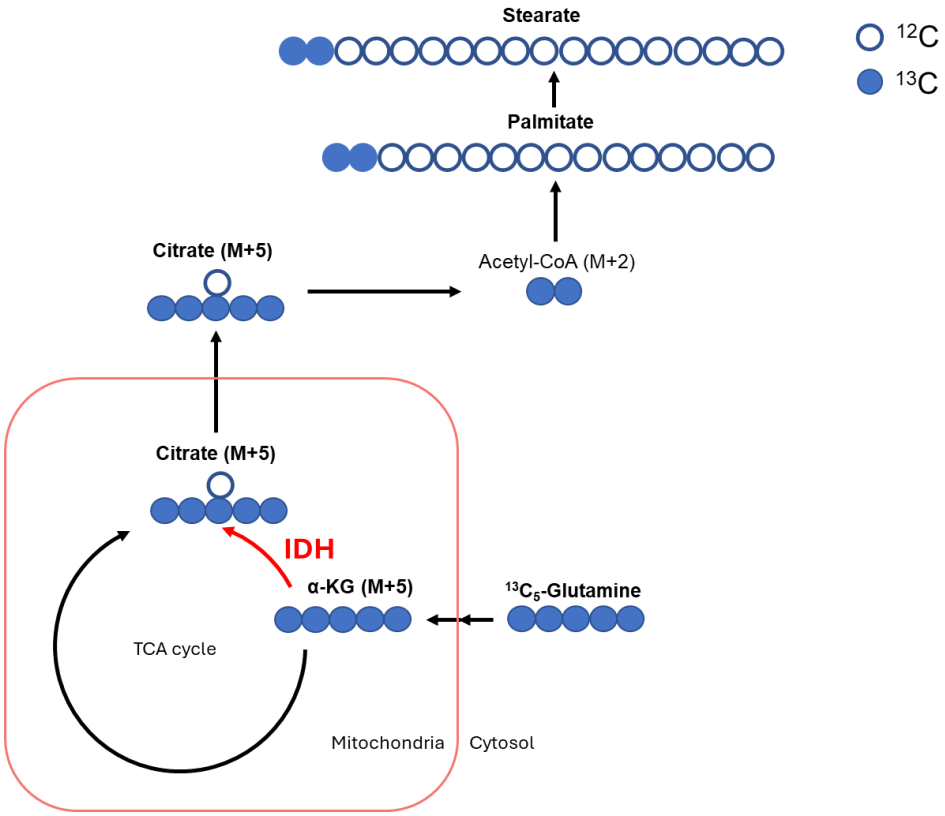


Figure 3.16 Schematics of the ^{13}C enrichment patterns of the TCA cycle and FA *de novo* synthesis using $^{13}C_5$-glutamine as a tracer.

α-KG is labelled M+5 and undergoes reductive carboxylation by IDH to produce M+5 citrate (shown in red). After transporting out of mitochondria, M+5 citrate is cleaved to M+2 acetyl-CoA. Multiple iterations of condensation of acetyl-CoA molecules produce palmitate (16:0). Further elongation of palmitate by incorporating a molecule of acetyl-CoA generates stearate (18:0).

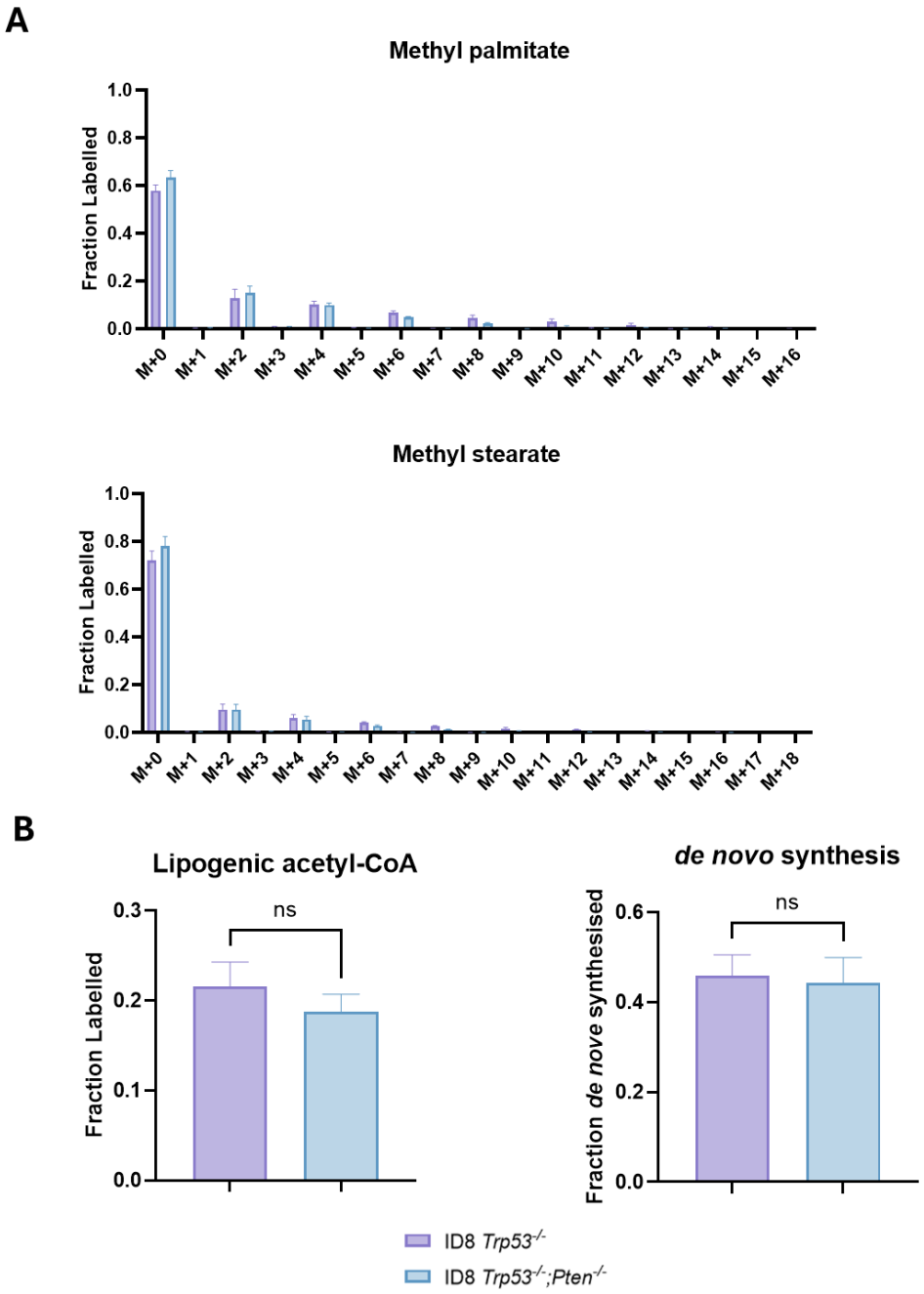


Figure 3.17 There was a downward trend, albeit not significant, of glutamine contribution to FA de novo synthesis in ID8 *Trp53*$^{-/-}$*; Pten*$^{-/-}$ cells.

(A) MID of methyl palmitate and methyl stearate. ID8 *Trp53*$^{-/-}$ cells and ID8 *Trp53*$^{-/-}$*; Pten*$^{-/-}$ cells were cultured in media with 2mM $^{13}C_5$-glutamine for 24h. Intracellular metabolites were then extracted and analysed by GC-MS. (B) The fraction of lipogenic acetyl-CoA (left, parameter D) and newly synthesized FA during tracer incubation (right, parameter g(t)). D and g(t) were estimated by ISA modelling using the MID of methyl palmitate. Data represent mean ± SD from three independent biological repeats. Statistical significance was calculated by t tests. ns, not significant.

3.2.5 Investigating the alternative carbon source of citrate synthesis in ID8 cells

As described in sections 3.2.3 and 3.2.4, glucose and glutamine contribute to approximately 23% and 20% of citrate synthesis respectively at 24h in ID8 cells regardless of Pten status (Figure 3.12 and Figure 3.15C). Thus, alternative carbon sources were investigated. Lactate has been reported to undergo oxidation to pyruvate and therefore (*291*), fuel the TCA cycle in cancer cells. To understand the relative contribution of lactate, ID8 *Trp53*$^{-/-}$ cells were incubated with 3-^{13}C-lactate and the aqueous metabolites were analysed by GC-MS. The schematics of ^{13}C enrichment was shown in Figure 3.18A. Pyruvate is labelled M+1 through the LDH-catalysed oxidation of 3-^{13}C-lactate and enters the TCA cycle via the PDH flux, which generates M+1 labelled intermediates of the TCA cycle. ^{13}C enrichment into pyruvate was detected and roughly 15% of the TCA cycle intermediates were labelled M+1 (Figure 3.18B), thereby suggesting lactate is a carbon source of citrate.

Acetate is a member of short chain fatty acids (SCFA), and previous reports demonstrate that acetate can be converted to acetyl-CoA by acetyl-CoA synthetase 1 (ACSS1) and contribute to citrate synthesis in cancer cells (*435*). Thus, the metabolic fate of acetate was examined. ID8 *Trp53*$^{-/-}$ cells were incubated with $^{13}C_2$-acetate for 24h and metabolites were analysed by GC-MS. Appendix Figure 3.4A illustrates the ^{13}C enrichment pattern of the TCA cycle intermediates. M+2 acetyl-CoA is generated from $^{3}C_2$-acetate and thus, the downstream intermediates are labelled M+2. My results showed that no significant levels of ^{13}C enrichment in citrate or α-KG was detected (Appendix Figure 3.4B), which suggests that acetate may not be a carbon source of citrate in ID8 cells.

Branched-chain amino acids (BCAAs, i.e., leucine, isoleucine and valine) is another potential carbon source for citrate in cancer cells (*436*). BCAAs undergo deamination by BCAA transaminases 1 and 2 (BCAT1/2) to produce branched-chain keto acids (BCKAs) that is further metabolised into acetyl-CoA to feed the TCA cycle (*436*). To examine whether BCAAs are actively metabolised, ID8 *Trp53*$^{-/-}$ cells were incubated with DMEM media (containing BCAAs: leucine and isoleucine = 0.80mM, valine = 0.80mM) incubated for 24h. Changes in

BCAA concentrations in media at the start and end of incubation were measured by NMR. My data showed a net decrease in BCAA concentrations (i.e., negative CORE values) (Appendix Figure 3.5), thereby suggesting BCAA contributes to metabolism in ID8 cells. Additionally, ketone body (3-hydroxybutarate, acetoacetate and acetone) has been shown to be metabolised to acetyl-CoA and contribute to the TCA cycle (*437*). However, no significant levels of ketone body can be detected in media by NMR (data not shown), which suggests that ketone body may not be a carbon source of citrate in the 2D culture system employed in this study.

Interestingly, short incubation (i.e., 4h) with $^{3}C_{6}$-glucose or 3-^{13}C-lactate yielded almost fully unlabelled citrate although significant ^{13}C enrichment into pyruvate was detected (Appendix Figure 3.6A-B). The MIDs of downstream intermediates (e.g., α-KG and succinate) showed similarly low levels of ^{13}C enrichment at 4h (Appendix Figure 3.6A-B). Likewise, M+5 α-KG and M+4 downstream TCA cycle intermediates (i.e., succinate) were detected when the ID8 cells were incubated with $^{13}C_{5}$-glutamine (Appendix Figure 3.6C). However, no ^{13}C enrichment into citrate (M+4 or M+5) could be observed (Appendix Figure 3.6C). These data indicate the low flux of citrate synthesis or the fast diversion of citrate for other metabolic pathways.

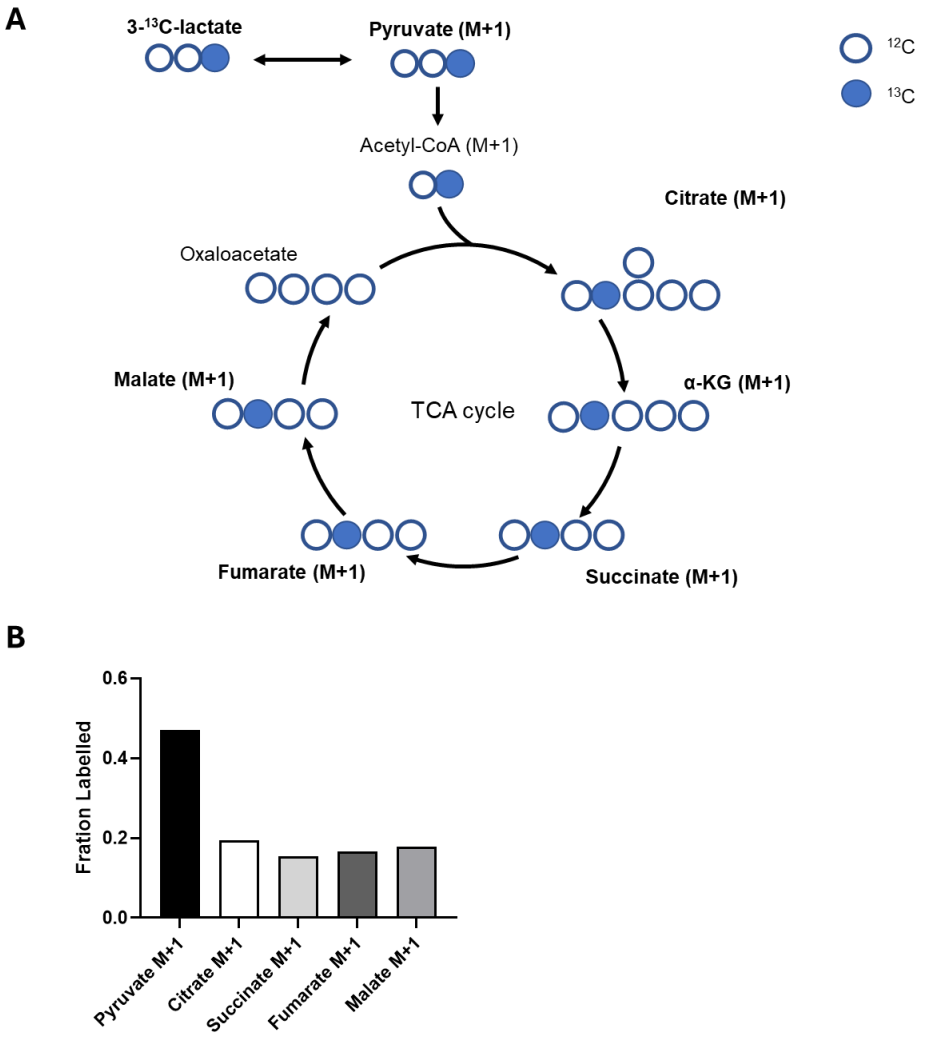


Figure 3.18 Exogenous lactate was a carbon source for the TCA cycle in ID8 *Trp53*$^{-/-}$ cells. (A) Schematics of the labelling patterns of the TCA cycle using 3-^{13}C-lactate as a tracer. M+1 pyruvate and acetyl-CoA are generated. After condensing with unlabelled oxaloacetate, the TCA cycle intermediates (e.g., citrate) are labelled M+1. (B) Fraction of M+1 pyruvate and TCA cycle intermediates. ID8 *Trp53*$^{-/-}$ cells were incubated with 10mM 3-^{13}C-lactate for 24h. Intracellular metabolites were extracted and analysed by GC-MS. Data represent mean from one biological repeat.

3.3 Discussion

In summary, my data provide insights into the metabolic pathways that undergo reprogramming secondary to Pten loss in ovarian HGSC. Briefly, the activity of glucose metabolism, lipid synthesis and oxidation, metabolic co-factor synthesis (e.g., NAD and CoA)

and arginine synthesis pathways are altered.

Previous publications reveal that Akt signalling is a key regulator of glucose metabolism in cancer cells. For instance, glucose uptake rates and glycolytic flux are enhanced in cancer cells with hyperactive Akt pathway (*83, 107, 111, 112*). Here, my results from 2D cultured ID8 cells confirmed upregulated glucose uptake and glycolysis in cells with Pten loss, which are in line with these reports. In addition, multiple pathways branch off of glycolysis, including PPP, serine and glycine synthesis and alanine synthesis. The Akt pathway also promotes the flux of PPP by enhancing the expression of various enzymes (e.g., G6PD) (*116*). However, my data showed that Pten loss has no impact on L/G ratio that estimates the relative flux between glycolysis and branch-off pathways. Of note, the L/G ratio possesses the limitation of masking any changes in PPP flux. This is because any changes in the ratio result from the diversion of PPP intermediate ribose 5-phosphate into PRPP synthesis, which reduces lactate production. However, ribose 5-phosphate can re-join glycolysis via the non-oxidative branch of PPP, and therefore an equal amount of lactate is produced (*438*). Such limitation can be overcome by SIRM using 1,2-$^{13}C_2$-glucose as a tracer (*357*). Glycolysis generates only M+2 lactate while the combined oxidative and non-oxidative PPP produces M+1 lactate (*439*). Thus, the ratio between M+1/M+2 lactate is an accurate indicator of PPP overflow to glycolysis. M+1 and M+2 ribose 5-phosphate is produced from the oxidative and non-oxidative branch, respectively (*357*). Therefore, the total abundance of M+1 and M+2 ribose 5-phosphate is a direct measure of PPP flux and the ratio of M+1/M+2 ribose 5-phosphate reflects the source of ribose (i.e., oxidative vs non-oxidative branch).

Glucose metabolism via the TCA cycle is also subject to regulation by the Akt pathway. In this regard, under conditions of hypoxia, Akt is recruited to mitochondria to directly phosphorylate and activate PDK1 which in turn phosphorylates and inhibits PDH to reduce pyruvate entry into the TCA cycle (*440*). In addition, HIF1α induces the expression of PDK to negatively regulate pyruvate input to the TCA cycle (*441*). As HIF1α is downstream effector of Akt pathway, it has been proposed that Akt regulates the TCA cycle indirectly via the HIF-1α/PDK1 axis at hypoxia (*428*). However, my data reveal that Pten loss fails to modulate glucose contribution to the TCA cycle. One possible explanation is that the ID8 cells were

cultured at normoxia. Of note, the above-mentioned studies suggest the hypoxia-induced downregulation as a protective mechanism against apoptosis, autophagy and oxidative stress during hypoxia(*440, 441*). Thus, SIRM experiments under hypoxia is required.

Akt signalling has also been reported to regulate glutamine uptake and metabolism indirectly via MYC induction (*96*). Glutamine uptake is enhanced by MYC-induced expression of glutamine transporters SLC1A5 (*142, 442*). MYC also upregulates the expression of the rate-limiting enzyme in glutamine metabolism GLS (*142, 442, 443*). However, my results indicate Pten loss has no impact on glutamine uptake rates and its metabolism via the canonical TCA cycle or reductive carboxylation pathway. The contradiction may be caused by the context-dependent induction of MYC downstream of Akt activation. In this regard, the regulatory inputs of MYC expression may be derived from pathways other than the Akt signalling. Here, the two ID8 cell lines tested harbour *Trp53* gene deletion and p53 is a negative regulator of MYC expression by a combination of transcriptional and post-translational control (i.e., microRNA-mediated silencing) (*444, 445*). Therefore, Akt signalling activation may not cause a further increase in MYC expression in the ID8 cells with *Trp53* gene deletion. Likewise, the activation of Ras signalling is sufficient to sustain MYC expression in multiple cancer types because the inhibition of PI3K fails to reduce MYC levels (*446-448*). Additional work is required to examine MYC abundance to understand non-significant changes in glutamine metabolism.

The Akt pathway has been reported to promote *de novo* FA and cholesterol synthesis by phosphorylating and activating ACLY to enhance the production of cytosolic acetyl-CoA and activating SREBP to upregulate nearly all the lipogenic enzymes (*83, 133, 135, 449*). Here, my data reveal that the flux of FA synthesis using glucose or glutamine as a substrate is unchanged regardless of Pten deletion. Given that NADPH provides the reducing equivalent essential for FA synthesis (*40*), the lack of increase in FA synthesis may result from a limited supply of NADPH. Indeed, my data show no increase in PPP flux, the major pathway for cytosolic NADPH production, in Pten deficient cells. Another possible explanation is that the flux of FA synthesis has reached its maximal level in ID8 *Trp53*$^{-/-}$ cells since almost 90% of FA is newly synthesized. Indeed, p53 has been reported to repress FA synthesis by

transcriptionally inhibition of SREBP1 expression (*450*). Thus, Akt activation may not cause a further increase in FA synthesis flux. Additional research is required to understand the dominant regulator of FA synthesis by investigating ID8 cells with wild-type *Trp53* gene. It is also possible that acetyl-CoA is diverted away from FA synthesis for protein acetylation (*451*). Indeed, there is a strong correlation between histone acetylation and Akt phosphorylation (*452*). And the supply of the acetylation substrate acetyl-CoA is enhanced due to Akt-mediated ACLY activation (*452*). Thus, additional work is required to probe for acetyl-CoA metabolism and investigate histone acetylation levels.

Interestingly, it is found that Pten loss increases glucose, but not glutamine, contribution to FA synthesis in this chapter. This result is inconsistent to the similar proportion of glucose-derived citrate in ID8 cells. One possible explanation is that metabolite extraction performed in this study is not specific to subcellular compartment. Cytosolic, but not mitochondrial, citrate is the source of FA synthesis. However, an average of citrate in the two compartments is presented here. Therefore, mitochondria separation is required prior to metabolite extraction which may reveal the differences in fraction of glucose-derived citrate. Alternatively, selective cell sampling (SCS) techniques can be applied to extract subcellular compartments to avoid metabolic artifacts due to extra sample processing during mitochondria separation (*453*).

Of note, no significant ^{13}C enrichment into cholesterol was detected regardless of Pten status in this study. This may be caused by insufficient tracer incubation time since 24h was chosen. Indeed, longer incubation of 48 or 72h has been suggested (*454*) and therefore, the SIRM experiment can be improved with longer incubation. Another explanation is that the major source of cholesterol in ID8 cells is uptake instead of *de novo* biosynthesis. Indeed, the expression of low-density lipoprotein receptor (LDLR), the major mediator of extracellular cholesterol uptake, is upregulated in endometrioid and clear cell ovarian carcinoma (*455*). Moreover, Pten loss in prostate cancer cells has been reported to enhance LDLR expression and lead to accumulation of intracellular cholesterol ester (*456*). Therefore, additional research is required to study the source of cholesterol in ovarian HGSC cells.

In addition, the Akt pathway regulates fatty acid oxidation (FAO) in cancer cells. Mitochondrial oxidation of FA requires carnitine palmitoyltransferase 1 (CPT1) which mediates the rate-limiting step of cytosolic FA transport into mitochondria. The expression of CPT1 is suppressed by the Akt signalling which blunts FAO activity in hematopoietic cells (*457*). Moreover, CPT1 is allosterically inhibited by high concentrations of malonyl-CoA which is produced from acetyl-CoA (*458*). As Akt signalling activates cytosolic acetyl-CoA synthesis by stimulating ACLY, CPT1 activity and FAO is reduced (*458*). However, my data show higher levels of acyl carnitines, the products of CPT1, in Pten deficient tumours. As there is no published data about Akt-mediated regulation of FAO enzymes downstream of CPT1, it is challenging to interpret the effects of Akt activation on FAO in ID8 tumours. Of note, *in vivo* studies show that ovarian cancer cells preferentially metastasise to lipid-rich omental tissue (*459*). Indeed, ovarian cancer cells induce lipolysis in adipocytes in omentum and utilise the produced FA for energy production, which promotes tumour growth (*459*). Given the early onset of omental metastasis and higher aggressiveness of Pten deficient ID8 tumours (*391*), it is possible that Akt-mediated CPT1 inhibition is context-dependent. Additional research is required to examine FAO activity using ^{13}C labelled FA (e.g., palmitate).

Furthermore, the PI3K/Akt pathway has been reported to regulate choline metabolism in cancer cells. In this regard, choline kinase (CHK) is activated by the combined PI3K and RAL GTPase guanine nucleotide dissociation stimulator (RALGDS) signalling pathways in NIH3T3 fibroblasts (*460*). CHK catalyses the phosphorylation of choline to produce PhoC and therefore, the ratio of PhoC to choline is increased in ovarian cancer cells with upregulated CHK activity (*461*). However, my data showed no significant difference between tumours with and without Pten loss. Indeed, the abundance of both choline and PhoC is decreased in Pten deficient tumours. This may result from the increased activity of CTP:phosphocholine cytidylyltransferase (CCT) which catalyses the conversion of PhoC to citicholine. This interpretation is supported by the increased citicholine levels in ID8 *Trp53*$^{-/-}$*; Pten*$^{-/-}$ tumours. However, it remains unclear whether the accumulation of citicholine is caused by the reduction in activity of diacylglycerol cholinephosphotransferase (DAG-CPT) that catalyses PtdCho synthesis using citicholine. Of note, there is no literature about the roles of Akt

signalling activation in CCT or DAG-CPT expression and activity. The major limitation is the lack of data about PtdCho levels and therefore, it is challenging to interpret the effects of Pten loss on PtdCho synthesis. Nevertheless, these data suggest Pten loss modulates PtdCho synthesis pathway in ovarian HGSC cells. Further investigation is required and includes stable isotope labelling experiments using ^{13}C labelled choline as a tracer and lipidomics profiling.

Apart from serving as a structural component of cellular membranes, PtdCho undergoes catabolism to generate lipid messengers including lysoPC, arachidonic acid (ARA), phosphatidic acid (PA) and diacylglycerol (DAG) (*462*). My results indicate decreased abundance of lysoPC(18:1) and increased levels of GPC, the breakdown product of lysoPC, in tumours with Pten loss. This may result from: 1) increased activity of lysophospholipase (lyso-PL) that cleaves lysoPC into GPC; 2) reduced activity of GPC-PDE (also known as glycerophosphodiester phosphodiesterases (GDPDs)) or endometrial differential 3 (EDI3) that convert GPC to choline (*463, 464*); 3) reduced activity of phospholipase A_2 (PLA_2) that catabolises PtdCho into lysoPC. The expression of PLA_2 has been reported to be reduced in ovarian cancer cells (*461*). However, with no published data about the impact of Akt pathway on these enzymes, it remains unclear how the activity of lysoPC metabolism is regulated. Of note, my data show that the levels of PDG_2, a lipid messenger, is significantly downregulated in Pten deficient tumours. Previous report shows that PDG_2 inhibits growth rates of human ovarian cancer cells (*465*), which may explain the higher aggressiveness of Pten deficient ID8 tumours (*391*). PDG_2 is produced using ARA as a substrate via sequential reactions catalysed by multiple enzymes with cyclooxygenase (COX) as the key regulator (*466*). However, Akt signalling induces COX expression through NF-κB/IκB pathway in endometrial cancer cells (*467*) and breast cancer cells (*468*), which suggests the reduced PDG_2 levels may result from changes in ARA production. One major limitation in this study is that the untargeted metabolic profiling method is not optimised for measurement of lipids. Therefore, additional lipidomics studies are needed to provide more data about lipid metabolic reprogramming induced by Pten loss.

My data also show that the activity of metabolic cofactor coenzyme A (CoA) synthesis is influenced by Pten loss in ID8 tumours. CoA is the major carrier of activated acyl groups in

cells (e.g., acetyl-CoA) and is involved in multiple metabolic processes including lipid synthesis, central carbon metabolism and histone acetylation (*469, 470*). In this study, the abundance of pantothenate, a substrate for CoA synthesis, is significantly reduced in tumours with Pten loss. This may reflect an increase in pantothenate metabolism for CoA synthesis. Indeed, Akt signalling promotes CoA de novo synthesis by phosphorylating and activating the rate-limiting enzyme pantothenate kinase 2 (PANK2) (*471*). Akt also relieves the inhibition of PANK4 on CoA synthesis (*471*). However, as there is no literature about Akt regulation of pantothenate uptake, it remains unclear whether Pten loss downregulates pantothenate uptake which also leads to a reduction in intracellular pantothenate levels. Therefore, SIRM studies using ($^{13}C_3$ $^{15}N_1$)-labelled pantothenate is required to monitor CoA synthesis activity.

Moreover, my results show that Pten loss have no impact on the ratio of lactate to pyruvate concentrations in media, which indicates that cellular NADH/NAD^+ ratio was not significantly changed. These data suggest that Akt signalling activation may not be sufficient to alter redox balance under basal conditions. However, this does not rule out the possibility that Pten loss may impact the cellular defensive mechanisms against ROS. In this regard, a reduction in the levels of ascorbic acid, a key scavenger of free radicals and ROS, is detected in tumours with Pten loss in this study. The limited abundance of ascorbic acid may impair ROS clearance, which suggests that Pten deficient tumours may be more vulnerable under oxidative stress. In addition, Akt signalling has been shown to promote the production of NADPH, a reducing equivalent, by upregulating the oxidative branch of PPP (*472*). My data showed that the ratio of lactate production to glucose consumption (L/G ratio) was not significantly altered by Pten loss, which implies that the PPP flux and NADPH production may not be changed. However, the non-oxidative branch of PPP mediates the conversion of ribulose 5-phosphate (the product of the oxidative branch of PPP) to glyceraldehyde 3-phosphate and re-joins glycolysis (*438*). Therefore, direct measurements of PPP fluxes using 1,2-$^{13}C_2$-glucose are required. CoA has also been reported to function as a cellular antioxidant due to the thiol group that is reactive with ROS (*473*). CoA is also a substrate of protein PTM called CoAlation that protects the protein against oxidation of the surface cysteine residues (*474*). This in turn prevents protein inactivation and degradation under conditions of oxidative stress (*474*). In

this study, the potential increase in CoA synthesis in Pten deficient tumours may maintain the redox balance. Nevertheless, it would be interesting to examine the responses to oxidative stress (e.g., apoptosis) to understand the combinational effects of changes in the above-mentioned metabolic pathways.

In addition, my results show that Pten loss alters the activity of the salvage pathway of NAD^+ synthesis. The reduced levels of nicotinamide, the breakdown product of NAD^+, and the increased abundance of NAD^+ indicate a potential upregulation in the salvage pathway. NAD^+ is a substrate of PARylation by PARP1 for DNA damage sensing and resolution (*217*). The loss of Pten has been reported to inhibit repair of DNA DSBs and suppress nucleotide excision repair (NER) (*475*), which may lead to unresolved DNA damage and increased PARP1 activation with enhanced NAD^+ consumption. Therefore, the salvage pathway may be activated as an adaptive mechanism to recycle nicotinamide and maintain the supply of NAD^+ for DNA damage repair in tumours with Pten loss. NAD^+ can also be synthesized from the *de novo* synthesis pathway and the Preiss-Handler (PH) pathway and therefore, the increase in NAD^+ levels may also result from activation in these pathways. However, no data about the abundance of intermediates in these pathways are available in this study. Thus, SIRM studies using labelled tryptophan, nicotinic acid and NAD^+ can be performed to probe for the flux in each pathway.

Moreover, my data show that arginine metabolism is altered in tumours with Pten loss. In this regard, the decrease in arginine abundance is detected in Pten deficient cells. This may result from a decrease in arginine synthesis, an increase in arginine catabolism or a decrease in arginine uptake. However, data from our lab show that there is no expression of argininosuccinate synthetase 1 (ASS1), the enzyme catalyses arginine synthesis, in ID8 *Trp53*$^{-/-}$ cells (personal communications with Flora McKinney). Therefore, the ID8 cells are arginine-auxotrophic (i.e., dependent on exogenous supply of arginine) and the reduction in arginine levels may not result from a decrease in synthesis. Instead, my data supports the notion that Pten loss may enhance arginine catabolism. In this case, the decreased aspartate observed in this study may reflect its diversion for other pathways including nucleotide synthesis in Pten deficient tumours. The downstream effector of Akt activation, mTORC1, promotes pyrimidine

synthesis by stimulating CAD that catalyses the first three steps of pyrimidine synthesis (*137, 138*). Aspartate is also a substrate of purine synthesis which is promoted by ATF4 downstream of mTORC1 (*139, 476*). Indeed, my data show that the abundance of IMP, the intermediate of purine synthesis, is decreased in Pten deficient tumour, which may reflect an increase in purine synthesis. The accumulation of citrulline may result from the cessation of ASS1 activity and/or an increase in arginine breakdown that produces citrulline. Both arginase and NOS catalyse the catabolic metabolism of arginine and produces ornithine and citrulline, respectively (*477*). The catabolism of amino acids (e.g., glutamate and asparagine) involves the disposal of nitrogen in the form of urea which is readily exported from cells (*478*). Therefore, the decrease in urea on its own is not specific enough to indicate a reduction in arginase activity. Indeed, the increase in spermidine levels may indicate an upregulation in polyamine pathway. As ornithine, the product of arginase pathway, is the substrate of the polyamine metabolism, my data suggest that arginine catabolism via the arginase pathway may be upregulated in tumours with Pten loss. NOS expression in cells with epithelial origin is limited in general. Instead, NOS is expressed in neurons (neuronal NOS; nNOS), endothelial cells (endothelial NOS; eNOS) and macrophages in response to stimulants including bacterial lipopolysaccharide and cytokines (inducible NOS; iNOS) (*479*). Thus, this further supports the enhanced activity of arginase pathway. However, it is difficult to rule out the potential that diminished arginine import acts as a mechanism of the reduced intracellular concentration because there is no published data about Akt-mediated regulation of arginine uptake. Therefore, SIRM studies using labelled arginine are required to further the understandings in arginine uptake and metabolism.

One limitation about the untargeted metabolomics data is the lack of support from targeted metabolomic data. Although the SWATH method used in this chapter maximizes the coverage of metabolites, the quantitation and target identification can be challenging (*380*). Alternatively, targeted method (e.g., multiple reaction monitoring (MRM)) is considered as a golden standard for metabolite quantification (*380*). Therefore, MRM methods optimised for each metabolic pathway shown in Figure 3.4-3.10 should be performed for validation.

Interestingly, my results show that carbon sources other than glucose and glutamine

contribute to citrate synthesis in ID8 *Trp53*$^{-/-}$ cells. In this regard, citrate synthesis can be fuelled by extracellular lactate. This is in line with previous reports showing lactate uptake and metabolism via the TCA cycle in multiple cancer types (*288, 291, 480*). Of note, ovarian cancer cells preferentially metastasise to lipid-rich omentum and induce lipolysis in the adipocytes for energy production via FAO, which promotes tumour growth. However, my data show no contribution of acetate, a SCFA, to citrate synthesis, which indicates that ID8 *Trp53*$^{-/-}$ cells cannot metabolise SCFA via the TCA cycle. Thus, it would be interesting to perform SIRM studies to examine whether exogenous long chain fatty acid (LCFA), including palmitate, is a carbon source for the TCA cycle. Acetate is also a substrate of histone acetylation which is catalysed by ACSS2 (*481, 482*). Therefore, additional research is required to investigate whether exogenous acetate contributes to histone modification. Moreover, my data show net uptake of BCAA in ID8 *Trp53*$^{-/-}$ cells. As BCAA is a source of acetyl-CoA (*483*), this result suggests its potential as a TCA cycle substrate. However, BCAA is also a substrate of protein synthesis and thus, the intracellular metabolic fate cannot be examined with cellular uptake data only. SIRM studies using ^{13}C labelled BCAA are required. Ketone bodies can also function as a carbon source of the TCA cycle. However, my data show the concentrations of ketone bodies (i.e., acetone, acetoacetate and 3-hydroxybutarate) are below limitation of detection (LOD) using NMR techniques. Thus, in the 2D cultured system, ketone bodies may not be incorporated into the TCA cycle. However, the concentrations of ketone bodies are generally less than 0.5mM in blood of healthy individuals and can increase 6-7.5mM during prolonged fasting (*484, 485*). Thus, it remains unclear whether ketone bodies are utilised via the TCA cycle in ovarian cancer cells *in vivo*. SIRM studies using ^{13}C labelled ketones can be performed in mice or human patients.

Noticeably, my data show a low ^{13}C enrichment of TCA cycle intermediates (e.g., citrate and α-KG) at 4h regardless of the tracers used in this study. One possible explanation is the defects of citrate synthesis in ovarian cancer cells. In this regard, the expression of mitochondrial elongation factor 2 (MIEF2) has been reported to be upregulated in ovarian cancer (*486*). MIEF2 is a key regulator of mitochondrial dynamics that mainly refers to fission and fusion (*487*). In general, mitochondria fusion is associated with enhanced metabolic capacity while

mitochondria fission allows mitochondria degradation (i.e., mitophagy) (*487*). The upregulated MIEF2 expression leads to reduced concentrations of the TCA cycle intermediates (e.g., citrate and α-KG) and increased levels of glycolytic intermediates (e.g., G6P) (*488*). Mutations in mitochondria DNA have also been reported and are associated with dysfunctional OXPHOS in ovarian cancer cells (*489, 490*). However, my data show that almost 90% of FA is *de novo* synthesised using citrate generated from glucose and glutamine, which suggests that citrate synthesis must be active. Thus, the lack of ^{13}C enrichment in the TCA cycle intermediates may result from the active utilisation of citrate for FA synthesis. To test this hypothesis, MIDs of citrate can be measured in cells treated with ACL inhibitor in the presence of ^{13}C labelled glucose or glutamine.

Taken together, untargeted metabolic profiling and SIRM studies show that Pten loss promotes glucose uptake and glycolysis but has no impact on glutamine uptake or its metabolism via the canonical TCA cycle or reductive carboxylation. Pten deletion also enhances glucose, but not glutamine, contribution to FA *de novo* synthesis in ovarian HGSC cells, although the flux of FA synthesis remains unchanged. Although the metabolite abundance data from the untargeted profiling study is not conclusive in interpreting the directions of pathway activity changes, they warrant further investigation using tracer studies. These pathways include PtdCho metabolism, NAD^+ salvage synthesis pathway, arginine catabolism, CoA synthesis pathway and FA oxidation.

CHAPTER 4

Mutations in the Ras/PI3K pathway sensitized the combination of FK866 and Olaparib in ovarian cancer cells

---

Chapter 4 Mutations in the Ras/PI3K pathway sensitized the combination of FK866 and Olaparib in ovarian cancer cells

4.1 Introduction

As described in Section 1.4.5, NAD^+ depletion has been reported to improve Olaparib sensitivity in various types of cancer cells (*285, 286, 388*). Given the roles of Ras/PI3K signalling in regulating metabolism and NAD^+ as a metabolic cofactor, dual NAMPT and PARP inhibition may provide additional benefits to this patient group. Indeed, preliminary data from our laboratory showed that in a panel of 10 ovarian cancer cell lines, mutations in the Ras/PI3K pathway improved sensitivity to NAMPT inhibition by FK866 (Appendix Figure 4.1A) (*393*). Of note, high levels of association between IC_{50} values of FK866 and NAD^+ concentration reduction were found (Appendix Figure 4.1B), which indicates the on-target effect of FK866. Additionally, FK866 improved Olaparib sensitivity in ovarian cancer cells regardless of the mutational status of Ras/PI3K (Figure 1.19) (*393*). However, the cells with mutations in the genes involved in the Ras/PI3K signalling (referred to as 'Ras/PI3K mutant' in this thesis) displayed greater reduction of cell growth rates when the same dose of FK866 and Olaparib were applied (Figure 1.19) (*393*). Thus, in this chapter, I set out to validate the sensitization effects of Ras/PI3K mutations and investigate the underlying mechanisms.

Here, a subgroup of 4 cell lines was chosen from the pool of 10 cell lines investigated previously to model ovarian cancer cells with and without Ras/PI3K pathway mutations. A2780, TOV21G and OVCAR8 cells were included in the experiment group because they harbour genetic alterations (i.e., A2780: PI3K/BRAF mutations and PTEN deletion; TOV21G: PI3K/KRAS mutations and PTEN deletion; OVCAR8: KRAS mutation). Of note, enhanced growth reduction was found in A2780, TOV21G and OVCAR8 cells treated with FK866 alone or in combination with Olaparib. COV318 cells were used to represent the unaltered group due to its lack of mutations in the Ras/PI3K pathway.

4.2 Results

4.2.1 Mutations in the Ras/PI3K pathway sensitised human EOC cells to dual PARP and NAMPT inhibition

To validate the sensitization effects observed in the preliminary data, cellular apoptosis was examined. In brief, a panel of epithelial ovarian cancer cells (Ras/PI3K wild-type cell line: COV318; Ras/PI3K mutant cell lines: A2780, TOV21G, OVCAR8) were treated with FK866 and/or Olaparib for 48h and caspase-3/7 activity was measured. My data showed that single drug treatment of FK866 or Olaparib failed to induce significant levels of caspase-3/7 and the combination treatment did not induce further caspase-3/7 activity in COV318 cells (Figure 4.1A). In contrast, A2780 and TOV21G cells treated with the combination of FK866 and Olaparib exhibited significantly higher levels of caspase-3/7 activity compared to single drug treatment group (Figure 4.1B-C). However, dual inhibition of NAMPT and PARP failed to induce caspase activation in OVCAR8 cells (Figure 4.1D).

To validate these results, flow cytometry analysis against annexin V and propidium iodide (PI) was performed on the cells treated with FK866 and/or Olaparib. Annexin V staining is marker of cellular apoptosis and PI is used as a dye to indicate cell viability. Thus, this technique allows the identification of early apoptotic cells (Annexin V^+ and PI^-) and late apoptotic cells (Annexin V^+ and PI^+). My results showed that the combination of FK866 and Olaparib significantly increased the percentage of late apoptotic A2780 and TOV21G cells (Figure 4.2A-B). Of note, early apoptotic A2780 cells were also upregulated by FK866 and Olaparib combination (Figure 4.2A). However, these effects were not observed in COV318 cells (Figure 4.2C). Collectively, these results indicate that Ras/PI3K mutations may increase the sensitivity of FK866 and Olaparib combination treatment in ovarian cancer cells.

To further verify the observed sensitization is a result of NAMPT inhibition, a rescue experiment was performed. Briefly, the EOC cells were cultured in media with or without the

supplementation of β-NMN, the product of NAMPT, and treated with the same dosing regimen as described in the previous paragraph. The data confirmed that FK866 and Olaparib combination induced significantly higher levels of apoptosis than individual treatment in A2780, but not COV318 cells (Figure 4.3A-B). Importantly, the supplementation of β-NMN abolished the increase of cellular apoptosis in A2780 cells treated with the drug combination (Figure 4.3A-B). Therefore, these data suggest that the on-target inhibition of FK866 on NAMPT and the subsequent decrease in NAD^+ levels are necessary for the sensitization effects of Ras/PI3K mutations on FK866 and Olaparib combination.

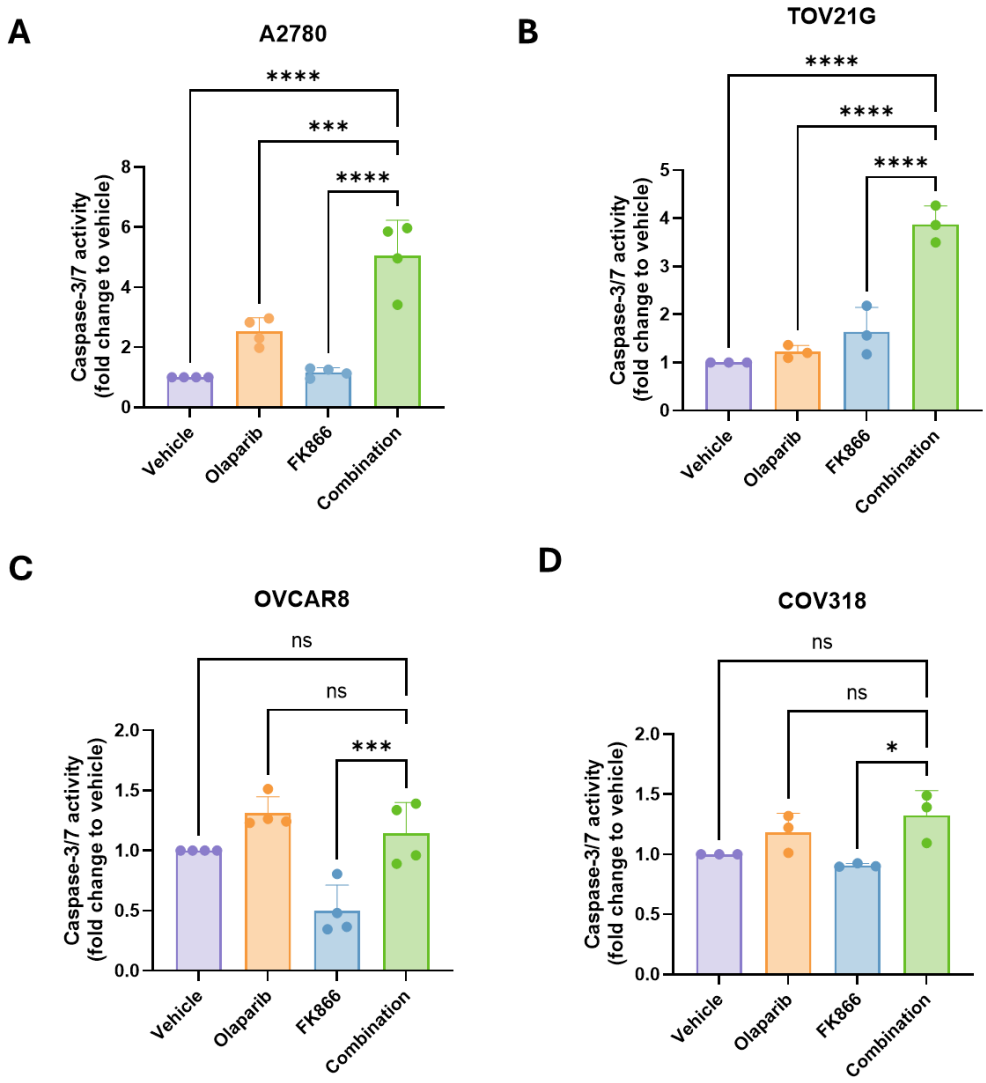


Figure 4.1 The combination of FK866 and Olaparib induced caspase-3/7 activation in ovarian cancer cells with mutations in the Ras/PI3K pathway (except OVCAR8 cells).
COV318 (A), A2780 (B), TOV21G (C) and OVCAR8 (D) cells were treated with 0.2% (v/v) DMSO, or 5nM FK866, or 10μM Olaparib or the combination for 48h before measuring caspase-3/7 activity using the Promega Caspase-Glo® 3/7 assay. Cell density was also measured by the SRB assay. The caspase-3/7 readout was normalised against cell density and the data were expressed as fold changes. Data represent the mean ± SD of three independent biological replicates. Statistical significance was calculated by one-way ANOVA followed by post-hoc Tukey test. * $p < 0.05$, *** $p < 0.001$, **** $p < 0.0001$, ns: not significant.

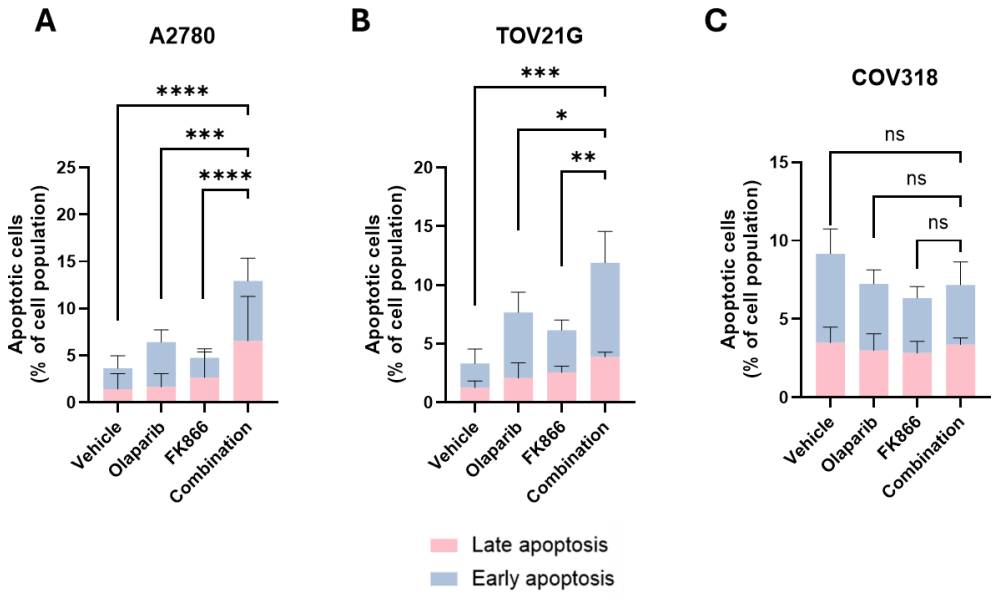


Figure 4.2 FK866 and Olaparib combination upregulated the proportion of apoptotic cells in Ras/PI3K mutant ovarian cancer cells.

A2780 (A), TOV21G (B) and COV318 (C) cells were treated with 0.2% (v/v) DMSO, or 5nM FK866, or 10μM Olaparib or the combination for 24h. Apoptosis was measured by flow cytometry against annexin V and propidium iodide (PI). Data were represented using stacked bar charts. Data represent the mean ± SD of three independent biological replicates. Statistical significance was calculated using the fraction of total apoptotic cells (i.e., combination of early and late apoptotic cells) by one-way ANOVA followed by post-hoc Tukey test. * $p < 0.05$, ** $p < 0.01$, *** $p<0.001$, **** $p<0.0001$ ns: not significant. For the gating strategies, refer to Appendix Figure 4.2. The flow cytometry experiments were performed with the help from the PhD student Yurui Ma and data were analysed by me.

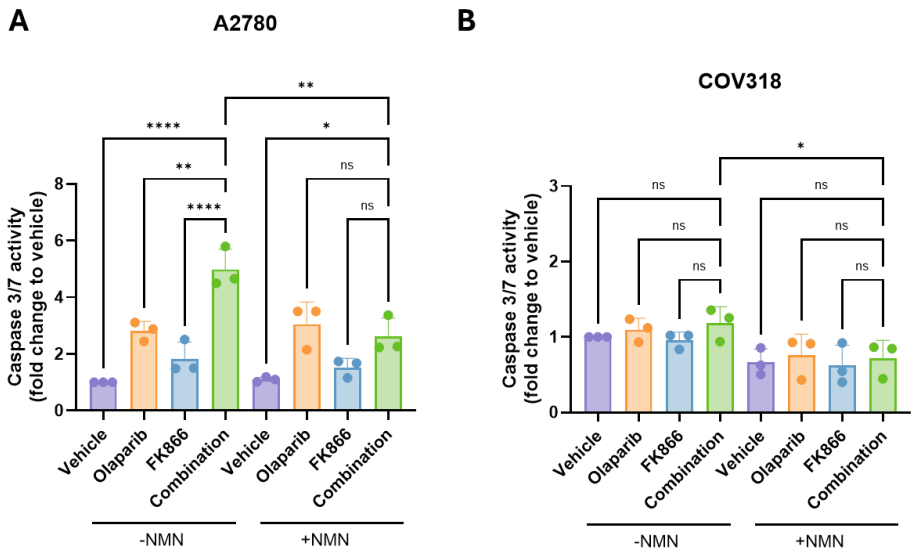


Figure 4.3 Supplementation of NMN rescues apoptosis induced by FK866 and Olaparib combination in A2780 cells.

A2780 (A) and COV318 (B) cells were treated with 0.2% (v/v) DMSO, or 5nM FK866, or 10μM Olaparib or the combination in media with or without 250μM NMN for 24h before measuring caspase-3/7 activity using the Promega Caspase-Glo® 3/7 assay. Cell density was also measured by the SRB assay. The caspase-3/7 readout was normalised against cell density and the data were expressed as fold changes. Data represent the mean ± SD of three independent biological replicates. Statistical significance was calculated by two-way ANOVA followed by post-hoc Tukey test. * $p < 0.05$, ** $p < 0.01$, **** $p<0.0001$, ns: not significant. The experiments were performed by the Master's student Chris An under my supervision and data were re-analysed and re-plotted.

4.2.2 Olaparib and FK866 combination induced higher DNA damage in EOC cells with mutations in the Ras/PI3K signalling

The underlying mechanisms of sensitization were then investigated. It was first hypothesized that Ras/PI3K mutations increase NAMPT expression and/or downregulate NAPRT levels, which may increase the dependency on NAD^+ production via the salvage pathway. This in turn enhances the sensitivity to FK866 and its combination with Olaparib. Such hypothesis is based on the preliminary data from our lab showing that a lower concentration of NAD^+ was detected in Ras-mutant OVCAR8 cells than Ras-WT COV318 cells under basal conditions (Appendix Figure 4.3). It was also found that FK866 alone or in combination with Olaparib caused a nearly complete depletion of NAD^+ in OVCAR8 cells, but not COV318 cells (Appendix Figure 4.3), which indicates that the higher reliance on NAMPT to maintain the cellular NAD^+ pools in OVCAR8 cells. This hypothesis is also supported by published data showing the regulatory roles of the Ras and PI3K signalling pathways on NAMPT expression. In this regard, the downstream effector of Akt, FOXO1, downregulates NAMPT expression in breast cancer cells (*491*). NAPRT is the rate-limiting enzyme of the alternative PH pathway of NAD^+ synthesis. Its inhibition or depletion has been shown to increase the dependency on NAMPT for NAD^+ production and enhance sensitivity to NAMPT inhibition (*492*).

To test this hypothesis, the expression of NAMPT and NARPT under basal conditions was measured by WB. The data showed that the expression of NAPRT, but not NAMPT, was reduced in A2780 in comparison to COV318 cells (Appendix Figure 4.4). In HEY-A8 cells which also displayed increased sensitivity to FK866 and Olaparib combination in our preliminary data (*393*), NAMPT levels were reduced and NAPRT expression was below detection limit (Appendix Figure 4.4). This suggests that the dependency on NAMPT for NAD^+ production is higher in A2780 and HEY-A8 cells. However, the same pattern of NAMPT and NAPRT expression could not be found in OVCAR8 or TOV21G cells where sensitization was also observed (Appendix Figure 4.4). Indeed, the data showed that in OVCAR8 cells, no NAMPT expression beyond detection limit was observed and NAPRT expression was increased in comparison to COV318 cells (Appendix Figure 4.4), which implies a greater reliance on the

PH pathway. Collectively, these data suggest that there is no clear association between Ras/PI3K mutations and NAMPT/NAPRT expression. Interestingly, no obvious corelation between Ras/PI3K mutations and hyperactivity in Ras/PI3K signalling (i.e., increased pERK and pAkt) was detected under basal conditions (Appendix Figure 4.5), which may explain the above data. Therefore, these results indicate that the sensitization effects may not result from the modulation of NAMPT/NAPRT levels by Ras/PI3K mutations.

Next, DNA damage was investigated as a potential mechanism. It has been reported that the combination of NAD^+ depletion and PARP1 inhibition enhances DNA damage which contributes to the improved Olaparib sensitivity (*286, 287, 493*). Given the greater depletion of NAD^+ pool in the Ras mutant OVCAR8 cells treated with FK866 and Olaparib combination as shown in the preliminary data from our lab, it was then hypothesized that the sensitization effects may result from the increased DNA damage induced by the drug combination in Ras/PI3K mutant EOC cell lines than WT cell lines. To test this hypothesis, immunofluorescence experiments against the DNA damage marker γH2AX were performed. Here, the data showed that single agent treatment of Olaparib, but not FK866, induced significantly higher γH2AX foci per nucleus in TOV21G cells with mutations in the Ras/PI3K pathway (Figure 4.4, Appendix Figure 4.6). Of note, the combination of FK866 and Olaparib resulted in even higher γH2AX foci per nucleus (Figure 4.4, Appendix Figure 4.6), thereby suggesting higher levels of DNA damage. In contrast, individual or combination treatment of FK866 and Olaparib had no effects on γH2AX foci per nucleus in COV318 cells (Figure 4.4, Appendix Figure 4.6). Thus, these data suggest that FK866 and Olaparib combination enhanced DNA damage in Ras/PI3K mutant EOC cells.

In response to DNA damage, eukaryotic cells activate the DDR signalling which consists of DNA damage sensors, signal transducers and effector proteins (*494*). Once activated by sensors (e.g., MRN), the protein kinases ATM and ataxia telangiectasia and Rad3-related protein serine/threonine kinase (ATR) transduce the signal by autophosphorylation and phosphorylating multiple effector protein, including checkpoint kinase 1 (Chk1), checkpoint kinase 2 (Chk2) and histone protein H2AX (*494-497*). The overall function of the DDR pathway is to mediate DNA damage repair, cell cycle arrest or cellular apoptosis in the event of

excessive DNA damage. Thus, the activity of DDR pathway was examined by measuring phosphorylation levels of ATM, ATR, Chk1 and Chk2 using WB. The results showed that the ratio of phospho-ATM/total-ATM and phosphor-Chk2/total-Chk2 was not significantly altered by Olaparib, FK866 or the combination treatment in A2780 and COV318 cells (Figure 4.5, Appendix Figure 4.7-4.8). However, large variations (e.g., phospho-ATM/total-ATM and phospho-Chk2/total-Chk2 ratio in combination treated A2780 cells) could be observed and additional repeats are thus required. The activation of the DDR pathway under basal conditions is in line with the high levels of γH2AX intensity per nucleus in COV318 cells as shown in Figure 4.4. Moreover, none of the treatment could significantly change the ratio of phospho-ATR/total-ATR in A2780 and COV318 cells (Figure 4.5, Appendix Figure 4.7-4.8). Interestingly, the combination treatment significantly increased the ratio of phospho-Chk1/total-Chk1 ratio in COV318, but not A2780, cells (Figure 4.5, Appendix Figure 4.7-4.8). However, the ratio could not be significantly altered by single agent treatment in both A2780 and COV318 cells (Figure 4.5, Appendix Figure 4.7-4.8). Collectively, these data suggest that the combination of FK866 and Olaparib did not induce greater activation of DDR signalling in Ras/PI3K mutant cell lines.

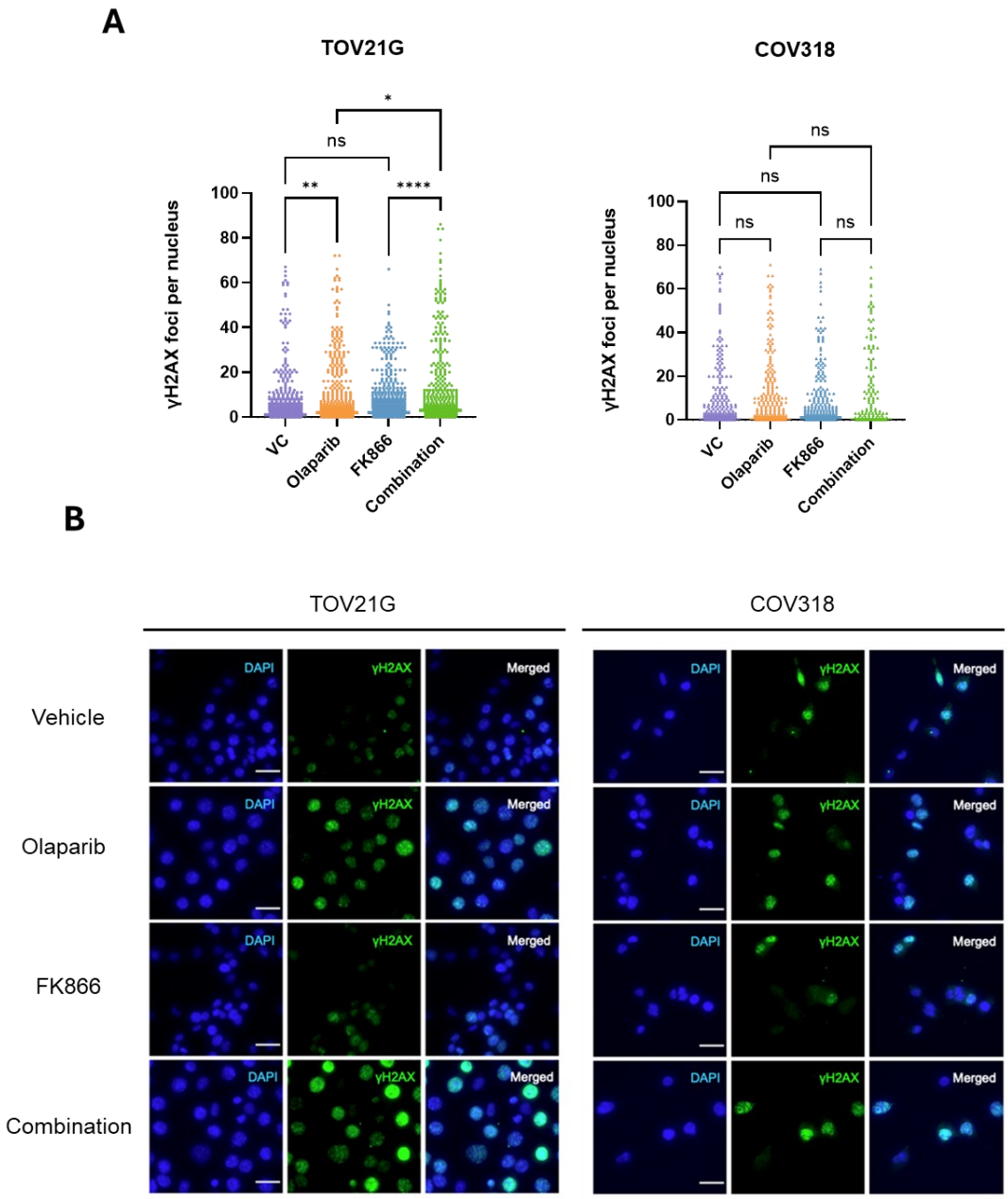
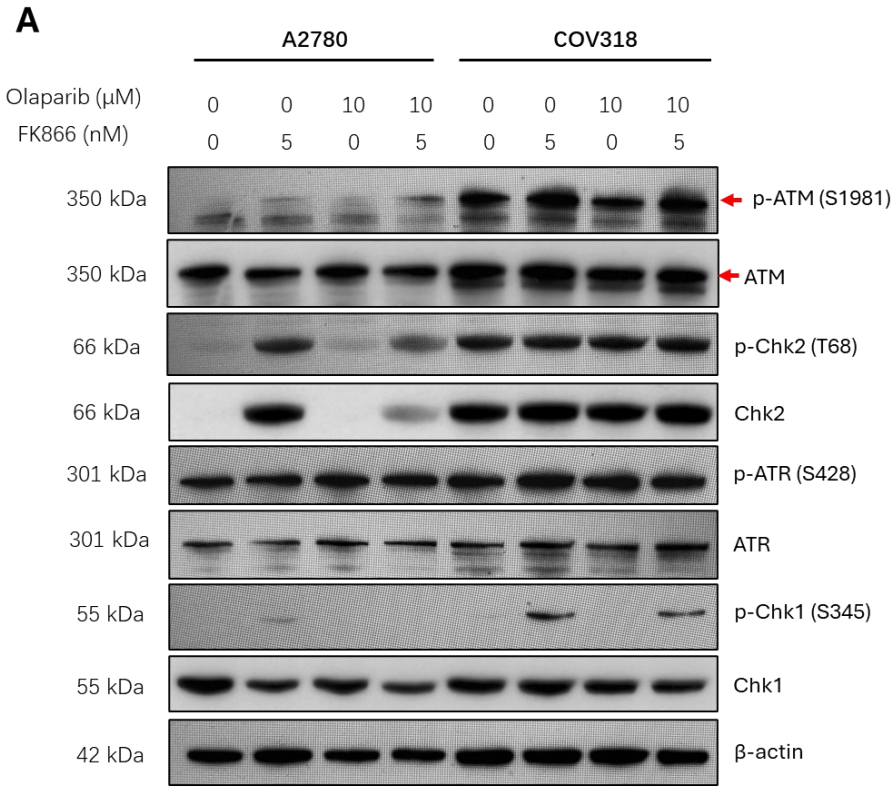


Figure 4.4 The combination of FK866 and Olaparib upregulated γH2AX intensity in Ras/PI3K mutant ovarian cancer cells.

TOV21G and COV318 cells were treated with 0.2% (v/v) DMSO, or 5nM FK866, or 10μM Olaparib or the combination for 24h before immunostaining for γH2AX. (A) Scatter plots showing γH2AX foci per cell. Data were from one representative repeat and the second biological repeat is shown in Appendix Figure 4.6. Because the data are not normally distributed (i.e., skewed), Kruskal-Wallis test and Dunn's multiple comparisons tests were performed to calculate p values. * $p<0.05$, ** $p<0.01$, **** $p< 0.0001$, ns: not significant. (B) Representative IF image showing γH2AX staining. Scale bar = 30μm. TOV21G and COV318 cells were also treated with 10 μM cisplatin for 24h as a positive control and to help identify γH2AX foci. The representative images are shown in Appendix Figure 4.6. The experiments were performed by the Master's student Chris An under my supervision and data were re-analysed and re-plotted.



(to be continued on the next page)

B

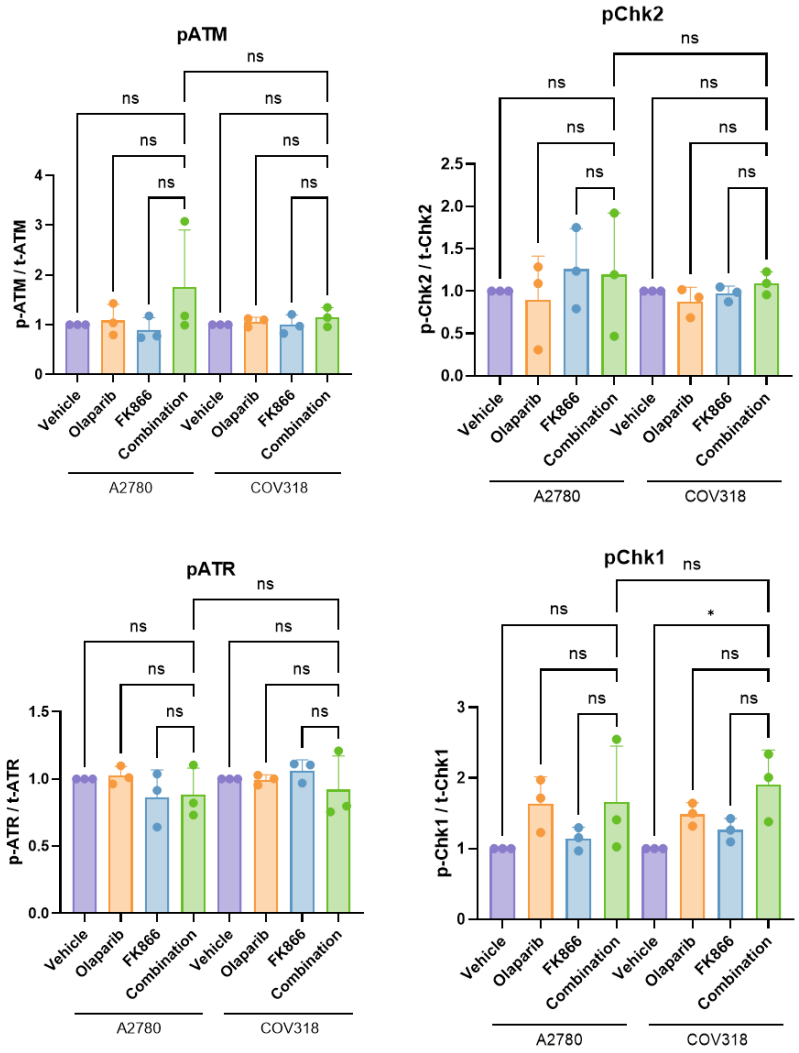


Figure 4.5 The combination of FK866 and Olaparib did not induce further activation of DDR signalling in ovarian cancer cells.

(A) Images of WB blots. A2780 and COV318 cells were treated with 0.2% (v/v) DMSO, or 5nM FK866, or 10μM Olaparib or the combination for 24h. DDR signalling activity was then measured by WB against phospho-ATM, phospho-ATR, phospho-Chk1 and phospho-Chk2. WB data from one representative biological repeat were shown and the rest two repeats were in Appendix Figure 4.7 and Appendix Figure 4.8. Arrows indicate target proteins. (B) Densitometry analysis. The levels of phospho-ATM, phospho-ATR, phospho-Chk1, and phospho-Chk2 were normalized to the levels of respective total proteins. Data represent mean ± SD from three biological repeats. Two-way ANOVA followed by post-hoc Tukey tests were performed to calculate the statistical significance. * $p<0.05$, ns: not significant. WB were performed by the Master's student Chris An under my supervision and densitometry was re-performed by me

4.2.3 FK866 and Olaparib combination caused cell cycle arrest at the G2/M phase in ovarian cancer cells with Ras/PI3K mutations

It has been reported that NAMPT or PARP inhibitors, when treated as a single agent, induce cell cycle arrest secondary to DNA damage (*498-501*). Given the higher DNA damage in Ras/PI3K mutant cells, it was therefore hypothesized that the combination of FK866 and Olaparib could induce greater cell cycle arrest. To test this hypothesis, flow cytometry was performed for phase identification during cell cycle progression. In brief, cells were labelled with the nucleotide analogue IdU to tag replicating DNA during the S phase. PI staining was also performed to quantify DNA content to distinguish G1 and G2/M phase. The data showed that in A2780 and TOV21G cells, Olaparib monotherapy induced an upregulation in the fraction of G2/M phase cells (Figure 4.6A-B). Of note, dual NAMPT and PARP inhibition caused a further increase in the proportion of A2780 and TOV21G cells at G2/M phase (Figure 4.6A-B). Interestingly, there was a decrease in the percentage of S phase A2780 cells when treated with the combination. In contrast, FK866 and Olaparib alone or in combination did not cause increase in the fraction of G2/M phase COV318 cells (Figure 4.6C). Therefore, these data suggest that FK866 and Olaparib combination caused cell cycle arrest at G2/M phase in Ras/PI3K mutant, but not wild-type, ovarian cancer cells.

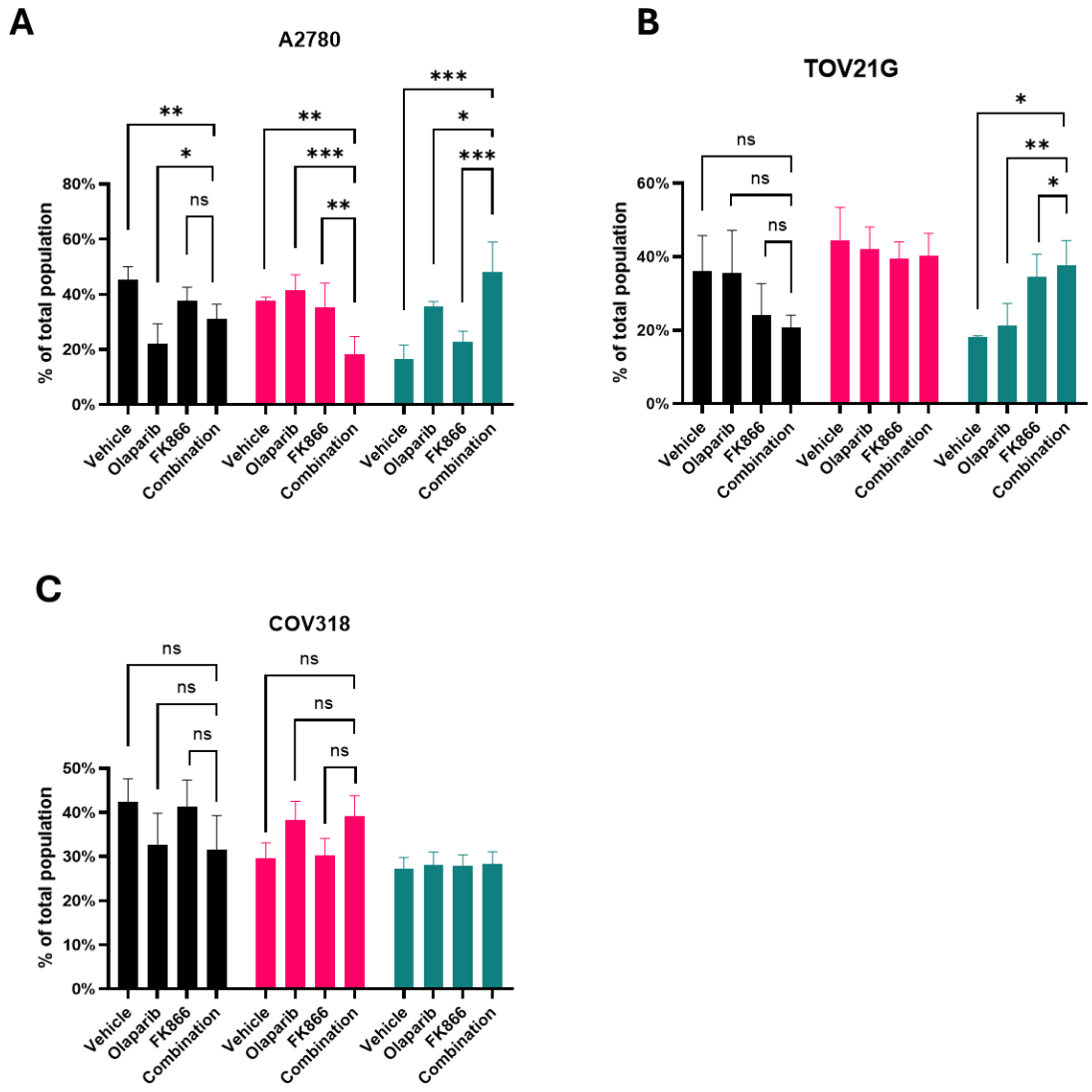


Figure 4.6 The combination of FK866 and Olaparib caused cell cycle arrest at G2/M phase in ovarian cancer cells with mutant Ras/PI3K.

A2780 (A), TOV21G (B) and COV318 (C) cells were treated with 0.2% (v/v) DMSO, or 5nM FK866, or 10μM Olaparib or the combination for 24h. Cell cycle phase were identified by flow cytometry staining of PI and IdU. Data represent mean ± SD of three independent biological replicates. Statistical significance was calculated by one-way ANOVA followed by post-hoc Tukey test. * $p < 0.05$, ** $p < 0.01$, *** $p<0.001$, ns: not significant. For the gating strategies, refer to Appendix Figure 4.9. The flow cytometry experiments were performed with the help from the PhD student Yurui Ma and data were analysed by me.

4.2.4 No enhancement in PARP trapping could be detected with combined PARP inhibitor/FK866 treatment

Next, the mechanisms underlying DNA damage were investigated. It has been reported that the combination of FK866 and Olaparib induces further reduction in PARylation in comparison to monotherapies in Ewing sarcoma cells (*286*). As PARP1 autoPARylation is essential for its release from DNA strands, it was then hypothesized that the higher DNA damage observed in Ras/PI3K mutant cells treated with FK866 and Olaparib combination may result from more PARP1 trapping. To test this hypothesis, a subcellular fractionation assay was performed to separate cytosolic, chromatin-bound and nucleus soluble proteins. My data showed that the chromatin protein histone 3 and the cytoplasmic protein actin could only be detected in the chromatin-bound and cytosolic fraction (Figure 4.7A), thereby confirming the effectiveness of the separation. In A2780 cells, PARP1 levels in the nucleus-soluble fraction were slightly decreased after treatment of Olaparib alone or in combination with FK866 (Figure 4.7A). However, the ratio of nuclear soluble PARP1 and chromatin bound PARP1 remained unchanged regardless of treatment in TOV21G cells (Figure 4.7B). Therefore, these data indicate that the combination of FK866 and Olaparib may not cause PARP1 trapping at the selected timepoint and drug doses. However, it should be noted that the sensitivity of this technique may be limited as chromatin-bound PARP1 could only be detected after long exposure in TOV21G cells.

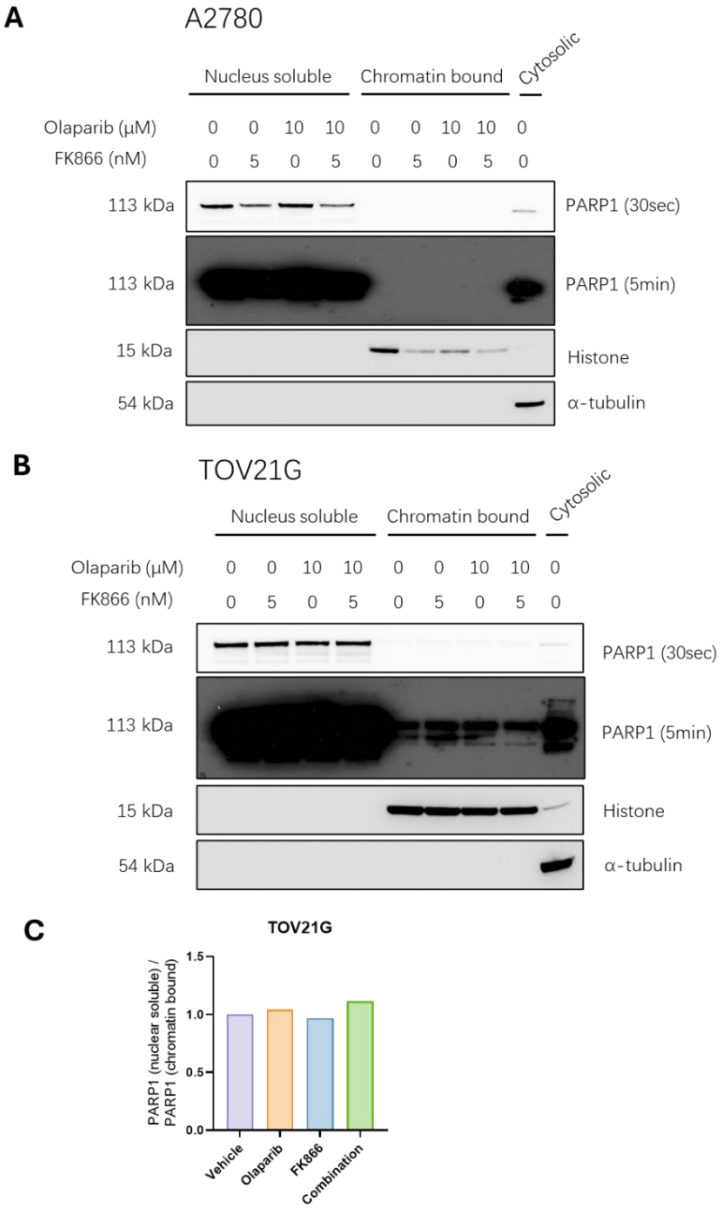


Figure 4.7 No increase in PARP trapping could be detected with FK866 and Olaparib combination treatment.

(A-B) Images of WB blots. A2780 (A) and TOV21G (B) cells were treated with 0.2% (v/v) DMSO, or 5nM FK866, or 10μM Olaparib or the combination for 24h. At the end of drug treatment, subcellular fractionation was performed and protein levels of PARP in different subcellular compartment were analysed by WB. WB images from one representative biological replicate was shown. Histone 3 and α-tubulin were used as positive control for chromatin-bound and cytosolic compartment. (C) Densitometry analysis. The relative levels of nuclear soluble PARP1 (short exposure) were normalized against chromatin bound PARP1 (long exposure) in TOV21G cells. Data represent mean from one biological repeat. Such normalisation could not be performed in A2780 cells because no band of chromatin bound PARP1 was detected. Normalisation of nuclear soluble PARP1 against loading control was not possible because no internal control was available.

4.2.5 The combination of Olaparib and FK866 resulted in more ROS accumulation in Ras/PI3K mutant ovarian cancer cells

$NADP^+$ and NADPH, the product of NAD^+, are essential for regulating the redox balance (*217*) and therefore, NAD^+ depletion by FK866 has been reported to induce oxidative stress and apoptosis in haematological cancer cells (e.g., chronic lymphocytic leukaemia and acute myeloid leukaemia cells) (*502, 503*). Interestingly, Olaparib monotherapy results in ROS production which is essential to its cytotoxic effects in bladder cancer cells and HR-proficient cancer cells (*504, 505*). As ROS causes oxidative damage to cellular macromolecules (e.g., DNA, lipids and proteins) (*64, 71*), it was then hypothesized that the combination of FK866 and Olaparib may induce higher levels of oxidative stress in Ras/PI3K mutant cells than Ras/PI3K WT cells, which in turn causes more DNA damage and apoptosis. To test this hypothesis, H_2O_2 levels was measured as an indicator of ROS accumulation and oxidative stress. H_2O_2 measurement was chosen because 1) it has the longest half-life among ROS species (e.g., superoxide, hydroxyl radical and singlet oxygen) (*506*) and is convenient to detect; 2) a range of ROS species can be converted to H_2O_2 and its levels reflect general changes in ROS (*506, 507*). The data showed that FK866 and Olaparib monotherapy caused a slight increase in ROS accumulation in A2780 cells (Figure 4.8A). Of note, the combination of FK866 and Olaparib resulted in a further increase in ROS levels (Figure 4.8A). In contrast, ROS accumulation remained unchanged regardless of drug treatment in COV318 cells (Figure 4.8B). Therefore, these data suggest that FK866 and Olaparib combination induces higher oxidative stress in EOC cells with Ras/PI3K mutations.

NAD^+ is an essential metabolic cofactor in the TCA cycle and OXPHOS in mitochondria (*217*). Its depletion by FK866 mediated NAMPT inhibition has been reported to compromise mitochondria metabolism (*502, 508-510*). In a viable mitochondrion, the TCA cycle generates reducing equivalent NADH and $FDAH_2$ which are subsequently oxidised in ETC (*511*). The electron transport during oxidation establishes proton gradient to maintain mitochondria membrane potential ($\Delta\Psi m$) that is next utilized by ATP synthase for ATP production (*511*). It has been demonstrated that FK866 treatment causes the reduction of oxygen consumption

rates, the loss of ΔΨm and the decrease in ATP production (*502, 508-510*). Given that mitochondrial dysfunction is a source of ROS production (*512*), it was then hypothesized that the combination of FK866 and Olaparib resulted in higher levels of mitochondrial dysfunction in Ras/PI3K mutant cells than wild-type cells, which in turn contributes to ROS generation. To test this hypothesis, ΔΨm was measured as an indicator of mitochondrial metabolic function. The results showed that FK866 and Olaparib monotherapy causes disruption in ΔΨm in A2780 cells (Figure 4.9A). There was an upward, but not statistically significant, trend in ΔΨm disruption in A2780 cells treated with FK866 and Olaparib combination (Figure 4.9A). In contrast, no compromise in ΔΨm was found in COV318 cells regardless of drug treatment (Figure 4.9B). Thus, these data suggest that dual NAMPT and PARP1 inhibition may not lead to further disruption in mitochondrial metabolism.

To examine whether the increased ROS accumulation is essential for cytotoxicity in Ras/PI3K mutant cells treated with FK866 and Olaparib combination, a rescue experiment was conducted. N-acetylcysteine (NAC) is an antioxidant drug and provides cysteine as a substrate for the synthesis of glutathione which is another potent antioxidant utilised by glutathione peroxidase (*513, 514*). Thus, cells were pre-incubated with NAC and treated with FK866 and/or Olaparib before cellular apoptosis was measured. The results showed that FK866 and Olaparib combination resulted in a further increase in the fraction of apoptotic cells in A2780, but not COV318 cells (Figure 4.10A-B), thereby confirming the sensitization effects in Ras/PI3K mutant cells. Intriguingly, dual NAMPT and PARP1 inhibition failed to further upregulate apoptotic cell population in A2780 cells pre-treated with NAC (Figure 4.10A). Indeed, the cells treated with the combination phenocopied those received Olaparib monotherapy (Figure 4.10A). Likewise, combination treatment caused the highest levels of caspase-3/7 activation in A2780 but not COV318 cells (Figure 4.11A-B). Of note, NAC supplementation significantly reduced caspase activity in A2780 cells treated with the combination (Figure 4.11A-B). In addition, ascorbic acid, a direct scavenger of ROS (*515*), was employed as another antioxidant to validate these results. However, the data showed that its supplementation even at low micromolar reduced cell growth under basal conditions (data not shown), and thus, the rescue experiment could not be performed. Collectively, these data

suggest that the sensitization effects of Ras/PI3K mutations on FK866 and Olaparib combination may result from the higher levels of ROS accumulation.

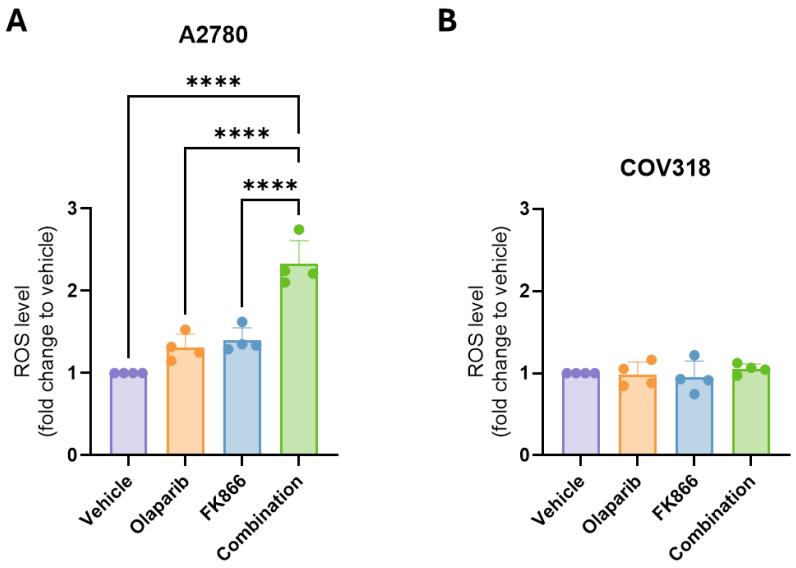


Figure 4.8 The combination of FK866 and Olaparib induced ROS accumulation in ovarian cancer cells with mutations in the Ras/PI3K pathway.

A2780 (A) and COV318 (B) cells were treated with 0.2% (v/v) DMSO, or 5nM FK866, or 10μM Olaparib or the combination for 24h before H_2O_2 measurement by ROS-Glo™ H_2O_2 assay. Data represent mean ± SD of four independent biological replicates performed by me and the Master's student Chris An under my supervision. Statistical significance was calculated by one-way ANOVA followed by post-hoc Tukey test. **** $p<0.0001$.

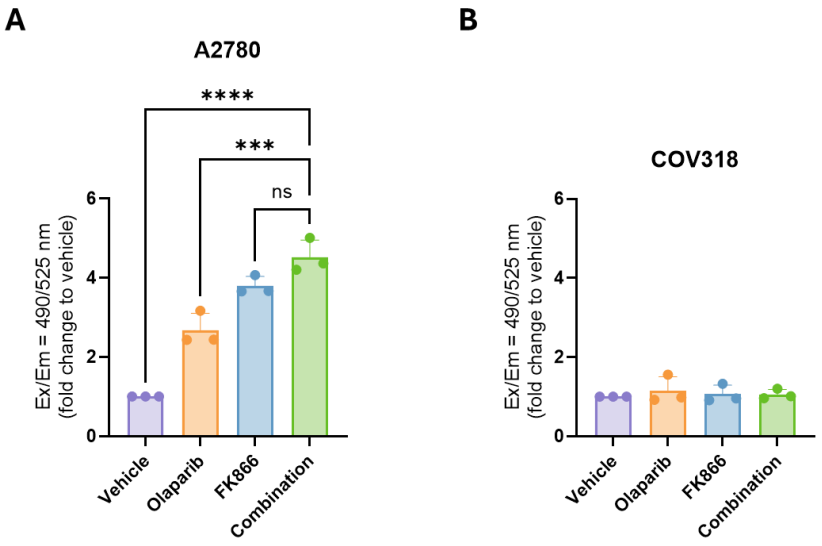


Figure 4.9 The combination of FK866 and Olaparib caused mitochondrial dysfunction in Ras/PI3K mutant ovarian cancer cells.

A2780 (A) and COV318 (B) cells were treated with 0.2% (v/v) DMSO, or 5nM FK866, or 10μM Olaparib or the combination for 48h before mitochondrial membrane potential measurement by JC-10 assay. Cell density was also measured by SRB assay. The readouts of the JC-10 assay (i.e., the emission intensity at 520nm wavelength when excited at 490nm wavelength) were normalised to cell density and the data were expressed as fold changes to vehicle (DMSO). Data represent mean ± SD of three independent biological replicates performed by me and the Master's student Chris An under my supervision. Statistical significance was calculated by one-way ANOVA followed by post-hoc Tukey test. *** $p<0.001$, **** $p<0.0001$, ns: not significant.

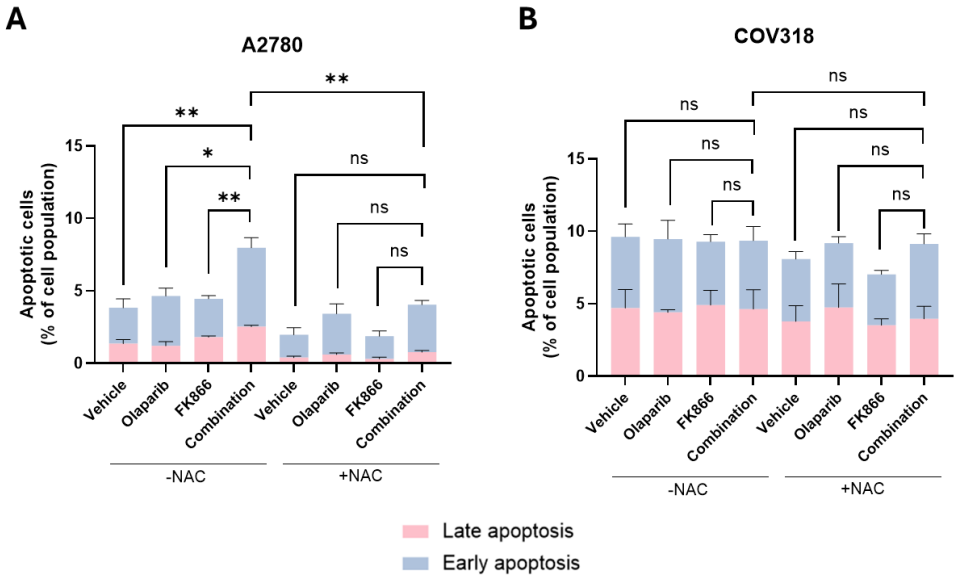


Figure 4.10 Supplementation of NAC rescued apoptosis in A2780 cells treated with the combination of FK866 and Olaparib.

A2780 (A) and COV318 (B) cells were pre-treated with 10mM NAC for 2h to boost GSH synthesis before treatment by 0.2% (v/v) DMSO, or 5nM FK866, or 10μM Olaparib or the combination for 24h in media with or without 5mM NAC. At the end of treatment, apoptosis was examined by flow cytometry against annexin V and propidium iodide (PI). Data were represented using stacked bar charts. Data represent mean ± SD of three independent biological replicates. Statistical significance was calculated using the fraction of total apoptotic cells (i.e., combination of early and late apoptotic cells) by two-way ANOVA followed by post-hoc Tukey test. * $p<0.05$, ** $p<0.01$, ns: not significant. For the gating strategies, refer to Appendix Figure 4.10. The experiments were performed by the Master's student Chris An under my supervision and data were re-analysed and re-plotted.

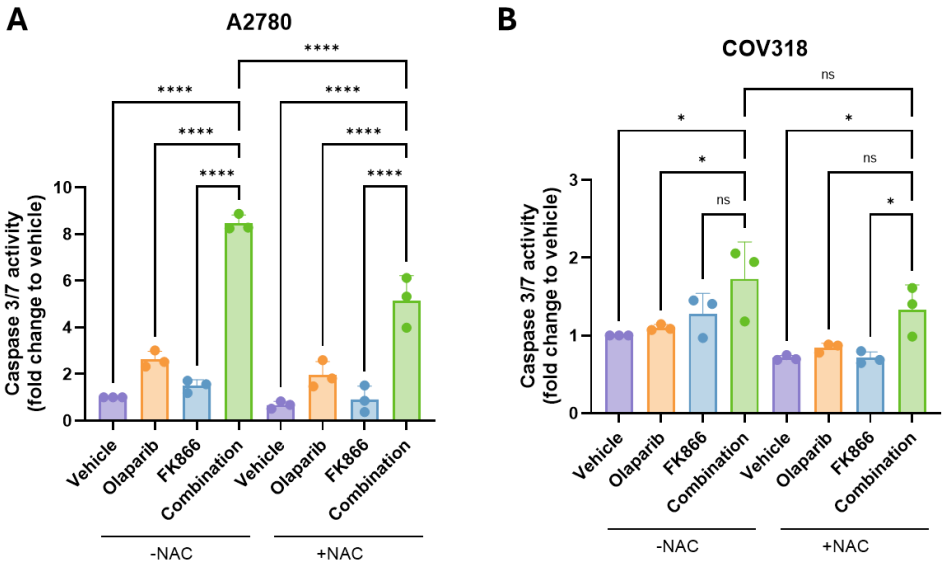


Figure 4.11 NAC supplementation rescued caspase-3/7 induction by the combination of FK866 and Olaparib in A2780 cells.

A2780 (A) and COV318 (B) cells were pre-treated with 10mM NAC for 2h to boost GSH synthesis before treatment by 0.2% (v/v) DMSO, or 5nM FK866, or 10μM Olaparib or the combination for 24h in media with or without 5mM NAC. At the end of treatment, caspase-3/7 activity was measured using the Promega Caspase-Glo® 3/7 assay. Cell density was also measured by the SRB assay. The caspase-3/7 readout was normalised against cell density and the data were expressed as fold changes to vehicle without NAC supplementation. Data represent the mean ± SD of three independent biological replicates. Statistical significance was calculated by two-way ANOVA followed by post-hoc Tukey test. * $p < 0.05$, **** $p < 0.0001$, ns: not significant. The experiments were performed by the Master's student Chris An under my supervision and data were re-analysed and re-plotted.

4.3 Discussion

Recent clinical trials support the application of PARP inhibitors beyond ovarian cancer patients with HR defects albeit with less therapeutic benefits (*264, 516*). In particular, Akt mutations are associated with poorer responses (*259*). Indeed, genetic alterations in the Ras/PI3K signalling are frequent in all the subtypes of ovarian cancer and, for instance, present in 45% of HGSC patients (i.e., the most common subtype) (*153, 169*), which highlights the need to improve PARP inhibitor sensitivity. One strategy is the combination of PARP inhibitors with FK866 to enhance PARP trapping and DNA damage. Indeed, the efficacy of this combination and increased DNA damage have been reported in various types of cancer, including triple-negative breast cancer (TNBC), Ewing sarcoma and ovarian HGSC cells with intrinsic or acquired resistance to PARP inhibitors (*286, 287, 493*). Activation of the Ras/PI3K pathway has been shown to stimulate central carbon metabolism which requires NAD^+ as a key co-factor (*96, 517*). Therefore, it was hypothesized that ovarian cancer cells with mutations in the Ras/PI3K signalling may be more vulnerable to the combination of NAD^+ depletion and PARP inhibitors.

In this chapter, I validated the preliminary data from our lab which showed dual NAMPT and PARP inhibition caused greater growth reduction in ovarian cancer cells with Ras/PI3K pathway mutations. Using a panel of human ovarian cancer cell lines, I showed the higher apoptosis in Ras/PI3K mutant cells when treated with the combination of FK866 and Olaparib. Of note, the sensitization effects were abolished by the supplementation of NMN, the product of NAMPT, in the media, which indicates the sensitization results from the on-target effects of FK866. Therefore, these data support the hypothesis and suggests NAD^+ depletion could be an effective strategy to sensitize patients with dysregulated Ras/PI3K pathway to Olaparib. Additionally, these findings indicate Ras/PI3K mutations may function as a biomarker to guide the clinical application. In this regard, clinical trials showed the dose-limiting toxicity of FK866 monotherapy (e.g., thrombocytopenia) (*518-520*). Although Olaparib was considered as a relative safe agent, haematological adverse drug events (e.g., neutropenia and thrombocytopenia) have been noticed in patients (*521, 522*). Thus, sensitization biomarkers

are required to lower the doses and limit toxicity. In this regard, BRCA1/2 deletion has been shown in a pre-clinical study to enhance the sensitivity in TNBC cells and thus may be used as biomarkers (*493*). However, it remains unclear whether other genetic mutations may predict the responses to dual NAMPT and PARP inhibition particularly in ovarian cancer. Here, novel evidence was provided to support the use of Ras/PI3K mutations, common genetic alterations in ovarian cancer, as a sensitization biomarker.

Interestingly, FK866 single agent treatment induced significantly lower levels of caspase-3/7 activity in OVCAR8 cells. This may not necessarily suggest reduced levels of cell death because caspase independent cell death (CICD) mechanisms have been reported (*523*). In this regard, mitochondrial outer membrane permeabilization (MOMP) results in the release of pro-apoptotic proteins (e.g., apoptosis-inducing factor (AIF) and endonuclease G) from mitochondria intermembrane space, which in turn induces CICD (*524*). Indeed, FK866 treatment has been reported to induce mitochondrial dysfunction, which in turn leads to the release of AIF and endonuclease G and thus, CICD in adult T-cell leukemia/lymphoma (ATL) (*525*). Thus, it would be interesting to examine the protein levels of AIF and endonuclease G in the cytosol compared to mitochondria by WB.

The correlation between Ras/PI3K pathway mutations and expression of NAMPT and NAPRT was also examined as a potential mechanism of sensitization by Ras/PI3K mutations. NAPRT expression is lower in A2780 cells than COV318 cells while similar levels of NAMPT expression were observed. This indicates that A2780 cells are more dependent on NAMPT for NAD^+ generation and thus, more sensitive to FK866. However, no clear pattern of association could be observed in the panel of 10 human ovarian cancer cell lines, which suggests that alterations in NAMPT and NAPRT expression may not sensitize ovarian cancer cells to the combination of FK866 and Olaparib. This contrasts with the previous published report which showed the regulatory roles of Ras/PI3K signalling in NAMPT expression (*491*). One possible explanation is the lack of association between Ras/PI3K mutations and activity in the signalling. It should be noted that the correlation was measured under conditions with 10% FBS in media. Therefore, these experiments should be repeated after serum starvation.

Regarding the underlying mechanisms, increased DNA damage and cell cycle arrest at G2/M phase were found in TOV21G cells, but not COV318 cells, treated with FK866 and Olaparib combination. The enhanced DNA damage induced by the drug combination is in line with previous studies. In this regard, higher levels of the DNA damage marker γH2AX have been reported in dual NAMPT and PARP inhibitor treated TNBC, Ewing sarcoma and ovarian HGSC cells (*286, 287, 493*). It was also found that the basal levels of DNA damage were higher in COV318 cells than TOV21G cells, which was associated with enhanced activity of DDR signalling. One possible explanation is the loss of p53, which is essential for maintaining genomic integrity (*526*), in COV318 cells and therefore, its deletion results in higher genetic instability.

Interestingly, the activity of DDR pathway did not correlate with γH2AX observed in the treatment groups. However, it should be noted that γH2AX and DDR pathway activity were measured in two different cell lines: TOV21G and A2780 cells, respectively. Therefore, DDR pathway activity and γH2AX should be measured for each cell line. Assuming that dual NAMPT and PARP inhibition caused the highest DNA damage in A2780 cells, the slight increase in pATM and reduction in pChk2 suggest the transduction of the DDR signalling through alternative effectors other than Chk2. In this regard, Abelson non-receptor tyrosine kinase (c-Abl) is a downstream effector of ATM and its phosphorylation in turn activates p73 to induce apoptosis (*527*). p53 is another effector regulated by ATM via direct phosphorylation or indirect c-Abl-mediated phosphorylation (*528, 529*). Once activated, p53 induces the transcription of pro-apoptotic genes (*530*). Indeed, signal transduction through c-Abl and p53 is supported by the highest apoptosis in A2780 cells treated with the drug combination. Alternatively, p73 and p53 induce cell cycle arrest at G1 phase by upregulating the expression of p21 which is a cyclin-dependent kinase (CDK) inhibitor (*531, 532*). p53 also arrests cell cycle at G2/M phase via 14-3-3 mediated inhibition of the Cdc2/cyclin B complex (*533*). Previously published reports showed that PARP or NAMPT inhibitors causes cell cycle arrest at G2/M phase individually (*498-501*) although little is known about the combination effects. Here, we provide the evidence that FK866 and Olaparib combination further increases the percentage of A2780 and TOV21G cells at G2/M phase. To understand the signal

transduction via DDR pathway and its link with cell cycle arrest and apoptosis, these downstream effectors of DDR signalling should be probed by WB.

To understand the source of DNA damage, PARP trapping was measured by western blotting against PARP1 localised in different subcellular compartments. However, no increase in chromatin-bound PARP1 could be detected although nucleus-soluble PARP1 was slightly decreased in A2780 cells treated with Olaparib alone or in combination with FK866. Typically, the cells are co-treated with methyl methanesulfonate (MMS) to increase basal DNA damage, which allows detection of chromatin-bound PARP1 (*243*). However, MMS depletes cellular NAD^+ pool and thus may interfere with FK866 in our system (*534*). Given that NAD^+ is a substrate of PARP1 autoPARylation for its release from DNA strands (*234*), it would be interesting to examine PARP1 trapping using a fluorescent sensor to overcome the sensitivity limitations of the subcellular fractionation and WB assay (*535*).

As NADP(H), the product of NAD^+, is essential for regulating redox balance and oxidative stress causes DNA damage, ROS levels were examined. Here, we found that the combination of FK866 and Olaparib induced a further increase of ROS levels in A2780 cells, but not COV318 cells. Surprisingly, FK866 monotherapy did not induce ROS accumulation although similar levels of $\Delta\Psi m$ disruption was observed in FK866 monotherapy and combination treated cells. In addition, previous data from our lab showed similar concentrations of NAD^+ in cells treated with FK866 alone or in combination with Olaparib. It is likely that there is a threshold of NAD^+ content and $\Delta\Psi m$ disruption beyond which cell death may occur and since the two parameters were measured only in viable cells, combination treated cells may not distinguish from FK866 monotherapy treated cells. However, it is also possible that NAD^+ depletion and the consequent mitochondrial dysfunction alone may not suffice to cause a further increase of ROS accumulation in the combination group. Published data showed that both FK866 and Olaparib monotherapy induce oxidative stress. However, the underlying mechanisms involve the opposite modulation on NAD^+ content. In this regard, FK866 single agent depletes NAD^+ and interferes with mitochondria metabolism as evidenced by reduced $\Delta\Psi m$, which in turn leads to oxidative stress (*503, 508*). In contrast, Olaparib treatment inhibits NAD^+ consumption by PARP and causes NAD^+ accumulation in macrophages (*536*). This rewires mitochondria

metabolism and diverts NAD^+ for reduction via the reverse electron transport (RET) which is a source of ROS production (*536, 537*). Moreover, PARP inhibition has been shown to upregulate mitochondrial oxidative metabolism via NAD^+ accumulation in mouse brown adipose and muscle tissue (*538*). Although NAD^+ content was not examined, bladder cancer cells treated with Olaparib displayed higher ROS levels (*504*). Collectively, these results indicate that alternative sources may contribute to the highest oxidative stress found in the combination group. For instance, approximately 3.5% of the transcriptome is regulated by PARP1, including metabolic genes (*539*). The mechanisms involve chromatin structure modulation and direct binding to DNA elements (*540*). In this regard, PARP1 can simultaneously bind to several nucleosomes and generate highly compacted chromatin structure (i.e., supranucleosomes), which in turn inhibits gene transcription by limiting the access to transcription machinery (*541*). PARP1 also directly interacts with promoter region of specific genes, which leads to the release of inhibitory co-regulators and recruitment of stimulatory co-regulators (*542, 543*). Given that dual NAD^+ depletion and PARP inhibition may further reduce PARP1 autoPARylation and increase DNA binding, the modulation of gene expression may be more profound in the combination group. For instance, genes involved in the ROS defensive system may be further repressed by dual NAMPT and PARP inhibition. Thus, a transcriptomics/proteomics study may help to understand the source of ROS accumulation.

Of note, supplementation of NAC, an antioxidant drug (*513*), lowered apoptosis in the combination treated A2780 cells to similar levels observed in Olaparib monotherapy group. This indicates that enhanced ROS accumulation may be a mechanism underlying the sensitization effects of Ras/PI3K mutation. Although caspase-3/7 activity showed a partial rescue, increasing the concentration of NAC or choosing a different antioxidant (e.g., vitamin E) may improve the rescue effects. ROS levels should also be measured in cells treated with NAC to confirm the reduction of oxidative stress. In addition, γH2AX should be measured in cells co-treated with NAC and FK866/Olaparib to establish the causal relationship between ROS accumulation to DNA damage. Alternatively, oxidized bases (e.g., 8-Oxo-2'-deoxyguanosine (8-oxo-dG)) can be measured by LC-MS/MS of immunofluorescence (*544,*

545).

In conclusion, evidence from this chapter showed that Ras/PI3K mutations may sensitize ovarian cancer cells to the combination of FK866 and Olaparib and the underlying mechanisms involve higher DNA damage and oxidative stress. One major limitation in this chapter is that no isogenic pair of cell lines was used. Given the different genetic landscape among the cell lines, the association between higher sensitivity to dual NAMPT and PARP inhibition and Ras/PI3K mutations should be further validated. This will be addressed in the next chapter.

CHAPTER 5

Investigating NAD^+ depletion as a strategy to improve Olaparib sensitivity in isogenic models of ovarian HGSC

Chapter 5 Investigating NAD^+ depletion as a strategy to improve Olaparib sensitivity in isogenic models of ovarian HGSC

5.1 Introduction

As described in the previous chapter, the Ras/PI3K mutations sensitized human ovarian cancer cells to the combination of FK866 and Olaparib. However, the main limitation is the complex genetic landscape of the cell lines used. Therefore, isogenic pairs of cell lines should be employed to validate the above results. Additionally, *in vivo* studies are required to support these *in vitro* data.

In this chapter, a panel of ID8 cells (ID8 *Trp53*$^{-/-}$, *Trp53*$^{-/-}$*; Nf1*$^{-/-}$, *Trp53*$^{-/-}$*; Pten*$^{-/-}$ cells) were used as an isogenic pair. Using CRISPR KO techniques, all the ID8 cells harbour Trp53 deletion to recapitulate human patients with HGSC. The loss of Nf1 and Pten models hyperactivation in the Ras and PI3K pathway, respectively. Of note, a syngeneic mouse model can be generated by implanting ID8 cells into the mice of the same inbred strain, which allows the investigation of the drug combination in the presence of a functional immune system. The ID8 *in vivo* model also develops ascites and peritoneal metastasis which recapitulates human patients.

5.2 Results

5.2.1 Mutations in Ras/PI3K pathway enhanced apoptosis induction capacity of FK866 and Olaparib combination in ID8 ovarian HGSC cells *in vitro*

To validate the sensitization effects of Ras/PI3K mutations on FK866 and Olaparib

combination, a panel of isogenic cell lines (ID8 *Trp53*$^{-/-}$, *Trp53*$^{-/-}$*; Nf1*$^{-/-}$, *Trp53*$^{-/-}$*; Pten*$^{-/-}$ cells) were used. The loss of NF1 and PTEN and hyperactivity of Ras/PI3K signalling were verified by WB. My data showed increased Ras and PI3K pathway in Nf1 and Pten depleted ID8 cells respectively with no crosstalk (Appendix Figure 3.2). Preliminary data from our laboratory showed that the combination of FK866 and Olaparib induced higher levels of caspase-3/7 activation in ID8 cells with Nf1 and Pten depletion (*393*). Therefore, for further validation, cellular apoptosis was measured by flow cytometry analysis against annexin V and PI. The data showed that FK866 monotherapy significantly upregulated the proportion of apoptotic ID8 *Trp53*$^{-/-}$*; Pten*$^{-/-}$ cells, but not ID8 *Trp53*$^{-/-}$ cells (Figure 5.1A-B). The combination of FK866 and Olaparib caused the highest levels of apoptotic cells in both cell lines and noticeably, the fraction was higher in ID8 cells with Pten deletion (Figure 5.1A-B). These data suggest that Pten loss might enhance the capacity of the FK866 and Olaparib combination to induce apoptosis.

To understand whether the combination of FK866 and Olaparib causes higher levels of growth inhibition in ID8 cells with Nf1 and Pten loss, cell mass was measured after drug treatment for 72h. My data showed that the addition of FK866 resulted in a left and downward shift in the dose-response curves of Olaparib in ID8 cells regardless of Nf1 and Pten mutational status (Figure 5.2A). These data suggest an improved sensitivity of Olaparib by FK866. Next, IC_{50} values were calculated. In comparison to HR-deficient ID8 cells (Brca1/2 depleted), all the ID8 cells were relative resistant to Olaparib monotherapy with nearly 5-fold higher IC_{50} values (Figure 5.2B). However, the combination of 5nM FK866 reduced Olaparib IC_{50} values in all the three HR-proficient ID8 cell lines to similar levels found in HR-deficient ID8 cells (Figure 5.2B). Surprisingly, ID8 *Trp53*$^{-/-}$ cells showed a greater reduction in IC_{50} values than ID8 *Trp53*$^{-/-}$*; Nf1*$^{-/-}$, *Trp53*$^{-/-}$*; Pten*$^{-/-}$ cells when treated low doses of FK866 (Figure 5.2B), which indicates that Nf1 and Pten loss failed to enhance growth inhibition by FK866 and Olaparib combination.

Collectively, these data suggest that FK866 sensitized Olaparib in ID8 cells, and the loss of Nf1 and Pten further improved the sensitization effects of apoptosis induction.

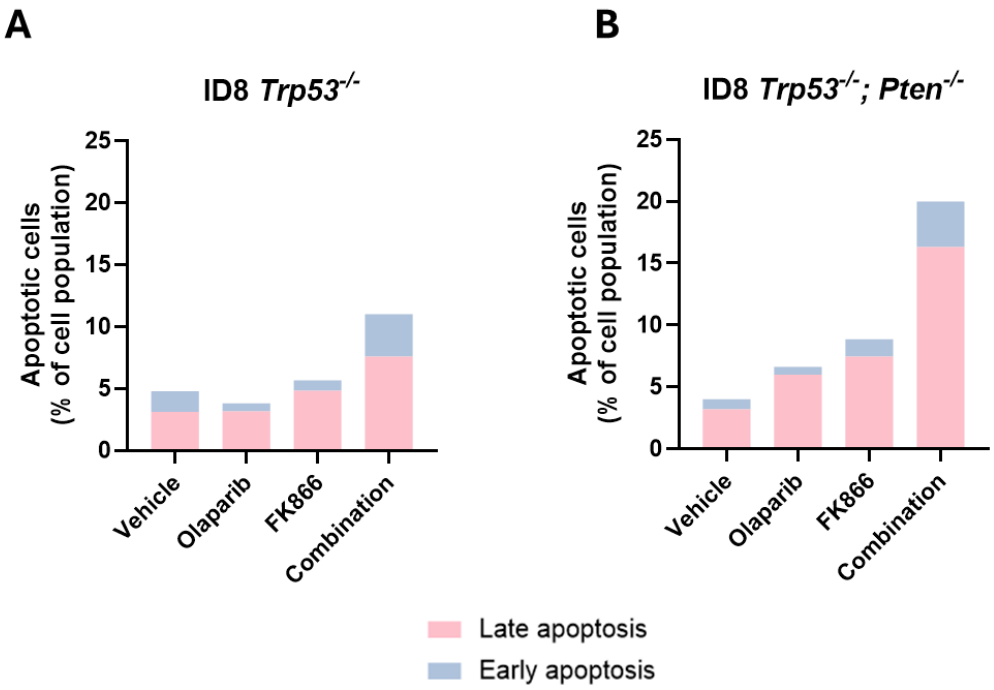


Figure 5.1 The combination of FK866 and Olaparib might induce higher levels of apoptosis in ID8 *Trp53*$^{-/-}$; *Pten*$^{-/-}$ cells compared to ID8 *Trp53*$^{-/-}$ cells.

ID8 *Trp53*$^{-/-}$ cells (A) and ID8 *Trp53*$^{-/-}$; *Pten*$^{-/-}$ cells (B) were treated with 0.2% (v/v) DMSO, or 5nM FK866, or 10μM Olaparib or the combination for 24h. Apoptosis was measured by flow cytometry against annexin V and propidium iodide (PI). Data were represented using stacked bar charts. Data represent mean from one biological replicate. For the gating strategies, refer to Appendix Figure 5.1. The experiments were performed by the Master's student Chris An under my supervision and data were re-analysed and re-plotted.

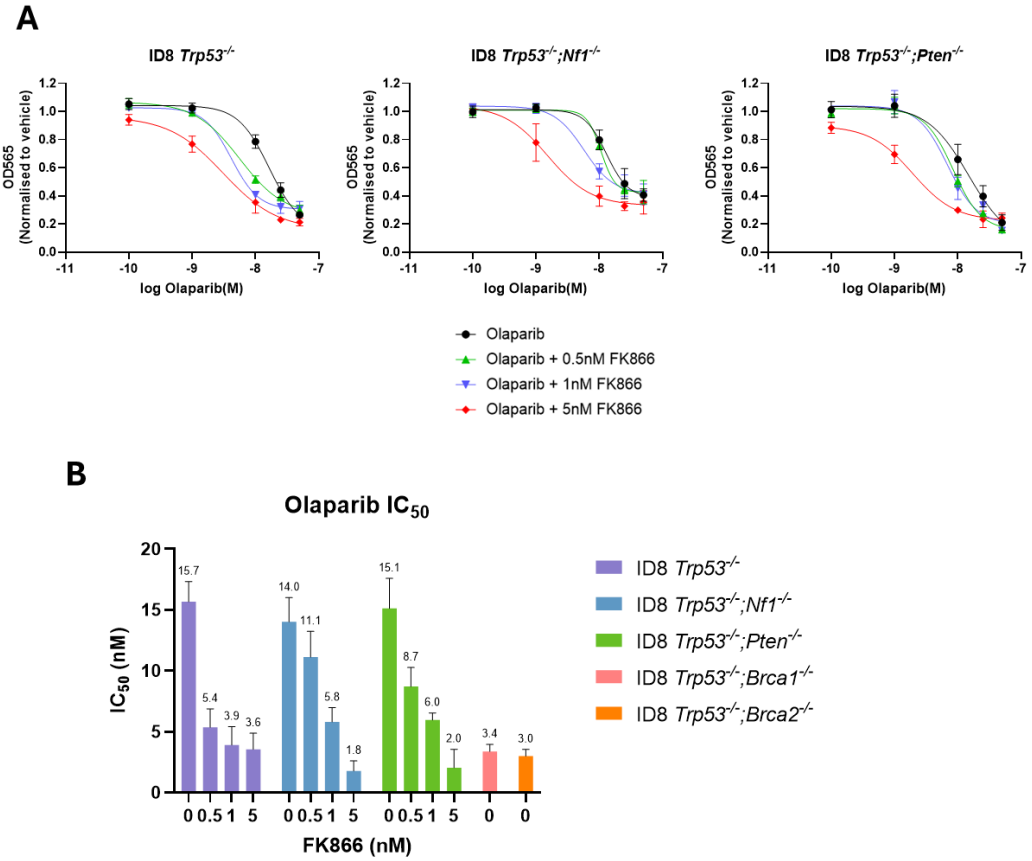


Figure 5.2 FK866 enhanced the growth inhibitory effects of Olaparib in a panel of ID8 cells. (A) Dose-response curves of Olaparib with or without FK866. A panel of ID8 cells (i.e., ID8 Trp*53*$^{-/-}$, ID8 *Trp53*$^{-/-}$*;Nf1*$^{-/-}$, ID8 *Trp53*$^{-/-}$*;Pten*$^{-/-}$ cells) were treated with various doses of Olaparib (0.1, 1, 10, 25, 50μM) in combination with 0.5, 1 or 5nM FK866 or DMSO. After 72h of treatment, cell density was measured by SRB assay. Data were normalized against vehicle groups and represent mean ± SD of four independent biological repeats. (B) IC_{50} values of Olaparib. IC_{50} values were calculated based on dose-response curves from (A) by non-liner regression fitting (least square fitting) in GraphPad (version 10.2.3). Data represent mean ± 95% confidence interval.

5.2.2 FK866 induced similar levels of NAD^+ decrease in ID8 ovarian HGSC cells *in vitro*

To understand the mechanisms of sensitization on apoptosis by Nf1 and Pten loss, NAD^+ and NADH concentrations were measured in ID8 cells treated with various doses of FK866 monotherapy. My data showed a gradual decrease in the concentrations of total NAD (NAD^+ and NADH) as the dose of FK866 increased (Figure 5.3A). Interestingly, treating ID8 cells with a dose higher than 5nM did not lead to a further reduction in total NAD pool, thereby suggesting that alternative pathways may contribute to NAD generation. Of note, ID8 cells showed similar levels of reduction in total NAD pool regardless of Nf1 or Pten loss (Figure 5.3A). Likewise, a dose-dependent decrease in NAD^+ and NADH concentrations were observed with no differences in responses to FK866 across the three ID8 cell lines (Figure 5.3B-C). Given that oxidative stress is essential to the sensitization effects observed in the human EOC cell lines (Section 4.2.6), NAD^+/NADH ratio was calculated as an indicator of cellular redox balance. My results showed that the NAD^+/NADH ratio was gradually decreased with higher dose of FK866 and Nf1 or Pten loss did not lead to a further reduction in the ratio (Figure 5.3D). Interestingly, similar levels of NAMPT and NAPRT expression was found between ID8 *Trp53*$^{-/-}$ and *Trp53*$^{-/-}$;*Pten*$^{-/-}$ cells under basal conditions (Appendix Figure 5.3). Collectively, these data suggest that the sensitization to apoptosis by Nf1 and Pten loss may not involve manipulation of NAD^+ levels.

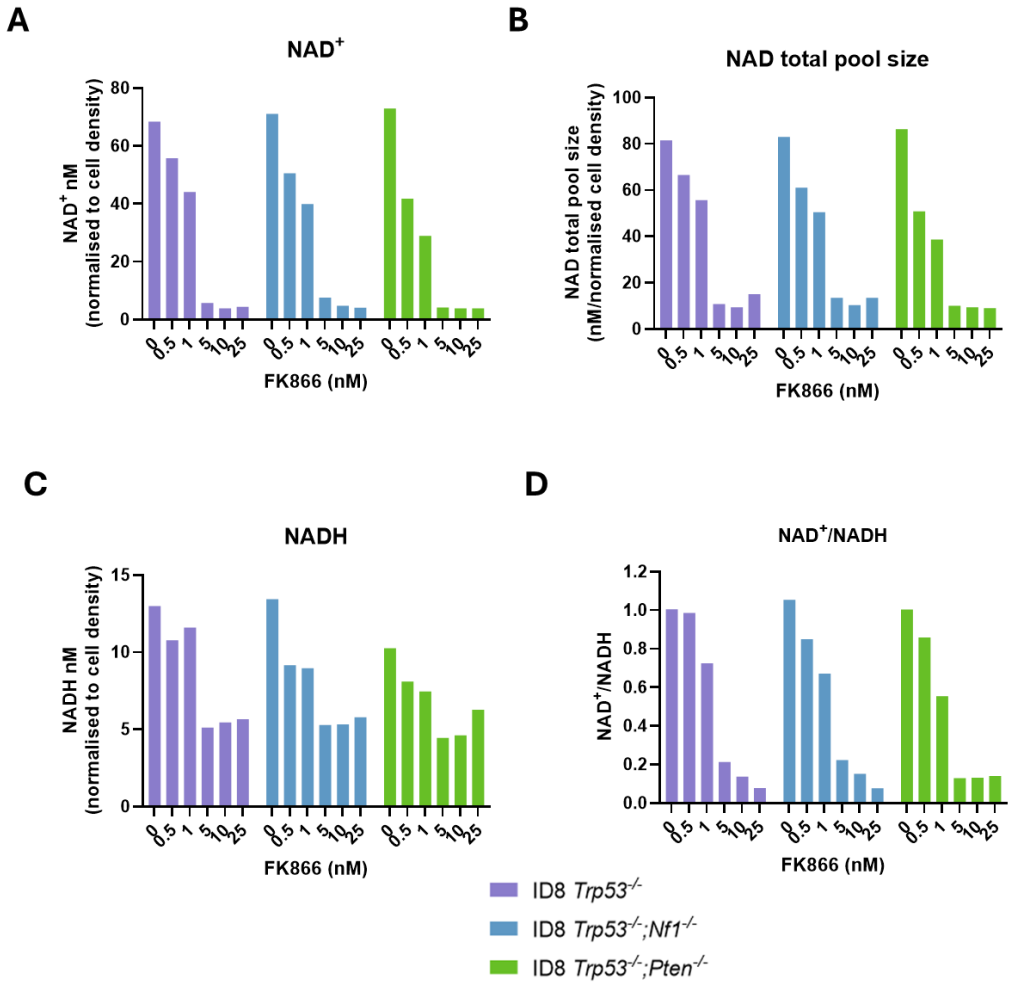


Figure 5.3 FK866 reduces NAD pool size and interferes with NAD$^+$/NADH ratio in ID8 cells. (A) NAD total pool size, (B) NAD$^+$ levels, (C) NADH levels and (D) NAD$^+$/NADH ratio in a panel of ID8 cells (i.e., ID8 Trp*53*$^{-/-}$, ID8 *Trp53*$^{-/-}$*;Nf1*$^{-/-}$, ID8 *Trp53*$^{-/-}$*;Pten*$^{-/-}$ cells). ID8 cells were treated with various doses of FK866 (0.5, 1, 5, 10 or 25nM) for 24h. NAD$^+$ and NADH levels were measure using the Promega NAD$^+$/NADH Glo Assay. Data represent mean of the first biological replicate. The data of the second biological replicate are shown in Appendix Figure 5.2.

5.2.3 FK866 and Olaparib combination caused ROS accumulation in ID8 cells *in vitro*

Given the essential roles of ROS accumulation in sensitizing FK866 and Olaparib combination in human EOC cells (section 4.2.6), ROS levels were then measured. The data showed that in both ID8 *Trp53*$^{-/-}$ and *Trp53*$^{-/-}$*; Pten*$^{-/-}$ cells, the combination of FK866 and Olaparib induced the highest levels of ROS (Figure 5.4A). However, FK866 monotherapy and its combination with Olaparib induced greater ROS accumulation in ID8 *Trp53*$^{-/-}$ cells compared to ID8 *Trp53*$^{-/-}$*; Pten*$^{-/-}$ cells (Figure 5.4A). To understand whether oxidative stress underlies Olaparib sensitization by FK866, a ROS recue experiment was performed. Briefly, ID8 *Trp53*$^{-/-}$*; Pten*$^{-/-}$ cells were treated with FK866 and/or Olaparib in the presence or absence of NAC for 48h. The data confirmed the further increase of apoptosis in cells treated with FK866 and Olaparib combination (Figure 5.4B). Surprisingly, the supplementation of NAC reduced apoptosis marginally in the combination group (Figure 5.4B). However, the rescue experiments were performed only once due to the limited time and resources. Thus, we cannot rule out increased oxidative stress as a sensitization mechanism of FK866 on Olaparib, although these data indicate that the sensitization effects on apoptosis by Nf1 and Pten loss may not involve ROS accumulation.

Collectively, the data from the ID8 cells diverge from those in the human EOC cells. One possible explanation is the supplementation of pyruvate in culture media of ID8 cells, which is a routine culture condition for ID8 cells (*390, 391, 408*). Given that pyruvate is the end product of glycolysis and NAD^+ is a key co-factor in this pathway, cellular responses to FK866 monotherapy were measured in media with or without pyruvate. The results showed that pyruvate withdrawal caused a left and downward shift of the dose-response curves in ID8 *Trp53*$^{-/-}$*; Pten*$^{-/-}$ cells but not ID8 *Trp53*$^{-/-}$ cells (Appendix Figure 5.5). Indeed, the IC_{50} values of FK866 were reduced from 5.6nM to 1.1nM by pyruvate withdrawal in ID8 *Trp53*$^{-/-}$*; Pten*$^{-/-}$ cells. These data indicate that pyruvate supplementation may impact the growth inhibitory effects of FK866 monotherapy and its combination with Olaparib.

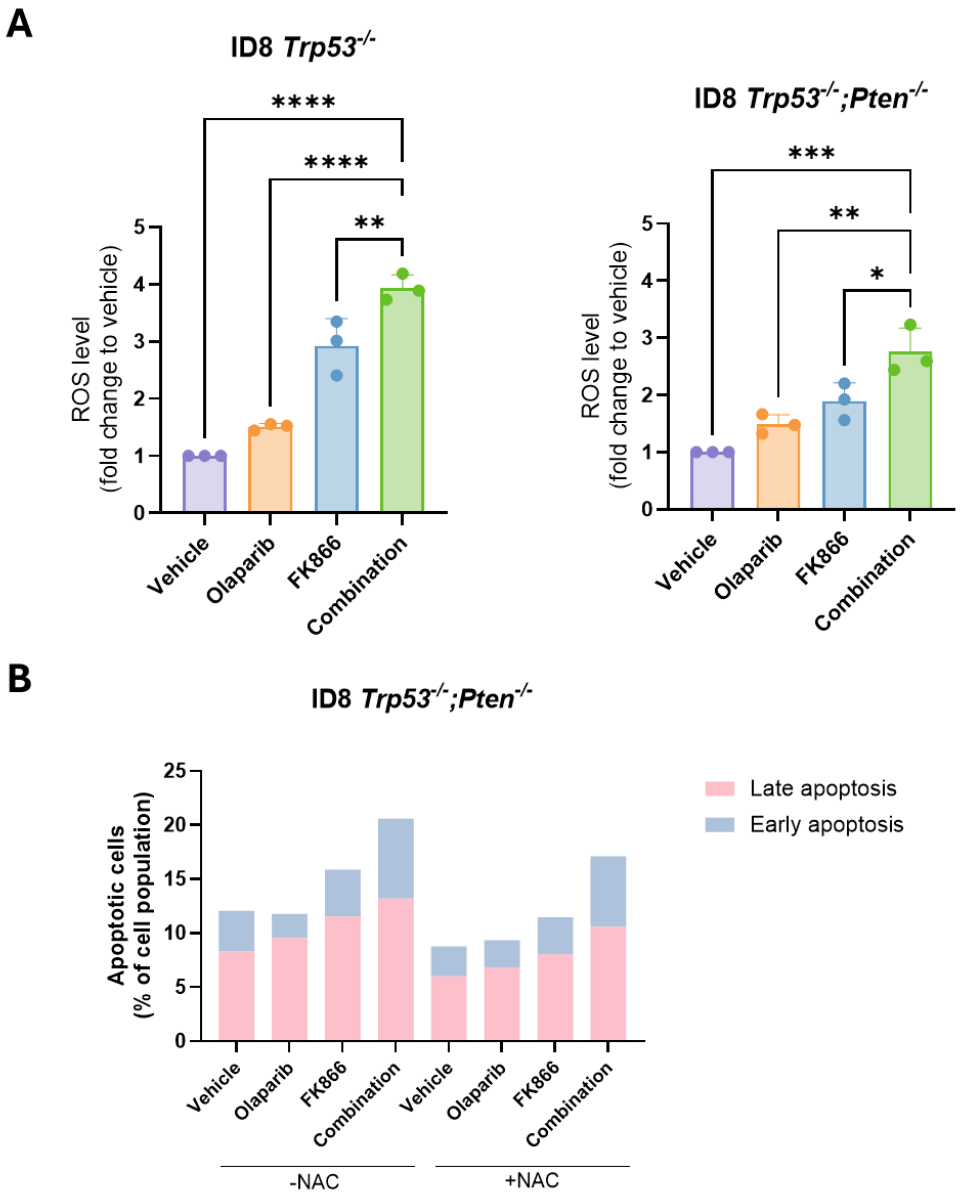


Figure 5.4 The combination of FK866 and Olaparib induced ROS accumulation in ID8 cells. (A) ROS levels. ID8 Trp*53*$^{-/-}$ and ID8 *Trp53*$^{-/-}$;*Pten*$^{-/-}$ cells were treated with 0.2% (v/v) DMSO, or 5nM FK866, or 10μM Olaparib or the combination for 48h. ROS and cell density were measured by Promega ROS-Glo™ H_2O_2 assay and SRB assay, respectively. ROS levels were then normalized against cell density. Data represent mean ± SD of three independent biological replicates. Statistical significance was calculated by one-way ANOVA followed by post-hoc Tukey test. * p<0.05, ** p<0.01, *** p<0.001, **** p<0.0001. (B) Fraction of apoptotic cells. ID8 Trp*53*$^{-/-}$ and ID8 *Trp53*$^{-/-}$;*Pten*$^{-/-}$ cells were pre-treated with 10mM NAC for 2h to boost GSH synthesis before treatment by 0.2% (v/v) DMSO or 5nM FK866 and/or 10μM Olaparib for 48h in media with or without 5mM NAC. At the end of treatment, apoptosis was examined by flow cytometry against annexin V and propidium iodide (PI). Data were represented using stacked bar charts. Data represent mean from one replicate. For the gating strategies, refer to Appendix Figure 5.4. The experiments were performed by the Master's student Chris An under my supervision and data were re-analysed and re-plotted.

5.2.4 The combination of FK866 and Olaparib inhibited growth of ID8 *Trp53*$^{-/-}$*; Pten*$^{-/-}$ tumours and increased overall survival *in vivo*

Nevertheless, the above data confirmed that NAMPT inhibition increases Olaparib sensitivity in ID8 cells *in vitro* and the underlying mechanisms may involve NAD^+ depletion. Of note, the preliminary data from our laboratory showed that FK866 enhanced DNA damage induced by Olaparib in ID8 cells (*393*). Collectively, these results suggest that FK866-induced Olaparib sensitization in ID8 cells may involve the same mechanisms as found in human EOC cells (i.e., NAD^+ depletion and DNA damage). Thus, the ID8 *Trp53*$^{-/-}$*; Pten*$^{-/-}$ model was chosen to perform *in vivo* studies for validation of the *in vitro* results. As mentioned in the section 3.1, the ID8 mouse model possesses additional advantages over xenograft models, including the presence of immune cells in TME and the recapitalization of omentum metastasis and ascites formation as seen in human patients.

To start with, a toxicology study was performed to understand the tolerability of FK866 and Olaparib and the effects of drug treatment on omental tumour growth. In brief, the mice injected with ID8 *Trp53*$^{-/-}$*; Pten*$^{-/-}$ cells were randomised into 7 groups (Figure 5.5A) and drug treatment started at day 15 after ID8 cell implantation because previous data showed significant omental tumour formation at day 14. Drug treatment involved two cycles of daily injection (5 days each) with a 2-day drug holiday to minimise toxicity (Figure 5.5A). The doses of Olaparib and FK866 were 50mg/kg and 30mg/kg (highest) respectively as chosen in previous studies (*394, 546*). The mice were sacrificed 24h after the last drug injection and blood and omental tumours were collected. The data showed no significant reduction in mouse body weight (more than 10%) apart from one mouse in combination B group (FK866: 20mg/kg; Olaparib: 50mg/kg) and two mice in FK866 monotherapy group (FK866: 30mg/kg) (Appendix Figure 5.6). The mice in FK866 monotherapy group showed signs of discomfort on the day of significant decrease of body weight (approximately 10%), including general inactivity, hunching, piloerection, narrowed eyes and laboured breathing. Because they demonstrated maximal tolerable adverse effects as specified in the project license, these two mice were immediately culled, and an autopsy was performed. Both mice showed faecal

impaction and one of them has intestine full of bile-like fluid. Intriguingly, both mice experienced FK866-induced toxicity at the end of drug injection cycle (i.e., the 5th and 10th injection), which indicates that 5-day FK866 injection at 30mg/kg is too toxic and lower dose or shorter drug exposure is required. The FK866 monotherapy group was then repeated at a lower dose of 10mg/kg in an independent study. The mouse in combination B group showed a 14% reduction in body weight but recovered on the following day. Given that there were no signs of discomfort, this mouse was not culled and received the remaining injection. For consistency, the FK866 monotherapy group at 10mg/kg was repeated in an independent study.

The data of showed that Olaparib monotherapy (50mg/kg) had no significant impact on omental tumour weight (Figure 5.5B). The mice in FK866 single agent treatment group (10 and 30mg/kg) showed similar omental tumour weight to vehicle mice (Figure 5.5B). Treatment with a combination of Olaparib and FK866 at various doses resulted in significant decreases of omental tumour weight compared to mice received vehicle or monotherapies of Olaparib or FK866 (Figure 5.5B). Interestingly, there was a decreasing trend in tumour weight with the increasing FK866 doses although the decrease across the combination groups did not reach statistical significance (Figure 5.5B). Taken together, these data suggest that FK866 enhanced Olaparib-induced inhibition in growth of ID8 *Trp53*$^{-/-}$*; Pten*$^{-/-}$ tumours.

Next, a survival study was performed to examine whether the combination of FK866 and Olaparib increased overall survival. Based on the toxicology study, the dose of FK866 was lowered to 20mg/kg in monotherapy group and two doses of KF866 were chosen in the combination groups (i.e., 10 and 20mg/kg). Therefore, the mice were randomised into 6 groups and drug dosing started 2 weeks after ID8 *Trp53*$^{-/-}$*; Pten*$^{-/-}$ cell implantation (Figure 5.6A). A total of 8 daily drug injections were performed with a three-day drug holiday after the 4th injection. Mice groups were then blinded to avoid bias in deciding whether to cull a mouse and survival was monitored. Surprisingly, four mice received 20mg/kg FK866 alone or in combination with Olaparib (two in FK866 monotherapy group and two in combination group) showed signs of discomfort (e.g., inactivity, piloerection, hunting, narrowed eyes and laboured breathing) and were culled. The surviving mice in these two groups received

10mg/kg FK866 to reduce toxicity and therefore, the groups with FK866 alone or in combination with Olaparib (FK866: 20mg/kg; Olaparib: 50mg/kg) were excluded from subsequent survival analysis. The FK866 monotherapy group was repeated at 10mg/kg in an independent study.

The survival curves are shown in Figure 5.6B. The results show that Olaparib, but not FK866 monotherapy, significantly increased mice survival (Figure 5.6B). Of note, the treatment of Olaparib and FK866 combination caused a further increase in mice survival (Figure 5.6B). The results were validated by analysis of mean of survival. In this regard, Olaparib alone provided a moderate but significant increase in mean survival (Olaparib: 36 days vs Vehicle: 31.3 days) and FK866 monotherapy had a smaller but significant effect on mean survival (FK866: 31.8 days vs Vehicle: 31.3 days) (Figure 5.6C). Of note, the mice received the combination of FK866 and Olaparib showed the longest mean survival (i.e., 41.7 days) and the survival benefit was approximately twice than that of Olaparib monotherapy (Combination: 10.4 days vs Olaparib: 4.7 days) (Figure 5.6C). Taken together, these data suggest that FK866 improved Olaparib sensitivity in mice with ID8 *Trp53*$^{-/-}$*; Pten*$^{-/-}$ tumours.

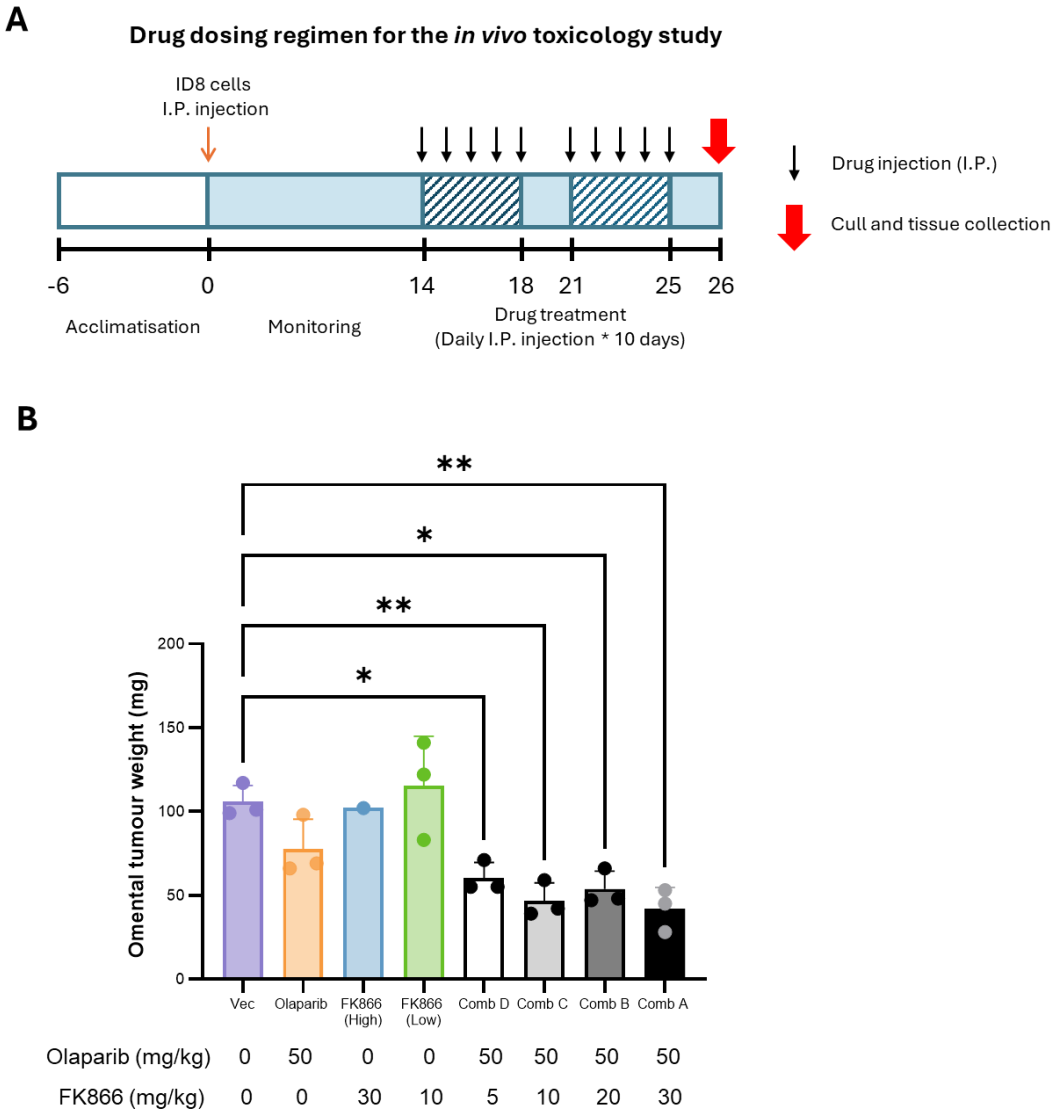
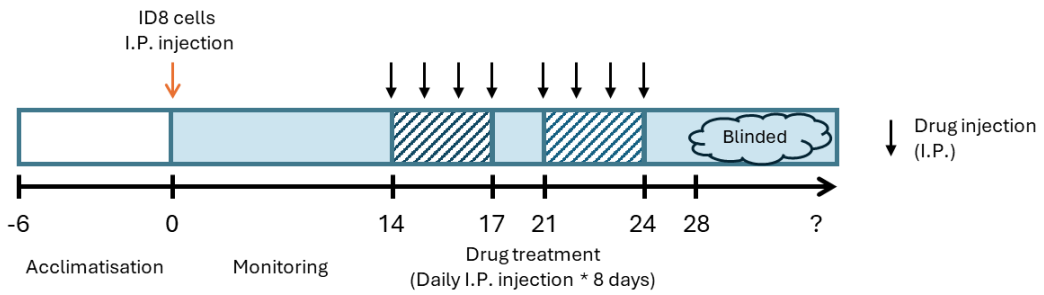


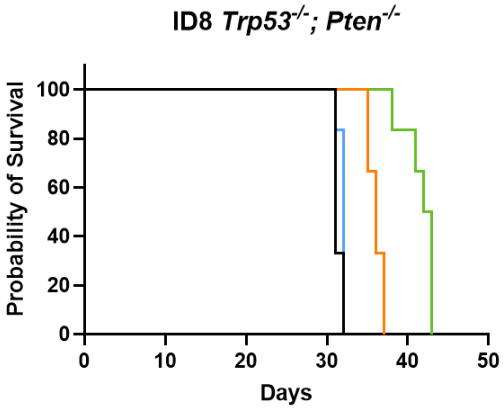
Figure 5.5 The combination of FK866 and Olaparib reduced tumour weight in the ID8 *Trp53*$^{-/-}$*; Pten*$^{-/-}$ model.

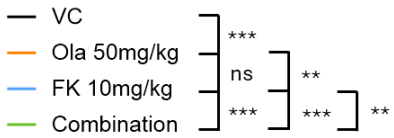
(A) Schematics of drug treatment regimen. C57BL/6 mice were intraperitoneally injected with ID8 *Trp53*$^{-/-}$*; Pten*$^{-/-}$ cells and monitored for 14 days before drug treatment (i.e., vehicle, FK866, Olaparib or the combination of FK866 and Olaparib). The drugs were administered daily in two cycles of five consecutive days separated by a two-day drug holiday. (B) Omental tumour weight. The mice were culled 24h after the last injection of drugs and omental tumours were collected and weighed. Except the FK866 monotherapy group, data represent mean ± SD of three mice. Statistical significance was calculated by one-way ANOVA followed by post-hoc Tukey test. The FK866 (30mg/kg) group was excluded for statistical tests. * $p<0.05$, ** $p<0.01$. The *in vivo* study was performed in collaboration with Dr Michael Gruet in our group.

A



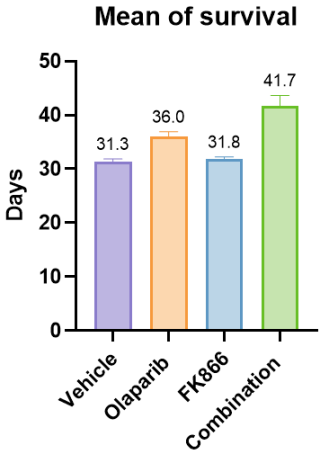
B





Log-rank (Mantel-Cox) test			
p values	FK866	Olaparib	Combination
Vehicle	0.0926	0.0006	0.0006
FK866	NA	0.0012	0.0012
Olaparib	NA	NA	0.0007

C





One-way ANOVA and post-hoc Tukey test			
p values	FK866	Olaparib	Combination
Vehicle	0.8687	<0.0001	<0.0001
FK866	NA	<0.0001	<0.0001
Olaparib	NA	NA	<0.0001

(Figure legends: see the next page

Figure 5.6 FK866 improved Olaparib sensitivity in mice with ID8 *Trp53*$^{-/-}$*; Pten*$^{-/-}$ tumours.
(A) Schematics of drug treatment regimen. C57BL/6 mice were injection with ID8 *Trp53*$^{-/-}$*; Pten*$^{-/-}$ cells and randomised into groups of 6 (n=6). Drug treatment started 14 days after ID8 cell implantation and involves two cycles of 4 consecutive daily intraperitoneal injection which were separated by a three-day drug holiday. In the survival study, the following doses were used: Olaparib (50mg/kg), FK866 (10 or 20mg/kg) and the combination (i.e., 50mg/kg Olaparib with 10 or 20mg/kg FK866). Mice injected with 20mg/kg FK866 alone or in combination with Olaparib were excluded due to drug related toxicity. The 10mg/kg FK866 monotherapy treatment was repeated in an independent study. To avoid bias in deciding the humane end point of mice, the researchers were blinded after the last drug injection. (B) Survival chart showing mice treated with vehicle, Olaparib (50mg/kg), FK866 (10mg/kg) and the combination (i.e., 50mg/kg Olaparib with 10mg/kg FK866). Log-rank (Mantel-Cox) tests were performed on the survival curves to determine statistical significance. The attached table shows p-values. ** $p<0.01$, *** $p<0.001$, ns: not significant. (C) Mean of survival. Error bars represent SD. One-way ANOVA and post-hoc Tukey tests were performed to calculate significance. The attached table shows p-values. The *in vivo* study was performed in collaboration with Dr Michael Gruet in our group.

5.2.5 FK866 and Olaparib combination resulted in higher DNA damage *in vivo*

To understand whether FK866 enhances Olaparib-induced DNA damage *in vivo*, DNA damage marker γH2AX and activation of DDR signalling pathway were investigated. Briefly, proteins in the omental tumour tissue from the toxicology study were extracted and analysed by WB. Preliminary data from Dr Michael Gruet the combination of FK866 and Olaparib resulted in an increase in γH2AX intensity, thereby suggesting that dual NAMPT and PARP1 inhibition caused DNA damage in vivo. Thus, I examined the activity of DDR signalling. Here, the results showed that the ratio of phospho-Chk1/total Chk1 was significantly increased in tumours treated with the combination although large variation could be observed (Figure 5.7A). However, neither Olaparib or FK866 single agent treatment could significantly change the ratio. Taken together, these data suggest that dual NAMPT and PARP1 inhibition induced higher levels of DNA damage in ID8 *Trp53*$^{-/-}$*; Pten*$^{-/-}$ tumours.

It has been reported that NAMPT inhibition induces autophagic cell death by inhibiting ERK and mTOR pathway in multiple myeloma cells (*546*). Interestingly, the inhibition of mTOR pathway resulted in a feedback activation of Akt (*546*). To understand whether the

combination of FK866 and Olaparib regulates these signalling pathways, WB against pErk1/2 and pAkt was performed using the same protein extracts. The data showed high levels of phospho-Erk1/2 and total-Erk1/2 ratio under basal conditions and a slight, but statistically significant, decrease was detected in the combination treated samples. However, variability existed and no pErk1/2 was detected in two samples (one from Olaparib monotherapy group and one from the combination group) (Figure 5.7B). Although variability existed in phospho-Akt and total-Akt ratio in vehicle, FK866 and Olaparib monotherapy group, there was an upward trend in the ratio of combination treated tumour samples (Figure 5.7B). Thus, these data indicate that dual NAMPT and PARP1 inhibition may regulate ERK and Akt pathway.

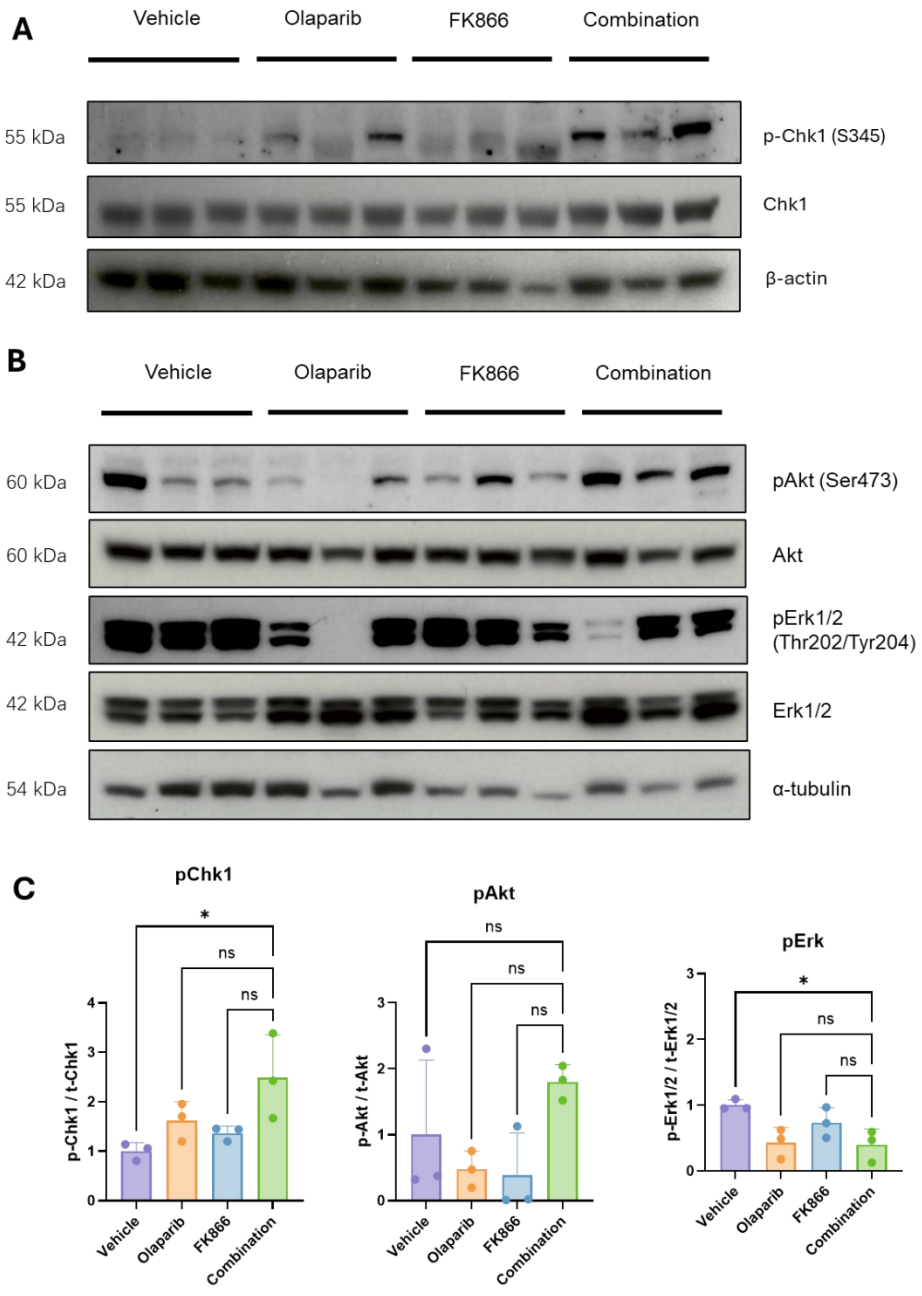


Figure 5.7 The impact of FK866 and Olaparib combination on DDR, Akt and Erk signalling pathway in ID8 *Trp53*$^{-/-}$*; Pten*$^{-/-}$ tumours.

(A-B) Images of WB blots. The activity of (A) Chk1 in DDR and (B) Akt and Erk signalling in omental tumours measured by WB. Proteins were extracted from omental tumours in mice treated with vehicle, Olaparib (50mg/kg), FK866 (10mg/kg) and the combination (i.e., 50mg/kg Olaparib with 10mg/kg FK866). Note that the samples from mice received 10mg/kg FK866 monotherapy were collected from an independent study. Protein extraction of samples from all groups was performed on the same day. Protein extraction was performed with help from Dr Michael Gruet in our group. (C) Densitometry analysis. The levels of phospho-Chk1, phospho-Akt and phospho-Erk1/2 were normalized against the respective total protein levels. Data represent mean ± SD from three biological repeats. p-values were calculated using t tests. * $p<0.05$, ns: not significant.

5.2.6 The combination of FK866 and Olaparib resulted in NAD^+ depletion in ID8 *Trp53*$^{-/-}$*; Pten*$^{-/-}$ tumours

To validate the depletion of NAD^+ and understand the metabolic effects of FK866 and Olaparib combination, untargeted metabolic profiling was performed. In brief, metabolites were extracted from the omental tumour tissue collected from the toxicology study. Due to the limited availability of the ZenoTOF 7600 LC-MS/MS platform, analysis of samples from the repeating toxicology study (3 mice of FK866 10mg/kg monotherapy) was delayed after the targeted profiling performed by Dr Michael Gruet in our group. As a result, very low peak intensity and very few peaks could be detected due to sample degradation (data not shown). Therefore, only the samples from the first toxicology study (vehicle, Olaparib monotherapy, combination groups and one mouse from the 30mg/kg FK866 monotherapy group) were profiled by the untargeted method and included in the subsequent analysis.

Untargeted profiling of omental tumours showed that excluding the FK866 monotherapy group with only one sample, NAD^+ is the only feature with significant changes in abundance among the 125 annotated metabolites (Figure 5.8A). Olaparib monotherapy resulted in a slight but not significant reduction in NAD^+ pool (Figure 5.8B). The NAD^+ pool of the tumour sample from the surviving mouse in FK866 monotherapy group was almost halved compared to that of vehicle group (Figure 5.8B). Of note, combination group A and C, which received 30 and 10mg/kg FK866 in combination with 50mg/kg Olaparib respectively, displayed greater NAD^+ depletion than combination group D (FK866: 5mg/kg; Olaparib: 50mg/kg) (Figure 5.8B). Although there was no statistical significance across the combination groups, the trend suggests FK866 dose-dependent reduction of NAD^+ pool. Collectively, these data confirmed the on-target effects of FK866 on NAMPT inhibition (i.e., NAD^+ depletion) in omental tumours.

To validate oxidative stress in combination treated omental tumours, the pool size of total glutathione and the ratio of reduced glutathione (GSH) to oxidized glutathione (GSSG) were examined. My data showed that the pool size of total glutathione was reduced in the combination groups A and C than the vehicle group (Figure 5.9A). The treatment of FK866 or Olaparib individually did not influence the pool size (Figure 5.9A). Thus, these data indicate

that FK866 and Olaparib combination may impair the ROS defensive mechanisms. Moreover, there was a decreasing trend in the GSH/GSSG ratio in the combination groups B and D compared to the vehicle group although huge variations were observed (Figure 5.9B). Additionally, a decreasing trend in ascorbic acid, an antioxidant, was detected in combination treated samples (Figure 5.9C).

In addition, the biomarkers for oxidation products of lipids were examined. Polyunsaturated fatty acids (PUFA) are readily oxidized by free radicals (i.e., lipid peroxidation) and the major products are hydroperoxides which are unstable and readily reduced to corresponding hydroxides in cells (*547*). Arachidonic acid (20:4) is a species of PUFA and the lipid peroxidation product is hydroperoxyeicosatetraenoic acid (HPETE) which is a chemically unstable hydroperoxide (*547*). HPETE undergoes further reduction by glutathione peroxidase or selelnoprotein P to produce hydroxyeicosatetraenoic acid (HETE) which is the corresponding hydroxide (Figure 5.10A) (*547*). My data showed that apart from the combination group B, the ratio of HETE to arachidonic acid was gradually upregulated as the FK866 dose increased from the Olaparib monotherapy group to the combination group A (Figure 5.10B), thereby suggesting a FK866 dose-dependent upregulation of arachidonic acid peroxidation. However, large variations were observed in the vehicle group (Figure 5.10B), which impedes the comparison against basal condition. Peroxidation of arachidonic acid also produces isoprostanes (isoP) among which F_2-isoPs have been most extensively studied (Figure 5.10A) (*548, 549*). My results showed that the ratio of F_2-isoP to arachidonic acid was higher in the combination group C and D in comparison to the vehicle group (Figure 5.10C). Olaparib monotherapy did not impact on the ratio and large variations existed in the combination group A (Figure 5.10C). Linoleic acid (18:2) is the most abundant PUFA species in vivo and the hydroxide product is hydroxyoctadecadienoic acid (HODE) (Figure 5.10D) (*547*). The data showed that the ratio of HODE to linoleic acid was reduced in the combination group A and B (Figure 5.10E). Although none of the oxidative stress biomarkers described above reached statistical significance, these data imply that the combination of FK866 and Olaparib may disrupt the redox balance *in vivo*.

To understand the global effects of FK866 on cellular metabolism, correlation analysis

between FK866 dose and metabolite abundance was performed. Excluding the combination group B which did not show the dose-dependent reduction in NAD^+ levels, metabolite data from the Olaparib monotherapy group and combination groups A, C and D were subject to Pearson correlation analysis. The data showed that NAD^+ was negatively correlated with FK866 doses (Figure 5.11A), consistent with the on-target effects of FK866. Interestingly, ascorbic acid levels were decreased as the doses of FK866 increased although the correlation was not significant (Figure 5.11B), which indicates that FK866 may disrupt the redox balance. Negative correlation was also found in IMP, CDP, acetylcarnitine, glutamate and adenine, and aspartate was positively correlated with FK866 doses (Figure 5.11D-G and J-K). Although the correlation was not significant, the abundance of carnitine, AMP, ADP and lactate was decreased as the doses of FK866 increased (Figure 5.11 C, H-I and L). Interestingly, it has been reported that NAMPT inhibition by FK866 caused depletion of adenine and supplementation of adenine rescued the apoptosis priming effects of FK866 in TNBC cells (*550*). Therefore, we examined whether adenine could rescue the apoptosis in A2780 cells treated with FK866 and Olaparib combination. The data showed that adenine reduced the activity of caspase-3/7 in A2780 cells treated with FK866 monotherapy and in combination with Olaparib (Appendix Figure 5.7).

To validate the correlation results from NAD^+ depletion by FK866, correlation analysis between NAD^+ and metabolite abundance was performed on the same dataset. Positive correlation was observed in adenine, adenine nucleotides (i.e., adenosine, AMP and ADP) (Figure 5.12A-D), which is opposite to the negative correlation with FK866 doses. Interestingly, IMP, guanine and CDP displayed positive association (Figure 5.12E-G). The abundance of ascorbic acid and total levels of glutathione were positively correlated with NAD^+ levels (Figure 5.12 H-I), which implies that the anti-oxidation capacity may be limited. Aspartate and glutamate were negatively and positively correlated to NAD^+ levels, respectively (Figure 5.12 J-K), which is opposite to the direction of correlation to FK866 doses. 1-methylnicotinamide, lactate and acetyl-carnitine were found to be positively associated with NAD^+ content (Figure 5.12L-N). Taken together, these data suggest that the modulation of metabolism by FK866 may result from its on-target inhibition on NAMPT.

PCA analysis of the annotated features showed that samples in different treatment groups did not separate (Figure 5.13A). However, samples from vehicle and Olaparib monotherapy group were more closely clustered. Hierarchical clustering analysis also confirmed the similarities of metabolite abundance between vehicle and Olaparib monotherapy group as evidenced by the short distance (Figure 5.13B). Therefore, these data suggest that Olaparib alone may have limited effects on cellular metabolism in omental tumours. Low levels of clustering were found between vehicle groups and all the combination groups although full separation of the 95% confidence regions was missing (Figure 5.13A). This is also supported by the hierarchical clustering results which showed the combination groups formed separate clusters from vehicle/Olaparib groups (Figure 5.13B). Among the different combination groups, close clustering was observed although outliers existed as shown in the PCA plot (Figure 5.13A). Collectively, these results suggest that the FK866 and Olaparib combination may impact metabolism.

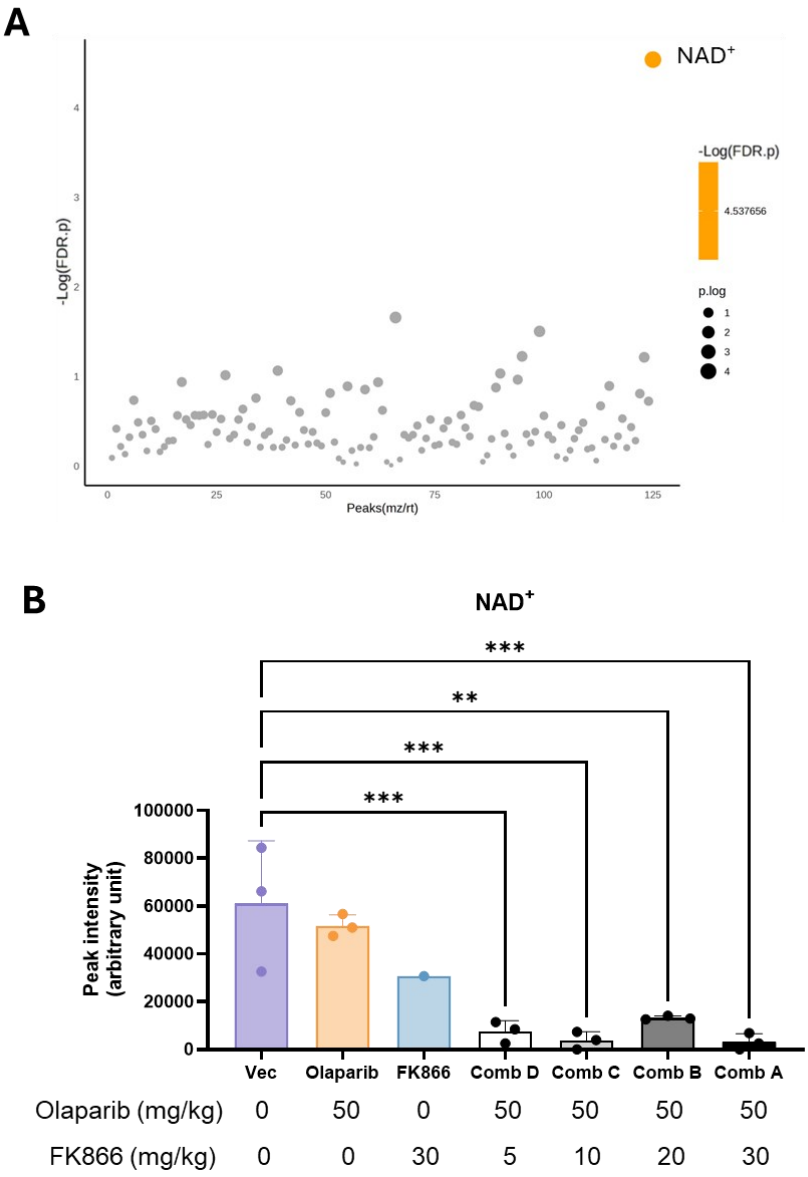


Figure 5.8 The combination of FK866 and Olaparib depleted NAD$^+$ in omental tumours.
(A) One-way ANOVA tests showing metabolites with significantly changed abundance. Untargeted metabolic profiling was performed using the omental tumour tissue from mice treated with vehicle, Olaparib (50mg/kg), FK866 (10mg/kg) and the combination (i.e., 50mg/kg Olaparib with 10mg/kg FK866). Note that the samples from mice received 10mg/kg FK866 monotherapy were collected from an independent study. Metabolite extraction of all the treatment groups was performed on the same day. The data were normalised against the sum of abundance of identified metabolites. The dataset was then subjected to a one-way ANOVA test using Metaboanalyst (v.5.0.). The metabolites with an FDR less than 0.05 were considered significantly changed and are highlighted in yellow. (B) NAD$^+$ levels in omental tumours. Data represent mean ± SD from three mice (except FK866 monotherapy group where data represent mean from one mouse). Statistical significance was calculated by one-way ANOVA followed by post-hoc Tukey test. The FK866 monotherapy group was excluded for statistical tests. ** $p<0.01$, *** $p<0.001$.

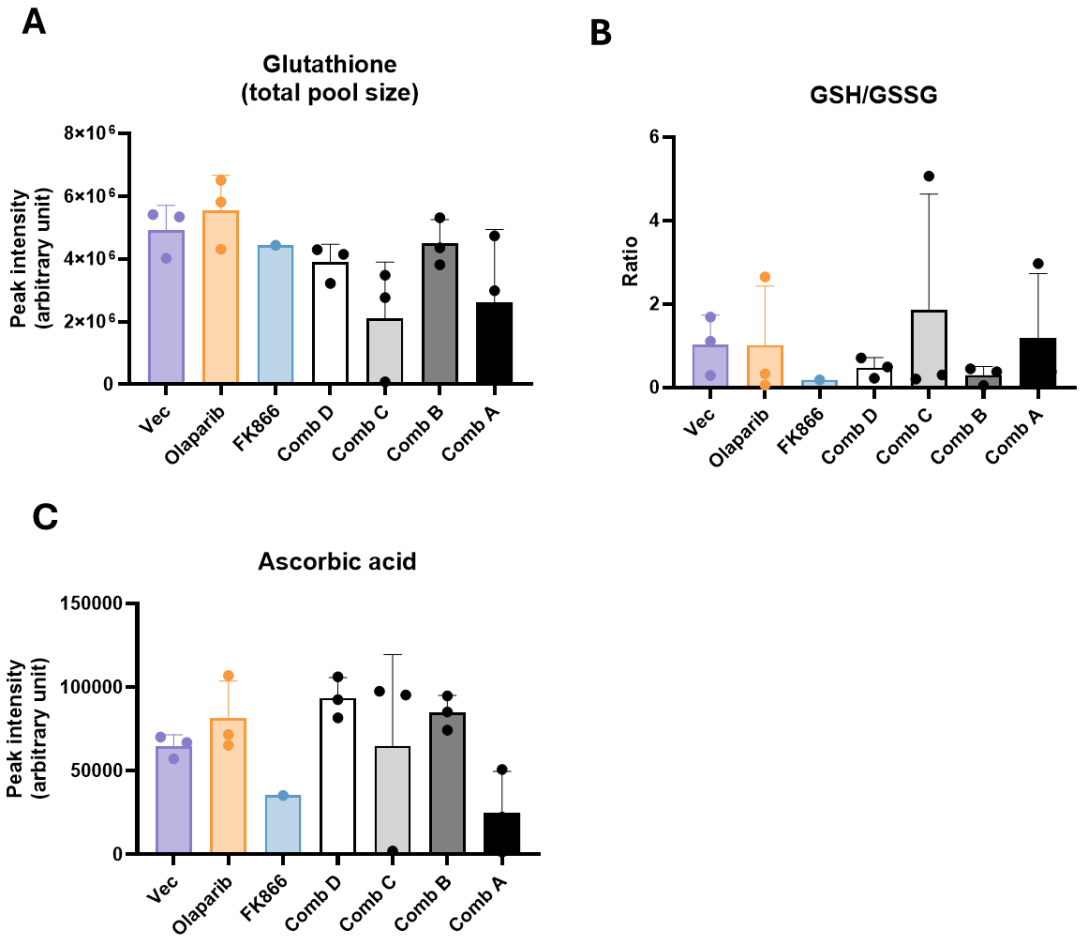
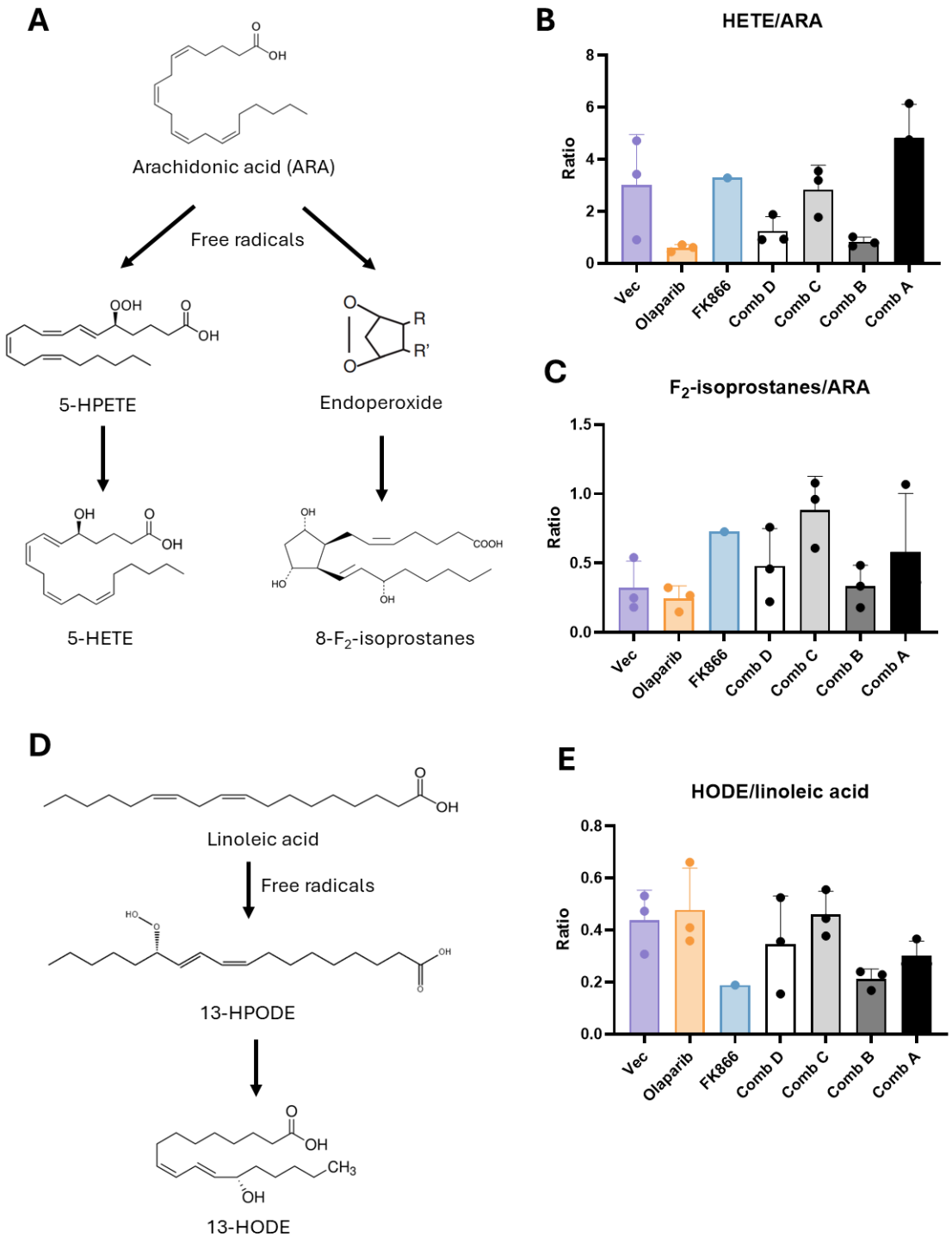


Figure 5.9 The combination of FK866 and Olaparib may induce oxidative stress in omental tumours.

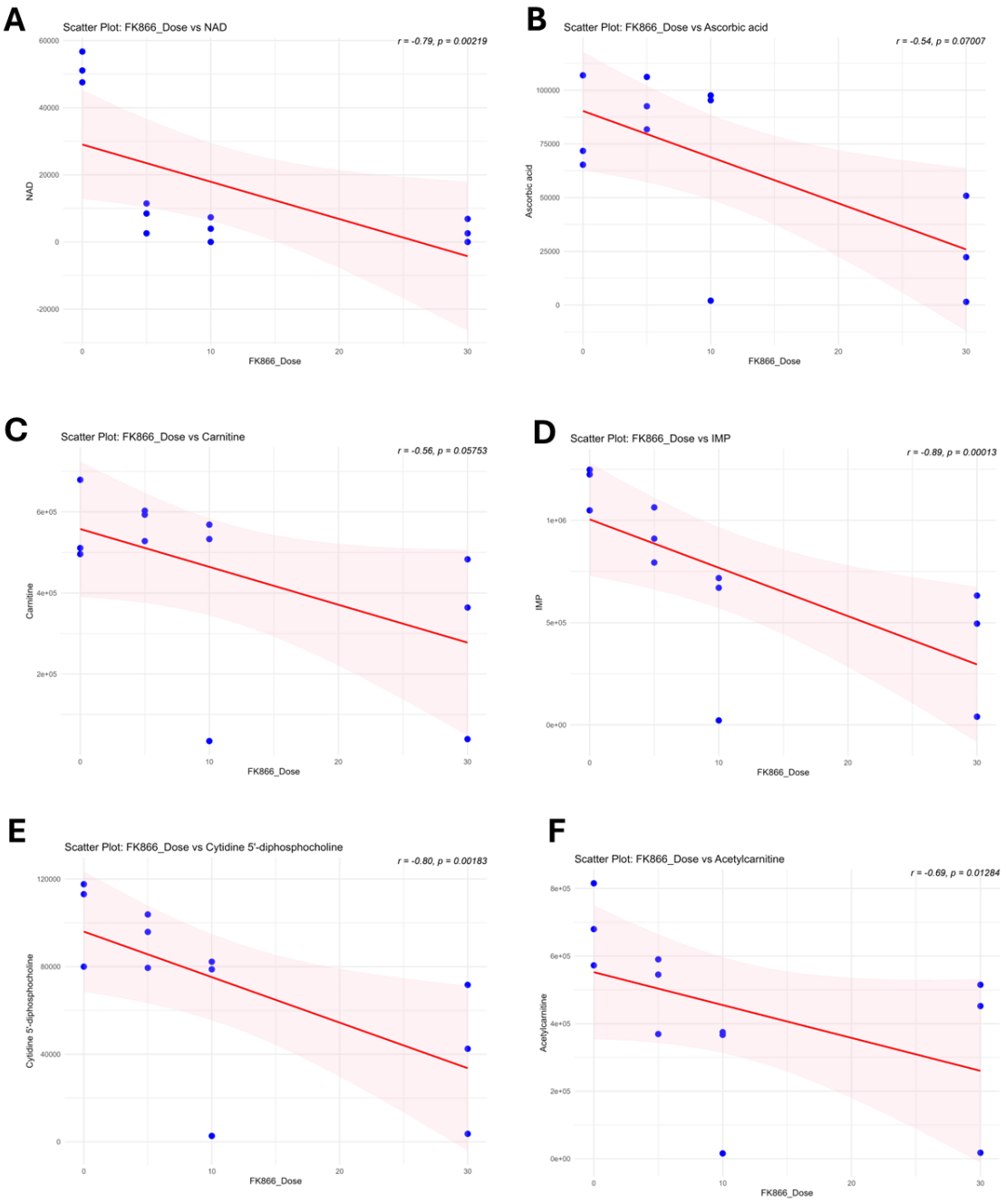
(A) Pool size of total glutathione, (B) GSH/GSSG ratio, (C) ascorbic acid abundance. The data were obtained from the same untargeted metabolomic profiling study as described in Figure 5.9. Data represent mean ± SD from three mice (except FK866 monotherapy group where data represent mean from one mouse). Statistical significance was calculated by one-way ANOVA followed by post-hoc Tukey test. The FK866 monotherapy group was excluded for statistical tests. No significance could be detected between any two groups.



(Figure 5.10 legend: see next page)

Figure 5.10 The combination of FK866 and Olaparib may cause oxidative damage to lipids in omental tumours.

(A) Schematics of products of arachidonic acid (ARA) peroxidation. ARA undergoes peroxidation by free radicals to produce hydroperoxides (e.g., HPETE) and endoperoxide which are not chemically stable. HPETE and endoperoxide are subsequently converted to stable HETE and F_2-isoprostanes. For simplicity, only one regioisomers is shown. (B) HETE/arachidonic acid ratio. (C) F_2-isoprostanes/arachidonic acid ratio. (D) Schematics of products of linoleic acid peroxidation. Hydroperoxide (e.g., HPODE) is produced when linoleic acid is peroxidised by free radicals. The unstable HPODE is subsequently converted to HODE. For simplicity, only one regioisomers is shown. (E) HODE/linoleic acid ratio. (B, C and E) were plotted based on the untargeted metabolic profiling study described in Figure 5.9. Data represent mean ± SD from three mice (except FK866 monotherapy group where data represent mean from one mouse). Statistical significance was calculated by one-way ANOVA followed by post-hoc Tukey test. The FK866 monotherapy group was excluded for statistical tests. No significance could be detected between any two groups.



(Figure 5.11: to be continued on the next page)

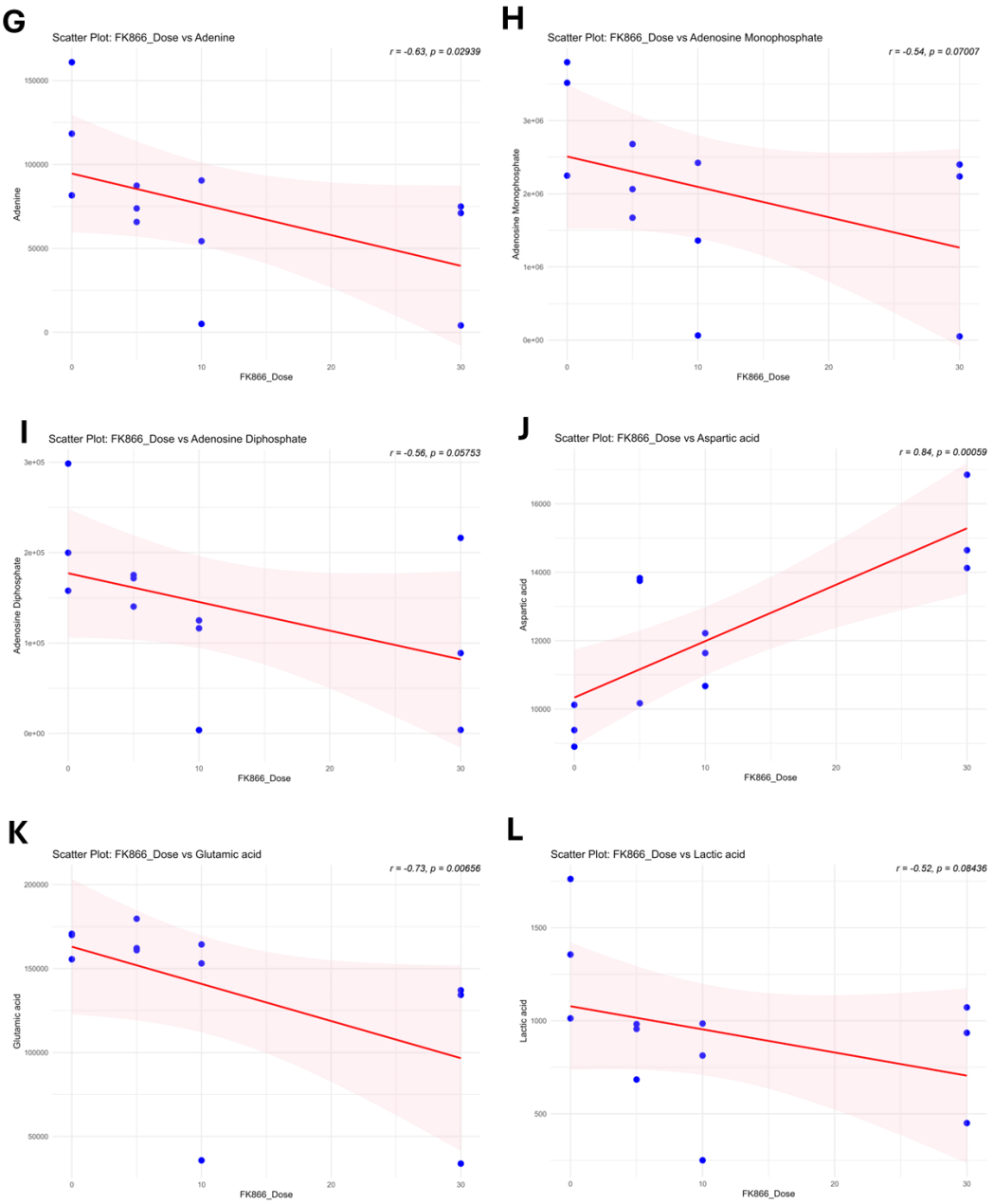
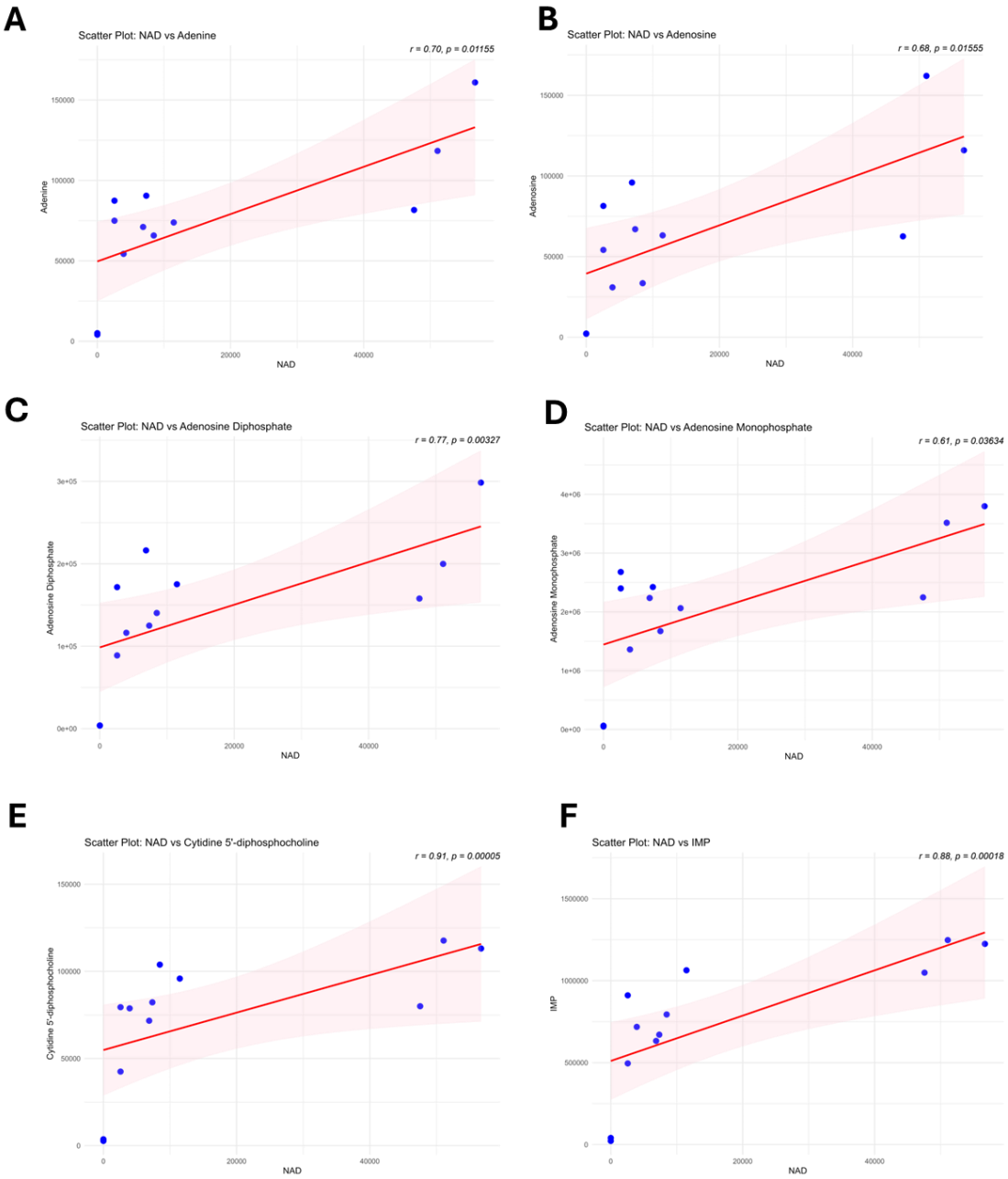
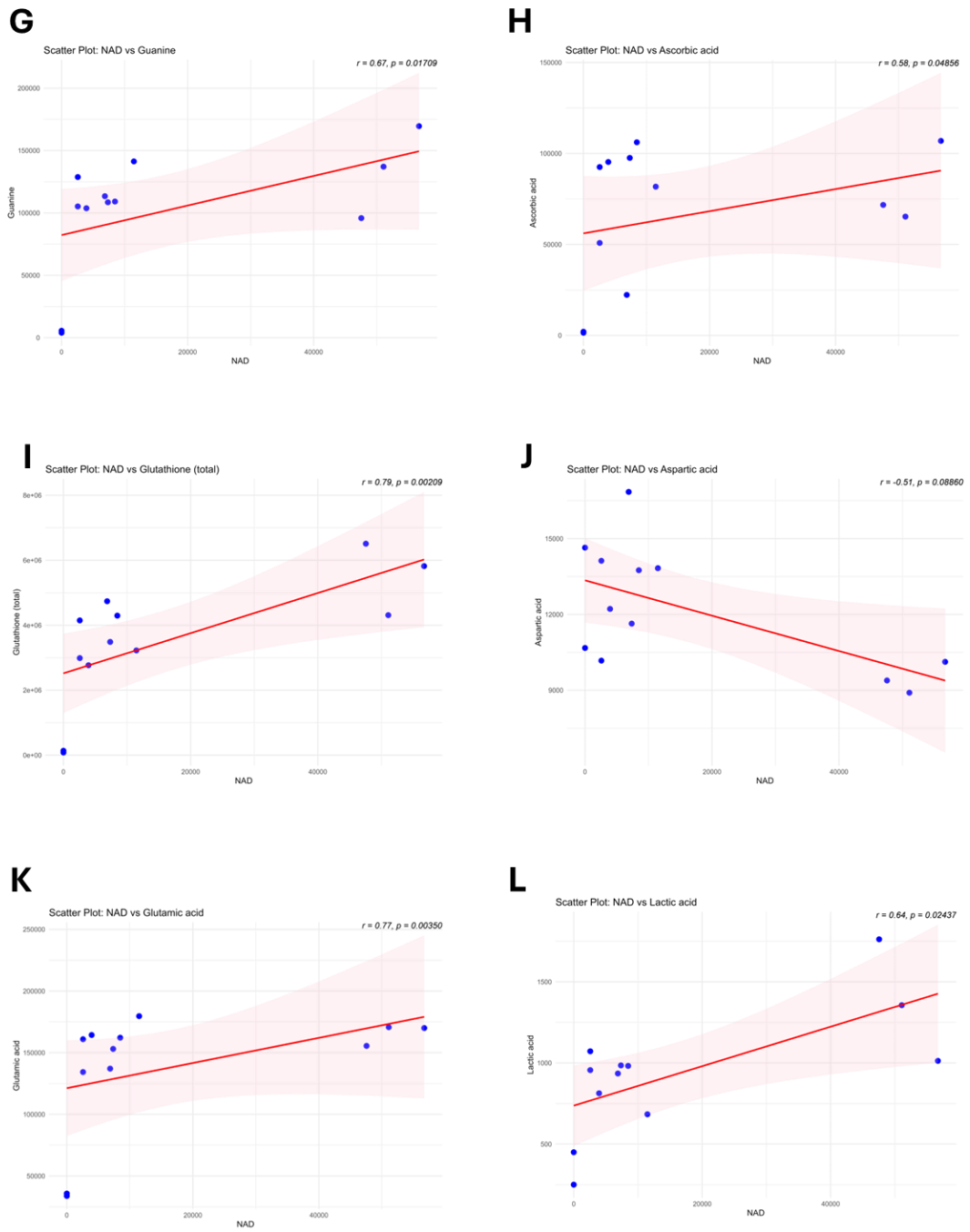


Figure 5.11 FK866 doses were correlated to a subset of metabolites in omental tumour tissue. Spearman's correlation analysis between FK866 doses and metabolite abundance in Olaparib monotherapy and combination groups (except combination group B) was performed by R studios (function cor.test() from the package *stats* version 4.3.2). The metabolic dataset was obtained from the untargeted metabolic profiling study in Figure 5.9. Only metabolites with a correlation coefficient higher than 0.5 or lower than -0.5 are displayed. Grey area and blue solid lines indicate the 95% confidence area and trend lines, respectively. The Spearman's correlation coefficient and related p values are also displayed.



(Figure 5.12: to be continued on the next page)



(Figure 5.12: to be continued on the next page)

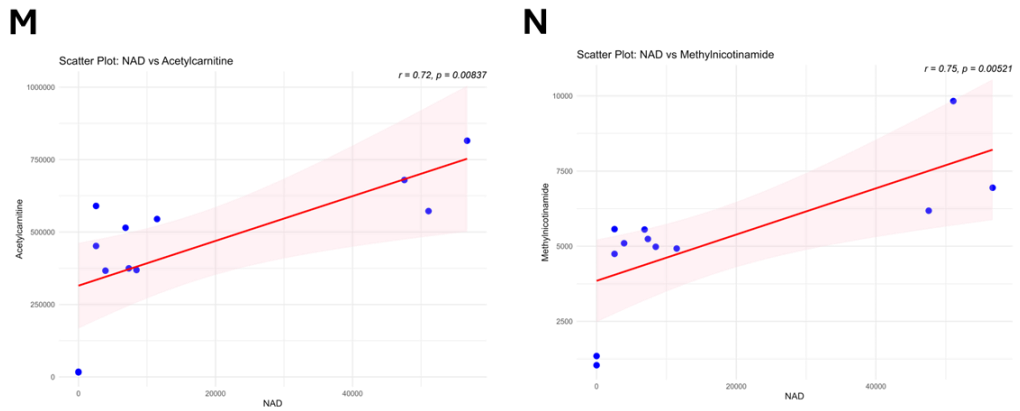


Figure 5.12 NAD^+ levels were correlated to a subset of metabolites in omental tumour tissue. Spearman's correlation analysis between NAD^+ levels and metabolite abundance in Olaparib monotherapy and combination groups (except combination group B) was performed by performed by R studios (function cor.test() from the package *stats* version 4.3.2). The metabolic dataset was obtained from the untargeted metabolic profiling study in Figure 5.9. Only metabolites with a correlation coefficient higher than 0.5 or lower than -0.5 are displayed. Grey area and blue solid lines indicate the 95% confidence area and trend lines, respectively. The Spearman's correlation coefficient and related p values are also displayed.

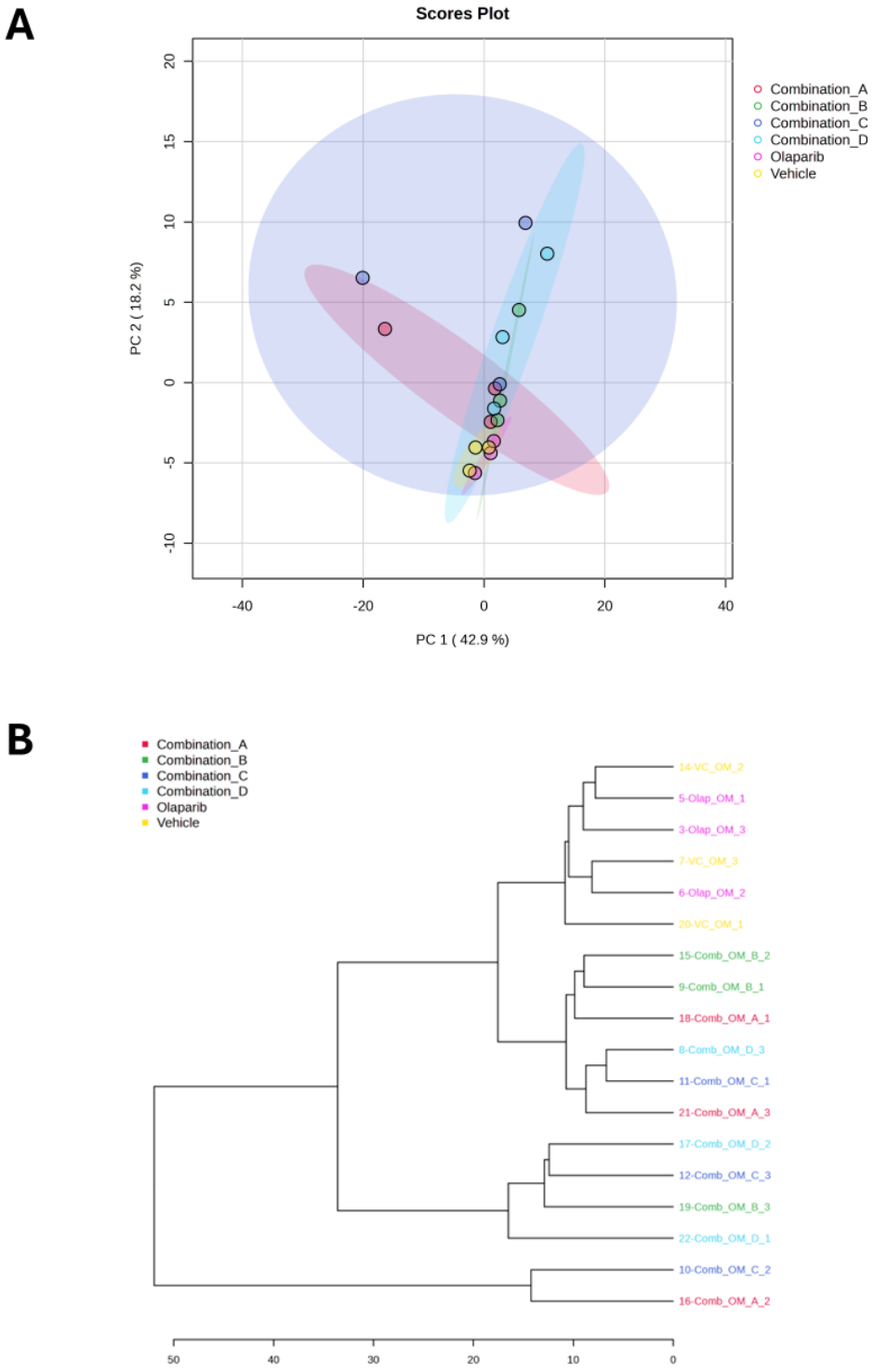


Figure 5.13 PCA analysis and hierarchical clustering analysis of the untargeted metabolomics dataset.

(A) PCA analysis and (B) hierarchical clustering analysis by Metaboanalyst (v.5.0.). Vehicle and Olaparib treated samples cluster closely while low levels of clustering was observed between vehicle and combination treated samples. However, outliers existed and no full separation of the 95% confidence regions was detected.

5.3 Discussion

In this chapter, I demonstrated that FK866 improved the capacity of Olaparib to induce apoptosis and growth inhibition in both ID8 *Trp53*$^{-/-}$ cells and ID8 *Trp53*$^{-/-}$*; Pten*$^{-/-}$ cells. The underlying mechanisms bear resemblance to those observed in the human ovarian cancer cell lines (see Section 4.3). In this regard, NAD^+ depletion by FK866 monotherapy was observed and the preliminary data from our lab showed that NMN supplementation rescued the combination treatment, which indicates that FK866 induced Olaparib sensitization may result from its on-target effect of NAMPT inhibition (*393*). Additionally, the combination of FK866 and Olaparib induced the highest level of ROS accumulation. Surprisingly, NAC supplementation only marginally reduced apoptosis in ID8 *Trp53*$^{-/-}$*; Pten*$^{-/-}$ cells treated with FK866 and Olaparib combination. However, it should be noted that mouse cells have a higher mitochondria density and ROS production rate than human cells (*551-553*) and therefore, the concentration of NAC used in this study may not be sufficient to scavenge ROS. Measurement of ROS levels are thus essential to understand whether NAC at the chosen dose is sufficient. Further investigations with increased NAC concentrations or alternative antioxidant drugs (e.g., ascorbic acid and α-tocopherol (*554*)) are required. It would also be interesting to examine the mitochondrial membrane potential to understand the effects of combination treatment on mitochondrial metabolism. Given our preliminary data from our laboratory showed the combination of FK866 and Olaparib induced the highest levels of DNA damage (*393*), these data suggest that in the ovarian HGSC model tested here, the sensitization mechanisms may involve NAD^+ depletion, oxidative stress and DNA damage.

Importantly, the FK866 induced sensitization of Olaparib was also observed in the *in vivo* studies. In this regard, the reduction in tumour weight in mice treated with Olaparib monotherapy was not significant. However, the combination treatment caused a significant decrease. Interestingly, increasing the doses of FK866 from 5mg/kg to 30mg/kg did not lead to a further decrease in tumour weight. One explanation is that the lowest dose of FK866 caused NAD^+ content depletion. Indeed, almost complete NAD^+ content depletion was observed in combination treated mice regardless of FK866 doses. Regarding mice overall

survival, the combination of FK866 and Olaparib more than doubled the therapeutic benefits of Olaparib monotherapy. Although FK866 has been shown to sensitize Olaparib in several types of tumours including ovarian HGSC (*285, 286, 388*), this study is the first to report the therapeutic benefits of the combination in Pten deleted ovarian HGSC tumours. Given that Akt mutations lead to rucaparib resistance as shown in a clinical trial (*266*), the findings in this study indicate that this patient subgroup may benefit from the combination. Of note, the untargeted metabolic profiling data showed NAD^+ depletion in the omental tumours from the mice treated with the combination. Interestingly, among the combination treated mice (except combination group B), there was a reverse correlation between cellular NAD^+ content and the dose of FK866, which indicates the NAD^+ depletion may result from the on-target effects of FK866. Surprisingly, the tumour sample from the surviving mouse treated with FK866 monotherapy showed only a 50% reduction in NAD^+ abundance. However, it should be noted that the surviving mouse may display resistance to FK866, and the data may not be representative of the whole treatment group. Indeed, the targeted metabolomics study performed by Dr Michael Gruet in our laboratory demonstrated that FK866 monotherapy and its combination with Olaparib achieved NAD^+ depletion in tumours (*393*). Taken together, these data indicate the sensitization may be caused by the on-target effects of NAMPT inhibition.

Mechanistically, data from the *in vivo* studies supported the *in vitro* studies. In this regard, the combination of FK866 and Olaparib induced the highest levels of pChk1, which indicates the activation of the DDR pathway. The preliminary data from Dr Michael Gruet which showed the DNA damage marker γH2AX was significantly upregulated to the highest levels in tumours treated with the combination. Collectively, these data suggest that FK866 enhanced DNA damage induced by Olaparib *in vivo*. However, given the crosstalk between Chk1 and Chk2 in DDR signalling, Chk2, ATM and ATR should be probed for further validation. Interestingly, my data showed a decreasing trend in pEKR1/2 and an increase in pAkt in the tumour samples treated with the combination. Previous publications reported that NAD^+ depletion induced by NAMPT inhibition activates autophagy in neuroblastoma and NAD^+ supplementation reverted the autophagy phenotype (*555*). In multiple myeloma cells, autophagic cell death

was induced by NAMPT inhibition and the mechanisms involve the downregulation of mTOR and ERK pathway activity (*546*). Surprisingly, pAkt was increased due to the feedback regulation between mTOR signalling and Akt (*546*). However, inconsistency has been reported regarding the effects of Olaparib on autophagy induction and the roles of autophagy in therapeutic benefits in ovarian cancer cells. In this regard, Olaparib inhibited growth of BRCA1 expressing UWB ovarian cancer cells (*556*). Autophagic cell death was observed, and the inhibition of autophagy abolished the growth inhibitory effects of Olaparib (*556*). In contrast, pharmacological inhibition of autophagy by chloroquine and hydroxychloroquine is synergistic with Olaparib in inducing apoptosis and growth inhibition of OVCAR8 and HEYA8 ovarian cancer cells (*557*). In A2780 and SKOV3 cells, Olaparib downregulated autophagy and enhanced apoptosis (*558*). Therefore, although the changes in Erk and Akt signalling may indicate that autophagy induction, direct measurement of autophagy flux (e.g., LC3II/LC3I ratio and autophagosome formation) is required. Additionally, inhibitors of autophagy can be used to assess the roles of autophagy in therapeutic effects of dual NAMPT and PARP inhibition.

Moreover, a combination of markers suggests that dual NAMPT and PARP inhibition induced oxidative stress in tumour samples. For instance, the pool size of total glutathione and the ratio of reduced to oxidised glutathione (i.e., GSH/GSSG) was reduced in combination treated groups. The combination treatment also reduced the abundance of ascorbic acid. The ratio between HETE/F_2-isoprostane and arachidonic acids (20:4) was also increased in combination treated groups. Surprisingly, the ratio between HODE and linoleic acid (18:2) was decreased by FK866 and Olaparib combination. However, it should be noted that PUFA (e.g., arachidonic acid and linoleic acid) can be oxidized through enzyme-catalysed pathways apart from free radical mediated oxidation. For instance, lipoxygenase (LOX) and cytochrome P450 (CYP) enzyme can catalyse HETE and HODE production while cyclooxygenases (COXs) can catalyse isoprostanes production (*559*). In addition, these lipid peroxidation biomarkers can undergo further metabolism or even excretion via kidney. HODE, for example, can be converted to oxo-octadecadienoic acid (oxoHODE) by hydroxy fatty acid dehydrogenase (*560*). Another limitation in the untargeted profiling is the failure to differentiate regioisomers of the lipid

peroxidation products that may have opposite effects on inflammation (*561, 562*). For instance, 12-HETE has been shown to stimulate the integrin-linked kinase/NF-κB pathway in ovarian cancer and promote inflammation while 15-HETE is anti-inflammatory (*563-565*). Therefore, it would be interesting to measure the regioisomers and characterise the inflammatory microenvironment of tumours to understand the immunological effects of the combination. Additionally, oxidation of cholesterol produces 7-hydroxycholesterol (7-OHCh) and 7-ketocholesterol (7-KCh) which are collectively known as oxysterols (*566, 567*). They are commonly measured by GC-MS (*568-570*) and therefore, it would be interesting to examine oxysterols to support the findings in this study.

Given the non-specific nature of free radical oxidation, measurement of different biomarkers is highly recommended to avoid biased results (*547*). Here, attempts were made to detect a range of biomarkers of oxidative DNA and protein damage (e.g., 8-Oxo-2'-deoxyguanosine (8-oxo-dG) (*571*) and tyrosine dimers (*572*)) by untargeted metabolic profiling. However, none of them could be detected in this study (data not shown) and this may be explained by the metabolite extraction method. Although oxidation of free nuclear bases can occur, DNA digestion may be necessary to extract oxidized bases incorporated to DNA strands to improve sensitivity (*573*). Importantly, the complete digestion also reduces variability across samples (*574*). Thus, DNA hydrolyzation should be performed on the tumour tissue samples in the future. Interestingly, oxidative products of free nuclear bases can be detected in human serum and urine (*544, 575*) and therefore, it would be interesting to profile these biological samples from the *in vivo* study. Alternatively, IF studies against 8-oxo-dG can be performed on the tumour tissue (*576*). To further validate the roles of ROS in therapeutic benefits of the combination, it would be interesting to perform an *in vivo* ROS rescue experiment by intraperitoneal injection of NAC (*577*).

Correlation analysis between FK866 doses and metabolite abundance revealed the impact of FK866 on tumour metabolism. In this regard, negative association was observed between FK866 doses and abundance of NAD^+, which confirmed the on-target inhibition of NAMPT. Given that NAD^+ is a substrate of $NADP^+$, FK866 may also deplete $NADP^+$ in tumours. However, $NADP^+$ has been reported as an endogenous inhibitor of PARP in ovarian cancer cells and

overexpression NAD kinase, which catalyses the phosphorylation of NAD^+ to $NADP^+$, boosted cellular content of $NADP^+$ and enhanced Olaparib sensitivity (*277*). Therefore, it would be interesting to measure $NADP^+$ concentrations. Moreover, the abundance of ascorbic acid was reduced as the FK866 doses increased, which indicates the disruption of redox balance by FK866. Levels of carnitine was decreased with the increases in FK866 doses, although such negative correlation was not significant. This is in line with the previous report which showed a dose-dependent decrease of carnitine in HCT116 colon cancer cells (*578*). Carnitine is *de novo* synthesised using lysine and methionine as substrates and NAD^+ is also required as a co-factor. Carnitine mediates the transport of long chain fatty acid in the form of acyl-carnitine for β-oxidation in mitochondria (*579*). However, β-oxidation and the metabolism of the product acetyl-CoA produced in mitochondria requires NAD^+. Therefore, the negative correlation may reflect the inhibition of carnitine synthesis. Interestingly, acetylcarnitine was negatively correlated with FK866 doses, which may result from the decreased availability of carnitine. The decrease in lactate levels with higher doses of FK866 may indicate the inhibition of glycolysis because NAD^+ is an essential glycolytic co-factor. Glutamate and aspartate levels were negatively and positively correlated with FK866 doses, respectively. This is consistent with the previous report showing a dose-dependent increase in aspartate and a marginal decrease in glutamate (*578*). The increase in aspartate may result from the accumulation of oxaloacetate. In this regard, the attenuation of glycolysis decreases pyruvate levels and given that pyruvate enters the TCA cycle by condensation with oxaloacetate, FK866 may cause an increase in oxaloacetate. As a result, aspartate transaminase activity is directed towards aspartate production using oxaloacetate and glutamate as substrates. Indeed, inhibition of mitochondrial pyruvate carrier by Zaprinast reduces pyruvate entry into the TCA cycle and increases the abundance of aspartate at the expense of glutamate (*580*). For further validation, ^{15}N labelled glutamine can be used to probe aspartate synthesis.

Moreover, I found a dose-dependent reduction in adenine, IMP and CDP abundance. These data contrast with the published data which showed FK866 induced accumulation of adenine and IMP (*550, 578*). This may reflect cell-specific responses to FK866. In this regard, Tolstikov et al argued the accumulation of IMP in A2780 cells is caused by inhibition of IMP

dehydrogenase (IMPDH) that requires NAD^+ as a cofactor (*578*). Consequently, IMP is diverted away from GMP synthesis via IMPDH towards AMP production and the catabolism of AMP generates adenine (*578*). However, the substrate of IMP *de novo* synthesis is PRPP which is derived from PPP and $NADP^+$ is a co-factor (*581*). In ID8 tumour samples, PPP and IMP de novo synthesis fluxes may be higher than GMP and AMP synthesis fluxes and therefore, FK866 may be more likely to cause IMP and adenine depletion. However, labelling studies using ^{13}C labelled glucose are required to probe PPP and purine metabolism. Of note, we found that adenine supplementation might rescue the apoptosis induction by FK866 monotherapy and its combination with Olaparib. These data are in line with a previous report showing that FK866 induced adenine depletion, and the apoptosis priming effects could be rescued by adenine supplementation in TNBC cells (*550*). However, these authors reported adenine supplementation did not increase the NAD^+ levels (*550*). One possible explanation is that adenine levels modulate mTORC1 activity, which in turn regulates apoptosis. In this regard, it has been reported that adenine depletion inhibits mTORC1 signalling and addition of exogenous adenine reactivates mTORC1 activity (*582*). mTORC1 has been reported to play dual roles in regulating apoptosis (*583, 584*). For instance, mTORC1 induces apoptosis by inducing autophagy-mediated degradation of the anti-apoptotic protein B cell lymphoma 2 (Bcl-2) (*585*). In contrast, mTORC1 promotes mitochondria translocation of Bax to activate apoptosis (*586*). Therefore, it would be interesting to probe the activity of mTORC1 and downstream effectors.

Interestingly, correlation analysis between NAD^+ levels and metabolite abundance showed opposite results to FK866 dose correlation analysis, which indicates the FK866 induced metabolic changes are caused by on-target effect of NAMPT inhibition. For instance, adenine, IMP and aspartate showed opposite results. Surprisingly, CDP was negatively correlated with both NAD^+ content and FK866 doses. This may result from the distribution of data points. Indeed, there were two clusters of data points: one with very low NAD^+ content and the other with high NAD^+ content (Figure 5.13), which may negatively impact the correlation analysis. Moreover, adenosine, ADP, AMP and guanine were positively correlated with NAD^+ content. The pool size of total glutathione was also positively correlated with NAD^+ content. Given that

ATP is required for glutathione *de novo* synthesis (*587*), glutathione depletion may result from the reduction in ATP secondary to NAD^+ depletion. Interestingly, ascorbic acid and total levels of glutathione were positively correlated with NAD^+ content, which suggests that NAD^+ depletion may limit anti-oxidation capacity. In addition, lactate and acetyl-carnitine levels were positively correlated with NAD^+ content. Given lactate is an end-product of glycolysis, these data indicate that FK866 treatment attenuated glycolytic flux. Acetyl-carnitine is synthesised using carnitine and acetyl-CoA in mitochondria (*588*). Given that PHD catalyses the conversion of pyruvate to acetyl-CoA, these results suggest the reduction of energy production in FK866 treated tumours. Interestingly, the abundance of 1-methylnicotinamide was positively associated with NAD^+ content. 1-methylnicotinamide has been reported to induce the production and release of tumour promoting cytokine tumour necrosis factor α (TNFα) from T cells in TME of ovarian HGSC tumours (*589*). 1-methylnicotinamide also suppresses T-cell mediated cytotoxicity (*589*). Therefore, it would be interesting to examine the immunomodulatory effects of the combination treatment.

PCA analysis and clustering analysis suggest that Olaparib and vehicle treated tumour samples cluster closely. This contrasts with previously published data showing that Olaparib treated samples separate from vehicle treated samples (*590, 591*). In addition, Olaparib downregulates glutamine, alanine, pyruvate and lactate in MCF-7, MDA-MB-231 and HCC1937 breast cancer cells (*590, 591*). However, the magnitude of such alterations compared to vehicle group is limited with fold change less than 2 (*590, 591*). Given that the TME consists of not only tumour cells but also stromal cells (e.g., immune cells and cancer associated fibroblasts), these changes may be masked in this study which profiles the metabolites in tumour samples. Samples in the combination treated groups were clustered away from vehicle group although full separation of the 95% confidence regions was not observed. Collectively, these data suggest that alterations in metabolism mainly result from FK866. The major limitation is the missing of FK866 monotherapy treated samples and therefore, additional metabolic profiling is needed.

Of note, the combination of FK866 and Olaparib induced higher levels of apoptosis in ID8 *Trp53*$^{-/-}$*; Pten*$^{-/-}$ cells compared to ID8 *Trp53*$^{-/-}$ cells. However, Pten loss failed to enhance the

growth inhibitory effects of Olaparib. Mechanistically, FK866 induced similar levels of NAD^+ depletion and NAD^+/NADH ratio perturbation regardless of genetic background in ID8 cells. Surprisingly, the combination treatment induced greater ROS accumulation in ID8 *Trp53*$^{-/-}$ cells. Although the *in vivo* study using ID8 *Trp53*$^{-/-}$*; Pten*$^{-/-}$ cells proved the efficacy of the combination, it should be repeated with ID8 *Trp53*$^{-/-}$ cells to understand the impact of Pten deletion *in vivo*. Nevertheless, the data in this chapter indicate the discrepancy with human ovarian cancer cell lines.

One possible explanation is the addition of pyruvate in ID8 cell culture media. In this chapter, pyruvate withdrawal sensitized FK866 in ID8 *Trp53*$^{-/-}$*; Pten*$^{-/-}$ cells but not ID8 *Trp53*$^{-/-}$ cells. FK866 treatment has been reported to inhibit glycolysis (*590, 591*) and given NAD^+ as a key co-factor of glycolysis, pyruvate supplementation may impact FK866 responses. Moreover, pyruvate can react non-enzymatically with H_2O_2 (*592*) and therefore, ROS may not accumulate sufficiently to differentiate ID8 *Trp53*$^{-/-}$*; Pten*$^{-/-}$ cells with ID8 *Trp53*$^{-/-}$ cells. However, pyruvate addition is a routine culture condition for ID8 cells (*390, 391, 408*) and therefore, pyruvate was added in this study. Thus, it would be interesting to repeat the experiments in ID8 cells cultured in media without pyruvate. In addition, except OVCAR8 cells, none of the human cell lines harbour P53 deletion (*593*). Therefore, these cell lines are classified as type I ovarian cancer (i.e., CCOC, LGSC, MOC, EnOC) (*594*). However, ID8 cells used in this study harbour TP53 deletion and are a model of Type II EOC (i.e., HGSC) (*391*). Thus, isogenic models of human cell lines with Ras/PI3K mutations should be generated to assess the combination of FK866 and Olaparib. Moreover, Pten deletion and Ras activating mutations are not functionally equivalent although similar pAkt could be detected (*595, 596*). Tumours with Pten loss generally progress more aggressively (*595, 596*). Thus, ID8 cells or human cell lines (e.g., COV318 cells) with knock-in mutations in the Ras/PI3K pathways should be generated. Given that Olaparib is approved mainly for ovarian HGSC treatment (*597*), ID8 cells with activating mutations are particularly relevant.

In summary, data from this chapter show that FK866 sensitized the ID8 model of ovarian HGSC to Olaparib therapy *in vivo*, and that the effect is likely a consequence of the on-target effect of FK866 to inhibit NAMPT, reduce NAD^+ levels and cause downstream metabolic stress.

CHAPTER 6

Investigating the kinetics of lactate metabolism in cancer cells

Chapter 6 Investigating the kinetics of lactate metabolism in cancer cells

6.1 Introduction

As described in section 1.5, lactate is more than a metabolic waste in cancer cells and contributes to the TCA cycle as a carbon source (*289-291, 598, 599*). Of note, data described in section 3.2.5 also show lactate as a potential source of the TCA cycle intermediates in ovarian HGSC cells. Additionally, we and other groups reported that lactate functions as an alternative carbon source when glucose supply is limited by the treatment of anti-angiogenic drugs and inhibitors of oncogenic signalling (e.g., Akt inhibitors) (*600-602*). This in turn leads to lactate-induced resistance to these therapies. Lactate has also been shown to modify histone and regulate gene expression in tumour associated macrophages (*603*).

The preliminary data described in section 1.7.4 may add a further layer of regulation of lactate metabolism (i.e., intracellular compartmentation). In brief, using $^{13}C_6$-glucose and $^{13}C_3$-lactate as tracers in two independent labelling studies, similar levels of ^{13}C enrichment of pyruvate were detected regardless of the tracer used (Figure 1.18). However, the fraction of labelled TCA cycle intermediates was significantly higher in cells incubated with $^{13}C_3$-lactate (Figure 1.18). These data suggest that lactate acidosis uncoupled glycolysis to the TCA cycle, which can be rationalized by the lactate metabolon model (Figure 1.14). Therefore, it was hypothesised that there are two kinetically resolved pools of pyruvate and lactate in HCT116 cells.

Additionally, our preliminary data showed that pharmacological inhibition or genetic deletion of MCT1, but not MCT4, increased glucose contribution to the TCA cycle (Figure 1.19). Also, dual blockage of MCT1 and MCT4 completely shifted pyruvate and citrate labelling, and glucose was the major carbon source of the TCA cycle (Figure 1.19). Thus, these data indicate that the lactate metabolon model is dependent on MCT1 and MCT4, especially MCT1. Thus, these preliminary data should be validated.

In this chapter, dual isotope labelling experiments were performed. In contrast to the parallel labelling experiments in which a single tracer was used at a time, the major advantage of dual labelling techniques is that measurements are made within the same sample, which allows for direct and more accurate comparison. Chemical inhibitors of MCT1 and MCT4 (AZD3965 and AZD0095, respectively) were used to investigate their roles in regulating the lactate metabolon model. HCT116 cells were chosen as the model in this chapter for reasons of consistency with our preliminary data. Published data also confirmed the expression of both MCT1 and MCT4 in HCT116 cells (*604*). HCT116 cells can server as a test tube for investigating lactate metabolism in cancer cells and these results may be validated and generalised to other cancer cell lines in the future.

6.2 Results

6.2.1 Dual labelling experiments supported the canonical model of lactate metabolism

To validate the preliminary data from our lab, dual isotope labelling experiments were performed. Here, the HCT116 cells were treated with 5.6mM $^{13}C_6$-glucose and 10mM 3-^{13}C-lactate simultaneously for 0.5, 1, 2, 4, 8 and 24h. The ^{13}C enrichment patterns of pyruvate and the TCA cycle intermediates are illustrated in Figure 6.1. In brief, glucose-carbon labelled pyruvate and TCA cycle intermediates in the first cycle are M+3 and M+2, respectively (Figure 6.1). Exogenous lactate-derived pyruvate and TCA cycle intermediates are M+1 (Figure 6.1).

My data showed that the fraction of M+3 intracellular pyruvate was stable at approximately 15% until 8h incubation and increased to about 41% after 24h incubation (Figure 6.2A). Interestingly, there was a gradual increase in M+3 intracellular lactate and M+2 TCA cycle intermediates (e.g., citrate and α-KG) from 30min to 8h incubation and a more profound upregulation was observed after 24h (Figure 6.2B-D, Appendix Figure 6.1). These data indicate metabolic activity of glycolysis and the time-dependent accumulation glucose-

derived carbons. This was also reflected by the gradual increase in the proportion of M+3 pyruvate and lactate in the media (Figure 6.3A-B). In contrast, approximately 96% of intracellular lactate was labelled M+1 after 30min incubation (Figure 6.2B), which suggests the high flux of uptake of exogenous 3-^{13}C-lactate. The majority of intracellular pyruvate was the M+1 isotopologue at 30min and its fraction was upregulated with longer incubation until 8h (Figure 6.2A). The decrease in M+1 intracellular pyruvate fraction in 24h may result from the dilution by M+3 pyruvate. There was also a similar increase in the fraction of M+1 TCA cycle intermediates (e.g., citrate and α-KG) with longer incubation time and the M+1 intermediate fraction was higher than the M+2 fraction (Figure 6.2C-D, Appendix Figure 6.1). The extracellular M+1 pyruvate and lactate also followed the same trend (Figure 6.3). Collectively, these data suggest the high initial incorporation of exogenous lactate derived carbons into the TCA cycle and the time-dependent increase in the contribution of glucose derived carbons.

To understand which lactate metabolic model better fits the data, the ratio between $^{13}C_6$-glucose and 3-^{13}C-lactate derived intracellular pyruvate, citrate and extracellular lactate was calculated. In the canonical model, the relative contribution of glucose and lactate to citrate should mirror that of intracellular pyruvate (Figure 6.4A). In contrast, in the lactate metabolon model, exogenous lactate derived pyruvate, but not glycolysis derived pyruvate, fuels the TCA cycle and therefore, the ratio between $^{13}C_6$-glucose and 3-^{13}C-lactate derived citrate should be close to that of extracellular pyruvate (Figure 6.4B). My results showed that the ratio of extracellular M+3 and M+1 lactate was gradually increased (Figure 6.4C). However, the M+2/M+1 citrate ratio was closer to the M+3/M+1 pyruvate ratio at all the timepoints examined (Figure 6.4C). Thus, these data are more consistent with the canonical lactate metabolic model.

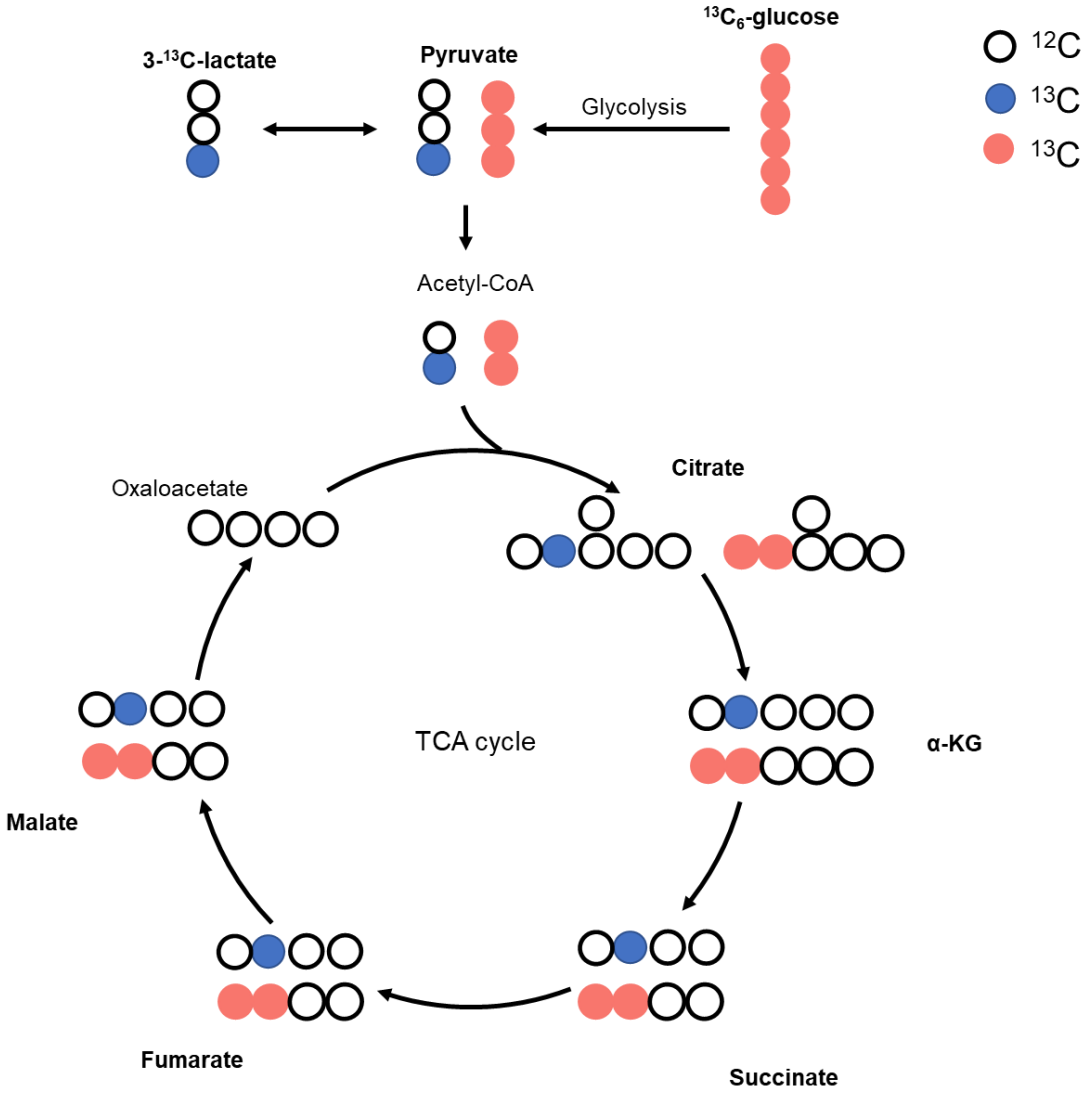


Figure 6.1 Schematics of ^{13}C enrichment patterns in dual labelling studies using $^{13}C_6$-glucose and 3-^{13}C-lactate as tracers.

$^{13}C_6$-glucose produces M+3 pyruvate and therefore the TCA cycle intermediates are labelled M+2. In contrast, 3-^{13}C-lactate generates M+1 pyruvate and thus M+1 downstream TCA cycle intermediates.

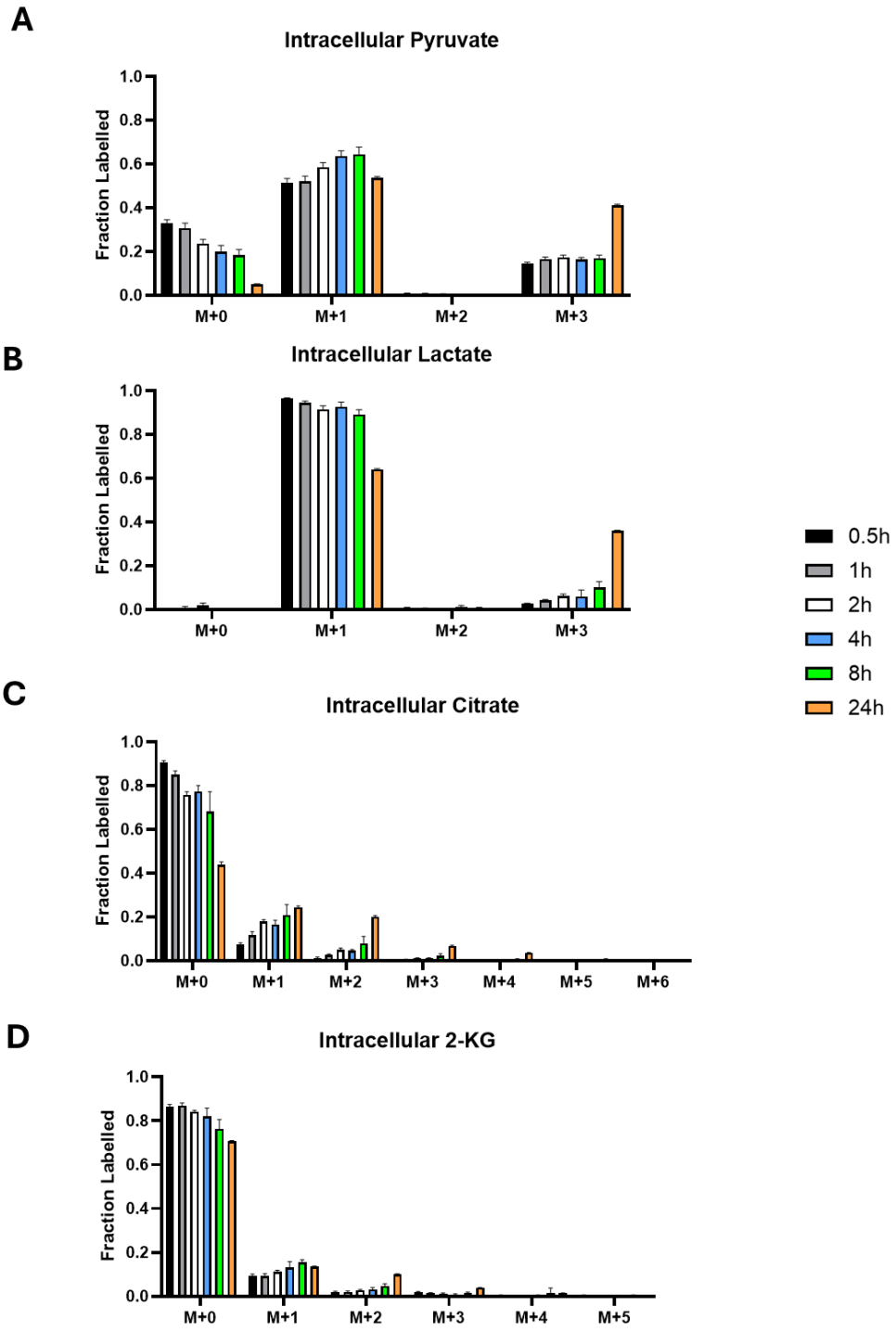


Figure 6.2 The metabolic fluxes of exogenous lactate fuelling the TCA cycle were high initially and there was a time-dependent increase in glucose contribution.

MIDs of intracellular pyruvate (A), intracellular lactate (B), citrate (C) and α-KG (D). HCT116 cells were incubated with 5.6mM $^{13}C_6$-glucose and 10mM 3-^{13}C-lactate simultaneously for various periods of time (e.g., 0.5, 1, 2, 4, 8 and 24h). At the end of incubation, intracellular metabolites were extracted and analysed by GC-MS. Data represent mean ± SD from three independent biological repeats.

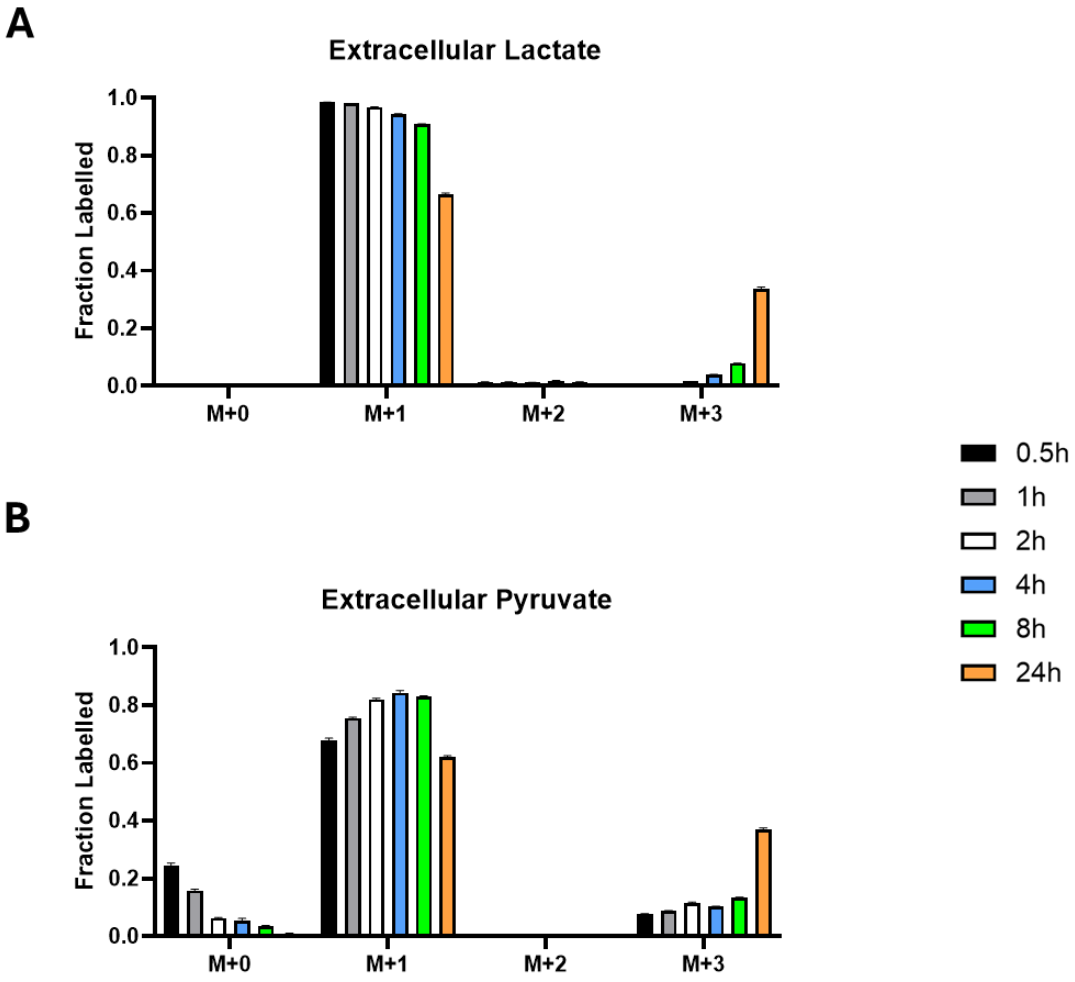
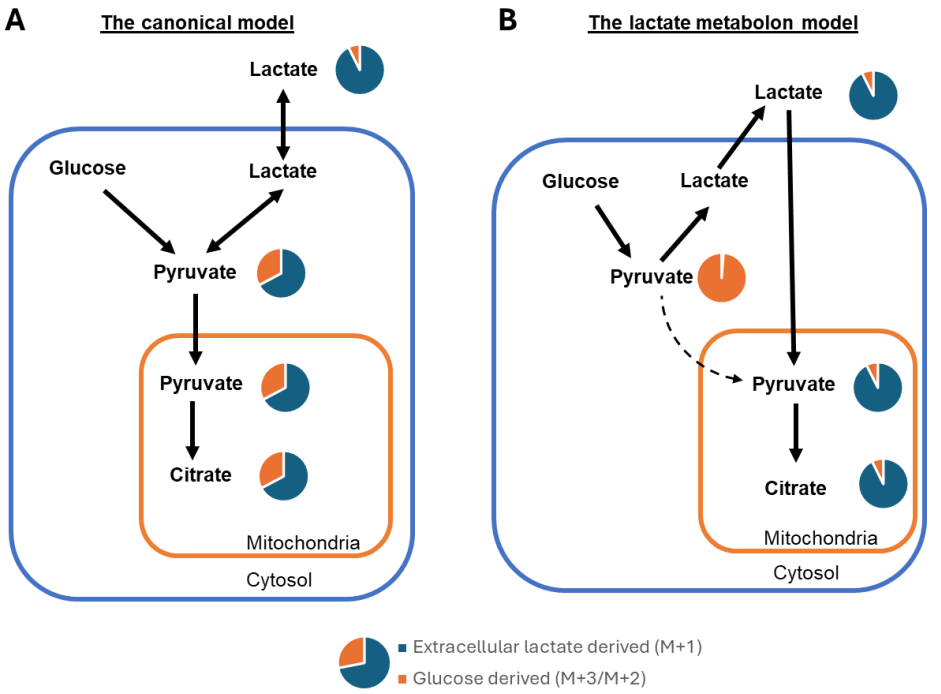


Figure 6.3 There was a time-dependent increase in glucose derived pyruvate and lactate in media.

MIDs of extracellular lactate (A) and extracellular pyruvate (B). Media were collected from the same dual labelling experiment as described in Figure 6.2. Briefly, at the end of incubation with 5.6mM $^{13}C_6$-glucose and 10mM 3-^{13}C-lactate, media were harvested and centrifuged to remove floating cells or cell debris. The metabolites were then extracted and analysed by GC-MS. Data represent mean ± SD from three independent biological repeats.



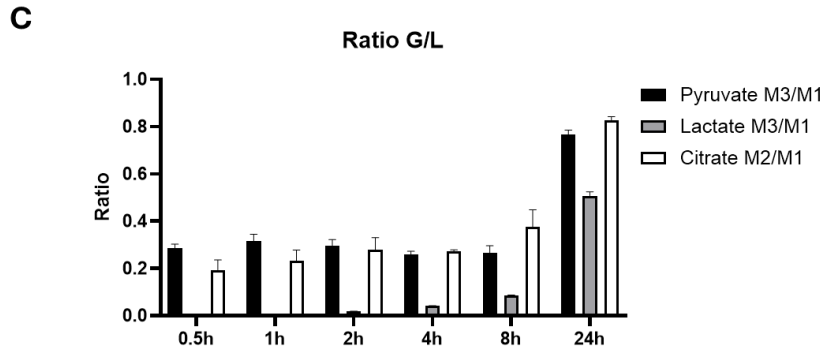


Figure 6.4 Higher agreement between the ratio of glucose/exogenous lactate derived citrate and that of intracellular pyruvate.

(A-B) Schematics showing the ratio of glucose/exogenous lactate derived (G/L ratio) citrate, intracellular pyruvate and extracellular lactate. (A) In the canonical model, glucose and exogenous lactate derived pyruvate are well mixed and fuels the TCA cycle. Thus, the G/L ratio of citrate should follow that of intracellular pyruvate. (B) In the lactate metabolon model, exogenous lactate fuels the TCA cycle without mixing with the glucose derived pool. Thus, the G/L ratio of citrate should follow that of extracellular lactate. The G/L ratio was indicated as a pie chart. Orange and blue represent exogenous lactate and glucose derived carbons, respectively. (C) The G/L ratio of citrate, intracellular pyruvate and extracellular lactate. The ratio was calculated using MID from the same dual labelling study as described in Figure 6.2. Data represent mean ± SD from three independent biological repeats.

6.2.2 Dual inhibition of MCT1 and MCT4 increased glucose contribution to the TCA cycle

Although the above-described data do not support the lactate metabolon model, the roles of MCT1 and MCT4 in lactate and glucose metabolism were still yet to be elucidated. To this end, HCT116 cells were treated with the MCT1 inhibitor AZD3965 and/or the MCT4 inhibitor AZD0095. AZD3965 is a potent inhibitor of MCT1 (K_i = 1.6nM) with 6-fold selectivity over MCT2 (K_i = 9.6nM) and no inhibition of MCT4 at 10uM (*605*). The treatment of AZD3965 has been reported to block lactate transport, increase intracellular lactate concentrations and reduce cell proliferation of lymphoma cells and breast cancer cells (*605-607*). AZD0095 has recently been discovered as a potent MCT4 inhibitor (K_i = 1.3nM) and is more than 1000 times selective over MCT1 (*608, 609*). AZD0095 inhibits MCT4-mediates lactate efflux in SKBr3 breast cancer cells and reduces the proliferation of MCT4, but not MCT1, expressing NCI-H358 non-small cell lung cancer cells (*608*). Historical data from our lab validated the specificity of AZD3965 on MCT1 inhibition. In this regard, LS174T WT colon cancer cells treated with AZD3965 phenocopied LS174T MCT1$^{-/-}$ cells as evidenced by similar reduction in exogenous lactate derived pyruvate (Figure 1.21). Moreover, no further reduction was observed when LS174T MCT1$^{-/-}$ cells were treated with AZD3965 (Figure 1.21), which suggests its high selectivity and no off-target inhibition on other MCT isoforms (e.g., MCT4).

A pilot experiment was conducted to optimize the doses of AZD3965 and AZD0095 in HCT116 cells. Briefly, the HCT116 cells were treated with various doses of AZD3965 and/or AZD0095 for 24h. The export rates of lactate and pyruvate and the uptake rates of glucose were then calculated by measuring the changes in their concentrations in media using NMR spectroscopy. My data showed that MCT1 inhibitor AZD3965 monotherapy, but not the MCT4 inhibitor AZD0095 treatment, caused a slight decrease in net lactate export rates (Figure 6.5A). This suggests that functional redundancy of lactate transport exists between MCT1 and MCT4. However, dual MCT1 and MCT4 inhibition resulted in an approximately 60% reduction in net lactate export rates and increasing doses of either AZD3965 or AZD0095 did not induce a further decrease (Figure 6.5A). These data indicate that alternative transporters of lactate may

mediate its secretion. Net pyruvate export rates were dramatically reduced by AZD3965, but not AZD0095, monotherapy, and a further decrease was observed when AZD3965 was combined with AZD0095 (Figure 6.5B). Interestingly, increasing AZD3965, but not AZD0095, had additional inhibitory effects of net pyruvate export (Figure 6.5B). Thus, these results indicate that MCT1 may act as the major pyruvate transporter although functional redundancy exists. Moreover, the combination of AZD3965 and AZD0095 resulted in a decrease in glucose uptake rates and treatment of higher doses had no significant impact (Figure 6.5C). Given the clear inhibition of net lactate and pyruvate export, 0.1μM was chosen as the optimal doses for both AZD3965 and AZD0095 to limit potential off-target effects.

Next, the HCT116 cells were treated with 0.1μM AZD3965 and/or AZD0095 in the presence of 5.6mM $^{13}C_6$-glucose and 10mM 3-^{13}C-lactate. My data showed that the abundance of intracellular M+1 lactate was significantly reduced in HCT116 cells treated with the combination of AZD3965 and AZD0095 (Figure 6.6A). This suggests the inhibition of exogenous lactate uptake. Interestingly, the levels of M+1 lactate in media was not changed (Figure 6.6B), which may reflect the large pool size of extracellular lactate than that of intracellular lactate. The abundance of intracellular and extracellular M+1 pyruvate, the product of M+1 lactate by LDH catalysed oxidation, was also reduced by dual MCT1 and MCT4 inhibition (Figure 6.6C-D), which may result from the reduced lactate import. However, it should be noted that reduction in M+1 pyruvate in media may also reflect decreased pyruvate export. Furthermore, dual MCT1 and MCT4 inhibition also caused an increase in the abundance of intracellular M+3 lactate and a reduction in M+3 lactate levels in media (Figure 6.7A-B), thereby indicating the inhibition of lactate export. Additionally, there was an upward trend of the intracellular M+3 pyruvate levels while the abundance of M+3 pyruvate in media was reduced by dual MCT1 and MCT4 inhibition (Figure 6.7C-D), which suggests the blockage of pyruvate export. Moreover, the abundance of M+2 and M+1 citrate was upregulated and downregulated by AZD3965 and AZD0095 combination, respectively (Figure 6.8A-B). Likewise, the downstream intermediates of the TCA cycle (e.g., α-KG) follow the same trend (Figure 6.8C-D, Appendix Figure 6.2). Taken together, these data indicate that dual MCT1 and MCT4 inhibition reduced lactate contribution but enhanced glucose contribution to the TCA

cycle.

AZD3965 single agent treatment resulted in a slight, but not significant, decrease in intracellular M+1 lactate concentrations (Figure 6.6A). Intracellular and extracellular M+3 lactate levels were upregulated and reduced, respectively (Figure 6.7A-B). This indicates that blockage of MCT1 alone mainly reduced lactate export. There was also a dramatic decrease in the abundance of intracellular and extracellular M+1 pyruvate (Figure 6.6C-D). Likewise, the levels of M+3 pyruvate in cells and media were decreased by AZD3965 monotherapy (Figure 6.7C-D). These data suggest the blockage of pyruvate export induced by the inhibition of MCT1 alone. Moreover, AZD3965 single agent treatment upregulated the levels of M+2 TCA cycle intermediates (Figure 6.8B). Of note, the above observed effects were less profound compared to those in the combination group. Interestingly, there was a paradoxical increase in the abundance of M+1 TCA cycle intermediates in HCT116 cells treated with AZD3965 monotherapy (Figure 6.8A). In contrast, AZD0095 alone had no major impact on ^{13}C enrichment of lactate, pyruvate and TCA cycle intermediates (Figure 6.6, 6.7 and 6.8). Collectively, these data suggest that MCT1 is the major regulator of lactate metabolism in HCT116 cells.

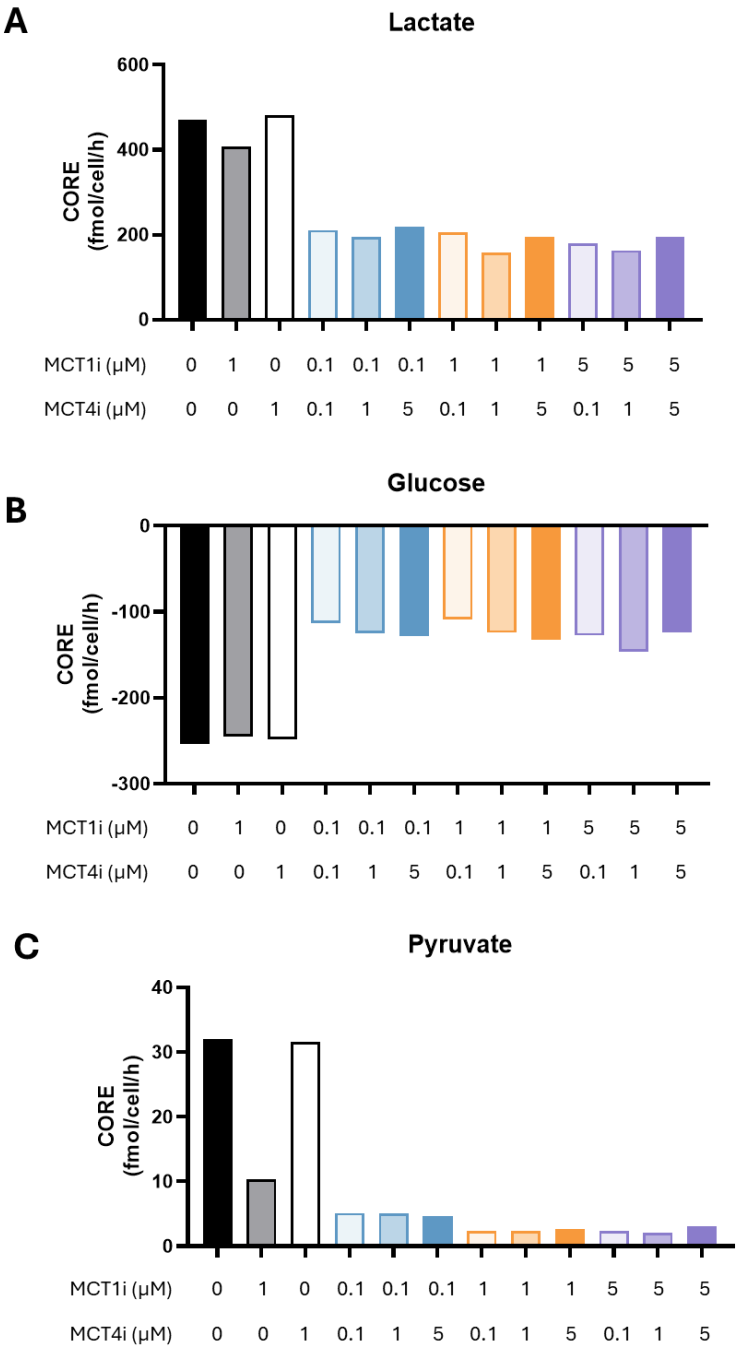


Figure 6.5 Dual inhibition of MCT1 and MCT4 may reduce net lactate and pyruvate export and glucose uptake rates.

The consumption/release (CORE) rates of lactate (A), pyruvate (B) and glucose (C). HCT116 cells were treated with AZD3965 (MCT1 inhibitor) and/or AZD0095 (MCT4 inhibitor) at various doses indicated in the Figure. At the start and end of 24h incubation, media were collected, and cells were countered. The concentrations of glucose, lactate and pyruvate in media were measured by NMR spectroscopy. CORE rates were calculated by dividing the changes in concentrations with cell density. Negative and positive CORE values indicate net consumption and release, respectively. Data represent mean from one biological repeat.

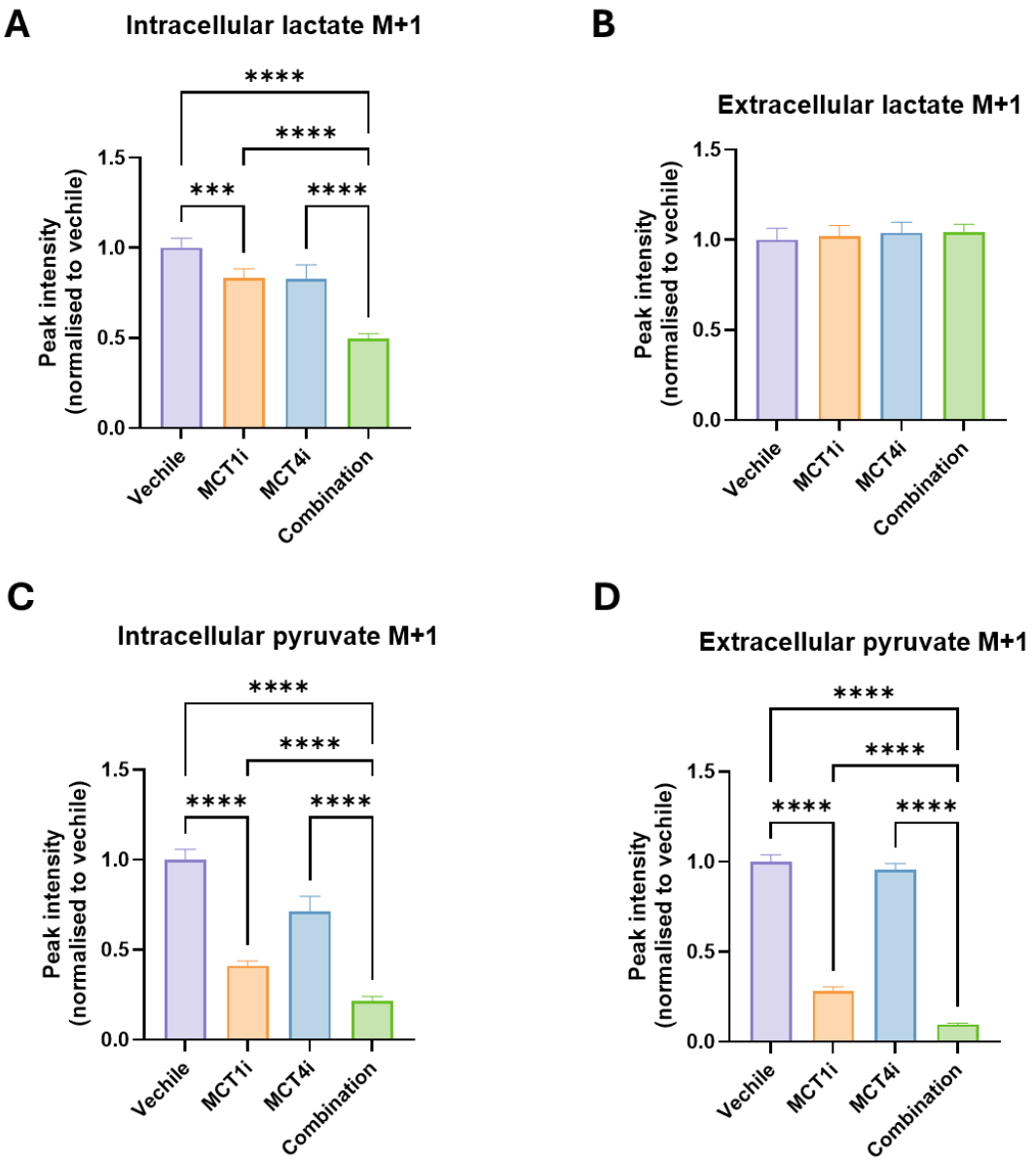


Figure 6.6 Dual MCT1 and MCT4 inhibition reduced lactate uptake.

Abundance of M+1 lactate in cells (A) and media (B) and M+1 pyruvate in cells (C) and media (D). HCT116 cells were treated with 0.2% (v/v) DMSO or 0.1μM AZD3965 and/or 0.1μM AZD0095 in media supplemented with both 5.6mM $^{13}C_6$-glucose and 10mM 3-^{13}C-lactate. At the end of the 2h incubation, media were collected, and cells were harvested. Metabolites were then extracted and analysed by GC-MS. Peak areas in drug treated groups were normalised to vehicle group (DMSO). Data represent mean ± SD from three independent biological repeats. Statistical significance was calculated by one way ANOVA with post-hoc Tukey tests. *** $p<0.001$, **** $p<0.0001$.

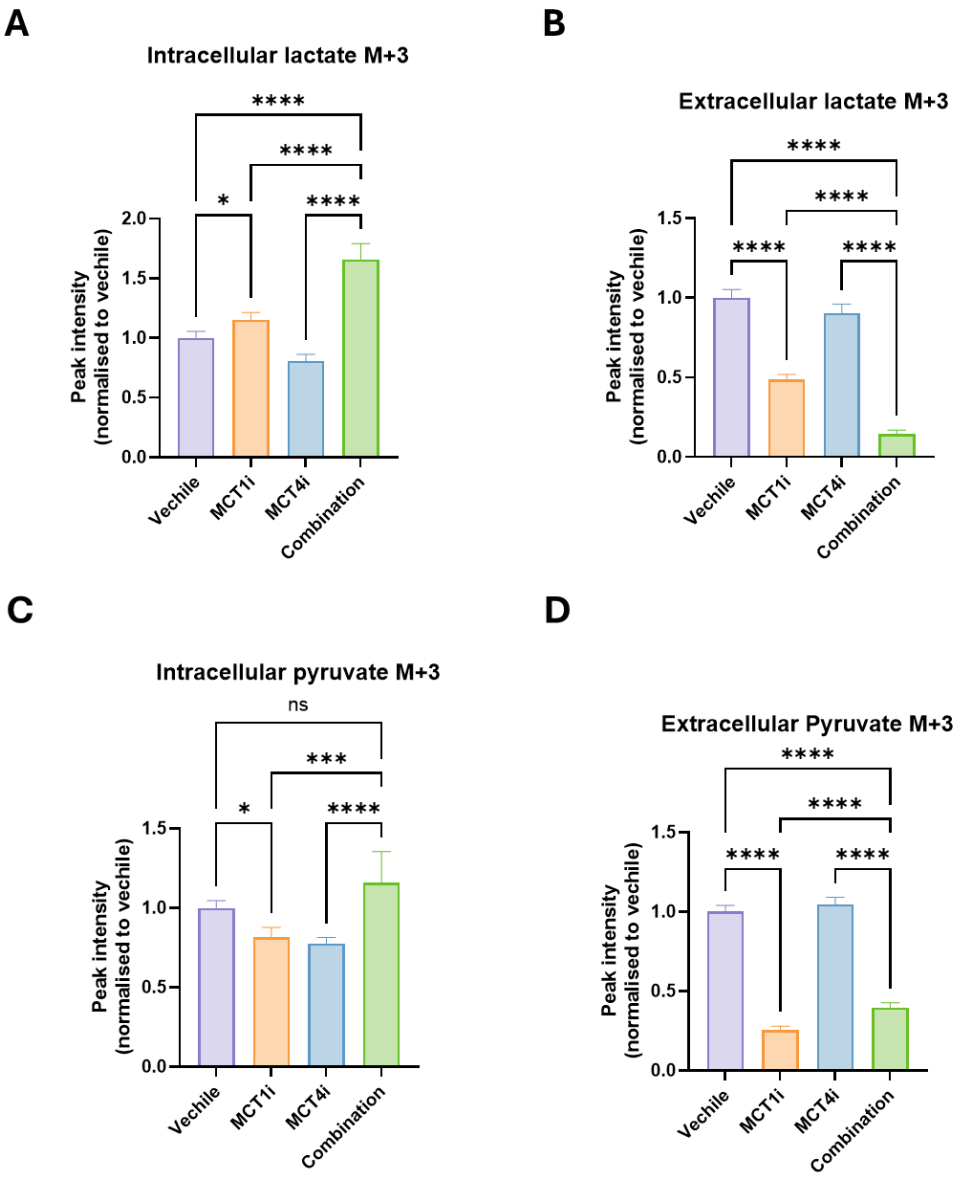


Figure 6.7 Dual MCT1 and MCT4 inhibition decreased lactate and pyruvate export.
Abundance of M+3 lactate in cells (A) and media (B) and M+3 pyruvate in cells (C) and media (D). The data were obtained from the same experiment described in Figure 6.6. Briefly, HCT116 cells were treated with 0.1μM AZD3965 and/or 0.1μM AZD0095 in the presence of 5.6mM $^{13}C_6$-glucose and 10mM 3-^{13}C-lactate. Metabolites were extracted and analysed by GC-MS. Peak areas were normalised to the vehicle groups. Data represent mean ± SD from three independent biological repeats. Statistical significance was calculated by one way ANOVA with post-hoc Tukey tests. * $p<0.05$, *** $p<0.001$, **** $p<0.0001$, ns: not significant.

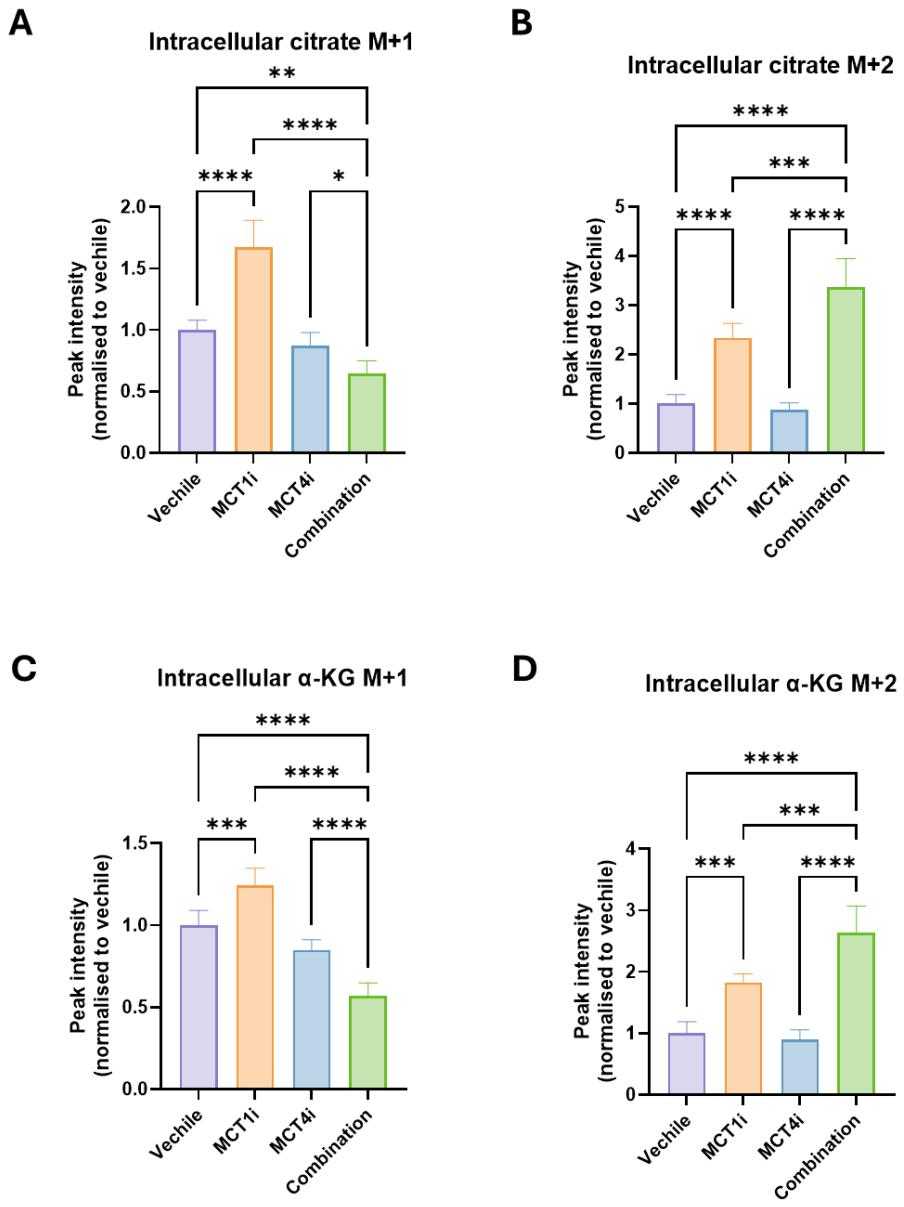


Figure 6.8 Dual MCT1 and MCT4 inhibition shifted the relative contribution of glucose and exogenous lactate to the TCA cycle.

Abundance of M+1 (A) and M+2 (B) citrate and M+1 (A) and M+2 (B) α-KG. The data were obtained from the same experiment described in Figure 6.6. In brief, HCT116 cells were treated with 0.1μM AZD3965 and/or 0.1μM AZD0095 in the presence of 5.6mM $^{13}C_6$-glucose and 10mM 3-^{13}C-lactate. Metabolites were extracted and analysed by GC-MS. Peak areas were normalised to the vehicle groups. Data represent mean ± SD from three independent biological repeats. Statistical significance was calculated by one way ANOVA with post-hoc Tukey tests. * p<0.05, ** p<0.01, *** p<0.001, **** p<0.0001.

6.3 Discussion

Subcellular compartmentation of metabolism provides advantages for the maintenance of cellular homeostasis (*610*). Such compartmentation can be achieved by membrane-dependent physical separation including mitochondria, cytoplasm and nucleus (*610, 611*). One example is NAD^+ metabolism (*612*). The subcellular localization of the three isoforms of NMNAT, which are key enzymes in NAD^+ synthesis, allows site-specific functions. The nuclear isoform NMNAT1 preferentially catalyses NAD^+ synthesis while the Golgi isoform NMNAT2 and mitochondrial isoform NMNAT3 mainly produce NADH (*612, 613*). Given the identical equilibrium constant of the interconversion between NAD^+ and NADH, the reaction direction is determined by the local concentrations (*614*). Thus, the compartmentation of NMNAT isoforms allows reduction and oxidation in the same cell (*613, 614*). Metabolic compartmentation can also be achieved by membrane-independent mechanisms which are described by the term 'metabolon' (*343*). Metabolon is defined as the assembly of sequential metabolic enzymes and cellular structural elements (e.g., actin) into a supramolecule complex (*343*). For instance, multiple glycolytic enzymes and gluconeogenic enzymes are organized into a multi-protein complex called 'glucosome' (*615*). Such spatial organization is proposed to facilitate the regulation of glucose flux (*615*). More recently, Pareek et al reported that the nine enzymes involved in purine *de novo* synthesis form a metabolic complex called 'purinosome' (*616*). The benefits include quick channelling of the intermediates for purine synthesis to allow synergistic action of these enzymes (*616*).

Subcellular compartmentation of lactate metabolism has been reported previously. In this regard, Chen et al detected LDH in mitochondria which catalyses lactate oxidation to pyruvate for the TCA cycle (*288*). Therefore, such localization of LDH enables simultaneous pyruvate reduction to lactate (i.e., the Warburg effect) and lactate oxidation to pyruvate in the same cell (*288*). However, it remains unclear whether lactate metabolism compartmentation occurs in the same subcellular fraction (e.g., the cytoplasm). Given that we and other groups found the uncoupling of glycolysis and the TCA cycle (*292*), it was then proposed that such phenomenon can be rationalized by the lactate metabolon model. Specifically, there are two

kinetically resolved pools of pyruvate and lactate in the cytoplasm (Figure 1.14). The glycolysis derived pyruvate and lactate (i.e., the glycolysis pool) are preferentially exported instead of entering the TCA cycle. Without mixing with the glycolysis pool, exogenous derived lactate is oxidized to pyruvate which is the preferred carbon source of the TCA cycle. Such lactate metabolon model can be achieved by the spatial organization of mitochondria. In this regard, mitochondria located close to the plasma membrane preferentially channels exogenous lactate (or the oxidized product pyruvate) to fuel the TCA cycle.

In this chapter, the parallel single labelling studies previously performed in our lab was validated by a dual labelling study. My data showed the high initial levels of the TCA cycle intermediates labelling from exogenous lactate and that there was a time-dependent dilution by glucose derived carbons labelling in HCT116 cells. Of note, I found that the ratio of $^{13}C_6$-glucose and 3-^{13}C-lactate derived citrate correlated better with that of intracellular pyruvate than extracellular lactate. Because exogenous lactate fuels the TCA cycle without mixing with the glycolysis pool according to the lactate metabolome model, the labelling patterns of the TCA cycle intermediates should associate with exogenous lactate. In contrast, glycolysis and exogenous lactate derived pyruvate is well mixed before entering the TCA cycle in the canonical model and therefore, the TCA cycle intermediate labelling should correlate with intracellular pyruvate. Thus, the results from the dual labelling study agreed better with the canonical model. The obvious discrepancy between the dual labelling and parallel single labelling data may result from the subtle differences including cell passage numbers and FBS composition contributed to the discrepancy. They may in turn modulate the interaction between mitochondria and plasma membrane and therefore, regulate channelling of exogenous lactate into mitochondria.

However, there are limitations and gaps in the dual labelling study and additional research is required to decide which lactate metabolic model to choose. For instance, the MID of intracellular pyruvate and lactate reflects the average of glycolysis and exogenous lactate derived metabolites. Thus, if the glycolysis and exogenous pool are not well-mixed, the measured pyruvate MID may deviate from that of the glycolysis pool, which in turn may skew the correlation analysis with citrate MID. Additionally, it should be noted that the repeated

cycling of the TCA cycle can produce other isotopologues. Indeed, M+1 and M+2 TCA cycle intermediates can be generated from $^{13}C_6$-glucose and 3-^{13}C-lactate labelling, respectively. Historical data from our lab showed limited levels of repeated cycling of the TCA cycle even after 24h incubation (i.e., less than 2% and 3% from $^{13}C_6$-glucose and 3-^{13}C-lactate, respectively) (data not shown). Given the limited time and resources, such calibration using $^{13}C_6$-glucose or 3-^{13}C-lactate as single tracers was not performed in this study. Since the carbon atoms of the TCA cycle intermediates at different positions are labelled by the tracers, efforts were made to examine the fragments of the intermediates. However, such fragments could not distinguish labelling from $^{13}C_6$-glucose or 3-^{13}C-lactate (data not shown). Therefore, correction by single tracer parallel labelling studies is required.

Moreover, ^{13}C-metabolic flux analysis (^{13}C-MFA) of the dual labelling data should be performed. ^{13}C-MFA quantitates metabolic fluxes to provide a systematic understanding of metabolic network and phenotypes in cancer cells (*362, 617*). Mathematically, ^{13}C-MFA can be viewed as least-square parameter estimation of metabolic fluxes (i.e., unknown parameters of the metabolic network) based on the measured MID (*362, 617*). ^{13}C-MFA generally starts with random values of metabolic fluxes and simulates MID for each metabolite in the network (*362, 617*). Through multiple iterations, ^{13}C-MFA optimises the estimated metabolic fluxes to minimize the difference between the simulated and measured MID (i.e., global minimal sum of squared residuals (SSR)) (*362, 617*). Historically, ^{13}C-MFA can only be performed on metabolic network with both metabolic and isotopic steady state. Recent developments allow its application in metabolic or isotopic non-steady state and software packages are available (e.g., OpenFlux) (*618*). Given that net lactate secretion into media and the time-dependent increase in ^{13}C enrichment were observed, non-steady MFA should be used and the lactate model with better fitting (i.e., lower SSR) should be chosen. Here, efforts have been made to model the dual labelling data using the algorithm OpenFlux although no stable model representing the lactate metabolon model could be found (data not shown). Thus, additional work is required to improve such model.

Lactate transport across the plasma membrane is mainly mediated by MCT1 and MCT4 in cancer cells. MCT1 has been reported to facilitate bi-directional lactate transport while MCT4

mainly mediate lactate efflux (*619*). MCT1 also shows higher affinity for lactate than MCT4 (*295*). Much effort has been devoted to understanding the individual roles of and interaction between MCT1 and MCT4. However, such effort is challenged by the lack of MCT4 specific chemical inhibitors and therefore, these studies rely on genetic manipulation of MCT1 or MCT4 is an alternative (*295, 619*). MCT1 specific inhibitors (e.g., AZD3965) and dual MCT1 and MCT4 inhibitors have been developed and a phase I clinical trial was initiated for AZD3965 (*620, 621*). However, MCT4 specific inhibitors are not available until recently. In 2021, VB124 (*335*) and MSC-4381 (*622*) were made available and well-validated *in vitro* and *in vivo* and later in 2023, AZD0095 was discovered (*608*). Using AZD3965 (MCT1 specific inhibitor) and VB124 (MCT4 specific inhibitor), Sheng et al demonstrated the functional redundancy and heterogeneity of MCT1 and MCT4 in osteosarcoma cells (*334*). In this regard, MCT1 mediates lactate export to avoid intracellular lactate acidosis and feedback inhibition on glycolysis (*334*). MCT1 is also responsible for the import of extracellular lactate that in turn enters the TCA cycle (*334*). In contrast, MCT4 maintains glycolysis under conditions of high intracellular lactate levels by mediating lactate efflux (*334*). Additionally, Babl et al reported that the combination of AZD3965 and AZD0095, but not monotherapy, reduced lactate efflux in HCT116 colon cancer cells (*604*). However, no further characterisation about the functional redundancy and heterogeneity was performed.

In this study, the functional redundancy in mediating lactate transport was confirmed in HCT116 cells. In this regard, the inhibition of MCT1 or MCT4 individually was not sufficient to significantly reduce the net lactate secretion rates. Indeed, such decrease was only observed in cells treated with the combination of AZD3965 and AZD0095. Interestingly, increasing the drug doses could not abolish net lactate export completely, which may reflect that other lactate transporters were active. For instance, sodium coupled monocarboxylate transporters mediates lactate transport albeit at a much lower affinity (e.g., SCL5A8: K_m=159μM) (*623, 624*). Given that MCTs mediate bi-directional lactate transport (*295*), a dual labelling study that uses $^{13}C_6$-glucose and 3-^{13}C-lactate as tracers was performed to differentiate lactate influx and efflux. My data showed that dual MCT1 and MCT4 inhibition caused the most profound increase in intracellular levels of M+3 lactate and pyruvate (i.e., the LDH product)

accompanied by a reduction in extracellular abundance, which suggests that MCT1 and MCT4 are redundant in lactate efflux. Moreover, the combination of AZD3965 and AZD0095 caused the highest reduction in intracellular levels of M+1 lactate and pyruvate. Combination treatment did not upregulate the abundance of M+1 lactate in media, which may reflect that the amount of lactate imported in vehicle group was neglectable during the 2h incubation. Nevertheless, these data indicate the functional redundancy in lactate influx.

Functional heterogeneity also exists. In this regard, MCT1 inhibition, but not MCT4 inhibition, significantly reduced the abundance of M+3 lactate in media, which indicates MCT1 as the major MCT isoform of lactate efflux. This is in line with the higher affinity of MCT1 for lactate (*295*). Interestingly, MCT1 inhibition alone did not reduce lactate influx as evidenced by the unchanged intracellular levels of M+1 lactate. This contrasts with the previous publication showing MCT1 as the major transporter for lactate import (*334*). The discrepancy may be explained by differences in incubation length and media composition (e.g., lactate and glucose concentrations) (*334*).

Given that MCT1 and MCT4 are carriers of other monocarboxylates (e.g., pyruvate) (*625*), pyruvate transport across the plasma membrane was also examined. Inhibition of MCT1, but not MCT4, significantly reduced net pyruvate export and blockage of both MCT1 and MCT4 caused a greater reduction. These data suggest that MCT1 is the major pyruvate transporter, which is in line with the higher affinity of MCT1 for pyruvate. MCTs also mediate transport of ketone bodies (*625*) and therefore, it would be interesting to understand the functional redundancy and heterogeneity of MCT1 and MCT4 in ketone body transport.

Additionally, my data showed that dual MCT1 and MCT4 inhibition upregulated glucose contribution while reduced exogenous lactate contribution to the TCA cycle. Interestingly, the glucose uptake rates were also reduced by the combined MCT1 and MCT4 inhibition. Therefore, these data indicate that blocking both MCT1 and MCT4 inhibited glycolysis flux although glucose was diverted towards the TCA cycle. This is in line with the previous report showing that knockout of both MCT1 and MCT4 reduced glycolysis and enhanced OXPHOS (*331, 626*). The reduction in glycolysis may result from the feedback inhibition due to lactate

accumulation. End-product inhibition of LDH caused by lactate accumulation limited the regeneration of NAD^+ which is key co-factor of glycolysis (*331, 626*). Consequently, the cells were more reliant on the OXPHOS for energy production (*331, 626*). Indeed, blocking OXPHOS by metformin, the inhibitor of mitochondrial complex I in ETC, is synthetic lethal with dual MCT1 and MCT4 inhibition (*331, 626*). Thus, it would be interesting to test the efficacy of the combination of AZD3965 and AZD0095 in cancer cells with mitochondria defects or low expression of PDH or PC (i.e., enzymes catalysing pyruvate entry to the TCA cycle). Moreover, the inhibition of LDH may also shift cellular redox balance (*627*). In this regard, blocking lactate export by inhibiting MCT1 reduced NADPH levels and GSH synthesis, which in turn caused oxidative stress and cytotoxicity (*331*). Therefore, it would be interesting to investigate redox balance and ROS levels in cells treated with combined AZD3965 and AZD0095.

Interestingly, MCT1 inhibition alone was sufficient to upregulate glucose entry into the TCA cycle. Given that no reduction in glucose uptake rates was observed, intracellular lactate concentrations may not suffice to block LDH and glycolysis. Such upregulation may therefore result from the blockage of MCT1-dependent pyruvate efflux. However, Braga et al reported that AZD3965 inhibited PDH activity and reduced glucose incorporation into the TCA cycle in diffuse large B-cell lymphoma (*628*). Thus, it would be interesting to examine the phosphorylation levels of PDH in HCT116 cells since its phosphorylation inhibits the activity. Surprisingly, MCT1 inhibition alone caused an increase in exogenous lactate contribution to the TCA cycle regardless of the decrease in exogenous lactate derived pyruvate. One possible explanation is that MCT1 inhibition blocked pyruvate transport across the plasma membrane. However, single inhibition of MCT1 was not sufficient to block lactate transport (i.e., MCT4 could mediate lactate import under this condition). Consequently, the accumulation of intracellular pyruvate derived from glucose and exogenous lactate can increase the contribution of both carbon sources to the TCA cycle. However, these data should be validated by MCT1 knock out studies to rule out the off-target effects of AZD3965.

In conclusion, data from this chapter support the canonical lactate metabolic model rather than the existence of a lactate metabolon, and evidence functional redundancy and

heterogeneity between MCT1 and MCT4.

CHAPTER 7

Final discussion and future directions

Chapter 7 Final discussion and future directions

7.1 Characterisation of metabolic reprogramming in ovarian HGSC cells with Pten loss

The roles of the Akt pathway in metabolic reprogramming have been reported in various types of cancer (e.g., hepatic cancer) (*83*). However, it remains unclear how the Akt signalling regulates cellular metabolism in ovarian HGSC cells. In this study, I found that Akt pathway activation induced by Pten loss results in metabolic reprogramming in ovarian HGSC cells. In short, glucose metabolism, lipid synthesis and oxidation, metabolic cofactor synthesis and arginine metabolism are modulated by Akt signalling. However, there are limitations and gaps, and additional research is needed.

One of the major gaps is the lack of data about changes of enzyme expression induced by Pten loss. Previous studies have reported that the metabolic reprogramming in Akt hyperactivated cancer cells are mediated by 1) transcriptional regulation of enzymes or transporters; and 2) acute phosphorylation (*83*). For instance, the molecular mechanisms of glucose uptake and glycolysis include both enhanced expression and direct stimulation by phosphorylation of GLUT1/4 and glycolytic enzymes including hexokinases and PFK1 (*83, 111, 117*). Therefore, it would be interesting to characterise the effects of Pten loss on total and phosphorylated levels of metabolic enzymes and transporters (refer to section 7.4 for details).

Of note, bulk mouse tumour tissue was used for the untargeted metabolic profiling in this study. However, the TME is heterogenous and consists of different types of cells (e.g., immune cells, cancer associated fibroblasts) and extracellular matrix (ECM) (*631*). In addition, oxygen tension and concentrations of nutrients, including glucose, amino acids and lipids, are highly heterogeneous (*598, 632*). Thus, these factors impact on metabolism of cancer cells and spatial heterogeneity in cancer metabolism is generated (*598, 632*). In this regard, ovarian cancer cells preferentially metastasise to omentum rich in adipocytes and show enhanced FA

uptake and oxidation after localising to the proximity of adipocytes (*459*). Although metabolomics performed using the bulk omental tumour tissue provide insights into metabolic reprogramming, the limitations of this approach include 1) the inability to examine the metabolic phenotypes of individual cancer cells at different location in TME; and 2) the failure to differentiate cancer cells with stromal cells (e.g., adipocytes). Therefore, spatial metabolomics can be performed (refer to section 7.4 for details).

Although the ID8 model recapitulates key features of human ovarian HGSC (e.g., p53 deletion, metastasis to omentum and ascites production), the major limitation is the ID8 cells are derived from mouse ovarian epithelial cells. Recently, it has been suggested that the progenitors of human ovarian HGSC cells are the secretory epithelial cells of the distal fallopian tubes (*634-636*). Moreover, the data in this study are derived from a single clone of ID8 cells and therefore, validation using additional clones is required.

7.2 Mutations in the Ras/PI3K signalling sensitized ovarian cancer cells to the combination of FK866 and Olaparib

Previous published reports have demonstrated that NAD^+ depletion by FK866 enhances Olaparib sensitivity in various types of cancer cells, including ovarian HGSC cells (*285, 286, 388*). Here, our findings confirmed these reports and contributed by showing that FK866 enhanced Olaparib sensitivity in ovarian HGSC cells with Pten deletion. In a panel of type I ovarian cancer cell lines, we also found that mutations in the Ras/PI3K pathway as sensitization biomarkers of FK866 and Olaparib combination. The underlying mechanisms involve NAD^+ depletion, DNA damage and oxidative stress. Our results have the potential to improve Olaparib efficacy in Ras/PI3K mutant patients who show worse responses to PARP inhibitors and may allow the application of lower doses to limit toxicity. Interestingly, NAMPT inhibition has been shown to sensitize Olaparib in NAPRT-silenced renal cell carcinoma (*637*), which indicates NAPRT may be an another potential biomarker for the combination. Thus, these

data highlight the importance of better understanding the specific susceptibility of genetic subtypes within a specific tumour type.

However, there are a few gaps in this study and additional research is required. As highlighted in section 5.3 and 7.1, the models used in Chapter 4 and 5 have limitations. For instance, except OVCAR8, none of the EOC cell lines used in Chapter 4 harbour TP53 mutation and thus, represent type I ovarian cancer. They are also characterised by different genetic landscape. The ID8 model has been improved to better recapitulate ovarian HGSC by knocking-out Trp53. However, the origin of the ID8 cells (ovarian epithelial cells) differ from human patients (i.e., distal fallopian tube). Also, Pten deletion may not be functional equivalent to oncogenic mutations in Ras or PIK3CA genes. Therefore, additional models should be used to validate the data. In addition, the causal relationship between oxidative stress and DNA damage is missing. Despite our best efforts, no enhancement of PARP1 trapping could be detected regardless of drug treatment. The mechanisms of ROS accumulation also remain unknown.

In this study, we focused on cell autonomous events to illustrate the mechanisms. However, multiple lines of evidence indicate that the combination of FK866 and Olaparib may have immunomodulatory effects. For instance, 1-methylnicotinamide, which negatively regulates T-cell mediated cytotoxicity (*589*), was positively correlated with NAD^+ content in omental tumours. Additionally, ROS accumulation has been shown to modulate anti-cancer immunity (*640*). In this regard, post translational modification of cysteine residues in proteins by ROS may alter the antigenicity (*641*). ROS also induces the expression of T cell co-stimulatory molecule CD80 via the JNK and MAPK signalling in colon cancer cells (*642*). In contrast, oxidative stress in TME has been reported to suppress anti-cancer immunity. For instance, ROS accumulation impairs T cell proliferation and activation, and recruitment of immunosuppressive regulatory T cells (*643-646*). Given the combination of FK866 and Olaparib induced the highest levels of ROS, it would be interesting to examine immune cell population and function in omental tumour samples from the syngeneic ID8 model.

7.3 Investigating the kinetics of lactate metabolism in cancer cells

As described in Section 1.5.4, cytosolic compartmentation of lactate metabolism has been suggested in glioma and cardiomyocytes. However, they lack support from genetic and cell imaging studies. Lactate-induced uncoupling of glycolysis and the TCA cycle observed previously in our lab and other groups led to the hypothesis of two kinetically resolved pools of pyruvate and lactate in cancer cells. These preliminary data suggest the urgent need to further examine the kinetics of lactate metabolism. Here, using $^{13}C_6$-glucose and 3-^{13}C-lactate as tracers, the dual labelling study, however, showed higher agreement with the canonical model where lactate and pyruvate pools are well mixed regardless of the origin.

There are gaps and limitations in this study which should be addressed for deeper understanding of lactate metabolism. As described in Section 6.3.1, MID was not corrected for repeated cycling of the TCA cycle although our historical data showed very limited interference. Non-steady MFA was performed to assess the agreement with the two models of lactate metabolism. However, no stable model could be found.

Although the results are not supportive of the lactate metabolon model, the roles of MCT1 and MCT4 in regulating lactate and glucose metabolism were examined. This is because such investigation has been challenged by the lack of MCT4 specific chemical inhibitors. The recent development of VB124, a specific inhibitor of MCT4, allowed such characterisation (*335*). In osteosarcoma cells, MCT1 mediates bi-directional transport of lactate while MCT4 mainly facilitate lactate efflux (*334*). Later, Babl et al showed in colon cancer cells, dual inhibition of MCT1 and MCT4 blocked lactate export (*604*). Here, data from this study using AZD3965 and AZD0095 (MCT1 and MCT4 inhibitor, respectively) contributed by showing the functional redundancy in regulating transport of lactate and pyruvate, and glucose metabolism in HCT116 colon cancer cells. However, MCT1 is the dominant lactate and pyruvate transporter and the major regulator of glucose metabolism.

The major limitation is the lack of support from *in vivo* models. Here, the concentration of

lactate in media was 10mM. However, lactate concentrations in TME can be as high as 40mM and vary depending on oxygen supply (*647*). Also, the pH of the TME can be decreased (i.e., lactate acidosis) to 6.3-6.9 (*648-650*), which differs from the pH-buffered media of the in vitro system. Therefore, the inhibitor studies should be repeated using *in vivo* models. In addition, the data were generated using chemical inhibitors only and the specificity of the MCT4 inhibitor AZD0095 was not verifies in this study.

7.4 Future work

As described in section 7.1, there are limitations and gaps in the untargeted metabolic profiling study. To address the lack of data about Pten loss induced modulation of enzyme and metabolite transporter expression, WB against the metabolic targets of Akt signalling can be performed (e.g., phosphorylated HK). The metabolomics data acquired in this study can also be integrated with transcriptomics, proteomics and phosphoproteomics. Recently, the integrated multi-omics approach has been applied in various cancer types to simultaneously investigate mRNA, protein, phosphor-protein and metabolites (370, 629, 630). This allows the input of all the biological data into one unified model and identification of the association of biological events at different levels.

To perform spatial analysis of metabolic phenotypes, matrix-assisted laser desorption/ionization (MALDI)-mass spectrometry imaging (MSI) can be used (598). This in situ technique achieves spatial visualization of metabolites by ionizing metabolites directly on the tissue section (633). Combined with histological staining, metabolic heterogeneity of cancer and non-cancer cells within TME can be interrogated.

A different model of ovarian HGSC should be used to validate the results generated in Chapter 3. In this regard, human ovarian HGSC cell lines and genetic engineered mouse (GEM) models are required for further validation. For instance, OVCAR4 cells recapitulates TP53 deletion (593) and CRISPR techniques can be used to knock out PTEN gene. The mouse model developed by Perets et al resembles the fallopian tube origin, molecular and histological

features of human ovarian HGSC (635).

In addition, new hypotheses can be generated by the metabolic profiling data in Chapter 3 and warrants further investigation. For instance, the increase in the abundance of acyl carnitines, the product of CPT1, in Pten deleted tumour samples implies that FAO may be promoted. Thus, tracer studies using ^{13}C labelled FA (e.g., palmitate) are required. The expression of CPT1, the rate-limiting step in FAO, should also be examined using WB. Moreover, the abundance of several metabolites in PtdCho metabolism pathway was altered, which implies the activity may be regulated by Pten. To understand the direction of such modulation, tracer studies using ^{13}C labelled choline can be performed. My data also suggest that arginine metabolism via arginase may be regulated and ^{13}C and ^{15}N labelled arginine should be used to probe these pathways. The decrease in pantothenate abundance implies enhanced CoA synthesis and ^{13}C and ^{15}N labelled pantothenate should be used to validate. Moreover, my data showed Pten might regulate the salvage pathway of NAD^+ synthesis. Given that Pten loss inhibits DNA repair and result in enhanced NAD^+ consumption due to PARP1 activation (*475*), tracer studies using deuterium labelled NAD^+ can be performed to quantify the fluxes of NAD^+ synthesis and breakdown.

As described in section 7.2, additional work is required to support the findings in Chapter 4 and 5. To address the limitations in the models, isogenic pairs of the EOC cell lines used in Chapter 4 can be generated. For instance, knock-in mutations in Ras or PI3K can be introduced to COV318 cells. The ID8 can be improved by introducing knock-in oncogenic mutations of Ras or PI3CA. An additional model of ovarian HGSC (e.g., the genetically engineered HGS2 model) can also be used to better recapitulate the distal fallopian tube origin of human ovrian HGSC patients (*638*). Moreover, the DNA damage marker γH2AX and activity of DDR signalling should be examined in cells treated with NAC and the drug combination. Thus, the causal relationship between oxidative stress and DNA damage can be established. The high sensitive fluorescence sensor developed by Steffen et al is based on the fluorescent resonance energy transfer (FRET) technology to capture structural changes of PARP1 in response to DNA damage (*535*). Thus, this fluorescence sensor can be used to understand the impact of the combination of Olaparib and FK866 on PARP1 trapping.

Furthermore, it would be interesting to perform proteomics or transcriptomics studies to understand the global impact of combination treatment. These datasets may also provide information about novel mechanisms apart from DNA damage and ROS accumulation.

The data in Chapter 4 and 5 also imply that the combination of Olaparib and FK866 may modulate anti-cancer immunity. Therefore, the syngeneic ID8 model should be used to investigate the potential changes in immune cell population and function. Moreover, the data suggest the potential of the drug combination for a clinical trial to improve the efficacy of Olaparib in EOC patients with Ras/PI3K mutations. However, further validation using *in vivo* models is required. For instance, the survival study should be repeated in the ID8 models with WT Pten to validate Ras/PI3K mutations as a sensitizing biomarker. In addition, a different *in vivo* model (e.g., HGS2 model (*638*)) should be used for further validation.

As described in section 7.3, additional work is required to understand the kinetics of lactate metabolism. For instance, the MID from the dual labelling studies should be corrected for repeated cycling of the TCA cycle. The model in the non-steady state MFA should be improved (e.g., adjusting metabolic fluxes). If the lactate metabolon model is supported, the physical basis for such channelling of lactate should be probed. For instance, the interaction between plasma membrane and mitochondria and mitochondria dynamic under different MCT status should be examined. An *in vivo* model (e.g., xenograft model) should be used to assess the roles of MCT1 and MCT4 and to support the *in vitro* data found in this thesis. Additionally, genetic knock-out models of HCT116 cells should be generated to support the data obtained using chemical inhibitors.

The data about the roles of MCT1 and MCT4 in regulating lactate and glucose metabolism also have therapeutic implications. In this regard, the functional redundancy in regulating lactate and glucose metabolism indicates that dual inhibition of MCT1 and MCT4 may be necessary to target cancer cells. Indeed, MCT4 expression has been suggested as a resistance mechanism of MCT1 specific inhibitors (*606*). Interestingly, genetic deletion and long-term treatment of inhibitors of MCT1 or MCT4 caused a trend of enhanced expression of the other MCT isoform (*334*). Therefore, dual inhibitors of MCT1 and MCT4 may overcome such

resistance and adaptation mechanisms. For instance, the combined targeting of MCT1 and MCT4 by MD-1 has been reported to impair mitochondria metabolism and inhibit tumour growth of feline oral squamous cell carcinoma (*651*). Thus, it would be interesting to examine the efficacy of MD-1 in HCT116 cells that co-express MCT1 and MCT4.

Blocking MCT1 and MCT4 may also impact the TME. In this regard, high lactate concentrations in the TME produced by cancer cells impair anti-tumour immunity (*652*). For instance, MCT1/4 mediated lactate efflux skews macrophage polarization towards the immunosuppressive M2 phenotype (*653-655*). Indeed, MCT1 and MCT4 silencing in melanoma cells has been shown to inhibit lactate efflux, enhance T cell function and boost the efficacy of immune checkpoint inhibitors (ICB) (*604*). However, MCT1-mediated lactate efflux is essential for cytokine production and cytotoxicity of $CD8^+$ T cells (*656*). Indeed, single MCT4 blockage enhanced the efficacy of ICB in MC38 murine model of colon cancer (*604*). However, the dual inhibition of MCT1 and MCT4 failed to further increase ICB efficacy (*604*). Thus, it would be interesting to investigate the roles of MCT1 and MCT4 in modulating anti-cancer immunity in other types of cancer.

In addition, MCT1 has been reported to promote metastasis in a model of melanoma (*657*). In this regard, MCT1 inhibition had minimal impact on primary tu mour cells but caused a reduction in circulating tumour cells (*657*). Mechanistically, inhibition of MCT1 altered the redox balance and oxidative stress as evidenced by increased NAD^+/NADH ratio (*657*). Interestingly, MCT1 expression was low in primary site but upregulated in metastatic lesions of osteosarcoma (*334*). However, it remains unclear about the roles of MCT4 in metastasis and thus, additional research is needed.

7.5 Conclusions

This study highlights the roles of the PI3K/Akt signalling in regulating cellular metabolism in a mouse model of ovarian HGSC. In particular, Pten loss enhanced glycolysis, and modulated NAD^+ metabolism and arginine synthesis. Furthermore, we highlight that such metabolic

reprogramming induced by hyperactive PI3K and Ras signalling may create a metabolic bottleneck which can be therapeutically exploited by dual inhibition of NAMPT and PARP. Finally, we highlight the functional redundancy and heterogeneity of MCT1 and MCT4 in colorectal cancer cells, which suggests that dual targeting may be necessary for therapeutic purposes.

Reference

1. O. Warburg, S. Minami, Versuche an Überlebendem Carcinom-gewebe. *Klinische Wochenschrift* **2**, 776-777 (1923).
2. M. V. Liberti, J. W. Locasale, The Warburg Effect: How Does it Benefit Cancer Cells? *Trends Biochem Sci* **41**, 211-218 (2016).
3. D. Hanahan, R. A. Weinberg, Hallmarks of cancer: the next generation. *Cell* **144**, 646-674 (2011).
4. R. J. DeBerardinis, N. S. Chandel, Fundamentals of cancer metabolism. *Sci Adv* **2**, e1600200 (2016).
5. N. N. Pavlova, J. Zhu, C. B. Thompson, The hallmarks of cancer metabolism: Still emerging. *Cell Metab* **34**, 355-377 (2022).
6. A. M. Navale, A. N. Paranjape, Glucose transporters: physiological and pathological roles. *Biophys Rev* **8**, 5-9 (2016).
7. X. M. Luo, S. H. Zhou, J. Fan, Glucose transporter-1 as a new therapeutic target in laryngeal carcinoma. *J Int Med Res* **38**, 1885-1892 (2010).
8. A. N. McCracken, A. L. Edinger, Nutrient transporters: the Achilles' heel of anabolism. *Trends in Endocrinology & Metabolism* **24**, 200-208 (2013).
9. I. A. Simpson *et al.*, The facilitative glucose transporter GLUT3: 20 years of distinction. *Am J Physiol Endocrinol Metab* **295**, E242-253 (2008).
10. V. Ganapathy, M. Thangaraju, P. D. Prasad, Nutrient transporters in cancer: Relevance to Warburg hypothesis and beyond. *Pharmacology & Therapeutics* **121**, 29-40 (2009).
11. M. Sastrasinh, S. Sastrasinh, Effect of acute pH change on mitochondrial glutamine transport. *Am J Physiol* **259**, F863-866 (1990).
12. M. Hassanein *et al.*, SLC1A5 mediates glutamine transport required for lung cancer cell growth and survival. *Clin Cancer Res* **19**, 560-570 (2013).
13. X. Li *et al.*, Role of glutamine and its metabolite ammonia in crosstalk of cancer-associated fibroblasts and cancer cells. *Cancer Cell Int* **21**, 479 (2021).
14. M. van Geldermalsen *et al.*, ASCT2/SLC1A5 controls glutamine uptake and tumour growth in triple-negative basal-like breast cancer. *Oncogene* **35**, 3201-3208 (2016).
15. H. Okudaira *et al.*, Putative transport mechanism and intracellular fate of trans-1-amino-3-18F-fluorocyclobutanecarboxylic acid in human prostate cancer. *J Nucl Med* **52**, 822-829 (2011).
16. M. Morotti *et al.*, Increased expression of glutamine transporter SNAT2/SLC38A2 promotes glutamine dependence and oxidative stress resistance, and is associated with worse prognosis in triple-negative breast cancer. *Br J Cancer* **124**, 494-505 (2021).
17. I. Böhme-Schäfer, S. Lörentz, A. K. Bosserhoff, Role of Amino Acid Transporter SNAT1/SLC38A1 in Human Melanoma. *Cancers (Basel)* **14**, (2022).
18. F. F. Zhou *et al.*, SLC38A1 promotes proliferation and migration of human colorectal cancer cells. *J Huazhong Univ Sci Technolog Med Sci* **37**, 30-36 (2017).
19. T. Nakanishi *et al.*, Structure, function, and tissue expression pattern of human SN2, a subtype of the amino acid transport system N. *Biochem Biophys Res Commun* **281**, 1343-1348 (2001).

20. T. Nakanishi *et al.*, Cloning and functional characterization of a new subtype of the amino acid transport system N. *Am J Physiol Cell Physiol* **281**, C1757-1768 (2001).
21. N. Gupta *et al.*, Upregulation of the amino acid transporter ATB0,+ (SLC6A14) in colorectal cancer and metastasis in humans. *Biochim Biophys Acta* **1741**, 215-223 (2005).
22. N. Gupta *et al.*, Up-regulation of the amino acid transporter ATB(0,+) (SLC6A14) in carcinoma of the cervix. *Gynecol Oncol* **100**, 8-13 (2006).
23. S. Karunakaran *et al.*, Interaction of tryptophan derivatives with SLC6A14 (ATB0,+) reveals the potential of the transporter as a drug target for cancer chemotherapy. *Biochem J* **414**, 343-355 (2008).
24. Q. Wang, J. Holst, L-type amino acid transport and cancer: targeting the mTORC1 pathway to inhibit neoplasia. *Am J Cancer Res* **5**, 1281-1294 (2015).
25. M. Nachef, A. K. Ali, S. M. Almutairi, S. H. Lee, Targeting SLC1A5 and SLC3A2/SLC7A5 as a Potential Strategy to Strengthen Anti-Tumor Immunity in the Tumor Microenvironment. *Front Immunol* **12**, 624324 (2021).
26. M. T. Snaebjornsson, S. Janaki-Raman, A. Schulze, Greasing the Wheels of the Cancer Machine: The Role of Lipid Metabolism in Cancer. *Cell Metabolism* **31**, 62-76 (2020).
27. N. Koundouros, G. Poulogiannis, Reprogramming of fatty acid metabolism in cancer. *British Journal of Cancer* **122**, 4-22 (2020).
28. R. J. Deberardinis, N. Sayed, D. Ditsworth, C. B. Thompson, Brick by brick: metabolism and tumor cell growth. *Curr Opin Genet Dev* **18**, 54-61 (2008).
29. V. Chajès, M. Cambot, K. Moreau, G. M. Lenoir, V. Joulin, Acetyl-CoA carboxylase alpha is essential to breast cancer cell survival. *Cancer Res* **66**, 5287-5294 (2006).
30. K. Brusselmans, E. De Schrijver, G. Verhoeven, J. V. Swinnen, RNA interference-mediated silencing of the acetyl-CoA-carboxylase-alpha gene induces growth inhibition and apoptosis of prostate cancer cells. *Cancer Res* **65**, 6719-6725 (2005).
31. G. Hatzivassiliou *et al.*, ATP citrate lyase inhibition can suppress tumor cell growth. *Cancer Cell* **8**, 311-321 (2005).
32. E. S. Pizer *et al.*, Inhibition of fatty acid synthesis delays disease progression in a xenograft model of ovarian cancer. *Cancer Res* **56**, 1189-1193 (1996).
33. F. P. Kuhajda *et al.*, Fatty acid synthesis: a potential selective target for antineoplastic therapy. *Proc Natl Acad Sci U S A* **91**, 6379-6383 (1994).
34. F. Pietrocola, L. Galluzzi, José M. Bravo-San Pedro, F. Madeo, G. Kroemer, Acetyl Coenzyme A: A Central Metabolite and Second Messenger. *Cell Metabolism* **21**, 805-821 (2015).
35. A. R. Mullen *et al.*, Reductive carboxylation supports growth in tumour cells with defective mitochondria. *Nature* **481**, 385-388 (2011).
36. S. R. Nagarajan, L. M. Butler, A. J. Hoy, The diversity and breadth of cancer cell fatty acid metabolism. *Cancer & Metabolism* **9**, 2 (2021).
37. R. J. DeBerardinis *et al.*, Beyond aerobic glycolysis: Transformed cells can engage in glutamine metabolism that exceeds the requirement for protein and nucleotide synthesis. *Proceedings of the National Academy of Sciences* **104**, 19345-19350 (2007).
38. Z. T. Schug *et al.*, Acetyl-CoA synthetase 2 promotes acetate utilization and maintains cancer cell growth under metabolic stress. *Cancer Cell* **27**, 57-71 (2015).
39. M. Inigo, S. Deja, S. C. Burgess, Ins and Outs of the TCA Cycle: The Central Role of

Anaplerosis. *Annu Rev Nutr* **41**, 19-47 (2021).
40. J. Fan *et al.*, Quantitative flux analysis reveals folate-dependent NADPH production. *Nature* **510**, 298-302 (2014).
41. C. A. Lewis *et al.*, Tracing compartmentalized NADPH metabolism in the cytosol and mitochondria of mammalian cells. *Mol Cell* **55**, 253-263 (2014).
42. A. Benito *et al.*, Glucose-6-phosphate dehydrogenase and transketolase modulate breast cancer cell metabolic reprogramming and correlate with poor patient outcome. *Oncotarget* **8**, 106693-106706 (2017).
43. X. Wang *et al.*, Glucose-6-phosphate dehydrogenase expression is correlated with poor clinical prognosis in esophageal squamous cell carcinoma. *European Journal of Surgical Oncology (EJSO)* **41**, 1293-1299 (2015).
44. R. Nagashio *et al.*, Prognostic significance of G6PD expression and localization in lung adenocarcinoma. *Biochimica et Biophysica Acta (BBA) - Proteins and Proteomics* **1867**, 38-46 (2019).
45. L. M. Fernandes *et al.*, Malic Enzyme 1 (ME1) is pro-oncogenic in ApcMin/+ mice. *Scientific Reports* **8**, 14268 (2018).
46. C. Shao *et al.*, Cytosolic ME1 integrated with mitochondrial IDH2 supports tumor growth and metastasis. *Redox Biology* **36**, 101685 (2020).
47. A. E. Calvert *et al.*, Cancer-Associated IDH1 Promotes Growth and Resistance to Targeted Therapies in the Absence of Mutation. *Cell Reports* **19**, 1858-1873 (2017).
48. N. Pardo-Lorente, S. Sdelci, MTHFD2 in healthy and cancer cells: Canonical and non-canonical functions. *npj Metabolic Health and Disease* **2**, 3 (2024).
49. H.-Q. Ju *et al.*, Modulation of Redox Homeostasis by Inhibition of MTHFD2 in Colorectal Cancer: Mechanisms and Therapeutic Implications. *JNCI: Journal of the National Cancer Institute* **111**, 584-596 (2019).
50. E. L. Lieu, T. Nguyen, S. Rhyne, J. Kim, Amino acids in cancer. *Exp Mol Med* **52**, 15-30 (2020).
51. N. Vié *et al.*, Overexpression of phosphoserine aminotransferase PSAT1 stimulates cell growth and increases chemoresistance of colon cancer cells. *Molecular Cancer* **7**, 14 (2008).
52. N. Vidula, C. Yau, H. S. Rugo, Glutaminase (GLS1) gene expression in primary breast cancer. *Breast Cancer* **30**, 1079-1084 (2023).
53. L. Xiang *et al.*, Glutaminase 1 expression in colorectal cancer cells is induced by hypoxia and required for tumor growth, invasion, and metastatic colonization. *Cell Death Dis* **10**, 40 (2019).
54. M. Chiu, G. Taurino, M. G. Bianchi, M. S. Kilberg, O. Bussolati, Asparagine Synthetase in Cancer: Beyond Acute Lymphoblastic Leukemia. *Front Oncol* **9**, 1480 (2019).
55. T. Takahara, Y. Amemiya, R. Sugiyama, M. Maki, H. Shibata, Amino acid-dependent control of mTORC1 signaling: a variety of regulatory modes. *Journal of Biomedical Science* **27**, 87 (2020).
56. D. Meng *et al.*, Glutamine and asparagine activate mTORC1 independently of Rag GTPases. *J Biol Chem* **295**, 2890-2899 (2020).
57. A. Stincone *et al.*, The return of metabolism: biochemistry and physiology of the pentose phosphate pathway. *Biol Rev Camb Philos Soc* **90**, 927-963 (2015).

58. H. Ying *et al.*, Oncogenic Kras maintains pancreatic tumors through regulation of anabolic glucose metabolism. *Cell* **149**, 656-670 (2012).
59. I. M.-J. Xu *et al.*, Transketolase counteracts oxidative stress to drive cancer development. *Proceedings of the National Academy of Sciences* **113**, E725-E734 (2016).
60. C. Wang *et al.*, Identification of transaldolase as a novel serum biomarker for hepatocellular carcinoma metastasis using xenografted mouse model and clinic samples. *Cancer Lett* **313**, 154-166 (2011).
61. M. M. Zarou, A. Vazquez, G. Vignir Helgason, Folate metabolism: a re-emerging therapeutic target in haematological cancers. *Leukemia* **35**, 1539-1551 (2021).
62. R. Nilsson *et al.*, Metabolic enzyme expression highlights a key role for MTHFD2 and the mitochondrial folate pathway in cancer. *Nature Communications* **5**, 3128 (2014).
63. J. Koseki *et al.*, Enzymes of the one-carbon folate metabolism as anticancer targets predicted by survival rate analysis. *Sci Rep* **8**, 303 (2018).
64. J. D. Hayes, A. T. Dinkova-Kostova, K. D. Tew, Oxidative Stress in Cancer. *Cancer Cell* **38**, 167-197 (2020).
65. M. Schieber, Navdeep S. Chandel, ROS Function in Redox Signaling and Oxidative Stress. *Current Biology* **24**, R453-R462 (2014).
66. M. P. Murphy, How mitochondria produce reactive oxygen species. *Biochem J* **417**, 1-13 (2009).
67. M. P. Murphy, Mitochondrial thiols in antioxidant protection and redox signaling: distinct roles for glutathionylation and other thiol modifications. *Antioxid Redox Signal* **16**, 476-495 (2012).
68. T. Finkel, From sulfenylation to sulfhydration: what a thiolate needs to tolerate. *Sci Signal* **5**, pe10 (2012).
69. Y. M. Janssen-Heininger *et al.*, Redox-based regulation of signal transduction: principles, pitfalls, and promises. *Free Radic Biol Med* **45**, 1-17 (2008).
70. E. Naik, V. M. Dixit, Mitochondrial reactive oxygen species drive proinflammatory cytokine production. *J Exp Med* **208**, 417-420 (2011).
71. H. Sies, C. Berndt, D. P. Jones, Oxidative Stress. *Annual Review of Biochemistry* **86**, 715-748 (2017).
72. M. C. Jaramillo, D. D. Zhang, The emerging role of the Nrf2-Keap1 signaling pathway in cancer. *Genes Dev* **27**, 2179-2191 (2013).
73. G. Hoxhaj *et al.*, Direct stimulation of NADP⁺ synthesis through Akt-mediated phosphorylation of NAD kinase. *Science* **363**, 1088-1092 (2019).
74. I. Pérez-Torres, V. Guarner-Lans, M. E. Rubio-Ruiz, Reductive Stress in Inflammation-Associated Diseases and the Pro-Oxidant Effect of Antioxidant Agents. *International Journal of Molecular Sciences* **18**, 2098 (2017).
75. R. P. Goodman *et al.*, Hepatic NADH reductive stress underlies common variation in metabolic traits. *Nature* **583**, 122-126 (2020).
76. L. Zhang, K. D. Tew, in *Advances in Cancer Research,* K. D. Tew, P. B. Fisher, Eds. (Academic Press, 2021), vol. 152, pp. 383-413.
77. H. Zhang *et al.*, Glutathione-dependent reductive stress triggers mitochondrial oxidation and cytotoxicity. *Faseb j* **26**, 1442-1451 (2012).
78. X. Zhang *et al.*, Involvement of reductive stress in the cardiomyopathy in transgenic mice

with cardiac-specific overexpression of heat shock protein 27. *Hypertension* **55**, 1412-1417 (2010).
79. T. Weiss-Sadan *et al.*, NRF2 activation induces NADH-reductive stress, providing a metabolic vulnerability in lung cancer. *Cell Metabolism* **35**, 487-503.e487 (2023).
80. N. S. Rajasekaran *et al.*, Human αB-Crystallin Mutation Causes Oxido-Reductive Stress and Protein Aggregation Cardiomyopathy in Mice. *Cell* **130**, 427-439 (2007).
81. M. Ge, T. Papagiannakopoulos, L. Bar-Peled, Reductive stress in cancer: coming out of the shadows. *Trends in Cancer* **10**, 103-112 (2024).
82. M. S. Lawrence *et al.*, Discovery and saturation analysis of cancer genes across 21 tumour types. *Nature* **505**, 495-501 (2014).
83. G. Hoxhaj, B. D. Manning, The PI3K–AKT network at the interface of oncogenic signalling and cancer metabolism. *Nature Reviews Cancer* **20**, 74-88 (2020).
84. J. Schlessinger, Cell signaling by receptor tyrosine kinases. *Cell* **103**, 211-225 (2000).
85. J. A. Engelman, J. Luo, L. C. Cantley, The evolution of phosphatidylinositol 3-kinases as regulators of growth and metabolism. *Nat Rev Genet* **7**, 606-619 (2006).
86. R. Katso *et al.*, Cellular function of phosphoinositide 3-kinases: implications for development, homeostasis, and cancer. *Annu Rev Cell Dev Biol* **17**, 615-675 (2001).
87. S. Jean, A. A. Kiger, Classes of phosphoinositide 3-kinases at a glance. *J Cell Sci* **127**, 923-928 (2014).
88. L. M. Thorpe, H. Yuzugullu, J. J. Zhao, PI3K in cancer: divergent roles of isoforms, modes of activation and therapeutic targeting. *Nat Rev Cancer* **15**, 7-24 (2015).
89. Y. Shi, B. E. Paluch, X. Wang, X. Jiang, PTEN at a glance. *J Cell Sci* **125**, 4687-4692 (2012).
90. D. A. Fruman *et al.*, The PI3K Pathway in Human Disease. *Cell* **170**, 605-635 (2017).
91. D. R. Alessi *et al.*, Mechanism of activation of protein kinase B by insulin and IGF-1. *Embo j* **15**, 6541-6551 (1996).
92. D. R. Alessi *et al.*, Characterization of a 3-phosphoinositide-dependent protein kinase which phosphorylates and activates protein kinase Balpha. *Curr Biol* **7**, 261-269 (1997).
93. D. D. Sarbassov, D. A. Guertin, S. M. Ali, D. M. Sabatini, Phosphorylation and regulation of Akt/PKB by the rictor-mTOR complex. *Science* **307**, 1098-1101 (2005).
94. B. Dummler, B. A. Hemmings, Physiological roles of PKB/Akt isoforms in development and disease. *Biochem Soc Trans* **35**, 231-235 (2007).
95. B. D. Manning, A. Toker, AKT/PKB Signaling: Navigating the Network. *Cell* **169**, 381-405 (2017).
96. G. Hoxhaj, B. D. Manning, The PI3K-AKT network at the interface of oncogenic signalling and cancer metabolism. *Nat Rev Cancer* **20**, 74-88 (2020).
97. R. M. Memmott, P. A. Dennis, Akt-dependent and -independent mechanisms of mTOR regulation in cancer. *Cell Signal* **21**, 656-664 (2009).
98. A. J. Valvezan, B. D. Manning, Molecular logic of mTORC1 signalling as a metabolic rheostat. *Nature Metabolism* **1**, 321-333 (2019).
99. S. Menon *et al.*, Spatial control of the TSC complex integrates insulin and nutrient regulation of mTORC1 at the lysosome. *Cell* **156**, 771-785 (2014).
100. A. Szwed, E. Kim, E. Jacinto, Regulation and metabolic functions of mTORC1 and mTORC2. *Physiological Reviews* **101**, 1371-1426 (2021).
101. D. A. Cross, D. R. Alessi, P. Cohen, M. Andjelkovich, B. A. Hemmings, Inhibition of glycogen

synthase kinase-3 by insulin mediated by protein kinase B. *Nature* **378**, 785-789 (1995).
102. S. Frame, P. Cohen, R. M. Biondi, A common phosphate binding site explains the unique substrate specificity of GSK3 and its inactivation by phosphorylation. *Mol Cell* **7**, 1321-1327 (2001).
103. C. Sutherland, What Are the bona fide GSK3 Substrates? *Int J Alzheimers Dis* **2011**, 505607 (2011).
104. Y. Jiramongkol, E. W. Lam, FOXO transcription factor family in cancer and metastasis. *Cancer Metastasis Rev* **39**, 681-709 (2020).
105. A. Brunet *et al.*, Akt promotes cell survival by phosphorylating and inhibiting a Forkhead transcription factor. *Cell* **96**, 857-868 (1999).
106. R. Augustin, The protein family of glucose transport facilitators: It's not only about glucose after all. *IUBMB Life* **62**, 315-333 (2010).
107. A. N. Waldhart *et al.*, Phosphorylation of TXNIP by AKT Mediates Acute Influx of Glucose in Response to Insulin. *Cell Rep* **19**, 2005-2013 (2017).
108. N. Wu *et al.*, AMPK-dependent degradation of TXNIP upon energy stress leads to enhanced glucose uptake via GLUT1. *Mol Cell* **49**, 1167-1175 (2013).
109. S. Y. Hong, F. X. Yu, Y. Luo, T. Hagen, Oncogenic activation of the PI3K/Akt pathway promotes cellular glucose uptake by downregulating the expression of thioredoxin-interacting protein. *Cell Signal* **28**, 377-383 (2016).
110. D. J. Roberts, V. P. Tan-Sah, J. M. Smith, S. Miyamoto, Akt phosphorylates HK-II at Thr-473 and increases mitochondrial HK-II association to protect cardiomyocytes. *J Biol Chem* **288**, 23798-23806 (2013).
111. K. Gottlob *et al.*, Inhibition of early apoptotic events by Akt/PKB is dependent on the first committed step of glycolysis and mitochondrial hexokinase. *Genes Dev* **15**, 1406-1418 (2001).
112. J. Deprez, D. Vertommen, D. R. Alessi, L. Hue, M. H. Rider, Phosphorylation and activation of heart 6-phosphofructo-2-kinase by protein kinase B and other protein kinases of the insulin signaling cascades. *J Biol Chem* **272**, 17269-17275 (1997).
113. L. Hue, M. H. Rider, Role of fructose 2,6-bisphosphate in the control of glycolysis in mammalian tissues. *Biochem J* **245**, 313-324 (1987).
114. G. V. Thomas *et al.*, Hypoxia-inducible factor determines sensitivity to inhibitors of mTOR in kidney cancer. *Nat Med* **12**, 122-127 (2006).
115. E. Laughner, P. Taghavi, K. Chiles, P. C. Mahon, G. L. Semenza, HER2 (neu) signaling increases the rate of hypoxia-inducible factor 1alpha (HIF-1alpha) synthesis: novel mechanism for HIF-1-mediated vascular endothelial growth factor expression. *Mol Cell Biol* **21**, 3995-4004 (2001).
116. K. Düvel *et al.*, Activation of a metabolic gene regulatory network downstream of mTOR complex 1. *Mol Cell* **39**, 171-183 (2010).
117. G. L. Semenza, Targeting HIF-1 for cancer therapy. *Nat Rev Cancer* **3**, 721-732 (2003).
118. Z. E. Stine, Z. E. Walton, B. J. Altman, A. L. Hsieh, C. V. Dang, MYC, Metabolism, and Cancer. *Cancer Discov* **5**, 1024-1039 (2015).
119. M. J. West, M. Stoneley, A. E. Willis, Translational induction of the c-myc oncogene via activation of the FRAP/TOR signalling pathway. *Oncogene* **17**, 769-780 (1998).
120. A. Csibi *et al.*, The mTORC1/S6K1 pathway regulates glutamine metabolism through the

eIF4B-dependent control of c-Myc translation. *Curr Biol* **24**, 2274-2280 (2014).

121. M. Welcker *et al.*, The Fbw7 tumor suppressor regulates glycogen synthase kinase 3 phosphorylation-dependent c-Myc protein degradation. *Proc Natl Acad Sci U S A* **101**, 9085-9090 (2004).
122. M. A. Gregory, Y. Qi, S. R. Hann, Phosphorylation by glycogen synthase kinase-3 controls c-myc proteolysis and subnuclear localization. *J Biol Chem* **278**, 51606-51612 (2003).
123. R. Sears *et al.*, Multiple Ras-dependent phosphorylation pathways regulate Myc protein stability. *Genes Dev* **14**, 2501-2514 (2000).
124. W. Zhang *et al.*, FoxO1 regulates multiple metabolic pathways in the liver: effects on gluconeogenic, glycolytic, and lipogenic gene expression. *J Biol Chem* **281**, 10105-10117 (2006).
125. K. S. Jensen *et al.*, FoxO3A promotes metabolic adaptation to hypoxia by antagonizing Myc function. *Embo j* **30**, 4554-4570 (2011).
126. C. Bouchard, J. Marquardt, A. Brás, R. H. Medema, M. Eilers, Myc-induced proliferation and transformation require Akt-mediated phosphorylation of FoxO proteins. *Embo j* **23**, 2830-2840 (2004).
127. I. A. Potapova, M. R. El-Maghrabi, S. V. Doronin, W. B. Benjamin, Phosphorylation of recombinant human ATP:citrate lyase by cAMP-dependent protein kinase abolishes homotropic allosteric regulation of the enzyme by citrate and increases the enzyme activity. Allosteric activation of ATP:citrate lyase by phosphorylated sugars. *Biochemistry* **39**, 1169-1179 (2000).
128. D. C. Berwick, I. Hers, K. J. Heesom, S. K. Moule, J. M. Tavare, The identification of ATP-citrate lyase as a protein kinase B (Akt) substrate in primary adipocytes. *J Biol Chem* **277**, 33895-33900 (2002).
129. J. D. Horton, J. L. Goldstein, M. S. Brown, SREBPs: activators of the complete program of cholesterol and fatty acid synthesis in the liver. *J Clin Invest* **109**, 1125-1131 (2002).
130. D. Kim *et al.*, AKT/PKB signaling mechanisms in cancer and chemoresistance. *Front Biosci* **10**, 975-987 (2005).
131. J. L. Yecies *et al.*, Akt stimulates hepatic SREBP1c and lipogenesis through parallel mTORC1-dependent and independent pathways. *Cell Metab* **14**, 21-32 (2011).
132. S. J. Ricoult, J. L. Yecies, I. Ben-Sahra, B. D. Manning, Oncogenic PI3K and K-Ras stimulate de novo lipid synthesis through mTORC1 and SREBP. *Oncogene* **35**, 1250-1260 (2016).
133. K. H. Kim *et al.*, Regulatory role of glycogen synthase kinase 3 for transcriptional activity of ADD1/SREBP1c. *J Biol Chem* **279**, 51999-52006 (2004).
134. A. Sundqvist *et al.*, Control of lipid metabolism by phosphorylation-dependent degradation of the SREBP family of transcription factors by SCF(Fbw7). *Cell Metab* **1**, 379-391 (2005).
135. A. M. Gouw *et al.*, The MYC Oncogene Cooperates with Sterol-Regulated Element-Binding Protein to Regulate Lipogenesis Essential for Neoplastic Growth. *Cell Metab* **30**, 556-572.e555 (2019).
136. A. Saha *et al.*, Akt phosphorylation and regulation of transketolase is a nodal point for amino acid control of purine synthesis. *Mol Cell* **55**, 264-276 (2014).
137. I. Ben-Sahra, J. J. Howell, J. M. Asara, B. D. Manning, Stimulation of de novo pyrimidine synthesis by growth signaling through mTOR and S6K1. *Science* **339**, 1323-1328 (2013).

138. A. M. Robitaille *et al.*, Quantitative phosphoproteomics reveal mTORC1 activates de novo pyrimidine synthesis. *Science* **339**, 1320-1323 (2013).
139. I. Ben-Sahra, G. Hoxhaj, S. J. H. Ricoult, J. M. Asara, B. D. Manning, mTORC1 induces purine synthesis through control of the mitochondrial tetrahydrofolate cycle. *Science* **351**, 728-733 (2016).
140. Y. C. Liu *et al.*, Global regulation of nucleotide biosynthetic genes by c-Myc. *PLoS One* **3**, e2722 (2008).
141. K. Hayashi, P. Jutabha, H. Endou, N. Anzai, c-Myc is crucial for the expression of LAT1 in MIA Paca-2 human pancreatic cancer cells. *Oncol Rep* **28**, 862-866 (2012).
142. D. R. Wise *et al.*, Myc regulates a transcriptional program that stimulates mitochondrial glutaminolysis and leads to glutamine addiction. *Proc Natl Acad Sci U S A* **105**, 18782-18787 (2008).
143. Y. Park, A. Reyna-Neyra, L. Philippe, C. C. Thoreen, mTORC1 Balances Cellular Amino Acid Supply with Demand for Protein Synthesis through Post-transcriptional Control of ATF4. *Cell Rep* **19**, 1083-1090 (2017).
144. M. E. Torrence *et al.*, The mTORC1-mediated activation of ATF4 promotes protein and glutathione synthesis downstream of growth signals. *Elife* **10**, (2021).
145. I. Shimomura, H. Shimano, B. S. Korn, Y. Bashmakov, J. D. Horton, Nuclear sterol regulatory element-binding proteins activate genes responsible for the entire program of unsaturated fatty acid biosynthesis in transgenic mouse liver. *J Biol Chem* **273**, 35299-35306 (1998).
146. S. J. Ricoult, C. C. Dibble, J. M. Asara, B. D. Manning, Sterol Regulatory Element Binding Protein Regulates the Expression and Metabolic Functions of Wild-Type and Oncogenic IDH1. *Mol Cell Biol* **36**, 2384-2395 (2016).
147. P. Rada *et al.*, SCF/{beta}-TrCP promotes glycogen synthase kinase 3-dependent degradation of the Nrf2 transcription factor in a Keap1-independent manner. *Mol Cell Biol* **31**, 1121-1133 (2011).
148. C. Tonelli, I. I. C. Chio, D. A. Tuveson, Transcriptional Regulation by Nrf2. *Antioxid Redox Signal* **29**, 1727-1745 (2018).
149. Y. Mitsuishi *et al.*, Nrf2 redirects glucose and glutamine into anabolic pathways in metabolic reprogramming. *Cancer Cell* **22**, 66-79 (2012).
150. H. Sasaki *et al.*, Electrophile response element-mediated induction of the cystine/glutamate exchange transporter gene expression. *J Biol Chem* **277**, 44765-44771 (2002).
151. H. R. Moinova, R. T. Mulcahy, Up-regulation of the human gamma-glutamylcysteine synthetase regulatory subunit gene involves binding of Nrf-2 to an electrophile responsive element. *Biochem Biophys Res Commun* **261**, 661-668 (1999).
152. A. C. Wild, H. R. Moinova, R. T. Mulcahy, Regulation of γ-Glutamylcysteine Synthetase Subunit Gene Expression by the Transcription Factor Nrf2*. *Journal of Biological Chemistry* **274**, 33627-33636 (1999).
153. G. C. Jayson, E. C. Kohn, H. C. Kitchener, J. A. Ledermann, Ovarian cancer. *The Lancet* **384**, 1376-1388 (2014).
154. D. Jelovac, D. K. Armstrong, Recent progress in the diagnosis and treatment of ovarian cancer. *CA: a cancer journal for clinicians* **61**, 183-203 (2011).

155. S. Lheureux, C. Gourley, I. Vergote, A. M. Oza, Epithelial ovarian cancer. *Lancet* **393**, 1240-1253 (2019).
156. R. L. Hollis, Molecular characteristics and clinical behaviour of epithelial ovarian cancers. *Cancer Lett* **555**, 216057 (2023).
157. D. D. Bowtell *et al.*, Rethinking ovarian cancer II: reducing mortality from high-grade serous ovarian cancer. *Nature reviews Cancer* **15**, 668-679 (2015).
158. R. J. Kurman, M. Shih Ie, Molecular pathogenesis and extraovarian origin of epithelial ovarian cancer--shifting the paradigm. *Hum Pathol* **42**, 918-931 (2011).
159. U. A. Matulonis *et al.*, Ovarian cancer. *Nature Reviews Disease Primers* **2**, 16061 (2016).
160. M. K. Ediriweera, K. H. Tennekoon, S. R. Samarakoon, Role of the PI3K/AKT/mTOR signaling pathway in ovarian cancer: Biological and therapeutic significance. *Semin Cancer Biol* **59**, 147-160 (2019).
161. J. Downward, Targeting RAS signalling pathways in cancer therapy. *Nat Rev Cancer* **3**, 11-22 (2003).
162. G. W. Reuther, C. J. Der, The Ras branch of small GTPases: Ras family members don't fall far from the tree. *Curr Opin Cell Biol* **12**, 157-165 (2000).
163. C. Anastasaki, P. Orozco, D. H. Gutmann, RAS and beyond: the many faces of the neurofibromatosis type 1 protein. *Dis Model Mech* **15**, (2022).
164. J. M. Shields, K. Pruitt, A. McFall, A. Shaub, C. J. Der, Understanding Ras: 'it ain't over 'til it's over'. *Trends Cell Biol* **10**, 147-154 (2000).
165. R. L. Hollis, C. Gourley, Genetic and molecular changes in ovarian cancer. *Cancer Biol Med* **13**, 236-247 (2016).
166. A. Gadducci, S. Cosio, Therapeutic Approach to Low-Grade Serous Ovarian Carcinoma: State of Art and Perspectives of Clinical Research. *Cancers (Basel)* **12**, (2020).
167. A. De Luca, M. R. Maiello, A. D'Alessio, M. Pergameno, N. Normanno, The RAS/RAF/MEK/ERK and the PI3K/AKT signalling pathways: role in cancer pathogenesis and implications for therapeutic approaches. *Expert Opin Ther Targets* **16 Suppl 2**, S17-27 (2012).
168. L. Huang, Z. Guo, F. Wang, L. Fu, KRAS mutation: from undruggable to druggable in cancer. *Signal Transduct Target Ther* **6**, 386 (2021).
169. C. G. A. R. Network, Integrated genomic analyses of ovarian carcinoma. *Nature* **474**, 609 (2011).
170. P. Smith *et al.*, The copy number and mutational landscape of recurrent ovarian high-grade serous carcinoma. *Nature Communications* **14**, 4387 (2023).
171. E. Colic, P. U. Patel, O. A. Kent, Aberrant MAPK Signaling Offers Therapeutic Potential for Treatment of Ovarian Carcinoma. *Onco Targets Ther* **15**, 1331-1346 (2022).
172. Integrated genomic analyses of ovarian carcinoma. *Nature* **474**, 609-615 (2011).
173. T. Moujaber *et al.*, BRAF Mutations in Low-Grade Serous Ovarian Cancer and Response to BRAF Inhibition. *JCO Precision Oncology*, 1-14 (2018).
174. M. H. Chui *et al.*, Spectrum of BRAF Mutations and Gene Rearrangements in Ovarian Serous Carcinoma. *JCO Precis Oncol* **5**, (2021).
175. P. Morice, S. Gouy, A. Leary, Mucinous Ovarian Carcinoma. *New England Journal of Medicine* **380**, 1256-1266 (2019).
176. J. M. Reyes-González, P. E. Vivas-Mejía, c-MYC and Epithelial Ovarian Cancer. *Front Oncol*

11, 601512 (2021).
177. A. Bellacosa *et al.*, Molecular alterations of the AKT2 oncogene in ovarian and breast carcinomas. *Int J Cancer* **64**, 280-285 (1995).
178. L. Shayesteh *et al.*, PIK3CA is implicated as an oncogene in ovarian cancer. *Nat Genet* **21**, 99-102 (1999).
179. U. A. Matulonis *et al.*, High throughput interrogation of somatic mutations in high grade serous cancer of the ovary. *PLoS One* **6**, e24433 (2011).
180. I. G. Campbell *et al.*, Mutation of the PIK3CA gene in ovarian and breast cancer. *Cancer Res* **64**, 7678-7681 (2004).
181. K. T. Kuo *et al.*, Frequent activating mutations of PIK3CA in ovarian clear cell carcinoma. *Am J Pathol* **174**, 1597-1601 (2009).
182. K. Obata *et al.*, Frequent PTEN/MMAC mutations in endometrioid but not serous or mucinous epithelial ovarian tumors. *Cancer Res* **58**, 2095-2097 (1998).
183. S. E. Wang *et al.*, HER2 kinase domain mutation results in constitutive phosphorylation and activation of HER2 and EGFR and resistance to EGFR tyrosine kinase inhibitors. *Cancer Cell* **10**, 25-38 (2006).
184. L. E. Kelemen, M. Köbel, Mucinous carcinomas of the ovary and colorectum: different organ, same dilemma. *Lancet Oncol* **12**, 1071-1080 (2011).
185. J. C. Amé, C. Spenlehauer, G. de Murcia, The PARP superfamily. *Bioessays* **26**, 882-893 (2004).
186. B. W. Durkacz, O. Omidiji, D. A. Gray, S. Shall, (ADP-ribose)n participates in DNA excision repair. *Nature* **283**, 593-596 (1980).
187. M. Rouleau, A. Patel, M. J. Hendzel, S. H. Kaufmann, G. G. Poirier, PARP inhibition: PARP1 and beyond. *Nature reviews cancer* **10**, 293-301 (2010).
188. G. Gradwohl *et al.*, The second zinc-finger domain of poly (ADP-ribose) polymerase determines specificity for single-stranded breaks in DNA. *Proceedings of the National Academy of Sciences* **87**, 2990-2994 (1990).
189. P. O. Hassa, M. O. Hottiger, The diverse biological roles of mammalian PARPS, a small but powerful family of poly-ADP-ribose polymerases. *Front Biosci* **13**, 3046-3082 (2008).
190. M. F. Langelier, K. M. Servent, E. E. Rogers, J. M. Pascal, A third zinc-binding domain of human poly(ADP-ribose) polymerase-1 coordinates DNA-dependent enzyme activation. *J Biol Chem* **283**, 4105-4114 (2008).
191. Z. Tao, P. Gao, D. W. Hoffman, H. W. Liu, Domain C of human poly(ADP-ribose) polymerase-1 is important for enzyme activity and contains a novel zinc-ribbon motif. *Biochemistry* **47**, 5804-5813 (2008).
192. M. Altmeyer, S. Messner, P. O. Hassa, M. Fey, M. O. Hottiger, Molecular mechanism of poly(ADP-ribosyl)ation by PARP1 and identification of lysine residues as ADP-ribose acceptor sites. *Nucleic Acids Res* **37**, 3723-3738 (2009).
193. Z. Tao, P. Gao, H.-w. Liu, Identification of the ADP-ribosylation sites in the PARP-1 automodification domain: analysis and implications. *Journal of the American Chemical Society* **131**, 14258-14260 (2009).
194. I. Kameshita, Z. Matsuda, T. Taniguchi, Y. Shizuta, Poly (ADP-ribose) synthetase. *J. Biol. Chem* **259**, 4770-4776 (1984).
195. A. Ray Chaudhuri, A. Nussenzweig, The multifaceted roles of PARP1 in DNA repair and

chromatin remodelling. *Nat Rev Mol Cell Biol* **18**, 610-621 (2017).
196. J. M. Dawicki-McKenna *et al.*, PARP-1 activation requires local unfolding of an autoinhibitory domain. *Molecular cell* **60**, 755-768 (2015).
197. J.-P. Gagne *et al.*, Proteome-wide identification of poly (ADP-ribose) binding proteins and poly (ADP-ribose)-associated protein complexes. *Nucleic acids research* **36**, 6959-6976 (2008).
198. S. Jungmichel *et al.*, Proteome-wide identification of poly(ADP-Ribosyl)ation targets in different genotoxic stress responses. *Mol Cell* **52**, 272-285 (2013).
199. M. Masson *et al.*, XRCC1 is specifically associated with poly(ADP-ribose) polymerase and negatively regulates its activity following DNA damage. *Mol Cell Biol* **18**, 3563-3571 (1998).
200. S. F. El-Khamisy, M. Masutani, H. Suzuki, K. W. Caldecott, A requirement for PARP-1 for the assembly or stability of XRCC1 nuclear foci at sites of oxidative DNA damage. *Nucleic Acids Res* **31**, 5526-5533 (2003).
201. M. Rose, J. T. Burgess, K. O'Byrne, D. J. Richard, E. Bolderson, PARP Inhibitors: Clinical Relevance, Mechanisms of Action and Tumor Resistance. *Frontiers in Cell and Developmental Biology* **8**, 564601 (2020).
202. J. F. Haince *et al.*, Ataxia telangiectasia mutated (ATM) signaling network is modulated by a novel poly(ADP-ribose)-dependent pathway in the early response to DNA-damaging agents. *J Biol Chem* **282**, 16441-16453 (2007).
203. R. Aguilar-Quesada *et al.*, Interaction between ATM and PARP-1 in response to DNA damage and sensitization of ATM deficient cells through PARP inhibition. *BMC Mol Biol* **8**, 29 (2007).
204. H. E. Bryant *et al.*, PARP is activated at stalled forks to mediate Mre11-dependent replication restart and recombination. *Embo j* **28**, 2601-2615 (2009).
205. M. L. Meyer-Ficca, R. G. Meyer, D. L. Coyle, E. L. Jacobson, M. K. Jacobson, Human poly(ADP-ribose) glycohydrolase is expressed in alternative splice variants yielding isoforms that localize to different cell compartments. *Exp Cell Res* **297**, 521-532 (2004).
206. V. Schreiber *et al.*, Poly(ADP-ribose) polymerase-2 (PARP-2) is required for efficient base excision DNA repair in association with PARP-1 and XRCC1. *J Biol Chem* **277**, 23028-23036 (2002).
207. J. Yélamos, V. Schreiber, F. Dantzer, Toward specific functions of poly(ADP-ribose) polymerase-2. *Trends Mol Med* **14**, 169-178 (2008).
208. J. Ménissier de Murcia *et al.*, Functional interaction between PARP-1 and PARP-2 in chromosome stability and embryonic development in mouse. *Embo j* **22**, 2255-2263 (2003).
209. W. M. Shieh *et al.*, Poly(ADP-ribose) polymerase null mouse cells synthesize ADP-ribose polymers. *J Biol Chem* **273**, 30069-30072 (1998).
210. F. R. Sallmann, M. D. Vodenicharov, Z. Q. Wang, G. G. Poirier, Characterization of sPARP-1. An alternative product of PARP-1 gene with poly(ADP-ribose) polymerase activity independent of DNA strand breaks. *J Biol Chem* **275**, 15504-15511 (2000).
211. H. Juarez-Salinas, J. L. Sims, M. K. Jacobson, Poly(ADP-ribose) levels in carcinogen-treated cells. *Nature* **282**, 740-741 (1979).
212. S. J. Berger, D. C. Sudar, N. A. Berger, Metabolic consequences of DNA damage: DNA

damage induces alterations in glucose metabolism by activation of poly (ADP-ribose) polymerase. *Biochem Biophys Res Commun* **134**, 227-232 (1986).

213. D. A. Carson, C. J. Carrera, D. B. Wasson, H. Yamanaka, Programmed cell death and adenine deoxynucleotide metabolism in human lymphocytes. *Adv Enzyme Regul* **27**, 395-404 (1988).
214. W. X. Zong, D. Ditsworth, D. E. Bauer, Z. Q. Wang, C. B. Thompson, Alkylating DNA damage stimulates a regulated form of necrotic cell death. *Genes Dev* **18**, 1272-1282 (2004).
215. C. Del Nagro, Y. Xiao, L. Rangell, M. Reichelt, T. O'Brien, Depletion of the Central Metabolite NAD Leads to Oncosis-mediated Cell Death*. *Journal of Biological Chemistry* **289**, 35182-35192 (2014).
216. J. Guo *et al.*, Unravelling oncosis: morphological and molecular insights into a unique cell death pathway. *Frontiers in Immunology* **15**, (2024).
217. A. Chiarugi, C. Dölle, R. Felici, M. Ziegler, The NAD metabolome—a key determinant of cancer cell biology. *Nature Reviews Cancer* **12**, 741-752 (2012).
218. I. Institute of Medicine Standing Committee on the Scientific Evaluation of Dietary Reference, O. B. V. its Panel on Folate, Choline, in *Dietary Reference Intakes for Thiamin, Riboflavin, Niacin, Vitamin B(6), Folate, Vitamin B(12), Pantothenic Acid, Biotin, and Choline*. (National Academies Press (US)

Copyright © 1998, National Academy of Sciences., Washington (DC), 1998).

219. A. Rongvaux *et al.*, Pre-B-cell colony-enhancing factor, whose expression is up-regulated in activated lymphocytes, is a nicotinamide phosphoribosyltransferase, a cytosolic enzyme involved in NAD biosynthesis. *Eur J Immunol* **32**, 3225-3234 (2002).
220. J. R. Revollo, A. A. Grimm, S. Imai, The NAD biosynthesis pathway mediated by nicotinamide phosphoribosyltransferase regulates Sir2 activity in mammalian cells. *J Biol Chem* **279**, 50754-50763 (2004).
221. B. Samal *et al.*, Cloning and characterization of the cDNA encoding a novel human pre-B-cell colony-enhancing factor. *Mol Cell Biol* **14**, 1431-1437 (1994).
222. P. Bieganowski, C. Brenner, Discoveries of nicotinamide riboside as a nutrient and conserved NRK genes establish a Preiss-Handler independent route to NAD+ in fungi and humans. *Cell* **117**, 495-502 (2004).
223. J. Preiss, P. Handler, Biosynthesis of diphosphopyridine nucleotide. I. Identification of intermediates. *J Biol Chem* **233**, 488-492 (1958).
224. J. Preiss, P. Handler, Biosynthesis of diphosphopyridine nucleotide. II. Enzymatic aspects. *J Biol Chem* **233**, 493-500 (1958).
225. G. Magni, G. Orsomando, N. Raffelli, S. Ruggieri, Enzymology of mammalian NAD metabolism in health and disease. *Front Biosci* **13**, 6135-6154 (2008).
226. F. Berger, C. Lau, M. Dahlmann, M. Ziegler, Subcellular compartmentation and differential catalytic properties of the three human nicotinamide mononucleotide adenylyltransferase isoforms. *J Biol Chem* **280**, 36334-36341 (2005).
227. C. Lau, M. Niere, M. Ziegler, The NMN/NaMN adenylyltransferase (NMNAT) protein family. *Front Biosci (Landmark Ed)* **14**, 410-431 (2009).
228. F. Berger, C. Lau, M. Ziegler, Regulation of poly(ADP-ribose) polymerase 1 activity by the phosphorylation state of the nuclear NAD biosynthetic enzyme NMN adenylyl transferase

1. *Proc Natl Acad Sci U S A* **104**, 3765-3770 (2007).
229. T. Zhang *et al.*, Regulation of poly(ADP-ribose) polymerase-1-dependent gene expression through promoter-directed recruitment of a nuclear NAD+ synthase. *J Biol Chem* **287**, 12405-12416 (2012).
230. F. Berger, M. a. H. Ramı´rez-Hernández, M. Ziegler, The new life of a centenarian: signalling functions of NAD(P). *Trends in Biochemical Sciences* **29**, 111-118 (2004).
231. N. J. O'Neil, M. L. Bailey, P. Hieter, Synthetic lethality and cancer. *Nature Reviews Genetics* **18**, 613-623 (2017).
232. H. E. Bryant *et al.*, Specific killing of BRCA2-deficient tumours with inhibitors of poly(ADP-ribose) polymerase. *Nature* **434**, 913-917 (2005).
233. H. Farmer *et al.*, Targeting the DNA repair defect in BRCA mutant cells as a therapeutic strategy. *Nature* **434**, 917-921 (2005).
234. C. J. Lord, A. Ashworth, PARP inhibitors: Synthetic lethality in the clinic. *Science* **355**, 1152-1158 (2017).
235. I. Brandsma, D. C. Gent, Pathway choice in DNA double strand break repair: observations of a balancing act. *Genome Integr* **3**, 9 (2012).
236. T. Aparicio, R. Baer, J. Gautier, DNA double-strand break repair pathway choice and cancer. *DNA Repair (Amst)* **19**, 169-175 (2014).
237. A. J. Davis, D. J. Chen, DNA double strand break repair via non-homologous end-joining. *Transl Cancer Res* **2**, 130-143 (2013).
238. J. Murai *et al.*, Trapping of PARP1 and PARP2 by Clinical PARP Inhibitors. *Cancer Research* **72**, 5588-5599 (2012).
239. S. J. Pettitt *et al.*, A genetic screen using the PiggyBac transposon in haploid cells identifies Parp1 as a mediator of olaparib toxicity. *PLoS One* **8**, e61520 (2013).
240. Y. Shen *et al.*, BMN 673, a novel and highly potent PARP1/2 inhibitor for the treatment of human cancers with DNA repair deficiency. *Clin Cancer Res* **19**, 5003-5015 (2013).
241. J. Murai *et al.*, Stereospecific PARP trapping by BMN 673 and comparison with olaparib and rucaparib. *Mol Cancer Ther* **13**, 433-443 (2014).
242. Y. Pommier, M. J. O'Connor, J. de Bono, Laying a trap to kill cancer cells: PARP inhibitors and their mechanisms of action. *Sci Transl Med* **8**, 362ps317 (2016).
243. J. Murai *et al.*, Trapping of PARP1 and PARP2 by Clinical PARP Inhibitors. *Cancer Research* **72**, 5588-5599 (2012).
244. J. Murai *et al.*, Rationale for poly(ADP-ribose) polymerase (PARP) inhibitors in combination therapy with camptothecins or temozolomide based on PARP trapping versus catalytic inhibition. *J Pharmacol Exp Ther* **349**, 408-416 (2014).
245. A. George, S. Kaye, S. Banerjee, Delivering widespread BRCA testing and PARP inhibition to patients with ovarian cancer. *Nature reviews Clinical oncology* **14**, 284-296 (2017).
246. Y. E. Choi *et al.*, Platinum and PARP inhibitor resistance due to overexpression of microRNA-622 in BRCA1-mutant ovarian cancer. *Cell reports* **14**, 429-439 (2016).
247. A. Maya-Mendoza *et al.*, High speed of fork progression induces DNA replication stress and genomic instability. *Nature* **559**, 279-284 (2018).
248. A. Quinet, A. Vindigni, Superfast DNA replication causes damage in cancer cells. *Nature* **559**, 186-187 (2018).
249. Y. Wu, S. Xu, S. Cheng, J. Yang, Y. Wang, Clinical application of PARP inhibitors in ovarian

cancer: from molecular mechanisms to the current status. *Journal of Ovarian Research* **16**, 6 (2023).

250. M. Smith, B. Pothuri, Appropriate Selection of PARP Inhibitors in Ovarian Cancer. *Curr Treat Options Oncol* **23**, 887-903 (2022).
251. P. C. Fong *et al.*, Inhibition of poly(ADP-ribose) polymerase in tumors from BRCA mutation carriers. *N Engl J Med* **361**, 123-134 (2009).
252. B. Kaufman *et al.*, Olaparib monotherapy in patients with advanced cancer and a germline BRCA1/2 mutation. *J Clin Oncol* **33**, 244-250 (2015).
253. S. M. Domchek *et al.*, Efficacy and safety of olaparib monotherapy in germline BRCA1/2 mutation carriers with advanced ovarian cancer and three or more lines of prior therapy. *Gynecol Oncol* **140**, 199-203 (2016).
254. P. DiSilvestro *et al.*, Overall Survival With Maintenance Olaparib at a 7-Year Follow-Up in Patients With Newly Diagnosed Advanced Ovarian Cancer and a BRCA Mutation: The SOLO1/GOG 3004 Trial. *J Clin Oncol* **41**, 609-617 (2023).
255. A. Poveda *et al.*, Olaparib tablets as maintenance therapy in patients with platinum-sensitive relapsed ovarian cancer and a BRCA1/2 mutation (SOLO2/ENGOT-Ov21): a final analysis of a double-blind, randomised, placebo-controlled, phase 3 trial. *Lancet Oncol* **22**, 620-631 (2021).
256. J. A. Ledermann, E. Pujade-Lauraine, Olaparib as maintenance treatment for patients with platinum-sensitive relapsed ovarian cancer. *Ther Adv Med Oncol* **11**, 1758835919849753 (2019).
257. R. Penson *et al.*, Final overall survival results from SOLO3: Phase III trial assessing olaparib monotherapy versus non-platinum chemotherapy in heavily pretreated patients with germline BRCA1 - and/or BRCA2-mutated platinum-sensitive relapsed ovarian cancer (026). *Gynecologic Oncology* **166**, S19-S20 (2022).
258. R. S. Kristeleit *et al.*, Efficacy and safety of rucaparib treatment in patients with BRCA-mutated, relapsed ovarian cancer: final results from Study 10. *British Journal of Cancer* **128**, 255-265 (2023).
259. E. M. Swisher *et al.*, Rucaparib in relapsed, platinum-sensitive high-grade ovarian carcinoma (ARIEL2 Part 1): an international, multicentre, open-label, phase 2 trial. *The Lancet Oncology* **18**, 75-87 (2017).
260. B. J. Monk *et al.*, A Randomized, Phase III Trial to Evaluate Rucaparib Monotherapy as Maintenance Treatment in Patients With Newly Diagnosed Ovarian Cancer (ATHENA–MONO/GOG-3020/ENGOT-ov45). *Journal of Clinical Oncology* **40**, 3952-3964 (2022).
261. R. L. Coleman *et al.*, Rucaparib maintenance treatment for recurrent ovarian carcinoma after response to platinum therapy (ARIEL3): a randomised, double-blind, placebo-controlled, phase 3 trial. *The Lancet* **390**, 1949-1961 (2017).
262. R. Kristeleit *et al.*, Rucaparib versus standard-of-care chemotherapy in patients with relapsed ovarian cancer and a deleterious BRCA1 or BRCA2 mutation (ARIEL4): an international, open-label, randomised, phase 3 trial. *The Lancet Oncology* **23**, 465-478 (2022).
263. J. M. Del Campo *et al.*, Niraparib Maintenance Therapy in Patients With Recurrent Ovarian Cancer After a Partial Response to the Last Platinum-Based Chemotherapy in the ENGOT-OV16/NOVA Trial. *J Clin Oncol* **37**, 2968-2973 (2019).

264. A. González-Martín *et al.*, Niraparib in Patients with Newly Diagnosed Advanced Ovarian Cancer. *N Engl J Med* **381**, 2391-2402 (2019).
265. K. N. Moore *et al.*, Niraparib monotherapy for late-line treatment of ovarian cancer (QUADRA): a multicentre, open-label, single-arm, phase 2 trial. *Lancet Oncol* **20**, 636-648 (2019).
266. E. M. Swisher *et al.*, Molecular and clinical determinants of response and resistance to rucaparib for recurrent ovarian cancer treatment in ARIEL2 (Parts 1 and 2). *Nature Communications* **12**, 2487 (2021).
267. P. Soberanis Pina, S. Lheureux, Overcoming PARP inhibitor resistance in ovarian cancer. *Int J Gynecol Cancer* **33**, 364-376 (2023).
268. C. Sun *et al.*, Rational combination therapy with PARP and MEK inhibitors capitalizes on therapeutic liabilities in RAS mutant cancers. *Sci Transl Med* **9**, (2017).
269. D. Wang *et al.*, Effective use of PI3K inhibitor BKM120 and PARP inhibitor Olaparib to treat PIK3CA mutant ovarian cancer. *Oncotarget* **7**, 13153-13166 (2016).
270. A. Juvekar *et al.*, Combining a PI3K inhibitor with a PARP inhibitor provides an effective therapy for BRCA1-related breast cancer. *Cancer Discov* **2**, 1048-1063 (2012).
271. T. A. Yap *et al.*, Phase I Trial of the PARP Inhibitor Olaparib and AKT Inhibitor Capivasertib in Patients with BRCA1/2- and Non-BRCA1/2-Mutant Cancers. *Cancer Discov* **10**, 1528-1543 (2020).
272. S. Westin *et al.*, SOLAR: Phase Ib Dose Expansion of Selumetinib (MEK Inhibitor) and OLAparib (PARP Inhibitor) Combination in Solid Tumors with RAS Pathway Alterations and in PARP Inhibitor-Resistant Ovarian Cancer (LBA 9). *Gynecologic Oncology* **176**, S33 (2023).
273. K. C. Kurnit *et al.*, Abstract CT020: Phase I dose escalation of olaparib (PARP inhibitor) and selumetinib (MEK Inhibitor) combination in solid tumors with Ras pathway alterations. *Cancer Research* **79**, CT020-CT020 (2019).
274. D. Gaglio *et al.*, Oncogenic K-Ras decouples glucose and glutamine metabolism to support cancer cell growth. *Mol Syst Biol* **7**, 523 (2011).
275. C. R. Amendola *et al.*, KRAS4A directly regulates hexokinase 1. *Nature* **576**, 482-486 (2019).
276. T. Schild *et al.*, NADK is activated by oncogenic signaling to sustain pancreatic ductal adenocarcinoma. *Cell Rep* **35**, 109238 (2021).
277. C. Bian *et al.*, NADP+ is an endogenous PARP inhibitor in DNA damage response and tumor suppression. *Nature Communications* **10**, 693 (2019).
278. D. Varshavi *et al.*, Metabolic characterization of colorectal cancer cells harbouring different KRAS mutations in codon 12, 13, 61 and 146 using human SW48 isogenic cell lines. *Metabolomics* **16**, 51 (2020).
279. L. Brunelli, E. Caiola, M. Marabese, M. Broggini, R. Pastorelli, Capturing the metabolomic diversity of KRAS mutants in non-small-cell lung cancer cells. *Oncotarget* **5**, 4722-4731 (2014).
280. A. Menssen *et al.*, The c-MYC oncoprotein, the NAMPT enzyme, the SIRT1-inhibitor DBC1, and the SIRT1 deacetylase form a positive feedback loop. *Proc Natl Acad Sci U S A* **109**, E187-196 (2012).
281. S. Chowdhry *et al.*, NAD metabolic dependency in cancer is shaped by gene amplification and enhancer remodelling. *Nature* **569**, 570-575 (2019).

282. V. Audrito *et al.*, Tumors carrying BRAF-mutations over-express NAMPT that is genetically amplified and possesses oncogenic properties. *Journal of Translational Medicine* **20**, 118 (2022).
283. Q. Zhang *et al.*, Chimeric kinase ALK induces expression of NAMPT and selectively depends on this metabolic enzyme to sustain its own oncogenic function. *Leukemia* **37**, 2436-2447 (2023).
284. M. Ohanna *et al.*, Pivotal role of NAMPT in the switch of melanoma cells toward an invasive and drug-resistant phenotype. *Genes Dev* **32**, 448-461 (2018).
285. I. Bajrami *et al.*, Synthetic lethality of PARP and NAMPT inhibition in triple-negative breast cancer cells. *EMBO Molecular Medicine* **4**, 1087-1096 (2012).
286. C. M. Heske *et al.*, Matrix Screen Identifies Synergistic Combination of PARP Inhibitors and Nicotinamide Phosphoribosyltransferase (NAMPT) Inhibitors in Ewing Sarcoma. *Clinical Cancer Research* **23**, 7301-7311 (2017).
287. A. Sauriol *et al.*, Inhibition of nicotinamide dinucleotide salvage pathway counters acquired and intrinsic poly(ADP-ribose) polymerase inhibitor resistance in high-grade serous ovarian cancer. *Sci Rep* **13**, 3334 (2023).
288. Y. Chen, Jr. *et al.*, Lactate metabolism is associated with mammalian mitochondria. *Nature Chemical Biology* **12**, 937-943 (2016).
289. P. Sonveaux *et al.*, Targeting lactate-fueled respiration selectively kills hypoxic tumor cells in mice. *J Clin Invest* **118**, 3930-3942 (2008).
290. S. Pavlides *et al.*, The reverse Warburg effect: aerobic glycolysis in cancer associated fibroblasts and the tumor stroma. *Cell Cycle* **8**, 3984-4001 (2009).
291. B. Faubert *et al.*, Lactate Metabolism in Human Lung Tumors. *Cell* **171**, 358-371.e359 (2017).
292. S. Hui *et al.*, Glucose feeds the TCA cycle via circulating lactate. *Nature* **551**, 115-118 (2017).
293. S. Liu, Z. Dai, D. E. Cooper, D. G. Kirsch, J. W. Locasale, Quantitative Analysis of the Physiological Contributions of Glucose to the TCA Cycle. *Cell Metab* **32**, 619-628.e621 (2020).
294. M. Ying, C. Guo, X. Hu, The quantitative relationship between isotopic and net contributions of lactate and glucose to the tricarboxylic acid (TCA) cycle. *J Biol Chem* **294**, 9615-9630 (2019).
295. N. Draoui, O. Feron, Lactate shuttles at a glance: from physiological paradigms to anti-cancer treatments. *Dis Model Mech* **4**, 727-732 (2011).
296. C. L. Markert, J. B. Shaklee, G. S. Whitt, Evolution of a gene. Multiple genes for LDH isozymes provide a model of the evolution of gene structure, function and regulation. *Science* **189**, 102-114 (1975).
297. M. Gallo *et al.*, Lactic dehydrogenase and cancer: an overview. *Front Biosci (Landmark Ed)* **20**, 1234-1249 (2015).
298. G. Claps *et al.*, The multiple roles of LDH in cancer. *Nature Reviews Clinical Oncology* **19**, 749-762 (2022).
299. P. Wu, T. Zhu, Y. Huang, Z. Fang, F. Luo, Current understanding of the contribution of lactate to the cardiovascular system and its therapeutic relevance. *Frontiers in Endocrinology* **14**, (2023).

300. A. Nagao, M. Kobayashi, S. Koyasu, C. C. T. Chow, H. Harada, HIF-1-Dependent Reprogramming of Glucose Metabolic Pathway of Cancer Cells and Its Therapeutic Significance. *Int J Mol Sci* **20**, (2019).
301. T. L. He *et al.*, The c-Myc-LDHA axis positively regulates aerobic glycolysis and promotes tumor progression in pancreatic cancer. *Med Oncol* **32**, 187 (2015).
302. H. Shim *et al.*, c-Myc transactivation of LDH-A: implications for tumor metabolism and growth. *Proc Natl Acad Sci U S A* **94**, 6658-6663 (1997).
303. J. Cui *et al.*, FOXM1 promotes the warburg effect and pancreatic cancer progression via transactivation of LDHA expression. *Clin Cancer Res* **20**, 2595-2606 (2014).
304. W. Jiang, F. Zhou, N. Li, Q. Li, L. Wang, FOXM1-LDHA signaling promoted gastric cancer glycolytic phenotype and progression. *Int J Clin Exp Pathol* **8**, 6756-6763 (2015).
305. J. Cui *et al.*, Suppressed expression of LDHB promotes pancreatic cancer progression via inducing glycolytic phenotype. *Med Oncol* **32**, 143 (2015).
306. A. Leiblich *et al.*, Lactate dehydrogenase-B is silenced by promoter hypermethylation in human prostate cancer. *Oncogene* **25**, 2953-2960 (2006).
307. D. Fu *et al.*, HMGB2 is associated with malignancy and regulates Warburg effect by targeting LDHB and FBP1 in breast cancer. *Cell Commun Signal* **16**, 8 (2018).
308. X. Zha *et al.*, Lactate dehydrogenase B is critical for hyperactive mTOR-mediated tumorigenesis. *Cancer Res* **71**, 13-18 (2011).
309. S. Hu *et al.*, miR-200b is a key regulator of tumor progression and metabolism targeting lactate dehydrogenase A in human malignant glioma. *Oncotarget* **7**, 48423-48431 (2016).
310. D. Zhao *et al.*, Lysine-5 acetylation negatively regulates lactate dehydrogenase A and is decreased in pancreatic cancer. *Cancer Cell* **23**, 464-476 (2013).
311. J. Fan *et al.*, Tyrosine phosphorylation of lactate dehydrogenase A is important for NADH/NAD(+) redox homeostasis in cancer cells. *Mol Cell Biol* **31**, 4938-4950 (2011).
312. L. Shi *et al.*, SIRT5-mediated deacetylation of LDHB promotes autophagy and tumorigenesis in colorectal cancer. *Mol Oncol* **13**, 358-375 (2019).
313. E. Y. Kim *et al.*, A Novel Lactate Dehydrogenase Inhibitor, 1-(Phenylseleno)-4-(Trifluoromethyl) Benzene, Suppresses Tumor Growth through Apoptotic Cell Death. *Sci Rep* **9**, 3969 (2019).
314. A. Le *et al.*, Inhibition of lactate dehydrogenase A induces oxidative stress and inhibits tumor progression. *Proceedings of the National Academy of Sciences* **107**, 2037-2042 (2010).
315. X. M. Hou, S. Q. Yuan, D. Zhao, X. J. Liu, X. A. Wu, LDH-A promotes malignant behavior via activation of epithelial-to-mesenchymal transition in lung adenocarcinoma. *Biosci Rep* **39**, (2019).
316. J. Zhao *et al.*, LDHA promotes tumor metastasis by facilitating epithelial-mesenchymal transition in renal cell carcinoma. *Mol Med Rep* **16**, 8335-8344 (2017).
317. A. Giatromanolaki *et al.*, Lactate dehydrogenase 5 (LDH-5) expression in endometrial cancer relates to the activated VEGF/VEGFR2(KDR) pathway and prognosis. *Gynecologic Oncology* **103**, 912-918 (2006).
318. A. P. Halestrap, The monocarboxylate transporter family--Structure and functional characterization. *IUBMB Life* **64**, 1-9 (2012).
319. A. P. Halestrap, Monocarboxylic acid transport. *Compr Physiol* **3**, 1611-1643 (2013).

320. I. Marchiq, J. Pouysségur, Hypoxia, cancer metabolism and the therapeutic benefit of targeting lactate/H(+) symporters. *J Mol Med (Berl)* **94**, 155-171 (2016).
321. A. W. De Bruijne, H. Vreeburg, J. Van Steveninck, Kinetic analysis of L-lactate transport in human erythrocytes via the monocarboxylate-specific carrier system. *Biochim Biophys Acta* **732**, 562-568 (1983).
322. A. W. de Bruijne, H. Vreeburg, J. van Steveninck, Alternative-substrate inhibition of L-lactate transport via the monocarboxylate-specific carrier system in human erythrocytes. *Biochim Biophys Acta* **812**, 841-844 (1985).
323. S. Galić, H. P. Schneider, A. Bröer, J. W. Deitmer, S. Bröer, The loop between helix 4 and helix 5 in the monocarboxylate transporter MCT1 is important for substrate selection and protein stability. *Biochem J* **376**, 413-422 (2003).
324. M. C. Wilson *et al.*, Basigin (CD147) Is the Target for Organomercurial Inhibition of Monocarboxylate Transporter Isoforms 1 and 4: THE ANCILLARY PROTEIN FOR THE INSENSITIVE MCT2 IS EMBIGIN (gp70)*. *Journal of Biological Chemistry* **280**, 27213-27221 (2005).
325. A. P. Halestrap, D. Meredith, The SLC16 gene family-from monocarboxylate transporters (MCTs) to aromatic amino acid transporters and beyond. *Pflugers Arch* **447**, 619-628 (2004).
326. M. S. Ullah, A. J. Davies, A. P. Halestrap, The Plasma Membrane Lactate Transporter MCT4, but Not MCT1, Is Up-regulated by Hypoxia through a HIF-1α-dependent Mechanism*. *Journal of Biological Chemistry* **281**, 9030-9037 (2006).
327. C. Juel, A. P. Halestrap, Lactate transport in skeletal muscle - role and regulation of the monocarboxylate transporter. *J Physiol* **517 (Pt 3)**, 633-642 (1999).
328. K. S. Dimmer, B. Friedrich, F. Lang, J. W. Deitmer, S. Bröer, The low-affinity monocarboxylate transporter MCT4 is adapted to the export of lactate in highly glycolytic cells. *Biochem J* **350 Pt 1**, 219-227 (2000).
329. J. E. Manning Fox, D. Meredith, A. P. Halestrap, Characterisation of human monocarboxylate transporter 4 substantiates its role in lactic acid efflux from skeletal muscle. *J Physiol* **529 Pt 2**, 285-293 (2000).
330. R. C. Poole, A. P. Halestrap, Transport of lactate and other monocarboxylates across mammalian plasma membranes. *Am J Physiol* **264**, C761-782 (1993).
331. J. R. Doherty *et al.*, Blocking Lactate Export by Inhibiting the Myc Target MCT1 Disables Glycolysis and Glutathione Synthesis. *Cancer Research* **74**, 908-920 (2014).
332. T. Hashimoto, R. Hussien, S. Oommen, K. Gohil, G. A. Brooks, Lactate sensitive transcription factor network in L6 cells: activation of MCT1 and mitochondrial biogenesis. *Faseb j* **21**, 2602-2612 (2007).
333. R. Boidot *et al.*, Regulation of Monocarboxylate Transporter MCT1 Expression by p53 Mediates Inward and Outward Lactate Fluxes in Tumors. *Cancer Research* **72**, 939-948 (2012).
334. G. Sheng, Y. Gao, H. Wu, Y. Liu, Y. Yang, Functional heterogeneity of MCT1 and MCT4 in metabolic reprogramming affects osteosarcoma growth and metastasis. *Journal of Orthopaedic Surgery and Research* **18**, 131 (2023).
335. A. A. Cluntun *et al.*, The pyruvate-lactate axis modulates cardiac hypertrophy and heart failure. *Cell Metab* **33**, 629-648.e610 (2021).

336. G. A. Brooks, The Science and Translation of Lactate Shuttle Theory. *Cell Metab* **27**, 757-785 (2018).
337. D. Bendahan, B. Chatel, T. Jue, Comparative NMR and NIRS analysis of oxygen-dependent metabolism in exercising finger flexor muscles. *American Journal of Physiology-Regulatory, Integrative and Comparative Physiology* **313**, R740-R753 (2017).
338. R. J. Connett, C. R. Honig, T. E. Gayeski, G. A. Brooks, Defining hypoxia: a systems view of VO2, glycolysis, energetics, and intracellular PO2. *Journal of Applied Physiology* **68**, 833-842 (1990).
339. W. L. Rumsey, C. Schlosser, E. M. Nuutinen, M. Robiolio, D. F. Wilson, Cellular energetics and the oxygen dependence of respiration in cardiac myocytes isolated from adult rat. *J Biol Chem* **265**, 15392-15402 (1990).
340. A. K. Bouzier *et al.*, Compartmentation of lactate and glucose metabolism in C6 glioma cells. A 13c and 1H NMR study. *J Biol Chem* **273**, 27162-27169 (1998).
341. J. C. Portais, R. Schuster, M. Merle, P. Canioni, Metabolic flux determination in C6 glioma cells using carbon-13 distribution upon [1-13C]glucose incubation. *Eur J Biochem* **217**, 457-468 (1993).
342. R. Bunger, Compartmented pyruvate in perfused working heart. *American Journal of Physiology-Heart and Circulatory Physiology* **249**, H439-H449 (1985).
343. T. Tian, J. Fan, S. E. Elf, Metabolon: a novel cellular structure that regulates specific metabolic pathways. *Cancer Commun (Lond)* **41**, 439-441 (2021).
344. J. B. German, B. D. Hammock, S. M. Watkins, Metabolomics: building on a century of biochemistry to guide human health. *Metabolomics* **1**, 3-9 (2005).
345. F. Danzi *et al.*, To metabolomics and beyond: a technological portfolio to investigate cancer metabolism. *Signal Transduct Target Ther* **8**, 137 (2023).
346. J. Han, Q. Li, Y. Chen, Y. Yang, Recent Metabolomics Analysis in Tumor Metabolism Reprogramming. *Front Mol Biosci* **8**, 763902 (2021).
347. D. R. Schmidt *et al.*, Metabolomics in cancer research and emerging applications in clinical oncology. *CA Cancer J Clin* **71**, 333-358 (2021).
348. A. V. Aderemi, A. O. Ayeleso, O. O. Oyedapo, E. Mukwevho, Metabolomics: A Scoping Review of Its Role as a Tool for Disease Biomarker Discovery in Selected Non-Communicable Diseases. *Metabolites* **11**, (2021).
349. S. Alseekh *et al.*, Mass spectrometry-based metabolomics: a guide for annotation, quantification and best reporting practices. *Nat Methods* **18**, 747-756 (2021).
350. A. Ribbenstedt, H. Ziarrusta, J. P. Benskin, Development, characterization and comparisons of targeted and non-targeted metabolomics methods. *PLoS One* **13**, e0207082 (2018).
351. A. C. Schrimpe-Rutledge, S. G. Codreanu, S. D. Sherrod, J. A. McLean, Untargeted Metabolomics Strategies-Challenges and Emerging Directions. *J Am Soc Mass Spectrom* **27**, 1897-1905 (2016).
352. W. Lu *et al.*, Metabolite Measurement: Pitfalls to Avoid and Practices to Follow. *Annu Rev Biochem* **86**, 277-304 (2017).
353. D. S. Wishart *et al.*, HMDB: the Human Metabolome Database. *Nucleic Acids Res* **35**, D521-526 (2007).
354. Y. Chen, E. M. Li, L. Y. Xu, Guide to Metabolomics Analysis: A Bioinformatics Workflow. *Metabolites* **12**, (2022).

355. M. Sugimoto, M. Kawakami, M. Robert, T. Soga, M. Tomita, Bioinformatics Tools for Mass Spectroscopy-Based Metabolomic Data Processing and Analysis. *Curr Bioinform* **7**, 96-108 (2012).
356. J. Chong *et al.*, MetaboAnalyst 4.0: towards more transparent and integrative metabolomics analysis. *Nucleic Acids Res* **46**, W486-w494 (2018).
357. C. Jang, L. Chen, J. D. Rabinowitz, Metabolomics and Isotope Tracing. *Cell* **173**, 822-837 (2018).
358. W. S. Ahn, M. R. Antoniewicz, Parallel labeling experiments with [1,2-(13)C]glucose and [U-(13)C]glutamine provide new insights into CHO cell metabolism. *Metab Eng* **15**, 34-47 (2013).
359. S. B. Crown, W. S. Ahn, M. R. Antoniewicz, Rational design of ^{13}C-labeling experiments for metabolic flux analysis in mammalian cells. *BMC Syst Biol* **6**, 43 (2012).
360. U. Sauer, Metabolic networks in motion: 13C-based flux analysis. *Mol Syst Biol* **2**, 62 (2006).
361. A. T. Kharroubi, T. M. Masterson, T. A. Aldaghlas, K. A. Kennedy, J. K. Kelleher, Isotopomer spectral analysis of triglyceride fatty acid synthesis in 3T3-L1 cells. *Am J Physiol* **263**, E667-675 (1992).
362. M. R. Antoniewicz, A guide to 13C metabolic flux analysis for the cancer biologist. *Experimental & Molecular Medicine* **50**, 1-13 (2018).
363. S. M. Fendt *et al.*, Metformin decreases glucose oxidation and increases the dependency of prostate cancer cells on reductive glutamine metabolism. *Cancer Res* **73**, 4429-4438 (2013).
364. G. Theodoridis, H. G. Gika, I. D. Wilson, Mass spectrometry-based holistic analytical approaches for metabolite profiling in systems biology studies. *Mass Spectrom Rev* **30**, 884-906 (2011).
365. T. M. Annesley, Ion suppression in mass spectrometry. *Clin Chem* **49**, 1041-1044 (2003).
366. J. W. Honour, Gas chromatography-mass spectrometry. *Methods Mol Biol* **324**, 53-74 (2006).
367. O. Fiehn *et al.*, Plasma metabolomic profiles reflective of glucose homeostasis in non-diabetic and type 2 diabetic obese African-American women. *PLoS One* **5**, e15234 (2010).
368. O. Fiehn, J. Kopka, R. N. Trethewey, L. Willmitzer, Identification of uncommon plant metabolites based on calculation of elemental compositions using gas chromatography and quadrupole mass spectrometry. *Anal Chem* **72**, 3573-3580 (2000).
369. R. S. Plumb *et al.*, Advances in high throughput LC/MS based metabolomics: A review. *TrAC Trends in Analytical Chemistry* **160**, 116954 (2023).
370. J. Feng *et al.*, Integration of Proteomics and Metabolomics Revealed Metabolite-Protein Networks in ACTH-Secreting Pituitary Adenoma. *Front Endocrinol (Lausanne)* **9**, 678 (2018).
371. S. Forcisi *et al.*, Liquid chromatography-mass spectrometry in metabolomics research: mass analyzers in ultra high pressure liquid chromatography coupling. *J Chromatogr A* **1292**, 51-65 (2013).
372. L. W. Sumner, D. V. Huhman, E. Urbanczyk-Wochniak, Z. Lei, Methods, applications and concepts of metabolite profiling: secondary metabolism. *Exs* **97**, 195-212 (2007).
373. D. Steinhauser, J. Kopka, Methods, applications and concepts of metabolite profiling: primary metabolism. *Exs* **97**, 171-194 (2007).

374. A. J. Chetwynd, A. David, A review of nanoscale LC-ESI for metabolomics and its potential to enhance the metabolome coverage. *Talanta* **182**, 380-390 (2018).
375. P. E. Miller, M. B. Denton, The quadrupole mass filter: Basic operating concepts. *Journal of Chemical Education* **63**, 617 (1986).
376. R. J. Cotter, Time-of-flight mass spectrometry: an increasing role in the life sciences. *Biomed Environ Mass Spectrom* **18**, 513-532 (1989).
377. C. J. Brais, J. O. Ibañez, A. J. Schwartz, S. J. Ray, RECENT ADVANCES IN INSTRUMENTAL APPROACHES TO TIME-OF-FLIGHT MASS SPECTROMETRY. *Mass Spectrom Rev* **40**, 647-669 (2021).
378. D. R. Allen, B. C. McWhinney, Quadrupole Time-of-Flight Mass Spectrometry: A Paradigm Shift in Toxicology Screening Applications. *Clin Biochem Rev* **40**, 135-146 (2019).
379. I. V. Chernushevich, A. V. Loboda, B. A. Thomson, An introduction to quadrupole-time-of-flight mass spectrometry. *J Mass Spectrom* **36**, 849-865 (2001).
380. M. Raetz, R. Bonner, G. Hopfgartner, SWATH-MS for metabolomics and lipidomics: critical aspects of qualitative and quantitative analysis. *Metabolomics* **16**, 71 (2020).
381. R. Bonner, G. Hopfgartner, SWATH data independent acquisition mass spectrometry for metabolomics. *TrAC Trends in Analytical Chemistry* **120**, 115278 (2019).
382. M. Raetz, E. Duchoslav, R. Bonner, G. Hopfgartner, Hybrid SWATH/MS and HR-SRM/MS acquisition for phospholipidomics using QUAL/QUANT data processing. *Anal Bioanal Chem* **411**, 5681-5690 (2019).
383. Y. Zhang *et al.*, The Use of Variable Q1 Isolation Windows Improves Selectivity in LC-SWATH-MS Acquisition. *J Proteome Res* **14**, 4359-4371 (2015).
384. G. Martin, M. Martin, J. Gouesnard, NMR Basic Principles and Progress. *Diehl, P*, 1-69 (1989).
385. T. L. James, Fundamentals of NMR. *Online Textbook: Department of Pharmaceutical Chemistry, University of California, San Francisco*, 1-31 (1998).
386. A. C. Dona *et al.*, A guide to the identification of metabolites in NMR-based metabonomics/metabolomics experiments. *Comput Struct Biotechnol J* **14**, 135-153 (2016).
387. H. Gungor *et al.*, Pharmacokinetic (PK)/pharmacodynamic (PD) analysis of escalating repeat doses of the AKT inhibitor GSK2141795 (GSK795) in patients (pts) with ovarian cancer. *Journal of Clinical Oncology* **29**, 5064-5064 (2011).
388. S. A. Sauriol *et al.*, Inhibition of nicotinamide dinucleotide salvage pathway counters acquired and intrinsic poly(ADP-ribose) polymerase inhibitor resistance in high-grade serous ovarian cancer. *Scientific Reports* **13**, 3334 (2023).
389. E. M. E. D. Yitao Xu, Hector C. Keun, Imperial College London, (2019).
390. J. Walton *et al.*, CRISPR/Cas9-Mediated Trp53 and Brca2 Knockout to Generate Improved Murine Models of Ovarian High-Grade Serous Carcinoma. *Cancer Research* **76**, 6118-6129 (2016).
391. J. B. Walton *et al.*, CRISPR/Cas9-derived models of ovarian high grade serous carcinoma targeting Brca1, Pten and Nf1, and correlation with platinum sensitivity. *Scientific Reports* **7**, 16827 (2017).
392. A. D. Association, Standards of medical care in diabetes--2014. *Diabetes Care*, (2014).
393. M. J. Gruet, Imperial College London, (2023).

394. Y. Xu *et al.*, Pharmacological depletion of RNA splicing factor RBM39 by indisulam synergizes with PARP inhibitors in high-grade serous ovarian carcinoma. *Cell Rep* **42**, 113307 (2023).
395. E. M. E. Doherty, Imperial College London, (2019).
396. A. Nijhuis *et al.*, Indisulam targets RNA splicing and metabolism to serve as a therapeutic strategy for high-risk neuroblastoma. *Nature Communications* **13**, 1380 (2022).
397. D. Y. Bang, S. K. Byeon, M. H. Moon, Rapid and simple extraction of lipids from blood plasma and urine for liquid chromatography-tandem mass spectrometry. *J Chromatogr A* **1331**, 19-26 (2014).
398. C. E. Lau, G. D. Tredwell, J. K. Ellis, E. W. Lam, H. C. Keun, Metabolomic characterisation of the effects of oncogenic PIK3CA transformation in a breast epithelial cell line. *Scientific Reports* **7**, 46079 (2017).
399. T. Kind *et al.*, FiehnLib: mass spectral and retention index libraries for metabolomics based on quadrupole and time-of-flight gas chromatography/mass spectrometry. *Anal Chem* **81**, 10038-10048 (2009).
400. V. Behrends, G. D. Tredwell, J. G. Bundy, A software complement to AMDIS for processing GC-MS metabolomic data. *Anal Biochem* **415**, 206-208 (2011).
401. G. D. Tredwell, H. C. Keun, convISA: A simple, convoluted method for isotopomer spectral analysis of fatty acids and cholesterol. *Metabolic Engineering* **32**, 125-132 (2015).
402. H. Tsugawa *et al.*, MS-DIAL: data-independent MS/MS deconvolution for comprehensive metabolome analysis. *Nature Methods* **12**, 523-526 (2015).
403. A. Klåvus *et al.*, "Notame": Workflow for Non-Targeted LC–MS Metabolic Profiling. *Metabolites* **10**, 135 (2020).
404. Z. Pang *et al.*, MetaboAnalyst 6.0: towards a unified platform for metabolomics data processing, analysis and interpretation. *Nucleic Acids Research*, (2024).
405. G. Hoxhaj *et al.*, Direct stimulation of NADP(+) synthesis through Akt-mediated phosphorylation of NAD kinase. *Science* **363**, 1088-1092 (2019).
406. M. Köbel *et al.*, The biological and clinical value of p53 expression in pelvic high-grade serous carcinomas. *The Journal of pathology* **222**, 191-198 (2010).
407. L. Alexandra, A. Edouard, P. Patricia, L. Catherine, in *Ovarian Cancer,* D. a.-P. Iván, Ed. (IntechOpen, Rijeka, 2013), pp. Ch. 13.
408. K. F. Roby *et al.*, Development of a syngeneic mouse model for events related to ovarian cancer. *Carcinogenesis* **21**, 585-591 (2000).
409. L. V. Yang, Tumor Microenvironment and Metabolism. *Int J Mol Sci* **18**, (2017).
410. I. Elia, M. C. Haigis, Metabolites and the tumour microenvironment: from cellular mechanisms to systemic metabolism. *Nature Metabolism* **3**, 21-32 (2021).
411. S. M. Davidson *et al.*, Environment impacts the metabolic dependencies of Ras-driven non-small cell lung cancer. *Cell metabolism* **23**, 517-528 (2016).
412. C. E. Ford, B. Werner, N. F. Hacker, K. Warton, The untapped potential of ascites in ovarian cancer research and treatment. *British journal of cancer* **123**, 9-16 (2020).
413. D. Ruiz-Perez, H. Guan, P. Madhivanan, K. Mathee, G. Narasimhan, So you think you can PLS-DA? *BMC Bioinformatics* **21**, 2 (2020).
414. J. Xia, D. S. Wishart, MSEA: a web-based tool to identify biologically meaningful patterns in quantitative metabolomic data. *Nucleic Acids Research* **38**, W71-W77 (2010).

415. C. E. Mountford, L. C. Wright, Organization of lipids in the plasma membranes of malignant and stimulated cells: a new model. *Trends in Biochemical Sciences* **13**, 172-177 (1988).
416. E. P. Kennedy, S. B. Weiss, THE FUNCTION OF CYTIDINE COENZYMES IN THE BIOSYNTHESIS OF PHOSPHOLIPIDES. *Journal of Biological Chemistry* **222**, 193-214 (1956).
417. M. Cheng, Z. M. Bhujwalla, K. Glunde, Targeting Phospholipid Metabolism in Cancer. *Front Oncol* **6**, 266 (2016).
418. C. W. Scull, W. C. Rose, Arginine metabolism: I. the relation of the arginine content of the diet to the increments in tissue arginine during growth. *Journal of Biological Chemistry* **89**, 109-123 (1930).
419. W. R. Featherston, Q. R. Rogers, R. A. Freedland, Relative importance of kidney and liver in synthesis of arginine by the rat. *Am J Physiol* **224**, 127-129 (1973).
420. V. Bronte, P. Zanovello, Regulation of immune responses by L-arginine metabolism. *Nature Reviews Immunology* **5**, 641-654 (2005).
421. S. M. Morris, Jr., Arginine: master and commander in innate immune responses. *Sci Signal* **3**, pe27 (2010).
422. M. E. Brosnan, J. T. Brosnan, Histidine Metabolism and Function. *The Journal of Nutrition* **150**, 2570S-2575S (2020).
423. A. Czumaj *et al.*, The Pathophysiological Role of CoA. *Int J Mol Sci* **21**, (2020).
424. Y.-M. Zhang, C. O. Rock, S. Jackowski, Feedback regulation of murine pantothenate kinase 3 by coenzyme A and coenzyme A thioesters. *Journal of Biological Chemistry* **280**, 32594-32601 (2005).
425. K. E. Tiedje, K. Stevens, S. Barnes, D. F. Weaver, β-Alanine as a small molecule neurotransmitter. *Neurochemistry International* **57**, 177-188 (2010).
426. O. Hayaishi, Y. Nishizuka, M. Tatibana, M. Takeshita, S. Kuno, Enzymatic studies on the metabolism of β-alanine. *Journal of Biological Chemistry* **236**, 781-790 (1961).
427. X. Lujuan, E. C. MacKenzie, Z. Hua, Z. Wangang, M. Yoshinori, Carnosine—a natural bioactive dipeptide: bioaccessibility, bioavailability and health benefits. *Journal of Food Bioactives* **5**, (2019).
428. X. Li *et al.*, Revving the engine: PKB/AKT as a key regulator of cellular glucose metabolism. *Front Physiol* **14**, 1320964 (2023).
429. W. Graboń *et al.*, Lactate Formation in Primary and Metastatic Colon Cancer Cells at Hypoxia and Normoxia. *Cell Biochemistry and Function* **34**, 483-490 (2016).
430. S. Go, T. T. Kramer, A. J. Verhoeven, R. P. J. Oude Elferink, J. C. Chang, The extracellular lactate-to-pyruvate ratio modulates the sensitivity to oxidative stress-induced apoptosis via the cytosolic NADH/NAD(+) redox state. *Apoptosis* **26**, 38-51 (2021).
431. S. Jitrapakdee *et al.*, Structure, mechanism and regulation of pyruvate carboxylase. *Biochem J* **413**, 369-387 (2008).
432. L. A. Broadfield, A. A. Pane, A. Talebi, J. V. Swinnen, S.-M. Fendt, Lipid metabolism in cancer: New perspectives and emerging mechanisms. *Developmental Cell* **56**, 1363-1393 (2021).
433. W. Luu, L. J. Sharpe, J. Stevenson, A. J. Brown, Akt acutely activates the cholesterogenic transcription factor SREBP-2. *Biochimica et Biophysica Acta (BBA)-Molecular Cell*

Research **1823**, 458-464 (2012).
434. R. A. Coleman, D. G. Mashek, Mammalian triacylglycerol metabolism: synthesis, lipolysis, and signaling. *Chem Rev* **111**, 6359-6386 (2011).
435. Z. T. Schug, J. Vande Voorde, E. Gottlieb, The metabolic fate of acetate in cancer. *Nature Reviews Cancer* **16**, 708-717 (2016).
436. S. Sivanand, M. G. Vander Heiden, Emerging Roles for Branched-Chain Amino Acid Metabolism in Cancer. *Cancer Cell* **37**, 147-156 (2020).
437. P. Puchalska, P. A. Crawford, Multi-dimensional Roles of Ketone Bodies in Fuel Metabolism, Signaling, and Therapeutics. *Cell Metab* **25**, 262-284 (2017).
438. T. TeSlaa, M. Ralser, J. Fan, J. D. Rabinowitz, The pentose phosphate pathway in health and disease. *Nature Metabolism* **5**, 1275-1289 (2023).
439. W. N. Lee *et al.*, Mass isotopomer study of the nonoxidative pathways of the pentose cycle with [1,2-13C2]glucose. *Am J Physiol* **274**, E843-851 (1998).
440. Y. C. Chae *et al.*, Mitochondrial Akt Regulation of Hypoxic Tumor Reprogramming. *Cancer Cell* **30**, 257-272 (2016).
441. J.-w. Kim, I. Tchernyshyov, G. L. Semenza, C. V. Dang, HIF-1-mediated expression of pyruvate dehydrogenase kinase: A metabolic switch required for cellular adaptation to hypoxia. *Cell Metabolism* **3**, 177-185 (2006).
442. P. Gao *et al.*, c-Myc suppression of miR-23a/b enhances mitochondrial glutaminase expression and glutamine metabolism. *Nature* **458**, 762-765 (2009).
443. B. Li, M. C. Simon, Molecular Pathways: Targeting MYC-induced metabolic reprogramming and oncogenic stress in cancer. *Clin Cancer Res* **19**, 5835-5841 (2013).
444. M. Sachdeva *et al.*, p53 represses c-Myc through induction of the tumor suppressor miR-145. *Proceedings of the National Academy of Sciences* **106**, 3207-3212 (2009).
445. N. Levy, E. Yonish-Rouach, M. Oren, A. Kimchi, Complementation by wild-type p53 of interleukin-6 effects on M1 cells: induction of cell cycle exit and cooperativity with c-myc suppression. *Mol Cell Biol* **13**, 7942-7952 (1993).
446. A. Wiegering *et al.*, Targeting Translation Initiation Bypasses Signaling Crosstalk Mechanisms That Maintain High MYC Levels in Colorectal Cancer. *Cancer Discov* **5**, 768-781 (2015).
447. S. Brondfield *et al.*, Direct and indirect targeting of MYC to treat acute myeloid leukemia. *Cancer Chemother Pharmacol* **76**, 35-46 (2015).
448. A. Safaroghli-Azar, D. Bashash, A. Kazemi, A. Pourbagheri-Sigaroodi, M. Momeny, Anticancer effect of pan-PI3K inhibitor on multiple myeloma cells: Shedding new light on the mechanisms involved in BKM120 resistance. *Eur J Pharmacol* **842**, 89-98 (2019).
449. G. Lee *et al.*, Post-transcriptional Regulation of De Novo Lipogenesis by mTORC1-S6K1-SRPK2 Signaling. *Cell* **171**, 1545-1558.e1518 (2017).
450. L.-L. Chen, W.-J. Wang, p53 regulates lipid metabolism in cancer. *International Journal of Biological Macromolecules* **192**, 45-54 (2021).
451. G. Chen *et al.*, Acetyl-CoA metabolism as a therapeutic target for cancer. *Biomedicine & Pharmacotherapy* **168**, 115741 (2023).
452. Joyce V. Lee *et al.*, Akt-Dependent Metabolic Reprogramming Regulates Tumor Cell Histone Acetylation. *Cell Metabolism* **20**, 306-319 (2014).

453. K. D. G. Saunders, H.-M. Lewis, D. J. V. Beste, O. Cexus, M. J. Bailey, Spatial single cell metabolomics: Current challenges and future developments. *Current Opinion in Chemical Biology* **75**, 102327 (2023).
454. J. D. Cybulski, K. S. Leung, C. O. N. Leung, D. M. Baker, T. K. W. Lee, Protocol to track the biosynthesis of cholesterol in cultured HCC cells using (13)C compound-specific stable isotopic tracers. *STAR Protoc* **4**, 102506 (2023).
455. W.-C. Chang *et al.*, LDLR-mediated lipidome–transcriptome reprogramming in cisplatin insensitivity. *Endocrine-related cancer* **27**, 81-95 (2020).
456. S. Yue *et al.*, Cholesteryl ester accumulation induced by PTEN loss and PI3K/AKT activation underlies human prostate cancer aggressiveness. *Cell Metab* **19**, 393-406 (2014).
457. R. J. Deberardinis, J. J. Lum, C. B. Thompson, Phosphatidylinositol 3-kinase-dependent modulation of carnitine palmitoyltransferase 1A expression regulates lipid metabolism during hematopoietic cell growth. *J Biol Chem* **281**, 37372-37380 (2006).
458. M. Buzzai *et al.*, The glucose dependence of Akt-transformed cells can be reversed by pharmacologic activation of fatty acid beta-oxidation. *Oncogene* **24**, 4165-4173 (2005).
459. K. M. Nieman *et al.*, Adipocytes promote ovarian cancer metastasis and provide energy for rapid tumor growth. *Nat Med* **17**, 1498-1503 (2011).
460. A. Ramírez de Molina, V. Penalva, L. Lucas, J. C. Lacal, Regulation of choline kinase activity by Ras proteins involves Ral–GDS and PI3K. *Oncogene* **21**, 937-946 (2002).
461. E. Iorio *et al.*, Activation of phosphatidylcholine cycle enzymes in human epithelial ovarian cancer cells. *Cancer Res* **70**, 2126-2135 (2010).
462. R. F. Saito, L. N. S. Andrade, S. O. Bustos, R. Chammas, Phosphatidylcholine-Derived Lipid Mediators: The Crosstalk Between Cancer Cells and Immune Cells. *Front Immunol* **13**, 768606 (2022).
463. J. D. Stewart *et al.*, Choline-releasing glycerophosphodiesterase EDI3 drives tumor cell migration and metastasis. *Proceedings of the National Academy of Sciences* **109**, 8155-8160 (2012).
464. K. Sonkar *et al.*, Focus on the glycerophosphocholine pathway in choline phospholipid metabolism of cancer. *NMR Biomed* **32**, e4112 (2019).
465. S. Malki *et al.*, Expression and biological role of the prostaglandin D synthase/SOX9 pathway in human ovarian cancer cells. *Cancer Lett* **255**, 182-193 (2007).
466. F. Antonio, E. Castro, M. Dias-Souza, Pharmacology of non-steroidal anti-inflammatory drugs: a prescription-based overview. (2021).
467. M. E. St-Germain, V. Gagnon, S. Parent, E. Asselin, Regulation of COX-2 protein expression by Akt in endometrial cancer cells is mediated through NF-kappaB/IkappaB pathway. *Mol Cancer* **3**, 7 (2004).
468. S. A. Glynn *et al.*, COX-2 activation is associated with Akt phosphorylation and poor survival in ER-negative, HER2-positive breast cancer. *BMC Cancer* **10**, 626 (2010).
469. F. Pietrocola, L. Galluzzi, J. M. Bravo-San Pedro, F. Madeo, G. Kroemer, Acetyl coenzyme A: a central metabolite and second messenger. *Cell Metab* **21**, 805-821 (2015).
470. S. Trefely, C. D. Lovell, N. W. Snyder, K. E. Wellen, Compartmentalised acyl-CoA metabolism and roles in chromatin regulation. *Mol Metab* **38**, 100941 (2020).
471. C. C. Dibble *et al.*, PI3K drives the de novo synthesis of coenzyme A from vitamin B5. *Nature* **608**, 192-198 (2022).

472. L. Chen *et al.*, NADPH production by the oxidative pentose-phosphate pathway supports folate metabolism. *Nature Metabolism* **1**, 404-415 (2019).
473. I. Gout, Coenzyme A: a protective thiol in bacterial antioxidant defence. *Biochemical Society Transactions* **47**, 469-476 (2019).
474. V. Filonenko, I. Gout, Discovery and functional characterisation of protein CoAlation and the antioxidant function of coenzyme A. *BBA Advances* **3**, 100075 (2023).
475. M. Ming, Y. Y. He, PTEN in DNA damage repair. *Cancer Lett* **319**, 125-129 (2012).
476. W. Wang *et al.*, The phosphatidylinositol 3-kinase/akt cassette regulates purine nucleotide synthesis. *J Biol Chem* **284**, 3521-3528 (2009).
477. A.-A. Martí i Líndez, W. Reith, Arginine-dependent immune responses. *Cellular and Molecular Life Sciences* **78**, 5303-5324 (2021).
478. T. Komoda, T. Matsunaga, in *Biochemistry for Medical Professionals,* T. Komoda, T. Matsunaga, Eds. (Academic Press, Boston, 2015), pp. 25-63.
479. U. Förstermann, W. C. Sessa, Nitric oxide synthases: regulation and function. *Eur Heart J* **33**, 829-837, 837a-837d (2012).
480. Z. H. Wang, W. B. Peng, P. Zhang, X. P. Yang, Q. Zhou, Lactate in the tumour microenvironment: From immune modulation to therapy. *EBioMedicine* **73**, 103627 (2021).
481. V. Bulusu *et al.*, Acetate Recapturing by Nuclear Acetyl-CoA Synthetase 2 Prevents Loss of Histone Acetylation during Oxygen and Serum Limitation. *Cell Reports* **18**, 647-658 (2017).
482. J.-F. Bolduc, L. Hany, C. Barat, M. Ouellet, J. Tremblay Michel, Epigenetic Metabolite Acetate Inhibits Class I/II Histone Deacetylases, Promotes Histone Acetylation, and Increases HIV-1 Integration in CD4+ T Cells. *Journal of Virology* **91**, 10.1128/jvi.01943-01916 (2017).
483. M. Holeček, Branched-chain amino acids in health and disease: metabolism, alterations in blood plasma, and as supplements. *Nutrition & Metabolism* **15**, 33 (2018).
484. P. Kanikarla-Marie, S. K. Jain, Hyperketonemia and ketosis increase the risk of complications in type 1 diabetes. *Free Radical Biology and Medicine* **95**, 268-277 (2016).
485. L. Laffel, Ketone bodies: a review of physiology, pathophysiology and application of monitoring to diabetes. *Diabetes/Metabolism Research and Reviews* **15**, 412-426 (1999).
486. R. Yu *et al.*, MIEF1/2 function as adaptors to recruit Drp1 to mitochondria and regulate the association of Drp1 with Mff. *Sci Rep* **7**, 880 (2017).
487. B. Westermann, Mitochondrial fusion and fission in cell life and death. *Nature Reviews Molecular Cell Biology* **11**, 872-884 (2010).
488. S. Zhao *et al.*, MIEF2 over-expression promotes tumor growth and metastasis through reprogramming of glucose metabolism in ovarian cancer. *J Exp Clin Cancer Res* **39**, 286 (2020).
489. H. Kobayashi, Recent advances in understanding the metabolic plasticity of ovarian cancer: A systematic review. *Heliyon* **8**, e11487 (2022).
490. L. Shen, X. Zhan, Mitochondrial Dysfunction Pathway Alterations Offer Potential Biomarkers and Therapeutic Targets for Ovarian Cancer. *Oxid Med Cell Longev* **2022**, 5634724 (2022).
491. B. Jeong, J. W. Park, J. G. Kim, B. J. Lee, FOXO1 functions in the regulation of nicotinamide

phosphoribosyltransferase (Nampt) expression. *Biochem Biophys Res Commun* **511**, 398-403 (2019).

492. F. Piacente *et al.*, Nicotinic Acid Phosphoribosyltransferase Regulates Cancer Cell Metabolism, Susceptibility to NAMPT Inhibitors, and DNA Repair. *Cancer Res* **77**, 3857-3869 (2017).
493. I. Bajrami *et al.*, Synthetic lethality of PARP and NAMPT inhibition in triple-negative breast cancer cells. *EMBO Mol Med* **4**, 1087-1096 (2012).
494. A. Maréchal, L. Zou, DNA damage sensing by the ATM and ATR kinases. *Cold Spring Harb Perspect Biol* **5**, (2013).
495. Y. Shiloh, ATM and related protein kinases: safeguarding genome integrity. *Nat Rev Cancer* **3**, 155-168 (2003).
496. T. Uziel *et al.*, Requirement of the MRN complex for ATM activation by DNA damage. *Embo j* **22**, 5612-5621 (2003).
497. J. Smith, L. Mun Tho, N. Xu, D. A. Gillespie, in *Advances in Cancer Research,* G. F. Vande Woude, G. Klein, Eds. (Academic Press, 2010), vol. 108, pp. 73-112.
498. B. K. Thakur *et al.*, Involvement of p53 in the cytotoxic activity of the NAMPT inhibitor FK866 in myeloid leukemic cells. *Int J Cancer* **132**, 766-774 (2013).
499. Y. Deng *et al.*, A Nicotinamide Phosphoribosyltransferase Inhibitor, FK866, Suppresses the Growth of Anaplastic Meningiomas and Inhibits Immune Checkpoint Expression by Regulating STAT1. *Front Oncol* **12**, 836257 (2022).
500. S. Camero *et al.*, PARP inhibitors affect growth, survival and radiation susceptibility of human alveolar and embryonal rhabdomyosarcoma cell lines. *Journal of Cancer Research and Clinical Oncology* **145**, 137-152 (2019).
501. P. Jelinic, D. A. Levine, New insights into PARP inhibitors' effect on cell cycle and homology-directed DNA damage repair. *Mol Cancer Ther* **13**, 1645-1654 (2014).
502. A. J. Cloux *et al.*, Reactive oxygen/nitrogen species contribute substantially to the antileukemia effect of APO866, a NAD lowering agent. *Oncotarget* **10**, 6723-6738 (2019).
503. I. Gehrke *et al.*, On-Target Effect of FK866, a Nicotinamide Phosphoribosyl Transferase Inhibitor, by Apoptosis-Mediated Death in Chronic Lymphocytic Leukemia Cells. *Clinical Cancer Research* **20**, 4861-4872 (2014).
504. Q. Liu *et al.*, PARP-1 inhibition with or without ionizing radiation confers reactive oxygen species-mediated cytotoxicity preferentially to cancer cells with mutant TP53. *Oncogene* **37**, 2793-2805 (2018).
505. X. Ma *et al.*, Downregulation of APE1 potentiates breast cancer cells to olaparib by inhibiting PARP-1 expression. *Breast Cancer Res Treat* **176**, 109-117 (2019).
506. A. A. Alfadda, R. M. Sallam, Reactive oxygen species in health and disease. *J Biomed Biotechnol* **2012**, 936486 (2012).
507. P. Newsholme *et al.*, Reactive oxygen and nitrogen species generation, antioxidant defenses, and β-cell function: a critical role for amino acids. *J Endocrinol* **214**, 11-20 (2012).
508. A. P. Oyarzún *et al.*, FK866 compromises mitochondrial metabolism and adaptive stress responses in cultured cardiomyocytes. *Biochemical Pharmacology* **98**, 92-101 (2015).
509. M. Pittelli *et al.*, Inhibition of nicotinamide phosphoribosyltransferase: cellular bioenergetics reveals a mitochondrial insensitive NAD pool. *J Biol Chem* **285**, 34106-

34114 (2010).
510. K. Pant *et al.*, The NAMPT Inhibitor FK866 in Combination with Cisplatin Reduces Cholangiocarcinoma Cells Growth. *Cells* **12**, 775 (2023).
511. Y. Shao, X. Li, J. W. Wood, J.-x. Ma, Mitochondrial dysfunctions, endothelial progenitor cells and diabetic retinopathy. *Journal of Diabetes and its Complications* **32**, 966-973 (2018).
512. C. Guo, L. Sun, X. Chen, D. Zhang, Oxidative stress, mitochondrial damage and neurodegenerative diseases. *Neural Regen Res* **8**, 2003-2014 (2013).
513. B. Pedre, U. Barayeu, D. Ezeriņa, T. P. Dick, The mechanism of action of N-acetylcysteine (NAC): The emerging role of H2S and sulfane sulfur species. *Pharmacology & Therapeutics* **228**, 107916 (2021).
514. B. Kalyanaraman, NAC, NAC, Knockin' on Heaven's door: Interpreting the mechanism of action of N-acetylcysteine in tumor and immune cells. *Redox Biology* **57**, 102497 (2022).
515. J. Kaźmierczak-Barańska, K. Boguszewska, A. Adamus-Grabicka, B. T. Karwowski, Two Faces of Vitamin C-Antioxidative and Pro-Oxidative Agent. *Nutrients* **12**, (2020).
516. R. C. Bonadio, M. D. P. Estevez-Diz, Perspectives on PARP Inhibitor Combinations for Ovarian Cancer. *Front Oncol* **11**, 754524 (2021).
517. S. Mukhopadhyay, M. G. Vander Heiden, F. McCormick, The Metabolic Landscape of RAS-Driven Cancers from biology to therapy. *Nat Cancer* **2**, 271-283 (2021).
518. K. Holen, L. B. Saltz, E. Hollywood, K. Burk, A.-R. Hanauske, The pharmacokinetics, toxicities, and biologic effects of FK866, a nicotinamide adenine dinucleotide biosynthesis inhibitor. *Investigational New Drugs* **26**, 45-51 (2008).
519. H. Tang *et al.*, Recent advances of targeting nicotinamide phosphoribosyltransferase (NAMPT) for cancer drug discovery. *Eur J Med Chem* **258**, 115607 (2023).
520. U. Galli *et al.*, Recent Advances in NAMPT Inhibitors: A Novel Immunotherapic Strategy. *Frontiers in Pharmacology* **11**, 656 (2020).
521. A. D. Ricci *et al.*, Specific Toxicity of Maintenance Olaparib Versus Placebo in Advanced Malignancies: A Systematic Review and Meta-analysis. *Anticancer Research* **40**, 597 (2020).
522. M. Friedlander, Y. C. Lee, W. P. Tew, Managing Adverse Effects Associated With Poly (ADP-ribose) Polymerase Inhibitors in Ovarian Cancer: A Synthesis of Clinical Trial and Real-World Data. *American Society of Clinical Oncology Educational Book*, e390876 (2023).
523. S. W. G. Tait, D. R. Green, Caspase-independent cell death: leaving the set without the final cut. *Oncogene* **27**, 6452-6461 (2008).
524. J. E. Chipuk, L. Bouchier-Hayes, D. R. Green, Mitochondrial outer membrane permeabilization during apoptosis: the innocent bystander scenario. *Cell Death & Differentiation* **13**, 1396-1402 (2006).
525. T. Kozako *et al.*, High expression of NAMPT in adult T-cell leukemia/lymphoma and anti-tumor activity of a NAMPT inhibitor. *European Journal of Pharmacology* **865**, 172738 (2019).
526. H. E. Marei *et al.*, p53 signaling in cancer progression and therapy. *Cancer Cell International* **21**, 703 (2021).
527. Z. M. Yuan *et al.*, p73 is regulated by tyrosine kinase c-Abl in the apoptotic response to DNA damage. *Nature* **399**, 814-817 (1999).

528. Q. Cheng, J. Chen, Mechanism of p53 stabilization by ATM after DNA damage. *Cell Cycle* **9**, 472-478 (2010).
529. Y. Nakamura, ATM: the p53 booster. *Nature Medicine* **4**, 1231-1232 (1998).
530. B. J. Aubrey, G. L. Kelly, A. Janic, M. J. Herold, A. Strasser, How does p53 induce apoptosis and how does this relate to p53-mediated tumour suppression? *Cell Death & Differentiation* **25**, 104-113 (2018).
531. R. L. Weinberg, D. B. Veprintsev, M. Bycroft, A. R. Fersht, Comparative binding of p53 to its promoter and DNA recognition elements. *J Mol Biol* **348**, 589-596 (2005).
532. A. M. Klein *et al.*, MDM2, MDMX, and p73 regulate cell-cycle progression in the absence of wild-type p53. *Proceedings of the National Academy of Sciences* **118**, e2102420118 (2021).
533. H. Hermeking *et al.*, 14-3-3σ Is a p53-Regulated Inhibitor of G2/M Progression. *Molecular Cell* **1**, 3-11 (1997).
534. J. C. Hoflack, M. J. Durand, G. G. Poirier, A. Maul, P. Vasseur, Alteration in methyl-methanesulfonate-induced poly(ADP-ribosyl)ation by 2-butoxyethanol in Syrian hamster embryo cells. *Carcinogenesis* **18**, 2333-2338 (1997).
535. J. D. Steffen, M. M. McCauley, J. M. Pascal, Fluorescent sensors of PARP-1 structural dynamics and allosteric regulation in response to DNA damage. *Nucleic Acids Res* **44**, 9771-9783 (2016).
536. L. Wang *et al.*, PARP-inhibition reprograms macrophages toward an anti-tumor phenotype. *Cell Reports* **41**, 111462 (2022).
537. F. Scialò, D. J. Fernández-Ayala, A. Sanz, Role of Mitochondrial Reverse Electron Transport in ROS Signaling: Potential Roles in Health and Disease. *Frontiers in Physiology* **8**, (2017).
538. P. Bai *et al.*, PARP-1 Inhibition Increases Mitochondrial Metabolism through SIRT1 Activation. *Cell Metabolism* **13**, 461-468 (2011).
539. H. Ogino *et al.*, Loss of Parp-1 affects gene expression profile in a genome-wide manner in ES cells and liver cells. *BMC Genomics* **8**, 41 (2007).
540. A. N. Weaver, E. S. Yang, Beyond DNA Repair: Additional Functions of PARP-1 in Cancer. *Frontiers in Oncology* **3**, (2013).
541. M. Y. Kim, S. Mauro, N. Gévry, J. T. Lis, W. L. Kraus, NAD+-Dependent Modulation of Chromatin Structure and Transcription by Nucleosome Binding Properties of PARP-1. *Cell* **119**, 803-814 (2004).
542. B.-G. Ju *et al.*, Activating the PARP-1 Sensor Component of the Groucho/ TLE1 Corepressor Complex Mediates a CaMKinase IIδ-Dependent Neurogenic Gene Activation Pathway. *Cell* **119**, 815-829 (2004).
543. R. Pavri *et al.*, PARP-1 Determines Specificity in a Retinoid Signaling Pathway via Direct Modulation of Mediator. *Molecular Cell* **18**, 83-96 (2005).
544. Y. Zou *et al.*, A robust LC-MS/MS method to measure 8-oxoGuo, 8-oxodG, and NMN in human serum and urine. *Analytical Biochemistry* **660**, 114970 (2023).
545. O. D'Augustin *et al.*, Identification of key residues of the DNA glycosylase OGG1 controlling efficient DNA sampling and recruitment to oxidized bases in living cells. *Nucleic Acids Research* **51**, 4942-4958 (2023).
546. M. Cea *et al.*, Targeting NAD+ salvage pathway induces autophagy in multiple myeloma cells via mTORC1 and extracellular signal-regulated kinase (ERK1/2) inhibition. *Blood* **120**,

3519-3529 (2012).
547. E. Niki, Biomarkers of lipid peroxidation in clinical material. *Biochimica et Biophysica Acta (BBA) - General Subjects* **1840**, 809-817 (2014).
548. J. D. Morrow *et al.*, A series of prostaglandin F2-like compounds are produced in vivo in humans by a non-cyclooxygenase, free radical-catalyzed mechanism. *Proc Natl Acad Sci U S A* **87**, 9383-9387 (1990).
549. G. L. Milne, H. Yin, K. D. Hardy, S. S. Davies, L. J. Roberts, 2nd, Isoprostane generation and function. *Chem Rev* **111**, 5973-5996 (2011).
550. V. W. Daniels *et al.*, Metabolic perturbations sensitize triple-negative breast cancers to apoptosis induced by BH3 mimetics. *Sci Signal* **14**, (2021).
551. L. Demetrius, Of mice and men. When it comes to studying ageing and the means to slow it down, mice are not just small humans. *EMBO Rep* **6 Spec No**, S39-44 (2005).
552. L. Demetrius, Caloric restriction, metabolic rate, and entropy. *J Gerontol A Biol Sci Med Sci* **59**, B902-915 (2004).
553. R. L. Perlman, Mouse models of human disease: An evolutionary perspective. *Evolution, Medicine, and Public Health* **2016**, 170-176 (2016).
554. M. Luo *et al.*, Antioxidant Therapy in Cancer: Rationale and Progress. *Antioxidants (Basel)* **11**, (2022).
555. R. A. Billington, A. A. Genazzani, C. Travelli, F. Condorelli, NAD depletion by FK866 induces autophagy. *Autophagy* **4**, 385-387 (2008).
556. E. Vescarelli *et al.*, MiR-200c sensitizes Olaparib-resistant ovarian cancer cells by targeting Neuropilin 1. *J Exp Clin Cancer Res* **39**, 3 (2020).
557. J. M. Santiago-O'Farrill *et al.*, Poly(adenosine diphosphate ribose) polymerase inhibitors induce autophagy-mediated drug resistance in ovarian cancer cells, xenografts, and patient-derived xenograft models. *Cancer* **126**, 894-907 (2020).
558. K. Wang, J. Zheng, Knockdown of BAG3 synergizes with olaparib to kill ovarian cancer cells via repressing autophagy. *J Investig Med*, (2020).
559. B. Wang *et al.*, Metabolism pathways of arachidonic acids: mechanisms and potential therapeutic targets. *Signal Transduction and Targeted Therapy* **6**, 94 (2021).
560. I. A. Kirpich, M. E. Miller, M. C. Cave, S. Joshi-Barve, C. J. McClain, Alcoholic Liver Disease: Update on the Role of Dietary Fat. *Biomolecules* **6**, 1 (2016).
561. M. Wang, S. Chen, X. He, Y. Yuan, X. Wei, Targeting inflammation as cancer therapy. *J Hematol Oncol* **17**, 13 (2024).
562. H. Yang *et al.*, Regulation of inflammation in cancer by dietary eicosanoids. *Pharmacology & Therapeutics* **248**, 108455 (2023).
563. F. Mao, M. Wang, J. Wang, W.-R. Xu, The role of 15-LOX-1 in colitis and colitis-associated colorectal cancer. *Inflammation Research* **64**, 661-669 (2015).
564. S. Chen, H. Zou, Key Role of 12-Lipoxygenase and Its Metabolite 12-Hydroxyeicosatetraenoic Acid (12-HETE) in Diabetic Retinopathy. *Curr Eye Res* **47**, 329-335 (2022).
565. Q. Liu *et al.*, 12-HETE facilitates cell survival by activating the integrin-linked kinase/NF-κB pathway in ovarian cancer. *Cancer Manag Res* **10**, 5825-5838 (2018).
566. L. Iuliano, Pathways of cholesterol oxidation via non-enzymatic mechanisms. *Chem Phys Lipids* **164**, 457-468 (2011).

567. R. C. Murphy, K. M. Johnson, Cholesterol, reactive oxygen species, and the formation of biologically active mediators. *J Biol Chem* **283**, 15521-15525 (2008).
568. L. Iuliano *et al.*, Measurement of oxysterols and alpha-tocopherol in plasma and tissue samples as indices of oxidant stress status. *Anal Biochem* **312**, 217-223 (2003).
569. S. Dzeletovic, O. Breuer, E. Lund, U. Diczfalusy, Determination of cholesterol oxidation products in human plasma by isotope dilution-mass spectrometry. *Anal Biochem* **225**, 73-80 (1995).
570. A. Babiker, U. Diczfalusy, Transport of side-chain oxidized oxysterols in the human circulation. *Biochim Biophys Acta* **1392**, 333-339 (1998).
571. J. Y. Hahm, J. Park, E.-S. Jang, S. W. Chi, 8-Oxoguanine: from oxidative damage to epigenetic and epitranscriptional modification. *Experimental & Molecular Medicine* **54**, 1626-1642 (2022).
572. C. L. Hawkins, M. J. Davies, Detection, identification, and quantification of oxidative protein modifications. *J Biol Chem* **294**, 19683-19708 (2019).
573. D. Mangal *et al.*, Analysis of 7,8-Dihydro-8-oxo-2′-deoxyguanosine in Cellular DNA during Oxidative Stress. *Chemical Research in Toxicology* **22**, 788-797 (2009).
574. X. Huang, J. Powell, L. A. Mooney, C. Li, K. Frenkel, Importance of complete DNA digestion in minimizing variability of 8-oxo-dG analyses. *Free Radic Biol Med* **31**, 1341-1351 (2001).
575. K. Kaneko *et al.*, Measurement of urinary 8-oxo-7,8-dihydro-2-deoxyguanosine in a novel point-of-care testing device to assess oxidative stress in children. *Clinica Chimica Acta* **413**, 1822-1826 (2012).
576. C. Li *et al.*, Deficiency of Pdk1 drives heart failure by impairing taurine homeostasis through Slc6a6. *Faseb j* **37**, e23134 (2023).
577. D. J. Wright *et al.*, N-Acetylcysteine improves mitochondrial function and ameliorates behavioral deficits in the R6/1 mouse model of Huntington's disease. *Translational Psychiatry* **5**, e492-e492 (2015).
578. V. Tolstikov, A. Nikolayev, S. Dong, G. Zhao, M. S. Kuo, Metabolomics analysis of metabolic effects of nicotinamide phosphoribosyltransferase (NAMPT) inhibition on human cancer cells. *PLoS One* **9**, e114019 (2014).
579. J. L. Flanagan, P. A. Simmons, J. Vehige, M. D. P. Willcox, Q. Garrett, Role of carnitine in disease. *Nutrition & Metabolism* **7**, 30 (2010).
580. J. Du *et al.*, Inhibition of mitochondrial pyruvate transport by zaprinast causes massive accumulation of aspartate at the expense of glutamate in the retina. *J Biol Chem* **288**, 36129-36140 (2013).
581. J. Chen *et al.*, De novo nucleotide biosynthetic pathway and cancer. *Genes & Diseases* **10**, 2331-2338 (2023).
582. G. Hoxhaj *et al.*, The mTORC1 Signaling Network Senses Changes in Cellular Purine Nucleotide Levels. *Cell Rep* **21**, 1331-1346 (2017).
583. Y. Xie, X. Lei, G. Zhao, R. Guo, N. Cui, mTOR in programmed cell death and its therapeutic implications. *Cytokine & Growth Factor Reviews* **71-72**, 66-81 (2023).
584. Z. Zou, T. Tao, H. Li, X. Zhu, mTOR signaling pathway and mTOR inhibitors in cancer: progress and challenges. *Cell & Bioscience* **10**, 31 (2020).
585. X. Hu *et al.*, Dual PI3K/mTOR inhibitor PKI-402 suppresses the growth of ovarian cancer cells by degradation of Mcl-1 through autophagy. *Biomedicine & Pharmacotherapy* **129**,

110397 (2020).
586. M. Castedo *et al.*, Human Immunodeficiency Virus 1 Envelope Glycoprotein Complex-Induced Apoptosis Involves Mammalian Target of Rapamycin/Fkbp12-Rapamycin–Associated Protein–Mediated P53 Phosphorylation. *Journal of Experimental Medicine* **194**, 1097-1110 (2001).
587. M. Marí *et al.*, Redox Control of Liver Function in Health and Disease. *Antioxidants & Redox Signaling* **12**, 1295-1331 (2009).
588. L. T. Izzo *et al.*, Acetylcarnitine shuttling links mitochondrial metabolism to histone acetylation and lipogenesis. *Science Advances* **9**, eadf0115 (2023).
589. M. K. Kilgour *et al.*, 1-Methylnicotinamide is an immune regulatory metabolite in human ovarian cancer. *Sci Adv* **7**, (2021).
590. D. Berardi *et al.*, The Differential Metabolic Signature of Breast Cancer Cellular Response to Olaparib Treatment. *Cancers (Basel)* **14**, (2022).
591. V. J. Bhute, S. P. Palecek, Metabolic responses induced by DNA damage and poly (ADP-ribose) polymerase (PARP) inhibition in MCF-7 cells. *Metabolomics* **11**, 1779-1791 (2015).
592. S. Desagher, J. Glowinski, J. Prémont, Pyruvate protects neurons against hydrogen peroxide-induced toxicity. *J Neurosci* **17**, 9060-9067 (1997).
593. S. Domcke, R. Sinha, D. A. Levine, C. Sander, N. Schultz, Evaluating cell lines as tumour models by comparison of genomic profiles. *Nature Communications* **4**, 2126 (2013).
594. R. J. Kurman, I.-M. Shih, The dualistic model of ovarian carcinogenesis: revisited, revised, and expanded. *The American journal of pathology* **186**, 733-747 (2016).
595. J. H. Mao *et al.*, Mutually exclusive mutations of the Pten and ras pathways in skin tumor progression. *Genes Dev* **18**, 1800-1805 (2004).
596. M. D. To, J. Pérez-Losada, J.-H. Mao, A. Balmain, Crosstalk Between Pten and Ras Signaling Pathways in Tumor Development. *Cell Cycle* **4**, 1185-1188 (2005).
597. P. C. Fong *et al.*, Poly(ADP)-ribose polymerase inhibition: frequent durable responses in BRCA carrier ovarian cancer correlating with platinum-free interval. *J Clin Oncol* **28**, 2512-2519 (2010).
598. M. Demicco, X.-Z. Liu, K. Leithner, S.-M. Fendt, Metabolic heterogeneity in cancer. *Nature Metabolism* **6**, 18-38 (2024).
599. S. Liu, Z. Dai, D. E. Cooper, D. G. Kirsch, J. W. Locasale, Quantitative Analysis of the Physiological Contributions of Glucose to the TCA Cycle. *Cell Metabolism* **32**, 619-628.e621 (2020).
600. E. M. E. Barnes *et al.*, Lactic acidosis induces resistance to the pan-Akt inhibitor uprosertib in colon cancer cells. *British Journal of Cancer* **122**, 1298-1308 (2020).
601. S. Park *et al.*, ERRα-Regulated Lactate Metabolism Contributes to Resistance to Targeted Therapies in Breast Cancer. *Cell Reports* **15**, 323-335 (2016).
602. E. Allen *et al.*, Metabolic Symbiosis Enables Adaptive Resistance to Anti-angiogenic Therapy that Is Dependent on mTOR Signaling. *Cell Rep* **15**, 1144-1160 (2016).
603. D. Zhang *et al.*, Metabolic regulation of gene expression by histone lactylation. *Nature* **574**, 575-580 (2019).
604. N. Babl *et al.*, MCT4 blockade increases the efficacy of immune checkpoint blockade. *J Immunother Cancer* **11**, (2023).
605. S. E. Critchlow *et al.*, Abstract 3224: Pre-clinical targeting of the metabolic phenotype of

lymphoma by AZD3965, a selective inhibitor of monocarboxylate transporter 1 (MCT1). *Cancer Research* **72**, 3224-3224 (2012).
606. R. Polański *et al.*, Activity of the monocarboxylate transporter 1 inhibitor AZD3965 in small cell lung cancer. *Clin Cancer Res* **20**, 926-937 (2014).
607. C. S. Hong *et al.*, MCT1 Modulates Cancer Cell Pyruvate Export and Growth of Tumors that Co-express MCT1 and MCT4. *Cell Reports* **14**, 1590-1601 (2016).
608. F. W. Goldberg *et al.*, Discovery of Clinical Candidate AZD0095, a Selective Inhibitor of Monocarboxylate Transporter 4 (MCT4) for Oncology. *J Med Chem* **66**, 384-397 (2023).
609. S. E. Critchlow *et al.*, Abstract 1207: Reversing lactate-driven immunosuppression using the novel, potent and selective MCT4 inhibitor AZD0095. *Cancer Research* **79**, 1207-1207 (2019).
610. T. H. More, K. Hiller, Complexity of subcellular metabolism: strategies for compartment-specific profiling. *Curr Opin Biotechnol* **75**, 102711 (2022).
611. B. Alberts *et al.*, in *Molecular Biology of the Cell. 4th edition*. (Garland Science, 2002).
612. X. A. Cambronne, W. L. Kraus, Location, Location, Location: Compartmentalization of NAD+ Synthesis and Functions in Mammalian Cells. *Trends in Biochemical Sciences* **45**, 858-873 (2020).
613. N. Xie *et al.*, NAD+ metabolism: pathophysiologic mechanisms and therapeutic potential. *Signal Transduction and Targeted Therapy* **5**, 227 (2020).
614. R. P. Goodman, S. E. Calvo, V. K. Mootha, Spatiotemporal compartmentalization of hepatic NADH and NADPH metabolism. *Journal of Biological Chemistry* **293**, 7508-7516 (2018).
615. C. L. Kohnhorst *et al.*, Identification of a multienzyme complex for glucose metabolism in living cells. *Journal of Biological Chemistry* **292**, 9191-9203 (2017).
616. V. Pareek, H. Tian, N. Winograd, S. J. Benkovic, Metabolomics and mass spectrometry imaging reveal channeled de novo purine synthesis in cells. *Science* **368**, 283-290 (2020).
617. N. Zamboni, 13C metabolic flux analysis in complex systems. *Current Opinion in Biotechnology* **22**, 103-108 (2011).
618. L.-E. Quek *et al.*, Dynamic 13C Flux Analysis Captures the Reorganization of Adipocyte Glucose Metabolism in Response to Insulin. *iScience* **23**, 100855 (2020).
619. A. P. Halestrap, N. T. Price, The proton-linked monocarboxylate transporter (MCT) family: structure, function and regulation. *Biochem J* **343 Pt 2**, 281-299 (1999).
620. R. A. Noble *et al.*, Inhibition of monocarboxyate transporter 1 by AZD3965 as a novel therapeutic approach for diffuse large B-cell lymphoma and Burkitt lymphoma. *Haematologica* **102**, 1247-1257 (2017).
621. M. Beloueche-Babari *et al.*, MCT1 Inhibitor AZD3965 Increases Mitochondrial Metabolism, Facilitating Combination Therapy and Noninvasive Magnetic Resonance Spectroscopy. *Cancer Res* **77**, 5913-5924 (2017).
622. T. Heinrich *et al.*, Discovery of 5-{2-[5-Chloro-2-(5-ethoxyquinoline-8-sulfonamido)phenyl]ethynyl}-4-methoxypyridine-2-carboxylic Acid, a Highly Selective in Vivo Useable Chemical Probe to Dissect MCT4 Biology. *J Med Chem* **64**, 11904-11933 (2021).
623. V. Ganapathy *et al.*, Sodium-coupled monocarboxylate transporters in normal tissues and in cancer. *Aaps j* **10**, 193-199 (2008).
624. M. J. Coady *et al.*, The human tumour suppressor gene SLC5A8 expresses a Na+-

monocarboxylate cotransporter. *J Physiol* **557**, 719-731 (2004).
625. S. J. Park *et al.*, An overview of MCT1 and MCT4 in GBM: small molecule transporters with large implications. *Am J Cancer Res* **8**, 1967-1976 (2018).
626. D. Benjamin *et al.*, Dual Inhibition of the Lactate Transporters MCT1 and MCT4 Is Synthetic Lethal with Metformin due to NAD+ Depletion in Cancer Cells. *Cell Rep* **25**, 3047-3058.e3044 (2018).
627. S. Passarella *et al.*, Mitochondria and L-lactate metabolism. *FEBS Lett* **582**, 3569-3576 (2008).
628. M. Braga *et al.*, Tracing Nutrient Flux Following Monocarboxylate Transporter-1 Inhibition with AZD3965. *Cancers (Basel)* **12**, (2020).
629. K. Maan *et al.*, Metabolomics and transcriptomics based multi-omics integration reveals radiation-induced altered pathway networking and underlying mechanism. *npj Systems Biology and Applications* **9**, 42 (2023).
630. T. Jendoubi, Approaches to Integrating Metabolomics and Multi-Omics Data: A Primer. *Metabolites* **11**, (2021).
631. K. E. de Visser, J. A. Joyce, The evolving tumor microenvironment: From cancer initiation to metastatic outgrowth. *Cancer Cell* **41**, 374-403 (2023).
632. J. Kim, R. J. DeBerardinis, Mechanisms and Implications of Metabolic Heterogeneity in Cancer. *Cell Metabolism* **30**, 434-446 (2019).
633. M. Aichler, A. Walch, MALDI Imaging mass spectrometry: current frontiers and perspectives in pathology research and practice. *Laboratory Investigation* **95**, 422-431 (2015).
634. K. Mehra *et al.*, STICS, SCOUTs and p53 signatures; a new language for pelvic serous carcinogenesis. *Front Biosci (Elite Ed)* **3**, 625-634 (2011).
635. R. Perets *et al.*, Transformation of the fallopian tube secretory epithelium leads to high-grade serous ovarian cancer in Brca; Tp53; Pten models. *Cancer cell* **24**, 751-765 (2013).
636. D. W. Kindelberger *et al.*, Intraepithelial carcinoma of the fimbria and pelvic serous carcinoma: Evidence for a causal relationship. *Am J Surg Pathol* **31**, 161-169 (2007).
637. K. J. Noronha *et al.*, NAPRT Silencing in FH-Deficient Renal Cell Carcinoma Confers Therapeutic Vulnerabilities via NAD+ Depletion. *Molecular Cancer Research* **22**, 973-988 (2024).
638. E. Maniati *et al.*, Mouse Ovarian Cancer Models Recapitulate the Human Tumor Microenvironment and Patient Response to Treatment. *Cell Reports* **30**, 525-540.e527 (2020).
639. A. Krüger, A. Bürkle, K. Hauser, A. Mangerich, Real-time monitoring of PARP1-dependent PARylation by ATR-FTIR spectroscopy. *Nature Communications* **11**, 2174 (2020).
640. A. Kotsafti, M. Scarpa, I. Castagliuolo, M. Scarpa, Reactive Oxygen Species and Antitumor Immunity-From Surveillance to Evasion. *Cancers (Basel)* **12**, (2020).
641. M. Martínez-Cayuela, Oxygen free radicals and human disease. *Biochimie* **77**, 147-161 (1995).
642. C. Marchiori *et al.*, Epithelial CD80 promotes immune surveillance of colonic preneoplastic lesions and its expression is increased by oxidative stress through STAT3 in colon cancer cells. *J Exp Clin Cancer Res* **38**, 190 (2019).
643. A. Kirtonia, G. Sethi, M. Garg, The multifaceted role of reactive oxygen species in

tumorigenesis. *Cell Mol Life Sci* **77**, 4459-4483 (2020).
644. S. E. Weinberg, L. A. Sena, N. S. Chandel, Mitochondria in the regulation of innate and adaptive immunity. *Immunity* **42**, 406-417 (2015).
645. D. Mougiakakos, C. C. Johansson, R. Kiessling, Naturally occurring regulatory T cells show reduced sensitivity toward oxidative stress-induced cell death. *Blood* **113**, 3542-3545 (2009).
646. Z. Yan, S. K. Garg, J. Kipnis, R. Banerjee, Extracellular redox modulation by regulatory T cells. *Nat Chem Biol* **5**, 721-723 (2009).
647. D. M. Brizel *et al.*, Elevated tumor lactate concentrations predict for an increased risk of metastases in head-and-neck cancer. *International Journal of Radiation Oncology*Biology*Physics* **51**, 349-353 (2001).
648. R. Oberhaensli *et al.*, BIOCHEMICAL INVESTIGATION OF HUMAN TUMOURS IN VIVO WITH PHOSPHORUS-31 MAGNETIC RESONANCE SPECTROSCOPY. *The Lancet* **328**, 8-11 (1986).
649. S. K. Parks, J. Chiche, J. Pouysségur, Disrupting proton dynamics and energy metabolism for cancer therapy. *Nature Reviews Cancer* **13**, 611-623 (2013).
650. S. J. Reshkin, M. R. Greco, R. A. Cardone, Role of pHi, and proton transporters in oncogene-driven neoplastic transformation. *Philosophical Transactions of the Royal Society B: Biological Sciences* **369**, 20130100 (2014).
651. A. Khammanivong *et al.*, A novel MCT1 and MCT4 dual inhibitor reduces mitochondrial metabolism and inhibits tumour growth of feline oral squamous cell carcinoma. *Veterinary and Comparative Oncology* **18**, 324-341 (2020).
652. X. Sun *et al.*, Role of Proton-Coupled Monocarboxylate Transporters in Cancer: From Metabolic Crosstalk to Therapeutic Potential. *Frontiers in Cell and Developmental Biology* **8**, (2020).
653. O. R. Colegio *et al.*, Functional polarization of tumour-associated macrophages by tumour-derived lactic acid. *Nature* **513**, 559-563 (2014).
654. T. Ohashi *et al.*, M2-like macrophage polarization in high lactic acid-producing head and neck cancer. *Cancer Sci* **108**, 1128-1134 (2017).
655. X. Mu *et al.*, Tumor-derived lactate induces M2 macrophage polarization via the activation of the ERK/STAT3 signaling pathway in breast cancer. *Cell Cycle* **17**, 428-438 (2018).
656. K. Fischer *et al.*, Inhibitory effect of tumor cell–derived lactic acid on human T cells. *Blood* **109**, 3812-3819 (2007).
657. A. Tasdogan *et al.*, Metabolic heterogeneity confers differences in melanoma metastatic potential. *Nature* **577**, 115-120 (2020).

Appendix Figurers and Tables

Tumour cells injected	Source	Mouse number	Survival days
ID8 *Trp53*$^{-/-}$ cells	Dr Yuewei Xu	1	45
ID8 *Trp53*$^{-/-}$ cells	Dr Yuewei Xu	2	50
ID8 *Trp53*$^{-/-}$ cells	Dr Yuewei Xu	3	47
ID8 *Trp53*$^{-/-}$ cells	Dr Yuewei Xu	4	39
ID8 *Trp53*$^{-/-}$ cells	Dr Yuewei Xu	5	47
ID8 *Trp53*$^{-/-}$ cells	Dr Yuewei Xu	6	46
ID8 *Trp53*$^{-/-}$; *Pten*$^{-/-}$ cells	Flora McKinney	1	28
ID8 *Trp53*$^{-/-}$; *Pten*$^{-/-}$ cells	Flora McKinney	2	29
ID8 *Trp53*$^{-/-}$; *Pten*$^{-/-}$ cells	Flora McKinney	3	29
ID8 *Trp53*$^{-/-}$; *Pten*$^{-/-}$ cells	Flora McKinney	4	29
ID8 *Trp53*$^{-/-}$; *Pten*$^{-/-}$ cells	Flora McKinney	5	29
ID8 *Trp53*$^{-/-}$; *Pten*$^{-/-}$ cells	Survivial study (refer to Section 5.2.4)	1	31
ID8 *Trp53*$^{-/-}$; *Pten*$^{-/-}$ cells	Survivial study (refer to Section 5.2.4)	2	31

Appendix Table 3.1 Survival days of mice injected with ID8 tumour cells.

The tumour tissue samples were obtained from the survival study described in Section 5.2.4 and kindly provided by Dr Yuwei Xu and Flora McKinney in our group. Briefly, C57BL/6 mice were injected with ID8 Trp*53*$^{-/-}$ cells or ID8 *Trp53*$^{-/-}$;*Pten*$^{-/-}$ cells. For mice with ID8 Trp*53*$^{-/-}$ cells, they received 11 daily injections of vehicle solution three weeks after tumour cell implantation. The mice with ID8 *Trp53*$^{-/-}$;*Pten*$^{-/-}$ cells received 8 daily injections of vehicle solution two weeks after ID8 cell implantation. The vehicle solution is saline with 3.5% DMSO and 6.5% Tween-80. The mice were monitored daily until they reached humane end point (e.g., signs of pain). The mice were then culled, and omental tumour tissue were collected.

No	Metabolite name
1	Pyrrolidine; CE10; RWRDLPDLKQPQOW-UHFFFAOYSA-N
2	Lactate
3	Glycine
4	Linolenic acid
5	2-Methylpyrrolidine; CE10; RGHPCLZJAFCTIK-UHFFFAOYSA-N
6	1-Methyladenosine
7	2-Methylpyrrolidine; CE30; RGHPCLZJAFCTIK-UHFFFAOYSA-N
8	PC 16:0
9	L-ALANINE
10	Lyso PC 15:0
11	Choline; CE30; OEYIOHPDSNJKLS-UHFFFAOYSA-N
12	2-Methylbutyryl-L-carnitine
13	Serine
14	2-Methylpyrrolidine
15	Pyrrole-2-carboxylic acid
16	3-(4-Hydroxyphenyl)lactic acid
17	Uracil; CE30; ISAKRJDGNUQOIC-UHFFFAOYSA-N
18	3',5'-Cyclic AMP
19	Uracil
20	3-Dehydrocholic acid
21	Proline
22	3-Hydroxy-3-methylglutaric acid
23	4-Hydroxy-4-methyl-2-pentanone
24	3-Hydroxybutyric acid
25	Guanidinoacetic acid
26	Norvaline
27	5-Hydroxyindoleacetic
28	Betaine
29	9-Hydroxyoctadecadienoic acid
30	Valine
31	Acetylcarnitine
32	Threonine
33	Benzoic acid
34	Adenosine
35	Nicotinamide
36	Adenosine 3',5'-cyclic monophosphate
37	Thymine
38	Adenosine 5'-diphosphoribose
39	4-IMIDAZOLEACETIC ACID
40	Adenosine diphosphate
41	L-Pyroglutamic acid; CE30; ODHCTXKNWHHXJC-VKHMYHEASA-N
42	Adenosine monophosphate

43	Adenosine triphosphate
44	L-Pipecolic acid; CE30; HXEACLLIILLPRG-YFKPBYRVSA-N
45	ADMA
46	N-Acetylalanine
47	Alpha-Hydroxydeoxycholic Acid
48	Isoleucine
49	Leucine
50	Arachidonic acid
51	Asparagine
52	Aspartic acid
53	Ascorbic acid
54	Benzothiazole
55	Adenine
56	Glycerophosphate
57	ADENINE
58	Bilirubin
59	2-Phenylacetamide
60	Allopurinol
61	b-Orcinolcarboxylic acid
62	HYPOXANTHINE
63	Butyryl carnitine
64	2-Aminobenzoic acid; CE30; RWZYAGGXGHYGMB-UHFFFAOYSA-N
65	Choline
66	Trigonelline
67	Urocanic acid
68	Citric acid
69	2-Naphthylamine
70	3-Formylindole
71	Cortisol
72	4-Hydroxyquinoline
73	Creatine
74	Leucine methyl ester
75	Creatine phosphate
76	4-aminobutyric acid betaine; CE30; JHPNVNIEXXLNTR-UHFFFAOYSA-N
77	Cytidine
78	Spermidine
79	Cytidine 2',3'-cyclic phosphate
80	Coumarin
81	Glutamine
82	Cytidine Monophosphate
83	Lysine
84	Glyceric acid
85	L-Glutamic acid; CE30; WHUUTDBJXJRKMK-VKHMYHEASA-N

86	Deoxyadenosine
87	Methionine
88	Deoxycytidine
89	1-(4-methoxyphenyl)ethanone
90	D-erythro-Sphingosine-1-phosphate
91	Guanine
92	Fructose-6-phosphate
93	Xanthine; CE30; LRFVTYWOQMYALW-UHFFFAOYSA-N
94	Dopamine
95	m-Anisic-acid
96	Flavin adenine dinucleotide
97	Histidine
98	5-Aminovaleric acid betaine; CE30; CDLVFVFTRQPQFU-UHFFFAOYSA-N
99	Fumaric acid
100	5-Aminovaleric acid betaine; CE10; CDLVFVFTRQPQFU-UHFFFAOYSA-N
101	gamma-Glutamylleucine
102	6-Methylcoumarin
103	Gamma-Glytamyl-L-glutamic acid
104	Carnitine
105	Glu-Ile
106	Phenylalanine
107	Glutamic acid
108	Phthalic acid; CE30; XNGIFLGASWRNHJ-UHFFFAOYSA-N
109	Glutamyltyrosine
110	2-Mercaptobenzothiazole
111	Oxidised glutathione
112	Uric acid; CE10; LEHOTFFKMJEONL-UHFFFAOYSA-N
113	Glycerophosphocholine
114	alpha-Methylhistidine
115	Arginine
116	Citrulline
117	l-ascorbic acid
118	Mephedrone
119	Guanosine 5'-diphospho-beta-L-fucose
120	Fusaric acid
121	GMP
122	Tyrosine
123	Hexanoyl-Carnitine
124	Phosphocholine
125	5-Hydroxyindole-3-acetic acid
126	Hypoxanthine
127	N-Acetylmethionine
128	Indole-carboxaldehyde

129	4-Hexylresorcinol
130	N,N-Dimethylarginine
131	Indoxyl sulfate
132	Spermine
133	Acetylcarnitine; CE30; RDHQFKQIGNGIED-UHFFFAOYSA-N
134	IMP
135	R-Deprenyl N-Oxide
136	Acetylcarnitine [M]+
137	L-alanine
138	TRYPTOPHAN
139	L-Aspartyl-L-phenylalanine
140	Indolelactic acid
141	NCGC00042134-05_C11H13NO3_N-Acetylphenylalanine
142	anthraquinone
143	L-glutamic acid
144	Kynurenine
145	2-Benzothiazolesulfonic acid
146	LPC 16:0
147	Denatonium_TP222
148	LPC 18:1
149	Cytidine; CE30; UHDGCWIWMRVCDJ-XVFCMESISA-N
150	LPE 16:0
151	Genipin
152	L-Pyroglutamic acid
153	5-butyl-3-methyl-7H-furo[3,2-g]chromen-7-one
154	L-Tryptophan
155	Lauric isopropanolamide
156	N,N-Dimethyltetradecylamine-N-oxide
157	Malate
158	Metobromuron
159	Malonyltryptophan
160	Curdione
161	Maltotriose
162	Hexanoyl-L-Carnitine
163	Imazapyr
164	Trimethyllysine
165	N6-Acetyl-L-lysine
166	methyl 2-((4-methyl-2-oxo-2H-chromen-7-yl)oxy)propanoate
167	N-Acetylarginine
168	8-acetyl-5,7-dimethoxy-2,2-dimethylchromene
169	N-Acetylglutamic
170	MMV688514
171	THYMIDINE

172	N-Acetylphenylalanine
173	4,7,8-trimethoxy-3,5-dimethylchromen-2-one
174	N-Alpha-Acetyllysine
175	Mirtazapine
176	N-Methylproline
177	Viramune
178	O-Acetyl-L-serine
179	Tri-N-butyl phosphate; CE10; STCOOQWBFONSKY-UHFFFAOYSA-N
180	Oleoyl ethylamide
181	Adenosine; CE0; OIRDTQYFTABQOQ-KQYNXXCUSA-N
182	Oleoyl-Carnitine
183	Inosine
184	Ophthalmic acid
185	Moclobemide
186	Pantothenic acid
187	alpha-santonin
188	Prostaglandin D2
189	reynosin
190	Phe-Glu_2
191	(E)-5-hydroxy-3-isobutyl-6-(3-methylbenzylidene)-1,6-dihydropyrazin-2(3H)-one
192	Phenylacetyl-L-glutamine
193	Lauryldiethanolamine
194	1-(3,4-Dimethoxycinnamoyl)piperidine
195	Phe-Phe
196	6-Shogaol
197	Phosphoric acid
198	Triphenylphosphine oxide
199	PI 34:1
200	15,16-Dihydrotanshinone I
201	PI 34:2
202	Dibutylphthalate
203	PI 36:2
204	?-linolenic acid
205	PI 36:4
206	Sulfamethoxypyridazine
207	PI 38:3
208	Dodemorph
209	PI 38:5
210	2-(4-oxoquinazolin-3(4H)-yl)ethyl isobutyrate
211	Hexaethylene glycol; CE0; IIRDTKBZINWQAW-UHFFFAOYSA-N
212	Pro-Phe
213	Guanosine

214	Propionic acid
215	9,10-alpha-Epoxy-eremanthin
216	Physcion
217	Pyrrolidine
218	Octanoyl-L-Carnitine
219	Pyruvic acid
220	OPHTHALMATE
221	Resveratrol 3-O-D-glucuronide
222	(S)-3-amino-4-(((S)-1-methoxy-1-oxo-3-phenylpropan-2-yl)amino)-4-oxobutanoic acid
223	FMN
224	NCGC00263645-02_C11H15N5O3S_5'-Methylthioadenosine
225	S-adenosyl-L-homocysteine
226	2,2'-(Tetradecylimino)diethanol
227	Benzalkonium chloride (C12)
228	(4S,4aR,8aS)-4-[(3R)-3-hydroxy-3-methylpent-4-enyl]-3,4a,8,8-tetramethyl-5,6,7,8a-tetrahydro-4H-naphthalen-1-one
229	"CYTIDINE 2',3'-CYCLIC PHOSPHATE"
230	Epigallocatechin
231	Succinic acid
232	Glutathione
233	Taurine
234	gamma-Glutamyltyrosine
235	Taurochenodeoxycholic acid
236	Malaoxon
237	h_55_metenolone-m
238	Niclosamide
239	Taurodeoxycholic acid
240	progesterone
241	Theophyline
242	Resmethrin
243	Adenosine Monophosphate
244	Thymidine
245	Tryptophan
246	INOSINE 5'-PHOSPHATE
247	7-hydroxy-1,4a-dimethyl-9-oxo-7-propan-2-yl-2,3,4,4b,5,6,10,10a-octahydrophenanthrene-1-carboxylic acid
248	Urea
249	5-[2-(furan-3-yl)ethyl]-8-hydroxy-5,6,8a-trimethyl-3,4,4a,6,7,8-hexahydronaphthalene-1-carboxylic acid
250	Uric acid
251	5-[5-hydroxy-3-(hydroxymethyl)pentyl]-8a-(hydroxymethyl)-5,6-dimethyl-3,4,4a,6,7,8-hexahydronaphthalene-1-carboxylic acid

252	Uridine
253	Uridine 5'-diphospho-N-acetylglucosamine
254	5-hydroxy-7-[2-(2-hydroxy-5-oxo-2H-furan-3-yl)ethyl]-7,8-dimethyl-5,6,6a,8,9,10-hexahydro-1H-benzo[d][2]benzofuran-3-one
255	Uridine monophosphate
256	(8S,9S,10R,11S,13S,14S,17R)-11,17-dihydroxy-17-(2-hydroxyacetyl)-10,13-dimethyl-2,6,7,8,9,11,12,14,15,16-decahydro-1H-cyclopenta[a]phenanthren-3-one
257	Uridine triphosphate
258	Finasteride
259	Riboflavin
260	Val-Gly
261	BIS(2-ETHYLHEXYL)PHTHALATE
262	(E)-3-(4-acetyloxy-2,3-dihydroxy-2,5,5,8a-tetramethyl-3,4,4a,6,7,8-hexahydro-1H-naphthalen-1-yl)prop-2-enoic acid
263	Xanthine
264	Palmitoylcarnitine
265	Uridine 5_-(trihydrogen diphosphate)
266	[4,5-dihydroxy-3,4-bis(hydroxymethyl)-4a,8,8-trimethyl-5,6,7,8a-tetrahydro-1H-naphthalen-1-yl] hexanoate
267	CHOLIC ACID
268	forskolin
269	N6-Threonylcarbamoyladenosine
270	NCGC00347704-02_C24H32O7_2H-Oxireno[1,10a]phenanthro[3,2-b]furan-10(11bH)-one, 5,7-bis(acetyloxy)-3,3a,4,5,6,7,7a,7b,8,8a-decahydro-4,4,7a,11-tetramethyl-, (1aS,3aR,5S,7S,7aR,7bS,8aR,11bR)-
271	Fludrocortisone acetate
272	Linoleyl Carnitine
273	Oleoyl-L-Carnitine
274	NCGC00384593-01![3-hydroxy-3-methyl-1-(7-oxofuro[3,2-g]chromen-9-yl)oxybutan-2-yl] 3-methylbutanoate [IIN-based on: CCMSLIB00000848938]
275	Gardenoside
276	Adenosine_Diphosphate
277	Stearoyl-L-Carnitine
278	Lancerin
279	Shanzhiside methylester
280	alpha-Tocopherol
281	(1R,3R,6R,8S,10R,13S,16S,17R)-8-tert-butyl-6,17-dihydroxy-16-methyl-2,4,14,19-tetraoxahexacyclo[8.7.2.0?,??.0?,?.0?,??.0??,??]nonadecane-5,15,18-trione
282	NCGC00380753-01_C16H28O12_6-O-Isobutyryl-alpha-D-glucopyranosyl alpha-D-glucopyranoside

283	narcotine
284	Chrysophanol-8-O-beta-D-glucopyranoside
285	NCGC00380314-01_C22H27NO7_3,5,7,9-Undecatetraenoic acid, 2-ethylidene-11-[4-hydroxy-4-(2-hydroxyethyl)-2-oxo-6-oxa-3-azabicyclo[3.1.0]hex-1-yl]-4,10-dimethyl-11-oxo-, methyl ester, (2Z,3E,5E,7E,9E)-
286	Ginkgolide C
287	Folic acid
288	NCGC00385345-01_C17H26O12_Cyclopenta[c]pyran-4-carboxylic acid, 1-(beta-D-glucopyranosyloxy)-1,4a,5,6,7,7a-hexahydro-5,6-dihydroxy-7-(hydroxymethyl)-, methyl ester, (1S,4aS,6R,7S,7aS)-
289	NCGC00385998-01_C17H26O12_Cyclopenta[c]pyran-4-carboxylic acid, 1-(beta-D-glucopyranosyloxy)-1,4a,5,6,7,7a-hexahydro-5,6,7-trihydroxy-7-methyl-, methyl ester, (1S,4aS,5S,6S,7R,7aS)-
290	Lovastatin hydroxy acid observed in lovastatin standard
291	methyl (2E,8E)-9-[3a-hydroxy-6,7-dimethyl-1-(2-methylpropyl)-3-oxo-2,4,7,7a-tetrahydro-1H-isoindol-4-yl]-4,5-dihydroxy-8-methylnona-2,8-dienoate
292	[(7R,8R,10R,13S)-17-(furan-3-yl)-4,4,8,10,13-pentamethyl-3,16-dioxo-6,7,9,11,12,17-hexahydro-5H-cyclopenta[a]phenanthren-7-yl] acetate
293	2-amino-3-[[(6E,9E)-5-hydroxy-8-methoxy-5,9,13,14-tetramethyl-2-oxo-1-oxacyclotetradeca-6,9-dien-4-yl]sulfanyl]propanoic acid
294	[(2E,6Z,10Z)-7,11-bis(acetyloxymethyl)-3,15-dimethylhexadeca-2,6,10,14-tetraenyl] acetate
295	Homoorientin
296	4-(3,4-dihydroxyphenyl)-7-hydroxy-5-[(2S,3R,4S,5S,6R)-3,4,5-trihydroxy-6-(hydroxymethyl)oxan-2-yl]oxychromen-2-one
297	"(3R,5R,7R,8R,9S,10S,12S,13R,14S,17R)-17-((2R)-6,7-dihydroxy-6-methylheptan-2-yl)-10,13-dimethylhexadecahydro-1H-cyclopenta[a]phenanthrene-3,7,12-triol"
298	Soyasapogenol A
299	4-[7-acetyloxy-5-chloro-3-[(1E,3E)-3,5-dimethylhepta-1,3-dienyl]-7-methyl-6,8-dioxoisoquinolin-2-yl]butanoic acid
300	4-((9S)-3,5,14-trihydroxy-10-((E)-((1-hydroxybutan-2-yl)imino)methyl)-13-methylhexadecahydro-1H-cyclopenta[a]phenanthren-17-yl)furan-2(5H)-one
301	Pralatrexate(Folotyn)
302	Speciosine
303	Vindoline
304	NCGC00380662-01_C20H27NO11_[(6-O-Hexopyranosylhexopyranosyl)oxy](phenyl)acetonitrile

305	NCGC00163699-03_C26H34O7_2,4,6,8-Decatetraenedioic acid, mono[5-methoxy-4-[2-methyl-3-(3-methyl-2-buten-1-yl)oxiranyl]-1-oxaspiro[2.5]oct-6-yl] ester, (2E,4E,6E,8E)-
306	3-((3a'S,6a'R)-5,7-dimethyl-2,4',6'-trioxo-5'-phenethyl-3',3a',4',5',6',6a'-hexahydro-2'H-spiro[indoline-3,1'-pyrrolo[3,4-c]pyrrol]-3'-yl)propanamide
307	methyl 3-hydroxy-5-(((1R,4aS)-7-isopropyl-1,4a-dimethyl-1,2,3,4,4a,9,10,10a-octahydrophenanthren-1-yl)methyl)-5H-pyrazolo[4,3-c]pyridine-7-carboxylate
308	NCGC00384770-01_C19H28O13_5-Hydroxy-2,3-dimethoxyphenyl 4-O-[(2S,3R,4R)-3,4-dihydroxy-4-(hydroxymethyl)tetrahydro-2-furanyl]-beta-D-glucopyranoside
309	Cytidine 5'-diphosphocholine
310	NCGC00180796-02_C28H38O6_(4beta,5beta,6beta,22R)-4,27-Dihydroxy-5,6:22,26-diepoxyergosta-2,24-diene-1,26-dione
311	(Z)-9-(4-hydroxyphenyl)-2-(2,3,4-trimethoxybenzylidene)-8,9-dihydro-2H-furo[2,3-f]chromene-3,7-dione
312	Lucidenic acid B
313	PharmaGSID_48519
314	Scutellarin methyl ester
315	Aconine
316	Taurodeoxycholate
317	Rhodamine B
318	Fexofenadine
319	25R-Inokosterone
320	"methyl (6R)-2-(hydroxymethyl)-6-((3R,5S,7R,9S,10S,12S,13R,14S,17R)-3,7,12-trihydroxy-10,13-dimethylhexadecahydro-1H-cyclopenta[a]phenanthren-17-yl)heptanoate"
321	3-(2-fluorophenyl)-10-(2-hydroxy-6-methoxyquinolin-3-yl)-9,10-dihydropyrano[2,3-f]chromene-4,8-dione
322	NCGC00380619-01_C27H37NO7_Spiro[2H-furo[2,3-e]isoindole-2,1'(2'H)-naphthalene]-7(3H)-butanoic acid, 3',4',4'a,5',6,6',7',8,8',8'a-decahydro-4,6',7'-trihydroxy-2',5',5',8'a-tetramethyl-6-oxo-, (2R,2'R,6'S,7'R,8'aS)-
323	NCGC00168968-03_C24H28O11_[(1aS,1bS,2S,5aR,6S,6aS)-2-(beta-D-Glucopyranosyloxy)-6-hydroxy-1b,5a,6,6a-tetrahydrooxireno[4,5]cyclopenta[1,2-c]pyran-1a(2H)-yl]methyl (2E)-3-phenylacrylate
324	NCGC00380484-01_C22H36O12_beta-D-Glucopyranose, 6-O-beta-D-glucopyranosyl-1-O-[(2,6,6-trimethyl-1-cyclohexen-1-yl)carbonyl]-
325	Telmisartan
326	Taurocholate
327	Tsugaric acid A
328	Lyso-PC 18:0

329	10'-(3-methoxy-4-((1-methyl-1H-imidazol-2-yl)methoxy)phenyl)-9',10'-dihydro-3'H-spiro[cyclohexane-1,2'-pyrano[2,3-f]chromene]-4',8'-dione
330	AVE3247
331	maltotriose
332	NCGC00380271-01_C24H40O11_2-Cyclohexen-1-one, 3,5,5-trimethyl-4-[3-[(6-O-beta-D-xylopyranosyl-beta-D-glucopyranosyl)oxy]butyl]-
333	NCGC00386012-01_C24H42O11_beta-D-Glucopyranoside, (1S,4R,5R)-4-[(1E,3R)-3-hydroxy-1-buten-1-yl]-3,3,5-trimethylcyclohexyl 6-O-[(2R,3R,4R)-tetrahydro-3,4-dihydroxy-4-(hydroxymethyl)-2-furanyl]-
334	"((4R)-4-((3R,5R,9S,10S,12S,13R,14S,17R)-3,12-dihydroxy-10,13-dimethylhexadecahydro-1H-cyclopenta[a]phenanthren-17-yl)pentanoyl)glycylglycine"
335	NCGC00169336-02_C24H28O12_2-Propenoic acid, 3-(4-hydroxyphenyl)-, [(1aS,1bS,2S,5aR,6S,6aS)-2-(beta-D-glucopyranosyloxy)-1b,5a,6,6a-tetrahydro-6-hydroxyoxireno[4,5]cyclopenta[1,2-c]pyran-1a(2H)-yl]methyl ester, (2E)-
336	(3R)-N-((2S,3R)-1-((benzo[d][1,3]dioxol-5-ylmethyl)amino)-3-methyl-1-oxopentan-2-yl)-2,2-dimethyl-5-oxo-2,3,5,9b-tetrahydrothiazolo[2,3-a]isoindole-3-carboxamide
337	(3S,4S,4aS,6R,6aS,6bS,7S,8R,8aR,9S,9aS,12S,15aS,15bS,16aR,16bS)-9,12,16b-trimethyldocosahydro-1H-4,16a-epoxybenzo[4,5]indeno[1,2-h]pyrido[1,2-b]isoquinoline-3,4,6,6b,7,8,9-heptaol
338	NCGC00381416-01![3-methyl-1-[3-methyl-1-oxo-1-(2,3,4,5,6-pentahydroxyhexoxy)pentan-2-yl]oxy-1-oxobutan-2-yl] 2-hydroxy-3-methylpentanoate [IIN-based on: CCMSLIB00000847843]
339	Ganoderic Acid G
340	Phytolaccagenin
341	"2-((4R)-4-((3R,5R,6S,7R,9S,10R,13R,14S,17R)-3,6,7-trihydroxy-10,13-dimethylhexadecahydro-1H-cyclopenta[a]phenanthren-17-yl)pentanamido)ethane-1-sulfonic acid"
342	Ceramide (d18:1/16:0)
343	ADENOSINE 5'-DIPHOSPHORIBOSE
344	Biliverdin
345	methyl 3-(2-(3,4-dihydroxyphenyl)-3,5,7-trihydroxy-4-oxo-4H-chromen-8-yl)-3-(2-hydroxy-6-methoxyquinolin-3-yl)propanoate
346	(1R,3aR,3bS,4aR,6S,7S,7aR,8R,8aR,9aR)-1,4a,8-tris(acetyloxy)-2,2,3b,6,8a-pentamethyl-4,9-dioxo-tetradecahydro-1H-cyclopenta[a]s-indacen-7-yl butanoate
347	lappaconitine
348	(4S,5Z,6S)-5-[2-[(E)-3-(4-hydroxyphenyl)prop-2-enoyl]oxyethylidene]-4-(2-methoxy-2-oxoethyl)-6-[(2S,3R,4S,5S,6R)-3,4,5-trihydroxy-6-(hydroxymethyl)oxan-2-yl]oxy-4H-pyran-3-carboxylic acid

349	NCGC00380937-01_C31H40O10_(1S,2R,4S,9R,10R,14S,15S,17S)-9-(3-Furyl)-1-hydroxy-15-(2-methoxy-2-oxoethyl)-10,14,16,16-tetramethyl-7,18-dioxo-3,8-dioxapentacyclo[12.3.1.0~2,4~.0~4,13~.0~5,10~]octadec-17-yl 2-methylpropanoate
350	Glutathione (oxidized form)
351	Crassostreaxanthin A
352	NAD
353	Subsessiline
354	FLAVIN ADENINE DINUCLEOTIDE
355	Typhaneoside
356	Picfeltarraenin IB
357	NCGC00347377-02_C41H66O14_1-O-[(2beta,3beta,5xi,9xi,18xi)-2,23-Dihydroxy-28-oxo-3-(beta-D-xylopyranosyloxy)olean-12-en-28-yl]-beta-D-glucopyranose
358	Solasonine
359	(9S,18R,21R)-15-benzyl-6-(4-((tert-butoxycarbonyl)oxy)benzyl)-21-(3-guanidinopropyl)-18-isobutyl-2,2,9-trimethyl-4,7,10,13,16,19-hexaoxo-3-oxa-5,8,11,14,17,20-hexaazadocosan-22-oic acid

Appendix Table 3.2 List of metabolites that were annotated by MS Dial with both MS1 and MS2 matching to the public library (version 17).

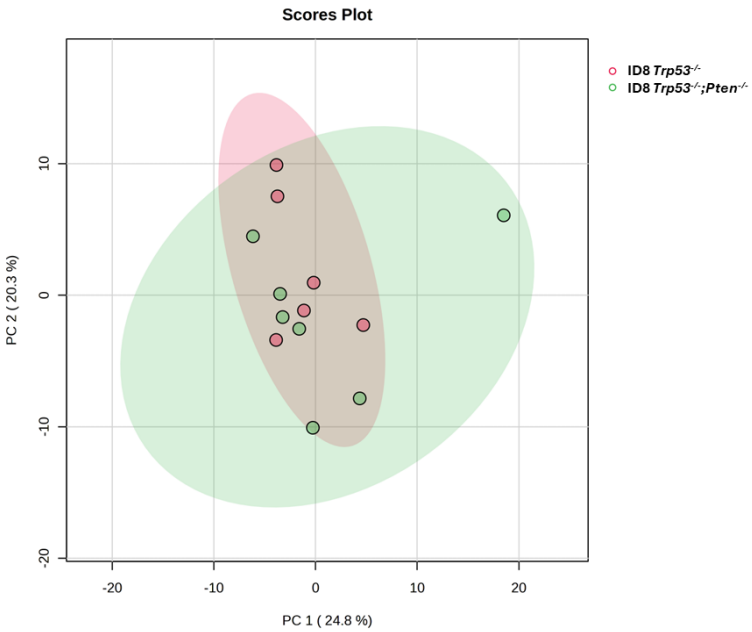
No	Metabolite name
1	Lactate
2	Linolenic acid
3	1-Methyladenosine
4	PC 16:0
5	Lyso PC 15:0
6	2-Methylbutyryl-L-carnitine
7	2-Methylpyrrolidine
8	2-Phenylacetamide
9	3-(4-Hydroxyphenyl)lactic acid
10	3',5'-Cyclic AMP
11	3-Dehydrocholic acid
12	3-Hydroxy-3-methylglutaric acid
13	3-Hydroxybutyric acid
14	5-Hydroxyindole-3-acetic acid
15	5-Hydroxyindoleacetic
16	9-Hydroxyoctadecadienoic acid
17	Acetylcarnitine
18	Adenine
19	Adenosine
20	Adenosine 3',5'-cyclic monophosphate
21	Adenosine 5′-diphosphoribose
22	Adenosine diphosphate
23	Adenosine monophosphate
24	Adenosine triphosphate
25	ADMA
26	Alpha-Hydroxydeoxycholic Acid
27	alpha-Methylhistidine
28	Arachidonic acid
29	Arginine
30	Ascorbic acid
31	Asparagine
32	Aspartic acid
33	Glycerophosphate
34	Betaine
35	Bilirubin
36	Biliverdin
37	b-Orcinolcarboxylic acid
38	Butyryl carnitine
39	Carnitine
40	Choline
41	Chrysophanol-8-O-beta-D-glucopyranoside
42	Citric acid

43	Citrulline
44	Cortisol
45	Creatine
46	Creatine phosphate
47	Cytidine
48	Cytidine 2',3'-cyclic phosphate
49	Cytidine 5'-diphosphocholine
50	Cytidine Monophosphate
51	Glyceric acid
52	Deoxyadenosine
53	Deoxycytidine
54	D-erythro-Sphingosine-1-phosphate
55	Fructose-6-phosphate
56	Dopamine
57	Flavin adenine dinucleotide
58	Folic acid
59	Fumaric acid
60	gamma-Glutamylleucine
61	gamma-Glutamyltyrosine
62	Gamma-Glytamyl-L-glutamic acid
63	Glu-Ile
64	Glutamic acid
65	Glutamyltyrosine
66	Glutathione
67	Oxidised glutathione
68	Glycerophosphocholine
69	Glycine
70	Guanidinoacetic acid
71	Guanine
72	Guanosine
73	Guanosine 5'-diphospho-beta-L-fucose
74	GMP
75	Hexanoyl-Carnitine
76	Histidine
77	Hypoxanthine
78	Indole-carboxaldehyde
79	Indolelactic acid
80	Indoxyl sulfate
81	Inosine
82	IMP
83	Isoleucine
84	L-alanine
85	L-Aspartyl-L-phenylalanine

86	Leucine
87	Leucine methyl ester
88	L-glutamic acid
89	Linoleyl Carnitine
90	LPC 16:0
91	LPC 18:1
92	LPE 16:0
93	L-Pyroglutamic acid
94	L-Tryptophan
95	Lyso-PC 18:0
96	Malate
97	Malonyltryptophan
98	Maltotriose
99	Methionine
100	Trimethyllysine
101	N6-Acetyl-L-lysine
102	N-Acetylalanine
103	N-Acetylarginine
104	N-Acetylglutamic
105	N-Acetylmethionine
106	N-Acetylphenylalanine
107	N-Alpha-Acetyllysine
108	N-Methylproline
109	O-Acetyl-L-serine
110	Oleoyl ethylamide
111	Oleoyl-Carnitine
112	Ophthalmic acid
113	Palmitoylcarnitine
114	Pantothenic acid
115	Prostaglandin D2
116	Phe-Glu_2
117	Phenylacetyl-L-glutamine
118	Phenylalanine
119	Phe-Phe
120	Phosphocholine
121	Phosphoric acid
122	PI 34:1
123	PI 34:2
124	PI 36:2
125	PI 36:4
126	PI 38:3
127	PI 38:5
128	Proline

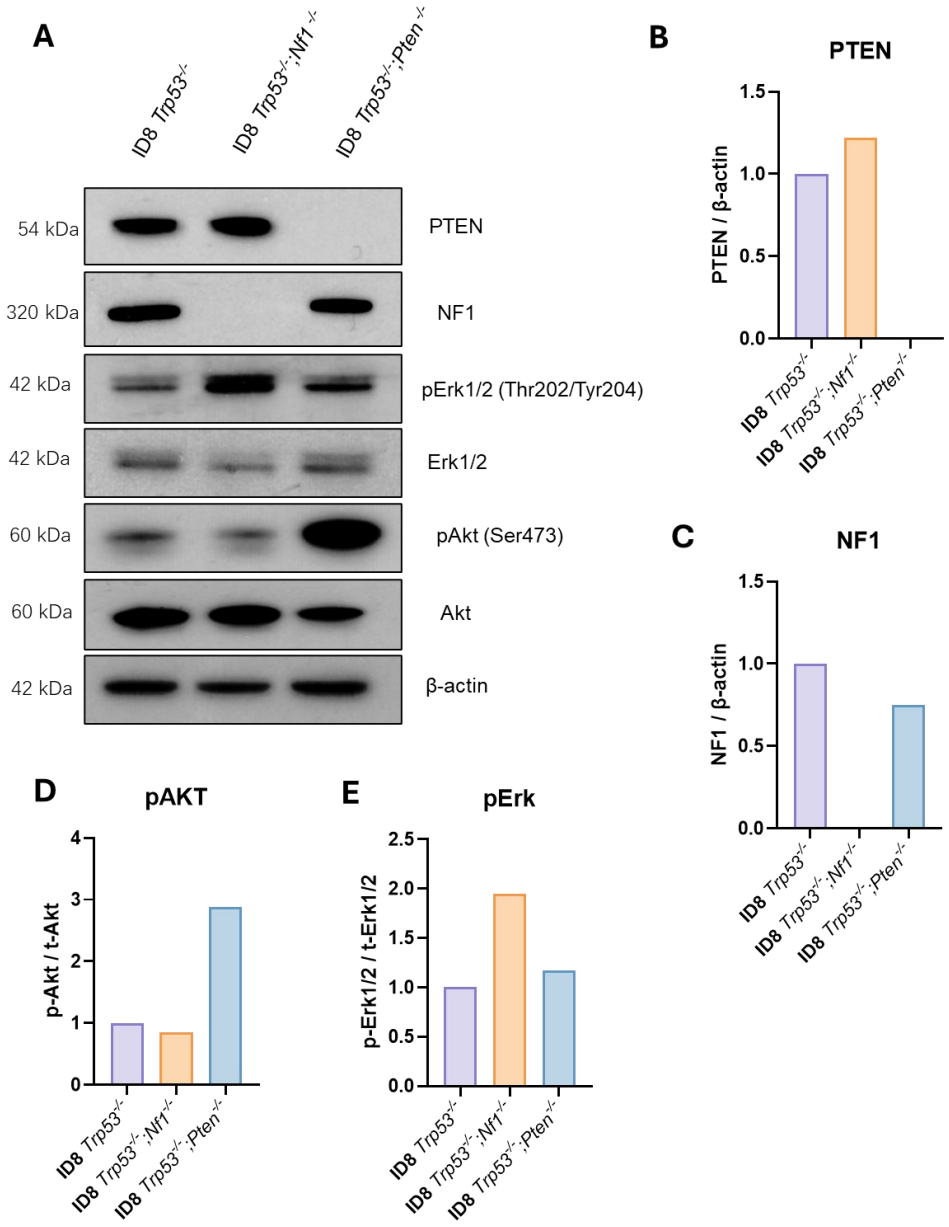
129	Pro-Phe
130	Propionic acid
131	Pyrrole-2-carboxylic acid
132	Pyrrolidine
133	Pyruvic acid
134	Resveratrol 3-O-D-glucuronide
135	Riboflavin
136	FMN
137	S-adenosyl-L-homocysteine
138	Serine
139	Spermidine
140	Spermine
141	Stearoyl-L-Carnitine
142	Succinic acid
143	Taurine
144	Taurochenodeoxycholic acid
145	Taurocholate
146	Taurodeoxycholate
147	Taurodeoxycholic acid
148	Theophyline
149	Threonine
150	Thymidine
151	Thymine
152	Tryptophan
153	Uracil
154	Urea
155	Uric acid
156	Uridine
157	Uridine 5'-diphospho-N-acetylglucosamine
158	Uridine monophosphate
159	Uridine triphosphate
160	Urocanic acid
161	Val-Gly
162	Valine
163	Xanthine
164	Nicotinamide
165	NAD

Appendix Table 3.3 List of metabolites that were cross-validated with MS1 and MS2 matching to the in-house built library.



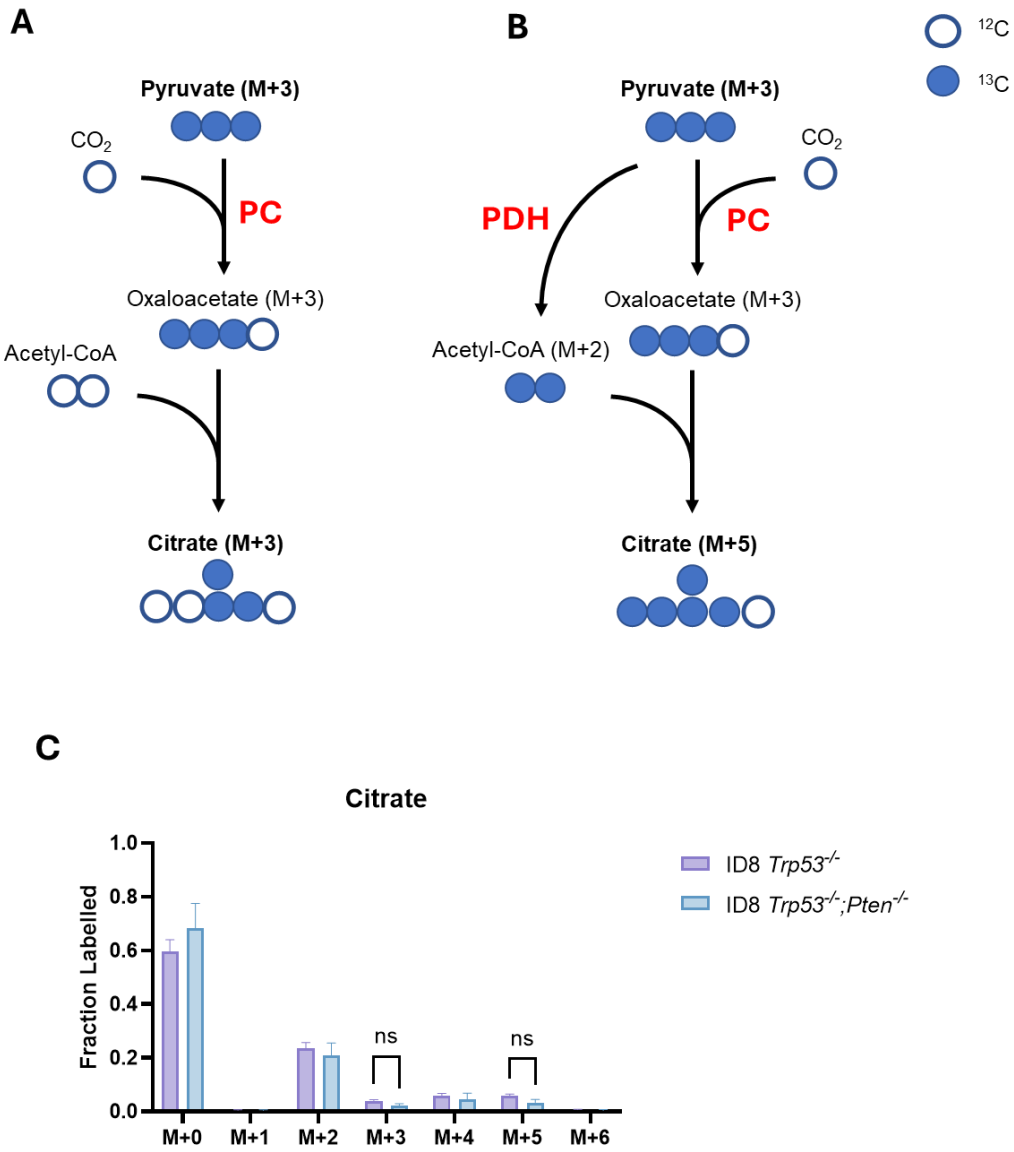
Appendix Figure 3. 1 PCA analysis showed that there was no separation between the ID8 *Trp53*$^{-/-}$ and *Trp53*$^{-/-}$*; Pten*$^{-/-}$ tumours.

Untargeted metabolic profiling was performed using mouse tumour tissue and the PCA plot was generated by Metaboanalyst (v.5.0.). Samples cluster closely regardless of Pten status. Coloured circles represent 95% confidence intervals.



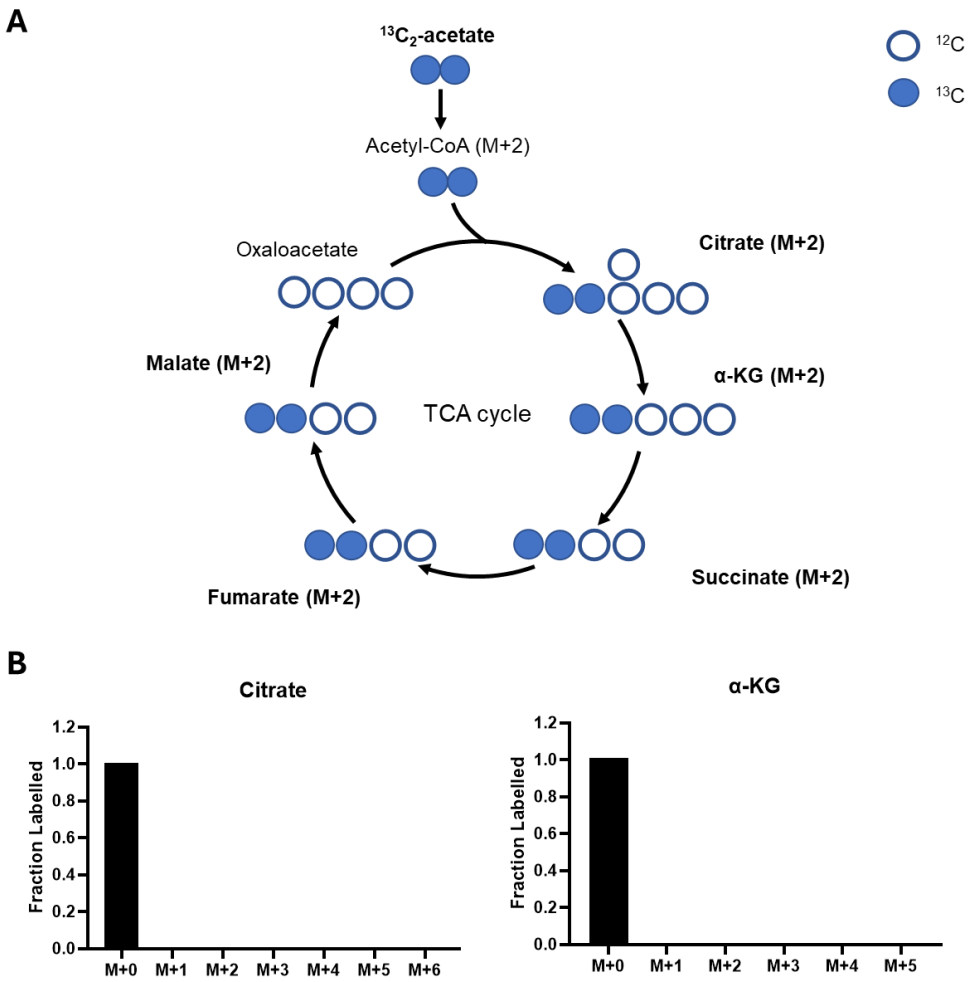
Appendix Figure 3.2 Validation of the panel of ID8 cell lines.

(A) Images of WB blots. ID8 Trp*53*$^{-/-}$, ID8 *Trp53*$^{-/-}$*;Nf1*$^{-/-}$, ID8 *Trp53*$^{-/-}$*;Pten*$^{-/-}$ cells were cultured in DMEM media with 10% FBS and 5.6mM glucose. Proteins were extracted and expression of NF1 and PTEN was examined by WB. Activity in the Erk1/2 and Akt pathways were also investigated by measuring phosphorylation levels using WB. (B-E) Densitometry analysis. The relative levels of PTEN (B) and NF1 (C) expression were normalized to β-actin (i.e., the internal control). The levels of phospho-Akt (D) and phospho-ERK1/2 (E) were normalized to respective total protein levels. Data are represented as mean from one biological repeat.

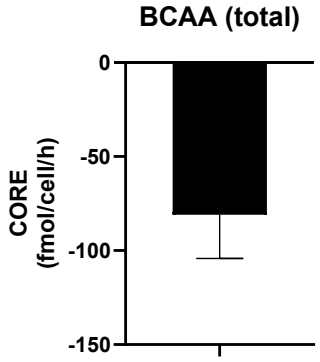


Appendix Figure 3.3 Extremely low levels of pyruvate carboxylase activity were observed in ID8 cells.

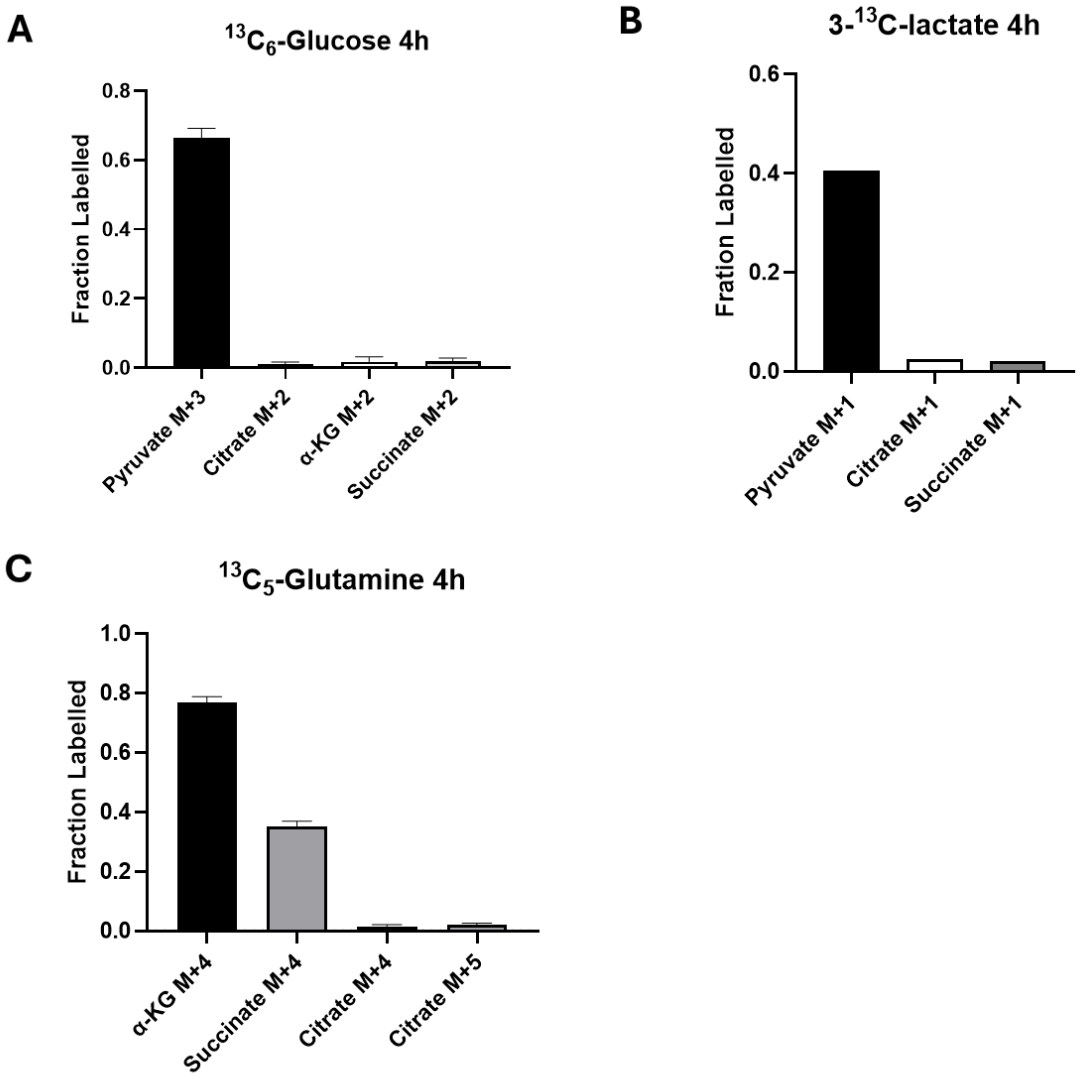
(A-B) Schematics showing pyruvate carboxylase (PC) flux using $^{13}C_6$-glucose as a tracer. PC catalyses the carboxylation of pyruvate to generate oxaloacetate. Given $^{13}C_6$-glucose produces M+3 pyruvate via glycolysis, oxaloacetate is labelled M+3. When oxaloacetate condenses with unlabelled or M+2 acetyl-CoA (i.e., from PDH flux), M+3 (A) and M+5 (B) citrate is generated, respectively. PC and PDH fluxes are indicated in red. (C) MID of citrate. ID8 Trp*53*$^{-/-}$ and ID8 *Trp53*$^{-/-}$;*Pten*$^{-/-}$ cells were incubated with 5.6mM $^{13}C_6$-glucose for 24h. Intracellular metabolites were extracted and analysed by GC-MS. Data represent mean ± SD from three independent biological repeats. One-way ANOVA and post-hoc Tukey tests were performed to determine statistical significance. ns, not significant.



Appendix Figure 3.4 Exogenous acetate might not be a carbon source of the TCA cycle.
(A) Schematics of the labelling patterns using $^{13}C_2$-acetate as a tracer. The conversion of acetate to acetyl-CoA is catalysed by acetyl-CoA synthetase (ACSS) and generates M+2 acetyl-CoA. After condensing with unlabelled oxaloacetate, the TCA cycle intermediates (e.g., citrate) are labelled M+2. (B) MID of citrate and α-KG. ID8 Trp*53*$^{-/-}$ cells were incubated with 500μM $^{13}C_2$-acetate for 24h. Intracellular metabolites were extracted and analysed by GC-MS. Data represent mean from one repeat.

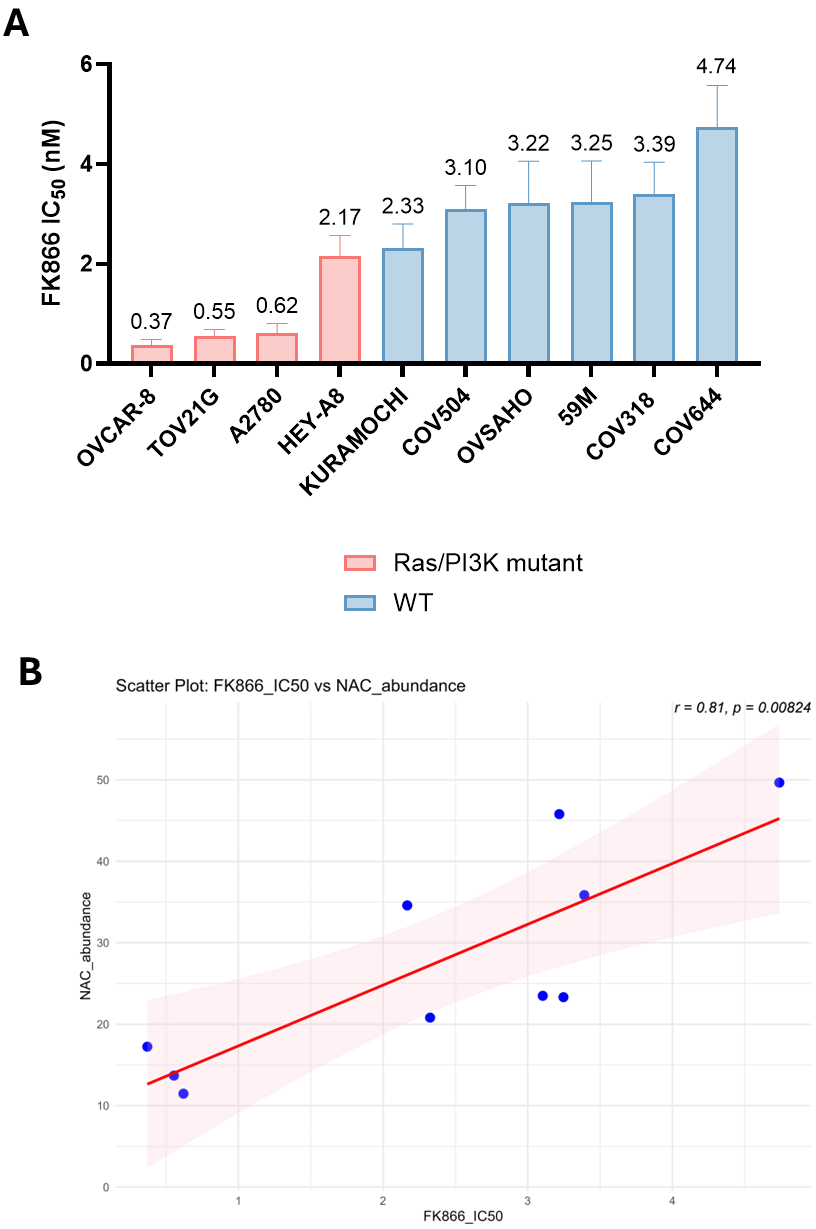


Appendix Figure 3.5 Net consumption of BCAA was observed in ID8 Trp*53*$^{-/-}$ cells.
CORE rates of total BCAA (i.e., valine, leucine and isoleucine) in ID8 Trp*53*$^{-/-}$ cells incubated without drug treatment. Media were collected at the start and end of the 24h incubation period and total BCAA levels were measured by NMR spectroscopy. Cells were also counted to calculate CORE rates. Negative CORE values indicate net consumption. Data represent mean ± SD from three biological repeats.



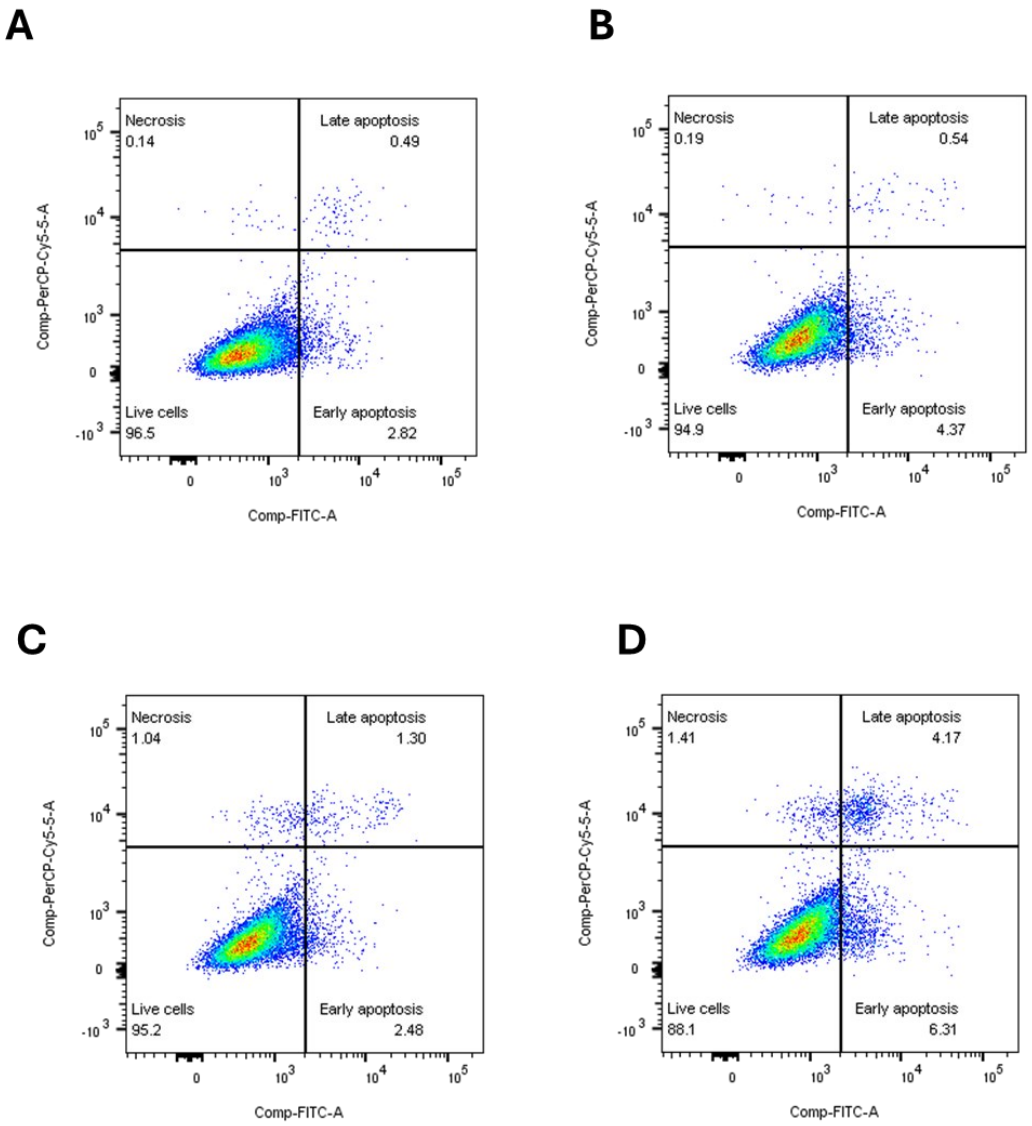
Appendix Figure 3.6 Extremely low levels of ^{13}C enrichment of citrate could be detected after short incubation with ^{13}C tracers.

(A) Fraction of M+3 pyruvate and M+2 TCA cycle intermediates. ID8 Trp*53*$^{-/-}$ cells were incubated with 5.6mM $^{13}C_6$-glucose. (B) Fraction of M+1 pyruvate and M+1 TCA cycle intermediates. ID8 Trp*53*$^{-/-}$ cells were incubated with 10mM 3-^{13}C-lactate. (C) Fraction of M+4 and M+5 TCA cycle intermediates. ID8 Trp*53*$^{-/-}$ cells were incubated with 2mM $^{13}C_5$-glutamine. After 4h incubation, intracellular metabolites were extracted and analysed by GC-MS. Data represent mean ± SD from three independent biological repeats (A-B) and mean from one repeat (C).

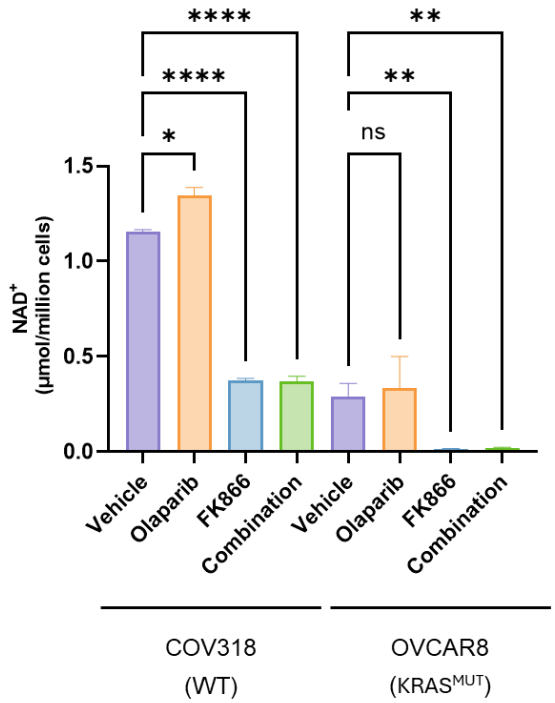


Appendix Figure 4.1 EOC cell lines with mutations in Ras/PI3K pathways are more sensitive to FK866.

(A) IC_{50} values of FK866 in a panel of EOC cells. These are preliminary data obtained by Dr Michael Gruet. Briefly, the EOC cells were treated with FK866 for 6 days before cell density measurement by SRB. IC_{50} values were calculated by least square fitting using Graph Pad (10.0.0). Data represent mean ± 95% confidence interval from three biological repeats. The figure was replotted. EOC cell lines with mutations in Ras/PI3K signalling and wild type are indicated in red and blue, respectively. (B) Spearman's correlation analysis of FK866 IC_{50} values with NAD^+ levels in cells treated with 0.5nM FK866 for 24h. These are preliminary data obtained by Dr Michael Gruet. Spearman's correlation was performed again and re-plotted by R studios (function cor.test() from package *stats* version 4.3.2). Pink areas indicate 95% confidence area, and the red line is the trend line.

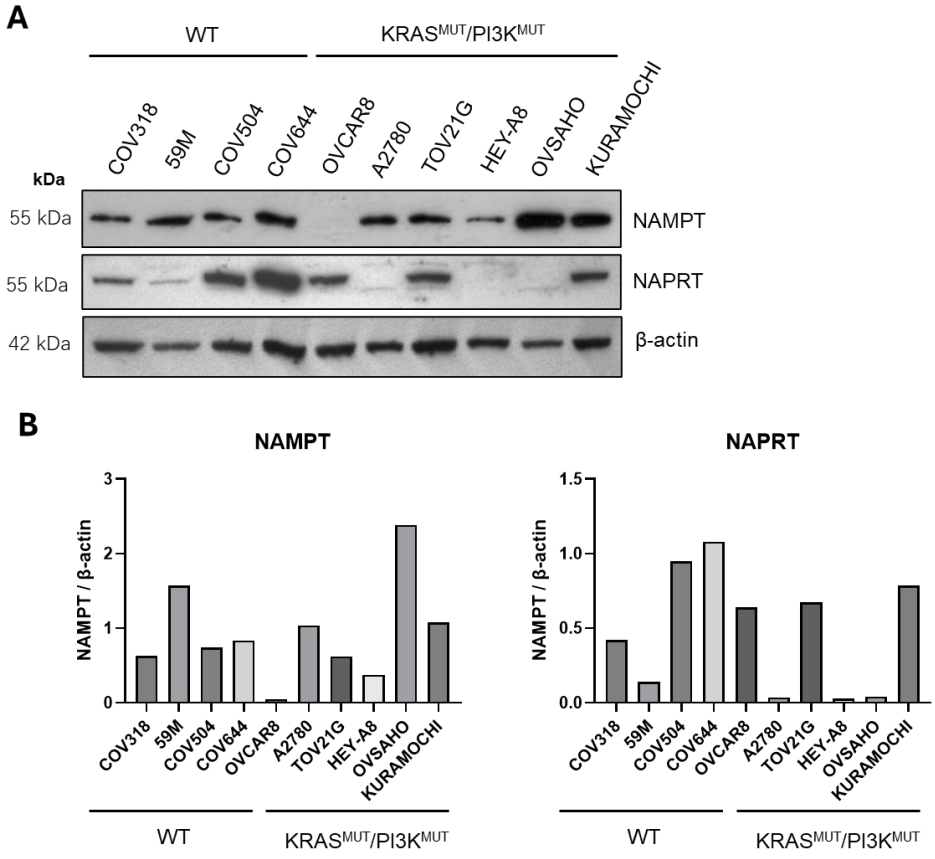


Appendix Figure 4.2 Gating strategy of the flow analysis as described in Figure 4.1.
Representative images of the flow analysis in A2780 cells treated with 0.2% (v/v) DMSO (A), 10μM Olaparib (B), 5nM FK866 (C) or the combination (D) are displayed. The same gating strategy was applied.



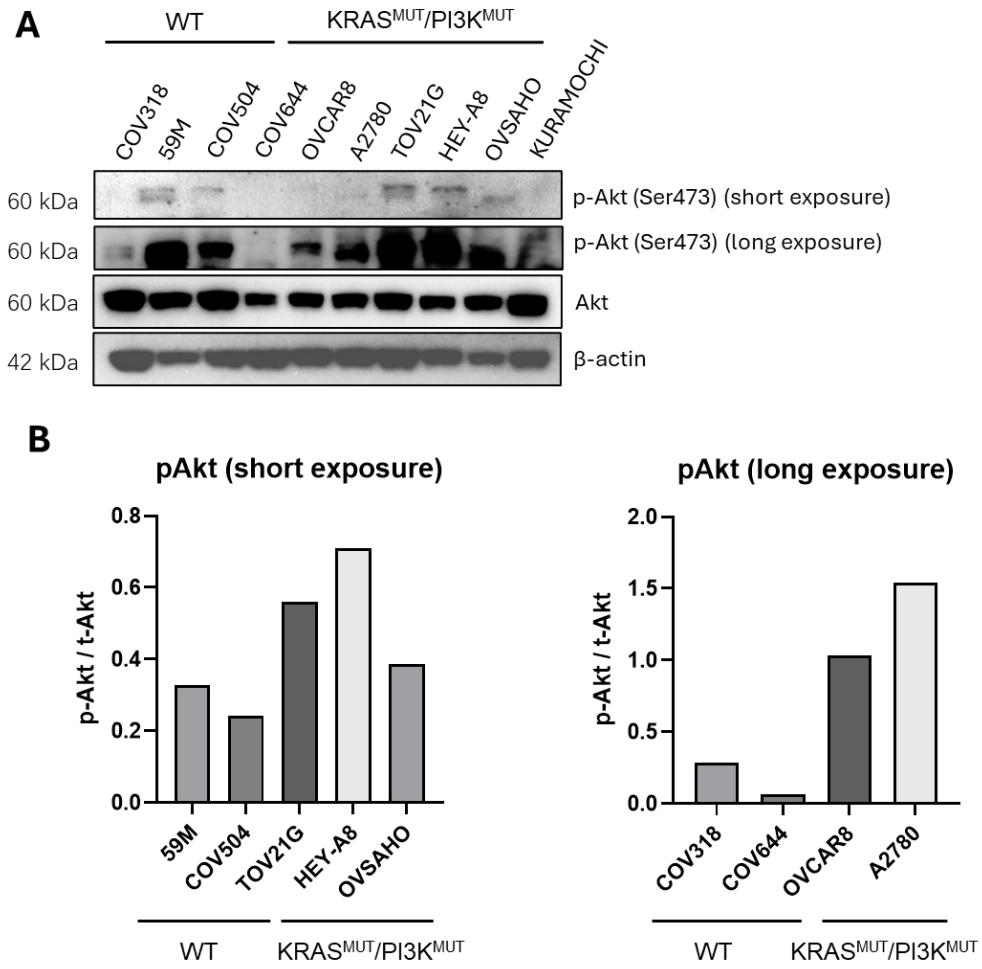
Appendix Figure 4.3 OVCAR8 (Ras mutant) cells had a smaller pool of NAD^+ and were more sensitive to NAD^+ depletion by FK866.

These are preliminary data obtained by Dr Michael Gruet. Briefly, OVCAR8 and COV318 cells were treated with 0.2% (v/v) DMSO, or 1nM FK866, or 1µM Olaparib or the combination for 24h and NAD^+ content was measured by LC-MS/MS. The figure was re-plotted. Data represent mean ± standard deviation of three biological repeats. One way ANOVA and post-hoc Tukey tests were performed to calculate statistical significance. * $p<0.5$, ** $p<0.01$, **** $p<0.0001$, ns: not significant.

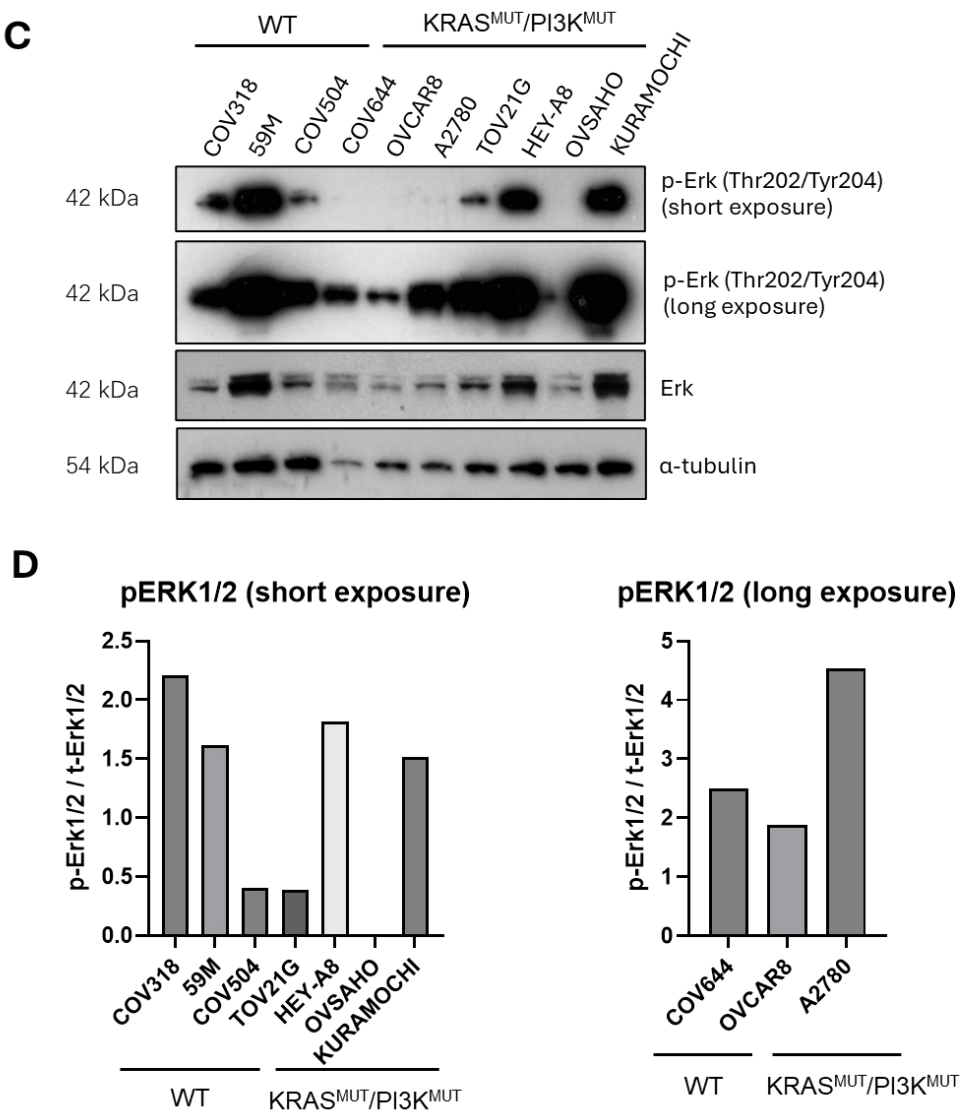


Appendix Figure 4.4 No association between Ras/PI3K pathway mutations and NAMPT or NAPRT expression in a panel of ovarian cancer cells.

(A) Images of WB blots. Basal protein levels of NAMPT and NAPRT were measured by WB in ovarian cancer cells in media with 10% FBS. (B) Densitometry analysis. The relative levels of NAMPT and NAPRT were normalized against the internal control β-actin. Data represent mean from one biological repeat. WB was performed by the Master's student Chris An under my supervision and densitometry analysis was re-performed by me.

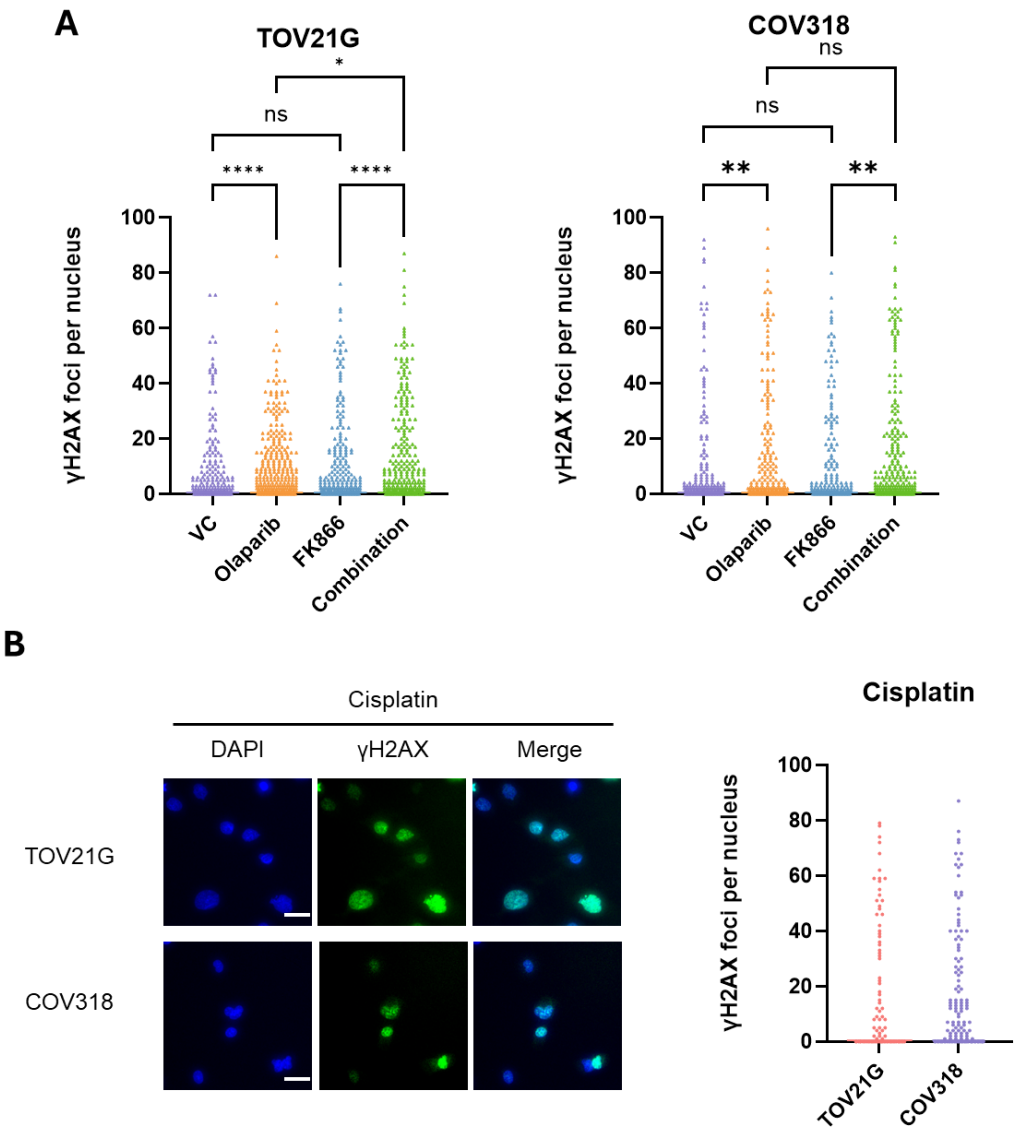


(to be continued on the next page)



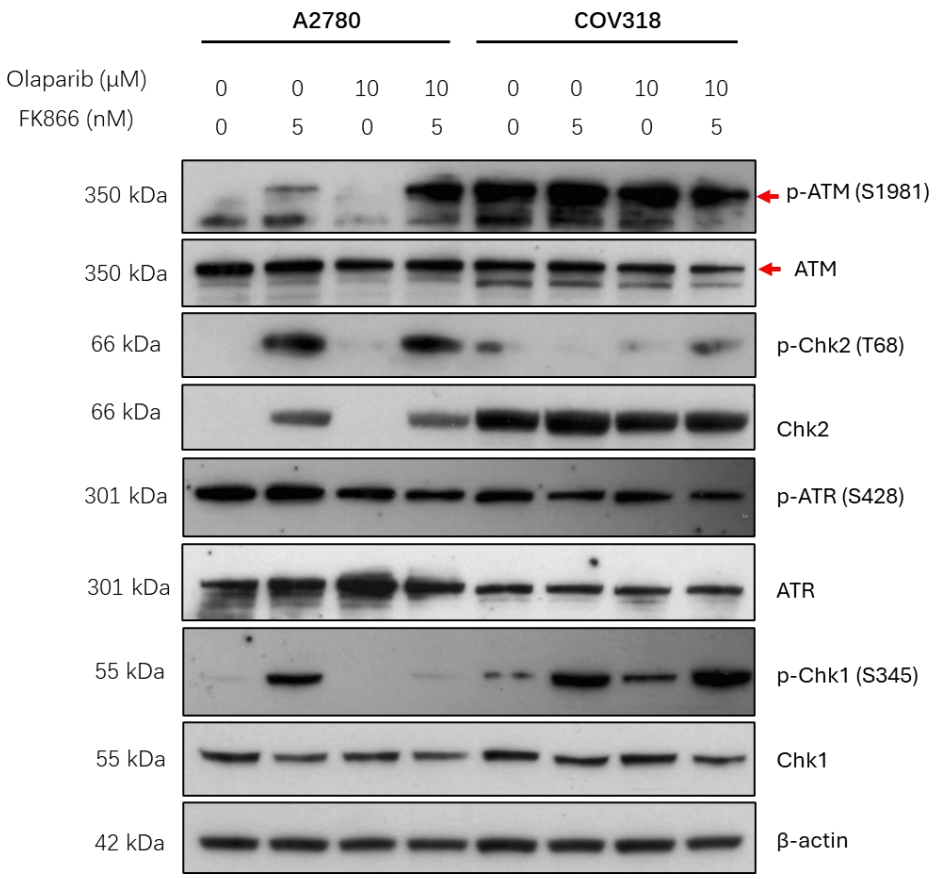
Appendix Figure 4.5 Inconsistent activation of the Ras/PI3K pathway across ovarian cancer cell line with or without Ras/PI3K mutations.

(A and C) Images of WB blots. Activity of Ras/Erk pathway and PI3K/Akt pathway was examined by WB against phosphorylated Erk and Akt, respectively. Proteins were extracted from a panel of ovarian cancer cells cultured in media with 10% FBS. (B and D) Densitometry analysis. The levels of phospho-Akt and phospho-Erk1/2 were normalized against the respective total protein levels. Because phospho-Akt and phospho-Erk1/2 could only be detected after long exposure for some cell lines, the normalization was performed using long exposure images. Data represent mean from one biological repeat. WB was performed by the Master's student Chris An under my supervision and densitometry analysis was re-performed by me.



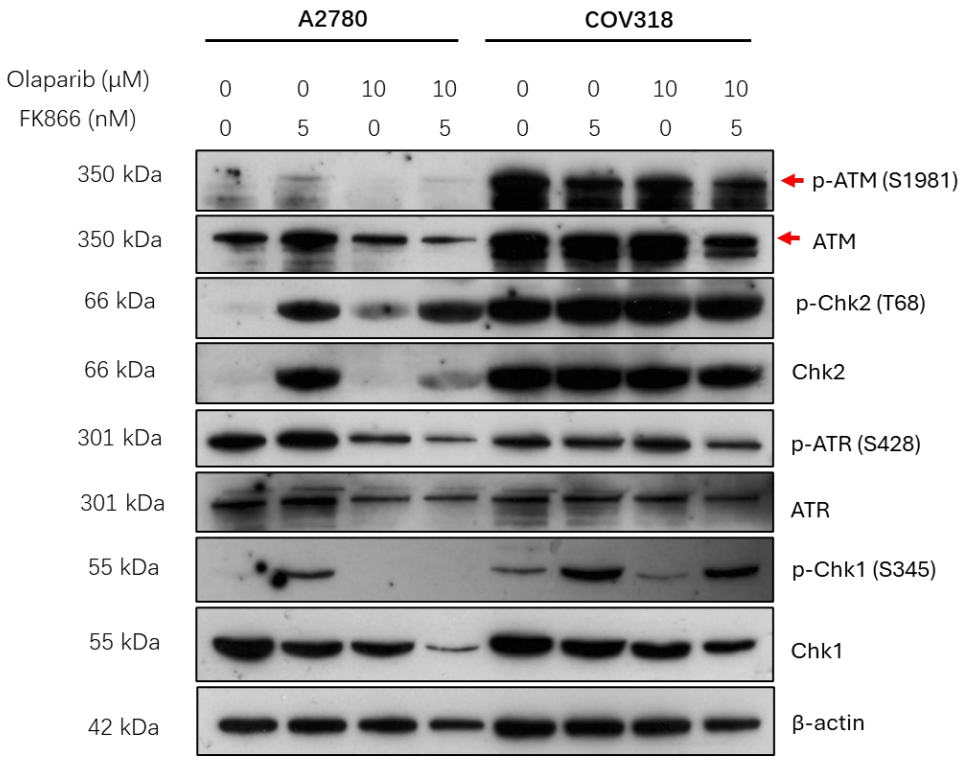
Appendix Figure 4.6 The combination of FK866 and Olaparib upregulated γH2AX intensity in Ras/PI3K mutant ovarian cancer cells.

(A) The second biological repeat was shown here. In brief, TOV21G and COV318 cells were treated with 0.2% (v/v) DMSO, or 5nM FK866, or 10μM Olaparib or the combination for 24h before immunostaining for γH2AX. Scatter plots showing γH2AX foci per cell. Because the data are not normally distributed (i.e., skewed), Kruskal-Wallis test and Dunn's multiple comparisons tests were performed to calculate p values. * $p<0.05$, ** $p<0.01$, **** $p< 0.0001$, ns: not significant. (B) Representative IF images of γH2AX staining in TOV21G and COV318 cells (left) and scatter plots (right) show γH2AX foci per nuclei. The TOV21G and COV318 cells were treated with 10μM cisplatin for 24h. Scale bar = 30μm. The experiments were performed by the Master's student Chris An under my supervision and data were re-analysed and re-plotted.



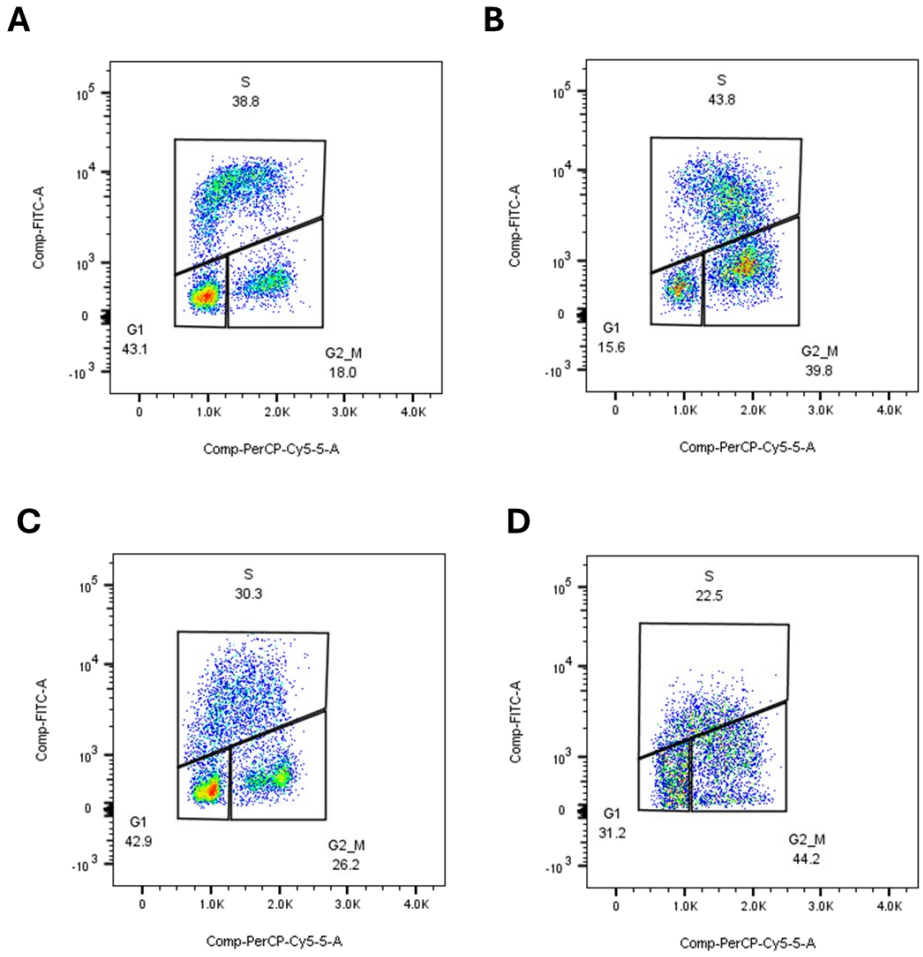
Appendix Figure 4.7 The combination of FK866 and Olaparib did not induce further activation of DDR signalling in ovarian cancer cells.

The second biological repeat was shown here. In brief, A2780 and COV318 cells were treated with 0.2% (v/v) DMSO, or 5nM FK866, or 10μM Olaparib or the combination for 24h. DDR signalling activity was then measured by WB against phosphor-ATM, phosphor-ATR, phosphor-Chk1 and phosphor-Chk2. Arrows indicate target proteins. Data were obtained by the Master's student Chris An under my supervision.

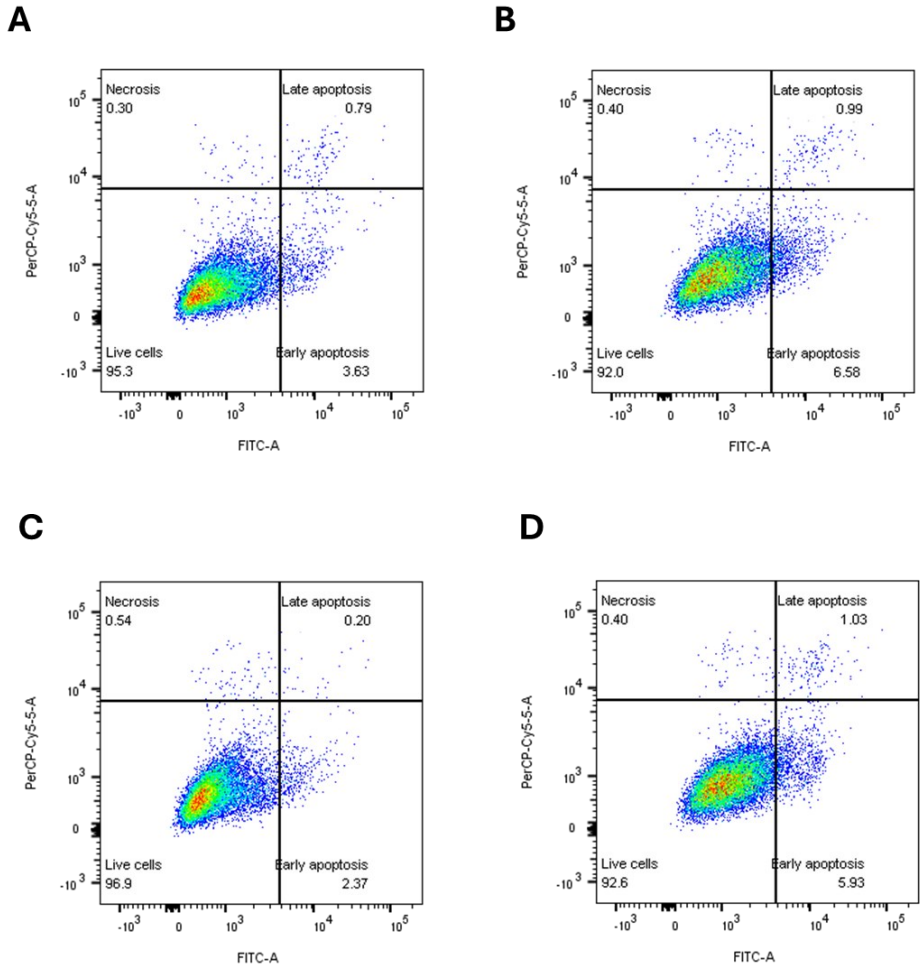


Appendix Figure 4.8 The combination of FK866 and Olaparib did not induce further activation of DDR signalling in ovarian cancer cells.

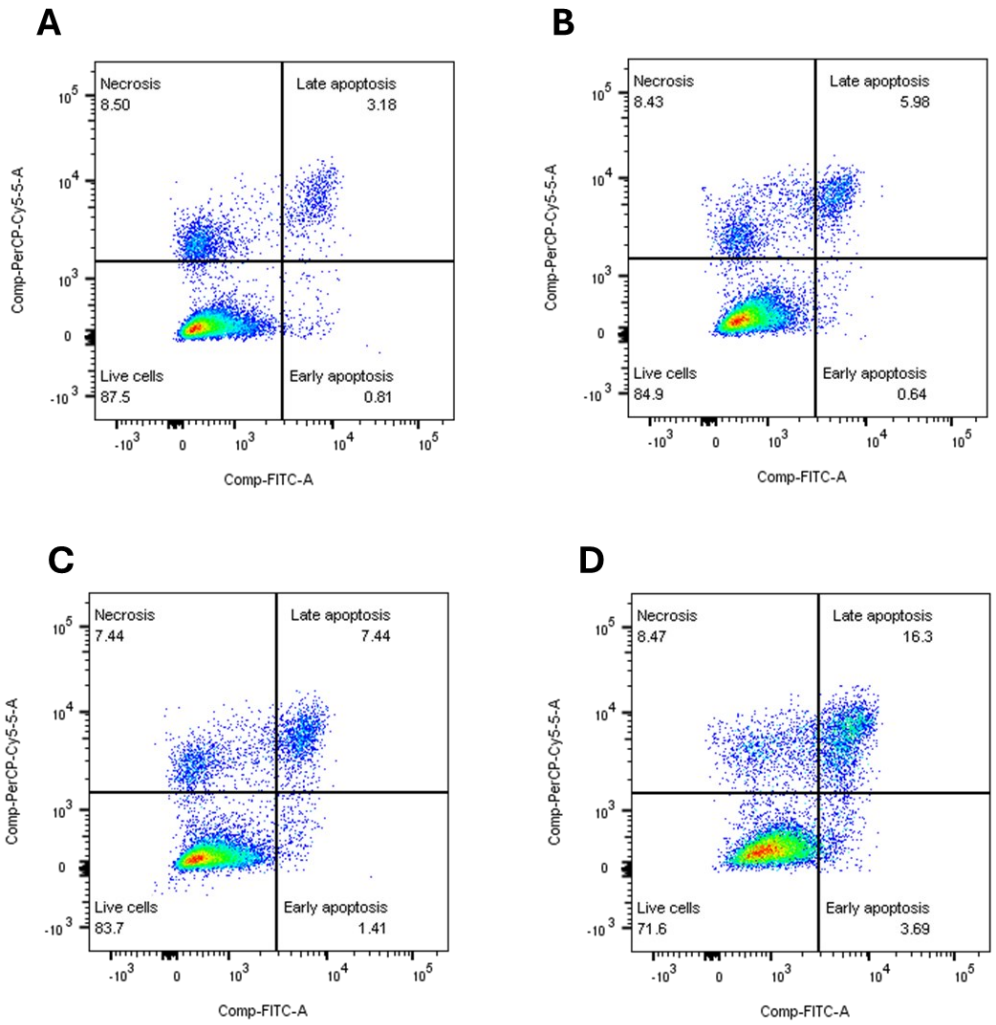
The third biological repeat was shown here. In brief, A2780 and COV318 cells were treated with 0.2% (v/v) DMSO, or 5nM FK866, or 10μM Olaparib or the combination. DDR signalling activity was then measured by WB against phosphor-ATM, phosphor-ATR, phosphor-Chk1 and phosphor-Chk2. Arrows indicate target proteins. Data were obtained by the Master's student Chris An under my supervision.



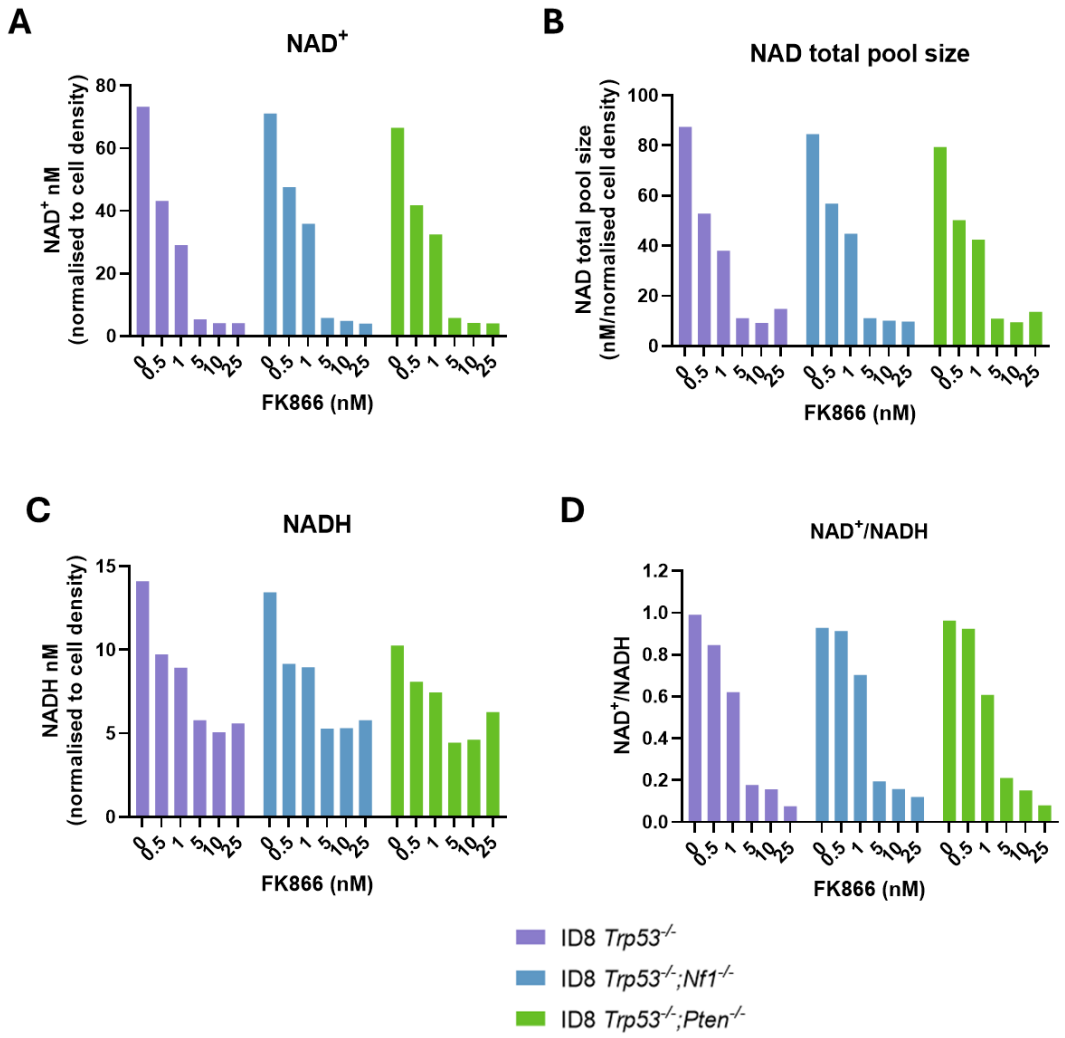
Appendix Figure 4.9 Gating strategy of the flow analysis as described in Figure 4.6.
Representative images of the flow analysis in A2780 cells treated with 0.2% (v/v) DMSO (A), 10μM Olaparib (B), 5nM FK866 (C) or the combination (D) are displayed. The same gating strategy was applied.



Appendix Figure 4.10 Gating strategy of the flow analysis as described in Figure 4.10.
Representative images of the flow analysis in A2780 cells treated with 0.2% (v/v) DMSO (A), 10μM Olaparib (B), 5nM FK866 (C) or the combination (D) in the presence of 5mM NAC are displayed. The same gating strategy was applied.

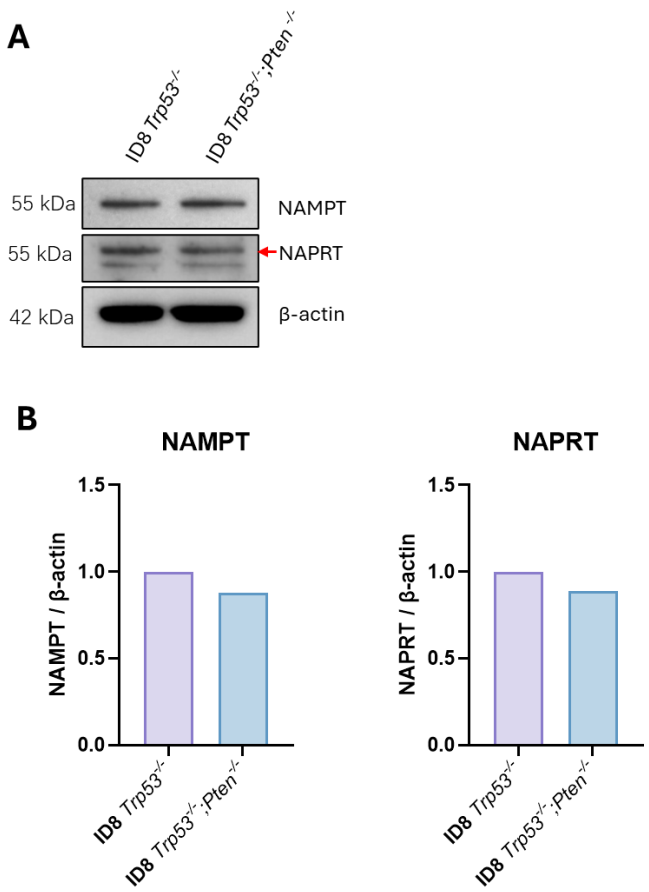


Appendix Figure 5.1 Gating strategy of the flow analysis as described in Figure 5.1.
Representative images of the flow analysis in ID8 *Trp53*$^{-/-}$;*Pten*$^{-/-}$ cells treated with 0.2% (v/v) DMSO (A), 10μM Olaparib (B), 5nM FK866 (C) or the combination (D) are displayed. The same gating strategy was applied.



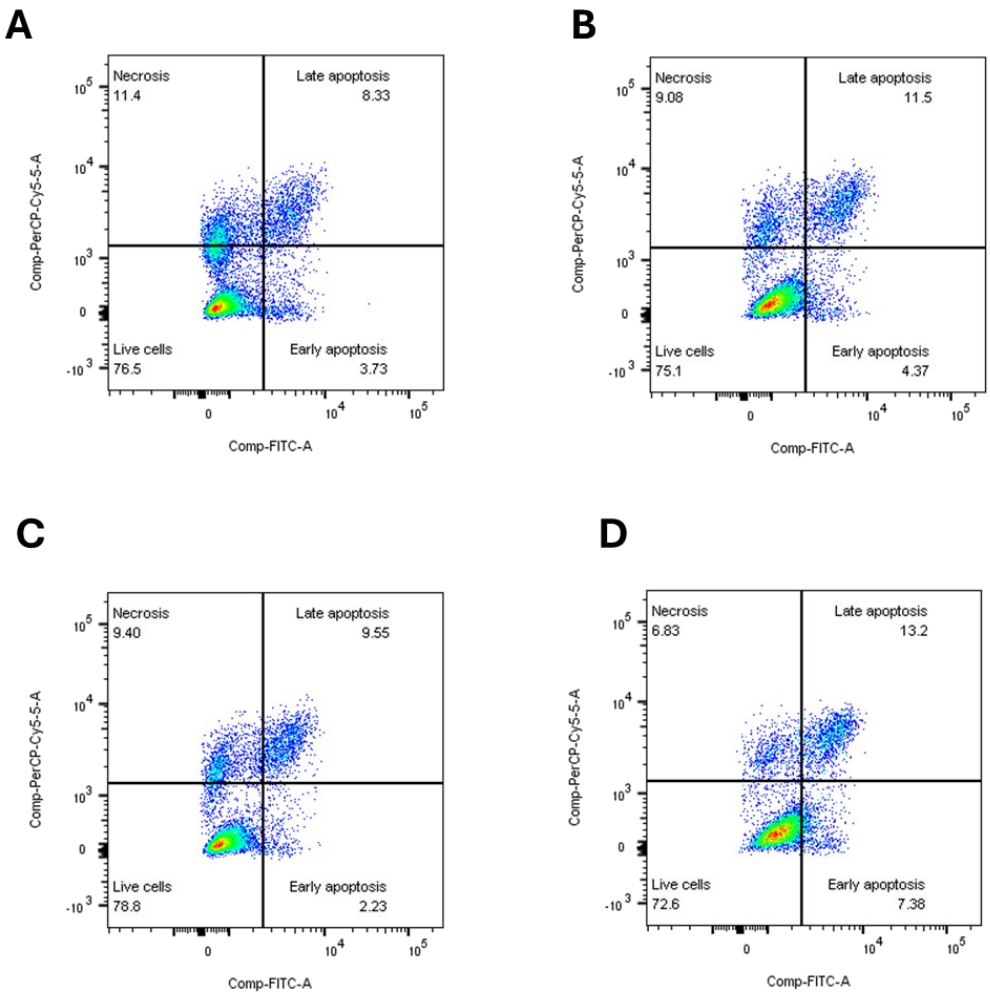
Appendix Figure 5.2 FK866 reduces NAD pool size and interferes with NAD$^+$/NADH ratio in ID8 cells.

(A) NAD total pool size, (B) NAD$^+$ levels, (C) NADH levels and (D) NAD$^+$/NADH ratio in a panel of ID8 cells (i.e., ID8 Trp*53*$^{-/-}$, ID8 *Trp53*$^{-/-}$*;Nf1*$^{-/-}$, ID8 *Trp53*$^{-/-}$*;Pten*$^{-/-}$ cells). ID8 cells were treated with various doses of FK866 (0.5, 1, 5, 10 or 25nM) for 24h. NAD$^+$ and NADH levels were measure using the Promega NAD$^+$/NADH Glo Assay. Data represent mean of the second biological replicate.

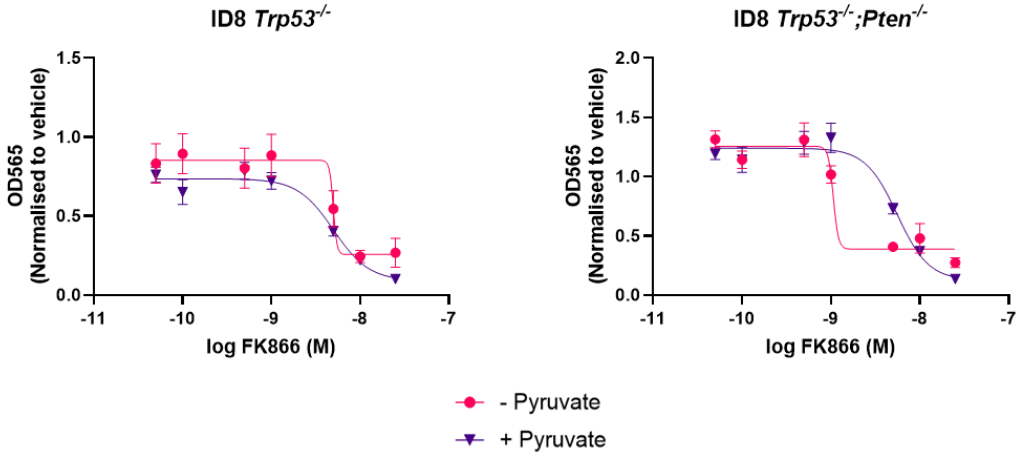


Appendix Figure 5.3 No correlation between NAMPT/NAPRT expression and Pten mutational status in ID8 cells.

(A) Images of WB blots. NAMPT and NAPRT protein expression was analysed by WB. The protein was extracted from ID8 Trp*53*$^{-/-}$ and ID8 *Trp53*$^{-/-}$*;Pten*$^{-/-}$ cells cultured with 10% FBS in media. (B) Densitometry analysis. The relative protein levels of NAMPT and NAPRT were normalized against the internal control β-actin, Data represent mean from one biological repeat. WB was performed by the Master's student Chris An under my supervision and densitometry analysis was re-performed by me.

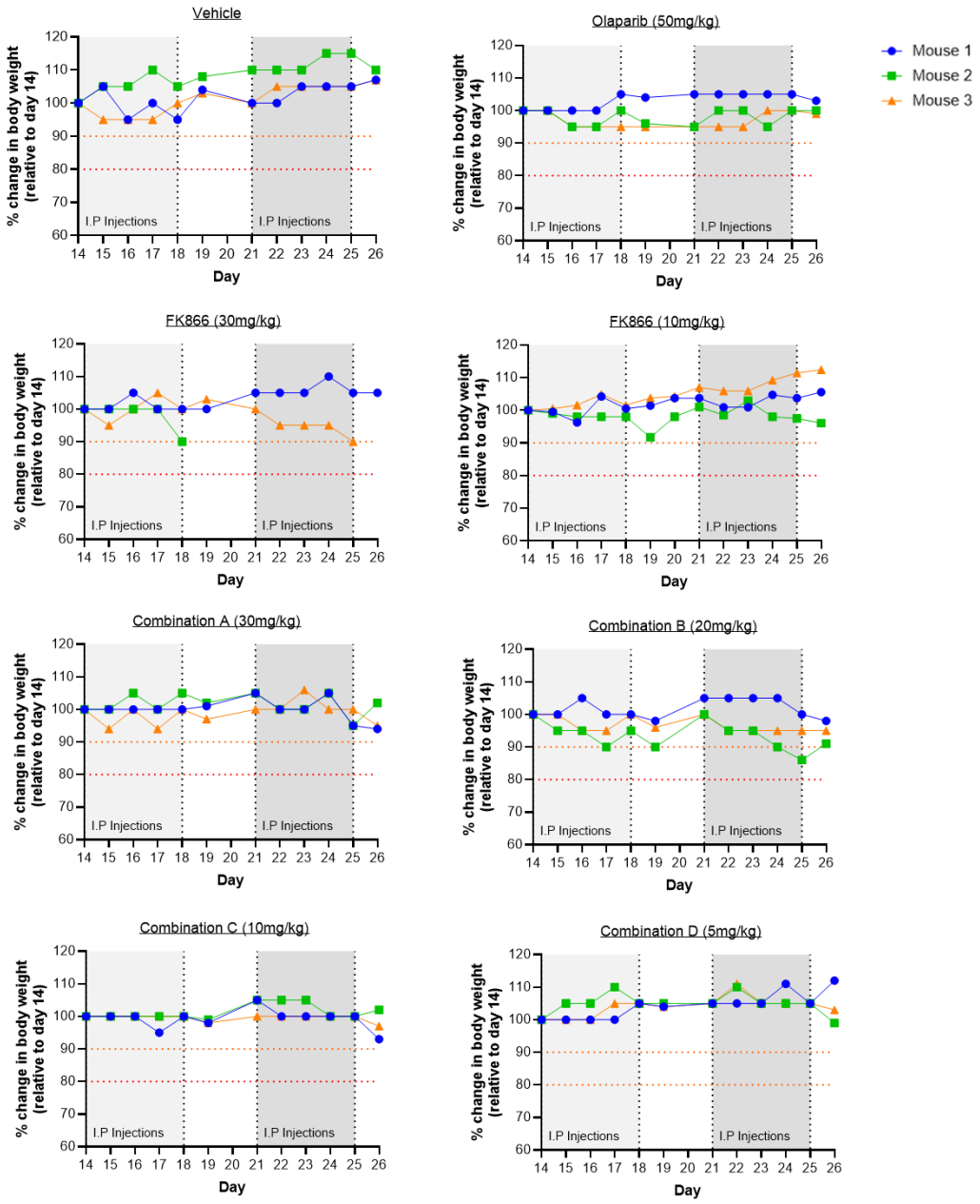


Appendix Figure 5.4 Gating strategy of the flow analysis as described in Figure 5.1.
Representative images of the flow analysis in ID8 *Trp53*$^{-/-}$;*Pten*$^{-/-}$ cells treated with 0.2% (v/v) DMSO (A), 10μM Olaparib (B), 5nM FK866 (C) or the combination (D) in the presence of 5mM NAC are displayed. The same gating strategy was applied.



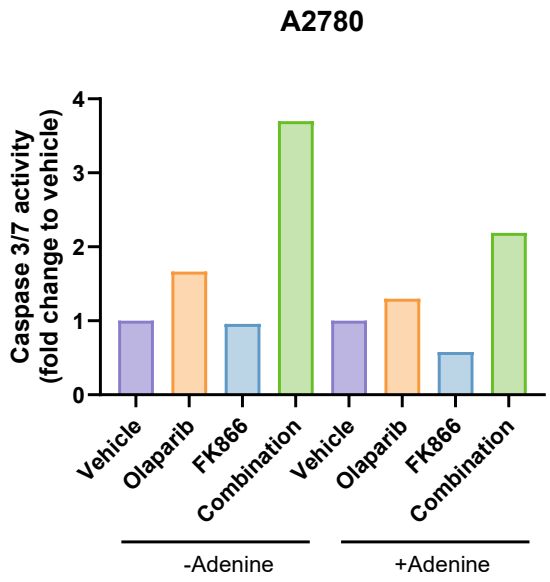
Appendix Figure 5.5 Pyruvate withdrawal enhanced sensitivity of FK866 in ID8 *Trp53*$^{-/-}$; *Pten*$^{-/-}$ cells but not ID8 *Trp53*$^{-/-}$ cells.

Dose-response curves of FK866. ID8 Trp*53*$^{-/-}$ and ID8 *Trp53*$^{-/-}$;*Pten*$^{-/-}$ cells were treated with various doses of FK866 (0.05, 0.1, 0.5, 1, 5, 10, 25nM) in media with or without 1mM sodium pyruvate for 72h. Cell density was measured by SRB assay. Data represent mean ± SD of one replicate. The experiments were performed by the Master's student Chris An under my supervision and data were re-analysed and re-plotted.



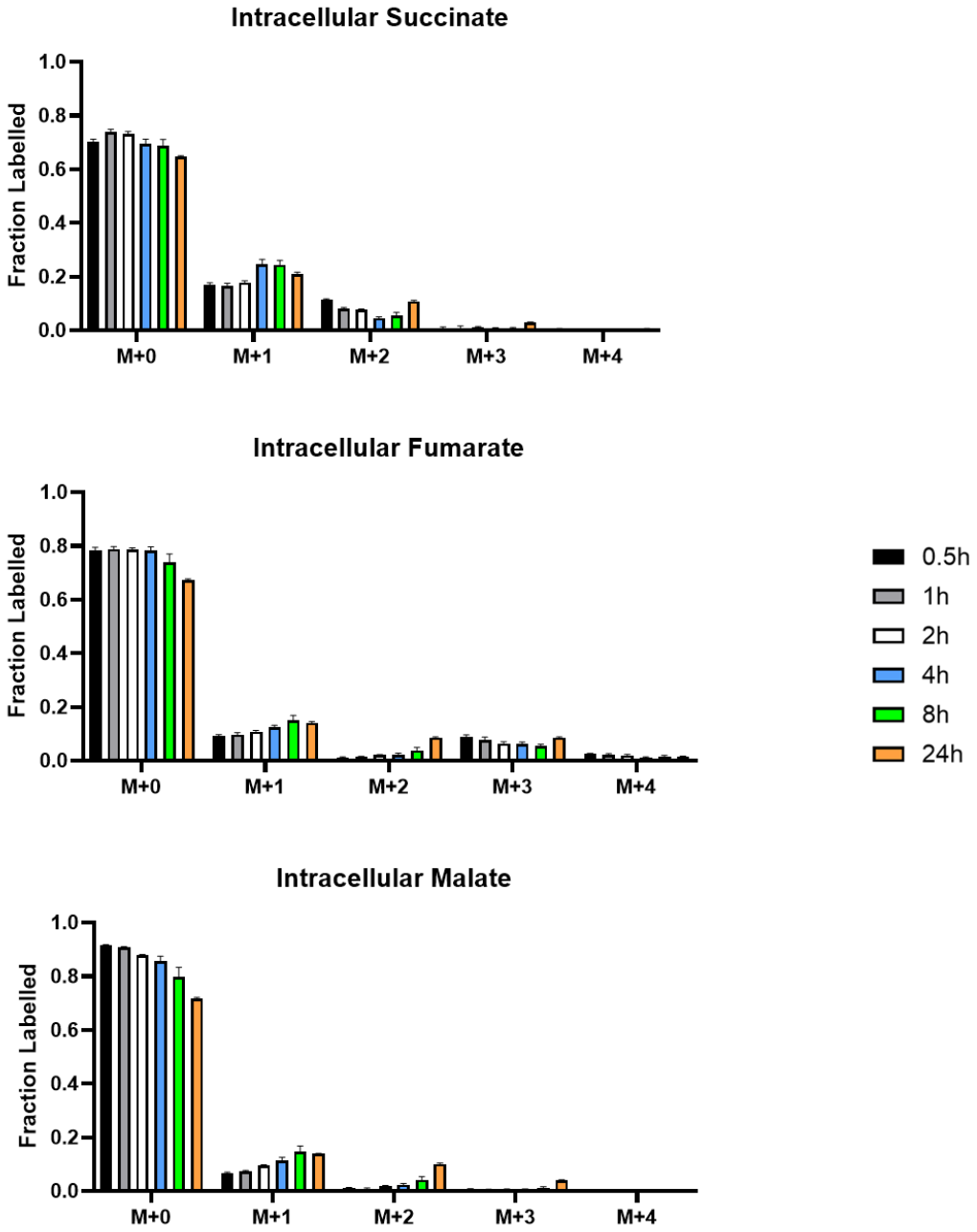
Appendix Figure 5.6 Relative changes of mouse weight during the toxicology study.

The mice were weighed daily starting from the first injection of drugs. Changes of mouse weight were expressed as % of the initial weight (i.e., on the day of the first drug injection). Two of the mice treated with 30mg/kg FK866 experienced signs of discomfort (e.g., constipation, narrowed eyes and piloerection) and 10% weight loss. They were culled before the study completed. Days of drug injection are indicated in grey areas and 10% and 20% weight loss are highlighted by dotted lines. The *in vivo* study was performed in collaboration with Dr Michael Gruet in our group.



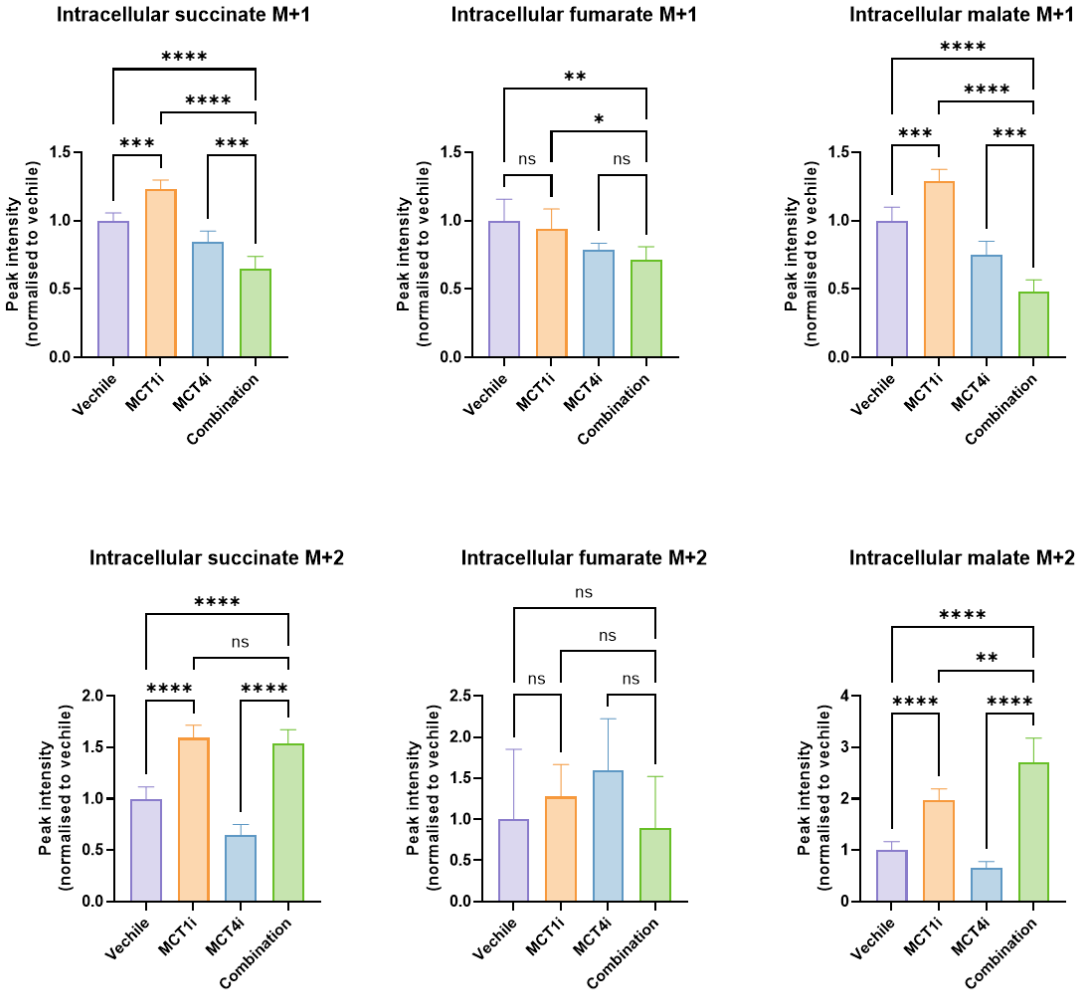
Appendix Figure 5.7 Adenine Supplementation rescued apoptosis in A2780 cells treated with FK866 and Olaparib combination.

A2780 cells were treated with 0.2% DMSO (v/v), 5nM FK866, 10μM Olaparib or the combination of 5nM FK866 and 10μM Olaparib in the presence or absence of 25μM adenine. After 48h treatment, the activity of caspase-3/7 was measured using the Promega Caspase-Glo® 3/7 assay. Cell density was also measured by the SRB assay. The caspase-3/7 readout was normalised against cell density and the data were expressed as fold changes. Data represent the mean of one biological replicate. The experiments were performed by the Master's student Chris An under my supervision and data were re-analysed and re-plotted.



Appendix Figure 6.1 Initial high fluxes of exogenous lactate fuelling the TCA cycle were observed and there was a time-dependent increase in glucose contribution.

MIDs of intracellular succinate, fumarate and malate. The data were obtained from the same experiment described in Figure 6.2. Briefly, HCT116 cells were incubated with 5.6mM $^{13}C_6$-glucose and 10mM 3-^{13}C-lactate simultaneously for various periods of time (e.g., 0.5, 1, 2, 4, 8 and 24h). At the end of incubation, intracellular metabolites were extracted and analysed by GC-MS. Data represent mean ± SD from three independent biological repeats.



Appendix Figure 6.2 Dual MCT1 and MCT4 inhibition altered the relative contribution of glucose and exogenous lactate to the TCA cycle.

The fraction of M+1 and M+2 succinate, fumarate and malate. The data were obtained from the same experiment described in Figure 6.6. In brief, HCT116 cells were treated with 0.1μM AZD3965 and/or 0.1μM AZD0095 in media Supplemented with both 5.6mM $^{13}C_6$-glucose and 10mM 3-^{13}C-lactate. At the end of the 2h incubation, media were collected, and cells were harvested. Metabolites were then extracted and analysed by GC-MS. Peak areas in drug treated groups were normalised to vehicle group. Data represent mean ± SD from three independent biological repeats. Statistical significance was calculated by one way ANOVA with post-hoc Tukey tests. * p<0.05, ** p<0.01, *** p<0.001, **** p<0.0001, ns: not significant.

Appendix Reports

Eurofins Genomics Europe Applied Genomics GmbH, Anzinger Str. 7 a, D-85560 Ebersberg

Chiharu Wickremesinghe
Imperial College, Surgery and Cancer
Du Cane Road
W12 0TX London
Great Britain

eurofins | Genomics

SOP_APG_Zelllinienauthentizität_A04_2.0

Person in charge: Dr. Torsten Brendel
Report date: 10.08.2023
Sample received on: 03.08.2023
Start / End of Analysis: 03.08.2023/10.08.2023

Analytical Report:
Cell Line Authentication Test
Order ID: 11108516443

Method:

Genetic characteristics were determined by PCR-single-locus-technology:
16 independent PCR-systems D8S1179, D21S11, D7S820, CSF1PO, D3S1358, TH01, D13S317, D16S539, D2S1338, AMEL, D5S818, FGA, D19S433, vWA, TPOX and D18S51 were investigated.
(ASN-0002 core markers are colored grey, Thermo Fisher, AmpFlSTR® Identifiler® Plus PCR Amplification Kit)
In parallel, positive and negative controls were carried out yielding correct results.
Method details are given in **SOP_APG_Zelllinienauthentizität_2.0**

Result:

Client Sample Name	PEO1 H2C5 DCAF15 KO	PEO1 NTC C2	PEO1	PEO4	KURAMOCHI	OVISE	OVSAHO	COV318	COV504	COV644
Sample Code	CL00014368	CL00014369	CL00014370	CL00014365	CL00014366	CL00014367	CL00014362	CL00014363	CL00014364	CL00014359
D8S1179	13,14	13,14	13,14	13,14	10,11	15,16	14,14	12,13	12,13	12,14
D21S11	32.2,32.2	32.2,32.2	32.2,32.2	30,32.2	30,32.2	28,30	31,31	30,30	29,29	29,29
D7S820	10,10	10,10	10,10	10,10	10,11	11,12	8,10	9,9	10,12	8,11
CSF1PO	10,12	10,12	10,12	10,12	11,12	9,11	10,12	11,13	12,13	10,10
D3S1358	16,16	16,16	16,16	16,16	18,18	14,15	15,15	14,16	16,16	17,18
TH01	9,3.9,3	9,3.9,3	9,3.9,3	9,3.9,3	9,9	9,9.3	6,6	9,3.9,3	6,7	8,8
D13S317	10,10	10,10	10,10	10,10	9,12	11,12	8,8	14,14	9,11	9,11
D16S539	9,9	9,9	9,9	9,9	10,10	9,9	9,9	9,12	9,11	11,12
D2S1338	20,21	20,21	20,21	20,21	18,18	19,24	23,23	17,27	17,19	17,18
D19S433	13,15	13,15	13,15	13,15	13,14	14,14.2	15.2,16.2	13,2,16	15,15	13,16.2
vWA	15,16	15,16	15,16	15,16	16,19	18,18	14,14	15,15	17,18	16,17
TPOX	9,11	9,11	9,11	9,11	8,12	8,8	8,11	8,11	8,9	9,11
D18S51	16,17	16,17	16,17	16,17	13,13	19,19	16,20	12,12	13,13	14,14*
AMEL	X,X	X,X	X,X	X,X	X,X*	X,X	X,X	X,X*	X,X	X,X
D5S818	11,12	11,12	11,12	11,12	12,12	10,10	12,13	11,13	11,11	10,11
FGA	20,20	20,20	20,20	20,20	21,23	19,23	24,24	20,23	22,22	21,23
Database Name	PEO1	PEO1	PEO1	PEO4	KURAMOCHI	OVISE	OVSAHO	COV318	COV504	COV644

The table shows the result of the cell line analysis and the comparison with the online database of the DSMZ (http://www.dsmz.de/de/service/services-human-and-animal-cell) and the Cellosaurus database (https://web.expasy.org/cellosaurus). Please note that only the PCR-systems according to ANSI/ATCC standard ASN-0002 were aligned (D5S818, D13S317, D7S820, D16S539, VWA, TH01, TPOX, CSF1PO, AMEL - colored grey).
* Weak signal

This report was created automatically and is therefore valid without a signature.

The laboratory is accredited acc. to **DIN EN ISO/IEC 17025:2018**. All analyses have been carried out with greatest care and on the basis of state of the art scientific knowledge. The results refer solely to the analysed samples, as received. The duplication and publication also in parts requires a written authorization by this laboratory. Our General Terms and Conditions apply exclusively and are available under eurofinsgenomics.com

Eurofins Genomics Europe Applied Genomics GmbH
Anzinger Straße 7 a
85560 Ebersberg
Germany

Tel.: +49 7531 816068
Fax: +49 8092 21084

Email: support-eu@genomics.eurofinseu.com
Web: eurofinsgenomics.com

Managing Directors: Dr. Mashal Alawi & Dr. Sonja Weidemann

Register Court Munich HRB 207710
VAT ID: DE815473648

HypoVereinsbank
IBAN: DE23 2073 0017 7000 0006 50
SWIFT: HYVEDEMME17

Appendix Report 1. STR profiling of KURAMOCHI, OVSAHO, COV318, COV504 and COV644 cell lines (highlighted by red rectangles).

Eurofins Genomics Europe Food/Environment/White Biotech Products & Services GmbH, Anzinger Str. 7 a, D-85560 Ebersberg

Chiharu Wickremesinghe
Imperial College, Surgery and Cancer
Du Cane Road
W12 0TX London
Great Britain

eurofins | Genomics

SOP_APG_Zelllinienauthentizität_A04_2.0

Analytical Report:
Cell Line Authentication Test
Order ID: 11108713272

Person in charge: Dr. Torsten Brendel
Report date: 04.01.2024
Sample received on: 22.12.2023
Start / End of Analysis: 22.12.2023/04.01.2024

Method:
DNA isolation was carried out from cell pellet (cell layer).
Genetic characteristics were determined by PCR-single-locus-technology:
16 independent PCR-systems D8S1179, D21S11, D7S820, CSF1PO, D3S1358, TH01, D13S317, D16S539, D2S1338, AMEL, D5S818, FGA, D19S433, vWA, TPOX and D18S51 were investigated.
(ASN-0002 core markers are colored grey, Thermo Fisher, AmpFISTR® Identifiler® Plus PCR Amplification Kit)
In parallel, positive and negative controls were carried out yielding correct results.
Method details are given in **SOP_APG_Zelllinienauthentizität_2.0**

Result:

Client Sample Name	59M	A2780	HEK293T	HEY-A8	IMR32	KELLY	KELLY NTC C3	KELL 3xC4	OVCAR4	OVCAR5
Sample Code	CL00014341	CL00014342	CL00014343	CL00014344	CL00014345	CL00014346	CL00014347	CL00014348	CL00014349	CL00014350
D8S1179	10,14	14,15,16,17,18	12,14	13,14	13,13	14,14	14,14	14,14	13,13	13,14
D21S11	31,31	27,28	28,30.2	30,30	30,31	28,30	28,30	28,30	28,31	31,31
D7S820	10,11	10,10	11,12	12,12	9,10	9,9	9,9	9,9	10,11	10,10
CSF1PO	13,13	10,11	12,12	10,11	11,12	12,12	12,12	12,12	10,10	10,10
D3S1358	15,17	14,15,16,17	15,17	16,16	16,16	14,16	14,16	14,16	15,15	15,16
TH01	7,7	6,6	7,9.3	8,9.3	7,9.3	9.3,9.3	9.3,9.3	9.3,9.3	9,9	7,9.3
D13S317	11,11	12,13.14	12,14	11,11	9,9	14,14	10,14	10,14	9,9	10,13
D16S539	9,9	11,12,13	9,13	8,12	8,8	12,13	12,13	12,13	11,11	11,11
D2S1338	19,20	20,21,22	19,19	24,25	23,24	17,20	17,20	17,20	23,23	17,23
D19S433	14,16	12,12	15,18	13,14	14,15	12,15.2	12,15.2	12,15.2	13,15	13,14
vWA	17,19	15,16,17	16,19	16,17	15,15	18,18	18,18	18,18	14,18	16,16
TPOX	8,8	8,10	11,11	11,11	11,11	8,10	8,10	8,10	8,8	8,11
D18S51	12,12	14,15,16,17,18,19	17,18	15,15	12,15	14,17	14,17	14,17	15,15	12,12
AMEL	X,X	X,X	X,X	X,X	X,Y	X,X	X,X	X,X***	X,X	X,X
D5S818	11,11	11,12	8,8	11,12	11,12	11,13	11,13	11,13	13,13	11,13
FGA	22,22.2	19,23.24	23,23	20,21	21,24	20,21	20,21	20,21	21,21	23,23
Database Name	59M*	A2780*	**	HEY A8	IMR-32	Kelly	94 % identity: Kelly	94 % identity: Kelly	OVCAR-4	OVCAR-5

The table shows the result of the cell line analysis and the comparison with the online database of the DSMZ (http://www.dsmz.de/de/service/services-human-and-animal-cell) and the Cellosaurus database (https://web.expasy.org/cellosaurus). Please note that only the PCR-systems according to ANSI/ATCC standard ASN-0002 were aligned (D5S818, D13S317, D7S820, D16S539, VWA, TH01, TPOX, CSF1PO, AMEL - colored grey).

* The sample could be identified as the stated cell line, although one or several PCR-Systems did show additional signals (see table). These signals could occur due to contamination of the cell line or possible mutations.

** Several HEK cell lines were identified
*** Weak Signal

This report was created automatically and is therefore valid without a signature.

The laboratory is accredited acc. to **DIN EN ISO/IEC 17025:2018**. All analyses have been carried out with greatest care and on the basis of state of the art scientific knowledge. The results refer solely to the analysed samples, as received. The duplication and publication also in parts requires a written authorization by this laboratory. Our General Terms and Conditions apply exclusively and are available under eurofinsgenomics.com

Eurofins Genomics Europe
Food/Environment/White Biotech Products & Services GmbH
Anzinger Straße 7 a
85560 Ebersberg
Germany

Tel.: +49 7531 816068
Fax: +49 8092 21084

Email: support-eu@genomics.eurofinseu.com
Web: eurofinsgenomics.com

Managing Directors: Dr. Mashal Alawi & Dr. Sonja Wiedemann

Register Court Munich HRB 207710
VAT ID: DE815473648

HypoVereinsbank

IBAN: DE23 2073 0017 7000 0006 50
SWIFT: HYVEDEMME17

Appendix Report 2. STR profiling of 59M, A2780 and HEY-A8 cell lines (highlighted by red rectangles).

Appendix Report 3. STR profiling of TOV21G cell lines (highlighted by red rectangles).

Eurofins Genomics Europe Food/Environment/White Biotech Products & Services GmbH, Anzinger Str. 7 a, D-85560 Ebersberg

Chiharu Wickremesinghe
Imperial College, Surgery and Cancer
Du Cane Road
W12 0TX London
Great Britain

eurofins | Genomics

SOP_APG_Zelllinienauthentizität_A04_2.0

Person in charge: Dr. Torsten Brendel
Report date: 04.01.2024
Sample received on: 22.12.2023
Start / End of Analysis: 22.12.2023/04.01.2024

Analytical Report:
Cell Line Authentication Test
Order ID: 11108713272

Method:
DNA isolation was carried out from cell pellet (cell layer).
Genetic characteristics were determined by PCR-single-locus-technology.
16 independent PCR-systems D8S1179, D21S11, D7S820, CSF1PO, D3S1358, TH01, D13S317, D16S539, D2S1338, AMEL, D5S818, FGA, D19S433, vWA, TPOX and D18S51 were investigated.
(ASN-0002 core markers are colored grey, Thermo Fisher, AmpFISTR® Identifiler® Plus PCR Amplification Kit)
In parallel, positive and negative controls were carried out yielding correct results.
Method details are given in **SOP_APG_Zelllinienauthentizität_2.0**

Result:

Client Sample Name	PC9	PC9 R5	PC9 R6	PC9 PI3KCA H1047R	PC9 PTEN KO	TOV21G	HCT116 3XC7	HCT116 3XC12	HCT116 NTC C1	HCT116 NTC C2
Sample Code	CL00014351	CL00014352	CL00014353	CL00014354	CL00014355	CL00014356	CL00014357	CL00014358	CL00014360	CL00014361
D8S1179	11,15	11,15	11,15	11,15	11,15	13,16	12,14	12,14	12,14	12,14
D21S11	29,30	29,30	29,30	29,30	29,30	28,34.2	29,30	29,30	29,30	29,30
D7S820	10,11	10,11	10,11	10,11	10,11	12,12	11,12	11,12	11,12	11,11
CSF1PO	11,11	11,11	11,11	11,11	11,11	12,13,14,15,16	7,10	7,10	7,10	7,10
D3S1358	16,16	16,16	16,16	16,16	16,16	14,16	12,17,18	12,17,18,19	12,19	12,19
TH01	7,7	7,7	7,7	7,7	7,7	7,9.3	8,9	8,9	8,9	8,9
D13S317	6,8	6,8	6,8	6,8	6,8	11,12	10,12	10,12	10,11	10,12
D16S539	9,9	9,9	9,9	9,9	9,9	10,12	11,12,13	11,12,13	11,12	11,13
D2S1338	19,20	19,20	19,20	19,20	19,20	17,17	16,16	16,16	16,16	16,16
D19S433	13,15.2	13,15.2	13,15.2	13,15.2	13,15.2	14,15.2,16.2	12,13	12,13	12,13	12,12
vWA	17,17	17,17	17,17	17,17	17,17	17,17	17,21,22,23	17,21,22,23	17,22	17,22
TPOX	11,11	11,11	11,11	11,11	11,11	8,11	8,8	8,8	8,8	8,8
D18S51	15,15	15,15	15,15	15,15	15,15	12,16	17,17	17,17	17,19	17,17
AMEL	X,X	X,X	X,X	X,X	X,X	X,X	X,X	X,X	X,X	X,X
D5S818	11,11	11,11	11,11	11,11	11,11	12,13	9,11	9,11	9,11	10,11
FGA	23,25	23,23	23,25	23,25	23,25	20,23	18,23	18,23	18,23	18,24
Database Name	PC-9	PC-9	PC-9	PC-9	PC-9	TOV-21G*	94 % identity: HCT116*	94 % identity: HCT116*	No hit	No hit

The table shows the result of the cell line analysis and the comparison with the online database of the DSMZ (http://www.dsmz.de/de/service/services-human-and-animal-cell) and the Cellosaurus database (https://web.expasy.org/cellosaurus). Please note t only the PCR-systems according to ANSI/ATCC standard ASN-0002 were aligned (D5S818, D13S317, D7S820, D16S539, VWA, TH01, TPOX, CSF1PO, AMEL - colored grey).

*The sample could be identified as the stated cell line, although one or several PCR-Systems did show additional signals (see table). These signals could occur due to contamination of the cell line or possible mutations.

This report was created automatically and is therefore valid without a signature.

The laboratory is accredited acc. to **DIN EN ISO/IEC 17025:2018**. All analyses have been carried out with greatest care and on the basis of state of the art scientific knowledge. The results refer solely to the analysed samples, as received. The duplication and publication also in parts requires a written authorization by this laboratory. Our General Terms and Conditions apply exclusively and are available under eurofinsgenomics.com

Eurofins Genomics Europe Food/Environment/White Biotech Products & Services GmbH
Anzinger Straße 7 a
85560 Ebersberg
Germany

Tel.: +49 7531 816068
Fax: +49 8092 21084

Email: support-eu@genomics.eurofinseu.com
Web: eurofinsgenomics.com

Managing Directors: Dr. Mashal Alawi & Dr. Sonja Wiedemann

Register Court Munich HRB 207710
VAT ID: DE815473648

HypoVereinsbank

IBAN: DE23 2073 0017 7000 0006 50
SWIFT: HYVEDEMME17

eurofins | Genomics

Eurofins Genomics Europe Applied Genomics GmbH, Anzinger Str. 7 a, D-85560 Ebersberg

Lisa Del Bel Belluz / Katie Tyson
Imperial College London
Surgery and Cancer
Du Cane Road
W12 0NN London

United Kingdom

Person in charge: Dr. Rainer Schubbert
Report date: 17.08.2022

Analytical Report: Murine Cell Line Authentication

Received on: 10.08.2022
Start / End of Analysis: 10.08.2022 / 17.08.2022

By order of Lisa Del Bel Belluz / Katie Tyson we were requested to perform a cell line authentication test for murine cell lines. Following samples were examined:

Our sample number	Client sample name
22_ZE_000702	ID8 C3
22_ZE_000703	ID8-F3
22_ZE_000704	ID8-B1
22_ZE_000705	ID8-B2
22_ZE_000706	ID8-PTEN
22_ZE_000707	ID8-NF1

Method:

DNA was isolated separately from the samples. Profiling of mouse cell line was done using highly-polymorphic short tandem repeat loci (STRs) published in Almeida et al. (2014) Mouse cell line authentication. Cytotechnology 66: 133-147. Fragment analysis was done on an ABI3130 (Life Technologies) and the resulting data were analyzed with GeneMapper Software (Applied Biosystems).

The laboratory is accredited acc. to **DIN EN ISO/IEC 17025:2018**. All analyses have been carried out with greatest care and on the basis of state of the art scientific knowledge. The results refer solely to the analysed samples, as received. The duplication and publication also in parts requires a written authorization by this laboratory. Our General Terms and Conditions apply exclusively and are available under eurofinsgenomics.com

Eurofins Genomics Europe Applied Genomics GmbH
Anzinger Straße 7 a
85560 Ebersberg
Germany

Tel.: +49 7531 816068
Fax: +49 8092 21084
Email: support-eu@eurofins.com
Web: eurofinsgenomics.com

Managing Director: Dr. Michael Hadem
Authorized Officer: Matthias Dittmer

Register Court Munich HRB 207710
VAT ID: DE815473648

HypoVereinsbank

IBAN: DE23 2073 0017 7000 0006 50

SWIFT: HYVEDEMME17

(Appendix Report 4: to be continued in the next page)

eurofins | Genomics

Results:

Marker / Sample	22_ZE_000702	22_ZE_000703	22_ZE_000704
18-3	17/17	17/17	17/17
4-2	19.3/19.3	19.3/19.3	19.3/19.3
6-7	15/15	15/15	15/15
9-2	18/18	18/18	18/19
15-3	22.3/22.3	21.3/22.3/23.3	21.3/22.3/23.3
6-4	18/18	18/18	18/18
12-1	17/17	17/17	17/17
5-5	17/17	17/18	17/18
X-1	27/27	27/27	27/27

Marker / Sample	22_ZE_000705	22_ZE_000706	22_ZE_000707
18-3	17/17	17/17	17/17
4-2	19.3/19.3	19.3/19.3	19.3/19.3
6-7	15/15	15/15	15/15
9-2	18/18	18/18	18/18
15-3	21.3/22.3/23.3	21.3/22.3/23.3	21.3/22.3/23.3
6-4	18/18	18/18	18/18
12-1	17/17	17/17	17/17
5-5	17/18	16/17/18	17/18
X-1	27/27	27/27	27/27

Profile Comparison to References:

Not possible due to missing reference database for murine cell lines.

This report was created automatically and is therefore valid without a signature.

The laboratory is accredited acc. to **DIN EN ISO/IEC 17025:2018**. All analyses have been carried out with greatest care and on the basis of state of the art scientific knowledge. The results refer solely to the analysed samples, as received. The duplication and publication also in parts requires a written authorization by this laboratory. Our General Terms and Conditions apply exclusively and are available under eurofinsgenomics.com

Eurofins Genomics Europe Applied Genomics GmbH
Anzinger Straße 7 a
85560 Ebersberg
Germany

Tel.: +49 7531 816068
Fax: +49 8092 21084
Email: support-eu@eurofins.com
Web: eurofinsgenomics.com

Managing Director: Dr. Michael Hadem
Authorized Officer: Matthias Dittmer
Register Court Munich HRB 207710
VAT ID: DE815473648

HypoVereinsbank
IBAN: DE23 2073 0017 7000 0006 50
SWIFT: HYVEDEMME17

Appendix Report 4. STR profiling of the panel of ID8 cell lines.

The deletion of Nf1 and Pten was validated by WB (refer to Appendix Figure 3.2).